



Energy Recovery System for a Gyrotron Backward Wave Oscillator

Liang Zhang

(B.Sc. (Hons.), University of Science & Technology of China)

(M.Sc., China Academy of Engineering Physics)

Department of Physics, SUPA

University of Strathclyde

Glasgow, UK

This thesis is submitted to the University of Strathclyde for the degree of Doctor of
Philosophy in the Faculty of Science.

March 2012

Copyright

The copyright of this thesis belongs to the author under the terms of the United Kingdom Copyright Acts as qualified by University of Strathclyde Regulation 3.51. Due acknowledgement must always be made of the use of any material contained in, or derived from, this thesis.

Dedication

I would like to dedicate this thesis to my wife Na La, and my parents for their unconditional love and support.

Contents

Acknowledgements	VII
Abstract	VIII
Abbreviation List	X
General Notation	XII
List of Figures	XV
List of Tables	XXII
Chapter 1	1
Introduction to Microwave Devices	1
1.1 Background	1
1.2 Microwave generation	2
1.2.1 Cherenkov radiation	2
1.2.2 Transition radiation	5
1.2.3 Bremsstrahlung	6
1.3 Gyro-BWOs	9
1.3.1 Introduction to the gyro-BWOs	9
1.3.2 Gyro-BWO research at the University of Strathclyde	12
1.3.3 The efficiency of gyro-BWOs	18
1.4 The purpose of the PhD study and achievements	20
1.5 Thesis structure	23
References	25
Chapter 2	32
Genetic Algorithm and Its Implementation	32
2.1 Why optimization algorithm is needed?	32
2.2 Why genetic algorithm?	33
2.3 The implementation of the genetic algorithm	37
2.4 Optimization of the depressed collector using MIT GALib	41
2.5 Conclusion	42
References	44
Chapter 3	45
Side-wall Coupler	45
3.1 The background	45
3.2 Bragg reflector	47
3.2.1 Sinusoidal ripple waveguide	48
3.2.2 Rectangular corrugation reflectors	50
3.2.3 Simulation result of the Bragg reflector	55
3.3 Side-wall coupler	60
3.3.1 The basics concept of the side-wall coupler	60
3.3.2 Side-wall coupler with cut-off waveguide	62

3.3.3	Side-wall coupler with Bragg reflector	67
3.4	Manufacture and measurement results	72
3.5	Conclusion	83
	References	85
Chapter 4	88
Microwave Window	88
4.1	The function of the window	88
4.2	Different types of microwave window	89
4.2.1	Block type window	90
4.2.1.1	The principle of the microwave window	90
4.2.1.2	Rectangular window	95
4.2.1.3	Circular window	99
4.2.2	Pillbox type window	102
4.3	Manufacture and measurement results	109
4.3.1	Three-layer window	109
4.3.2	Pillbox window	113
4.4	Conclusion	120
	References	122
Chapter 5	125
Depressed Collector	125
5.1	The principle of depressed collector	125
5.2	The derivation of depressed collector	129
5.3	Different types of depressed collector	131
5.3.1	Cylindrical tubes [4]	131
5.3.2	Electrostatic symmetric structure	133
5.3.3	Electrostatic asymmetric structure	135
5.3.4	Tilted electric field (TEF) structure	137
5.4	The effect of secondary electron emission	141
5.4.1	The effect of secondary emission	141
5.4.2	Models of secondary electron emission	142
5.4.2.1	Simulation of TSEs	143
5.4.2.2	TSE yield	144
5.4.2.3	Energy spectrum and angular distribution of the TSEs	150
5.4.3	Multiple scattering models for the BSEs	151
5.5	Conclusion	152
	References	154
Chapter 6	160
Simulation of the Depressed Collector	160
6.1	Simulation of gyro-BWO using MAGIC	160
6.2	Simulation results with Bragg reflectors	165
6.3	Collection efficiency	169
6.4	Simulation of depressed collector	175
6.4.1	Structure of the electrodes	175

6.4.2	Simulation results of the 4-stage depressed collector	176
6.4.3	Simulation results for different magnetic fields	179
6.5	Simulation with secondary electron emission	181
6.5.1	Material property for the depressed collector.....	181
6.5.2	Simulation results	181
6.6	Heat power density distribution on the collector	187
6.7	CAD model of the depressed collector	192
6.8	Conclusion.....	195
	References	197
	, Chapter 7	198
	Chapter 7	199
	Experimental setup and results	199
7.1	Experiment setup for W-band gyro-BWO.....	199
7.2	Construction of the depressed collector	209
7.3	Power supply	212
7.3.1	Double Blumlein line	212
7.3.2	Voltage dividers	217
7.3.3	Measurement of the voltages and currents.....	220
7.4	Experimental results of the microwave signal.....	224
	References	228
	Chapter 8	229
	Conclusions and future work.....	229
8.1	Introduction	229
8.2	Conclusions and future work.....	229
8.2.1	Conclusions	229
8.2.2	Future work	231
	References	233
Appendix I	Multi-mode Coupling Wave Theory	234
Appendix II	The Optimization Program.....	244
Appendix III	Non-uniform waveguide	251
Appendix IV	Author's Publications.....	256

Acknowledgements

I would like to thank Professor A.D.R. Phelps for his support and guidance as my supervisor throughout my research. Special thanks are due to Dr. Wenlong He (my second supervisor) and Dr. A.W. Cross (my third supervisor) for the many helpful discussions and conversations. I would also like to thank all my colleagues at the University of Strathclyde for providing me with a stimulating and exciting research environment.

Also, I would like to acknowledge the hard work of my fellow colleagues Dr. Craig R. Donaldson, Dr. Fengping Li, and Mr. Paul McElhinney for their help in the experimental side of the work in this thesis.

Furthermore, I would like to acknowledge the contributions of my colleagues Dr. Kevin Ronald, Dr. Colin G. Whyte and Dr. Craig W. Robertson for their help in construction of the depressed collector and the Vector Network Analyzer measurements.

Mr. D. Barclay is acknowledged for his technical skill and advice in constructing the depressed collector.

Financial support from the SUPA and ORSAS is gratefully acknowledged.

I am forever indebted to my family (my parents and my sisters) for their support, and, particularly, my wife, Na La, for her constant love, patience and kindness. None of these would be possible without the unconditional love from you.

Abstract

This thesis is based on the research project of a W-band gyrotron backward wave oscillator (gyro-BWO) using a helically corrugated waveguide which is currently being built and upgraded in the University of Strathclyde. The gyro-BWO was optimally designed through numerical simulations to achieve an output maximum power of ~ 10 kW with a -3 dB frequency tuning range of 84 - 104 GHz. To increase the overall efficiency of the W-band gyro-BWO, an energy recovery system of four-stage depressed collector was designed, numerically optimized and fabricated on the gyro-BWO. Microwave components including the Bragg reflectors, the side-wall coupler, the three-layer microwave window and the pillbox window were designed, simulated and measured to facilitate the practical use of the energy recovery system.

This thesis includes the analytically calculated results, the numerical simulations as well as the experimental results of the said components and system.

A 14-section Bragg reflector together with the side-wall coupler located at the upstream of the helically corrugated interaction cavity was used to couple the microwave radiation out. This allowed the installation of the depressed collector at the downstream side of the gyro-BWO. The transmission coefficient of the coupler was numerically optimized to achieve -1.0 dB over the frequency tuning range, from 84 - 104 GHz. The Bragg reflector measurement agrees well with the simulation. The input coupler achieves an average -13 dB reflection over the frequency in the measurement.

Theoretical analysis of the pillbox type window and multi-layer window based on mode-matching method was carried out. The simulation and optimization of the pillbox window achieved a reflection of less than -15 dB in the whole operating frequency range of 84 - 104 GHz. The three-layer window can achieve less than

-30 dB reflection in the frequency range of 84 - 104 GHz in the simulation. A three-layer window and a pillbox window which particularly optimized in frequency range of 90 - 100 GHz (the operating frequency range of the gyro-TWA that shares the same experimental setup as the gyro-BWO) were fabricated. With manufacturing constraints the design of the three-layer window achieved an average -10 dB measured reflection in 84 - 104 GHz and better than -15 dB in 90 - 100 GHz.

In the downstream side of the gyro-BWO, another 18-section Bragg reflector was used to reflect the radiation back into the upstream interaction cavity. And the transmission coefficient of -30 dB was obtained in the microwave measurements using a VNA, which means the microwave power leakage was less than 1%. The measurement results agreed well with the simulations.

A four-stage depressed collector was designed to recover the energy from the spent electrons. The 3D PIC code MAGIC and a genetic algorithm were used to simulate and optimize the geometry of the electrodes. Secondary electron emissions were simulated and a few emission models were compared to investigate their effects on the overall recovery efficiency and the backstreaming rate for the multistage collector. The optimization of the shape and dimensions of each stage of the collector using a genetic algorithm achieved an overall recovery efficiency of about 70%, with a minimized backstreaming rate of 4.9%. The heat distribution on the collector was calculated and the maximum heat density on the electrodes was $240\text{W}/\text{cm}^2$ and the generation of “hot spots” could be avoided. The electric field distribution inside the depressed collector was calculated and the geometries of these electrodes were properly shaped to avoid the voltage breakdown in vacuum.

Abbreviation List

API	Application Programming Interface
BSEs	Backscattered Electrons
BWO	Backward Wave Oscillator
CARM	Cyclotron Autoresonance Maser
CRM	cyclotron resonance masers
CVD diamond	Chemical Vapour Deposition diamond
CW	Continuous Wave
DCM	dielectric Cerenkov maser
DNP	dynamic nuclear polarization
ECM	Electron Cyclotron Maser / electronic countermeasures
ECRH	Electron Cyclotron Resonance Heating
ESR	electron spin resonance
FEL	Free Electron Laser
FDTD	Finite-difference Time-domain
FEM	Finite-element Method
GA	Genetic Algorithm
Gyro-TWT	Gyrotron Traveling Wave Tube
Gyro-BWO	Gyrotron Backward Wave Oscillator

HPM	High Power Microwave
IGBT	Insulated Gate Bipolar Transistor
LHC	Large Hadron Collider
MOSFET	Metal Oxide Semiconductor Field Effect Transistors
MW	Mega Watt
NMR	nuclear magnetic resonance
OMT	Ortho-mode Transducer
PCSS	Photoconductive Semiconductor Switch
PIC	Particle In Cell
SEY	Secondary Electron Yield
SNA	Scalar Network Analyzer
TE	Transverse Electric
TEF	Tilted Electric Field
TSEs	True Secondary Electrons
TM	Transverse Magnetic
TWT	Traveling Wave Tube
VBA	Visual Basic for Applications
VNA	Vector Network Analyzer
W.G.	Waveguide

General Notation

ε_0	Permittivity of a free space, $\varepsilon_0 = 8.854 \times 10^{-12}$ F/m
ε	Permittivity of a media
n	The refractive index
c	The speed of light in a free space, $c = 3.0 \times 10^8$ m/s
v	Electron velocity
c'	Speed of light in a media
ω	The electromagnetic wave angular frequency
k_z	The characteristic axial wavenumber
v_z	The axial drift velocity of the electrons
Ω	The electron cyclotron frequency
s	The resonant harmonic number
γ	the relativistic factor
B_0	The magnetic field
e	Charge on the electron, $e = 1.602 \times 10^{-19}$ C
m_0	The mass of the electron
λ_w	The period of a spatially varying undulator or wiggler

R	Radius, resistance
r_b	Beam radius
ω_{co}	The cutoff frequency of a waveguide mode
R_1	The corrugated depth, resistance
R_0	The mean radius of the helically corrugated waveguide, resistance
m_B	The folded number
d	The longitude period of the corrugation
S_{jm}	The coupling coefficient between the two coupled mode
h_j, h_m	The longitudinal wave numbers of the coupled modes
ξ_m, ξ_j	The root of the derivation of the Bessel function
k	The free-space wave number
α_j, α_m	The transversal wave numbers of mode j and m
P_z	The probability
V_i	The equivalent voltage of mode i
I_i	The equivalent current of mode i
β_i	The propagation coefficient
K_i	The wave impedance

T_{ip}, T_{pi}	The voltage and current transfer coefficients
A_i^+, A_i^-	The amplitudes of the forward and backward travelling waves
S_{ip}^+, S_{ip}^-	The forward and backward coupling coefficient
ψ	The wave function
Z_{mI}	The characteristic impedance of the mode
μ	The permittivity of the material filling in the cavity
k_b	The ripple period
R_{ef}	The reflection coefficient
T_{ran}	The transmission coefficient
φ_1, φ_2	The wave function

List of Figures

Fig. 1. 1 Structure of dielectric Cherenkov maser.....	3
Fig. 1. 2 The basic configuration of TWTs and BWOs.....	4
Fig. 1. 3 The basic configuration of a cylindrical magnetron (B is the magnetic field).....	5
Fig. 1. 4 Schematic diagram of a two-cavity klystron amplifier.....	6
Fig. 1. 5 Schematic diagram of a generic cyclotron resonance maser configuration.....	7
Fig. 1. 6 The interaction between the beam and the wiggler in an FEL [27].....	8
Fig. 1. 7 Basic vircator diagrams: (a) axial extraction and (b) side extraction. ...	9
Fig. 1. 8 Dispersion diagram of a gyro-BWO.....	10
Fig. 1. 9 (a) Profile of three-fold helically corrugated waveguide, (b) Electric field (c) magnetic field on the cross-section of the helically corrugated waveguide.....	14
Fig. 1. 10 The relation between the coupled waves and the new eigenwaves. ...	15
Fig. 1. 11 The operating dispersion of the helical waveguide.....	18
Fig. 1. 12 W-band gyro-BWO experimental setup, (a) schematic view, (b) 3D view.....	21
Fig. 2. 1 The flow chart of the genetic algorithm.....	38
Fig. 2. 2 Schematic diagram of encoding operation.....	38
Fig. 2. 3 Schematic diagram of crossover operation.....	39
Fig. 2. 4 Schematic diagram of encoding operation.....	40
Fig. 2. 5 Flow diagram of the optimization program.....	42
Fig. 3. 1 Diagram of the input and out of the gyro-BWO/TWA.....	46

Fig. 3. 2 Reflector with corrugated sections.....	50
Fig. 3. 3 Single module of discontinuous waveguide.....	50
Fig. 3. 4 The relation between the overall and local scattering matrices.....	54
Fig. 3. 5 The reflectivity when the parameters are $a=1.3\text{mm}$, $h=1.04\text{mm}$, $L=454.96\text{mm}$	56
Fig. 3. 6 The geometry (a) and the scattering parameter (b) of the optimized 18-section Bragg reflector.....	58
Fig. 3. 7 The scattering parameter considering the tolerance of the Bragg reflector (a) the whole bandwidth, (b) detail view.....	59
Fig. 3. 8 Geometry of the circular-to-rectangular coupler.....	60
Fig. 3. 9 Reflection and transmission coefficient of the coupler ($R=1.25\text{ mm}$, $a=1.88\text{ mm}$, $b=0.98\text{ mm}$).....	61
Fig. 3. 10 Circular-to-rectangular coupler with cut-off waveguide, (a) 3D view, (b) front view, (c) component connection.....	62
Fig. 3. 11 Cascading a 3-port S-matrix with a 2-port S-matrix.....	63
Fig. 3. 12 The transmission coefficient in (a) $L=0$, (b) $R_c=0$	64
Fig. 3. 13 The phase angle spread vs. the bandwidth.....	66
Fig. 3. 14 The geometry (a) and S-parameters (b) of optimized Bragg reflector with 14 corrugated sections.....	69
Fig. 3. 15 The transmission coefficient of the whole structure.....	70
Fig. 3. 16 The results by optimizing the whole structure.....	71
Fig. 3. 17 The transmission with consideration of the tolerances.....	72
Fig. 3. 18 The machining of the Bragg reflectors (a) the Aluminium former, (b) the 18-section Bragg reflector (c) the 14-section Bragg reflector.....	73
Fig. 3. 19 The Anritsu ME7808B VNA system.....	75
Fig. 3. 20 The measurement results of the Bragg reflector.....	77

Fig. 3. 21 The measurement results of the Bragg reflector.....	79
Fig. 3. 22 The CAD drawing and the machining of the input coupler.	80
Fig. 3. 23 The waveguide bend.	81
Fig. 3. 24 The results of the input coupler.	83
Fig. 4. 1 Schematic of the microwave windows (a) block type window, (b) pillbox type window.....	90
Fig. 4. 2 The schematic of the discontinuity in the media interface.....	92
Fig. 4. 3 The schematic of the single-layer window.....	94
Fig. 4. 4 The optimum result of the single-layer ceramic window and its size...96	
Fig. 4. 5 Different cases of the two-layer window.	97
Fig. 4. 6 The optimum results of the two-layer window and the optimum sizes.	98
Fig. 4. 7 Different cases of the three-layer window.	98
Fig. 4. 8 The optimum results of the three-layer windows and the optimum sizes.	99
Fig. 4. 9 The optimum result of the single-layer ceramic window and its size.100	
Fig. 4. 10 The optimum results of the two-layer ceramic window and their sizes.	100
Fig. 4. 11 The optimum results of the three-layer ceramic window and their sizes.	101
Fig. 4. 12 The optimum results of the three-layer ceramic window for W-band gyro-TWA.	101
Fig. 4. 13 (a) 3D view of the pillbox type window (b) the connection of the components.....	103
Fig. 4. 14 The cross-section view of the rectangular to circular step.	104
Fig. 4. 15 The simplified connection of the components.....	105

Fig. 4. 16 Convergence of the scattering parameter for TE ₁₀ mode.....	106
Fig. 4. 17 Comparison of the simulation results of the MATLAB code and CST microwave studio.	107
Fig. 4. 18 The optimum result of the pillbox window.	108
Fig. 4. 19 The geometry discontinuities of the three layer window.	109
Fig. 4. 20 The CAD drawing and the photo of the three-layer window.	111
Fig. 4. 21 The measurement of the three-layer window.	113
Fig. 4. 22 The pillbox window.	115
Fig. 4. 23 The measurement of the dielectric constant of the ceramic disk.	117
Fig. 4. 24 The measurement of the dielectric constant of the ceramic disk.	119
Fig. 4. 25 The measurement of pillbox window.....	120
Fig. 5. 1 Schematic diagram of a beam-type microwave tube.	125
Fig. 5. 2 Power supplies of the microwave device.	127
Fig. 5. 3 Schematic of multi-stage depressed collector.	128
Fig. 5. 4 Schematic diagram of the depressed collector with cylindrical tubes [4].	132
Fig. 5. 5 Beam trajectories of the electrons in the defocusing field.	133
Fig. 5. 6 Sketch of electrostatic symmetric structure and the beam trajectories [15].	134
Fig. 5. 7 Beam trajectories of the electrons in focusing field [21].	136
Fig. 5. 8 (a) Cross section of a 3-stage asymmetric structure and (b) electron trajectories [22].	137
Fig. 5. 9 Electron trajectory in cross field (a), cross section of depressed collection using cross field (b) [3].	138
Fig. 5. 10 (a) Schematic of the field configuration of tilted electric field structure, (b) the electron trajectories in a practical design [24].	139

Fig. 5. 11 Schematic of the generation of secondary electrons.....	141
Fig. 5. 12 The emitted-energy spectrum of the secondary electron energy.	143
Fig. 5. 13 The relation between SEY and the incident primary energy in different models for copper where $\delta_{0m}=1.3$, $E_{0m}=580\text{eV}$ and $s=1.44$	149
Fig. 6. 1 (a) Geometry of the helically corrugated waveguide and (b) the model in 3D PIC code MAGIC.....	162
Fig. 6. 2 (a) MAGIC simulation results of the output spectrum of 96.83 GHz, (b) mode pattern of TE_{11} mode and (c) beam trajectory.....	164
Fig. 6. 3 Simulated output frequency and power of the gyro-BWO as a function of tuning cavity magnetic field.	165
Fig. 6. 4 Simulated output frequency and power of the gyro-BWO as a function of tuning electron beam voltage when the magnetic field is 1.90 T.....	165
Fig. 6. 5 The overall magnetic field in the microwave tube.....	167
Fig. 6. 6 Simulated structure using the 3D PIC code MAGIC (a) the trajectory of the electron beam, (b) Output microwave power, (c) Lost microwave power.	169
Fig. 6. 7 Overall device efficiency as a function of collector efficiency at different electronic efficiency.....	171
Fig. 6. 8 (a) Energy distribution of the spent beam, (b) recovered energy from the spent electrons, under the condition of 40 kV electron beam voltage, 1.5 A beam current, beam alpha of 1.6 and a cavity magnetic field of 1.75 T.	173
Fig. 6. 9 Collection efficiency as a function of potential fluctuation on each electrode.	174
Fig. 6. 10 The basic geometry of an electrode.	176
Fig. 6. 11 Full geometry of 4-stage depressed collector.	177
Fig. 6. 12 Collection efficiency versus iteration number.....	178
Fig. 6. 13 Trajectories of the primary electrons and the secondary electrons in the optimized geometry.	183

Fig. 6. 14 Trajectories of the electrons in the depressed collector (using Vaughan's formulas).....	186
Fig. 6. 15 The collection efficiencies and the backstreaming rates over the frequency tuning range of the gyro-BWO.....	187
Fig. 6. 16 Two types of conductor surfaces.	188
Fig. 6. 17 Schematic of the conductors in case (a).....	189
Fig. 6. 18 Schematic of the conductors in case (b).....	190
Fig. 6. 19 The average and maximum heat power density as a function of the axial position in the depressed collector.....	191
Fig. 6. 20 The maximum heat power density and maximum average power density in different magnetic fields.....	191
Fig. 6. 21 The 3D view (a) and the cross-section view (b) of the depressed collector.	192
Fig. 6. 22 The electric field distribution inside the depressed collector (a) and inside the electrodes (b).....	194
Fig. 6. 23 The electric field distribution inside the depressed collector.	195
Fig. 7. 1 The schematic drawing of the experimental setup (Figure drawn by Craig Donoladson).	200
Fig. 7. 2 The setup of the gyro-BWO experiments.....	201
Fig. 7. 3 the properties of the cusp electron gun.	203
Fig. 7. 4 A photograph of the reverse coil.....	204
Fig. 7. 5 Photographs of the cavity solenoids.....	204
Fig. 7. 6 The simulation and measurement results of the reverse coil.....	205
Fig. 7. 7 The simulation and measurement results of the cavity solenoid.	207
Fig. 7. 8 The NADA power supply (one unit).....	208
Fig. 7. 9 The Farnell power supply for reverse coil.....	208

Fig. 7. 10 The construction of the depressed collector.	211
Fig. 7. 11 The schematic circuit of a pulse forming line.	212
Fig. 7. 12 The schematic of a single Blumlein line.	213
Fig. 7. 13 The schematic diagram of a double cable Blumlein line.	214
Fig. 7. 14 The schematic diagram of the double cable Blumlein in the experiments.....	215
Fig. 7. 15 The schematic of the three-electrode spark-gap switch and the picture of the one used in the experiment.	216
Fig. 7. 16 The schematic drawing of the power supply for the cathode.....	217
Fig. 7. 17 The schematic of the voltage divider for the depressed collector.....	218
Fig. 7. 18 A photograph of the voltage dividers.....	219
Fig. 7. 19 The schematic circuit of the voltage divider.	220
Fig. 7. 20 Basic schematic circuit of magnetic probe.....	221
Fig. 7. 21 Magnetic probe method to measure the current.....	223
Fig. 7. 22 The Rogowski coil.	223
Fig. 7. 23 The typical traces of the measured beam voltage and beam current.	224
Fig. 7. 24 The setup of the microwave detector.	225
Fig. 7. 25 The measured voltage and microwave signal.....	226

List of Tables

Table 4. 1 Comparison of the computing time of the MATLAB code and the CST microwave studio.....	106
Table 6. 1 Collection efficiency for different number of stages.....	173
Table 6. 2 Collected currents and collection efficiencies	179
Table 6. 3 The optimum potential on the electrodes	180
Table 6. 4 The collected currents and the collection efficiencies.....	180
Table 6. 5 The secondary electron yield of different materials.....	181
Table 6. 6 The collected currents and the collection efficiencies.....	184
Table 6. 7 The collection efficiency and the backstreaming rate in different cases.	184
Table 6. 8 The maximum electric fields of the four power feedthroughs.....	195
Table 7. 1 The minimum and maximum potentials on the electrodes.....	217

Chapter 1

Introduction to Microwave Devices

1.1 Background

The development of microwave sources which extends from approximately 300 MHz to 300 GHz in the electromagnetic spectrum began many years ago. The first artificial microwave was generated by Hertz to verify Maxwell's equations in 1887 [1]. Then microwaves in the lower frequency range were used in radio broadcasting in the early 20th century with the invention of the triode. In the 1930s, it was realized that high frequency could be obtained by using resonant cavities instead of electronic tubes [2]. During and after World War II, high power, high frequency microwaves were in great demand due to several military applications and it led to the development of various microwave vacuum electronic devices (MVEDs), such as magnetrons, traveling wave tubes (TWTs) and backward wave oscillators (BWOs). In the 1960s and 1970s, gyrotron devices were demonstrated [3]. As a result of the development of plasma physics and pulsed power technology during this period, electron beams with a current in excess of 10 kA at voltage of 1 MV made it possible to generate microwaves over a GW in peak power. From the late 1970s to the mid 1990s, the high power microwave (HPM) communities experienced a fabulously fast increase in radiation power. During this period, the development of relativistic devices such as gyrotron devices showed better performance compared with those conventional devices such as magnetrons and klystrons.

HPM refers to coherent electromagnetic radiation spanning the frequency range of approximately 1 GHz to over 100 GHz. "High power" has two interpretations. One is "high-average-power" microwaves, which imply long-pulse duration, high repetition

rate or continuous microwave (CW) sources. The other is “high-peak-power” microwaves, which imply short-pulse duration, low repetition rate even single-shot sources. The peak power of high-peak-power sources often exceeds 100 MW [4].

The high power microwave sources have become promising radiation sources and show their great potential in many research fields and industrial applications, such as controlled thermonuclear fusion [5,6], high resolution radar systems [7-9], atmosphere measurement and modification [10], advanced accelerators for high-energy physics research [11,12], and industrial processing of materials [13-18].

1.2 Microwave generation

Vacuum electronics devices use electrons to generate coherent radiation where electrons are gathered into micro bunches and produce spontaneous emission in random phases. There are three basic electromagnetic radiations generation mechanisms by charged particles. The first is Cherenkov, or Smith–Purcell, radiation of slow waves propagating with velocities less than the speed of light in vacuum. The second is the transition radiation and the third is the Bremsstrahlung [19].

1.2.1 Cherenkov radiation

Cherenkov radiation occurs when electrons move in a medium with a refractive index larger than 1, and the velocity of the electrons is larger than the phase velocity of the electromagnetic wave. The condition of Cherenkov radiation can be expressed as $v > c/n$, where n is the refractive index, c is the speed of light, and v is the electron velocity [20].

One of the Cherenkov devices is the dielectric Cherenkov maser (DCM) [21], as shown in Fig. 1.1. The phase velocity of the electromagnetic wave is reduced by inserting a dielectric material with large permittivity ϵ into the waveguide. The

dielectric material can be a sleeve inside the wall or a plasma layer in which the effective speed of light becomes

$$c' = c(\epsilon_0 / \epsilon)^{1/2} \quad (1.1)$$

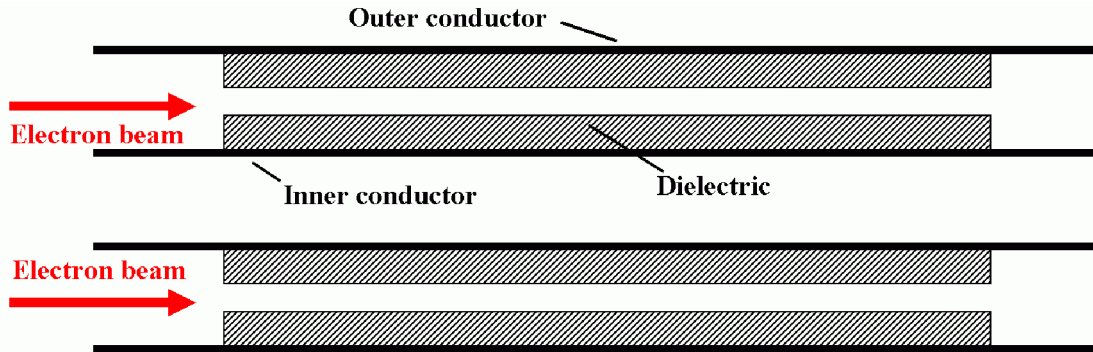
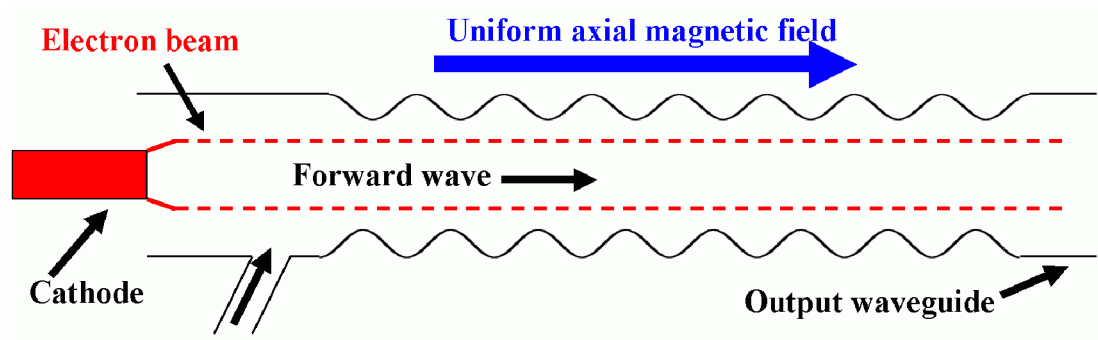


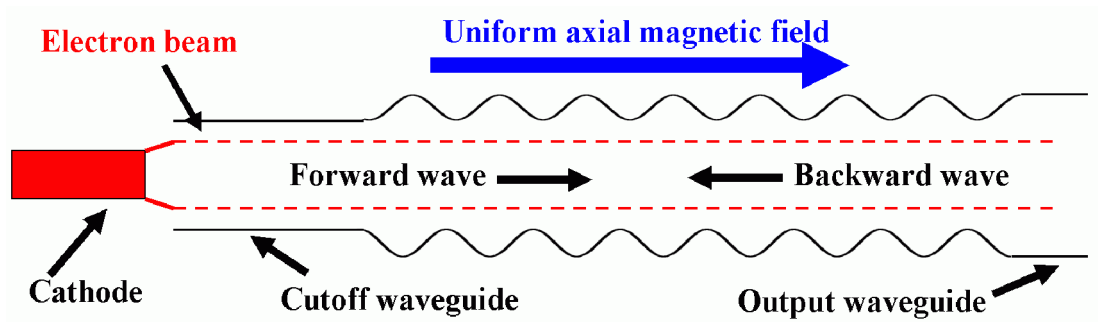
Fig. 1. 1 Structure of dielectric Cherenkov maser.

The other way to slow down the phase velocity of the electromagnetic wave is by modifying the waveguide to form a slow-wave structure, which can be implemented by periodically loading the waveguide with a resonant cavity or winding a helically wound wire around the inner wall of the waveguide, or periodically varying the radius of the waveguide [22].

The axial periodic slow-wave structures are the basis of microwave devices like relativistic backward wave oscillators (BWOs) and traveling wave tubes (TWTs). The difference between BWOs and TWTs is the intersection point between the dispersion curve of the waveguide and the beam line. For BWOs, the slope of the dispersion curve of the waveguide in the intersection is negative which represents a negative group velocity. While in TWTs, the slope is positive. The basic configuration of TWTs and the BWOs is shown in Fig. 1.2.



(a) The basic configuration of TWTs;



(b) The basic configuration of BWOs;

Fig. 1. 2 The basic configuration of TWTs and BWOs.

The azimuthal periodic slow-wave structure is the basis of magnetrons, as shown in Fig. 1.3 [5]. In magnetrons, the electrons are emitted directly from the cathode and then travel to the anode in the interaction region without the extra beam tunnel. Thus the structure of the magnetrons can be quite compact. The magnetrons are one of the most mature high power microwave devices. The anode and the cavity structure, the dimensions of the interaction region together with the axial length of the device play primary roles in determining the operating frequencies and the output mode. The magnetron has the disadvantage of being difficult to operate at high frequencies due to the dimensional limitations.

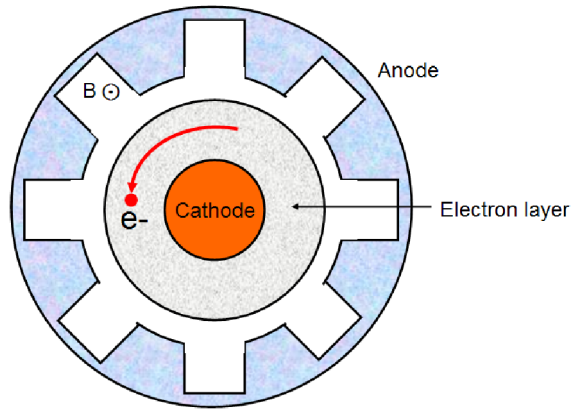


Fig. 1. 3 The basic configuration of a cylindrical magnetron (B is the magnetic field).

1.2.2 Transition radiation

Transition radiation [23] occurs when the electrons pass through a boundary between two media with different refractive indices, or through some perturbations in the media such as conducting grids, or plates. In radio-frequency tubes, these perturbations are grids. While in microwave tubes such as klystrons [24], they are short-gap cavities. The basic diagram of the klystron is shown in Fig. 1.4. In the first cavity, the beam interacts with a selected mode of the cavity and the fields associated with this electromagnetic mode modulate the axial drift velocities of the electrons. A space-charge wave is excited and the amplitude grows. In the drift space between the two cavities, the space-charge wave continues to grow and it bunches the electron beam at the same time. In the second cavity, the bunched electron beam excites the cavity mode and the electromagnetic fields is coupled out. Klystrons are the most common type of devices based on coherent transition radiation. Magnicons [25] are another type of transition radiation device and they have similar structures with klystrons.

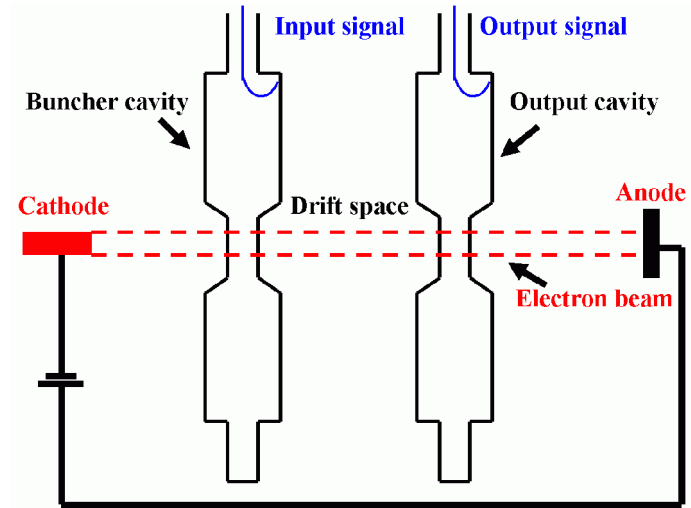


Fig. 1. 4 Schematic diagram of a two-cavity klystron amplifier.

1.2.3 Bremsstrahlung

Bremsstrahlung is stimulated when relativistic electrons undergo oscillations which are transverse to the direction of the beam motion by the action of an external magnetic and/or electric fields [26]. In Bremsstrahlung devices, the coherence radiation needs to meet the condition that the electromagnetic waves whose Doppler-shifted frequencies coincide either with the oscillation frequency of the electrons, or its harmonic, which is

$$\omega - k_z v_z = s\Omega, \quad (s = 1, 2, 3, \dots) \quad (1.2)$$

$(k_z v_z = \text{Doppler term})$

where Ω is the frequency of periodic motions of the electrons. s is the resonant harmonic number. ω and k_z are the wave angular frequency and characteristic axial wavenumber, respectively. v_z is the axial drift velocity of the electrons. Coherent Bremsstrahlung can occur when electron oscillations are induced either in constant or periodic fields.

The best known devices where the electrons oscillate in a constant magnetic field are the cyclotron resonance masers (CRMs). In CRMs, the Ω is the electron cyclotron frequency which follows

$$\Omega = eB_0/(m_0\gamma) \quad (1.3)$$

where B_0 is the axial magnetic field, and γ is the relativistic factor. It is the basis of a number of electron cyclotron maser devices, such as the gyromonotrons, gyrotron traveling wave amplifiers (gyro-TWTs), the gyrotron backward wave oscillators (gyro-BWOs), gyroklystrons, gyrotwistrons, and cyclotron autoresonant masers (CARMs). A schematic diagram of a generic cyclotron resonance maser is shown in Fig. 1.5. A hollow electron beam gyrating in its Larmor radius interacts with an electromagnetic wave in a cylindrical waveguide with a constant magnetic field in axial direction to generate the coherent Bremsstrahlung radiation.

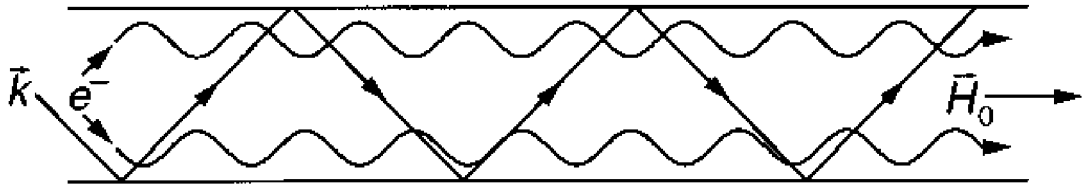


Fig. 1. 5 Schematic diagram of a generic cyclotron resonance maser configuration.

The most common devices based on the radiation produced when the electrons oscillate in a periodic magnetic field are the free-electron lasers (FELs) [27]. In FELs, the Ω is defined as

$$\Omega = k_w v_z = 2\pi v_z / \lambda_w \quad (1.4)$$

where λ_w is the period of a spatially varying undulator or wiggler which generates a periodic magnetic field. Fig. 1.6 is a basic diagram of the interaction between the beam and the wiggler in a FEL.

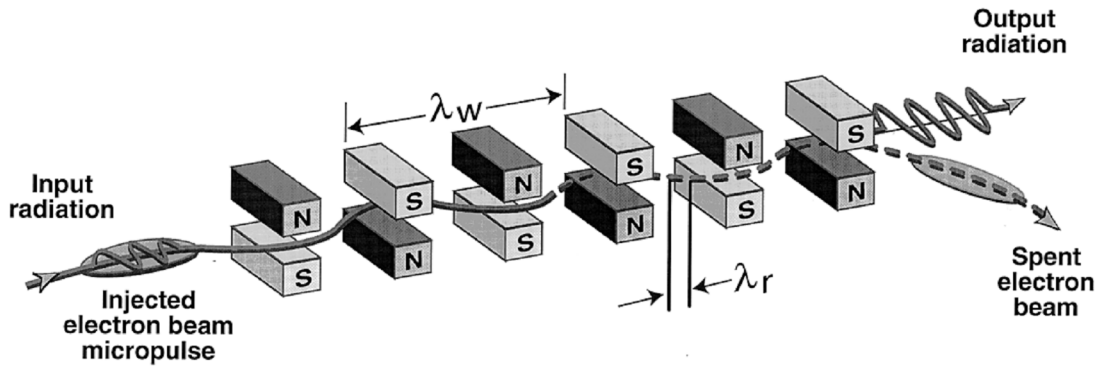


Fig. 1. 6 The interaction between the beam and the wiggler in an FEL [27].

Another special device can be arguably catalogued as Bremsstrahlung type is the vircator in which the electrons oscillate in their own electric fields [28, 29]. For a thin annular beam of radius r_b propagating in a tube with constant radius R , the space-charge limiting current is given by [30]

$$I_L = \frac{mc^2}{2e} \frac{(\gamma^{2/3} - 1)^{3/2}}{\ln(R/r_b)} \quad (1.5)$$

In vircators, an electron beam in its space-charge limiting current propagates into a cylindrical drift tube whose radius has a sudden increase. When the wall radius increases, the space-charge limiting current drops and makes the electron beam current smaller. The space-charge force slows the electron beam and some of the current reverses its direction, producing a region with high space-charge density and electrostatic potential depression known as a virtual cathode. The location of the virtual cathode moves back and forth at roughly the beam plasma frequency. The electrons are reflected between the cathode and the virtual cathode. The interaction between the electrons and the oscillating electric field produces microwave radiation.

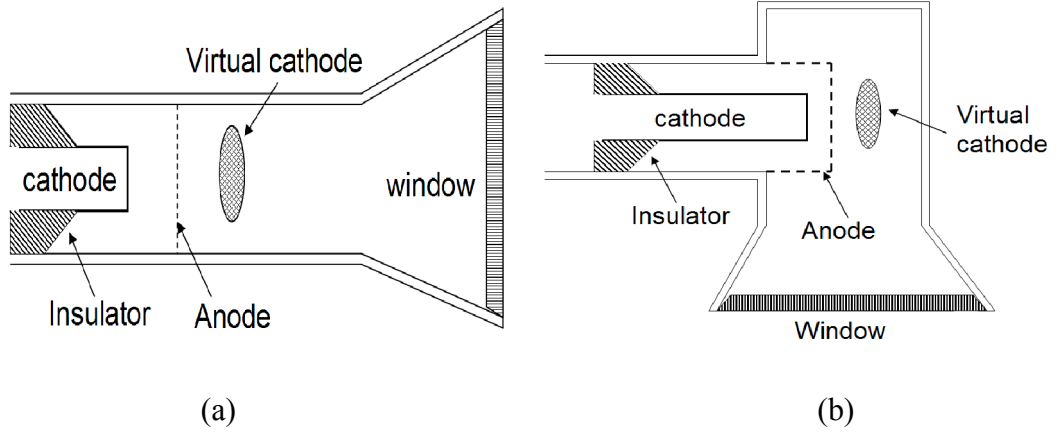


Fig. 1. 7 Basic vircator diagrams: (a) axial extraction and (b) side extraction.

1.3 Gyro-BWOs

1.3.1 Introduction to the gyro-BWOs

Gyrotron backward wave oscillators (gyro-BWOs) are gyro-devices based on the electron cyclotron maser instability [31-34]. In gyro-BWOs, the electrons gyrating in the external magnetic field interact with an oppositely propagating electromagnetic wave. Fig. 1.8 shows the dispersion diagram of a gyro-BWO with circular waveguide. The output frequency of the device can be described by the left intersection between the Doppler-shifted electron cyclotron mode and the electromagnetic waveguide mode. The electron cyclotron radiation line has the expression of

$$\omega = k_z v_z + s\Omega \quad (1.6)$$

where ω is the wave frequency. Ω is the electron cyclotron frequency described as equation 1.2. s is the resonant harmonic number. k_z is the characteristic axial wavenumber. v_z is the axial drift velocity of the electrons. The dispersion curve of the circular waveguide follows

$$\omega^2 = k_z^2 c^2 + \omega_{c0}^2 \quad (1.7)$$

where c is the speed of light and ω_{co} is the cutoff frequency of waveguide mode. As shown in Fig. 1.8, k_z in the interaction is negative and both of the group and phase velocities of the wave are negative which means an opposite propagating wave relative to the direction of motion of the electrons.

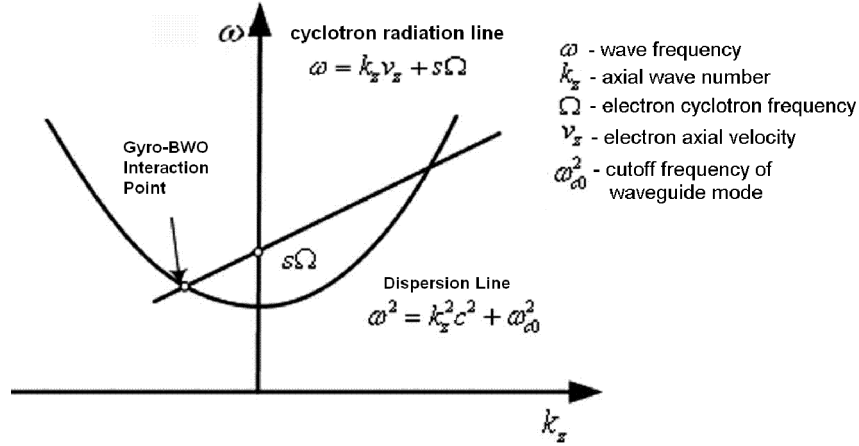


Fig. 1. 8 Dispersion diagram of a gyro-BWO.

The operation frequency of the gyro-BWOs can be continuously tuned over a broad frequency range above the cutoff frequency. It can be achieved either by tuning the magnetic field, which changes the electron cyclotron frequency Ω by the expression in Eq. 1.2, or by tuning the electron beam energy which changes the electron axial velocity v_z . Compared with the other gyro-devices, gyro-BWOs have the unique capability of wide frequency tunability, and they have attracted tremendous research attention because an increasing number of applications require frequency tunability of the microwave devices, such as electron spin resonance (ESR), plasma diagnostics, and enhancement of the sensitivity of nuclear magnetic resonance (NMR) using dynamic nuclear polarization (DNP) [35].

The theoretical study of gyro-BWOs began in the mid 1960s. The interaction of weakly relativistic gyrating electrons with an opposite wave of constant amplitude was studied in paper [36]. A self-consistent treatment of the gyro-BWOs in which the effect of an electron beam on the wave amplitude was taken into account was

published in paper [37]. It was shown that the gyro-BWO's equations could be reduced to the equations of the conventional BWO at small current and the maximum efficiency of the weakly relativistic gyro-BWO with constant external magnetic field was close to 20% if the electron velocity spread could be negligible. This formalism was later generalized for the case of relativistic gyro-BWOs [38]. In paper [38], the gyrating electrons were considered to interact with a transversely homogeneous electromagnetic wave propagating in a media with a phase velocity of c/n , where n is the refractive index. Then the procedure for deriving the equations in designing a relativistic gyro-BWO was described in detail in [39]. The gyro-BWO equations were derived in a general form allowing one to use them to design gyro-BWO's with an arbitrary geometry of the interaction region. Linear theory then served as the basis for gyro-BWO design to predict the start oscillation conditions since the 1980's. Orbit tracing techniques and particle simulations were then employed to investigate the nonlinear behaviour and to improve the design.

The experimental study of gyro-BWOs began in the early 1990s. Experimental results on tuning the operating frequency by changing the magnetic field or beam voltage was reported in paper [40-42]. In paper [43], it was show that operating close to the waveguide cutoff frequency, the efficiency of a gyro-BWO can reach around 20%. However, operating in the cutoff frequency region also means less frequency tuning range.

Gyro-BWOs are based on fast wave interaction. Thus they do not need a slow wave structure to adjust the phase velocity of the electromagnetic field. They show higher power capability in the millimetre and sub-millimetre range compared with the conventional BWOs, because a smooth bore cylinder structure with high-power handling capability can be employed in the fast wave interaction. In the experiments reported in paper [44], megawatt output power was achieved by using high-current relativistic electron beams.

To pursue high-frequency operation, a strong magnetic field usually provided by a superconducting magnet is required. However, the complexity and the cost increase as the amplitude of the magnetic field increases. An alternative choice is to operate the gyro-BWO in harmonic mode, where mode competition and high oscillation threshold will become serious problems. Nonstationary behaviour and selective suppression of high order axial modes in the gyro-BWOs drew great attention in recent years in order to find a solution [45]. One method proposed to control the spectral purity and phase of the output signal using an injection locking technique was reported by National Tsing Hua University, Taiwan in [46]. The other way to suppress the unwanted oscillations is by modifying the geometry of the interaction waveguide and several structures have been developed. A sliced waveguide developed at UC Davis to interrupt the wall current of unfavorable modes was applied to the TE_{21} second-harmonic gyrotron traveling-wave-tube amplifier (gyro-TWTA), and the output power exceeded 207 kW at 15.7GHz [47]. A helical corrugated structure that changed the dispersion curve of the interaction waveguide was designed by a united effort by Vladimir Bratman's group from the Institute of Applied Physics (IAP) in Russia and the group of Alan Phelps at the University of Strathclyde in the United Kingdom. It was reported that an X-band gyro-BWO with a helically corrugated waveguide achieved a frequency tuning range of 17% and 16.5% electronic efficiency in 2005 [48]. A slotted structure which was initially applied in magnetrons was designed for a second-harmonic TE_{21} gyro-BWO at the National Tsing Hua University, Taiwan. The gyro-BWO achieved an electronic efficiency of 23% with a 3 dB tuning bandwidth of 9% in Ka-band [49].

1.3.2 Gyro-BWO research at the University of Strathclyde

Conventional cylindrical waveguides were used in most of the gyro-devices. However, there are several disadvantages using cylindrical waveguide in gyro-BWOs. Firstly, when a gyro-BWO with cylindrical waveguide operating at a

frequency near cutoff with a weakly relativistic electron beam, the frequency tuning band is very narrow and the spurious gyrotron oscillations are easy to be excited if the group velocity and axial wave number are small. Secondly, when the gyro-BWO operates at frequency far from the cutoff with a relativistic electron beam, a much broader frequency tuning range can be obtained. However, they are very sensitive to the beam axial velocity spread which lowers the interaction efficiency.

Research on gyro-BWOs based on a helically corrugated waveguide demonstrated excellent results in achieving high power and wide frequency tuneability. Helically corrugated waveguide changes the smooth waveguide dispersion in the region of close-to-zero to make it have large group velocity which ensures a broadband operation with minimum negative impact of the velocity spread. The idea was first published in the 19th international conference on infrared and millimeter waves by a united group from the Institute of Applied Physics in Russia and the University of Strathclyde, UK.

The equation of the helical profile of the inner surface in a cylindrical coordinate system (r, θ, z) can be written as

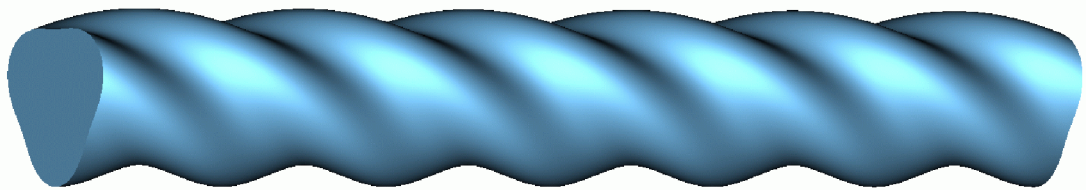
$$r(\theta, z) = R_0 + R_1 \cos(m_B \theta + 2\pi z / d) \quad (1.8)$$

where R_0 is the mean radius of the circular waveguide, R_1 is the corrugation depth, m_B is the folded number, and d is the longitudinal period of the corrugation. A profile of a three-fold helically corrugated waveguide is shown in Fig. 1.9 (a), and the electric field and magnetic field on the cross-section of the helically corrugated waveguide are shown in Fig. 1.9(b) and Fig. 1.9(c), respectively. At nonzero corrugation depth, two modes will couple when their axial and azimuthal wave numbers satisfy the synchronism conditions

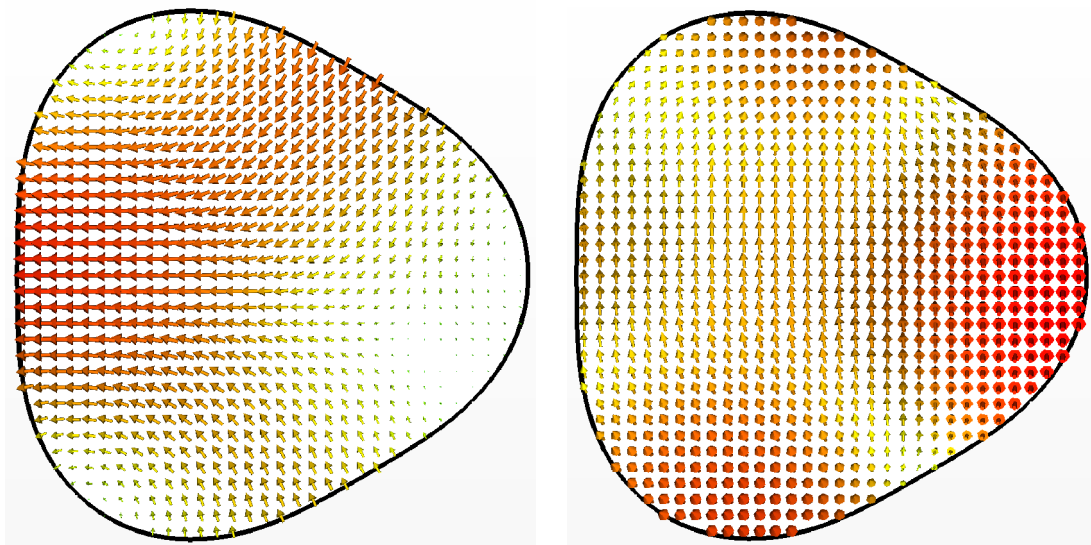
$$k_{z1} - k_{z2} = 2\pi / d, \quad m_1 - m_2 = m_B \quad (1.9)$$

where k_{z1} and k_{z2} are the axial wavenumbers of the two coupling modes, and m_1 and m_2 are the azimuthal indices of the two coupling modes.

In three-fold helically corrugated waveguide, the TE_{21} mode will be coupled with the TE_{11} circularly polarized mode of opposite rotation and generate a higher (W_2) and lower (W_1) operating mode, as shown in Fig. 1.10. The dispersion characteristics can be changed by choosing different corrugation depths and the corrugation periods to meet the needs in different applications. In the gyro-BWO, a constant group velocity in the operating frequency range is desired to achieve a wide frequency tuning band.



(a)



(b)

(c)

Fig. 1. 9 (a) Profile of three-fold helically corrugated waveguide, (b) Electric field (c) magnetic field on the cross-section of the helically corrugated waveguide

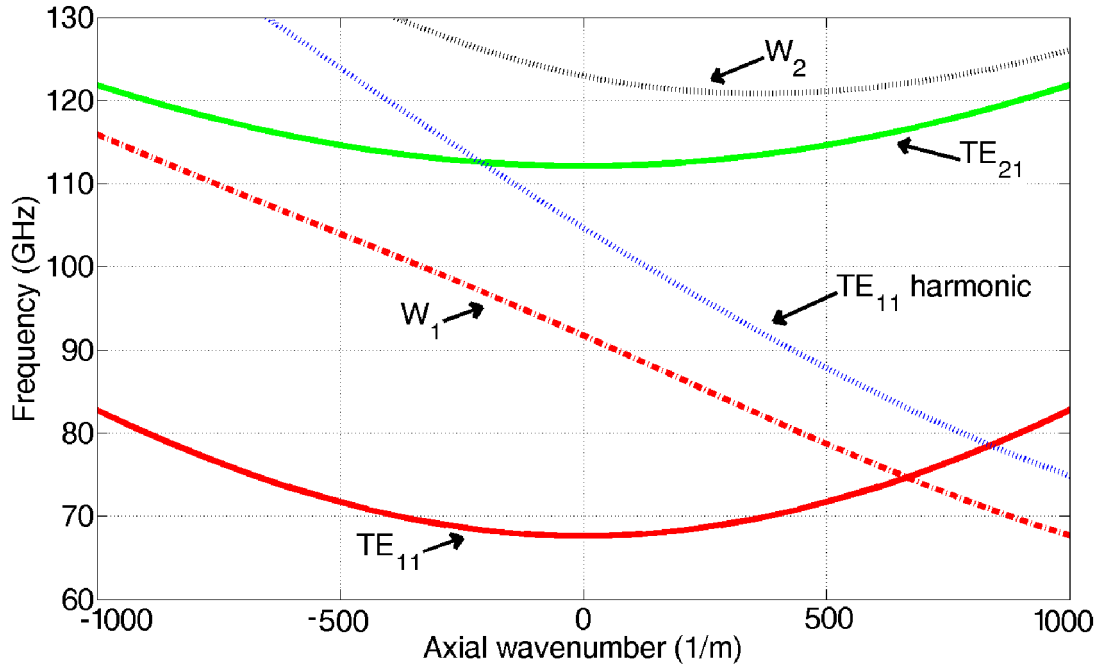


Fig. 1. 10 The relation between the coupled waves and the new eigenwaves.

An analytical method based on perturbation coupled wave theory has been developed to get a fast calculation of the dispersion curve of the operating mode [64]. The new dispersion curve caused by two coupled modes f_j, f_m will satisfy the following equation

$$f_j^2(h) \cdot f_m^2(h) = h_j^2 h_m^2 S_{jm}^2 \quad (1.10)$$

where S_{jm} is the coupling coefficient between the two coupled mode, from the perturbation theory, it has the following form

$$S_{jm} = \begin{cases} \frac{R_1[\xi_m^2 \xi_j^2 + (h_j h_m + k^2) jm R_0^2]}{h_j (h_j - h_m) R_0^3 \sqrt{\xi_m^2 - m^2} \sqrt{\xi_j^2 - j^2}}, & \text{(TE to TE mode)} \\ \frac{R_1(k^2 - h_j h_m)}{R_0 h_j (h_j - h_m)}, & \text{(TM to TM mode)} \\ -\frac{R_1 k m}{R_0 h_j \sqrt{\xi_m^2 - m^2}}, & \text{(TE to TM mode)} \end{cases} \quad (1.11)$$

The dispersion relation for a TE/TM mode in the circular waveguide can be written as

$$f_j^2(h) = k^2 - \alpha_j^2 - h^2 \quad (1.12)$$

While mode m is the negative spatial harmonic wave, the dispersion curve is left shifted by $2\pi/d$ due to the periodicity of the helically corrugated waveguide, which is

$$f_m^2(h) = k^2 - \alpha_m^2 - (h - 2\pi/d)^2 \quad (1.13)$$

α_j, α_m are the transversal wave numbers of mode j and m . h_j, h_m are the longitudinal wave numbers of the coupled modes, k is the free-space wave number. ξ_m, ξ_j are the root of the derivative of the Bessel function.

Eq. 1.10 is a fourth-order linear equation. Given a wave number k , four eigenvalues can be solved from the equation. However, only two of them have practical physical meaning. If there is no coupling between the two modes, which is $S_{jm} = 0$, the eigenfunction will degenerate into two separate dispersion curve functions as $f_j^2(h) = 0$, and $f_m^2(h) = 0$, which denote the previous uncoupled eigenwaves. A detailed description of the multi-mode coupling theory for a higher fold number of the helically corrugated waveguide and the comparison with a five-fold waveguide for pulse compression is described in Appendix I.

The output frequency of the gyro-BWO interaction can be calculated from the intersection of the dispersions of the eigenwaves and the electron beam cyclotron mode, as in the form of Eq. 1.6.

In analogy to gyrotron interactions and paper [50, 51], it is possible for one to derive the gyro-BWO beam-wave dispersion

$$\begin{aligned}
& [(h^2 - 2\delta)(h - \Delta_g + \delta / h_0) + 2S_{jm}^2 / h_0][h - (\delta - \Delta_H) / \beta_{z0}]^2 \\
& = C^3 (h - \Delta_g + \delta / h_0) \left\{ 1 + \frac{2s}{\alpha_0^2 \beta_{z0}} [h - (\delta - \Delta_H) / \beta_{z0}] \right\}
\end{aligned} \tag{1.14}$$

where α_0 and β_{z0} are the beam initial pitch angle and relative velocity in the longitudinal direction respectively. δ and Δ_g are the frequency and geometrical mismatches, respectively. Δ_H is the relative frequency mismatch defined by the s harmonic of the electron cyclotron frequency and the wave frequency. The interaction frequency of the gyro-BWO can be calculated by solving the uncoupled beam-wave equation by setting $C=0$ in Eq. 1.14, i.e. the intersection of the eigenwave W_1 and the beam dispersion line. In a general case, Eq. 1.14 has four $k(h)$ roots, with two real roots being the "hot" (electron beam present) eigenwaves, and a pair of conjugate complex roots, which are degenerate with the electron cyclotron mode due to the CRM interaction at and near the intersection when the beam parameters are suitably chosen. The negative imaginary number of the solution (Fig. 1.11, dashed line showing one such interaction for the gyro-BWO) gives rise to the oscillation that grows with time in the cavity and hence allows the starting condition and the small signal growth of the oscillation to be analyzed.

The dispersion of the operating eigenwave can be found by measuring the phase evolution of a counter-rotating circularly polarized wave when it propagates through the waveguide by using a vector network analyzer (VNA). It can also be measured by detecting the polarization angle of a linearly polarized wave when it propagates through the waveguide by using a scalar network analyzer (SNA) [59]. In Fig. 1.11 the measured results using the VNA method are shown and compared with the results simulated by MAGIC using the same operating eigenwave. In the simulation using the MAGIC code, a left-polarized circular wave of one frequency was injected into the right-hand helical waveguide, and a component of the electric field inside the waveguide was measured along the axial direction. The measured field was then

numerically analyzed and the axial wavenumber of the eigenwave was therefore obtained for that frequency [60, 61].

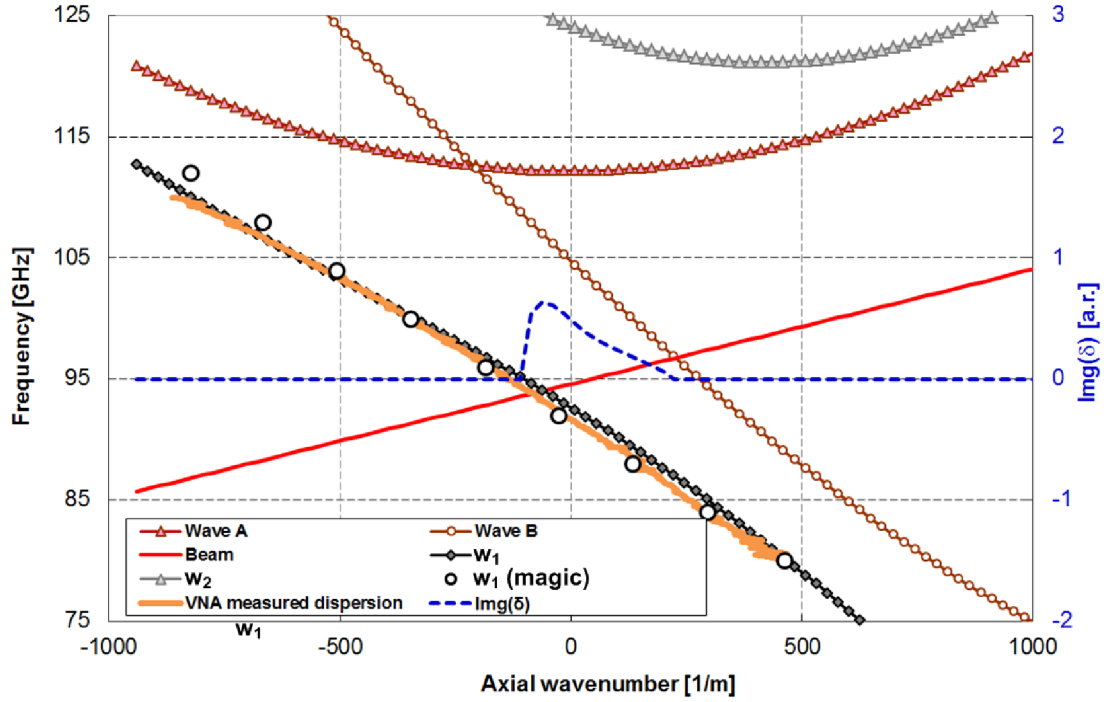


Fig. 1.11 The operating dispersion of the helical waveguide.

In the experimental research of helically corrugated waveguide, a Ka-band (26.5-40 GHz) gyro-BWO operating at the second cyclotron harmonic achieved a maximum output power of about 1 MW, 10% efficiency and a 15% frequency tuning range [52]. An X-band (7.0-12.5 GHz) gyro-BWO achieved a frequency tuning range of 17% and 16.5% electronic efficiency in 2005 [48]. As predicted in the study of a W-band (75-110GHz) gyro-BWO, it is possible to increase the frequency tuning band to more than 17% [53].

1.3.3 The efficiency of gyro-BWOs

The disadvantage of gyro-BWOs is the low interaction efficiency compared with the gyromonotrons and gyroklystrons. In gyro-BWOs, the amplitude of the RF field increases as the RF wave travels to the entrance. In the entrance, the amplitude of the

RF field reaches its maximum and it causes an abrupt electron bunching, while the RF field is weak at the exit of the interaction region resulting in a weak beam-wave interaction. The electrons lose less energy to the wave and the efficiency is low.

The overall efficiency is an important parameter for high-power microwave sources. For a given RF output power, higher efficiency means less primary power needed. Microwave sources with higher efficiency have less heat dissipation which means smaller cooling systems are needed. High efficiency is essential in space applications and some ground-based applications, such as deep space communication and mobile installations.

Several methods have been developed to improve the efficiency of beam-wave interaction. One is to change the profile of the waveguide to obtain a higher electronic efficiency, such as employing a slot structure, helical structure, slice structure, and so on. The other way is to use a tapered magnetic field or tapered wall radius instead of the constant values. The tapered magnetic field was first known in gyrotrons and it enhances the interaction efficiency dramatically from 36% to 75% [54]. The idea was then introduced to a gyro-BWO and it was demonstrated that a proper linear tapering of the magnetic field can enhance the electronic efficiency from 14% (in the case of constant magnetic field) to 32% [55]. The theory of a gyro-BWO with a tapered magnetic field and waveguide cross section was discussed in paper [56] and the numerical simulation of the effects of tapering the magnetic field was presented in paper [57].

Ways to improve the electronic efficiency have attracted a lot of attention. However, once the microwave device has been established, the electronic efficiency would be fixed. Another option for enhancing the efficiency is to recover energy from the spent beam using single, or multi-stage, depressed collectors. It has been proven that it is an efficient way to improve the overall efficiency of microwave tubes, such as conventional klystrons, BWOs and TWTs [62, 63]. However, it is still a challenge to

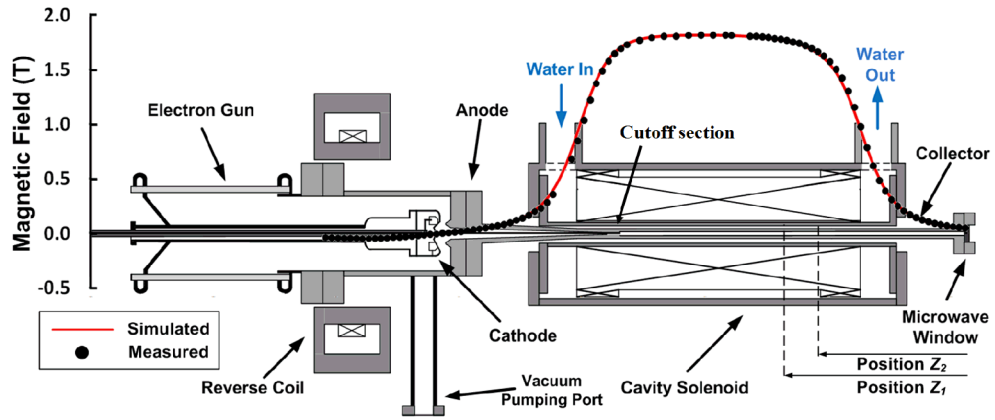
employ a multi-stage depressed collector in gyrotron devices because the electrons in gyrotron devices always have large transverse velocity which makes the electrons hard to be sorted. Furthermore, the gyro-BWO has frequency tunability. The spent-beam properties are different for different frequencies. Therefore it makes it difficult to build an energy recovery system for a gyro-BWO.

1.4 The purpose of the PhD study and achievements

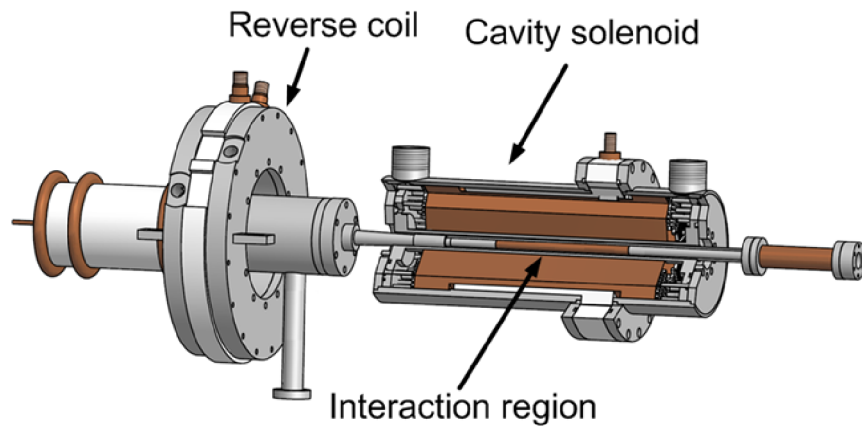
The purpose of the PhD study is to design an energy recovery system based on the current research of the W-band gyro-BWO at the University of Strathclyde.

A schematic diagram of a W-band gyro-BWO experimental setup is shown in Fig. 1.12. The W-band gyro-BWO was predicted to operate in the frequency range of 84 -104 GHz with a helically corrugated waveguide. It could achieve a frequency tuning range of 17% and 16.5% electronic efficiency [48].

The electron beam which was generated from the cusp electron gun [58] passed through the cutoff section and then entered into the interaction region. In the helically corrugated waveguide, the electron beam interacted with the backward propagating microwaves based on the cyclotron resonance maser instability and then was dumped onto a smooth waveguide which also acted as a beam collector. The generated microwaves firstly traveled in the upstream direction and then were reflected downstream because of the cutoff section and were finally extracted by a narrow band single-layer sapphire window. In the current experimental setup, there is no energy recovery system to collect the remaining energy from the spent electron beam. Thus the overall efficiency is completely determined by the electronic efficiency.



(a)



(b)

Fig. 1. 12 W-band gyro-BWO experimental setup, (a) schematic view, (b) 3D view.

As the depressed collector has been proven to be an efficient method in conventional microwave devices, it is meaningful to investigate the possibility of using it in the W-band gyro-BWO. Also, after applying the depressed collector, the method that couples out the radiation needs to be changed. An upgrade to the current gyro-BWO device with a novel coupler and broadband window is necessary. These required microwave components are also the purpose of this PhD study.

In this thesis, the following results have been achieved

1 A general-purpose optimization program based on a genetic algorithm was developed. It has the capability to work with various simulation programs such as CST microwave studio, Mician μ Wave Wizard, and the 3D PIC code MAGIC. The program provides the optimization routing for the design of the microwave components, such as the Bragg reflector, the side-wall coupler, the microwave windows, and also for the optimization of the potentials and the geometry of the depressed collector.

2 Simulation codes based on the mode matching method were developed to simulate the S parameters of the Bragg reflectors. The simulation results agreed well with the result obtained by CST microwave studio while it is much faster than the 3D simulation to make the optimization possible. The measurement results were found agreed well with the numerical simulations.

3 A side-wall coupler was simulated and optimized to extract the radiation out from the W-band gyro-BWO. The novel coupler has the advantage of not requiring a cut-off section to achieve a wide frequency band and a good coupling coefficient. Therefore, a high electron beam transportation rate to the interaction region can be achieved and to improve the interaction efficiency. The input coupler achieves an average -13 dB reflection over the designed frequency band.

4 Equations to calculate different types of microwave windows were induced and highly efficient simulation codes were developed. The simulation codes were able to provide a closely comparable simulation result to CST microwave studio in less than four minutes, while CST microwave studio needs a few hours to complete the simulations.

5 The depressed collector was designed and optimized by using the 3D PIC code MAGIC and 70% collection efficiency could be achieved by a four-stage depressed collector.

6 The experiment demonstrating the W-band gyro-BWO was carried out. Two Bragg reflectors, an input coupler, a pillbox window, and a three-layer window were machined and measured to compare with the simulation results.

1.5 Thesis structure

Chapter 1 presents the background of the microwave devices, and the basic principle of microwave generation. A brief introduction to the gyro-BWO is included as the background of this thesis.

Chapter 2 introduces various optimization algorithms including their advantages and disadvantages. The genetic algorithm is chosen to optimize the microwave components as well as the depressed collector after the comparison.

Chapter 3 presents the design of the side-wall coupler as well as the Bragg reflector. Detailed equations are included and the simulation and measurement results are discussed.

Chapter 4 discusses different types of microwave windows. In this chapter, the detailed equations used to calculate the performance of the block-type and the pillbox windows are derived. The optimized simulation results as well as the measurement results are also given.

Chapter 5 is a background study and a literature review of the depressed collector. The principle and different types of multi-stage depressed collectors were included and the models of the secondary electron emission were also discussed.

Chapter 6 presents the particle-in-cell simulation results of W-band gyro-BWO and the depressed collector. The simulation included the overall efficiency with and without the depressed collector, the optimum potentials and the geometry of the electrodes, the effect of the secondary electrons and the heat dissipation on the

electrodes. The electric field inside of the depressed collector has also been simulated.

Chapter 7 describes the gyro-BWO experiment setup and the experiment results, including electron beam voltage and current measurement, the magnetic field of the solenoid, and microwave radiation signal and the power supply for the depressed collector.

Chapter 8 concludes all the previous chapters and outlines the future work.

References

- [1] Heinrich Rudolph Hertz, "Electric waves: being researches on the propagation of electric action with finite velocity through space", Cornell University Library, 1893.
- [2] W. W. Hansen, "A Type of Electrical Resonator", J. Appl. Phys., vol. 9, no. 10, pp. 654-663, 1938.
- [3] J. L. Hirshfield and J. M. Wachtel, "Electron Cyclotron Maser", Phys. Rev. Lett., vol. 12, no. 19, pp. 533-536, 1964.
- [4] Robert J. Barker, and Edl Schamiloglu, "High-power Microwave Sources and Technologies", John Wiley & Sons Inc, 2001.
- [5] K. Kajiwara, Y. Ikeda, K. Sakamoto, et al, "High Power Operation of 110GHz Gyrotron at 1.2 MW on the JT-60 ECRF System", Fusion Engineering and Design, vol. 65, no. 4, pp. 493-499, 2003.
- [6] T. Fujita, H. Tamai, M. Matsukawa, et al, "Design Optimization for Plasma Performance and Assessment of Operation Regimes in JT-60SA", Nuclear Fusion, vol. 47, no. 11, pp. 1512-1523, 2007.
- [7] A. Blyakhman, D. Clunie, R. Harris, et al, "Nanosecond Gigawatt Radar: Indication of Small Targets Moving among Heavy Clutters", IEEE Radar Conference, pp. 61-64, 2007.
- [8] A. Blyakhman, D. Clunie, G. Mesyats, et al, "Analysis of Nanosecond Gigawatt Radar, in Quasi-Optical Control of Intense Microwave Transmission". Ed. J. Hirshfield and M. Petelin, NATO Science Series, vol. 203, Springer, pp. 283-296, 2005.
- [9] H. H. Song, D. B. McDermott, Y. Hirata, et al, "Theory and Experiment of a 94 GHz Gyrotron Traveling-wave Amplifier", Phys. Plasmas, vol. 11, no. 5, pp. 2935-2941, 2004.
- [10] A. V. Gaponov-Grekhov, and Victor L. Granatstein, "Applications of

- High-power Microwaves”, Artech House Press, 1994.
- [11] R.M. Phillips and D.W. Sprehn, “High-power klystrons for the Next Linear Collider”, Proceedings of the IEEE, vol. 87, no. 5, pp. 738-751, 1999.
- [12] Erk Jensen and Igor Syratchev, “CLIC 50 MW L-Band Multi-Beam Klystron”, High Energy Density and High Power RF: 7th Workshop on High Energy Density and High Power RF, AIP Conference Proceedings, vol. 807, pp. 90-99, 2006.
- [13] D. E. Clark, and W. H. Sutton, “Microwave Processing of Materials”, Annual Review of Materials Science, vol. 26, pp. 299-331, 1996.
- [14] James Benford, John A. Swegle, and Edl Schamiloglu, ”High Power Microwaves, second edition”, CRC press, Taylor Francis Group, 2006.
- [15] V. L. Granatstein, R. K. Parker, and C. M. Armstrong, “Vacuum Electronics at the Dawn of the Twenty-first Century”, Proceedings of the IEEE, vol. 87, no. 5, pp. 702-716, 1999.
- [16] Robert J. Barker, Neville C. Luhmann, Gregory S. Nusinovich, et al, “Modern Microwave and Millimeter-Wave Power Electronics”, IEEE Press, 2005.
- [17] E. Schamiloglu, “High power microwave sources: where do we go from here?”, Conference Record of the 25th International Power Modulator Symposium, and High-Voltage Workshop, July, pp. 694-698, 2002.
- [18] R. A. Cairns, and Alan D. R. Phelps, “Generation and Application of High Power Microwaves”, CRC Press, 1997.
- [19] Steven H. Gold, and Gregory S. Nusinovich, “Review of High-power Microwave Source Research”, Rev. Sci. Instruments, vol. 68, no. 11, pp. 3945-3974, 1997.
- [20] B. W. Hakki, “Cerenkov Radiation in Slow-wave Guiding Structures”, IRE Trans. Electron Devices, vol. 8, no. 6, pp. 497-508, 1961.
- [21] E. P. Garate, A. Fisher, and W. G. Main, “Coaxial Configuration of the

- Dielectric Cerenkov Maser”, IEEE Trans. Plasma Sci., vol. 18, no. 5, 1990, pp. 831-836.
- [22] A.S. Gilmour, “Microwave tubes”, Artech House, Inc, 1986.
- [23] U. Happek and A. J. Sievers, “Observation of Coherent Transition Radiation”, Phys. Rev. Lett. 67, vol. 67, no. 21, pp. 2962-2965, 1991.
- [24] A. M. Sessler, and S. S. Yu, “Relativistic klystron two-beam accelerator”, Phys. Rev. Lett., vol. 58, no. 23, pp. 2439 – 2442, 1987.
- [25] Oleg A. Nezhevenko, "Gyrocons and Magnicons: Microwave Generators with Circular Deflection of the Electron Beam", IEEE Trans. Plasma Sci., vol. 22, no. 5, pp. 756-772, 1994.
- [26] G. R. Blumenthal, and R. J. Gould, “Bremsstrahlung, Synchrotron Radiation, and Compton Scattering of High-Energy Electrons Traversing Dilute Gases”, Rev. Mod. Phys., vol. 42, no. 2, pp. 237-270, 1970.
- [27] H. P. Freund and G. R. Neil, “Free-electron Lasers: Vacuum Electronic Generators of Coherent Radiation”, Proceedings of the IEEE, vol. 87, no. 5, pp. 782-803, 1999.
- [28] W. Jiang, K. Masugata, and K. Yatsui, “Mechanism of Microwave Generation by Virtual Cathode Oscillation”, Phys. Plasmas, vol. 2, no. 3, pp. 982-986, 1995.
- [29] W. Jiang, and M. Kristiansen, “Theory of the virtual cathode oscillator”, Phys. Plasmas, vol. 8, no. 8, pp. 3781-3787, 2001.
- [30] R. B. Miller, “An Introduction to the Physics of Intense Charged Particle Beams”, Plenum, New York, 1982, Chapter 3.
- [31] K. R. Chu, “The Electron Cyclotron Maser”, Rev. Mod. Phys., vol. 76, no. 2, pp. 489-540, 2004.
- [32] V. A. Flyagin, A. V. Gaponov, M. I. Petelin, et al , “The Gyrotron”, IEEE Trans. Microwave Theory Tech., vol. MTT-25, no. 6, pp. 514-521, 1977.
- [33] J. L. Hirshfield and V. L. Granatstein, “The Electron Cyclotron Maser—An

- Historical Survey”, IEEE Trans. Microwave Theory Tech., vol. MTT-25, no. 6, pp. 522 – 527, 1977.
- [34] V.A. Flyagin, and G.S. Nusinovich, “Gyrotron oscillators”, Proceedings of the IEEE, vol. 76, no. 6, pp. 644-656, 1988.
- [35] L. R. Becerra, G. J. Gerfen, R. J. Temkin, et al, “Dynamic Nuclear Polarization with a Cyclotron Resonance Maser at 5 T”, Phys. Rev. Lett., vol. 71, no. 2, pp. 3561-3564, 1993.
- [36] G. N. Rapoport, A. K. Nematik, and V. A. Zhurakhovskiy, “Interaction of spiral electron beam with a large-amplitude fast electromagnetic wave”, Voprosy Radioelektroniki, Ser. I , Elektronika, no. 11, pp. 27-39, 1964.
- [37] V. K. Yulpatov, “Nonlinear theory of interaction between curvilinear periodic electron beam and electromagnetic field”, Voprosy Radioelektroniki, Ser 1. Elektronika, no. 12, pp. 15-23 (in Russian) , 1965.
- [38] N. S. Ginzburg, I. G. Zamitsyna, and G. S. Nusinovich, “Theory of relativistic cyclotron autoresonance maser with an opposite wave”, Radio Eng. Electron. Phys., vol. 24, no. 6, pp. 113-118, 1979.
- [39] A. Flifet, “Linear and nonlinear theory of the Doppler-shifted cyclotron resonance maser based on TE and TM waveguide modes”, Int. J. Electron., vol. 61, pp. 1049-1080, 1986.
- [40] S. Y. Park, R. H.Kyser, C.M. Armstrong, et al, “Experimental study of a Ka-band gyrotron backward-wave oscillator”, IEEE Trans. Plasma Sci., vol. 18, no. 3, pp. 321–325, 1990.
- [41] C. S. Kou, S. H. Chen, L. R. Barnett, et al, “Experimental study of an injection-locked gyrotron backward-wave oscillator”, Phys. Rev. Lett., vol. 70, no. 7, pp. 924-927, 1993.
- [42] M. A. Basten,W. C. Guss, K. E. Kreischer, et al, “Experimental investigation of a 140 GHz gyrotron-backward wave oscillator”, Int. J. Infrared Millimeter Waves, vol. 16, no. 5, pp. 889-905, 1995.

- [43] A. T. Lin and C. C. Lin, "Dependence of efficiency on magnetic field in gyro-backward wave oscillators", *Phys. Fluids B*, vol. 5, no. 7, pp. 2314-2317, 1993.
- [44] T.A. Spencer, C.E. Davis, K.J. Hendricks, et al, "Results from Gyrotron Backward Wave Oscillator Experiments Utilizing a High-current High-voltage Annular Electron Beam", *IEEE Trans. Plasma Sci.*, vol. 24, no. 3, pp. 630-635, 1996
- [45] T. H. Chang, C. T. Fan, K. F. Pao, et al, "Stability and tunability of the gyrotron backward-wave oscillator", *Appl. Phys. Lett.*, vol. 90, 191501, 2007.
- [46] C. S. Kou, S. H. Chen, L. R. Barnett, et al, "Experimental study of an injection-locked gyrotron backward-wave oscillator", *Phys. Rev. Lett.*, vol. 70, no. 7, pp. 924-927, 1993.
- [47] Q. S. Wang, D. B. McDermott, and N. C. Luhmann, "Demonstration of Marginal Stability Theory by a 200-kW Second-Harmonic Gyro-TWT Amplifier", *Phys. Rev. Lett.*, 75, 4322, 1995.
- [48] W. He, K. Ronald, A.R. Young, et al, "Gyro-BWO experiments using a helical interaction waveguide", *IEEE Trans. Electron Devices*, vol. 52, pp. 839-844, 2005.
- [49] N. C. Chen, C. F. Yu, and T. H. Chang, "A TE_{21} Second-harmonic Gyrotron Backward-wave Oscillator with Slotted Structure", *Phys. Plasmas*, vol. 14, 123105, 2007.
- [50] Simon J. Cooke and Gregory G. Denisov, "Linear Theory of a Wide-Band Gyro-TWT Amplifier Using Spiral Waveguide", *IEEE Trans. Plasma Sci.*, vol. 26, no. 3, pp. 519-530, 1998.
- [51] V. L. Bratman, G. G. Denisov, S.V. Samsonov, et al, "High-Efficiency Wideband Gyro-TWTs and Gyro-BWOs With Helically Corrugated Waveguides", *Radio Eng. Electron. Phys.*, vol. 50, no. 2, pp. 95-107, 2007.
- [52] S.V. Samsonov, G.G. Denisov, V.L. Bratman, et al, "Frequency-tunable CW

- gyro-BWO with a helically rippled operating waveguide”, IEEE Trans. Plasma Sci., vol. 32, pp. 884-889, 2004,.
- [53] W. He, A.D.R. Phelps, C.R. Donaldson, et al, “The Design and Simulation of a W-band Gyro-BWO”, Eighth IEEE International Vacuum Electronics Conference, Kitakyushu International Conference Center, Kitakyushu, Japan, May 15-17, 2007.
- [54] P. Sprangle and Robert A. Smith, “The nonlinear theory of efficiency enhancement in the electron cyclotron maser (gyrotron)”, J. Appl. Phys., vol. 51, no. 6, pp. 3001-3007, 1980.
- [55] A. K. Ganguly and S. Ahn, “Non-linear analysis of the gyro-BWO in three dimensions”, Int. J. Electronics, vol. 67, no. 2, pp. 261-276, 1989.
- [56] G. S. Nusinovich, and O. Dumbrajs, “Theory of gyro-backward wave oscillators with tapered magnetic field and waveguide cross section”, IEEE Trans. Plasma Sci., vol. 24, no. 3, pp. 620-629, 1996.
- [57] M.T. Walter, R.M. Gilgenbach, J.W. Luginsland, et al, “Effects of tapering on gyrotron backward-wave oscillators”, IEEE Trans. Plasma Sci., vol. 24, no. 3, pp. 636-647, 1996.
- [58] C. R. Donaldson, W. He, A. W. Cross, F. Li, A. D. R. Phelps, L. Zhang, K. Ronald, C. W. Robertson, C. G. Whyte, and A. R. Young, "A cusp electron gun for millimeter wave gyrodevices", Appl. Phys. Lett. 96, 141501, 2010.
- [59] G. Burt, S. V. Samsonov, K. Ronald, G. G. Denisov, A. R. Young, V. L. Bratman, A. D. R. Phelps, A. W. Cross, I. V. Konoplev, W. He, J. Thomson, and C. G. Whyte, “Dispersion of helically corrugated waveguides: Analytical, numerical, and experimental study,” Phys. Rev. E, vol. 70, no. 4, p. 046402, 2004..
- [60] W. He, C. R. Donaldson, F. Li, L. Zhang, A. W. Cross, A. D. R. Phelps, K. Ronald, C. W. Robertson, C. G. Whyte, and A. R. Young, "W-band gyro-devices using helically corrugated waveguide and cusp gun: design,

simulation and experiment", *Int. J. Terahertz Sci. and Tech.*, vol. 4 no. 1, pp. 9 – 19, 2011.

- [61] W. He, C. R. Donaldson, L. Zhang, K. Ronald, A. D. R. Phelps and A. W. Cross, "Numerical Simulation of a Gyro-BWO with a Helically Corrugated Interaction Region, Cusp Electron Gun and Depressed Collector", *Numerical Simulations / Book 2*, 2011.
- [62] W. Neugebauer, T. G. Mihran, "A ten-stage electrostatic depressed collector for improving klystron efficiency," *IEEE Trans. Electron Devices*, vol.19, no.1, pp. 111- 121, 1972.
- [63] J. D. Wilson, E. G. Wintucky, K. R. Vaden, D. A. Force, I. L. Krainsky, R. N. Simons, N. R. Robbins, W. L. Menninger, D. R. Dibb, D. E. Lewis, "Advances in Space Traveling-Wave Tubes for NASA Missions," *Proceedings of the IEEE*, vol.95, no.10, pp.1958-1967, 2007.
- [64] Liang Zhang, Wenlong He, Kevin Ronald, Alan D. R. Phelps, Colin G. Whyte, Craig W. Robertson, Alan R. Young, Craig R. Donaldson and Adrian W. Cross, "Multi-mode Coupling Wave Theory for Helically Corrugated Waveguide", *IEEE Trans. Microwave Theory Tech.*, vol. 60, no. 1, pp. 1-7, 2012.

Chapter 2

Genetic Algorithm and Its Implementation

2.1 Why optimization algorithm is needed?

Several problems in designing the energy recovery system are essentially relevant to the optimization issue. For example, when designing the input/output coupler and the microwave window, there is no rigorous theory to provide the ideal geometry parameters. When calculating the Bragg reflector, there is no equations available to predict how many corrugated sections and what the dimensions of the sections are required to achieve a total reflection over the interested frequency range. Also, it is hard to determine the stage number of the depressed collector and the potentials on the electrodes as well as the geometry of the electrodes to achieve optimum collection efficiency when designing the multi-stage depressed collector. The way to find the best parameter set by enumerating all the possibilities will take up too much computing time. For example, suppose a problem to be solved has 10 variables and each variable has 10 possibilities, then the overall possibilities would be 10^{10} . Unrealistic computing time is required to enumerate all the possibilities. Instead, an optimization algorithm by using a certain optimization strategy can be used to find an optimized solution in a reasonably short time.

The optimization process plays an important roll in designing microwave components. In this chapter, several optimization algorithms commonly used are introduced and compared in section 2.2. Section 2.3 introduces the important concepts when implementing the genetic algorithm. Section 2.4 gives a brief

summary on the optimization program which can invoke the 3D PIC code MAGIC, CST microwave studio and Mician μ Wave Wizard to evaluate the parameters.

2.2 Why genetic algorithm?

Several optimization algorithms have been developed. Such as

1 Enumerative method. In this method, every point in the searching space needs to be examined and the optimum solution is finally selected. The enumerative technique is easy to implement by changing each variable one at a time by a small step for a multi-variable problem. The results obtained from this method are reliable because all the possible values of the variables are evaluated and compared. However, it is the most costly option. The enumerative method should only be used in those problems where the number of variables is small as it's extremely low efficiency [1].

2 Hill-climbing method. It is the simplest heuristic optimization technology based on randomization technique and iterative improvement algorithm. It is derived from the strategy that people used when climbing to the peak of the hill in the shortest time. People always choose the steep position as their next step. In the hill-climbing method, the initial position is chosen randomly. The neighbour with the biggest ascent gradient of the current point is chosen as the current position. After some iterations, the algorithm reaches its local maximum when no neighbours have a larger value than the current position.

The hill-climbing method has the advantage that it is easy to implement. However, the derivative of the target function is required which means the objective function needs to be continuous in the searching space. It is not fulfilled for some complicated problems. The hill-climbing method can only provide locally optimum values, and these values depend on the selection of the starting points. Moreover, there is no general method to determine the errors between the local optima and the global optimum because the global optimum is still unknown. To avoid the hill-climbing

method being trapped in a locally optimal solution, a large number of different starting points can be chosen to repeat the same iterating process in the hope that at least some of these initial points have a path leading to the global optimum [2].

3 Simulated annealing method. It is based on the analogy between the simulation of the annealing of solids and the problem of solving large combinatorial optimization problems. In material physics, annealing denotes a physics process in which a solid is heated to liquid phase by increasing the temperature and then cooled down to solid phase. When the solid reaches its peak temperature, the particles of the solid randomly arrange themselves in the liquid phase. While as the temperature decreases, the particles arrange themselves in the low-energy ground state of corresponding lattices. At each given temperature, the solid reaches thermal equilibrium and the energy of the particles can be characterized by a Boltzmann distribution. When the solid reaches the quenching temperature, all the particles are frozen into the metastable amorphous structures resulting in a minimum energy. In a simulated annealing algorithm, a fixed point of the variable represents a particle in the solid, and the objective function is regarded as the energy of the particle. The objective function accepts a lower value with higher and higher probability as the temperature decreases.

Simulated annealing is essentially a modified version of the hill-climbing method. The difference is the hill-climbing method only chooses the neighbour having the biggest positive gradient as the next point while the simulated annealing algorithm has the chance to accept a worse point under the Metropolis criterion

$$P_z(i \Rightarrow j) = \begin{cases} 1, & \text{when } f(j) \leq f(i) \\ \exp\left(\frac{f(i) - f(j)}{z}\right), & \text{otherwise} \end{cases} \quad (2. 1)$$

Where $P_z(i \Rightarrow j)$ is the probability to accept the neighbour j as the current position i . z is the distance of each step and $f(i)$ is the objective function. The simulated

annealing algorithm thus has the ability of global optimization. However, it is not good in optimization problems that have multi-parameters [3].

4 Greedy algorithm. The greedy algorithm is an optimization strategy based on the truth that the optimum algorithms typically run through a sequence of steps. The strategy is simple and straightforward. For each choice of the steps, the algorithm always takes the action that looks best at the moment without worrying about the effect that these decisions may have in the future. That is, it always tries to reach the local optimum of each optimization step in the hope of reaching a global optimum. The greedy algorithm is easy to implement and quite efficient for some problems. However, the greedy algorithm does not always achieve a global optimum for it is shortsighted in taking the local optimum decision [4].

5 Ant colony optimization. The ant colony algorithm is derived from the observation of the real ant's behaviour. The real ants can always find an optimum path from the nest to the food by exchanging information through a certain pheromone. At first, the ants wander randomly. When they find food, they will lay down pheromone trails to their colony on their way. The other ants will follow the trail if they find such a path and reinforce the pheromone if they eventually find the food. In ant colony optimization, the artificial ants are designed to simulate the behaviour of real ants. They can choose those paths having more pheromone with higher probability, leaving more pheromone on the shorter way to the food, and communicate with other ants by pheromone.

The ant colony optimization can be used to solve computational problems which can be reduced to find good paths through graphics, such as the routing problem in telecommunications networks. It has the advantage over the other optimization algorithm when the graphic changes dynamically, such as the load in the routers. The ants have the ability to adapt their behaviour when the environment changes while

keeping a good path. The ant colony algorithm can be run continuously and adapt to changes in real time [5].

6 Genetic algorithm. It is a searching technology inspired by the mechanism of natural selection where stronger individuals have large a possibility to survive in a competing environment. In Darwin's theory of evolution, our physical feature is dominated by genes which are portions of chromosome. The stronger individuals can preserve their genetic information by inheritance and crossover to make their offspring have a higher probability of becoming the winner. The weaker ones also have the chance to be stronger by means of mutation. The final winner is thought to be the most fit in this environment. Genetic algorithm (GA) simulates the similar natural selection process when solving the optimization problems. It assumes that every possible solution of the problem is an individual (like the chromosome in biology) and it can be represented as a set of parameters (like the genes in biology). The individuals are examined by the fitness function (like natural selection) and then generate their offspring by inheritance, mutation and crossover. After a few generations, the one that has the best fitness is regarded as the optimum solution for the problem.

The idea of the genetic algorithm was first introduced in the 1960s [6]. It is a mature technology after 40 years of development and has been widely used in various applications. It has been proven that the genetic algorithm performs well in problems in which the fitness functions are complex, such as those that are discontinuous and with many local optima. The major advantage of the genetic algorithm as a global search method is its flexibility and robustness. The other advantage is that it is readily amenable to parallel implementation because the individuals in the same generation can be examined at the same time thus making it ideal for large problems especially where the evaluation of the fitness of the individuals is time consuming. The genetic algorithm provides a common solution to many problems because it does

not need to know much detail about the problem. The only information needed is the fitness function of the individuals and the rough range of the variables.

Among these methods, the enumerative method needs too much computing time when the searching space is large; hill-climbing method and greedy algorithm can find a local optimum solution, but not guaranteed to find a global optimum; simulated annealing algorithm is not very good at solving multi-variable problems and the ant colony optimization is only efficient at solving the problems that can be reduced into finding good paths through graphics [7, 8]. The design of a multi-stage depressed collector is a multi-variable problem, for each stage can be regarded as a variable. Moreover, there is no significant relationship between the objective function and the parameters. The genetic algorithm could be a better choice in designing the depressed collector than the other optimization algorithms. As a common solution, the genetic algorithm can also be used to optimize the dimension of the input/output coupler, the Bragg reflector and the microwave window.

2.3 The implementation of the genetic algorithm

The flow chart of the genetic algorithm is shown in Fig. 2.1.

At first, the variables of the problems acting as the genes are encoded and then joined together as bit strings which act as the chromosome. An individual which contains a chromosome is regarded as a possible solution of the problem. When the calculation begins, an initial population is generated with a number of individuals by a certain distribution function or randomness. The fitness of each individual in the population is then be evaluated and a proportion of the good individuals are preserved to be the members of the next generation. The other members are bred through genetic operations such as crossover and mutation. The evaluation and reproduction process are repeated until the evolution reaches the required generation number, or the optimum individual is thought to be good enough.

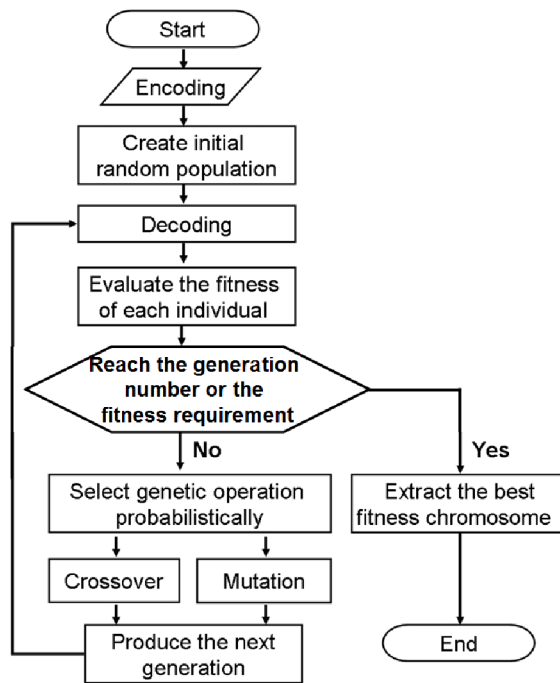


Fig. 2. 1 The flow chart of the genetic algorithm.

There are several important processes when implementing the genetic algorithm.

1 Encoding. Before the genetic algorithm runs, the variables are encoded as bit strings. Several encoding methods have been successfully developed, such as binary encoding, permutation encoding, value encoding and tree encoding. The binary encoding is the simplest and the most commonly used one. In binary encoding, the chromosome is encoded as a string of 0s and 1s. For example, a chromosome with four variables A, B, C, D can be encoded as binary string shown in Fig. 2.2.

Chromosome: 10110010 1010100 100100 100010
 Variables: A B C D

Fig. 2. 2 Schematic diagram of encoding operation.

Other encoding technology such as permutation encoding is useful for ordering problems. Value encoding is suitable for complicated objects associated with real

numbers and characters, however, specific crossover and mutation operation should be designed for each specific problem.

2 Selection. A good parent selection mechanism is necessary to produce good offspring. In general, the higher fitness the individual is, the higher possibility it is to be selected as a parent to reproduce the offspring. The most common selection technology is the Roulette Wheel Mechanism in which the probability of the individual being selected is proportional to the fitness of the individual.

3 Crossover. Crossover is one of the basic operations of the genetic algorithm. The simplest crossover operation is the single-point crossover. It randomly chooses a locus and exchanges the subsequences before and after that, the locus between two chromosomes to create a new offspring. For example, if a crossover happens in the 4th locus of the parent chromosome strings of 11001011 and 11011111, the offspring with chromosome of 11001111 is produced, as shown in Fig. 2.3.

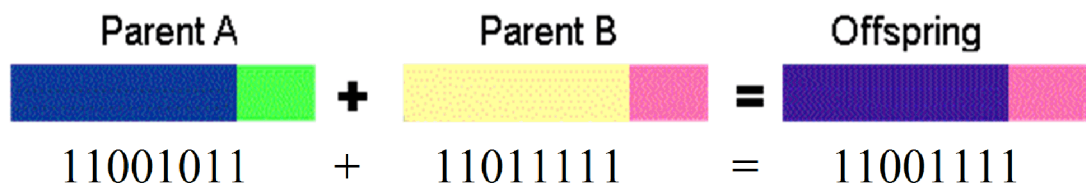


Fig. 2. 3 Schematic diagram of crossover operation.

Other crossover methods based on single-point crossover, such as two-point crossover, uniform crossover and arithmetic crossover were developed in the hope of exploring the searching space in a more efficient way.

4 Mutation. Mutation provides a small amount of random search in the solution space to ensure that every point in the solution space has non-zero probability to be searched. The operation is applied to the child individuals after crossover. The number of mutations is controlled by the mutation probability and the individuals are chosen randomly. For binary encoding, the mutation operation is implemented by flipping some bits (from 1 to 0 or 0 to 1) in the chromosome. For example, the

chromosome before and after the mutation operation applied on the 5th gene is shown in Fig. 2.4.

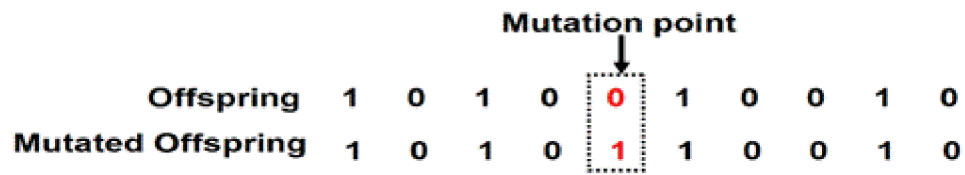


Fig. 2. 4 Schematic diagram of encoding operation.

5 Fitness function. It is derived from the problem to be solved and used to quantify the optimality of a possible solution. The fitness function gives a single numerical value that represents the “utility” or “ability” of the individual when given a particular chromosome (a possible solution). The efficiency of the genetic algorithm is greatly determined by the design of the fitness function. To reach a good efficiency, the fitness function should not have too many local maxima, or a very isolated global maximum.

Several genetic algorithm packages using different programming languages are available, such as Genetic Algorithm Library by Mladen Jankovic in C++ [9], Java Genetic Algorithms Package (JGAP) in JAVA [10], Genetic Algorithm and Direct Search Toolbox 2.4 in MATLAB [11], MIT GALib in C++ [12], and so on. In this thesis, MIT GALib was chosen to optimize the design of the depressed collector, and the Direct Search Toolbox was used to optimize the Bragg reflector and the microwave window. MIT GALib is a C++ Library developed by Massachusetts Institute of Technology which contains a set of C++ genetic algorithm objects. The library includes tools for using genetic algorithms to do optimization in any C++ program using any representation and genetic operators. The functions of the library could be easily modified and inserted into the multi-stage depressed collector simulation code which was also written in C++. The Bragg reflector code and microwave window codes were implemented in MATLAB by the mode matching method thus the Direct Search Toolbox was convenient to use.

2.4 Optimization of the depressed collector using MIT GALib

The modeling and simulation of the multistage collector is a challenging task because a large number of electrons including the secondary electrons need to be simulated in the electromagnetic fields in the collection region. Several particle-in-cell (PIC) codes can be used to simulate the multistage collector, including COCA, E-GUN 3D, MAFIA, MICHELLE, and MAGIC. However, most of these codes have a special purpose and are not available to our group and none of the source codes are available either for security or proprietary reason. The 3D PIC code MAGIC is commercial software and it is available in the university, thus it was chosen to simulate the multistage depressed collector.

Unfortunately, MAGIC does not contain any optimization routines, therefore, an optimization program based on the MIT GALib was developed to help in designing the depressed collector. In this program, the process of “Evaluate the fitness of each individual” in Fig. 2.1 was implemented by controlling the MAGIC without the need to know the source code. The flow diagram of this process is shown in Fig. 2.5.

The optimization program firstly created an input file by filling the new set of parameters generated by the genetic algorithm to the template input file for MAGIC. Then MAGIC was invoked to simulate the new geometry and the result was read by the optimization program to evaluate the parameters.

To invoke the MAGIC simulation program and monitor the state of the simulation, several API (Application Programming Interface) functions in the windows operating system were used [13]. The optimization program is able to run several MAGIC simulations at the same time to evaluate the individuals, therefore it can speed up the optimization process.

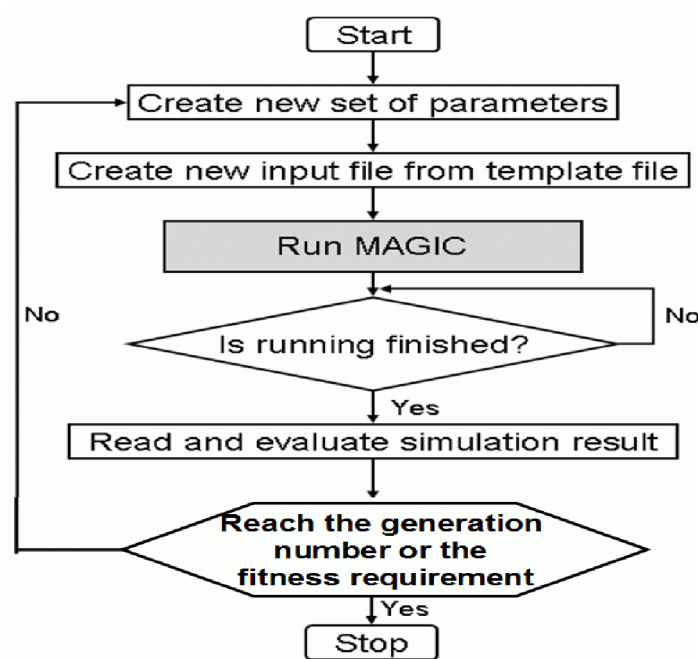


Fig. 2. 5 Flow diagram of the optimization program.

The optimization program was then released as a general program which provides an optimization algorithm to the programs used in microwave research field, such as the CST microwave studio and the Mician μ Wave Wizard in a similar approach. A detailed description on the program can be found in appendix II.

2.5 Conclusion

Optimization algorithms such as enumerative method, hill-climbing method, simulated annealing method, greedy algorithm, ant colony optimization and genetic algorithm could be used in the design of depressed collector. Among these algorithms, genetic algorithm has the advantage in parallel running, and solving problems without knowing much detail about the problems. The simulation of a depressed collector is challenging work, because the trajectories of the spent electrons are not only dependent on the initial states of the electrons but also related to the geometry of the electrode and the potentials on the electrodes. The genetic algorithm can provide a general solution to such a complicated problem and an optimization program based on the MIT GAlib was developed to help to design the

depressed collector. The other genetic algorithm packet Direct Search Toolbox in MATLAB was used to optimize the input/output coupler, Bragg reflector and the microwave window.

References

- [1] Lingfeng Wang, Kay Chen Tan and Chee Meng Chew, “Evolutionary Robotics: From Algorithms to Implementations”, World Scientific press, pp. 229, 2006
- [2] Zbigniew Michalewicz and David B. Fogel, “How to Solve it: Modern Heuristics”, Springer press, pp. 43, 2004
- [3] Peter J. M. Laarhoven and Emile H. L. Aarts, “Simulated Annealing: Theory and Applications”, Springer press, 1987
- [4] Thomas H. Cormen, Charles E. Leiserson, Ronald L. Rivest, et al, “Introduction to Algorithms”, MIT Press, 2001
- [5] Marco Dorigo and Thomas Stützle, “Ant Colony Optimization”, MIT Press, 2004
- [6] Alex Fraser, "Simulation of genetic systems by automatic digital computers. I: Introduction". Aust. J. Biol. Sci. vol. 10, pp. 484-491, 1957.
- [7] Melanie Mitchell, “An Introduction to Genetic Algorithms”, MIT Press, 1998
- [8] S. Kwong, K. F. Man, and K. S. Tang, “Genetic Algorithms: Concepts and Designs”, Springer press, 1999
- [9] <http://www.codeproject.com/KB/recipes/geneticlibrary.aspx>
- [10] <http://sourceforge.net/projects/jgap/>
- [11] <http://www.mathworks.com/products/gads/>
- [12] <http://lancet.mit.edu/ga/>
- [13] Jeffrey Richter, and Christophe Nasarre, “Windows Via C/C++”, Microsoft Press, 2007

Chapter 3

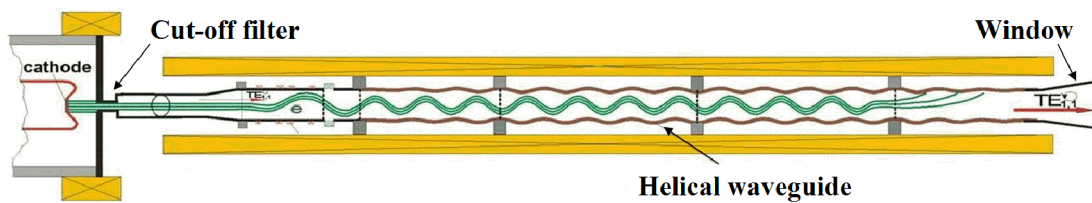
Side-wall Coupler

3.1 The background

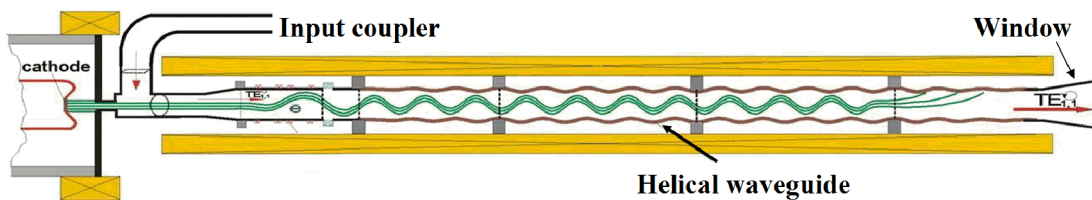
The initial experimental setup of the W-band gyro-BWO is shown in Fig. 3.1 (a). The hollow large orbit electron beam was emitted from the cusp electron gun and passed into the helically corrugated interaction waveguide to generate microwave radiation. A microwave cut-off filter was placed before the interaction waveguide to reflect the microwaves downstream, where it was extracted out by a microwave window. However, when we applied a depressed collector to recover the energy from the spent electrons at the end of the interaction region, the path for the microwaves would be blocked and the microwaves could not be extracted from the axis direction. An alternative method is to extract the generated microwave by a coupler from side of the beam tube either before or after the interaction region.

Meanwhile, a W-band gyro-TWA is under development based on the experimental setup of the gyro-BWO. They share the same cusp electron beam gun, the solenoid systems as well as the helically corrugated interaction waveguide with different dimensions. The gyro-TWA was predicted to achieve a saturated gain of 40 dB, and an output power of 5 kW in the frequency tuning band of 90 - 100 GHz [1]. As shown in Fig. 3.1 (b), the seed microwave is coupled into the system between the electron beam gun and the interaction region, and the amplified microwave is extracted out at the downstream from the input coupler by a broadband, low-reflection window. To meet the requirement of both devices, the coupler was placed upstream, between the cathode and the interaction waveguide [2, 3].

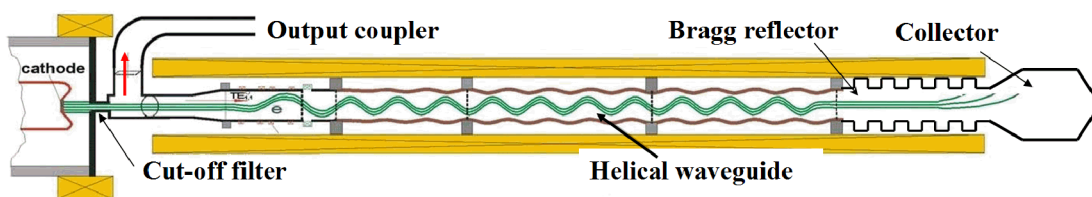
If the side-wall coupler can not extract the entire generated microwave radiation, the rest of the microwaves will travel downstream and enter into the collection region. To avoid the rest of the microwaves affecting the spent beam in the depressed collector and to increase the microwave output power, a Bragg reflector was inserted between the interaction region and the depressed collector to act as a waveguide short and to reflect the rest microwave radiation back upstream, as shown in Fig. 3.1 (c).



(a) Original experimental setup of the gyro-BWO;



(b) Experimental setup of the gyro-TWA;



(c) Experimental setup of the gyro-BWO with collector;

Fig. 3. 1 Diagram of the input and out of the gyro-BWO/TWA.

In this chapter, the design of a side-wall coupler and a Bragg reflector is introduced. The principle of the Bragg reflectors including the sinusoidal ripple waveguides and the rectangular corrugated waveguides are introduced and the simulation results are presented in section 3.2. In section 3.3, the side-wall coupler which was used to

convert the TE_{11} mode of the circular waveguide to the TE_{10} mode of the rectangular waveguide was designed and optimized for the gyro-BWO in frequency range of 84 - 104 GHz, which covers the frequency band of the gyro-TWA from 90 - 100 GHz.

3.2 Bragg reflector

The structure inserted between the interaction region and the depressed collector should have the function of reflecting the generated microwave radiation back upstream without blocking the path of the spent electrons to the collection region, which indicated that the designed structure should have high reflectivity in the operating frequency range, which is 84 - 104 GHz, and also the minimum radius of the structure should be larger than the radius of the beam tube.

Extensive theoretical and experimental research indicated that a near unity reflection could be achieved by a Bragg reflector composed of a cylindrically symmetric corrugated structure. One of the most important applications of Bragg reflectors was the Bragg resonator, which comprised two Bragg reflectors separated by a smooth waveguide. Bragg resonators had become the most suitable cavity structures for the cyclotron autoresonance maser (CARM) and the free electron laser (FEL) [4, 5].

There are basically two types of structures. One is the non-uniform waveguide with smooth variations on the cross section along the axis. The other is with discontinuous corrugations.

The study on the non-uniform waveguide with smooth variations on cross section along the axis was first studied by Solymar in 1959 [6]. In this paper, the non-uniform waveguide was regarded as a system of coupled transmission lines, where the coupling coefficients were functions of the z axis. The field intensities in the non-uniform waveguide were represented by equivalent voltages and currents. The reflectivity can be evaluated from solving the differential equation of the

generalized telegraphist's equation and the boundary conditions [7, 8]. The details can be referred from appendix III.

3.2.1 Sinusoidal ripple waveguide

A simple corrugated depth distribution is when the waveguide has a weak axisymmetric sinusoidal ripple in the waveguide wall having the expression [9, 10]

$$R'(z) = a + h \cos(k_b z) \quad (3.1)$$

where a is the mean radius, h is the corrugation amplitude, and $2\pi/k_b$ is the period of the ripple. Assume the generalised telegraphist's equations have a solution with the form of $A = f(z)e^{jk_z z}$, where k_z is the axial wavenumber. In this case, the reflected wave term is only important when the Bragg condition $2k_z - k_b = 0$ is satisfied. And the equations for the mode amplitude are a pair of first-order homogeneous linear differential equations as

$$\begin{cases} \frac{df^+}{dz} + j\Delta f^+ = -jGf^- \\ \frac{df^-}{dz} - j\Delta f^- = jGf^+ \end{cases} \quad (3.2)$$

where $G = H(\beta h / \tan \theta)$, $\Delta = 2k_z - k_b$, and H is defined by A.18 in appendix III.

The general solution of the equation is

$$\begin{cases} f^+(z) = c_1(-jG)e^{jz} + c_2(-jG)e^{-jz} \\ f^-(z) = c_1(j\Delta + \gamma)e^{\lambda z} + c_2(j\Delta - \gamma)e^{-\lambda z} \end{cases} \quad (3.3)$$

where $\gamma^2 = G^2 - \Delta^2$ and c_1 and c_2 are determined by the boundary condition. If the waveguide connected to both sides of the Bragg reflector are matched and no reflection is produced, the boundary conditions for the rippled waveguide are

$$\begin{cases} f^+(0) = 1 \\ f^-(L) = 0 \end{cases} \quad (3.4)$$

And the solution for the boundary conditions is

$$\begin{cases} f^+(z) = \frac{j\Delta \sinh \gamma(L-z) + \gamma \cosh \gamma(L-z)}{j\Delta \sinh \gamma L + \gamma \cosh \gamma L} \\ f^-(z) = \frac{-jG \sinh \gamma(L-z)}{j\Delta \sinh \gamma L + \gamma \cosh \gamma L} \end{cases} \quad (3.5)$$

The reflectivity in this case is

$$R(\Delta) = |f^-(0)|^2 = \left| \frac{\gamma \sinh \gamma L}{j\Delta \sinh \gamma L + \gamma \cosh \gamma L} \right|^2 \quad (3.6)$$

To obtain a high reflectivity, $G > \Delta$ which means $\gamma > 0$ is always chosen. At the centre of the reflection band ($\Delta = 0, \gamma = G$), the reflectivity is

$$R = \tanh^2(GL) \quad (3.7)$$

The expression of G can be simplified as

$$G = \begin{cases} \frac{h}{2} \left\{ \frac{x_{mn}^4 - m^2 a^2 (\omega^2 / c^2 + \beta^2)}{\beta a^3 (x_{mn}^2 - m^2)} \right\}, & \text{for TE modes,} \\ \frac{h}{2} \frac{\omega^2 / c^2 + \beta^2}{\beta}, & \text{for TM modes.} \end{cases} \quad (3.8)$$

Since G is linearly proportional to the ripple depth, the longer the reflect section is, and the deeper the ripple is, the higher reflectivity can be obtained. And also, the Bragg reflectors with deeper ripples have broad bandwidth.

3.2.2 Rectangular corrugation reflectors

The previous analytical theory assumes a slow and weakly varying corrugation in the reflector. However, the theory is not suitable for a reflector with step discontinuities, such as rectangular corrugation reflectors shown in Fig. 3.2. The sinusoidal ripple reflectors have a half period radius smaller than the beam tube, while the rectangular corrugation reflectors [11-15] do not have such limitation and the radii of the corrugated sections can be configured flexibly.

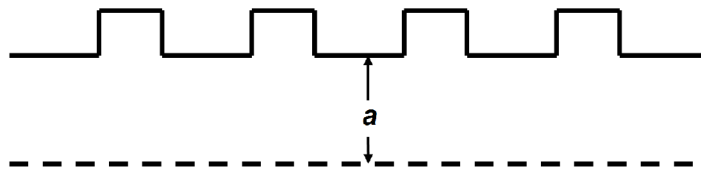


Fig. 3. 2 Reflector with corrugated sections.

The mode matching method can be used to carry out the numerical simulation of the reflectivity of the discontinuous waveguides. In this approach, the waveguide is decomposed into a discrete number of modules. Each module consists of an abrupt junction of two circular waveguides with different diameters, as shown in Fig. 3.3.

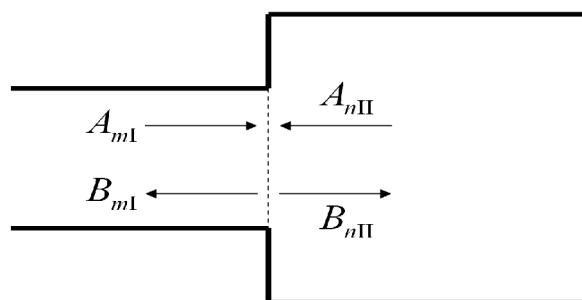


Fig. 3. 3 Single module of discontinuous waveguide.

The wave propagation in such a waveguide step can be analytically evaluated by matching the fields on the discontinuous position [17]. As shown in Fig. 3.3, the

transverse field \vec{E} and \vec{H} can be expressed in terms of the eigenmodes \vec{e}_i, \vec{h}_i of the waveguide in region I as

$$\begin{cases} \vec{E}_I = \sum_{m=1}^M (A_{mI} + B_{mI}) \vec{e}_{mI} \\ \vec{H}_I = \sum_{m=1}^M (A_{mI} - B_{mI}) / Z_{mI} \vec{h}_{mI} \end{cases} \quad (3.9)$$

where A_{mI} is the amplitude of the forward propagation wave (from region I to region II) and B_{mI} is the amplitude of backward propagation wave (from region II to region I). Z_{mI} is the characteristic impedance of the mode and M is the number of eigenmodes to be calculated. Theoretically, $M \rightarrow \infty$, while in practice, M is governed by the relative convergence phenomenon.

The field in region II can be expressed as

$$\begin{cases} \vec{E}_{II} = \sum_{n=1}^N (A_{nII} + B_{nII}) \vec{e}_{nII} \\ \vec{H}_{II} = \sum_{n=1}^N (A_{nII} - B_{nII}) / Z_{nII} \vec{h}_{nII} \end{cases} \quad (3.10)$$

where A_{nII} is the amplitude of forward propagation wave (from region II to region I) and B_{nII} is the amplitude of backward propagation wave (from region I to region II). Z_{nII} is the characteristic impedance of the mode in region II. N is the number of eigenmodes to be calculated. It is suggested that by choosing $N = Ma_{II} / a_I$ this help by converging to the correct values. Here a_I and a_{II} are the radius of the waveguide in region I and II, respectively.

Apply continuity of the tangential \vec{E} and \vec{H} across the discontinuous area and forcing zero tangential electric field on the wall of the larger guide, we have the following relation between the modal amplitudes of the forward and backward wave in the discontinuous waveguide.

$$\begin{cases} P[A_I + B_I] = I[A_{II} + B_{II}] \\ Z_I P^T Y_{II} [A_{II} - B_{II}] = I[A_I - B_I] \end{cases} \quad (3.11)$$

where I is the unit matrix; A_v and B_v ($v=I, II$) are column matrix composed by A_{kv} ($k=1 \dots M$) and B_{kv} ($k=1 \dots N$). Z_I is $M \times M$ diagonal matrix of the modal impedances in region I, that is

$$Z_I = \begin{bmatrix} Z_{I1} & \cdots & 0 \\ \vdots & \ddots & \vdots \\ 0 & \cdots & Z_{IM} \end{bmatrix} \quad (3.12)$$

Y_{II} is $N \times N$ diagonal matrix of the modal admittances for region II, that is,

$$Y_{II} = \begin{bmatrix} 1/Z_{II1} & \cdots & 0 \\ \vdots & \ddots & \vdots \\ 0 & \cdots & 1/Z_{IIN} \end{bmatrix} \quad (3.13)$$

P is $N \times M$ mode coupling matrix and given by

$$P_{ji} = \int_{CA} \vec{e}_{jII} \cdot \vec{e}_{iI}^* dA \quad (3.14)$$

The wave impedances for a circular waveguide with radius a are

$$Z_{mn} = \begin{cases} \frac{j\omega\mu}{\beta_{mn}}, & \text{TE mode} \\ -\frac{j\beta_{mn}}{\omega\epsilon}, & \text{TM mode} \end{cases} \quad (3.15)$$

where μ is the permittivity of the material filled in the cavity; ϵ is the dielectric constant of the material; ω is the frequency of the wave; β_{mn} is the propagation constant that can be expressed as

$$\beta_{mn} = \left(\left(\frac{\gamma_{mn}}{a} \right)^2 - \mu\epsilon\omega^2 \right)^{1/2} \quad (3.16)$$

where γ_{mn} is the n^{th} zero of J_m and J is the first kind of Bessel function.

There is no coupling between two waves with different azimuthal indices. In paper [14], the coupling coefficients for an axisymmetric waveguide were given as follows

$$P_{m,n_1 \rightarrow m,n_2} = \begin{cases} \frac{2(a_1/a_{II})\gamma'_{mn_2} J'(\gamma'_{mn_2} a_1/a_{II})}{J(\gamma'_{mn_2})(\gamma'^2_{mn_1} - m^2)^{1/2}(\gamma'^2_{mn_2} - m^2)^{1/2}(1 - (\gamma'_{mn_2}/\gamma'_{mn_1})^2(a_1/a_{II})^2)}, & \text{TE}_{mn_1} \rightarrow \text{TE}_{mn_2} \\ -\frac{2mJ(\gamma_{mn_2} a_1/a_{II})}{\gamma_{mn_2} J_{m+1}(\gamma_{mn_2})(\gamma'^2_{mn_1} - m^2)^{1/2}}, & \text{TE}_{mn_1} \rightarrow \text{TM}_{mn_2} \\ \frac{2J(\gamma_{mn_2} a_1/a_{II})}{\gamma_{mn_2} J_{m+1}(\gamma_{mn_2})(1 - (\gamma_{mn_1}/\gamma_{mn_2})^2(a_{II}/a_1)^2)}, & \text{TM}_{mn_1} \rightarrow \text{TE}_{mn_2} \\ 0, & \text{TM}_{mn_1} \rightarrow \text{TM}_{mn_2} \end{cases} \quad (3.17)$$

where γ'_{mn} is the n^{th} zero of J'_m and J' is the derivate of first kind of Bessel function.

The scattering matrix is then used to define the interaction between the initial state and the final state. For example, Eq. 3.11 can be rewritten by introducing the scattering matrix S .

$$\begin{pmatrix} B_I \\ B_{II} \end{pmatrix} = \begin{pmatrix} S_{11} & S_{12} \\ S_{21} & S_{22} \end{pmatrix} \begin{pmatrix} A_I \\ A_{II} \end{pmatrix} \quad (3.18)$$

The elements of S can be calculated from Eq. 3.11 and Eq. 3.18 and the results are

$$\begin{cases} S_{11} = [I + Z_1^{1/2} P^T Y_2 P Z_1^{1/2}]^{-1} [1 - Z_1^{1/2} P^T Y_2 P Z_1^{1/2}] \\ S_{12} = 2[1 + Z_1^{1/2} P^T Y_2 P Z_1^{1/2}]^{-1} Z_1^{1/2} P^T Y_2^{1/2} \\ S_{21} = Y_2^{1/2} P Z_1^{1/2} [I + S_{11}] \\ S_{22} = Y_2^{1/2} P Z_1^{1/2} S_{12} - I \end{cases} \quad (3.19)$$

Eq. 3.17 is used when $a_1 < a_{II}$. When $a_1 > a_{II}$, the scattering matrix becomes

$$S = \begin{pmatrix} S_{22} & S_{21} \\ S_{12} & S_{11} \end{pmatrix} \quad (3.20)$$

The scattering matrix for a waveguide length of L can be written as

$$S_{\text{wg}} = \begin{pmatrix} 0 & S_v \\ S_v & 0 \end{pmatrix} \quad (3.21)$$

S_V is a $V \times V$ diagonal matrix with the elements $S_{vv} = e^{-\beta_{mn}L}$. By cascading all the scattering matrixes along the discontinuity waveguide, we can obtain the overall scatter matrix S_0 . Consider a system with two scatter matrix shown in Fig. 3.4, the relation between the overall scattering matrix and the local scattering matrixes is

$$\begin{pmatrix} B_I \\ B_{II} \end{pmatrix} = \begin{pmatrix} S_{11}^a & S_{12}^a \\ S_{21}^a & S_{22}^a \end{pmatrix} \begin{pmatrix} A_I \\ A_{II} \end{pmatrix}, \quad \begin{pmatrix} C'_I \\ C'_{II} \end{pmatrix} = \begin{pmatrix} S_{11}^b & S_{12}^b \\ S_{21}^b & S_{22}^b \end{pmatrix} \begin{pmatrix} B'_I \\ B'_{II} \end{pmatrix}$$

and $A_{II} = C'_I$, $B_{II} = B'_I$ (3.22)

$$\begin{pmatrix} B_I \\ C'_{II} \end{pmatrix} = \begin{pmatrix} S_{11}^0 & S_{12}^0 \\ S_{21}^0 & S_{22}^0 \end{pmatrix} \begin{pmatrix} A_I \\ B'_{II} \end{pmatrix}$$

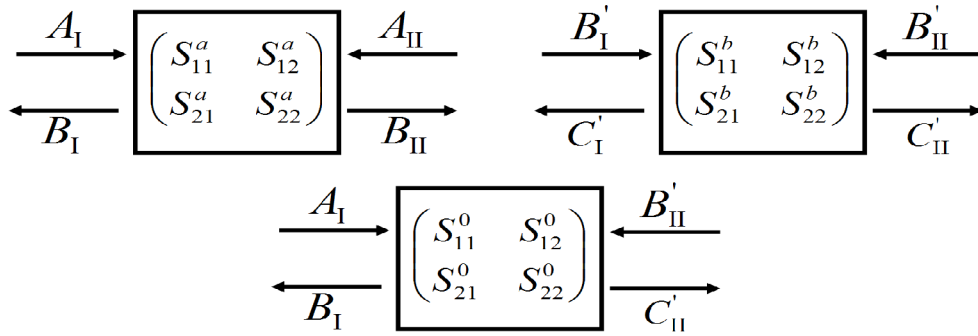


Fig. 3. 4 The relation between the overall and local scattering matrices.

The overall scattering matrix S_0 can be solved as

$$\begin{cases} S_{11} = S_{12}^a [I - S_{11}^b S_{22}^a]^{-1} S_{11}^b S_{21}^a + S_{11}^a \\ S_{12} = S_{12}^a [I - S_{11}^b S_{22}^a]^{-1} S_{12}^b \\ S_{21} = S_{21}^b [I - S_{22}^a S_{11}^b]^{-1} S_{21}^a \\ S_{22} = S_{21}^b [I - S_{22}^a S_{11}^b]^{-1} S_{22}^a S_{12}^b + S_{22}^b \end{cases} \quad (3.23)$$

The overall scatter matrix of the reflector with more than two scattering matrices can be calculated by repeating the process of cascading two scatter matrixes. Suppose the reflector is terminated by matching loads at the end of both sides, and a wave propagates from the left to the right, we have $B_{II}' = 0$. For the reflected modes, we have $B_I = S_{11}^0 A_I$; for the transmitted modes, we have $B_{II} = S_{21}^0 A_I$. The reflectivity of the reflector can be obtained from S_{11}^0 .

3.2.3 Simulation result of the Bragg reflector

A Bragg reflector with sinusoidal ripple waveguide was calculated. As in our application, the mode of the generated microwaves is TE_{11} . The frequency range is $84 \sim 104$ GHz, and the centre frequency is 94 GHz. The ripple period d can be evaluated from the Bragg condition, which is

$$k_b = 2k_z = 2\left(\left(\frac{x_{11}}{a}\right)^2 - \left(\frac{\omega_{center}}{c}\right)^2\right)^{1/2} = 2\left(\left(\frac{1.841}{1.3 \times 10^{-3}}\right)^2 - \left(\frac{2\pi \times 94 \times 10^9}{3.0 \times 10^8}\right)^2\right)^{1/2} = 2762 \text{ lm}^{-1} \quad (3.24)$$

$$d = 2\pi / k_b = 2.27 \text{ mm}$$

To have a high reflectivity (90%) in the centre of the frequency band, the value of $|GL|$ should be as large as possible, which means h, L should be as large as possible. However, the maximum bandwidth can reach is only 1.3 GHz, as shown in Fig. 3.5. It is obvious that the sinusoidal ripple Bragg reflector can not achieve this requirement.

A program based on the formula in section 3.2.2 was developed to calculate the scattering parameters of the rectangular corrugated reflector. In the simulation, it was found that the more corrugated sections, the wider the bandwidth of the higher reflectivity that could be achieved.

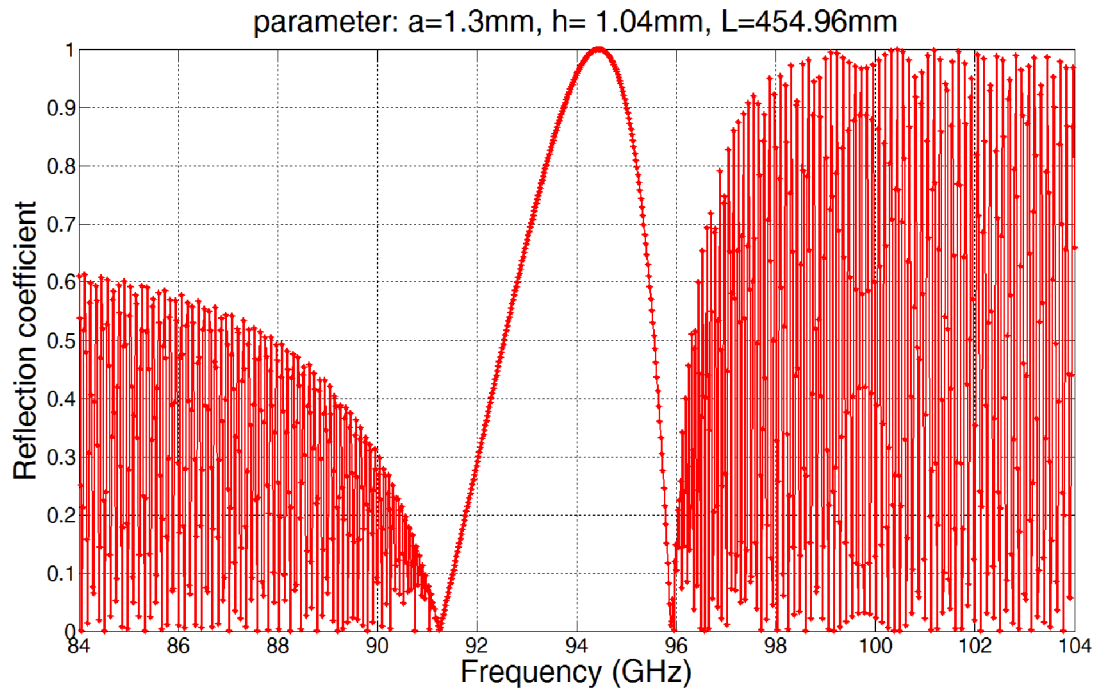


Fig. 3. 5 The reflectivity when the parameters are $a=1.3\text{mm}$, $h=1.04\text{mm}$, $L=454.96\text{mm}$.

The genetic algorithm described in chapter 2 was used to optimize the corrugated sections. To reduce the machining difficulty, all the lengths of the sections are set as the same value. The radii of the corrugated sections are set at different values. In our application, the magnetic field reduced as the distance away from to the solenoid increases, the radius of the spent electron beam increases. Thus we set the radius of the corrugated sections gradually increases as the distance to the solenoid. The optimized range of the radii of the corrugated section whose distance is less than 45 mm to the beginning position is in the [1.3mm, 2.0 mm] range. The radii of the corrugated section whose distance is larger than 45 mm to the beginning position is

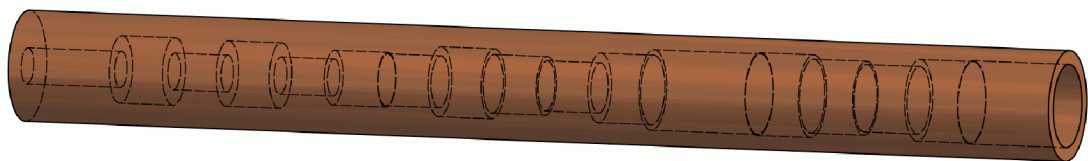
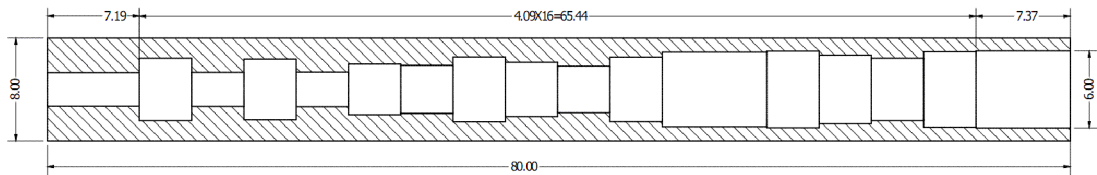
[2.0 mm, 3.0 mm]. The range of the length of the corrugated sections is [2.0 mm, 5.5 mm].

In the optimization program, the population, the crossover probability and the mutation probability were set as 20, 0.85, and 0.05, respectively. The evaluation function was chosen as

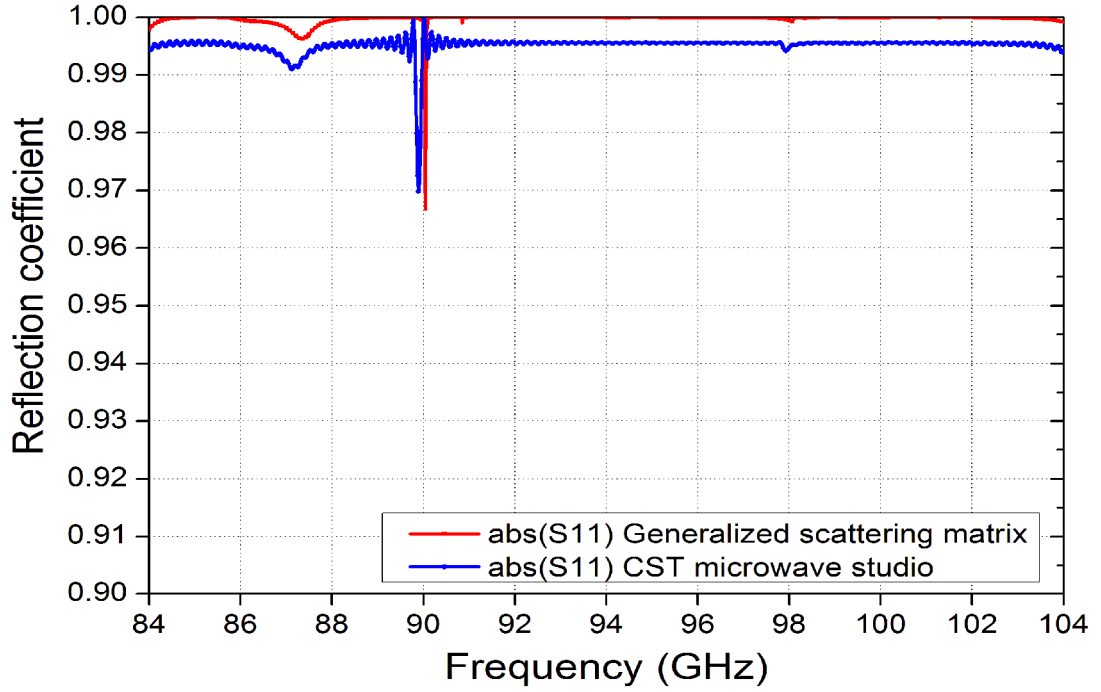
$$f(x_1, \dots, x_n) = \frac{\sum^N [A_{11}(x_1, \dots, x_n, F) - 1]^2}{N} \quad (3.25)$$

where x_1, \dots, x_n are the parameters to be optimized. F is the frequency index in the calculated frequency range, N is the number of frequencies to be calculated, A_{11} is the absolute value of the complex S_{11} parameter of the reflector for the TE_{11} mode in the calculated frequency point.

Fig. 3.6 shows the optimized result of a Bragg reflector with 18 corrugated sections. It achieved a high reflection over a much broader frequency band when comparing with the sinusoidal Bragg reflector. The outer diameter of the Bragg reflector was 8.00 mm. The diameter of the first section was set as the diameter of the helically corrugated waveguide, which was 2.60 mm. The diameter of the last section was set as 6.00 mm. The length of the first section and the last section were set as 7.19 mm and 7.37 mm, and the length between them was the optimized value of 4.09 mm.



(a)



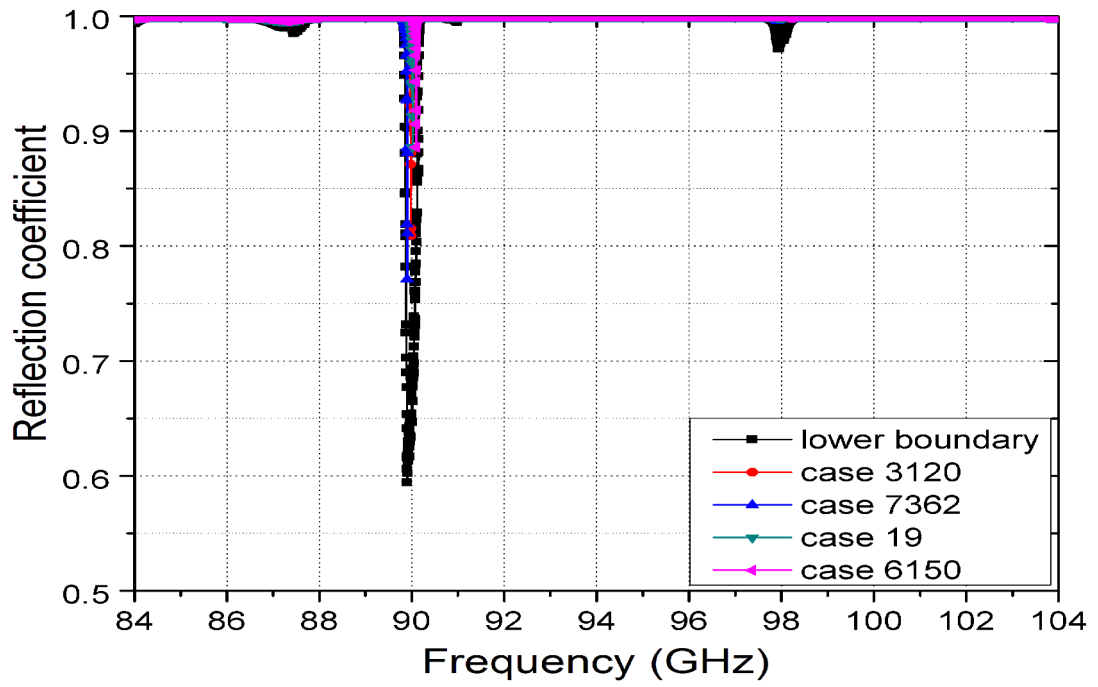
(b)

Fig. 3. 6 The geometry (a) and the scattering parameter (b) of the optimized 18-section Bragg reflector.

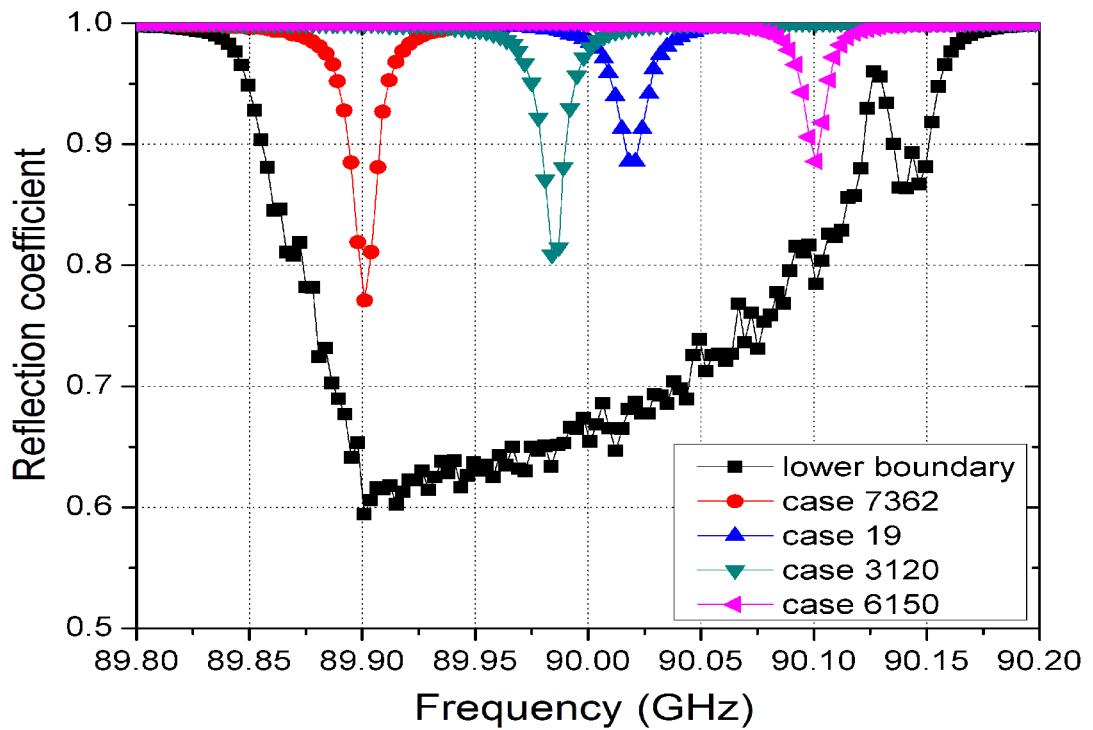
The machining tolerance of the Bragg reflector was also studied. The biggest tolerance in the machining process was set as $\pm 10 \mu\text{m}$. The evaluation function for the genetic algorithm can be revised as

$$f(x_1, \dots, x_n) = - \frac{\sum_{F=1}^N [A_{11}(x_1 - u_1, \dots, x_n - u_n, F) - 1]^2}{N} \quad (3.26)$$

where x_1, \dots, x_n are the diameters of the optimized Bragg reflector, as shown in Fig. 3.6. u_1, \dots, u_n are the machining tolerances of the corrugated sections. F is the frequency index in the calculated frequency range, N is the number of frequencies to be calculated, A_{11} is the absolute value of the complex S_{11} parameter of the Bragg reflector for the TE_{11} mode in the calculated frequency point. The lower boundary of the S_{11} parameter was recorded and is shown in Fig. 3.7. It shows that the reflection at frequency 89.8 GHz is sensitive to the tolerance which was set at $20 \mu\text{m}$.



(a)



(b)

Fig. 3. 7 The scattering parameter considering the tolerance of the Bragg reflector (a) the whole bandwidth, (b) detail view.

3.3 Side-wall coupler

3.3.1 The basics concept of the side-wall coupler

The general geometry of the side-wall coupler is a circular-to-rectangular T-junction, as shown in Fig. 3.8. The T-junction can be used in many applications, such as ortho-mode transducer (OMT) [18], polarizer and microwave filter [19]. The scattering parameters of the circular-to-rectangular T-junction can be easily calculated by software based on the finite-difference time-domain method (FDTD), such as CST microwave studio transient solver. However, finding an analytical solution for the T-junction is meaningful for it can not only greatly reduce the calculation time, especially when optimization of the structure is required but also can make high order mode information available. Several papers have been published on the calculation of the scattering matrix of the circular-to-rectangular T-junction using mode matching method or method of moments [16~19]. In our calculation, the formula developed in [17] was used.

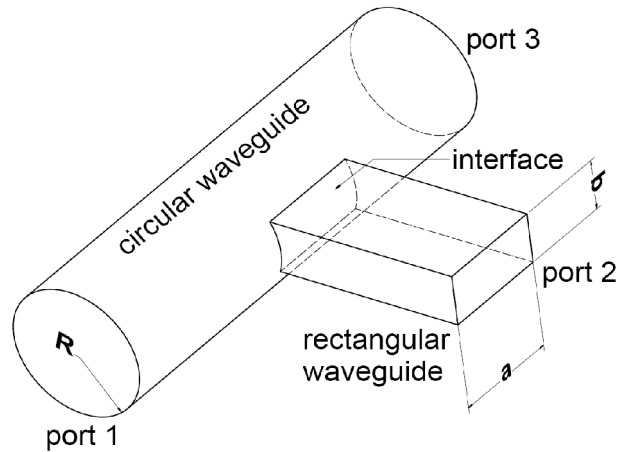


Fig. 3. 8 Geometry of the circular-to-rectangular coupler.

The transmission coefficient from TE_{10} mode of the rectangular waveguide to the TE_{11} mode of the circular waveguide can be simply evaluated by Eq. 31 in paper [19]. The formula can also be used to optimize the dimension of the rectangular slot (a ,

and b) to achieve an optimized transmission coefficient in the operating frequency range when the radius of the circular waveguide R is fixed.

A genetic algorithm was used in the optimization of the value of a and b . In the optimization, R was chosen as the real dimension of the designed gyro-BWO/TWA, which is 1.25 mm. The value range of a was chosen from 1.79 mm (cut-off frequency at 83.8 GHz for TE₁₀ mode) to 2.88 mm (a wavelength of TE₁₁ mode in the frequency of 104.0 GHz). $b = s \cdot a$, where $s = [0.4, 0.65]$. The calculation frequency range was 84 - 104 GHz. The evaluation function was set as

$$f(a, b) = \sum_F^N [A_{12}(a, b, F) - 1]^2 / N \quad (3.27)$$

where F was the frequency index in the calculated frequency range, N was the number of frequencies to be calculated, A_{12} was the absolute value of the complex S_{12} value of the TE₁₀ mode in port 2 coupled to the TE₁₁ mode in port 1. However, even under the optimized dimension, the transmission coefficient was still not good. As shown in Fig. 3.9, the transmission coefficient for TE₁₀ mode of port 2 to TE₁₁ mode of port 1 was only about -4 dB.

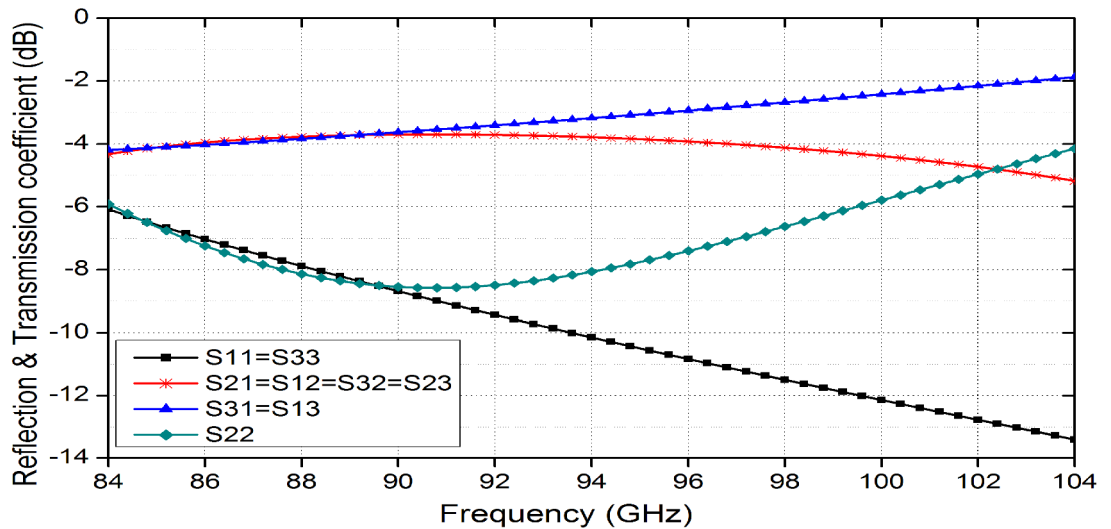


Fig. 3. 9 Reflection and transmission coefficient of the coupler ($R=1.25$ mm, $a=1.88$ mm, $b=0.98$ mm).

3.3.2 Side-wall coupler with cut-off waveguide

In practical application, a cut-off waveguide was always added to the end of circular waveguide to enhance the transmission coefficient [3, 20], as shown in Fig. 3.10.

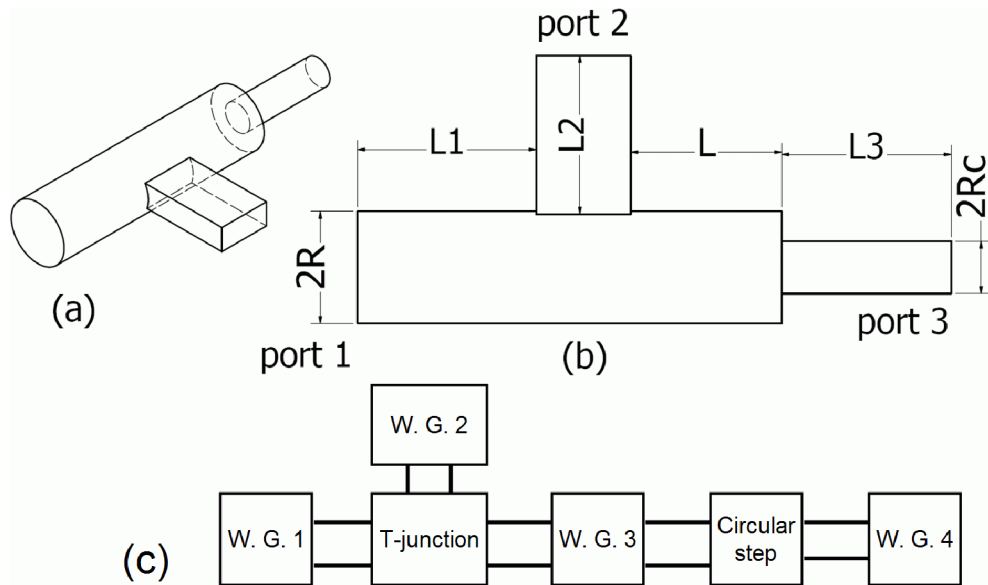


Fig. 3. 10 Circular-to-rectangular coupler with cut-off waveguide, (a) 3D view, (b) front view, (c) component connection.

A generalized scattering matrix method can be employed to analyze this structure [21]. The connection of the side-wall coupler with the cut-off waveguide is shown in Fig. 3.10 (c). The port 1 of the T-junction was connected with a circular waveguide with radius of R and length L_1 (W.G. 1). Port 2 is connected by a rectangular waveguide with dimension of a , b and length L_2 (W.G. 2). Port 3 is connected by a circular waveguide with radius R and length L and then followed by a step of circular waveguide with radius from R to R_c , then finally connected with the circular waveguide with radius R_c and length L_3 .

Among the waveguide components, the scattering matrix of a waveguide with length L , either circular or rectangular waveguide, can be written as Eq. 3.21. The scattering matrix of the circular waveguide step by using mode matching method can be

referred to section 3.2.2. The scattering matrix of the whole structure can therefore be calculated by cascading the scattering matrix of each component together.

Fig.3.11 shows a three port microwave component connecting with a two port microwave component, and the scattering matrix can be written as Eq. 3.28. The calculation process is similar to Eq. 3.22.

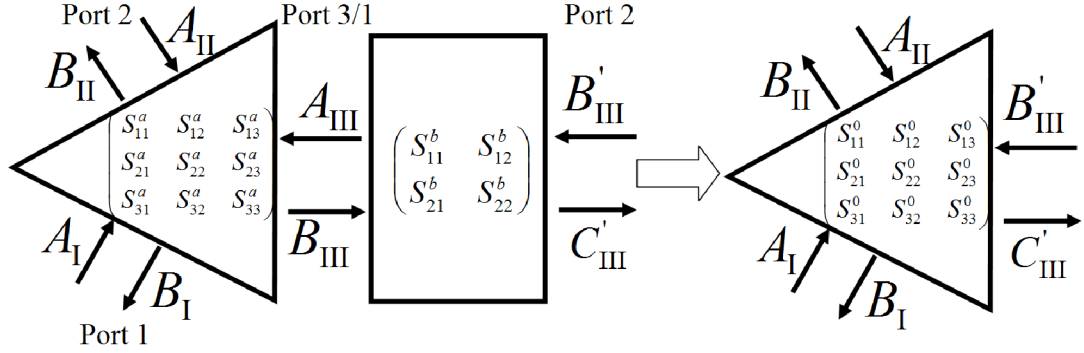
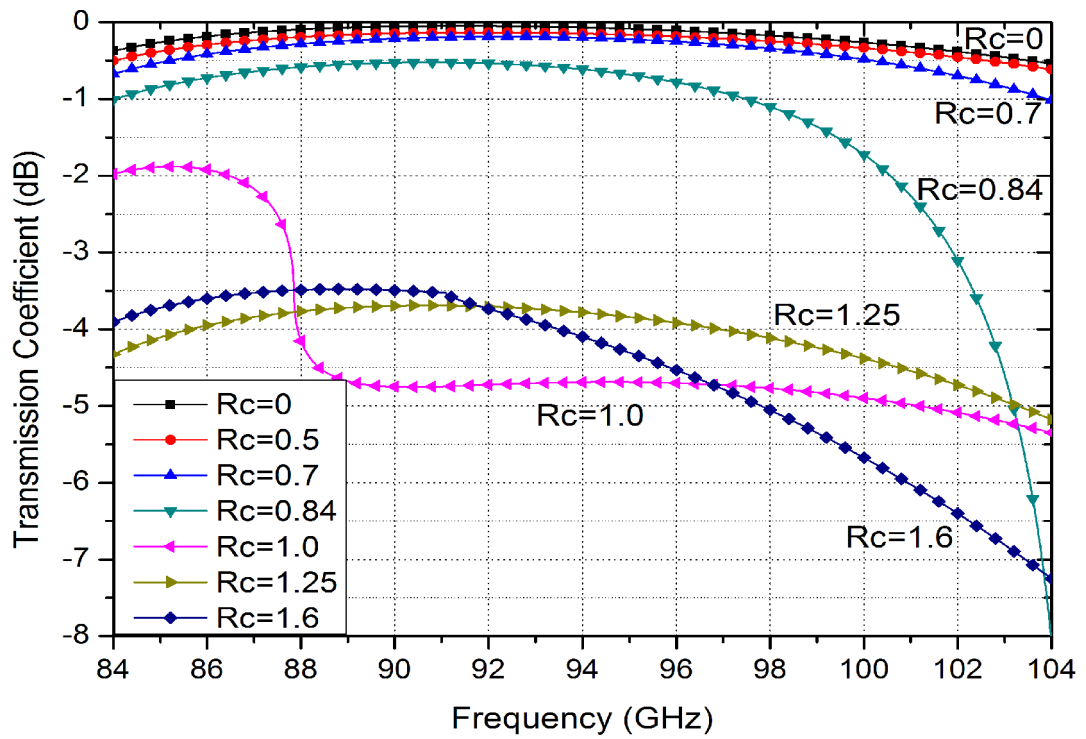


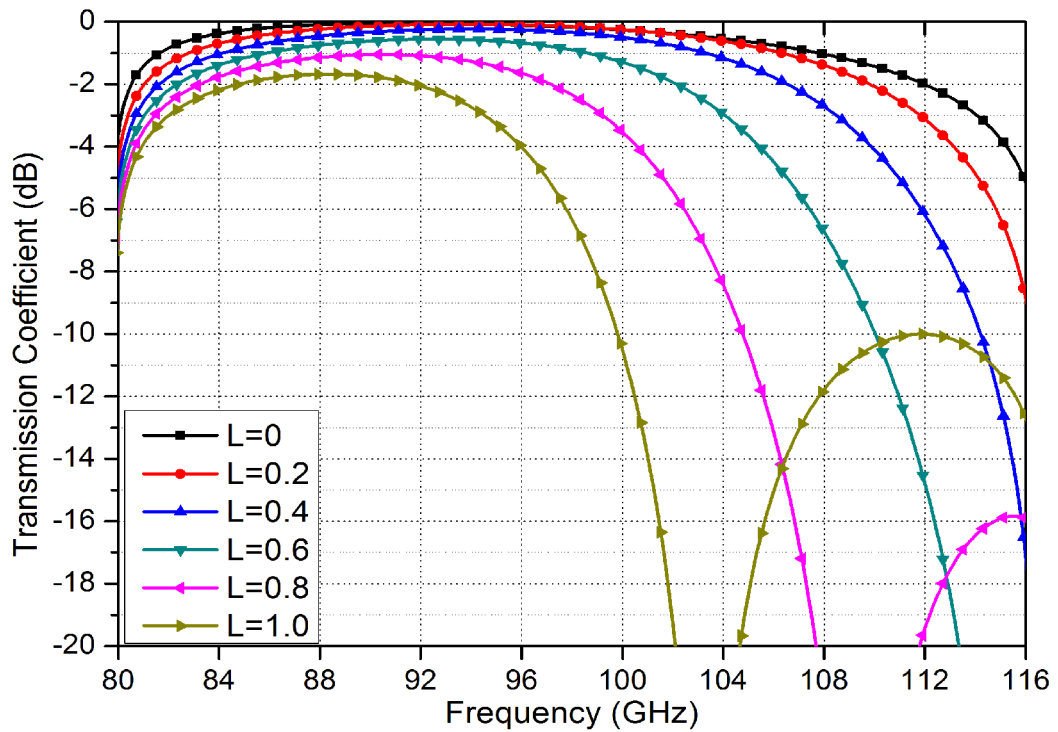
Fig. 3. 11 Cascading a 3-port S-matrix with a 2-port S-matrix.

$$\left\{ \begin{array}{l}
 S_{11}^0 = S_{13}^a W S_{11}^b S_{31}^a + S_{11}^a \\
 S_{12}^0 = S_{13}^a W S_{11}^b S_{32}^a + S_{12}^a \\
 S_{13}^0 = S_{13}^a W S_{12}^b \\
 S_{21}^0 = S_{23}^a W S_{11}^b S_{31}^a + S_{21}^a \\
 S_{22}^0 = S_{23}^a W S_{11}^b S_{32}^a + S_{22}^a \\
 S_{23}^0 = S_{23}^a W S_{12}^b \\
 S_{31}^0 = S_{21}^b (I + S_{33}^a W S_{11}^b) S_{31}^a \\
 S_{32}^0 = S_{21}^b (I + S_{33}^a W S_{11}^b) S_{32}^a \\
 S_{33}^0 = S_{21}^b S_{33}^a W S_{12}^b + S_{22}^b \\
 W = (I - S_{11}^b S_{33}^a)^{-1}
 \end{array} \right. \quad (3.28)$$

The transmission coefficient for the circular-to-rectangular waveguide connecting with a cut-off waveguide with different radius R_c and length L is shown in Fig. 3.12.



(a) ($L=0$, R_c is in mm)



(b) ($R_c=0$, L is in mm)

Fig. 3. 12 The transmission coefficient in (a) $L=0$, (b) $R_c=0$.

It can be seen from Fig. 3.12(a) that the transmission coefficient is improved by the reducing of R_c when $L=0$. A simple explanation is that the electromagnetic wave is stopped propagating to port 3 and it either travels back to port 1 or can be coupled out from port 2 to improve the transmission coefficient. As from the simulation, the higher reflection caused by the circular waveguide step, the higher transmission coefficient it can achieve. The waveguide short has a perfect reflectivity 1 in the whole frequency band and achieve the best transmission coefficient.

As shown in Fig. 3.12(b), the bandwidth of the coupler, which is defined as -1dB transmission, increases as the length is reduced of the connecting waveguide L when a waveguide short is connected ($R_c = 0$). Such cut-off waveguide has a unity reflectivity; the only parameter that can affect the bandwidth is the phase of the scattering parameter. The phase angle shift of the TE_{11} mode by a circular waveguide with length L can be evaluated by Eq. 3.21. The waveguide short has a constant phase angle shift of 180° . The overall phase shift by the cut-off waveguide is

$$P(\omega, L) = 2(\text{Angle}(e^{-(1.842/R)^2 - (\omega/c)^2}]) + 180 \quad (3.29)$$

where function Angle is used to calculate the phase angle of a complex value. The phase angle spread here is defined as

$$P_s(L) = 360 - (|P(L, \omega_1)| + |P(L, \omega_2)|) \quad (3.30)$$

where ω_1 and ω_2 are the start and stop frequency in the calculation. Fig. 3.13 shows the relationship between the phase angle spread and the frequency bandwidth for the coupler with a waveguide short. It can be seen that the phase angle spread in the frequency range becomes larger as L increases. The larger the phase angle spread, the narrower the bandwidth is. When $L=0$, $P(\omega)$ is a constant, no phase angle spread exist, thus it has the maximum bandwidth. Another interesting result is that the centre of the bandwidth is shifted as L changes. Thus it is possible for us to move the bandwidth to our desired range by changing the value of L .

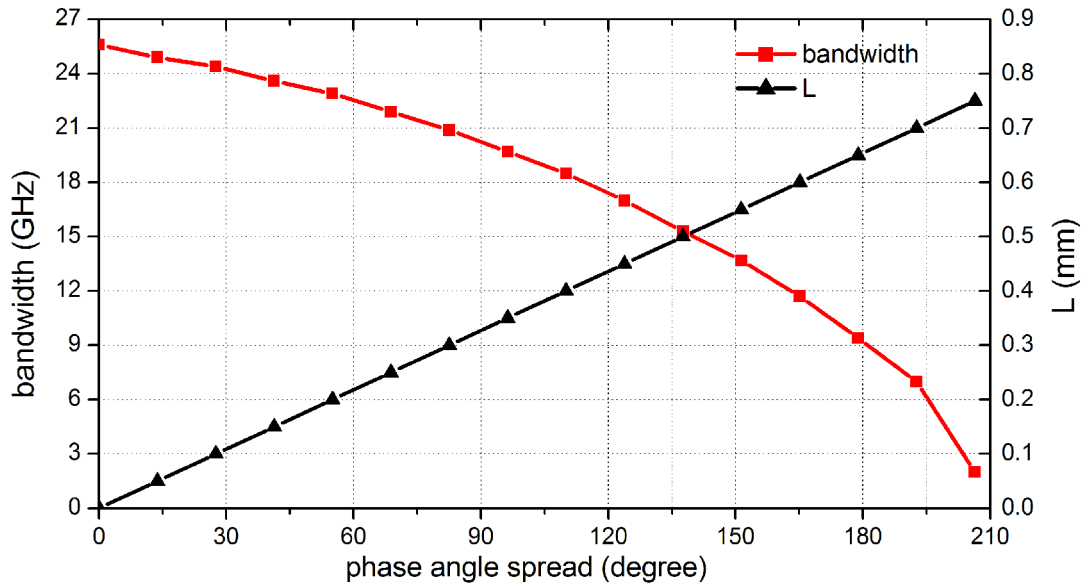


Fig. 3. 13 The phase angle spread vs. the bandwidth.

The cut-off waveguide is a normal solution to improve the transmission coefficient. The requirement is that the radius of the cut-off waveguide needs to be reasonably small. For a low frequency microwave device, such as the X-band gyro-BWO/TWA, it is easier to make the radius of the cut-off waveguide small to satisfy the requirement while keeping it larger than the radius of the electron beam generated from the electron gun. For the cusp electron gun designed for the W-band gyro-BWO/TWA, the average radius of the electron beam is about 0.42 mm when beam alpha is 1.56 [22], and the radius of the electron beam becomes larger with the increase of the alpha value. When conducting high alpha experiments, the cut-off waveguide will stop part of the electron beam from passing through, and seriously affect the performance of the device. It is important that if we are able to find a structure that can not only act like a cut-off waveguide, especially a waveguide short, but also let the electron beam pass through freely. In our application, the minimum radius of the structure is desired to be larger than beam tube of the W-band gyro-BWO/TWA, which is 1.25 mm.

3.3.3 Side-wall coupler with Bragg reflector

It is well known that, the structure with rectangular corrugated sections can act as a filter if it is properly designed. It can achieve high reflectivity in a wide frequency band just like a waveguide short. The detail of the Bragg reflector can be referred in section 3.2.

However, the phase spread of a normal Bragg reflector usually covers the whole phase range from -180° to 180° . As can be seen from Fig. 3.13, a large phase spread will limit the frequency band. Therefore, the designed Bragg reflector requires not only have a high reflectivity but also a small phase spread in the operating frequency range.

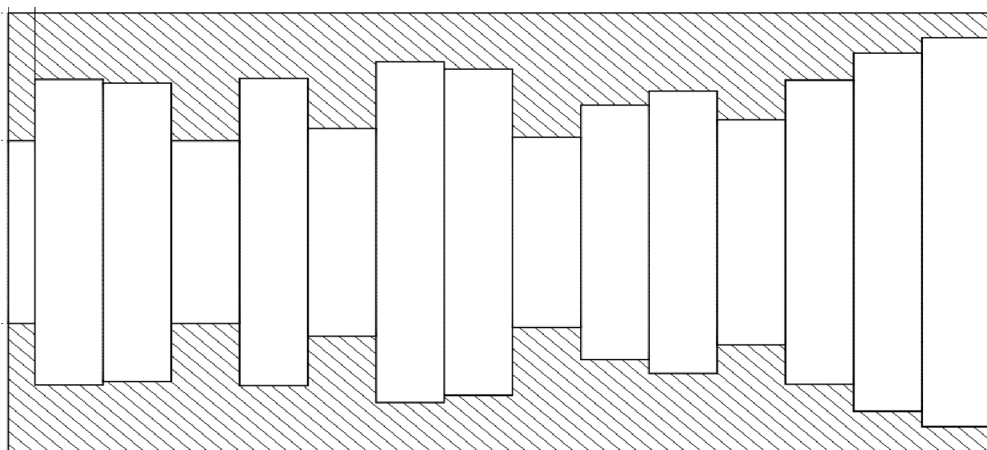
To find such a Bragg reflector, the optimization program using a genetic algorithm was used to optimize the parameters, including the radii and the length of the corrugated sections. The radius of the corrugated section was limited in the range of [1.25, 2.50 mm]. The length of the corrugated section was chosen in the range of [0.50, 2.00 mm]. And the evaluation function for the genetic algorithm was chosen as

$$f(x_1, \dots, x_n) = \frac{\sum_F^N [A_{11}(x_1, \dots, x_n, F) - 1]^2}{N} + W \cdot \frac{\sum_F^N [P_{11}(x_1, \dots, x_n, F) - \overline{P_{11}}(x_1, \dots, x_n, F)]^2}{N} \quad (3.49)$$

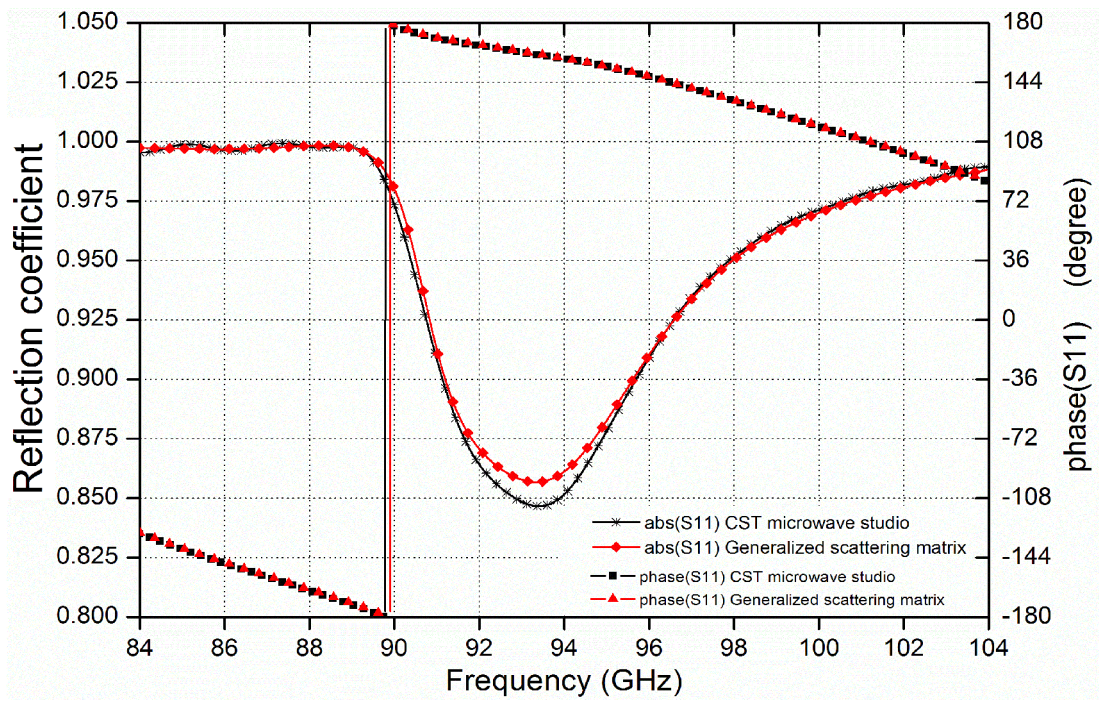
where x_1, \dots, x_n are the parameters to be optimized. F is the frequency index in the calculated frequency range, N is the number of frequencies to be calculated, A_{11} is the absolute value of the complex S_{11} parameter of the Bragg reflector for the TE_{11} mode in the calculated frequency point, P_{11} is the phase angle of the complex value of S_{11} , $\overline{P_{11}}$ is the average phase angle, and W is the weight of the phase angle spread compared with the reflectivity spread. In the simulation, we found that the phase angle spread has greater effect on the overall transmission coefficient. Therefore we chose the weight value as 2. A Bragg reflector with more sections can achieve wider

bandwidth of high reflectivity, but it is harder to get a small phase angle spread. In our optimization, the section number was chosen as 14. Fig. 3.14 shows the geometry and the result of the optimized structure. The reflectivity is larger than 0.85 and the phase angle spread is about 133° . From Fig. 3.13, it can be predicted that the bandwidth will be in the range of 15-18 GHz.

The Bragg reflector was then connected to the circular-to-rectangular coupler. The transmission coefficient of the whole structure is shown in Fig. 3.15. The -1 dB transmission band is from 83.5 - 101.0 GHz, about 17.5 GHz. It is excellent in the gyro-TWA operating frequency range from 90 - 100 GHz. However, the bandwidth is still not enough for the gyro-BWO. Since 17.5 GHz bandwidth was the maximum we could achieve when the beam tube was limited at 1.25 mm, we can only scale down the whole structure to achieve a ~ 20 GHz bandwidth. Fig. 3.15 shows the transmission coefficient when the scale factor is 0.96 (the radius of the beam tube is 1.20 mm), the bandwidth is about 19.5 GHz (from the result of CST microwave studio), and the other S parameters are shown in Fig. 3.15 (b). And the length of the corrugated sections also need some slight adjustment to get the best result. In this structure, the length of the first corrugated section was changed from 0.30 mm to 0.38 mm, and the length of the rest corrugated sections was changed from 0.77 mm to 0.76 mm.

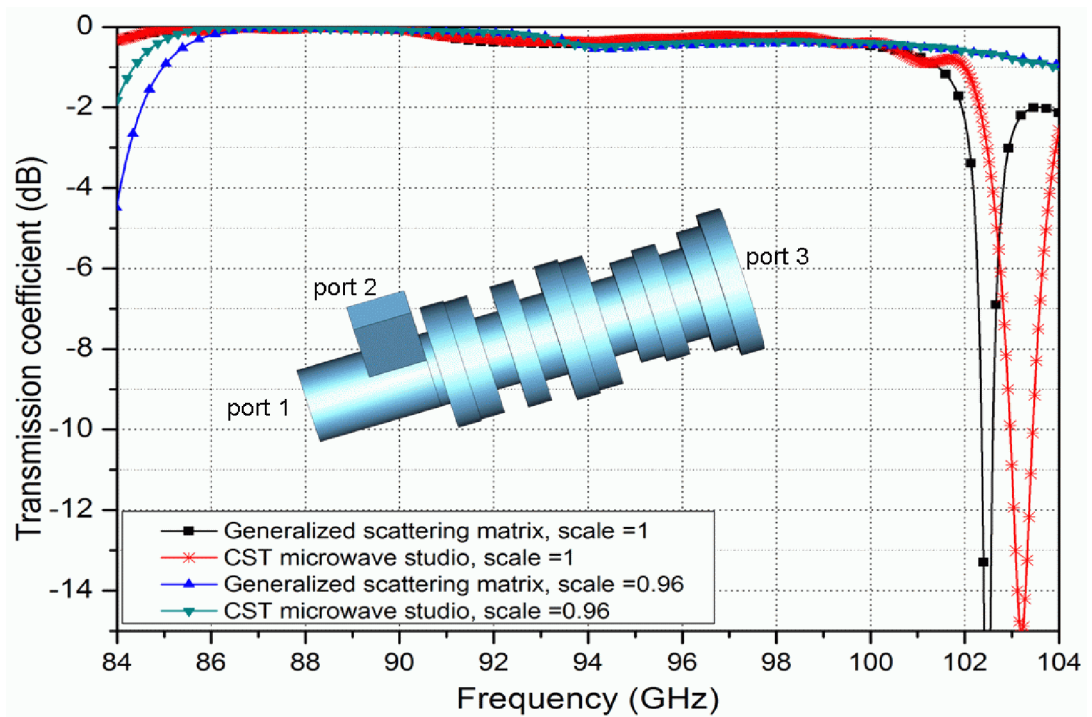


(a)

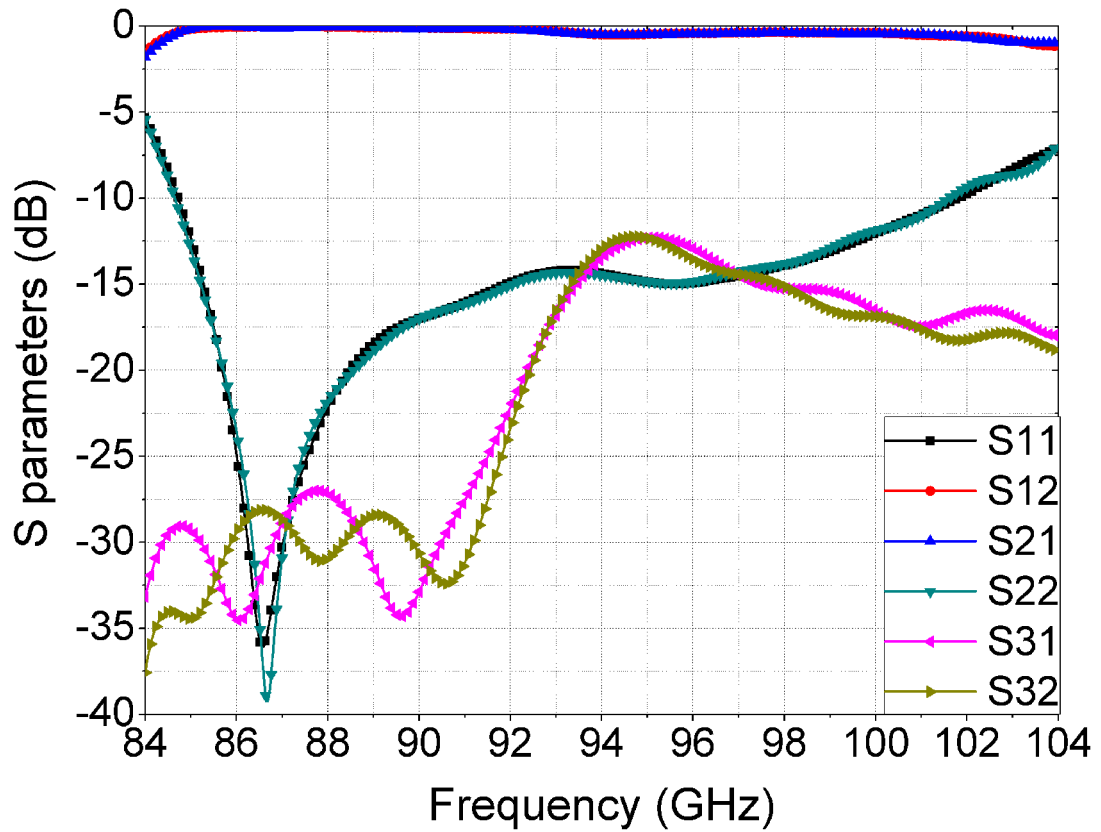


(b)

Fig. 3. 14 The geometry (a) and S-parameters (b) of optimized Bragg reflector with 14 corrugated sections.



(a) The simulation results by CST microwave studio and mode-matching method;



(b) the scattering parameters of the coupler;

Fig. 3. 15 The transmission coefficient of the whole structure.

Another optimization calculation was carried on by putting the whole coupler structure into the calculation. It was much more time consuming than only optimizing the Bragg reflector. However, we did not need to look at the phase angle spread caused by the Bragg reflector. The parameter we were concerned with was the transmission coefficient from TE_{10} mode in port 2 to TE_{11} mode in port 1. Fig. 3.16 shows the optimization results when the radius of the beam tube is 1.25 mm. It has the bandwidth of 18.0 GHz (from the result of CST microwave studio). The dimensions of the Bragg reflector in Fig. 3.15 and Fig. 3.16 are quite different. That means that there exist many possible solutions for such problem.

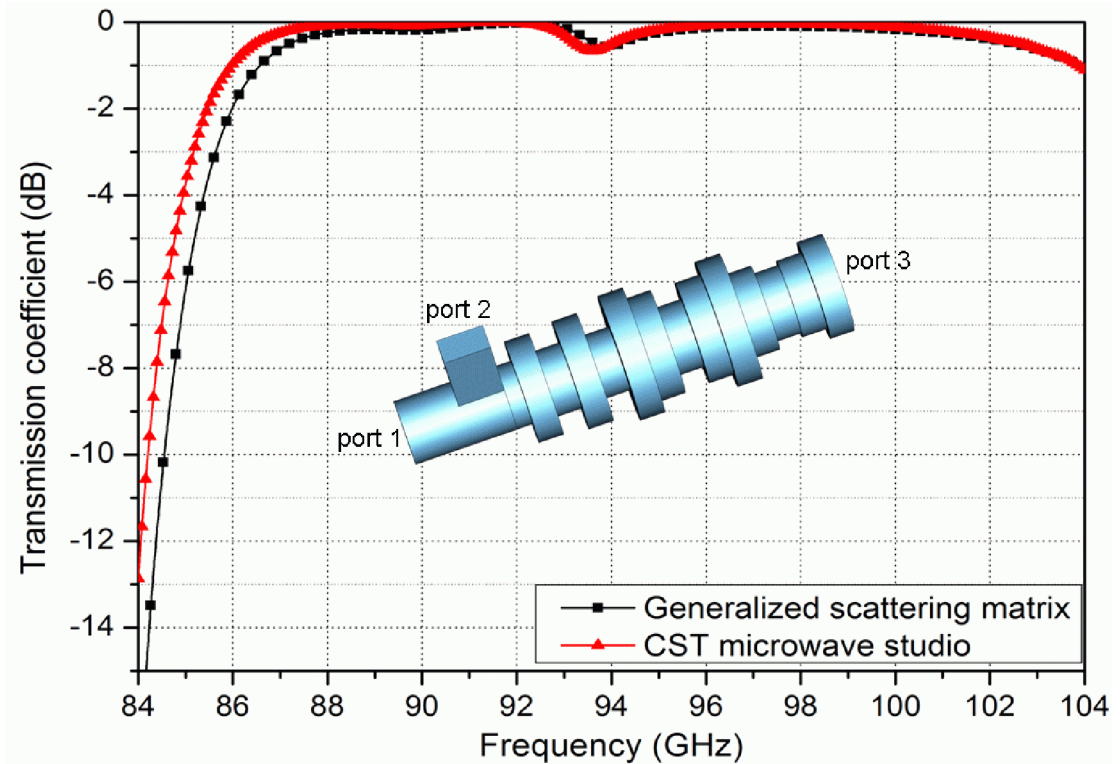


Fig. 3. 16 The results by optimizing the whole structure.

In our final design, the radius of the beam tube was chosen as 1.20 mm as it could provide wider bandwidth. The effect of the tolerance of the input/output coupler from machining was also calculated. Each parameter of the structure was with a machining tolerance between $\pm 5\mu\text{m}$. The lower boundary of the coupler coefficient was shown in Fig. 3.17. Case 3991 in Fig. 3.17 indicates one of the simulation results caused by the tolerance. It was found that the tolerance of the length of the first corrugated section brought the most serious effect to the transmission coefficient. It caused the shift of the frequency band, as we predicted in section 3.3.2. The other parameters did not cause much effect on the transmission coefficient.

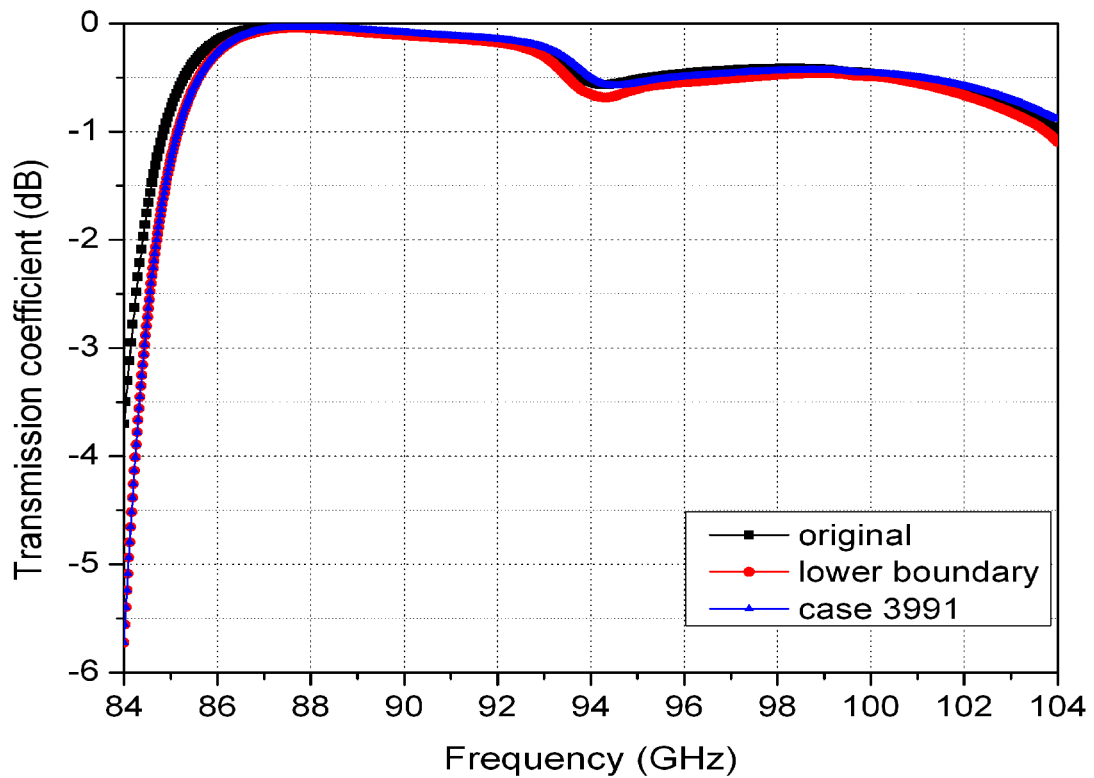


Fig. 3. 17 The transmission with consideration of the tolerances.

3.4 Manufacture and measurement results

The manufacture of the microwave components in W-band are difficult jobs because of the small size and tight tolerances required. As from the simulation, the tolerances of the dimensions should be within $10\ \mu\text{m}$. Also, for gyro-BWO experiments, the vacuum level is kept under 10^{-7} mBar in order to keep the thermionic cathode in a stable working condition. The vacuum sealing requirement makes the components even harder to be fabricate because some of them can not be machined in a single copper piece which results in a complicated brazing process.

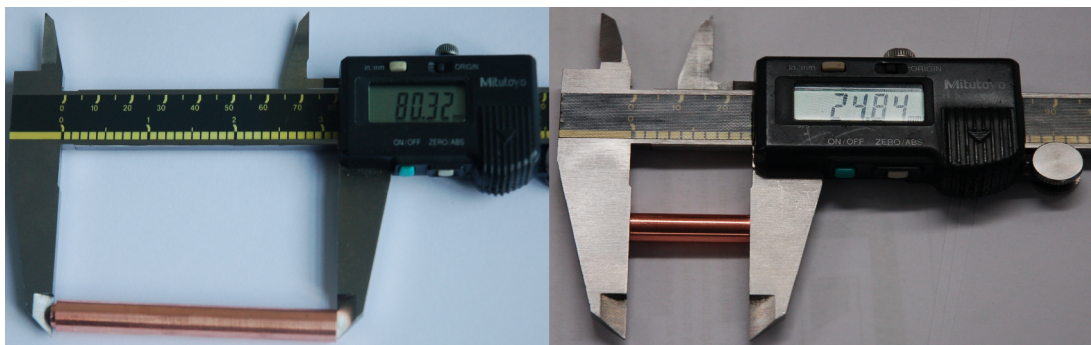
The Bragg reflectors were machined by an electrical chemical method. In this method, the positive formers of the components are machined from Aluminium, then copper was electroformed on the former, finally the Aluminium mandrel was dissolved away by an alkali solution so that the copper components are formed. The microwave components in this method are made by a single copper piece and they

are inherent vacuum tight. The drawback of this method is that the grown copper layer is not as solid as the copper bar because the component is actually grown layer by layer. It has some risk that it can not be brazed well with the other components like the pillbox window as the thermal properties of joining material do not match very well.

The Aluminium former of the Bragg reflector are shown in Fig. 3.18. The first one in Fig. 3.18(a) is the 18-section Bragg reflector placing between the interaction region and the depressed collector. The second one is the 14-section Bragg reflector for the side-wall input coupler. Fig. 3.18(b) and Fig.3.18(c) are the Bragg reflector after growing copper on the Aluminium former.



(a)



(b)

(c)

Fig. 3. 18 The machining of the Bragg reflectors (a) the Aluminium former, (b) the 18-section Bragg reflector (c) the 14-section Bragg reflector.

A network analyzer was used to measure the microwave properties of the components. The network analyzers are the most complex and versatile pieces of test equipments in microwave engineering. They have been widely used for research purpose and the product testing. There are two types of network analyzers; one is scalar network analyzer (SNA) which can only provide the amplitude of the transmission and reflection of the test waveguide components, the other is vector network analyzer (VNA) which can not only provide the amplitude information but also the phase information.

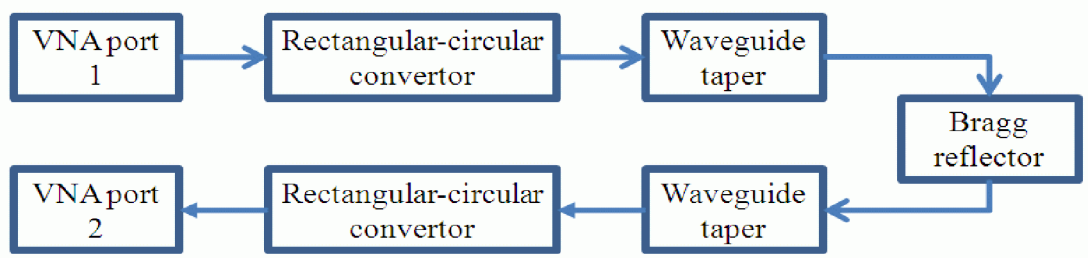
In the measurement, the Anritsu ME7808B VNA was used to measure the components, which is shown in Fig. 3.19. The ME7808B broadband VNA is a high performance measurement instrument that covers the frequency range from 40 MHz to 110 GHz in a single fast sweep. It was built on the advanced technology of the Anritsu Lightning 40 MHz to 65 GHz VNA and the 65 - 110 GHz millimetre Wave modules using a unique multiplexing coupler design. It consists of a Lightning 37397D 65 GHz VNA; two millimetre wave modules (3642A series) - extended W-band (WR-10) and two 20 GHz ultra-low phase noise frequency sources. With different extended oscillation heads its frequency range of operation can be extended to cover 140 - 220 GHz (WR-05 heads) and 325 - 500 GHz (V02.2VNA2-T/R 325 - 500 GHz high frequency heads) [23].

The setup for S-parameter measurement for the Bragg reflector used at the end of the interaction region is shown in Fig. 3.20 (a). As the output of the VNA port is a rectangular waveguide, two rectangular to circular waveguide converters were needed at both ends of the VNA output port. And also the waveguide holders at the both sides were used to keep the alignment of the Bragg reflector. Before measuring the Bragg reflector, the scattering parameters of the other components are measured as background. Then scattering parameters of the Bragg reflector are calculated from the results with and without the Bragg reflector. The results are shown in Fig. 3.20 (b) and Fig. 3.20 (c). The mode-matching and CST microwave studio simulation results

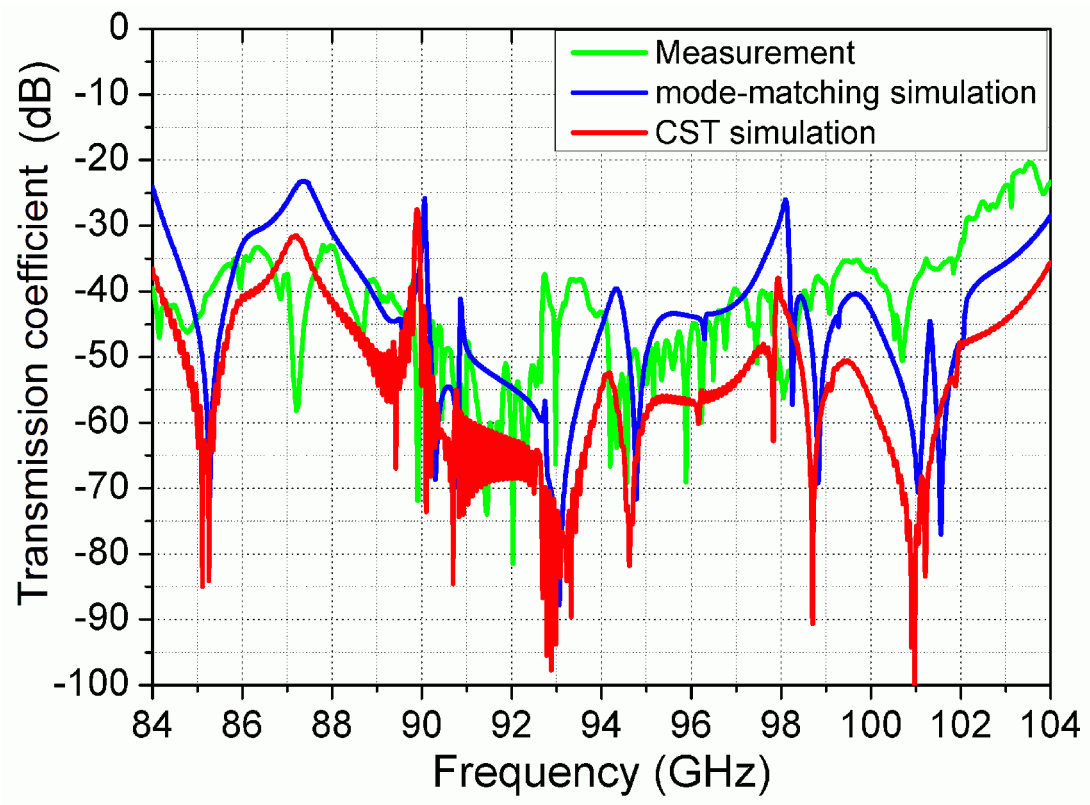
on the S_{21} agree well with the measurement result. The S_{11} measurement results agree well with the simulation results except in the frequency range 96 - 100 GHz. It is caused by the imperfect alignment of the circular taper and the Bragg reflector that make the energy in this frequency range trapped inside the Bragg reflector. This problem also exists when measuring the 14-section Bragg reflector as well as the microwave windows. A further improvement of the alignment is very difficult due to the small dimensions in the W frequency band. Even a small angle in the misalignment will cause a big difference in the measurement.



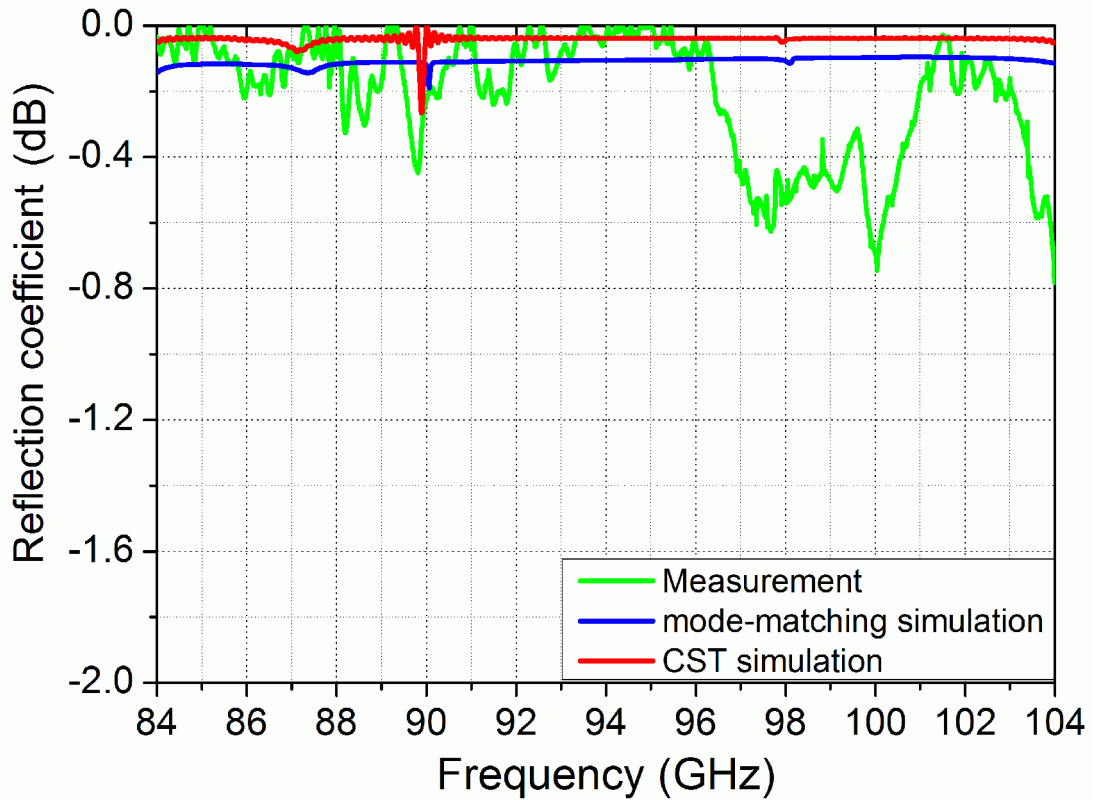
Fig. 3. 19 The Anritsu ME7808B VNA system.



(a) The measurement setup of the Bragg reflector;



(b) The transmission of the Bragg reflector;



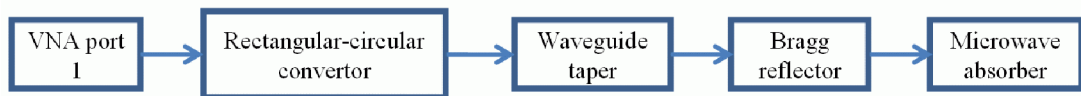
(c) The reflection of the Bragg reflector;

Fig. 3. 20 The measurement results of the Bragg reflector.

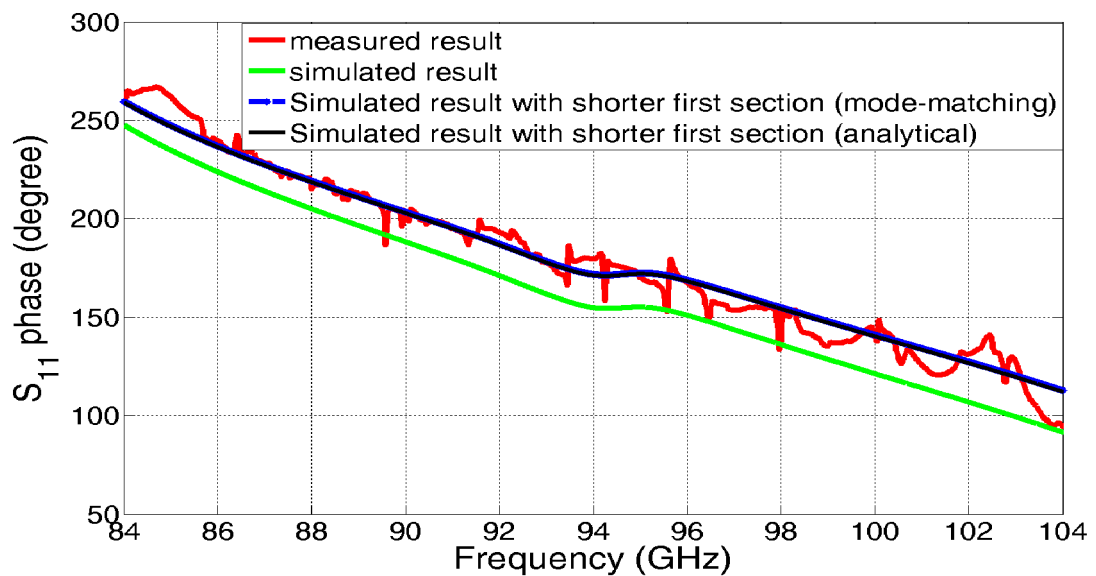
The one port measurement is applied to the Bragg reflector for the input coupler due to the lack of the extra circular waveguide taper shown in Fig. 3.21. Only the amplitude and the phase of the S_{11} can be measured in this case. The phase information is more important as discussed in section 3.3. To get the phase information of the Bragg reflector, the rectangular-to-circular converter, the waveguide taper and the microwave absorber were first measured as background and then the whole structure was measured. The phase of the Bragg reflector can be obtained by subtracting the two phase measurement. There are some differences between the simulation and the measurement. Then it is found that the length of the first section of the machined Bragg reflector is shorter than the design due to the inaccurate machining. The difference of the lengths is 0.12 mm from the simulation

prediction, and it matches with the practical measurement. A thin copper ring with the same dimension of the first Bragg section can then be used to fix this problem.

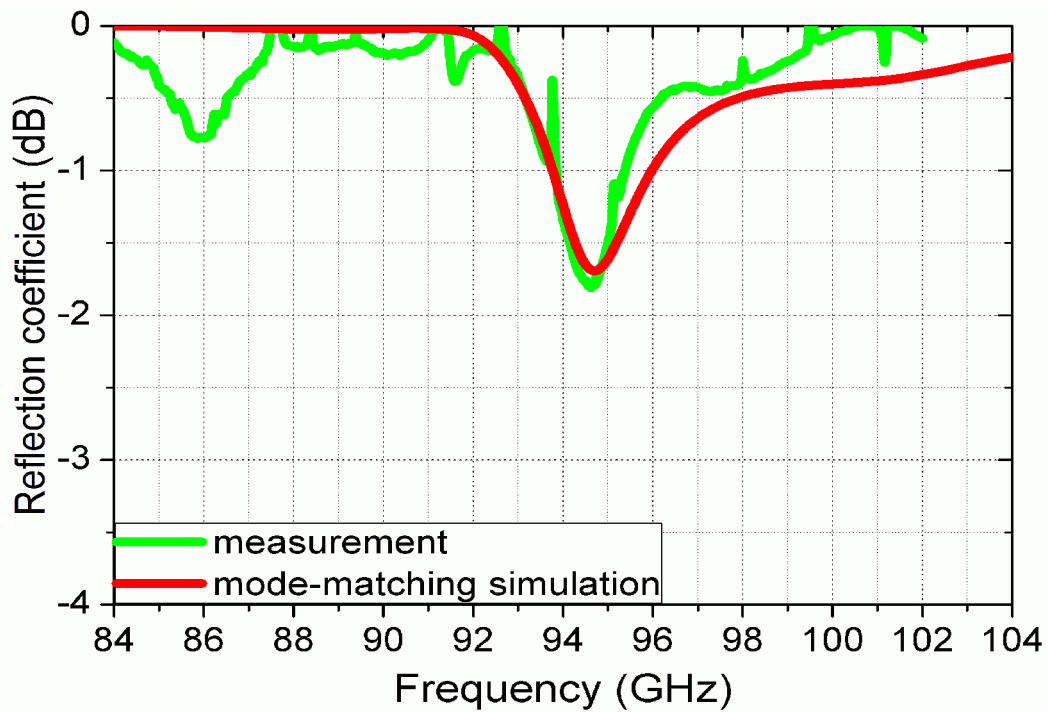
The reflection result had the same trend with the simulation. The difference could also be caused by the imperfect alignment of the taper and the Bragg reflector. Also, the microwave absorber is not ideal as it will cause additional reflection back to the measurement port.



(a) The measurement setup of the Bragg reflector for input coupler;



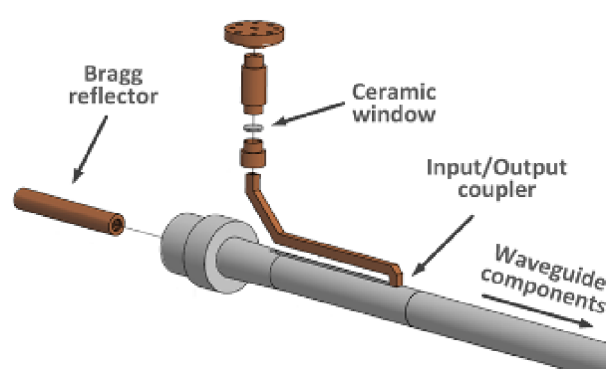
(b) The phase of S_{11} of the Bragg reflector;



(c) The reflection of the Bragg reflector;

Fig. 3. 21 The measurement results of the Bragg reflector.

In practical experimental setup, the space for the input coupler is quite limited due to the small gap between the beam tube and the cavity solenoid. There is not enough space to put the pillbox window close to the side-wall coupler and it has to be moved far away. A long waveguide bend is thus necessary to connect the input coupler and the pillbox window. It also included a rectangular taper from size $2.00 \text{ mm} \times 1.27 \text{ mm}$ to a standard waveguide with size $2.54 \text{ mm} \times 1.27 \text{ mm}$. The side view of the input coupler is shown in Fig. 3.22.



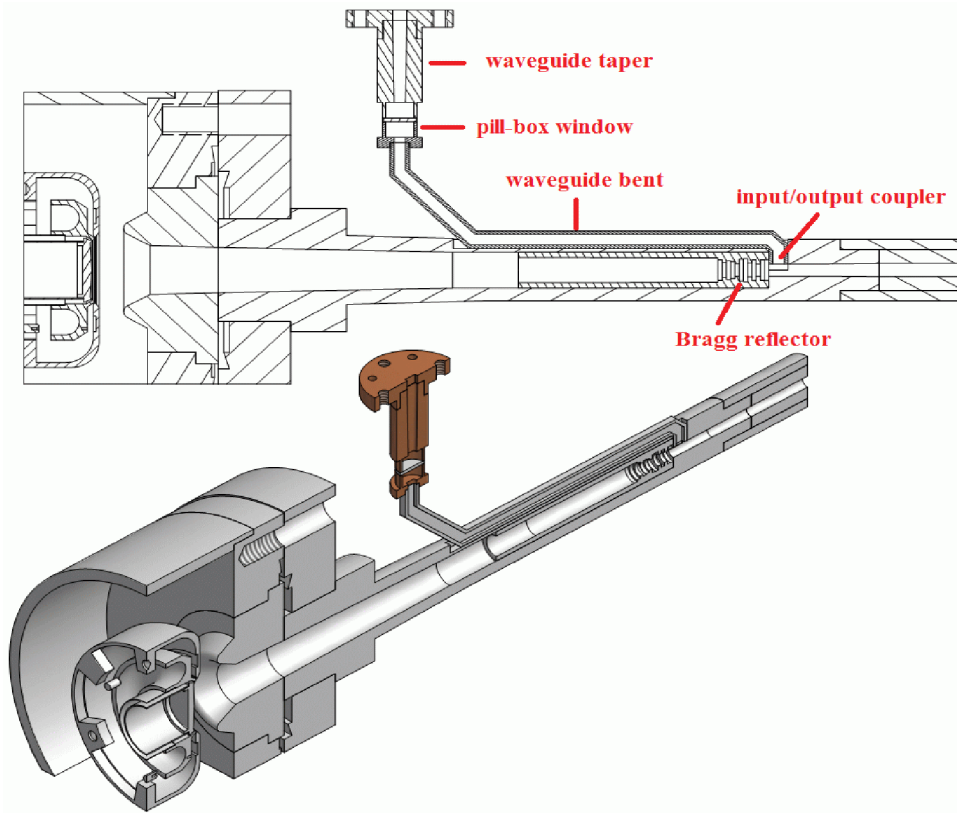


Fig. 3. 22 The CAD drawing and the machining of the input coupler.

Two methods were used to machine the waveguide bend. One is to separate the waveguide into two copper pieces, and each piece was machined by using the wire cutting technology. The final pieces are shown in Fig. 3.23. The later two pieces

were brazed together to make them a complete waveguide. With this method, the bend waveguide is easy to be machined and small tolerance can be achieved, however, it has more chance of vacuum leakage because of the large brazing area. Fortunately, both of the methods worked well in practical machining and we picked the one with the best vacuum sealing and with low dimensional tolerance.



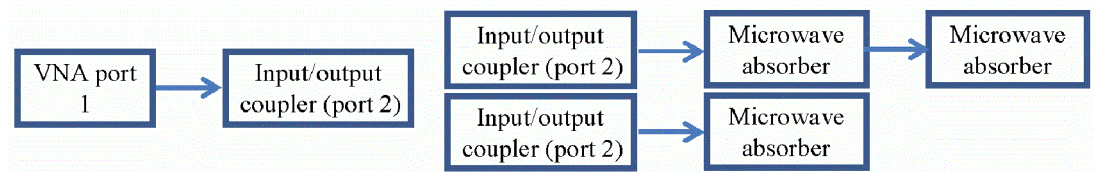
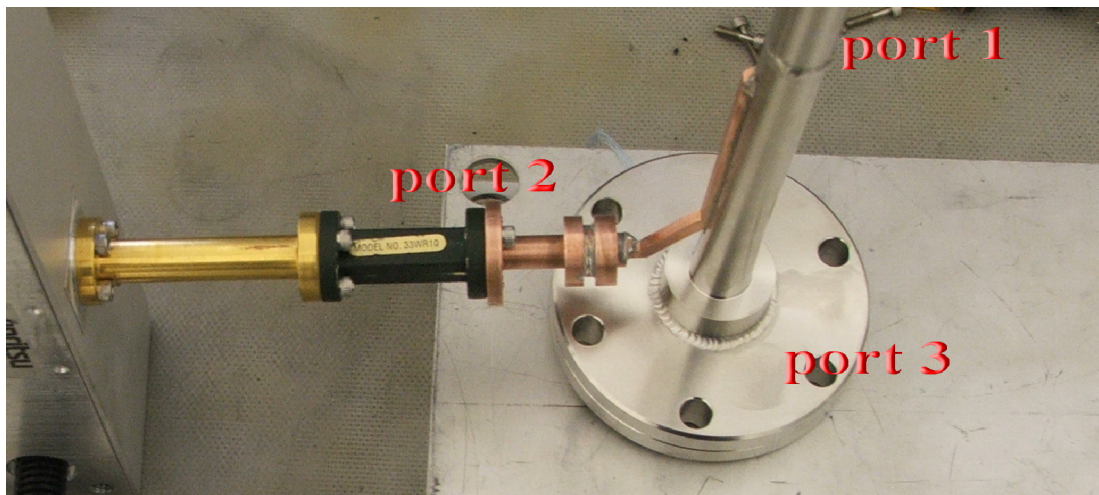
Fig. 3. 23 The waveguide bend.

The input coupler was manufactured in the beam tube which is much more oversized than the waveguide port, therefore, the full-port measurement can not be applied to the input coupler. The one port measurement with the setup shown in Fig. 3.24(a) was used. The VNA measurement port was connected to the pillbox window. The Bragg reflector was inserted into the beam tube from port 3. The microwave absorber was placed after the Bragg reflector and pressed tightly to make sure the Bragg reflector had tight connection with the input coupler. A long waveguide taper that tapers the radius from 1.2 mm to 4.0 mm was placed in port 1 to avoid the big discontinuity inside the beam tube. The microwave absorber was placed after the waveguide taper to reduce the reflection between the waveguide taper to free space.

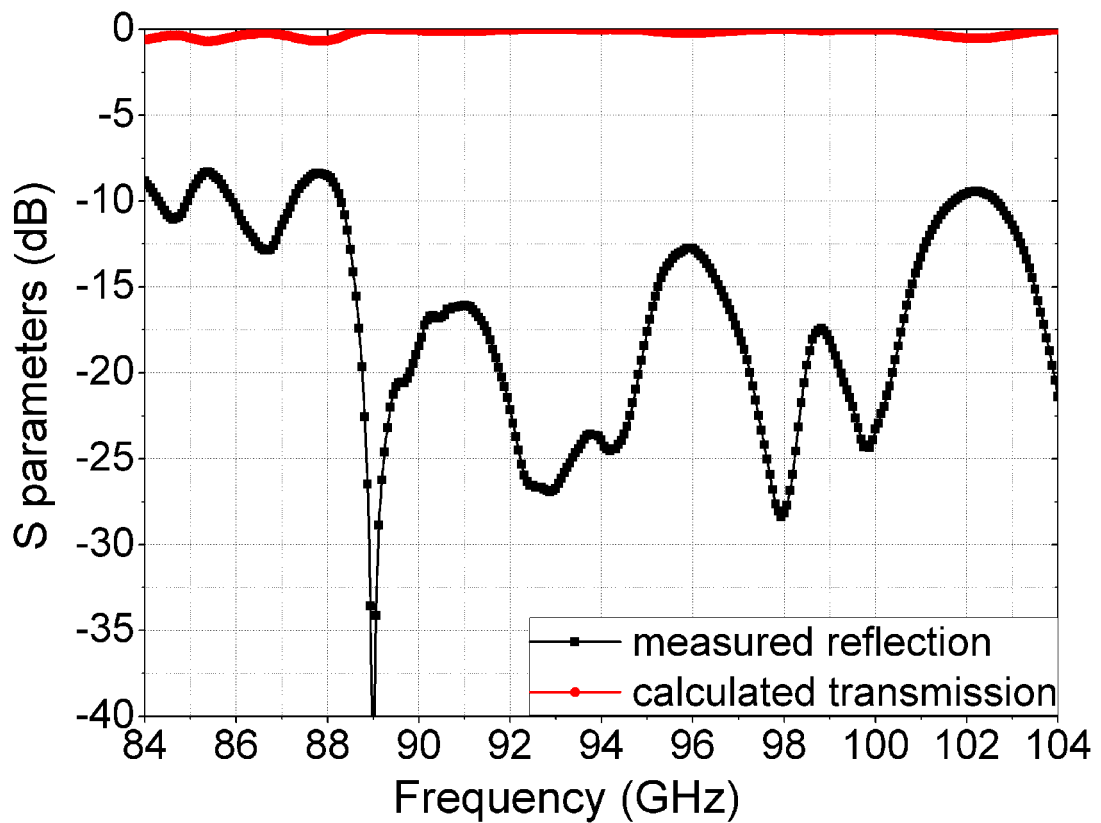
In the one port measurement, only the reflection at port 2 can be measured. In the measurement, the reflection of the input coupler at port 2 can achieve less than -13 dB at most of the frequency band. The big reflection in the frequency range of 84 - 88 GHz and 102 - 104 GHz is due to the high reflection of the pillbox window as it is specifically designed for the gyro-TWA to achieve low reflection in 90 -100 GHz. The transmission between port 1 and 2 is not able to obtain from the measurement directly, however, it can be calculated from the convergence of the energy if no loss is considered.

$$|S_{12}|^2 + |S_{22}|^2 + |S_{32}|^2 = 1 \quad (3.50)$$

From the simulation, It can be approximate that $|S_{32}| \ll |S_{12}|$, then the transmission can be calculated from the reflection in port 2. The result is shown in Fig. 3.24(b). It is around -1.0 dB and satisfied the designing requirement.



(a) The measurement setup of the coupler with the pillbox type window;



(b) the simulated and measured results of the coupler;

Fig. 3. 24 The results of the input coupler.

3.5 Conclusion

In this chapter, the principle of the Bragg reflector with sinusoidal ripple and rectangular corrugated sections were studied. A Bragg reflector with 18 rectangular corrugated sections was optimized to reflect the generated microwave to the upstream direction and then it was extracted out by a side-wall circular-to-rectangular coupler. The side-wall circular-to-rectangular coupler was designed and optimized to achieve a high transmission coefficient for a W-band gyro-BWO working in frequency range of 84 - 104 GHz as well as a W-band gyro-TWA working in frequency range of 90 - 100 GHz. In the design, a Bragg reflector was used instead of a cut-off waveguide to let the electron beam pass freely

into the interaction region. The designed side-wall coupler achieved a bandwidth (-1 dB transmission coefficient) of 17.5 GHz when the radius of the beam tube was 1.25 mm and 19.5 GHz when the radius of the beam tube was 1.20mm. The manufacture and measurement of the microwave components are also described in this chapter. The measured results of the Bragg reflectors show a good agreement with theory, and the input coupler with a pillbox window, which is designed to get a low reflection in the frequency range of 90 - 100 GHz, can achieve an average -13 dB transmission over the frequency band.

References

- [1] W. He, A. D. R. Phelps, A.W. Cross, C. R. Donaldson, and K. Ronald, “A W-band gyrotron travelling wave amplifier using a helically corrugated waveguide,” in Proc. 17th High-Power Particle Beams Conf. (Beams), Xi’an, China, 2008, p. 646.
- [2] G. G. Denisov, V. L. Bratman, A. W. Cross, W. He, A. D. R. Phelps, K. Ronald, S. V. Samsonov, and C. G. Whyte, “Gyrotron Traveling Wave Amplifier with a Helical Interaction Waveguide”, Phys. Rev. Lett., vol. 81, no. 25, pp. 5680-5683, December, 1998.
- [3] V. L. Bratman, A.W. Cross, G. G. Denisov, W. He, A. D. R. Phelps, K. Ronald, S.V. Samsonov, C. G. Whyte, and A. R. Young, “High-Gain Wide-Band Gyrotron Traveling Wave Amplifier with a Helically Corrugated Waveguide”, Phys. Rev. Lett., vol. 84, no. 12, March, 2000.
- [4] N. S. Ginzburg, A. A. Kaminsky, A. K. Kaminsky, et al, “High-Efficiency Single-Mode Free-Electron Maser Oscillator Based on a Bragg Resonator with Step of Phase of Corrugation”, Phys. Rev. Lett., vol. 84, no. 16, pp. 3574-3577, 2000.
- [5] T. J. Orzechowski, B. R. Anderson, J. C. Clark, et al, “High-efficiency Extraction of Microwave Radiation from a Tapered-wiggler Free-electron Laser”, Phys. Rev. Lett., vol. 57, no. 17, pp.2172-2175, 1986.
- [6] L. Solymar, “Spurious Mode Generation in Nonuniform Waveguide”, IRE Trans. Microwave Theory Tech., vol. 7, no. 3, pp. 379-383, 1959.
- [7] G Reiter, “Generalized Telegraphist’s Equation for Waveguides of Varying Cross-section”, Convention on Long Distance Transmission by Waveguide, London, England, January 19-30, 1959.
- [8] A.W. Fliflet, L.R. Barnett, J.M. Baird, “Mode Coupling and Power Transfer in a Coaxial Sector Waveguide with a Sector Angle Taper”, IEEE Trans. Microwave

- Theory and Tech., vol. 28, no. 12, pp. 1482 - 1486, 1980.
- [9] R. B. McCowan, A. W. Fliflet, S. H. Gold, et al, "Design of a waveguide resonator with rippled wall reflectors for a 100GHz CARM oscillator experiment", *Int. J. Electronics*, vol. 65, no. 3, pp. 463 – 475, 1988.
- [10] C.K. Chong, D.B. McDermott, M.M. Razeghi, et al, "Bragg reflectors", *IEEE Trans. Plasma Sci.*, vol. 20, no. 3, pp. 393-402, 1992.
- [11] G.L. James, "Analysis and Design of TE₁₁-to-HE₁₁ Corrugated Cylindrical Waveguide Mode Converters", *IEEE Trans. Microwave Theory Tech.*, vol. 29, no. 10, pp. 1059-1066, 1981.
- [12] Tak Sum Chu and T. Itoh, "Generalized Scattering Matrix Method for Analysis of Cascaded and Offset Microstrip Step Discontinuities", *IEEE Trans. Microwave Theory and Tech.*, vol. 34, no. 2, pp: 280- 284, 1986.
- [13] J. M. Neilson, P. E. Latham, M. Caplan, et al, "Determination of the Resonant Frequencies in a Complex Cavity Using the Scattering Matrix Formulation", *IEEE Trans. Microwave Theory and Tech.*, vol. 37, no. 8, pp. 1165-1170, 1989.
- [14] P. Borsboom and H. J. Frankena, "Field Analysis of Two-dimensional Integrated Optical Gratings", *J. Opt. Soc. Am. A*, vol. 12, no. 5, pp. 1134-1141, 1995.
- [15] S. Kondoh, A. Hirata, T. Shiozawa, "A Compact and Wide-band Metallic Reflector Grating in a Rectangular Waveguide", *IEEE Trans. Plasma Sci.*, vol. 32, no. 3, pp. 1318-1322, 2004.
- [16] P. Krauss, and F. Arndt, "Rigorous mode-matching method for the modal analysis of the T-junction circular to side coupled rectangular waveguide", *IEEE MTT-S International Microwave Symposium Digest*, vol.3, pp. 1355-1358, Orlando, USA, May 1995.
- [17] N. Yoneda, M. Miyasaki, T. Nishino, H. Asao, H. Nakaguro, and S. Betsudan, "Analysis of circular-to-rectangular waveguide T-junction using

- mode-matching technique”, *Electronics and Communications in Japan (Part II: Electronics)*, vol. 80, no. 7, pp. 37-46, 1998.
- [18] J. Zheng and M. Yu, “Rigorous mode-matching method of circular to off-center rectangular side-coupled waveguide junctions for filter applications”, *IEEE Trans. Microwave Theory Tech.*, vol. 55, no. 11, pp. 2365-2373, 2007.
- [19] K. Hwang and H. Eom, "Scattering analysis for a circular to rectangular T-junction", *Microwave Opt. Tech. Lett.*, vol. 41, no. 3, pp. 231-234, 2004.
- [20] T. H. Chang, C. H. Li, C. N. Wu, and C. F. Yu, "Exciting circular TE_{mn} modes at low terahertz region", *Appl. Phys. Lett.*, vol. 93, 111503, 2008.
- [21] T. Itoh, Ed., “Numerical techniques for microwave and millimeter-wave passive structures”, chapter 9 and 10, New York: Wiley, 1989.
- [22] C. R. Donaldson, W. He, A. W. Cross, F. Li, A. D. R. Phelps, L. Zhang, K. Ronald, C. W. Robertson, C. G. Whyte, and A. R. Young, "A cusp electron gun for millimeter wave gyrodevices", *Appl. Phys. Lett.* 96, 141501, 2010.
- [23] http://www.testequipmentconnection.com/specs/Anritsu_ME7808B.PDF.

Chapter 4

Microwave Window

4.1 The function of the window

The microwave window is an important component of the MVEDs. It separates the high vacuum inside the device from the atmospheric pressure outside as well as imports or exports the microwave power.

There are some basic requirements for the microwave window. The reflection of the window needs to be as small as possible to achieve a high transmission. The insertion loss of the window needs to be small so that it will not be much heat dissipation on the window. The window needs to have high power handling capability that it can be used in high power, long duration applications. And finally the window needs to have excellent mechanical strength and vacuum-tight seal [1, 2].

Due to the requirements, there are only a few materials suitable for window design, such as beryllia (BeO) ceramic, alumina (Al_2O_3) ceramic, alumina (Al_2O_3) sapphire, and chemical vapour deposition (CVD) diamond. The BeO ceramic has higher thermal conductivity than Al_2O_3 ceramic but it has the disadvantage of potential adverse health effects [3]. The sapphire has higher strength and lower absorbed power than the ceramic, but it is expensive to fabricate [2]. The CVD diamond has the highest strength and thermal conductivity. However, it is the most expensive among these materials. The CVD diamond is the best choice for the applications with MW power level, such as electron cyclotron resonance heating (ECRH) [4]. A more detail discussion on the specifications of the materials was reported in papers [5 - 9].

In the W-band gyro-BWO experiment, two windows are needed. The first one is placed at the end of the interaction region when the depressed collector is not applied, as shown in Fig. 3.1 (a). The other window is at the end of the input/output side-wall coupler when the depressed collector is applied, as shown in Fig. 3.1 (b, c). The alumina ceramic is chosen because it is the cheapest among the previously mentioned materials.

A further requirement of the windows for gyro-BWO is the bandwidth, as gyro-BWO is predicted to operate in the frequency range of 84-104 GHz. The windows need to keep a good transmission over the frequency range. To design a window in the millimetre range is challenging work. In low frequency band, the ceramic piece is thick and large, to make it easier to be brazed to the metal vacuum jacket and has better mechanical strength. As the operating frequency increases, the ceramic piece becomes thinner and thinner so that it is easier to break. It is also difficult to fabricate for the heat stress experienced in the vacuum braze process makes the window prone to breakage due to its small size.

4.2 Different types of microwave window

There are generally two types of microwave windows which are frequently used. The first is the block type, as shown in Fig. 4.1 (a). The ceramic piece is inserted into the connected waveguide, which can be in circular or rectangular cross section, and they are brazed together. The other is the pillbox type. It is composed by a cylindrical waveguide whose size is larger than the transmission rectangular waveguide. The ceramic piece is brazed with the cylindrical waveguide. A basic schematic of the pillbox type window is shown in Fig. 4.1 (b). In our study, simulations are done on both of the structures to find optimum geometries that have the better transmission and easier to be fabricated.

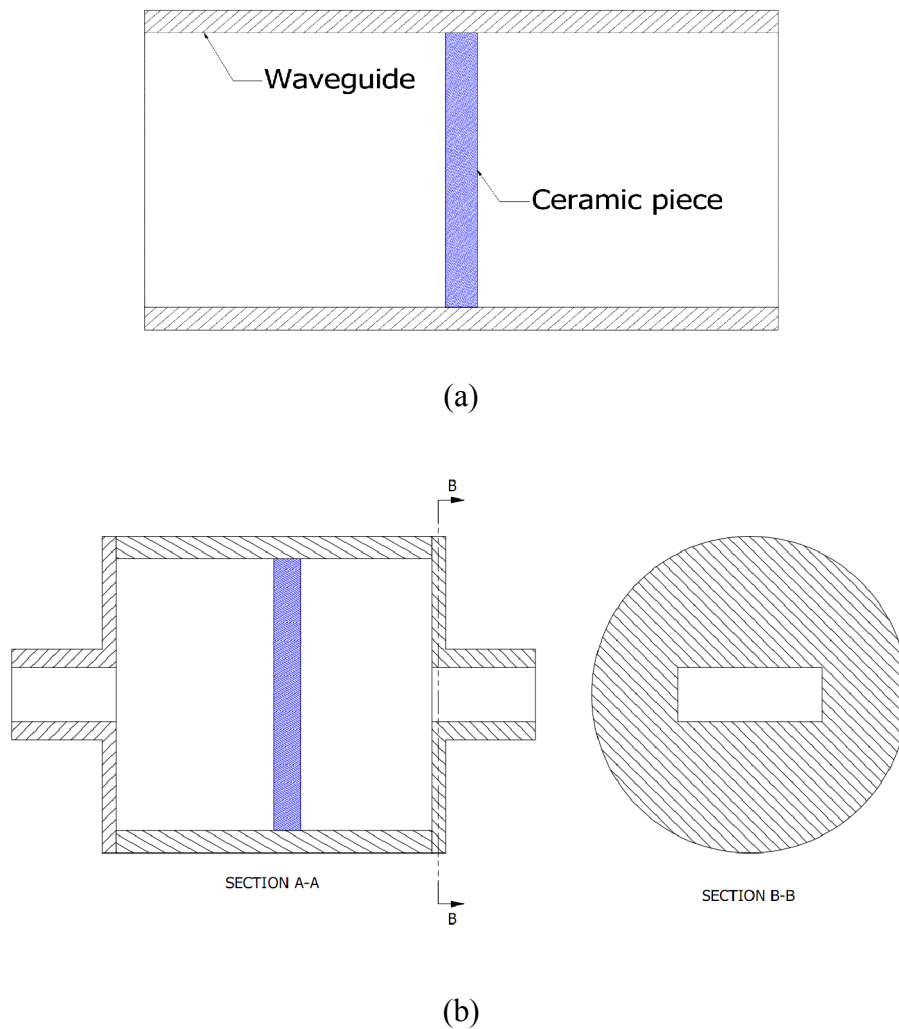


Fig. 4. 1 Schematic of the microwave windows (a) block type window, (b) pillbox type window.

4.2.1 Block type window

4.2.1.1 The principle of the microwave window

The mode-matching technology mentioned in chapter 3 can also be used to analyze the block type window. This window has no geometry discontinuities, but has discontinuities in the permittivity or permeability on the media interface. In paper [10, 11], a detail analysis of the transmission and reflection of the TE modes in single and multi-layer rectangular windows was represented. In this section, we extended this method to the circular waveguide as well as the TM modes. The scattering matrix for

the media discontinuity in the waveguide can finally be obtained from this analytical approach.

The general solution of the wave in a rectangular waveguide of size a , b can be written as [12]

$$\varphi(x, y, z) = \begin{cases} \sum_{m=0}^{\infty} \sum_{n=0}^{\infty} H_{mn} \cos\left(\frac{m\pi x}{a}\right) \cdot \cos\left(\frac{n\pi y}{b}\right) \cdot (Ae^{-ik_z z} + Be^{ik_z z}), & \text{TE modes} \\ \sum_{m=0}^{\infty} \sum_{n=0}^{\infty} E_{mn} \sin\left(\frac{m\pi x}{a}\right) \cdot \sin\left(\frac{n\pi y}{b}\right) \cdot (Ae^{-ik_z z} + Be^{ik_z z}), & \text{TM modes} \end{cases} \quad (4.1)$$

where

$$k_z = \sqrt{\omega^2 \varepsilon \mu - k_c^2} = \sqrt{\omega^2 \varepsilon \mu - \left(\left(\frac{m\pi}{a}\right)^2 + \left(\frac{n\pi}{b}\right)^2\right)} \quad (4.2)$$

The general solution of the wave in a circular waveguide of radius R can be written as [12]

$$\varphi(r, \phi, z) = \begin{cases} \sum_{m=0}^{\infty} \sum_{n=1}^{\infty} H_{mn} J_m(u'_{mn} r / R) \frac{\cos m\phi}{\sin m\phi} \cdot (Ae^{-ik_z z} + Be^{ik_z z}), & \text{TE modes} \\ \sum_{m=0}^{\infty} \sum_{n=1}^{\infty} E_{mn} J'_m(u_{mn} r / R) \frac{\cos m\phi}{\sin m\phi} \cdot (Ae^{-ik_z z} + Be^{ik_z z}), & \text{TM modes} \end{cases} \quad (4.3)$$

$$k_z = \sqrt{\omega^2 \varepsilon \mu - k_c^2} = \begin{cases} \sqrt{\omega^2 \varepsilon \mu - (u'_{mn} / R)^2}, & \text{TE mode} \\ \sqrt{\omega^2 \varepsilon \mu - (u_{mn} / R)^2}, & \text{TM mode} \end{cases} \quad (4.4)$$

where u'_{mn} is the n^{th} zero of J'_m and J' is the derivate of first kind of Bessel function.

u_{mn} is the n^{th} zero of J_m and J is the first kind of Bessel function. ε , μ are the permittivity and the permeability of the media in the waveguide.

It should be noticed that the wave modes in the transverse direction are only determined by the geometry. Therefore, if there are no discontinuities in the geometry, and only with different ε , μ of the media in the waveguide, as shown in Fig.

4.2, there will be no coupling between two different modes. Thus we only need to match the same mode on both sides of the media interface. To simplify the writing of Eq. 4.1 - 4.4, we use the following formula to identify the ξ, ζ modes either in rectangular or circular waveguide

$$\varphi(\xi, \zeta, z) = \varphi_0(\xi, \zeta) \cdot (Ae^{-ik_z z} + Be^{ik_z z}) \quad (4.5)$$

where $k_z = \sqrt{\omega^2 \varepsilon \mu - k_c^2}$. k_c is determined by different modes in different types of waveguides. It is also the function of the property of the media (ε and μ) in the waveguide.

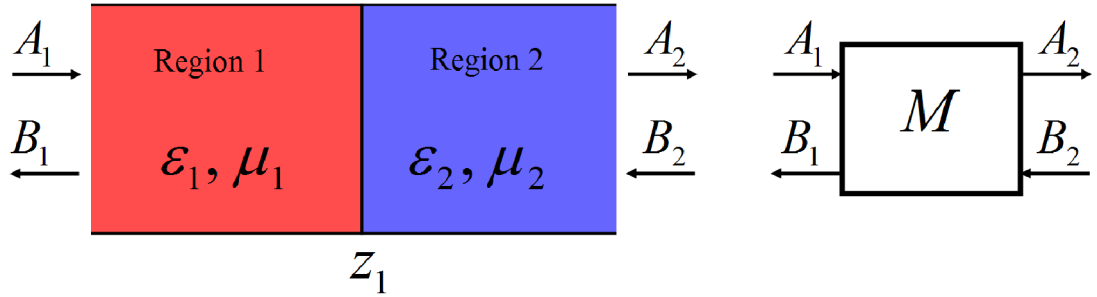


Fig. 4. 2 The schematic of the discontinuity in the media interface

The boundary conditions to match the TE mode in position Z_1 are

$$\begin{cases} \mu_1 \varphi_1(\xi, \zeta, z_1) = \mu_2 \varphi_2(\xi, \zeta, z_1) \\ \left. \frac{d}{dz} \varphi_1(\xi, \zeta, z_1) \right|_{z=z_1} = \left. \frac{d}{dz} \varphi_2(\xi, \zeta, z_1) \right|_{z=z_1} \end{cases} \quad (4.6)$$

Then we have

$$\begin{cases} \mu_1 \varphi_0(\xi, \zeta) \cdot (A_1 e^{-ik_{z1} z_1} + B_1 e^{ik_{z1} z_1}) = \mu_2 \varphi_0(\xi, \zeta) \cdot (A_2 e^{-ik_{z2} z_1} + B_2 e^{ik_{z2} z_1}) \\ -ik_{z1} \varphi_0(\xi, \zeta) \cdot (A_1 e^{-ik_{z1} z_1} - B_1 e^{ik_{z1} z_1}) = -ik_{z2} \varphi_0(\xi, \zeta) \cdot (A_2 e^{-ik_{z2} z_1} - B_2 e^{ik_{z2} z_1}) \end{cases} \quad (4.7)$$

From Eq. 4.7, we can get the relationship between $A_1, A_2, B_1,$ and B_2 in the form of matrix

$$\begin{bmatrix} B_1 \\ A_2 \end{bmatrix} = \begin{bmatrix} \frac{f-g}{f+g} e^{-i2k_{z1}z_1} & \frac{2}{g+f} e^{-i(k_{z1}-k_{z2})z_1} \\ \frac{2gf}{g+f} e^{-i(k_{z1}-k_{z2})z_1} & \frac{g-f}{f+g} e^{i2k_{z2}z_1} \end{bmatrix} \begin{bmatrix} A_1 \\ B_2 \end{bmatrix} = \begin{bmatrix} S_{11}^0 & S_{12}^0 \\ S_{21}^0 & S_{22}^0 \end{bmatrix} \begin{bmatrix} A_1 \\ B_2 \end{bmatrix} \quad (4.8)$$

where $f = k_{z1}/k_{z2}$, $g = \mu_1/\mu_2$.

The scattering matrix needs to satisfy $|s_{11}|^2 + |s_{12}|^2 = 1$, $|s_{12}| = |s_{21}|$. Thus the scattering matrix can be written as

$$S = \begin{bmatrix} \frac{f-g}{f+g} e^{-i2k_{z1}z_1} & \frac{2\sqrt{gf}}{g+f} e^{-i(k_{z1}-k_{z2})z_1} \\ \frac{2\sqrt{gf}}{g+f} e^{-i(k_{z1}-k_{z2})z_1} & \frac{g-f}{f+g} e^{i2k_{z2}z_1} \end{bmatrix} = \begin{bmatrix} S_{11} & S_{12} \\ S_{21} & S_{22} \end{bmatrix} \quad (4.9)$$

For TM mode, the boundary condition are

$$\begin{cases} \varphi_1(\xi, \zeta, z_1) = \varphi_2(\xi, \zeta, z_1) \\ \left. \frac{1}{\varepsilon_1} \frac{d}{dz} \varphi_1(\xi, \zeta, z_1) \right|_{z=z_1} = \left. \frac{1}{\varepsilon_2} \frac{d}{dz} \varphi_2(\xi, \zeta, z_1) \right|_{z=z_1} \end{cases} \quad (4.10)$$

Then we have

$$\begin{cases} \varphi_0(\xi, \zeta) \cdot (A_1 e^{-ik_{z1}z_1} + B_1 e^{ik_{z1}z_1}) = \varphi_0(\xi, \zeta) \cdot (A_2 e^{-ik_{z2}z_1} + B_2 e^{ik_{z2}z_1}) \\ \frac{-ik_{z1}}{\varepsilon_1} \varphi_0(\xi, \zeta) \cdot (A_1 e^{-ik_{z1}z_1} - B_1 e^{ik_{z1}z_1}) = \frac{-ik_{z2}}{\varepsilon_2} \varphi_0(\xi, \zeta) \cdot (A_2 e^{-ik_{z2}z_1} + B_2 e^{ik_{z2}z_1}) \end{cases} \quad (4.11)$$

The scattering matrix for TM modes can be obtained in the same way as the TE mode, as follows

$$S = \begin{bmatrix} \frac{fh-1}{fh+1} e^{-i2k_{z1}z_1} & \frac{2\sqrt{fh}}{fh+1} e^{-i(k_{z1}-k_{z2})z_1} \\ \frac{2\sqrt{fh}}{fh+1} e^{-i(k_{z1}-k_{z2})z_1} & \frac{1-fh}{fh+1} e^{i2k_{z2}z_1} \end{bmatrix} = \begin{bmatrix} S_{11} & S_{12} \\ S_{21} & S_{22} \end{bmatrix} \quad (4.12)$$

where $h = \varepsilon_2/\varepsilon_1$.

The relationship between the A_1 , A_2 , B_1 , and B_2 can be also written as the form of transfer matrix. For TE modes,

$$\begin{bmatrix} A_2 \\ B_2 \end{bmatrix} = \frac{1}{2} \begin{bmatrix} e^{i(k_{2z}-k_{1z})Z_1} \cdot (g+f) & e^{i(k_{2z}+k_{1z})Z_1} \cdot (g-f) \\ e^{i(-k_{2z}-k_{1z})Z_1} \cdot (g-f) & e^{i(-k_{2z}+k_{1z})Z_1} \cdot (g+f) \end{bmatrix} \begin{bmatrix} A_1 \\ B_1 \end{bmatrix} \quad (4.13)$$

For TM modes,

$$\begin{bmatrix} A_2 \\ B_2 \end{bmatrix} = \frac{1}{2} \begin{bmatrix} e^{i(k_{2z}-k_{1z})Z_1} \cdot (1+fh) & e^{i(k_{2z}+k_{1z})Z_1} \cdot (1-fh) \\ e^{i(-k_{2z}-k_{1z})Z_1} \cdot (1-fh) & e^{i(-k_{2z}+k_{1z})Z_1} \cdot (1+fh) \end{bmatrix} \begin{bmatrix} A_1 \\ B_1 \end{bmatrix} \quad (4.14)$$

In the calculation of the transmission of the block type window, the transfer matrix was used for it is easier to cascade than the scattering matrix.

The basic schematic of a single-layer window is shown in Fig. 4.3. It contains two discontinuities in the dielectric constant. The transfer matrix of the whole structure can be calculated by cascading each transfer matrix of the discontinuities from right to left. And we have

$$\begin{bmatrix} A_3 \\ B_3 \end{bmatrix} = [M_2] \times [M_1] \times \begin{bmatrix} A_1 \\ B_1 \end{bmatrix} = [M] \times \begin{bmatrix} A_1 \\ B_1 \end{bmatrix} = \begin{bmatrix} M_{11} & M_{12} \\ M_{21} & M_{22} \end{bmatrix} \times \begin{bmatrix} A_1 \\ B_1 \end{bmatrix} \quad (4.15)$$

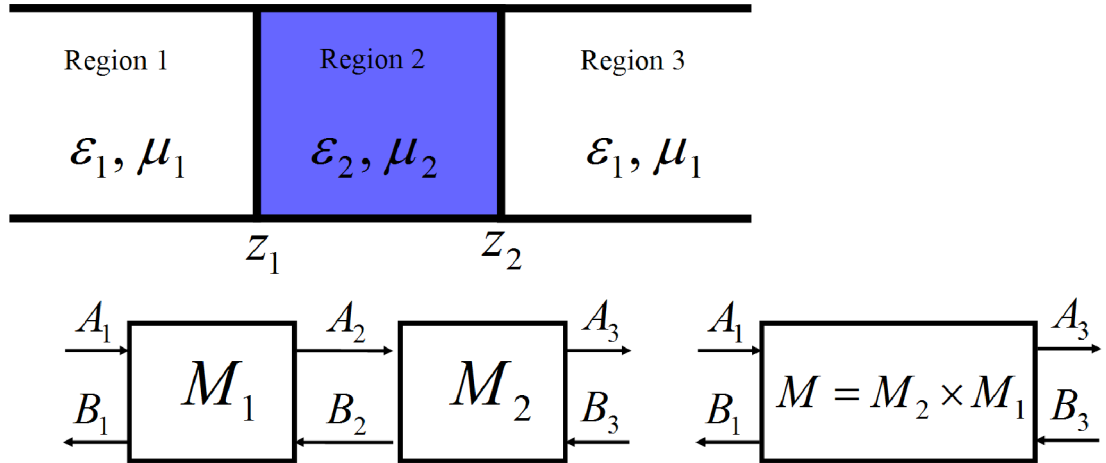


Fig. 4. 3 The schematic of the single-layer window

From paper [11], the reflection (R_{ef}) and transmission (T_{ran}) coefficient of the window can be written as

$$\begin{cases} R_{ef} = \left| -\frac{M_{21}}{M_{22}} \right|^2 \\ T_{ran} = \frac{\mu_1 k_2}{\mu_2 k_1} \left| \frac{M_{11} \cdot M_{22} - M_{12} \cdot M_{21}}{M_{22}} \right|^2 \end{cases} \quad (4.16)$$

The S -parameters in dB scale can be written as

$$\begin{cases} S_{11} \text{ (dB)} = 10 \cdot \log R_{ef} \\ S_{12} \text{ (dB)} = 10 \cdot \log T_{ran} \end{cases} \quad (4.17)$$

The performance of the window could be easily obtained and optimized. For the ceramic window from the given equations, we chose the relative permittivity as 9.7 for 99.5% purity alumina ceramic and the relative permeability as 1.

4.2.1.2 Rectangular window

To design a rectangular window for the input/output coupler, the size of the rectangular waveguide was $a = 2.00$ mm, $b = 1.30$ mm, which is the same size as the input/output coupler in chapter 3. The operating frequency range is 84 - 104 GHz. The optimized dimension and the reflection of the window for TE_{10} mode is shown in Fig. 4.4.

The single-layer window is narrow band, which is about 5% bandwidth with a 90% transmission (-10 dB). It can not fulfill the requirement of the gyro-BWO.

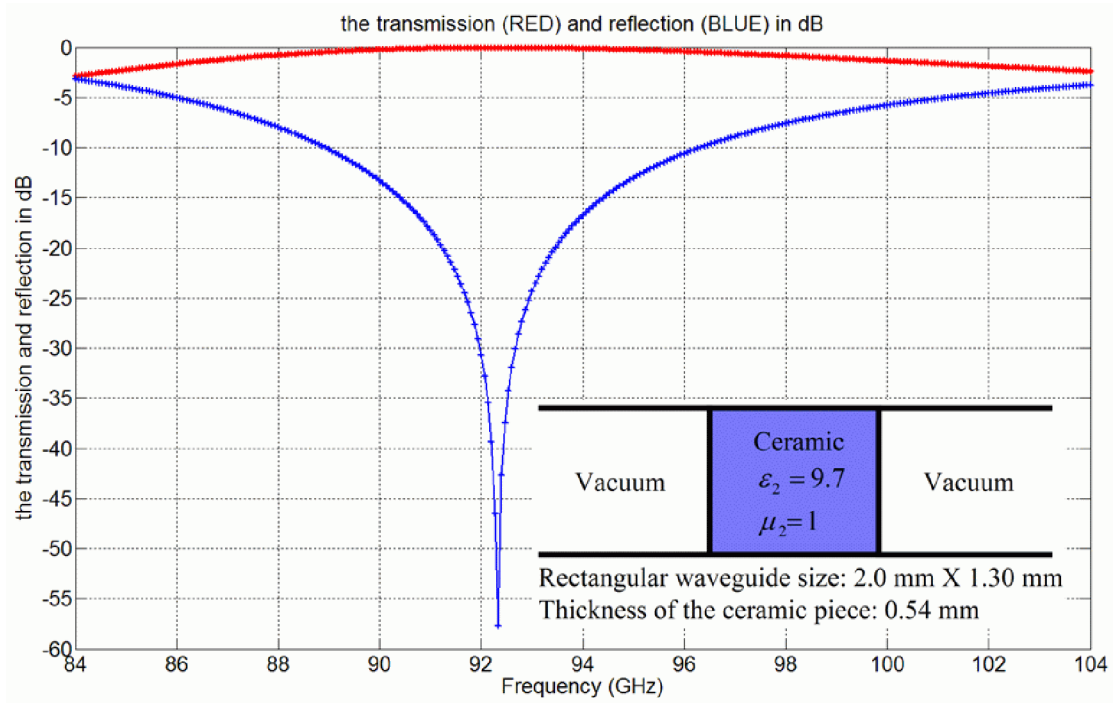


Fig. 4. 4 The optimum result of the single-layer ceramic window and its size.

To get a better performance, some iris pieces can be inserted into the window to compensate the reflection in some frequencies therefore make it a multi-layer window. To find such geometry, different types of window with one and two irises were investigated. The simulation of multi-layer window is similar with the single-layer window. The only difference is that more transfer matrices need to be cascaded. The inserted iris material was chosen as quartz, whose relative dielectric constant was chosen as 3.683.

Genetic algorithm was used to optimize the parameters. The evaluation function for genetic algorithm was chosen as

$$f(L_1, \dots, L_n) = \sum_F^N [R_{ef}(L_1, \dots, L_n, F) - 0]^2 \quad (4.18)$$

where L_1, \dots, L_n are the parameters to be optimized. F is the frequency index in the calculated frequency range. N is the number of frequencies to be calculated. In the calculation, it is 2001. R_{ef} is the reflection coefficient of the window.

The parameter range of the ceramic and quartz pieces was chosen as [0.05, 3.00] mm, and the length of the vacuum gap was chosen as [0.05, 6.00] mm.

There are four cases for the two-layer window, as shown in Fig. 4.5. The optimized dimensions and the reflection of the optimized dimension are shown in Fig. 4.6.

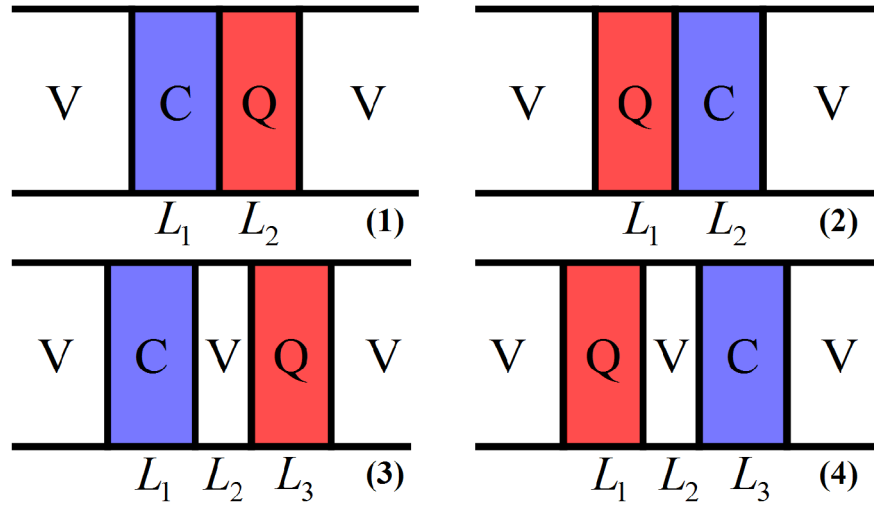


Fig. 4. 5 Different cases of the two-layer window.

(V=Vacuum, C=Ceramic, Q=quartz.)

The two-layer window still can not achieve -10 dB reflection over the whole frequency band. Case 1 and case 2, case 3 and case 4 have close optimum results, that is because the reciprocity of the geometry which has $S_{11} = S_{22}$. When considering the reciprocity, and taking out the cases that could degenerate into a two-layer window, there were five cases in all for a three-layer window, as shown in Fig. 4.7. The optimum results and geometries are shown in Fig. 4.8. Case 3 and 5 can reach a -10 dB (10% in power) reflection over the desired frequency band.

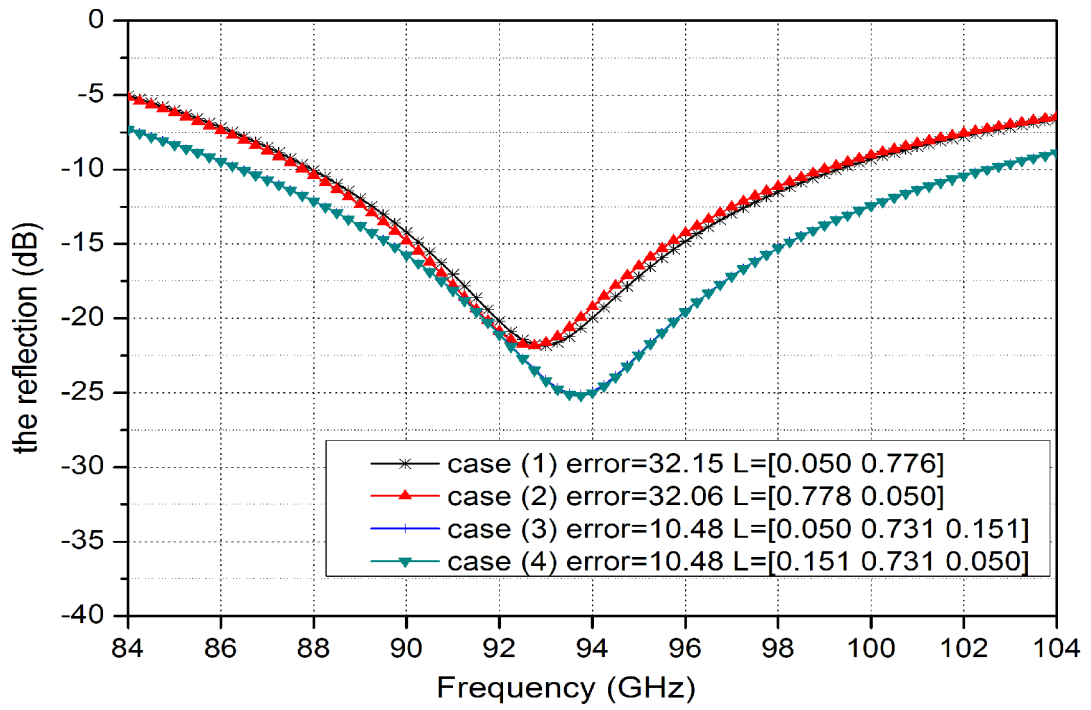


Fig. 4. 6 The optimum results of the two-layer window and the optimum sizes.

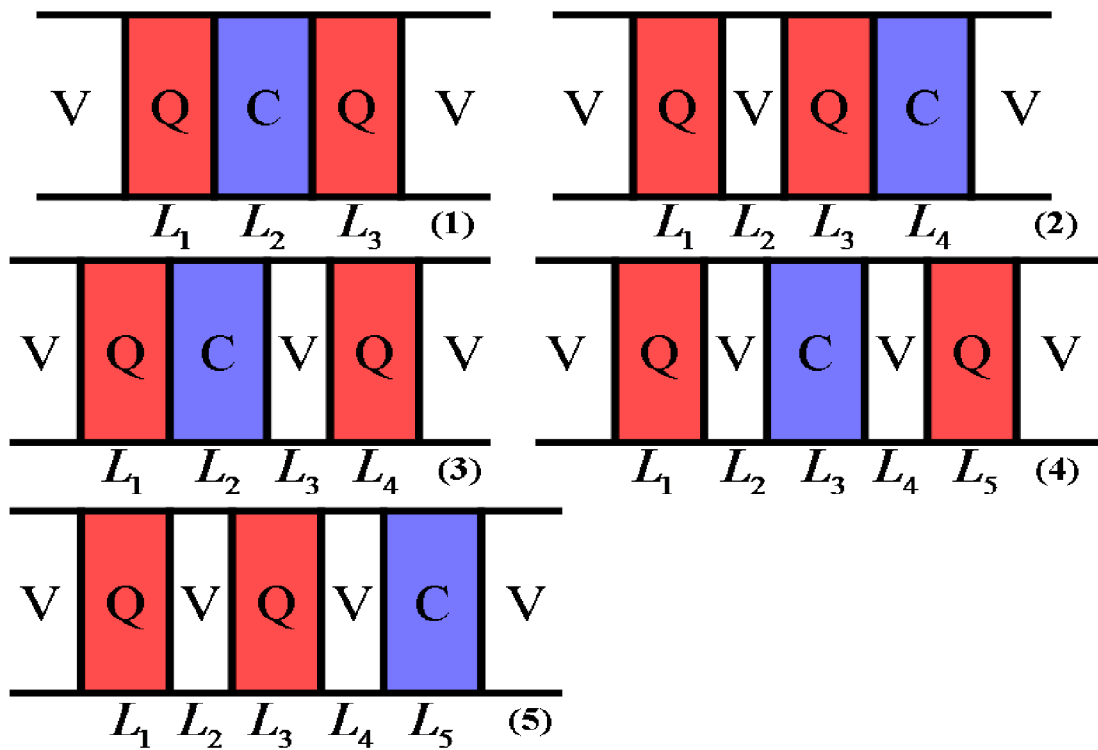


Fig. 4. 7 Different cases of the three-layer window.

(V=Vacuum, C=Ceramic, Q=quartz.)

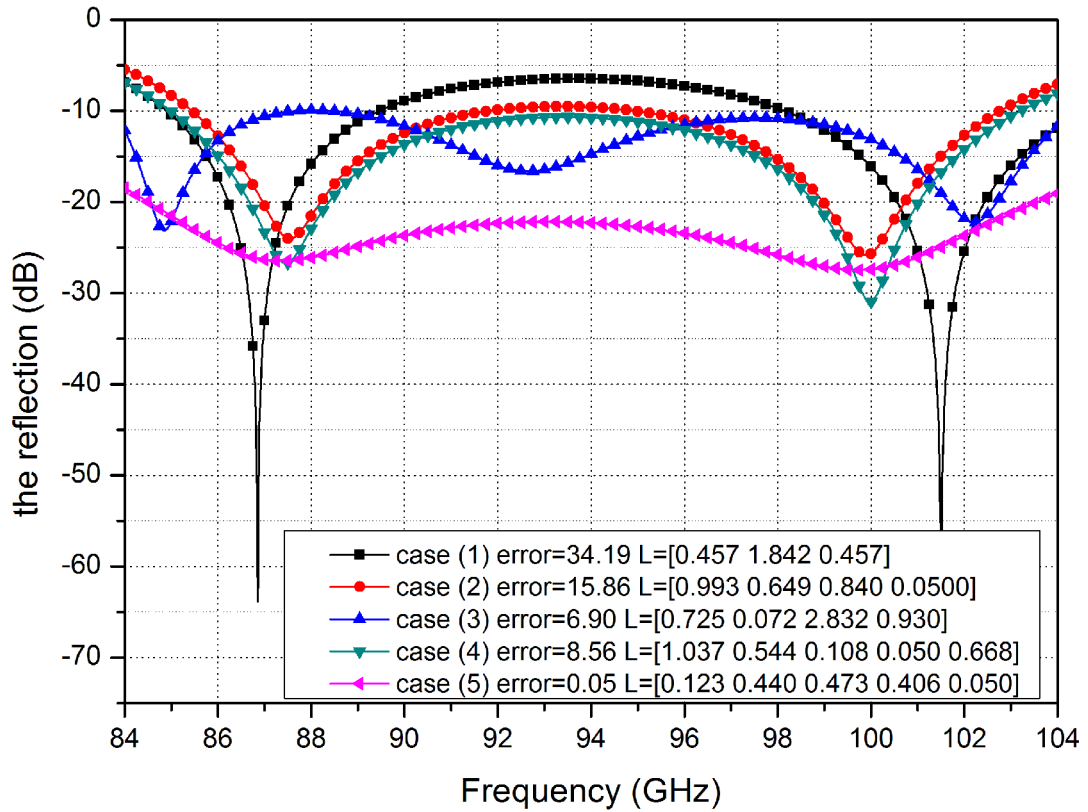


Fig. 4. 8 The optimum results of the three-layer windows and the optimum sizes.

4.2.1.3 Circular window

A circular window is required at the end of the interaction region of the gyro-BWO where the connected circular waveguide is with radius of 7.50 mm. In the simulation, the TE_{11} mode is considered and the windows in single-layer, two-layer, and three-layer cases are optimized. The results and the parameters of the geometries are shown in Fig. 4.9, 4.10 and 4.11, respectively. The three-layer window could reach a reflection lower than -25 dB over the frequency band in case 3 and 4.

Another optimization was done on the three-layer window on case 4, which is for the W-band gyro-TWA whose frequency band is 90-100 GHz. The desired reflection was aimed to less than -40 dB. The optimum result and geometry was shown in Fig. 4.12.

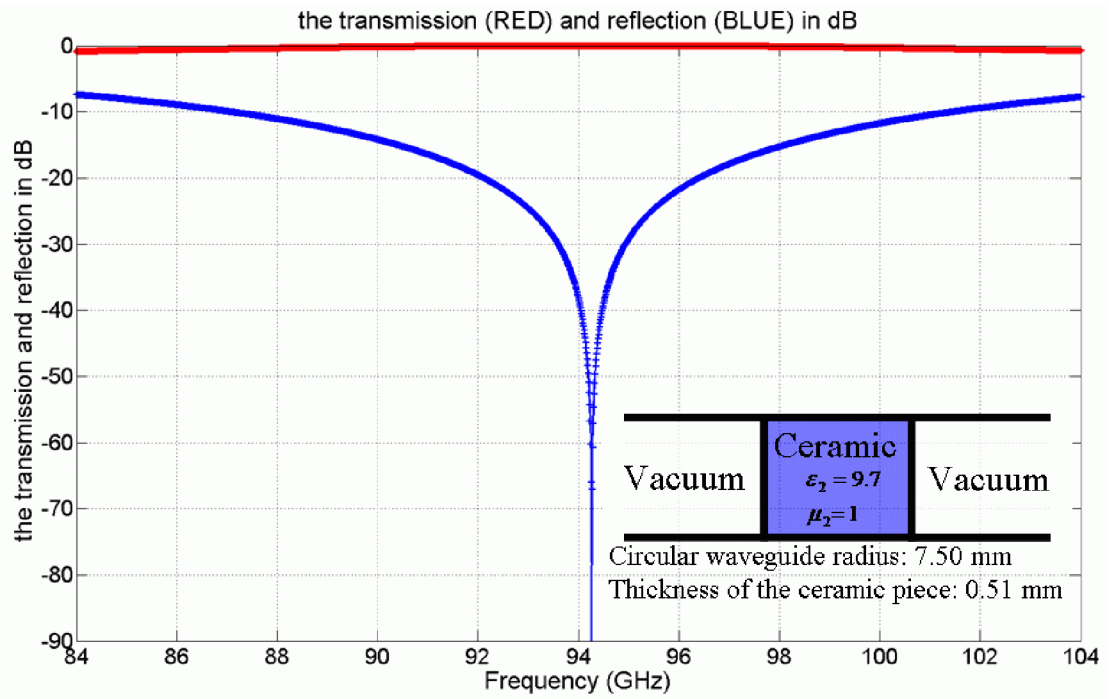


Fig. 4. 9 The optimum result of the single-layer ceramic window and its size.

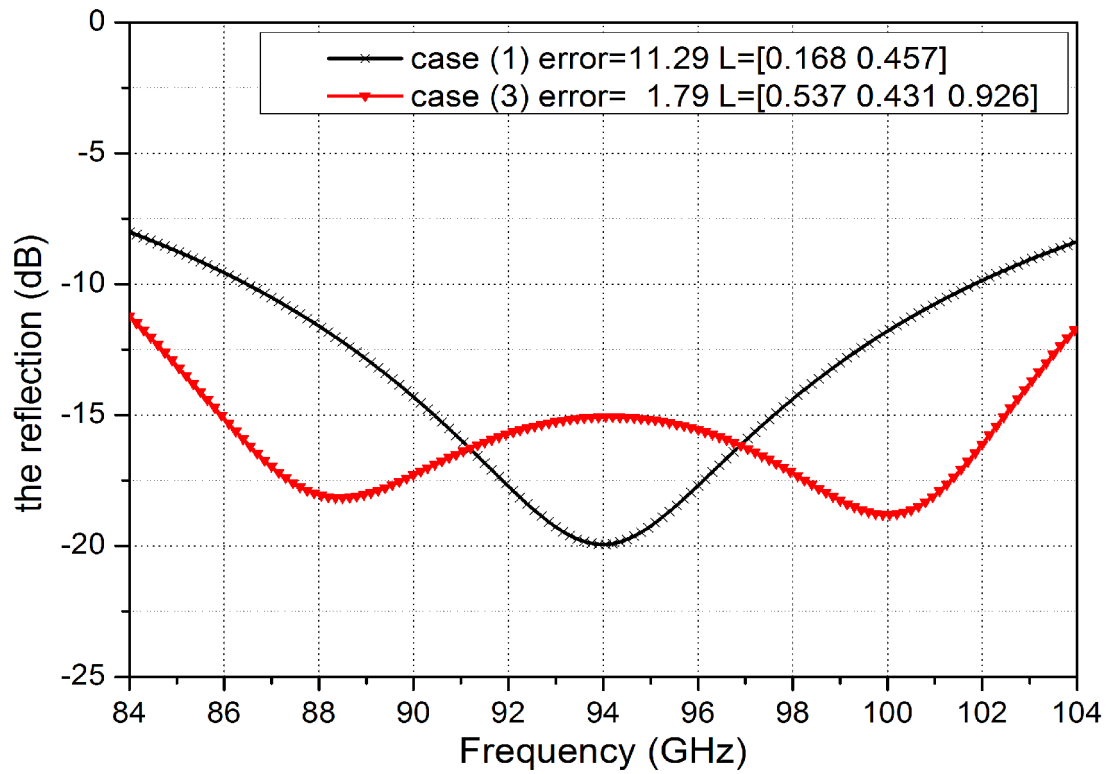


Fig. 4. 10 The optimum results of the two-layer ceramic window and their sizes.

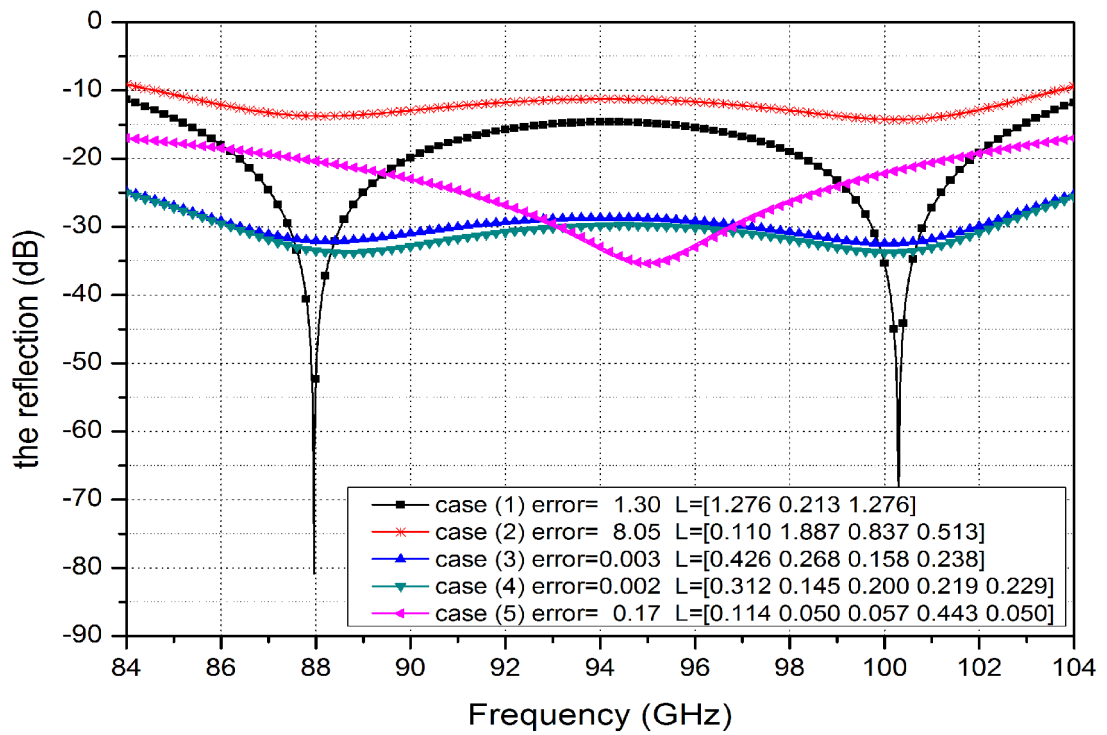


Fig. 4. 11 The optimum results of the three-layer ceramic window and their sizes.

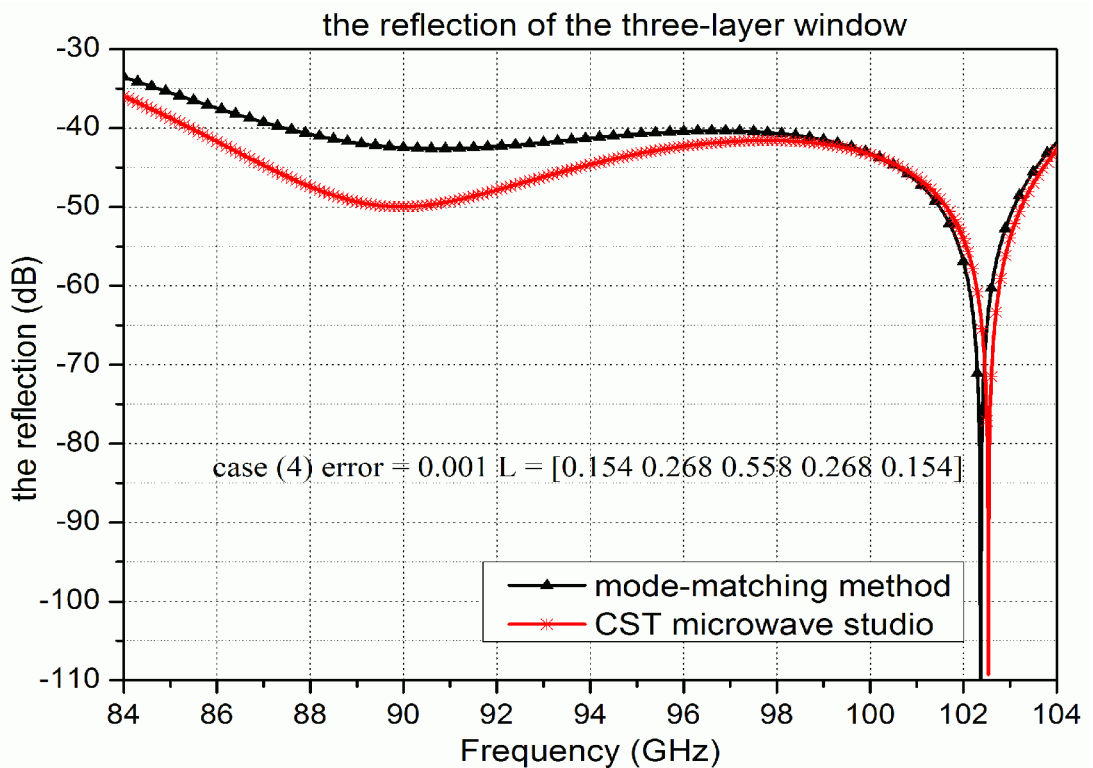


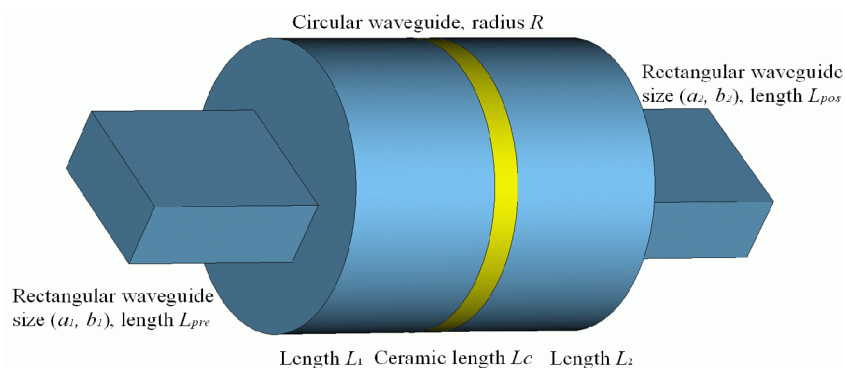
Fig. 4. 12 The optimum results of the three-layer ceramic window for W-band gyro-TWA.

4.2.2 Pillbox type window

The other type is the pillbox type window, as shown in Fig. 4.1 (b). This type of window has the advantages of broad band, high power capability, and easy to fabricate due to the large size. Several papers have been published in calculating this type of window, including the equivalent circuit method [13, 14] and the method of moment [15].

In our study, the mode-matching technology was used to achieve a full model analysis of the pillbox type window based on the results of E. K. Duerr's thesis [16], and reference [11].

When we look into the geometry, it can be divided into several basic components cascading together, as shown in Fig. 4.13 (a). From left to right, they are rectangular waveguide with size a_1, b_1 and length L_{pre} , rectangular to circular waveguide step (rectangular waveguide with size a_1, b_1 into a larger circular waveguide with radius R), empty circular waveguide (radius R and length L_1), the vacuum to ceramic step (the discontinuity in the dielectric constant), the ceramic piece (radius R and length L_c), the ceramic to vacuum step, empty circular waveguide (radius R and length L_2), the circular to rectangular waveguide step (from radius R to rectangular waveguide with size a_2, b_2), and finally with a empty rectangular waveguide (size a_2, b_2 and length L_{pos}). The connection of the components is shown in Fig. 4.13 (b).



(a)

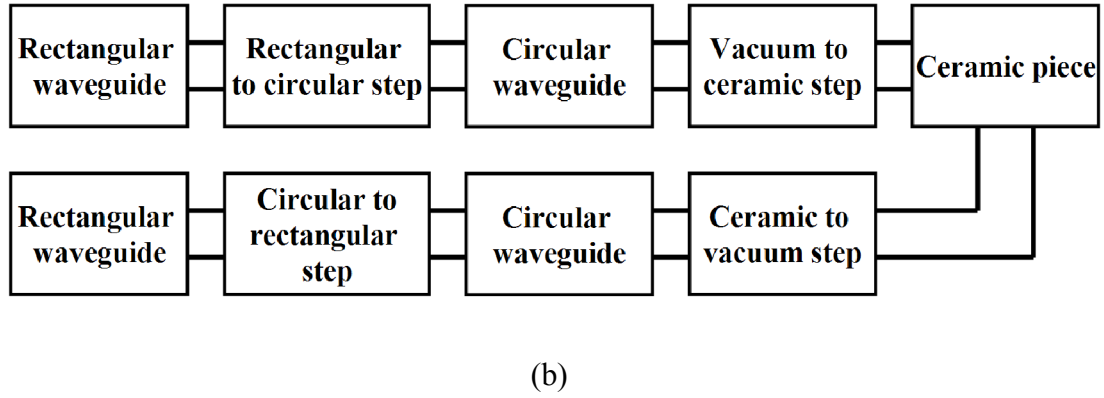


Fig. 4. 13 (a) 3D view of the pillbox type window (b) the connection of the components.

Among all these components, the scattering matrix of the empty waveguide and the ceramic piece is given in Eq. 3.39. The scattering matrix for the discontinuity in the material has been discussed in section 4.2.1. The only scattering matrices still unknown are the rectangular to circular waveguide and the circular to rectangular waveguide steps. Fortunately, several papers have reported on the calculation of small rectangular to larger circular waveguide step [16 - 19]. In [17], the basic notion of how to use mode-matching method for this kind of component is introduced. However, no detail is given on the overlap integrals between rectangular and circular eigenmodes, which is the most important step in the calculation. Reference [19] gives part of the results but mistakes in the formula are found in later study. In E. K. Duerr's thesis, the full process of getting the scattering matrix of the rectangular to circular step is discussed in detail, and the results are used in our calculation of the pillbox type window. Only a brief summary is given in this section.

The scattering matrix for the rectangular to circular step is $S = \begin{bmatrix} S_{11} & S_{12} \\ S_{21} & S_{22} \end{bmatrix}$, where

$$\begin{aligned}
S_{11} &= (I + Z_{\alpha}^{1/2} M^T Z_{\beta}^{-1} M Z_{\alpha}^{1/2})^{-1} (I - Z_{\alpha}^{1/2} M^T Z_{\beta}^{-1} M Z_{\alpha}^{1/2}) \\
S_{12} &= 2(I + Z_{\alpha}^{1/2} M^T Z_{\beta}^{-1} M Z_{\alpha}^{1/2})^{-1} Z_{\alpha}^{1/2} M^T Z_{\beta}^{-1/2} \\
S_{21} &= Z_{\beta}^{-1/2} M Z_{\alpha}^{1/2} (I + S_{11}) \\
S_{22} &= Z_{\beta}^{-1/2} M Z_{\alpha}^{1/2} S_{12} - I
\end{aligned} \tag{4.19}$$

In Eq. 4.19, Z_{α}, Z_{β} is the resistance matrix of the rectangular and circular waveguide, respectively, as defined in Eq. 3.30. The M matrix is determined by the geometry of the circular waveguide (with radius R), and the rectangular waveguide (size a, b and offset to the centre x_1, y_1 , as shown in Fig. 4.14). The formula on calculating matrix M is given in section 2.2.4 in E. K. Duerr's thesis in detail.

The scattering matrix of a larger circular waveguide to smaller rectangular waveguide step can be obtained from the rectangular to circular step. The two matrices have the following relationship

$$\begin{bmatrix} S'_{11} & S'_{11} \\ S'_{11} & S'_{11} \end{bmatrix} = \begin{bmatrix} S_{22} & S_{21} \\ S_{12} & S_{11} \end{bmatrix} \tag{4.20}$$

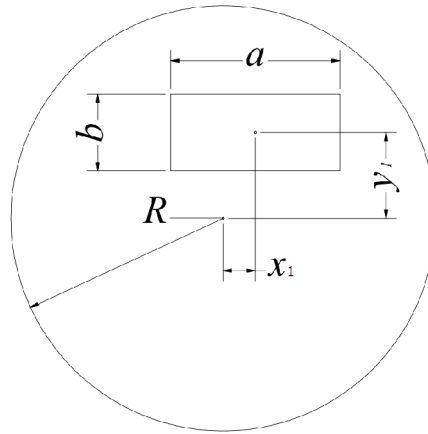


Fig. 4. 14 The cross-section view of the rectangular to circular step.

The scattering matrix of the whole pillbox window can be obtained by cascading all the scattering matrices of the components from left to right. It should be noticed that the scattering matrices of the empty waveguide, the ceramic piece, and the media

discontinuity are diagonal. Thus when cascading these components, the matrix multiply operation can be degenerated into a vector multiply operation, and significantly reduce the calculation time. And also, the rectangular waveguide in both ends only affect the phase of the S parameters. If only the amplitudes of the S parameters are desired, there is no need to include these two components in the calculation. Therefore, the connection of the components can be simplified as Fig. 4.15.

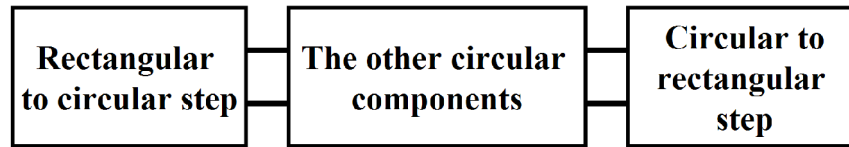


Fig. 4. 15 The simplified connection of the components.

A demonstration code was created in MATLAB environment and the convergence of different calculation modes was compared. As suggested in [19], if the calculated TE mode in the rectangular waveguide was N , then the TM mode was chosen as $N/2$.

The TE mode in the circular waveguide was chosen as $M = \frac{\pi R^2}{ab} N$, and the TM mode was $M/2$.

For a W-band pillbox window with the geometry parameters $a_1=a_2=2.54$ mm, $b_1=b_2=1.27$ mm, $x_1=x_2=y_1=y_2=0$, $R=2.44$ mm, $L_1=L_2=3.00$ mm, and $L_c=0.71$ mm, Fig. 4.16 shows the absolute S_{11} (TE_{10} to TE_{10}) value in different TE mode numbers. The calculation result converges when $N \geq 14$. The result was compared with CST microwave studio in Fig. 4.17 and the computing times for both of the codes are listed in table 4.1. The calculation was executed on a 4-core, 2.8 GHz PC and windows sever 2008 operating system.

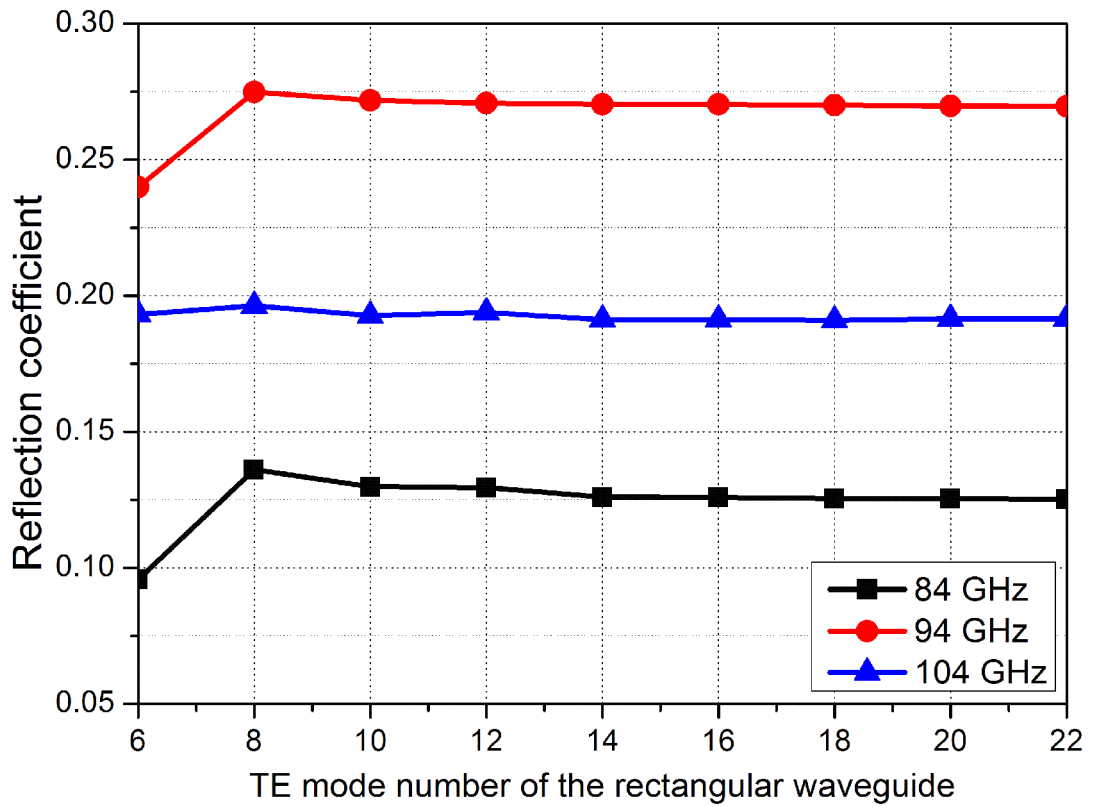


Fig. 4. 16 Convergence of the scattering parameter for TE₁₀ mode.

Table 4. 1 Comparison of the computing time of the MATLAB code and the CST microwave studio.

	N	Frequency points / cell number	CPU time (minutes)
MATLAB code	14	1001 points	1.65
	16	1001 points	2.37
	18	1001 points	3.29
CST microwave studio		1.11 million cells	141.8
		1.88 million cells	354.0

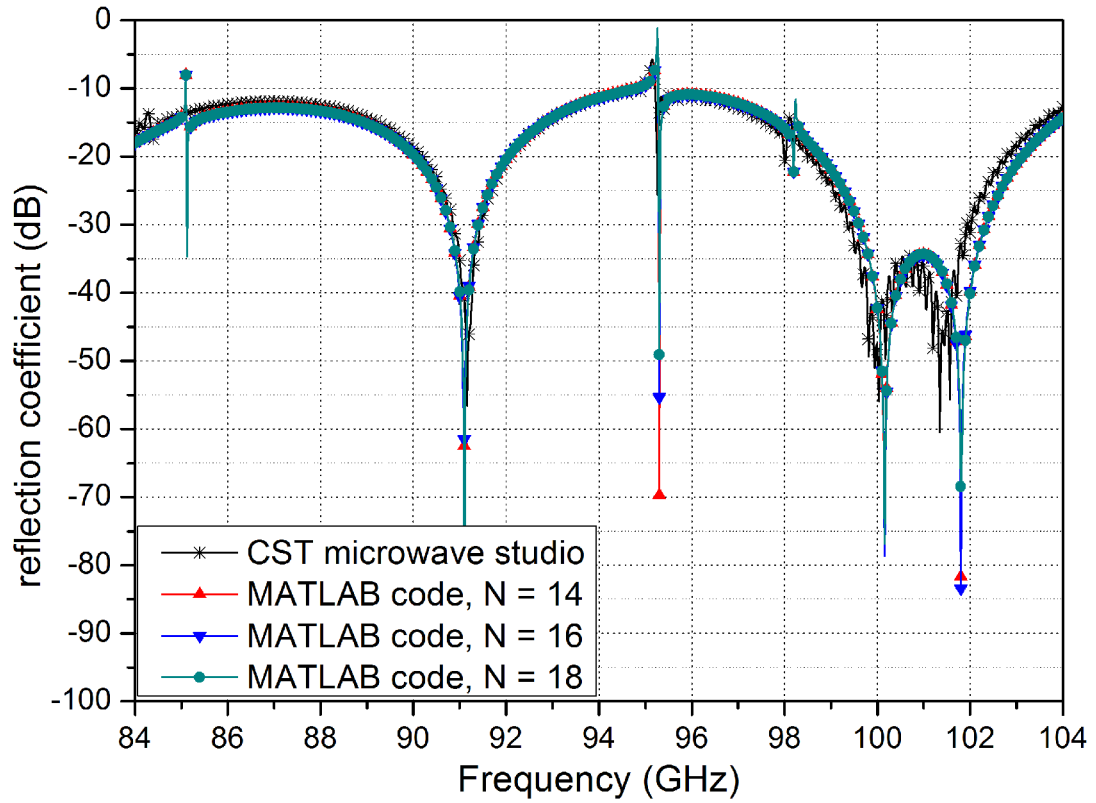


Fig. 4. 17 Comparison of the simulation results of the MATLAB code and CST microwave studio.

In our design, the dimensions of the rectangular waveguide in the left side were $a_1=2.00$ mm and $b_1=1.30$ mm. As the rectangular waveguide in the right side needs to connect with a standard WR-10 waveguide ($a=2.54$ mm, $b=1.27$ mm), its sizes were set as $a_2=2.00$ mm, $b_2=1.27$ mm. The reason that did not directly use the dimension of WR-10 waveguide to the rectangular waveguide in the right side was no good transmission over the frequency band could be obtained in the optimization. The offsets of the rectangular waveguide to the centre were chosen as $x_1 = y_1 = x_2 = y_2 = 0$ mm. To find a window structure with the optimum transmission over the frequency band, the genetic algorithm [20] was used to optimize the parameters of the geometry, which were R , L_1 , L_2 , and L_c . The evaluation function for the genetic algorithm was

$$f(R, L_1, L_2, L_c) = \sum_F^N [S_{11}(R, L_1, L_2, L_c, F) - 0]^2 \quad (4.21)$$

where F is the frequency index in the calculated frequency range, N is the number of frequencies to be calculated. S_{11} is the absolute value of S_{11} (TE₁₀ to TE₁₀) of the pillbox window.

The optimum geometry was $R=2.44$ mm, $L_1=L_2=3.00$ mm, and $L_c=0.72$ mm, and the reflection is shown in Fig. 4.18. It could reach a -10 dB reflection at most of the frequency band, but still had spikes in some frequency points. Each spike had nearly 20 MHz frequency band. The CST microwave studio could not capture such small frequency gap, and the result was smooth over the frequency range. As 20 MHz was only 0.1% of the whole 20 GHz frequency band, this kind of sharp spikes were acceptable in the practical applications.

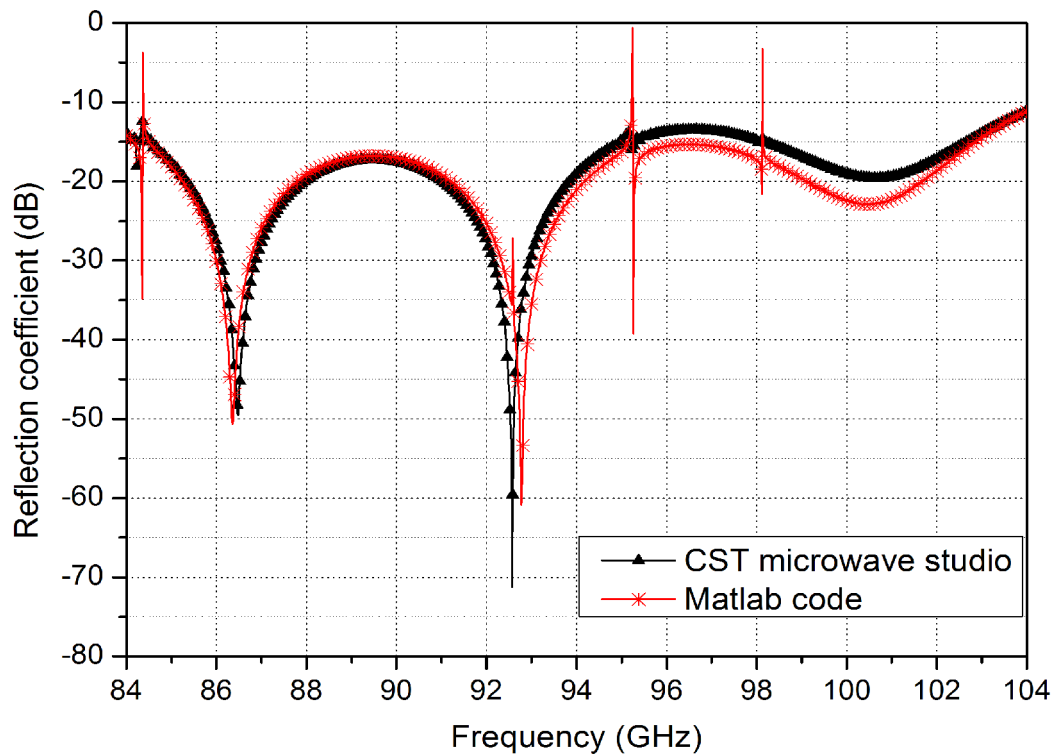


Fig. 4. 18 The optimum result of the pillbox window.

4.3 Manufacture and measurement results

4.3.1 Three-layer window

When manufacturing the three-layer window, it is very difficult to avoid geometry discontinuities either due to the brazing process or the physical connection. As from the optimization result in section 4.1, to achieve a high reflection over the operating frequency band, the thickness of the dielectric pieces such as the ceramic piece and the quartz pieces need to be very small. It is a tricky task to braze the ceramic piece and to hold the quartz pieces. Form the brazing requirement, the ceramic need to have a step in radius against the copper tube, as shown in Fig. 4.19. And also, there are geometry steps required for the quartz pieces as to hold them in the right position.

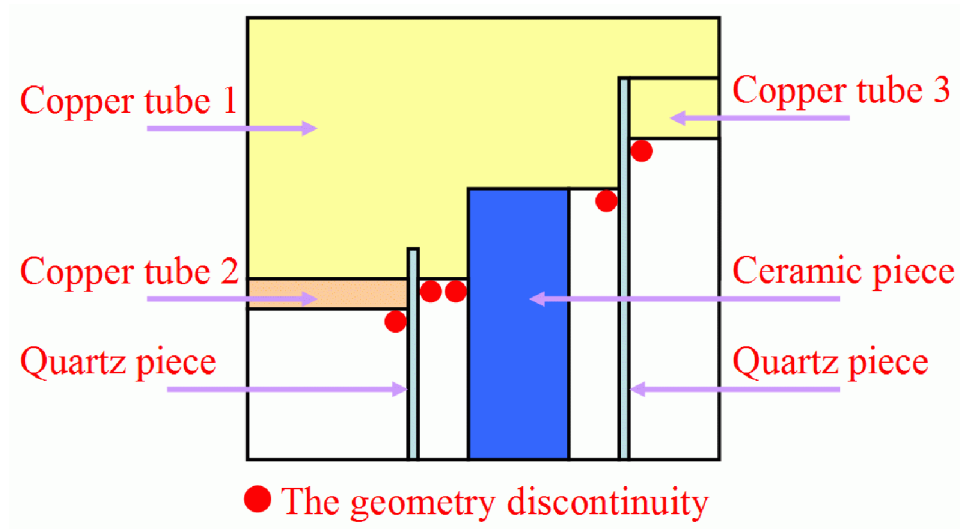
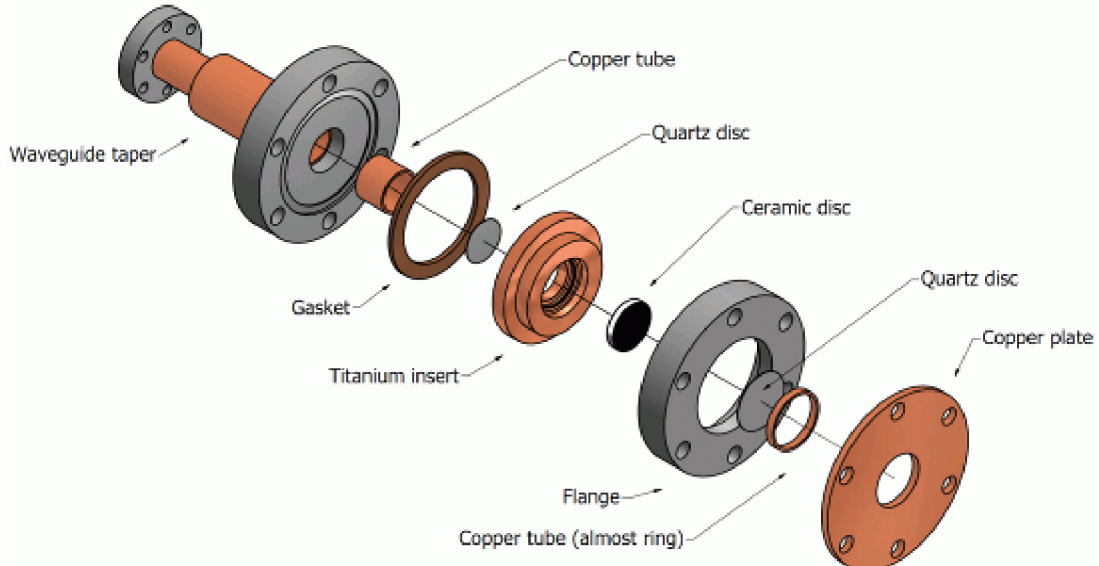


Fig. 4. 19 The geometry discontinuities of the three layer window.

However, as from the simulation, the geometry discontinuities are harmful to the performance. A small geometry discontinuity will cause a large reflection in a certain frequency to produce a spike in the figure of transmission coefficient. It can be simply explained by the impedance changing at the discontinuous position causing an impedance mismatching resulting in a large reflection. And a larger discontinuity has more serious effect. These spikes are acceptable for the experiment of the

gyro-BWO. However, they are not desired for the gyro-TWA experiments, as it requires a -40 dB reflection over the frequency band from 90 - 100 GHz. Therefore, another optimization based on the method described in section 4.1 was carried out with consider the practical restriction and the frequency band of 90 - 100 GHz. In the optimization, a minimum thickness of the ceramic piece of 2.0 mm was chosen to be thick enough for sufficient mechanical strength to hold vacuum. A discontinuity of 4.0 mm in diameter between the copper tube and the ceramic piece was set according to the technician's requirement to do the brazing job. To reduce the effect of the geometry discontinuities, the diameter of the window was chosen as 19.0 mm, which is much larger than the discontinuity. The practical three-layer window under the machining and brazing restrictions will not have a performance as good as the simulation results in section 4.2. However, the optimization routing can still provide the optimal solution under these restrictions. To connect the beam tube with the three-layer window, a long circular taper is required. The CAD drawing and the photo of the three-layer window are shown in Fig. 4.20.



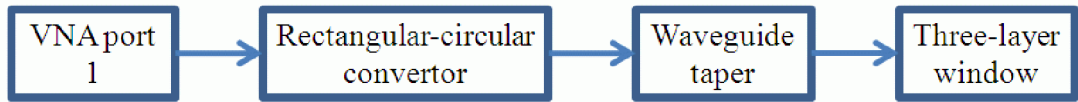
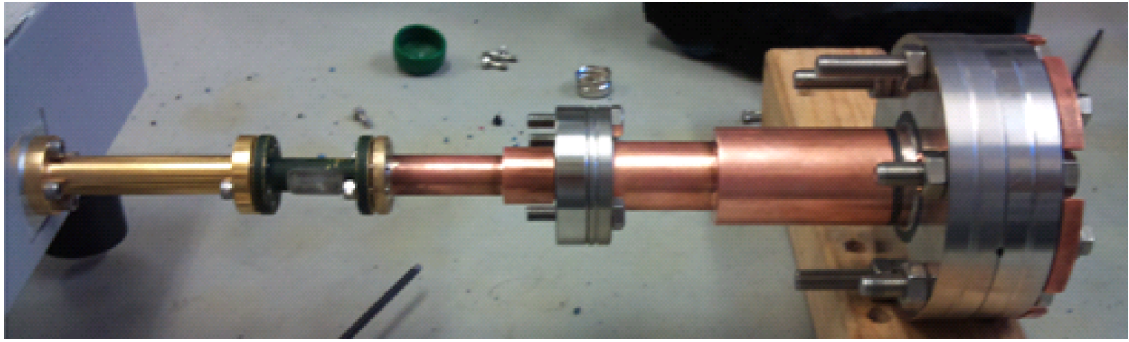
(a) CAD drawing of the three-layer window.



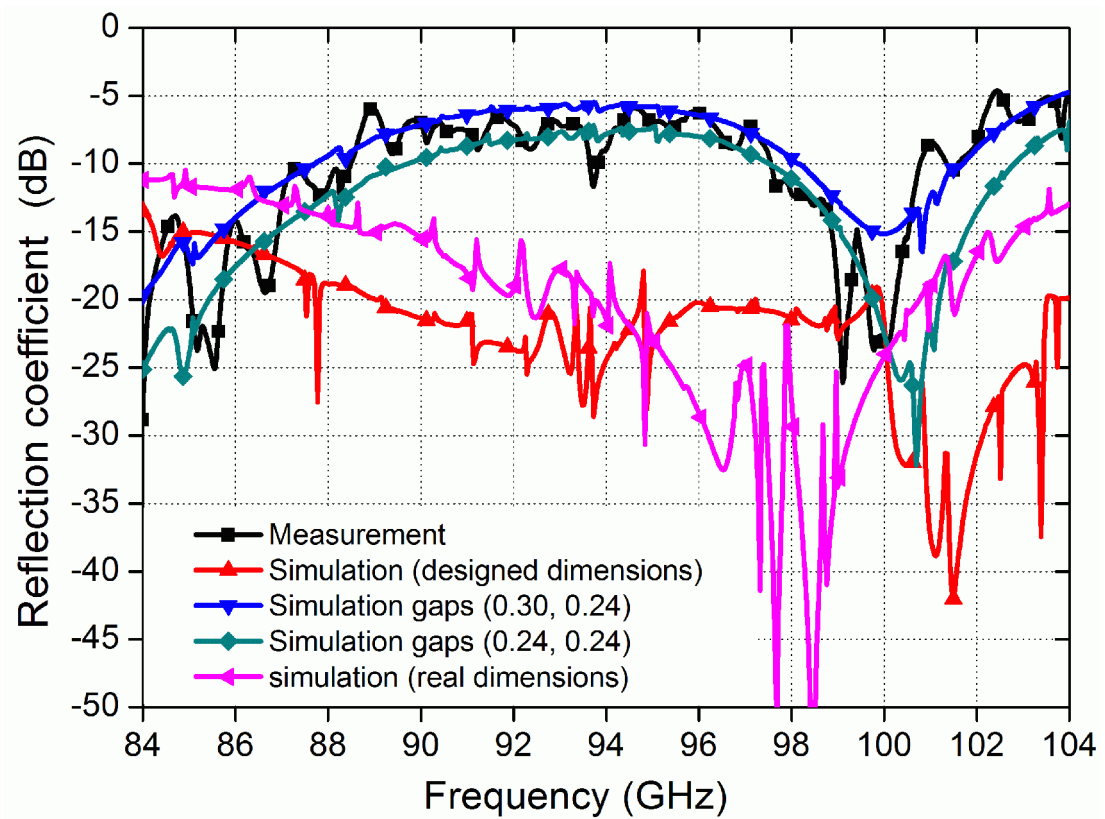
(b) The photograph of the three-layer window.

Fig. 4. 20 The CAD drawing and the photo of the three-layer window.

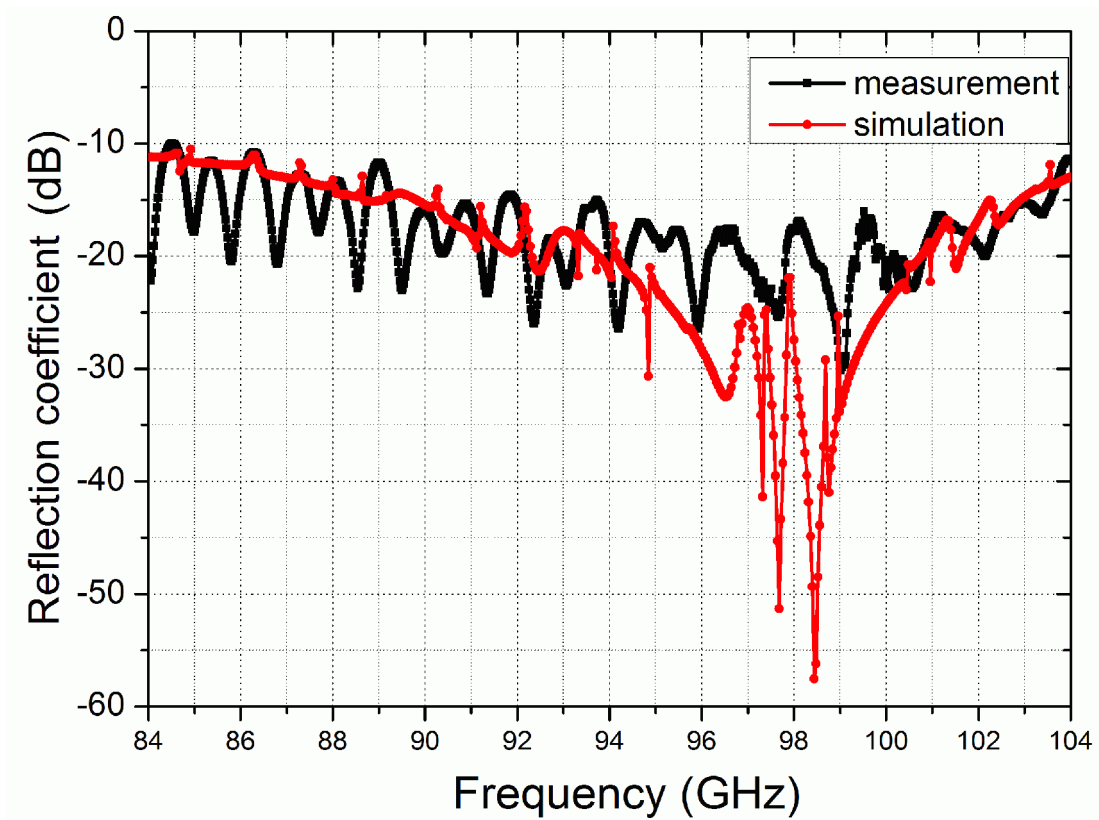
One port measurement was used when measuring the performance of the three-layer window. The setup is shown in Fig. 4.21(a). The measurement shows the performance of the three-layer window is very sensitive to the gap between the ceramic and the quartz pieces, as previously predicted from the simulation. Also, the tolerance from machining also makes the performance a little worse than the design, as seen from the comparison between the simulation results of the designed and measured dimensions from the manufactured window shown in Fig. 4.21(b). The first measurement is not as good a performance as expected, as shown in Fig. 4.21(b). The simulation result of the gaps of the ceramic disk and the quartz disks of 0.30 mm and 0.24 mm together with the real machined dimensions was found which agrees well with the experimental measurement. While in the design, the gaps are both 0.16 mm. A further adjustment on the gap between the ceramic disk and the quartz disks can be done by tightening or loosening the screws on the flanges. The best measurement result achieved is shown in Fig. 4.21(c). Better than -10 dB reflections can be obtained over the frequency band from 84 - 104 GHz and better than -15 dB can be achieved in frequency band 90 - 100 GHz.



(a) The measurement setup of the three-layer window;



(b) The first measurement;



(c) The best measurement result;

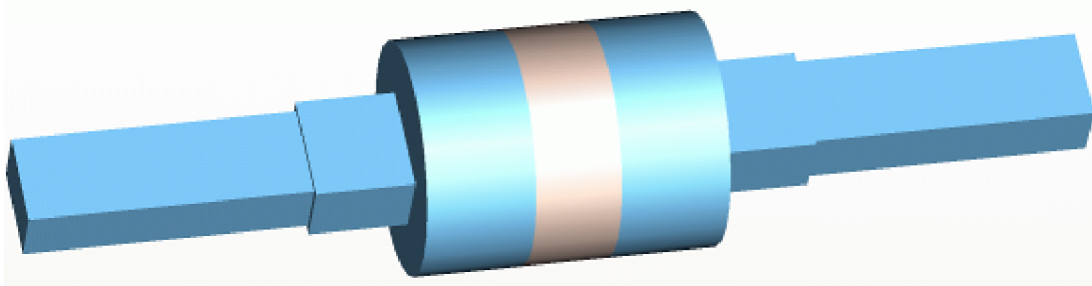
Fig. 4. 21 The measurement of the three-layer window.

4.3.2 Pillbox window

In the practical manufacture of the pillbox window, the ceramic piece was desired to have a large thickness to achieve high mechanical strength and also to make it have large brazing area which can reduce the possibility of vacuum leakage. In the previous optimization described in section 4.2, the ceramic thickness is 0.72 mm. It was suggested by the technician that it would be safer to increase the thickness to be thicker than 1.5 mm. Further more, to give consideration to the gyro-TWA experiments whose operating frequency band is 90 - 100 GHz, in the optimization routing, the performance in the frequency range was applied for larger weight. The optimization geometry by using the method described in section 4.2 under these restrictions is shown in Fig. 4.22(a). The final thickness of the ceramic piece is

1.82 mm, the diameter of the circular cavities is 4.93 mm and the lengths are 2.30 mm. The rectangular waveguides which connect to the circular waveguides are with dimensions of 2.29 mm and 1.50 mm, and finally connect to the rectangular waveguide one to the input coupler and the other to the standard waveguide. The simulation result is shown in Fig. 4.22(c). The optimized geometry has a very good performance in the frequency band 90 - 100 GHz according to the simulation, which can reach more than -30 dB reflection. However, it has worse performance in the other frequency bands than the one optimized for the whole frequency range 84 - 104 GHz.

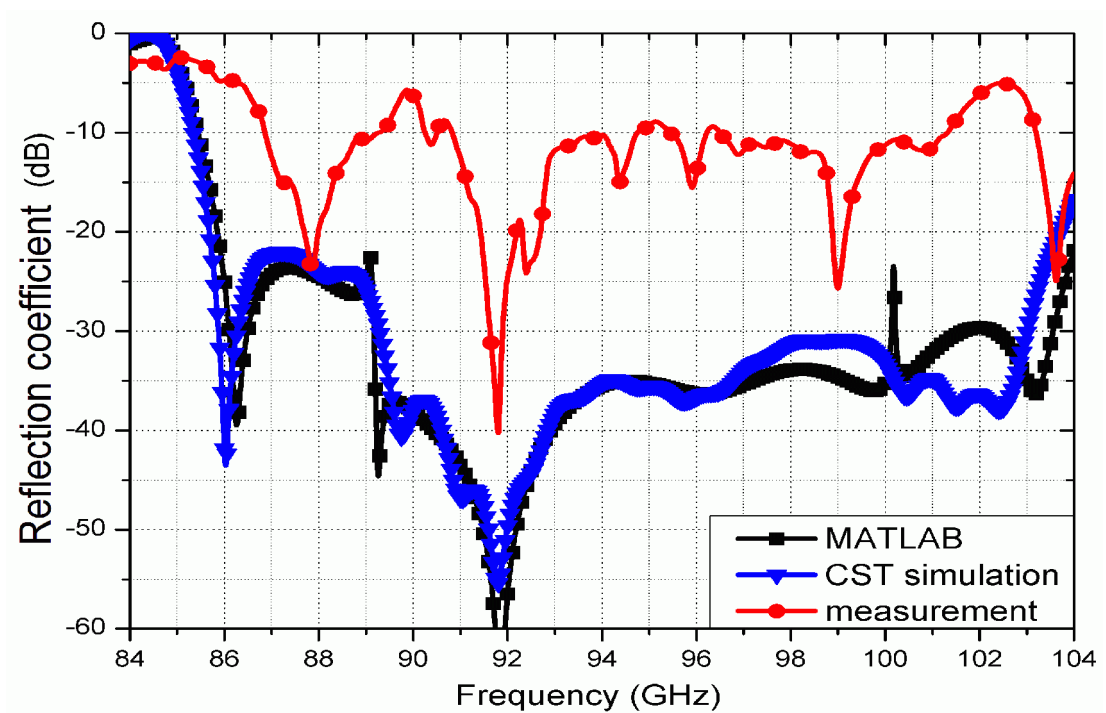
The pillbox window is composed from different parts, including the ceramic piece, the circular cavities, the waveguide taper, as well as the flange with a standard W-band rectangular waveguide. The ceramic disk was firstly brazed on the side edge to a Titanium tube that has a slot inside to avoid the discontinuity. Then the Titanium tube was brazed with a copper tube to produce the circular cavities. The reason to do this is the Titanium has similar thermal expansion as the ceramic which enables the vacuum seal to be made by melting the braze material to join the titanium sleeve to the ceramic. The waveguide taper was machined with the matching step using the spark erosion technique to produce a "cap" to hold the copper tube. All these machined parts are shown in Fig. 4.22(b), and finally they are brazed together as a single component after the measurement and vacuum leakage test.



(a) The model of the pillbox window;



(b) Photographs of the machined parts;

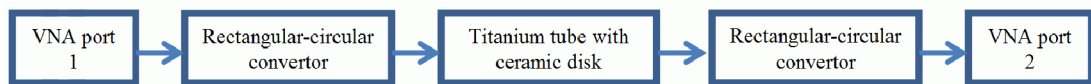


(c) The simulation result of the pillbox window;

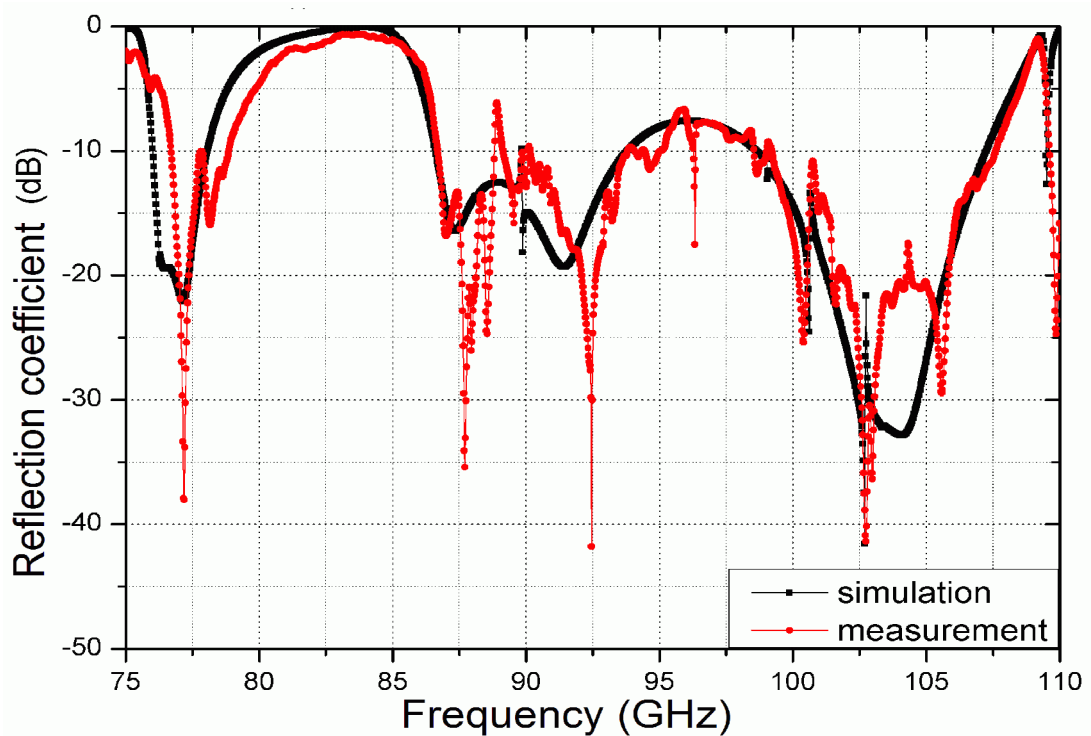
Fig. 4. 22 The pillbox window.

However, the measurement results were found quite different with the simulated result. Based on the experience on testing the three-layer window, the difference could be caused by the following reason, the dielectric constant of the ceramic piece, the tolerance of the machining, and the braze material that was left on the ceramic surface.

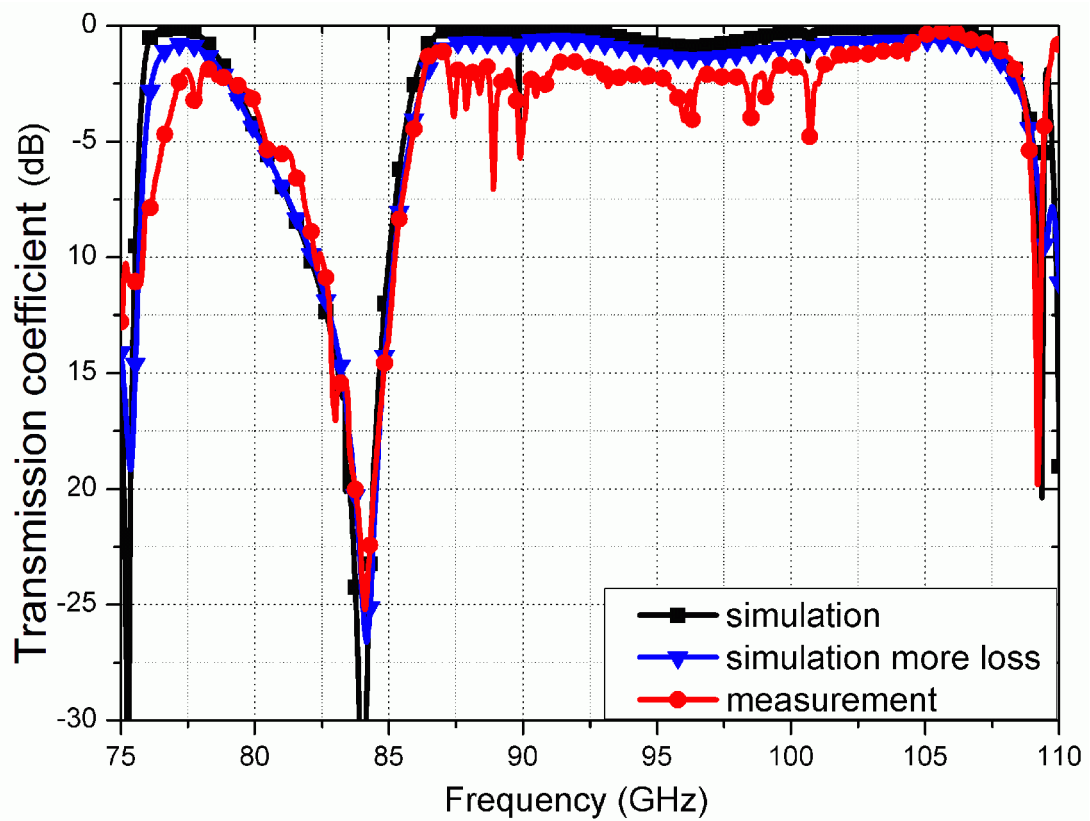
Several tests were carried out to investigate the mismatch between the simulation and the measurement. The dielectric constant of the ceramic piece was tested by the simplified structure, as shown in Fig. 4.23(a). When the dielectric constant was 9.52, the simulation result agrees well with the measurements as shown in Fig. 4.23(b). The dielectric constant value is slightly lower than the designed value 9.7. And the comparison between the simulation and the measurement also shows the ceramic disk has a large loss tangent up to 0.001.



(a) The setup to measure the dielectric constant of the ceramic disk;



(b) The simulation and measurement results of the reflection;

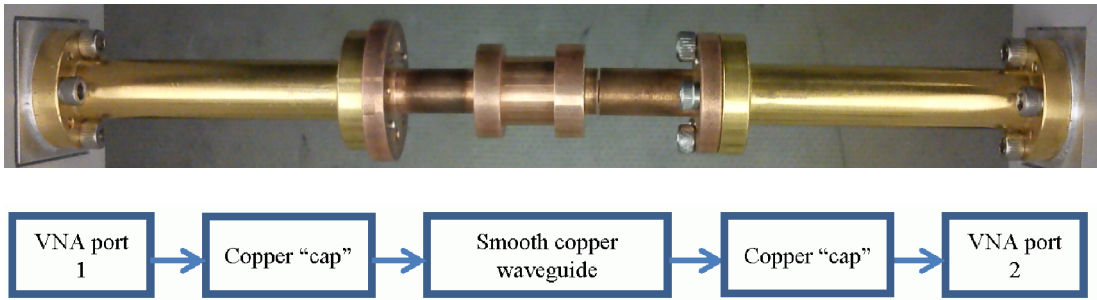


(c) The simulation and measurement results of the transmission (the rectangular-to-circular convertor has extra 1 dB loss);

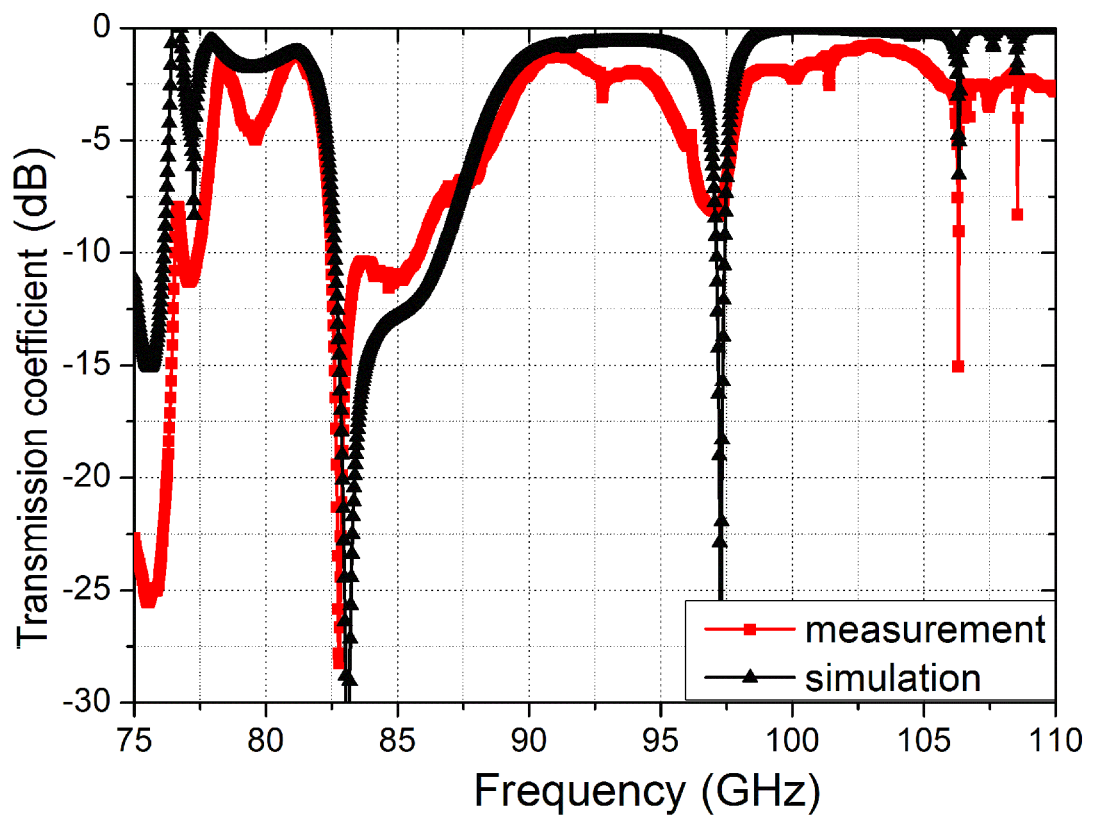
Fig. 4. 23 The measurement of the dielectric constant of the ceramic disk.

The copper "caps" had large machining tolerances, some dimensions were with more than 0.1 mm tolerance. More over, the rectangular steps did not align well with each other and had a 5 degree angle with respect to the axis. Their performance was tested by inserting a smooth waveguide between them, as shown in Fig. 4.24(a). It was found that accumulative tolerances resulted in an additional 1.5 dB loss as compared with the simulation results, and also a much larger loss in the lower frequency band. However, the simulation and measurements of the reflection did not match well in the high frequency range. This could be caused by poor machining of the copper "cap", resulting in misalignment of the matching section and the taper which was confirmed by measurement using a vernier caliper. Another reason may be a cavity effect. As there is a big discontinuity between the circular cavities, a part of the

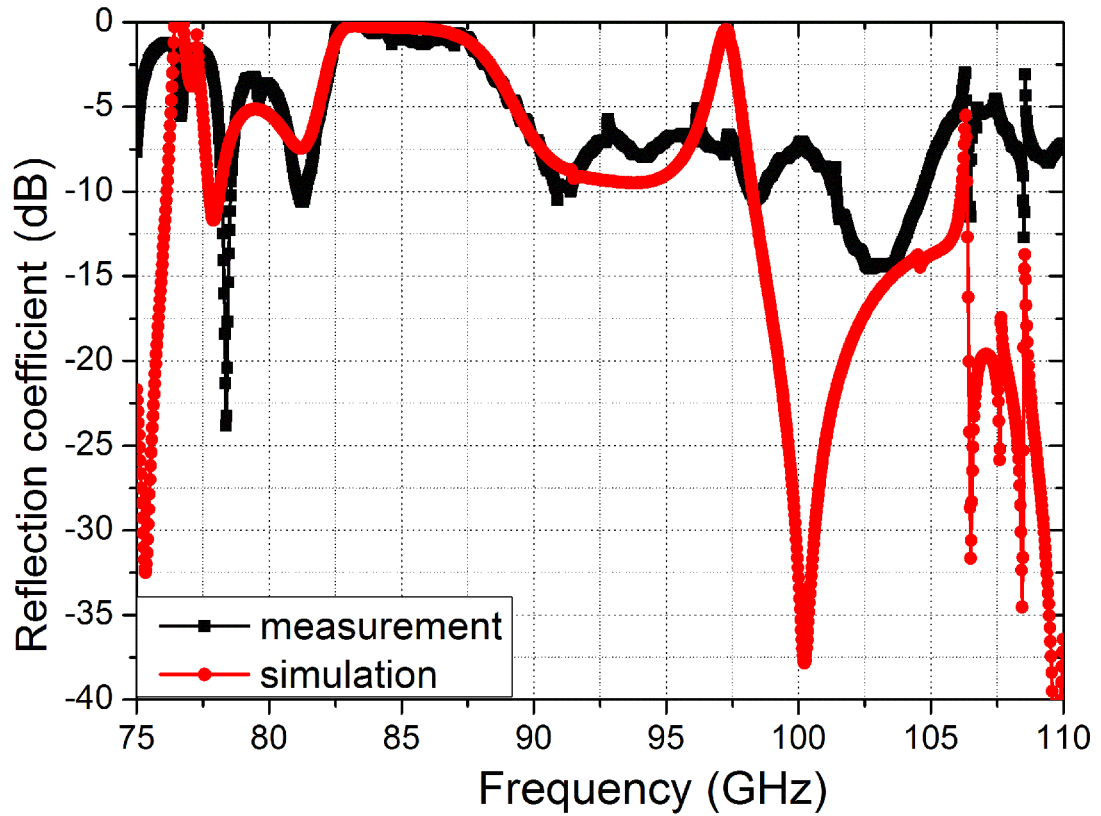
energy could be trapped between the copper "caps" in a sort of oscillation, which finally cause a large reflection.



(a) The measurement setup of the copper "cap";



(b) The measurement and simulation of the transmission;



(c) The measurement and simulation of the reflection;

Fig. 4. 24 The measurement of the dielectric constant of the ceramic disk.

Several attempts were carried out to improve the performance of the pillbox window, such as adjusting the cavity lengths and using nitride acid to clean the surface of the ceramic disk to remove the undesired braze material. However, it only had a slight improvement and the machining problem was still the dominant reason. The final measurements and the original predicted simulation results are shown in Fig. 4.25. Although the reflection result is still much worse than the design, it still can achieve an average -10 dB reflection in frequency range of 89 - 104 GHz.

Later measurements of the input coupler with this pillbox window, which is described in chapter 3, confirm the problems of the misalignments. After brazing the input coupler with the pillbox window, the reflection of the whole device is lower than the pillbox window itself before brazing. It should be not possible that multiple

components cascading together could achieve a lower reflection than a single component. However, after brazing the pillbox window with the input coupler, the connections of the pillbox window fill with brazing material which is conductor to avoid the small gaps. The cavity effects were therefore avoided. Furthermore, the pillbox window becomes one single piece after brazing then the misalignment problem was solved. As the pillbox window achieves a much lower reflection after brazing, it is possible for the input coupler with pillbox window to achieve better result than the pillbox window before brazing.

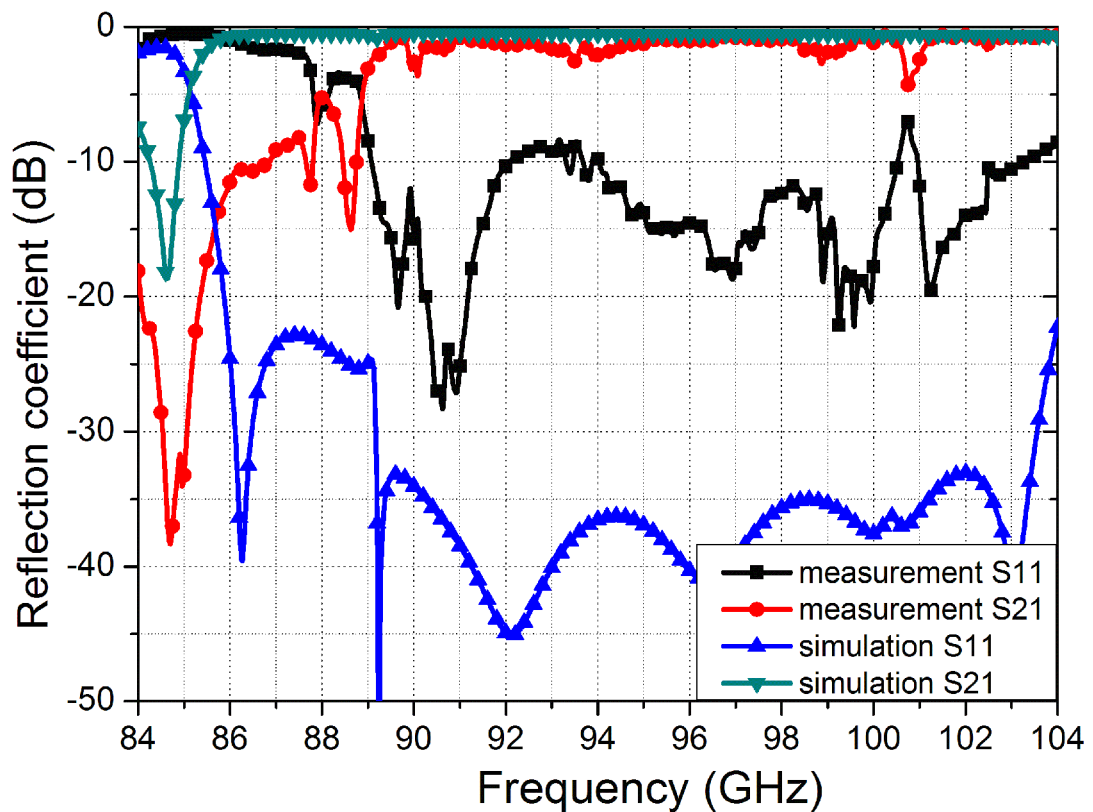


Fig. 4. 25 The measurement of pillbox window.

4.4 Conclusion

In summary, from the previous simulation, the block type window could achieve an excellent transmission when the number of the layers was more than three. The

pillbox type window can achieve a better transmission than the block type window if the number of the layers was less than three.

Comparison with the fabrication, a rectangular ceramic piece is much more difficult to machine than a circular one, and also there are a lot of technical difficulties to braze such a small ceramic piece (2.00 mm×1.30 mm). Therefore, we chose the pillbox type window for the coupler, and a three-layer block-type circular window at the end of the interaction section.

A three-layer window and a pillbox window were particularly designed for the gyro-BWO and the performance was measured using a VNA. The three-layer window achieved an average reflection less than -10 dB over the frequency range from 84 - 104 GHz and less than -15 dB in the 90 - 100 GHz frequency range. The pillbox window can achieve an average -10 dB over the 89 - 104 GHz frequency range. However, the performance was still worse than expected, which is mainly caused by the machining difficulty of the W-band microwave components due to the small size and critical tolerance limitation.

References

- [1] Liu Shunkang, "A fast computational technique for RF window in millimeter wave tubes", *Int. J. Infrared Milli.*, vol. 15, no. 5, pp.857-860, 1994
- [2] Stephen C. Bates, "Low Loss Sapphire Windows for High Power Microwave Transmission", <http://www.tvu.com/PLowLossSWinweb.htm>.
- [3] E. Savrun, V. Nguyen, and N. Gilmore, "High thermal conductivity aluminum nitride ceramics for high power microwave windows", 5th IEEE International Vacuum Electronics Conference (IVEC), California, April 27-29, 2004.
- [4] T. Manfred, "MPACVD-diamond windows for high-power and long-pulse millimeter wave transmission", *Diamond and related materials*, vol. 10, no. 9-10, pp. 1692-1699, 2001.
- [5] R. Heidinger, "Ceramic materials for microwave windows", *Int. J. Electronics*, vol. 64, no. 1, pp. 37 – 48, 1988.
- [6] V. V. P. Singh, E. Borie, A. K. Sinha, B. N. Basu and H. N. Bandopadhyay, "Thermo-Mechanical Analysis of Single-Disc Edge-Cooled Silicon Nitride Millimeter Wave Window for 200 kW CW Gyrotrons", *Int. J. Infrared Milli.*, vol. 21, no. 4, pp. 485-504, 2000.
- [7] L. Heikinheimo, J. A. Heikkinen, J. Lindén, A. Kaye, S. Orivuori, S. Saarelma, S. Tähtinen, R. Walton and F. Wasastjerna, "Dielectric window for reactor like ICRF vacuum transmission line", *Fusion Engineering and Design*, vol. 55, no. 4, pp. 419-436, 2001.
- [8] M. K. Ferber, H. D. Kimrey, and P. F. Becher, "Mechanical reliability of ceramic windows in high frequency microwave heating devices, Part 1 An analysis of temperature and stress distributions", *J. Mater. Sci.*, vol. 19, no. 11, pp. 3767-3777, 1984
- [9] R. Heidinger and F. Koniger, "Investigations on advanced ceramics for window applications in radiofrequency heating concepts", *J. Nucl. Mater.*, vol. 155-157,

pp. 344-347, 1988

- [10] Ming-Chieh Lin, Hao-Ming Chung and Alex Burke, “An analytical approach for the fast design of high-power waveguide windows”, *Wave Motion*, vol. 37, no. 2, pp. 183-188, 2003.
- [11] Ming-Chieh Lin, “A Multilayer Waveguide Window for Wide-Bandwidth Millimeter Wave Tubes”, *Int. J. Infrared Milli.*, vol. 28, no. 5, pp. 355-362, 2007.
- [12] Annapurna Das, Sisir K. Das, “Microwave engineering”, Mc Graw Hill Higher Education, 2007, chapter 4.
- [13] H. Nakatsuka, N. Yoshida, I. Fukai, “Three-dimensional analysis of a vacuum window connected to waveguide”, *IEEE Trans. Plasma Sci.*, vol. 16, no. 4, pp. 416-422, 1988.
- [14] Shunkang Liu, “A RF window for broadband millimeter wave tubes”, *Int. J. Infrared Milli.*, vol. 17, no. 1, pp. 121-126, 1996.
- [15] Hiroyuki Arai, Naohisa Goto, Yoshitaka Ikeda, and Tsuyoshi Imai, “An analysis of a vacuum window for lower hybrid heating”, *IEEE Trans. Plasma Sci.*, vol. PS-14, no. 6, pp. 947 – 954, 1986.
- [16] Erik Kurt Duerr, “Millimeter-wave Integrated Horn Antennas”, Master thesis, Massachusetts Institute Of Technology, 1998.
- [17] Keller Reinhard and Arndt Fritz, “Rigorous modal analysis of the asymmetric rectangular iris in circular waveguides”, *IEEE Microwave and Guided Wave Letters*, vol. 3, no. 6, pp. 185-187, 1993.
- [18] R. Keller and F. Arndt, “Rigorous CAD of Rectangular Aperture Coupled Circular Waveguide Multimode Filters”, *Proc. 23rd European Microwave Conference*, Cannes, pp. 1337-1342, 1994.
- [19] R. H. MacPhie and K. L. Wu, “Scattering at the junction of a rectangular waveguide and a larger circular waveguide,” *IEEE Trans. Microwave Theory Tech.*, vol. 43, no. 9, pp. 2041–2045, 1995.

[20] MATLAB GA Toolbox, Department of Automatic Control and Systems
Engineering, University of Sheffield, UK,
<http://www.acse.dept.shef.ac.uk/cgi-bin/gatbx-download>.

Chapter 5

Depressed Collector

5.1 The principle of depressed collector

In beam-type microwave tubes, the electrons are always emitted from a cathode and stopped at a collector, as shown in Fig. 5.1. In conventional design, the collector shares the same potential with the microwave tube which is grounded. The spent beam strikes on the surface of the collector and dissipates their kinetic energy into heat. Depressed collectors are a bit different from conventional design. “Depressed” here means the collector has a depressed potential as compared with the main body of the tube.

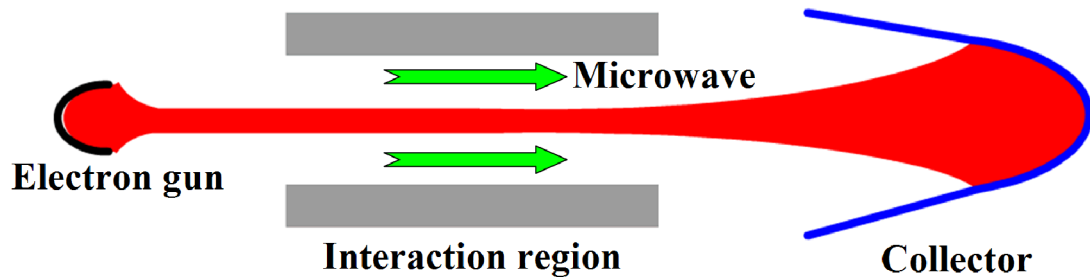


Fig. 5. 1 Schematic diagram of a beam-type microwave tube.

The principle of how the depressed collector works can be examined from the view of the electric circuit [1]. As seen from Fig. 5.2 (a), in this conventional microwave tube, a power equal to $P=V_0I_0$ is supplied to the cathode, and a microwave power of P_{mw} is generated. To make it simple, we assume that the whole circuit has no loss and there is no other power supply except the power supply between the cathode and beam tube. Then the overall efficiency of the microwave device can be written as

$$\eta_{overall} = \frac{P_{mw}}{P} = \frac{P_{mw}}{V_0 I_0} \quad (5.1)$$

The rest power of $P - P_{mw}$ in the spent beam will be dissipated into heat finally. Then if we apply another power supply between the collector and the cathode, and the microwave tube can still produce an output power of P_{mw} as we do not change any other parameters of the microwave structure, it can be seen that the power supply by the circuit loop is

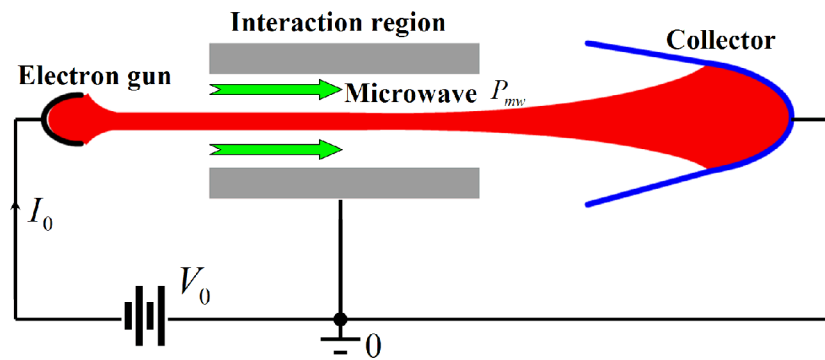
$$P = V_0 I_0' + V_1' I_1 \quad (5.2)$$

Then the overall efficiency can be written as

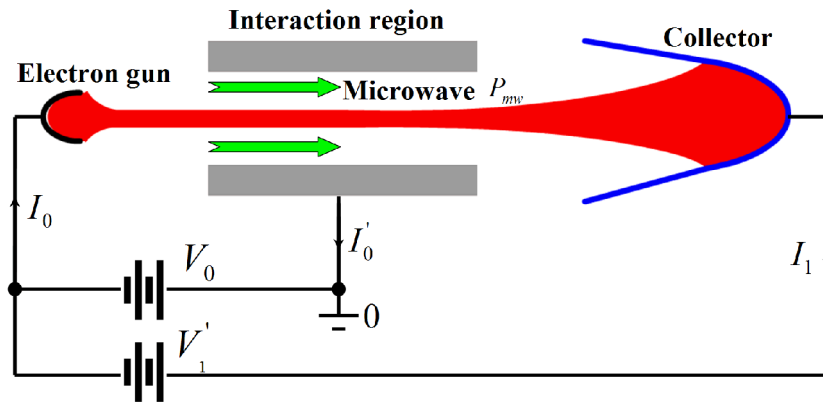
$$\eta_{overall} = \frac{P_{mw}}{P} = \frac{P_{mw}}{V_0 I_0' + V_1' I_1} \quad (5.3)$$

Suppose most of the electrons pass through the microwave structure, which is reasonable for most of the microwave devices, then we have $I_0' = 0, I_1 \approx I_0$. The overall efficiency then becomes

$$\eta_{overall} = \frac{P_{mw}}{P} \approx \frac{P_{mw}}{V_1' I_0} \approx \frac{P_{mw}}{V_0 I_0 - (V_0 - V_1') I_0} \quad (5.4)$$



(a) Conventional microwave tube;



(b) Microwave tube with voltage depression;

Fig. 5. 2 Power supplies of the microwave device.

Comparing Eq. 5.1 with Eq. 5.4, the overall efficiency improves if $V_0 > V_1'$ is satisfied. In general, there are two explanations of the term $(V_0 - V_1')I_0$. For power supply engineers, the depressed collector was regarded as a technology to reduce the input power from V_0I_0 to $V_1'I_0$. And the physics community considers the depressed collectors as passive converters that can transfer the kinetic energy of the spent electrons into potential electric energy. In this view, the electrons are accelerated between the cathode and microwave tube and contain an average kinetic energy of eV_0 when they travel out of the microwave tube. Then the electrons pass through the retarding electrostatic field between the microwave tube and the depressed collector. In this process, a proportion of the overall input power with the value of $e(V_0 - V_1')$ is converted into electric power. In this paper, we use “recovery” from the view of physics process.

Another conclusion from Eq. 5.4 is that to increase the overall efficiency, V_1' should be as small as possible. However, the depressed electric field between the beam tube and the collector should not exceed the kinetic energy of the spent beam or the electron beam will return back to the interaction region and cause undesired effect. The ideal depressed collector is aimed to sort all the electrons landing on the

collector with zero kinetic energy. As we know from electron cyclotron maser instability, the electrons interact with the electromagnetic field in different phases. Some are accelerated while the others are decelerated by the electromagnetic field. The spent electron beam has an energy spread when they enter the collection region. All the electrons can not be well sorted by a single electrode, and multi-stage depressed collector with multiple electrodes, shown in Fig. 5.3, was then developed to solve this problem soon after the single depressed collector was brought forward. The collected power or the reduced part of the input power can be written as

$$P_{col} = \sum_{i=1}^N V_i I_i \quad (5.5)$$

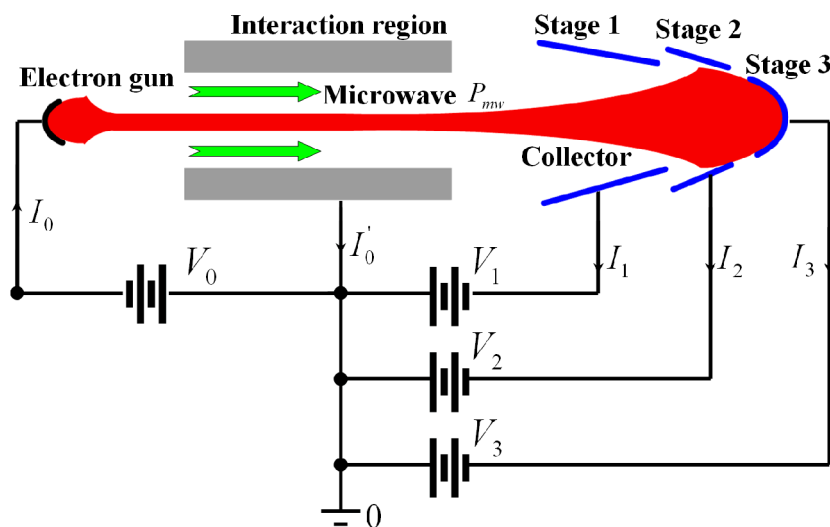


Fig. 5. 3 Schematic of multi-stage depressed collector.

Depressed collectors are important for high power microwave devices because they have following advantages:

1. By using the depressed collector, the DC power supply of the microwave tubes can be reduced, thus improve the overall efficiency. If we can recover the power from the spent electrons and double the overall efficiency, that means approximate half the cost of the power supply is required. For the applications that high power microwave tubes are used, such as high energy

accelerators and controlled thermonuclear fusion, a lot of money can be saved if the depressed collectors can be successfully applied.

2. The spent electrons lost a large proportion of their kinetic energy before landing on the surface of the depressed collector. Therefore, the heat dissipated on the electrodes can be reduced. In high power microwave devices, the cost of the cooling system can also be reduced. In medium power microwave devices, air cooling systems may be sufficient to make the whole device more compact.
3. The reducing of kinetic energy of the spent electrons also results in lower X-ray emission. It provides extra safety and reduces the shielding requirements around the microwave tubes.

5.2 The derivation of depressed collector

The earliest concept of depressed collectors started in the 1940s [2]. In the late 1950s, the theoretical calculation of the electron trajectories neglecting space charge in a crossed-field region was developed [3]. A two-stage depressed collector was used to improve the efficiency of a traveling wave tube (TWT) and achieved a collection efficiency of 56% [4]. However, when the number of the stages exceeded two, a tremendous amount of backstreaming was detected. The science of depressed collectors was first studied in more depth at the end of the 1960s [4]. It was based on full understanding of the mechanism of the electron beam collection. Several models of electrostatic or electromagnetic field were developed at the beginning of the 1970s [15, 21, 25]. After that, multistage collectors were successfully applied in many applications without the deleterious effects of the backstreaming. A ten-stage electrostatic depressed collector was tested on a klystron with 1 kW continuous wave (CW) output at 750 MHz and achieved a collection efficiency of 70% [5]. A four-stage depressed collector achieved a collection efficiency of 81% and 83% was tested on a dual band TWT [6]. Computers were then employed to simulate the

trajectories of the spent electrons to predict the performance of depressed collectors in linear beam devices in late 1970's [7].

In 1980s, research on gyrotrons proved the great potential in the applications of nuclear fusion and advanced accelerators [52]. These large projects need a large number of high power gyrotrons and the efficiency of gyrotrons is extremely important. However, it is much more difficult for depressed collectors to achieve high collection efficiency in gyrotron devices compared with those linear beam devices. The depressed collectors developed for the linear beam devices can only recover the energy associated with axial motion. However, in gyrotrons, most of the kinetic energy is in rotational motion. To achieve high collection efficiency, the rotational energy needs to be converted into axial motion. Moreover, the magnetic field in gyrotron devices is larger than in the linear beam tubes. The magnetic field needs to be reduced to a reasonable value otherwise the electrons would be focused in a small region and unable to be well sorted. The research on depressed collector for gyro-devices was first reported in the late 1980s [8]. In the University of Maryland, a double magnetic cusp gyrotron with a two-stage depressed collector was developed. The first cusp provided a large rotational velocity to the electrons after they were emitted from the cathode, and the second cusp was used to unwind the axis encircling electrons before proceeding towards the depressed collector [8, 9]. The unwinding cusp magnetic field provides a possible solution to sort the spent electrons in the gyrotron.

In recent years, various particle-in-cell (PIC) codes were developed to obtain a detail study on the design of the microwave tubes, and some of them were developed to simulate the multistage depressed collectors, such as GUN3D [10], LKOBRA [11], and so on. There were also some PIC codes specifically designed for simulating the depressed collectors, such as COCA [12] and MICHELLE [13].

Gyro-BWOs obtained great interest in recent years for their wide frequency tuning range. However, they are inheritably low efficiency. A depressed collector can significantly improve the performance if high collection efficiency can be achieved. It is more difficult to employ depressed collectors on gyro-BWOs than the other gyro devices. For gyrotrons and cavity-coupled TWTs, the operation frequency is rather narrow, and the depressed collector can always achieve optimum collection efficiency once it is designed. For a broadband helix TWT, the parameters of the spent beam only have small variations in the operating frequency band. Therefore, the depressed collector can achieve a high efficiency. However, for gyro-BWOs, the output microwave power changes when tuning the operating frequency. Therefore, the parameters of the spent electron beam are also changing and the depressed collector can no longer keep the optimum collection efficiency if the geometry and the potentials on the electrodes are unchangeable. To achieve a high performance over the frequency tuning range, the potentials on the electrodes of the depressed collector should be adjustable.

5.3 Different types of depressed collector

The depressed collectors were firstly applied to the linear microwave tubes, such as klystrons and TWTs. In 1970s, several types of collectors were designed and tested, such as electrostatic symmetric and asymmetric structures and electromagnetic asymmetric structures. In this section, the principle of these types of depressed collectors and the experimental results are introduced [14].

5.3.1 Cylindrical tubes [4]

The first experiment of the depressed collector was carried out in the late 1950s, where a two-stage depressed collector was applied to a low-efficiency helix TWT. The collector was composed by two cylindrical tubes, as shown in Fig. 5.4. The two cylindrical tubes were insulated from each other by mica and shielded from the

focusing magnetic field by a magnetic shield. The electrons travelled through the helix TWT waveguide and were finally collected by the cylindrical tubes. For the tested low-power, low-efficiency device, the radial and axial velocity spread were small, and almost all the spent electrons were collected by the back collector. Therefore, a significant improvement in overall efficiency could be obtained. However, the collection efficiency in the experiment was still far less than the theoretical maximum because of the backstreaming electrons including the secondary electrons and the reflected primary electrons. Furthermore, when looking into the electric field between the front and back collectors, it was clear that the boundary of the electrodes did not coincide with the equipotential surface. A fringing field with lens effect was formed and prevented the electrons with low energy to be collected and produced large backstreaming.

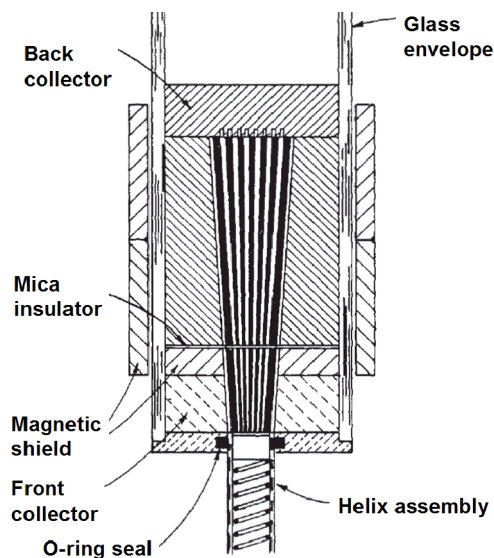


Fig. 5. 4 Schematic diagram of the depressed collector with cylindrical tubes [4].

For high-power microwave tubes with large velocity spread, the depressed collectors with cylindrical tubes were not successfully applied. As the development of the “scientific” depressed collectors based on better understanding of the mechanism of the electron collection, depressed collectors of this type were no longer used.

5.3.2 Electrostatic symmetric structure

The electrostatic symmetric structure employs a defocusing field to sort the spent electrons. The defocusing field is defined as those whose 2nd derivation of the potential is negative. That is

$$\frac{d^2V}{dz^2} < 0 \quad (5.6)$$

In the defocusing field, the equipotentials are concave surfaces. A parabolic defocusing fields is defined as

$$y^2 = \frac{4V^2}{V_0^2 A^2} \left(x + \frac{V^2}{V_0^2 A^2} \right) \quad (5.7)$$

where A is a constant, V is the equipotential value, V_0 is the beam voltage, and x and y indicate the coordinates. The beam trajectories in such an electric field and the equipotentials are shown in Fig. 5.5.

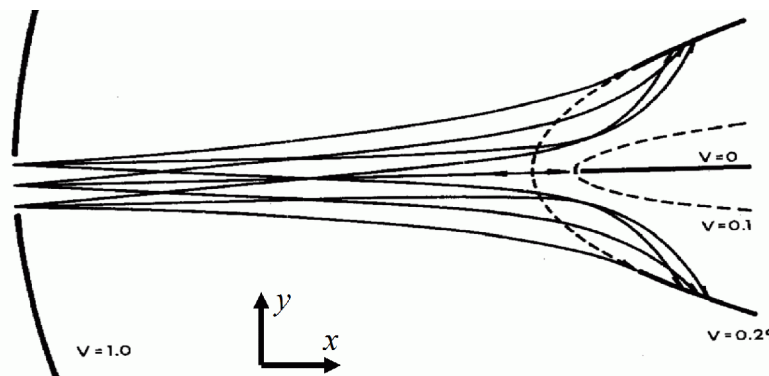


Fig. 5.5 Beam trajectories of the electrons in the defocusing field.

The parabolic defocusing fields can be implemented by a long symmetric spike with negative potential as shown in Fig. 5.6. The spent electrons are deflected from the axial direction and move towards the electrodes after they propagate down from the apex of the trajectories, as shown in Fig. 5.6. The electrostatic symmetric structure is

efficient in sorting the off-axis electrons. However, on-axis electrons will become backstreaming when their kinetic energies are less than the energy of the depressed electric field [15, 16].

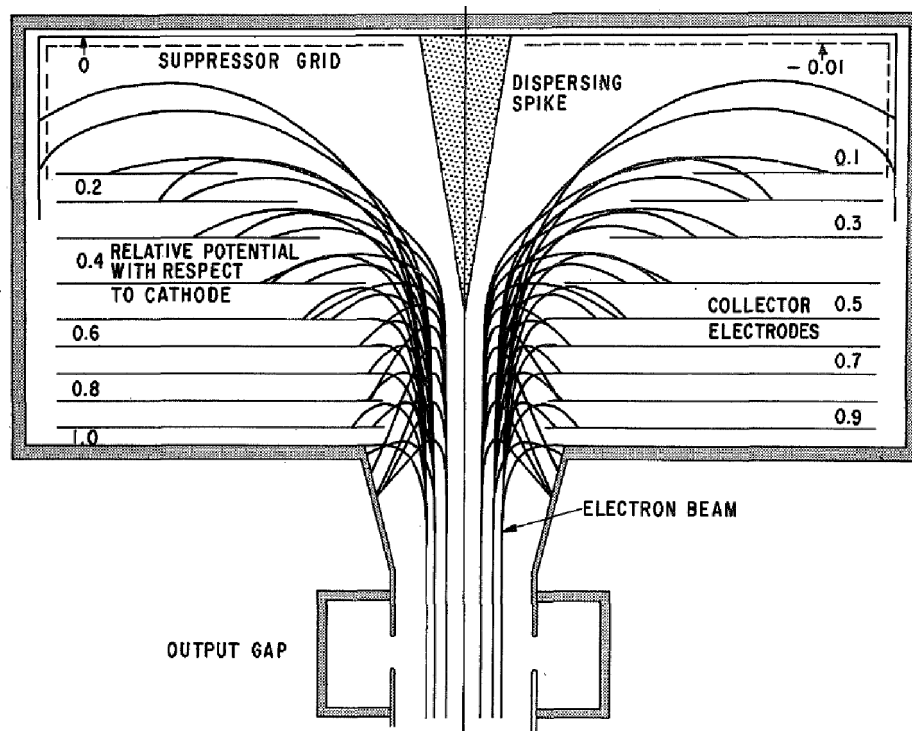


Fig. 5. 6 Sketch of electrostatic symmetric structure and the beam trajectories [15].

Most of the spent electrons are off-axis in gyro-devices, therefore, the depressed collectors with a symmetric structure in gyro devices may not cause serious backstreaming.

The symmetric multistage depressed collectors have been designed and tested in several gyrotron devices. A three-stage depressed collector with an efficiency of 76% was designed to improve a gyro-klystron from an electronic efficiency of 30% to an overall efficiency of 64% [9]. A two-stage depressed collector with collection efficiency of 60% was designed for a 110 GHz, 1 MW gyrotron. An overall efficiency of 60% was achieved and the heat dissipated on the collectors was lowered from 1.67 to 0.67 MW at an output power of 1 MW [17, 18]. A compact two-stage depressed collector was designed for a 1.5 MW coaxial cavity gyrotron operating at

165 GHz in the transverse electric TE_{31,17} mode by FZK, Karlsruhe, Germany. A collection efficiency of 73% was achieved resulting in an increase of the overall efficiency from 36.5% to 62.5% [19]. A Ku-band gyro-BWO with a single-stage depressed collector was reported in [20]. However, there is no paper on the experimental results of a gyro-BWO with a multi-stage depressed collector.

5.3.3 Electrostatic asymmetric structure

Another structure for a depressed collector uses an asymmetric focusing field. A focusing field is defined as those whose 2nd derivation of the potential is positive. That is

$$\frac{d^2V}{dz^2} > 0 \quad (5.8)$$

In the focusing field, the equipotentials are convex surfaces. One of the example is the two-dimensional hyperbolic focusing field

$$V = \frac{V_0(x^2 - y^2 - A^2)}{B^2 - A^2} \quad (5.9)$$

where A , B are constants, V_0 is the beam voltage and x and y are the coordinates. The electron trajectories in such a focusing field are shown in Fig. 5.7 [21].

The asymmetric structure has the advantage of reducing the probability of the backstreaming. Moreover, a well designed asymmetric structure has higher efficiency than a symmetric structure with the same number of stages, for the asymmetric structure is not as sensitive as symmetric structure to the angular spread of the spent electrons. However, the asymmetric structure is much more complicate than the symmetric one so that it is harder to manufacture.

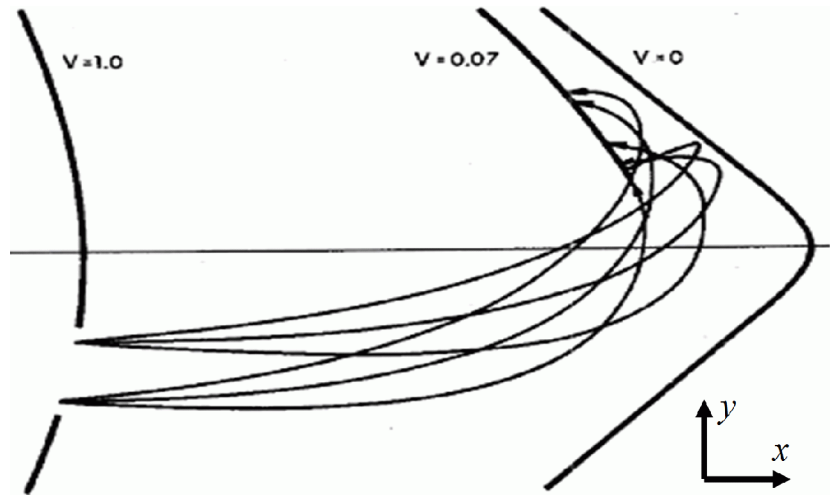


Fig. 5. 7 Beam trajectories of the electrons in focusing field [21].

Experiments on a three-stage asymmetry depressed collector were carried out by Litton Industries in 1976. The depressed collector was applied on a high-power dual-mode TWT for electronic countermeasure (ECM) applications [22, 23]. The cross section of the structure and the beam trajectories are shown in Fig. 5.8(b). In the real experimental setup, the curved surfaces in the ideal electrode geometry, shown in Fig. 5.8(b), were approximated by planar electrodes to simplify the manufacture. The 1st and 2nd electrodes were made from copper while the 3rd stage was fabricated from molybdenum wire mesh. The space between the 3rd electrode and the back wall was used to trap the secondary electrons. The potentials on the electrodes were $0.5V_0$, $0.75V_0$, and V_0 , respectively.

The collection efficiencies for the tested three-stage depressed collector on a dual mode TWT theoretically were 71% in the high mode and 79% in the low mode. In experiment, 71.1% efficiency in high mode and 75.6% efficiency in low mode were achieved.

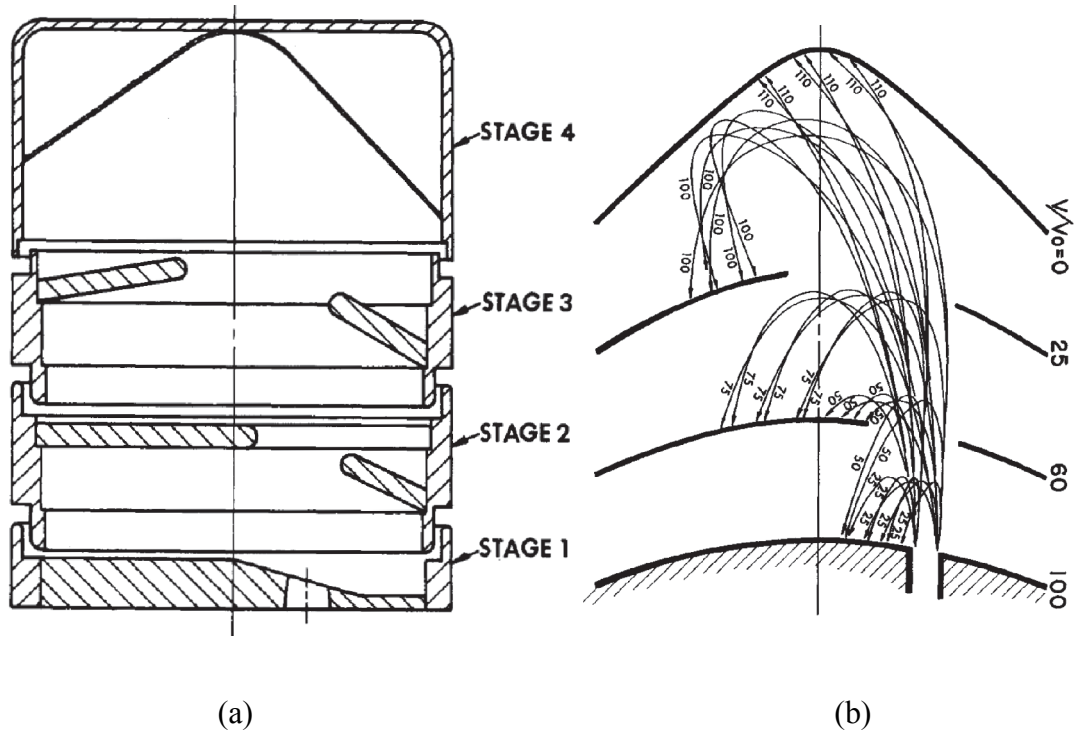


Fig. 5. 8 (a) Cross section of a 3-stage asymmetric structure and (b) electron trajectories [22].

5.3.4 Tilted electric field (TEF) structure

The other depressed collector is the tilted electric field (TEF) collector whose structure is also asymmetric. However, it is an electromagnetic collector for not only an electric field but also a magnetic field is employed to sort the spent electrons.

The idea of using a transverse magnetic field to sort the electron velocities in collectors was firstly published in 1959 [3]. In this paper, a cross field composed by a transverse electric field in the y axis and a magnetic field in x axis was used to sort the electrons to different electrodes as shown in Fig. 5.9 (Here suppose the electrons travelled in the z axis). The motion of the spent electrons follows the equations

$$\begin{cases} m\ddot{x} = eE_x - eB_y\dot{z} \\ m\ddot{z} = eB_y\dot{x} \end{cases} \quad (5.10)$$

From Eq. 5.10, the decrease of the kinetic energy of the spent electrons in the z axis is determined by the magnetic field B_y . The electrons did not lose much of their kinetic energies as the kinetic energies converted from the z component to y component. This type of collector was discounted after reports of such depressed collectors in the “scientific” press.

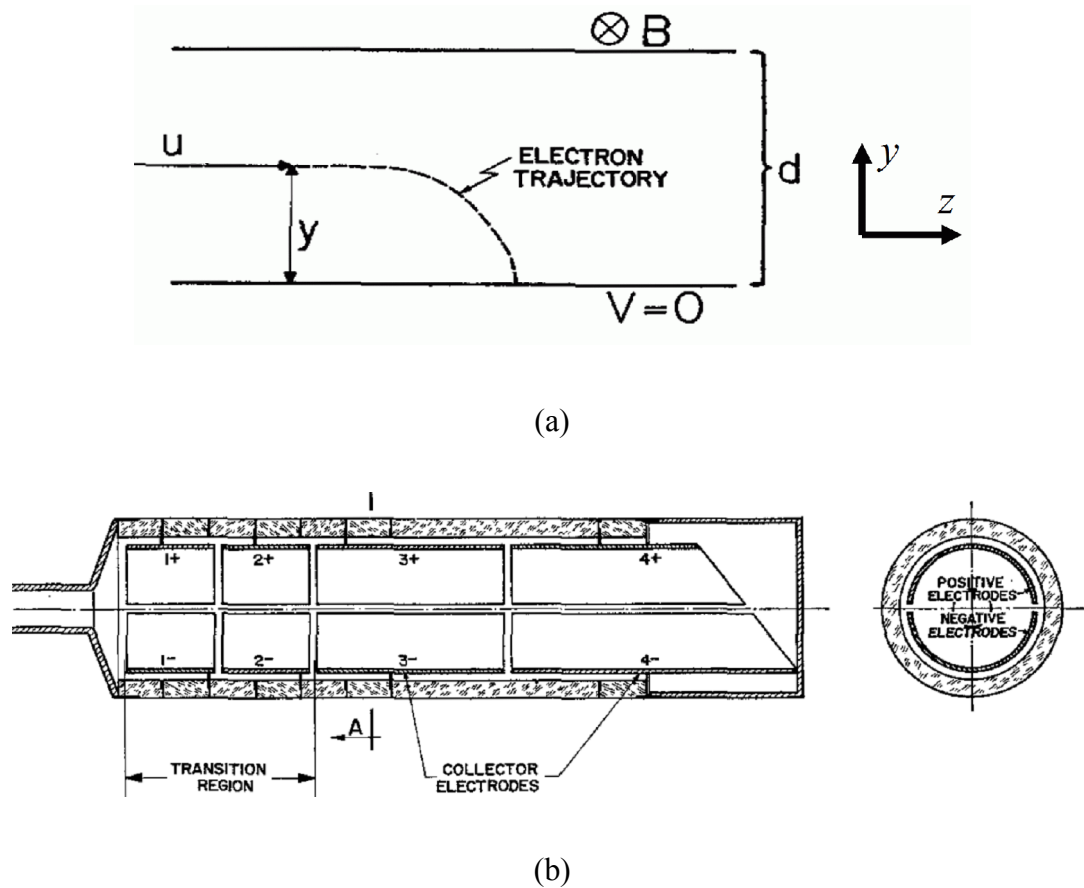
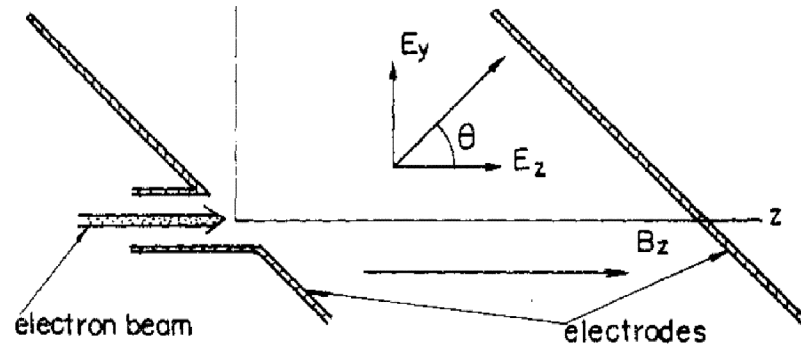
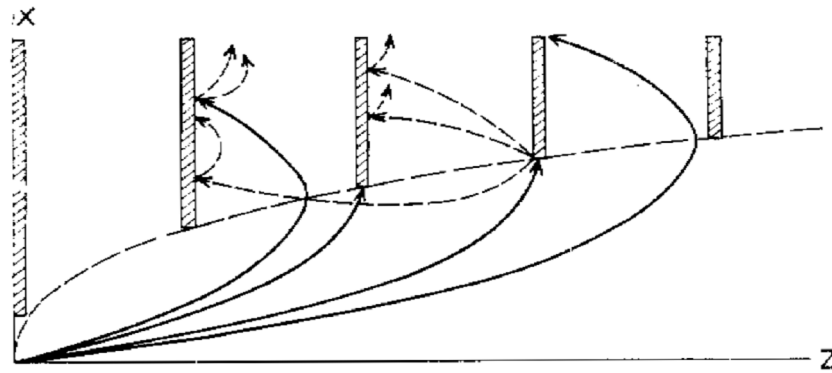


Fig. 5. 9 Electron trajectory in cross field (a), cross section of depressed collection using cross field (b) [3].

The tilted electric field collector contains a magnetic field parallel to the original beam axis throughout the collector volume as well as a set of plane parallel electrodes inclined at an angle with respect to the beam axis as shown in Fig. 5.10 [24, 25].



(a)



(b)

Fig. 5. 10 (a) Schematic of the field configuration of tilted electric field structure, (b) the electron trajectories in a practical design [24].

The equations of the motion of an electron in the electromagnetic field are

$$\begin{cases} m\ddot{x} = -eB_z\dot{y} \\ m\ddot{y} = -eE_z \tan\theta + eB_z\dot{x} \\ m\ddot{z} = -eE_z \end{cases} \quad (5.11)$$

where E_z and B_z are the electric and magnetic field in the z axis, respectively. θ is the tilt angle of the electric field with respect to the z axis. Suppose the initial conditions for time $t=0$ are $x = y = z = \dot{x} = \dot{y} = \dot{z} = 0$, and $\dot{z} = v_0$.

The solution of Eq. 5.10 becomes

$$\begin{cases} x(t) = E_z \tan \theta \frac{t - B_z - \sin \omega t}{\omega B_z} \\ y(t) = E_z \tan \theta \frac{\cos \omega t - 1}{\omega B_z} \\ z(t) = v_0 t - \frac{\omega E_z t^2}{2 B_z} \end{cases} \quad (5.12)$$

where $\omega = eB_z/m$ is the angular cyclotron frequency corresponding to B_z . In Eq. 5.12, the electron is uniformly decelerated in the z axis, thus it is possible to achieve a soft-landing collection. In the x axis, the motion is composed by a uniform drift with the speed of $E_z \tan \theta / B_z$ and there is a small cyclotron motion in x - y plane. The trajectories of electrons with different incident energies in the x - z plane of the collection region are shown in fig. 5.10 (b).

The advantage of the TEF collector is it completely eliminates the problems associated with electron backstreaming. When secondary electron emitted from the surface of the electrode, it will drift further in the x direction due to the uniform drift velocity in the x axis and never go back to the interaction region. The disadvantage of the TEF collector is its asymmetric structure and the requirement of a magnetic field. Moreover, a large axial magnetic field is required because the drift velocity in the x axis is inversely proportion to the magnitude of the magnetic field. A small magnetic field will cause a large radius of the collector.

An experiment of a five-stage TEF collector was carried out on a medium-power periodic-field type TWT. The overall efficiency of the microwave tube was improved from 19% to 46% [3].

5.4 The effect of secondary electron emission

5.4.1 The effect of secondary emission

Although the retarded electric field in the collection region can significantly reduce the kinetic energy of the spent electron beam, the rest kinetic energy is still large. When the spent electrons strike on the surface of the electrodes, the incident energy is large enough to produce the secondary electrons. A simple schematic of a primary electron with energy E_0 impacting with the material of the electrode and generating the secondary electrons with energy $E_1 \sim E_n$ is shown in Fig. 5.11.

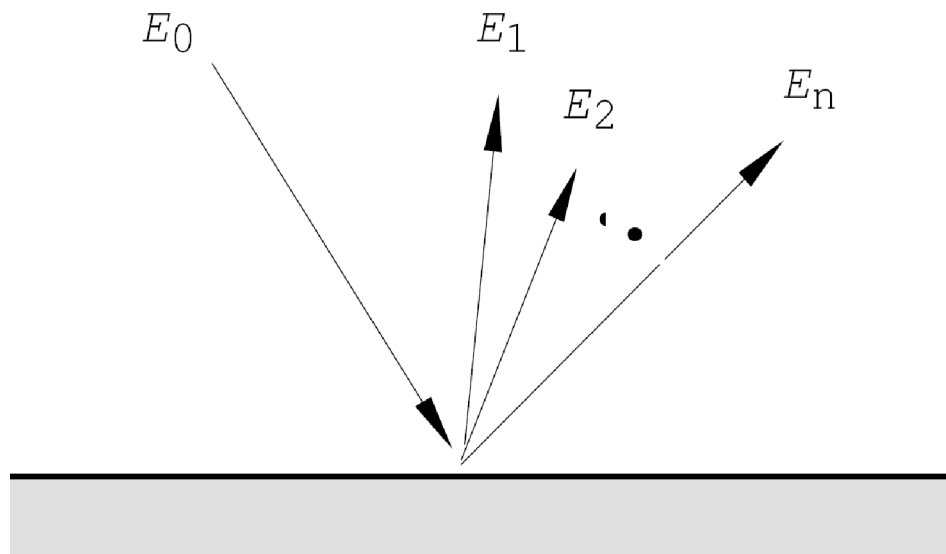


Fig. 5. 11 Schematic of the generation of secondary electrons

The secondary emission is an important issue in the design of multistage depressed collectors. The collection efficiency can be approximately 10% lower when the secondaries are taken into account. In reference [26], the collection efficiency of a two-stage depressed collector for 1-MW CW gyrotrons varied from 68% to 60% when the secondaries were considered.

The secondary electrons have several negative effects on high power microwave devices. First of all, secondary electrons carrying velocities with opposite direction to the primaries will be accelerated by the electrostatic field in the collection region and some of them will become backstreaming. The secondary electrons absorb energy from the electrostatic field and decrease the collection efficiency. Secondly, the backstreaming entered into the RF interaction region, which will generate noise on the microwave output and decrease the performance of the microwave tube. Thirdly, in high average power devices, the backstreaming may contribute an additional thermal power on the thermally stressed waveguide structure [27]. And also, multipacting caused by the secondary electrons may lead to RF breakdown in multihundred kW microwave devices [53]. Thus in depressed collectors, it is essential to reduce the current of secondary electrons to be as low as possible.

This section introduces the basic concept on the secondary emission and the physical models of the true secondary electrons and the scattered electrons. The simulation results of the depressed collector with the secondary electron emission will be represented in chapter 6.

5.4.2 Models of secondary electron emission

Secondary electrons are generally divided into three classes [28]. The first class is the true secondary electrons (TSEs) which are knocked out from the surface of the material due to the bombardment of the primary electrons. The true secondaries are always with energy less than a few tens of electronvolts, normally regarded as 50 eV. The second class is the rediffused electrons. The primary electron impacts with one or more atoms inside the material then is reflected back out. The collision is inelastic and the energy of the rediffused secondaries can be any value from a few tens of electronvolts to the incident energy. The other class is the backscattered elastic electrons in which the incident electron is reflected back without losing its kinetic energy. In the simulation, the rediffused electrons and the backscattered elastic

electrons were treated by a uniform model for they had the same physical nature. The term of "backscattered electron" (BSEs) was used to indicate these two types of secondary electrons. Fig. 5.12 shows an example of the contribution of the three components when an incident electron beam of energy of E bombards on a stainless steel surface.

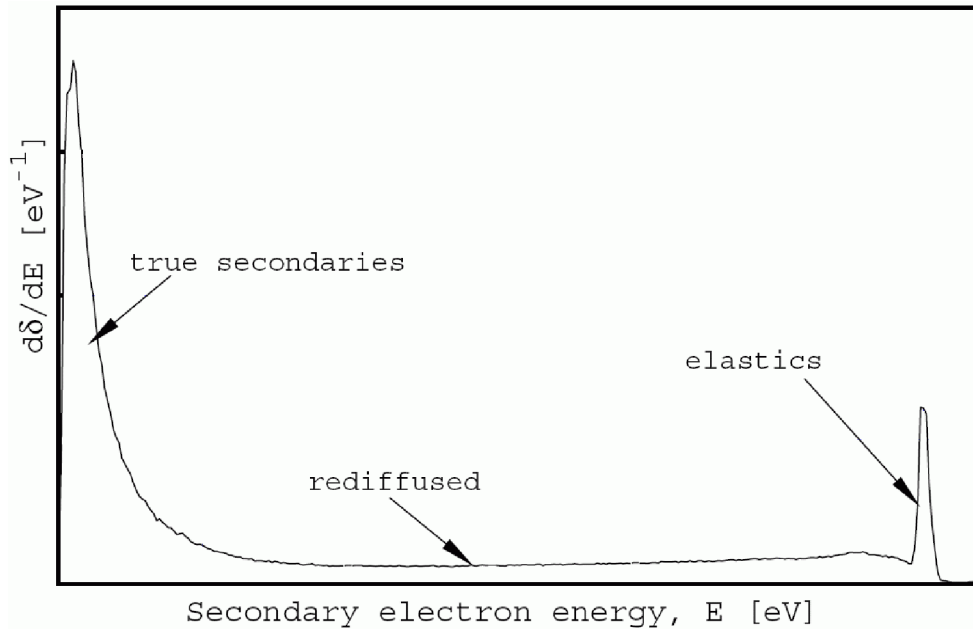


Fig. 5. 12 The emitted-energy spectrum of the secondary electron energy.

The secondary electrons play an important role to the performance of the depressed collector. Therefore, these models of the secondary electron emission should be applied in the simulation of the depressed collector using 3D PIC code MAGIC.

5.4.2. 1 Simulation of TSEs

In MAGIC, the numbers, the energies and the angles of the emitted TSEs were sampled from the probability function of the yield, the energy distribution and the angular distribution by using Monte Carlo algorithm. Therefore the true secondary yield, the emitted angular distribution and the emitted-energy spectrum are considered as important quantities in the simulation. The original data of the

secondary electron yield (SEY), the emitted angle distribution and the emitted-energy spectrum can be obtained from experiments, and several semiempirical formulas have been developed to fit the experimental data.

5.4.2. 2 TSE yield

The secondary electron yield (SEY) represents the number of secondary electrons emitted per incident particle, which is

$$\delta = I_s / I_0 = \delta_T + \eta \quad (5.13)$$

where I_0 is the incident electron beam current and I_s is the secondary current. SEY is composed by the true secondary yield δ_T and the backscatter coefficient η .

The true secondary yield δ_T can be calculated using the Eq. 5.13 because the secondary electron yield and the backscatter coefficient were measured by various parties and semi empirical formulas were obtained.

The first semi empirical model of the secondary electrons was published by Salow in 1940 [29]. It assumed that the SEY could be written as

$$\delta = \int_0^{\infty} n(x, E_0) f(x) dx \quad (5.14)$$

where $n(x, E_0)$ is the number of secondary electrons produced at a distance of x from the surface by a primary electron of energy E_0 . And a further assumption is that it is proportional to the energy loss per unit path length, which is

$$n(x, E_0) = -KdE / dx \quad (5.15)$$

where $1/K$ represents the energy required to produce a secondary electron. $f(x)$ is the probability that a secondary electron produced at x reaches and escapes from the

surface, and it is generally accepted that it follows Lenard absorption law [30] and has the expression

$$f(x) = e^{-ax} \quad (5.16)$$

where $1/a$ is the effective range of the secondaries in the material.

Various forms of $n(x, E_0)$ have been suggested where the first one assumed the energy loss was governed by the Thomson-Whiddington law [31], which was

$$\frac{dE}{dx} = \frac{A}{E(x)} \quad (5.17)$$

Braoody deduced the expression of SEY by using Thomson-Whiddington law in 1950, which was [32]

$$\delta / \delta_m = \frac{1}{F(0.92)} F(0.92E_0 / E_{0m}) \quad (5.18)$$

$$F(r) = e^{-r^2} \int_0^r e^{y^2} dy$$

where δ_m was the maximum yield occurring for a primary electron with energy E_{0m} , E_0 was the energy of the incident primary electron.

However, it was found that Eq. 5.18 did not agree with the data obtained in Young's experiment on aluminum oxide films. Then it was suggested that the energy loss was not given by a simple inverse relationship, but by some power law as [33]

$$\frac{dE}{dx} = \frac{A}{E^{1+n}(x)} \quad (5.19)$$

The SEY in the assumption of power law of the energy loss had the expression

$$\delta / \delta_m = \frac{1}{g_n(z_m)} g_n(z_m E_0 / E_{0m}) \quad (5.20)$$

$$g_n(z) = \frac{1 - \exp(-z^n + 1)}{z^n}$$

where z_m was the value of z for which $g_n(z)$ reached its maximum. Young suggested n to be 0.35 from the experimental data, and thus z_m and $g_n(z)$ could be solved as

$$z_m = 1.8432, g_n(z_m) = 0.7250 \quad (5.21)$$

The SEY in Eq. 5.20 can be rewritten as

$$\frac{\delta}{\delta_m} = 1.11(E_0 / E_{0m})^{-0.35} (1 - e^{-2.3(E_0 / E_{0m})^{1.35}}) \quad (5.22)$$

Eq. 5.22 agreed well with the secondary electron emission over a limited range of primary energy; however, it was less accurate at high primary energy according to experimental data in paper [34]. When $E_0 \gg E_{0m}$, Eq. 5.22 became

$$\delta = 1.11\delta_m (E_0 / E_{0m})^{-0.35} \quad (5.23)$$

In 1983, Seiler [35] modified Eq. 5.23 by using the experimental data from Ono and Kanaya [36]

$$\frac{\delta_m}{E_{0m} / \text{keV}} \approx k, 1.87 \leq k \leq 2.4 \quad (5.24)$$

When choosing $k = 2.1$ then the SEY for high primary energy became

$$\delta = 1.11\delta_m^{1.35} (E_0 / \text{keV})^{-0.35} \quad (5.25)$$

It is similar to Eq. 5.23 but with a correction factor of δ_m . In 1984, Thomas introduced another formula of the true SEY with the following form [37], and it becomes the build-in SEY model in MAGIC.

$$\frac{\delta}{\delta_m} = 7.40 \frac{E_0}{E_{0m}} e^{-2(\frac{E_0}{E_{0m}})^{1/2}} \quad (5.26)$$

However, a formula widely used for SEY was by Vaughan in 1993 [38, 39]. It followed

$$\delta / \delta_{0m} = (v e^{1-v})^k \quad (5.27)$$

where δ_{0m} was the maximum SEY. $v = (E_0 - E_{\min}) / (E_{0m} - E_{\min})$. E_0 was the energy of the incident primary electron. E_{\min} was the minimum primary energy that could generate the secondary electrons, which was commonly accepted as 12.5eV. E_{0m} was the energy of the incident primary electron producing the maximum SEY. The value of parameter k was suggested as

$$\begin{aligned} k &= k_1 = 0.56, \quad \text{for } v < 1 \\ k &= k_2 = 0.25, \quad \text{for } 1 < v \leq 3.6 \\ \delta &= 1.125 \delta_{0m} / v^{0.35}, \quad \text{for } v > 3.6 \end{aligned} \quad (5.28)$$

Vaughan compared Eq. 5.22 and Eq. 5.27 with the experimental data on a BeO surface used in cold-cathode CFA's, and proved that his formula fits the experimental data better than Young's.

Besides the incident primary energy E_0 , the incident angle is another important parameter of the secondary electron emission yield. The angular dependent SEY in Vaughan's formula was

$$\begin{cases} E_{0m}(\theta) = E_{0m}(0)(1 + k_{sE}\theta^2 / 2\pi) \\ \delta_{0m}(\theta) = \delta_{0m}(0)(1 + k_{s\delta}\theta^2 / 2\pi) \end{cases} \quad (5.29)$$

where θ was the incident angle and $0 \leq \theta < \pi/2$. $\delta_{0m}(0)$ was the maximum SEY normal to the surface. k_{sE} and $k_{s\delta}$ were the smooth factors for $E_{0m}(0)$ and $\delta_{0m}(0)$, respectively. They were normally set at a default value of 1.0 to represent the surface of the tube.

In 2002, Furman suggested another semi empirical formula based on a probability model and the experimental data from the large hadron collider (LHC) for the low primary energy part ($E_0 < 1\text{kV}$) of the electrons [40], and it is given by Eq. 5.30.

$$\frac{\delta}{\delta_{0m}} = \frac{s(E_0 / E_{0m})}{s - 1 + (E_0 / E_{0m})^s} \quad (5.30)$$

where s is a constant and $s > 1$.

The SEY with consideration of the incident angle in Furman's formula based on the experimental results obtained at the LHC was

$$\begin{cases} E_{0m}(\theta) = E_{0m}(0)[1 + t_1(1 - \cos^{t_2} \theta)] \\ \delta_{0m}(\theta) = \delta_{0m}(0)[1 + t_3(1 - \cos^{t_4} \theta)] \end{cases} \quad (0 \leq \theta \leq 84^\circ) \quad (5.31)$$

where t_1 , t_2 , t_3 , and t_4 were coefficients varying for different materials. Fig. 5.13 shows the SEY as a function of the incident energy of the primary electrons obtained by different researchers since 1950 [32 - 40].

The backscatter coefficient could be evaluated by the Hunger-Kuchler formula which was obtained by fitting the experimental data in the energy range of 4 ~ 40 keV [41].

$$\begin{aligned} \eta(E_0, Z) &= E_0^{m(Z)} C(Z) \\ m(Z) &= 0.13182 - 0.9211 / Z^{0.5} \\ C(Z) &= 0.1904 - 0.2236 \ln Z + 0.1292(\ln Z)^2 - 0.01491(\ln Z)^3 \end{aligned} \quad (5.32)$$

where Z was the atomic number of the material. The angular dependence of the backscatter coefficient can be evaluated by Eq. 5.33 [42].

$$\eta(\theta) = 0.89(\eta_0 / 0.89)^{\cos\theta} \quad (5.33)$$

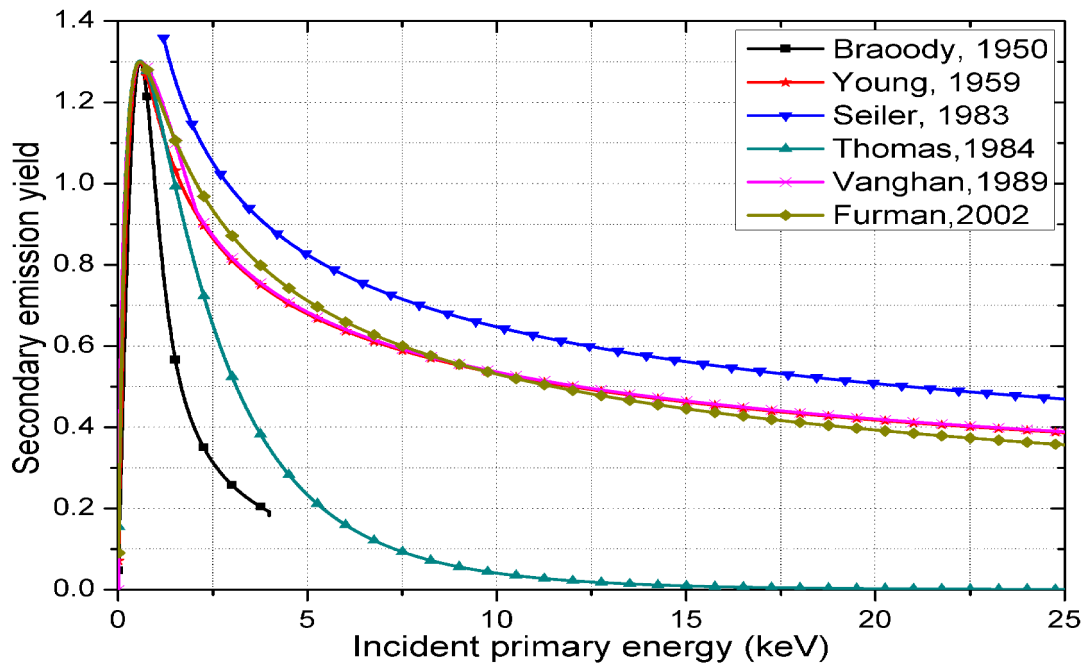


Fig. 5. 13 The relation between SEY and the incident primary energy in different models for copper where $\delta_{0m}=1.3$, $E_{0m}=580\text{eV}$ and $s=1.44$.

The TSE yield function in MAGIC is based on a formula derived by Thomas [37]. However, MAGIC also allows users to define their own SEY functions and the energy distribution function for true secondary electrons by using the command “EMISSION SECONDARY”. In the simulation Vaughan and Furman’s SEY formulas and the backscatter coefficient calculated from Eq. 5.32 were used to evaluate the true secondary yield as they have been proved to be in good agreement with the experimental data [38, 40].

Several particle-in-cell (PIC) codes have been developed with the model of secondary electron emission. The BSCAT [43], 3D PIC code MICHELLE [44] and LKOBRA [45] all employed the formula from Vaughan for the secondary electrons, and BSCAT employed a modified formula from Eq. 5.32 for backscattered electrons, which was

$$\begin{aligned}
\eta(E_0, Z) &= E_0^{m(Z)} C(Z) \\
\begin{cases} m(Z) = 0.0114Z - 0.329, & \text{for } Z < 23 \\ m(Z) = 0.00494Z - 0.0943, & \text{for } 23 \leq Z < 31 \\ m(Z) = 0.00494Z - 0.0943, & \text{for } 23 \leq Z < 31 \end{cases} & \quad (5.34) \\
\begin{cases} C(Z) = 0.0141Z - 0.0311, & \text{for } Z < 16 \\ C(Z) = 0.000173Z - 0.252, & \text{for } Z \geq 16 \end{cases}
\end{aligned}$$

The simulation code ESRAY used to simulate the depressed collector for the gyrotron and was also capable of modeling the secondary electrons. The theoretical model was based on the probabilistic description of the Furman's formulas [46].

5.4.2.3 Energy spectrum and angular distribution of the TSEs

It was found that the incident angle and energy of the primary electrons did not affect the energy distribution of the true secondary electrons [47]. Therefore in the simulation, the secondary energy distribution of the TSEs was assumed to have a peak at 7.5 eV with a full-width at half-maximum of 10 eV. While in MICHELLE [44], a normalized Maxwellian probability distribution function was suggested with the expression

$$f(E) = (E / E_{pk}^2) e^{-(E / E_{pk})} \quad (5.35)$$

where E_{pk} is the empirical energy peak which is regarded as 3.3 eV for copper material. In BSCAT code [43], a probability distribution function of

$$f(E) = 6u^2 E / (E + u)^4 \quad (5.36)$$

was used, where u is the work function of the material (4.7 eV for copper). Because the kinetic energy of the true secondary (always less than 50 eV) is much smaller than the electric potential difference between the electrodes of the designed depressed collector (larger than 10 kV), the differences caused by using these different energy distribution functions could be neglected.

The angular distribution of TSEs was chosen to be homogeneous in the MAGIC simulation, which is

$$f(\theta) = 1/\pi, \quad \theta \in [-\pi/2, \pi/2] \quad (5.37)$$

While a more accurate distribution was suggested to follow the cosine distribution [44]

$$f(\theta) = \cos \theta / 2, \quad \theta \in [-\pi/2, \pi/2] \quad (5.38)$$

5.4.3 Multiple scattering models for the BSEs

The way to deal with the BSEs was different from the TSEs in MAGIC. In the process of producing TSEs, the microcosmic interaction between the incident electrons and the target material was treated as a “black box”. However, in the process of producing BSEs, a real multiple scattering model between the incident electrons and the target material was used in the simulation. In the simulation, the traces of the electrons were divided into a sequence of random moves and interaction events that the electrons changed their directions and energies. The energy loss straggling (including collision energy-loss straggling and radiative energy-loss straggling) and angular deflection for each step were sampled from a multiple scattering distribution. The parameters for the multiple scattering models were the energy and angle of the incident electrons, as well as the properties of the target material. The backscatter coefficient, the emitted energy spectrum and angular distribution of the BSEs are obtained from the statistical results of a large number of interaction events in the multiple scattering process.

The research on the multiple scattering models began in the 1940’s by Goudsmit [48]. Several useful codes based on the Monte Carlo algorithm and multiple scattering models together with the experimental data, such as EGS4, GRANT, ETRAN, ITS, MCNP, PENELOPE, et al, have been developed and widely used in the study of the

transportation of the electrons and photons in various media. Reference [49], [50] are good review papers on the multiple scattering models and the electron-photon Monte Carlo calculations.

The scattering process in MAGIC was carried out by ITS (The integrated TIGER Series of Coupled Electron/Photon Monte Carlo Transport Codes) code and it has been proved that the simulation results of the ITS code were in good agreement with the experiments [51]. “BACKSCATTER” option in MAGIC allows ITS to be invoked automatically to simulate the emission of both the rediffused and backscattered elastic electrons.

5.5 Conclusion

In this chapter, the principle and the literature of the depressed collector are introduced in the first two sections. A detail description of the different types of depressed collectors is given in section 5.3. Section 5.4 gives a detail discussion on the SEE models, which is one of the most important issues in the designing of the depressed collector.

To design a depressed collector with higher efficiency, the following problems should be considered.

- a) Microwave coupler. It has been discussed in chapter 3.
- b) Decision of the potentials and the geometry of the electrodes to reach optimum collection efficiency. Different potentials on the electrodes result in different equipotential distributions in the collection region. To achieve high collection efficiency, the potentials on the electrodes should be chosen carefully.
- c) Secondary electrons. It was the motivation of the development of different types of depressed collectors in early 1970s. As the backstreaming could seriously affect the performance of the microwave tubes if it returned back

to the interaction region, it should be limited as small as possible.

- d)** Heat dissipation on the electrodes. When the electrons strike on the surface of the electrodes, the rest kinetic energy converts to heat energy and deposits on the electrodes. If the energy is not removed in time, the temperature of the surface will rise and may cause damage to the electrode, which is called “hot spot”. To avoid the “hot spot”, the maximum power density and average power density on the electrode needs to be examined.
- e)** Power supply system. The role of a depressed collector is to recover a proportion of the kinetic energy of the spent beam. Thus the power supply system should have the ability to reach this goal. Moreover, the requirements of a power supply system for a depressed collector are high performance, high reliability and low cost.

References

- [1] A. S. Gilmour, "Principle of Traveling Wave Tubes", chapter 14, Artech House, 1994.
- [2] A.V. Haeff, L.S. Nergaard, "Wide-Band Inductive-Output Amplifier", Proceedings of the IRE, vol. 28, no. 3, pp. 126-130, 1940.
- [3] D.A. Dunn, R.P. Borghi, G. Wada, "A crossed-field Multisegment Depressed Collector for Beam-type Tubes", IRE Trans. Electron Devices, vol. 7, no. 4, pp. 262-267, 1960.
- [4] F. Sterzer, "Improvement of traveling-wave tube efficiency through collector potential depression", IRE Trans. Electron Devices, vol. 5, no. 4, pp. 300-305, 1958
- [5] W. Neugebauer and T. G. Mihran, "A Ten-stage Electrostatic Depressed Collector for Improving Klystron Efficiency", IEEE Trans. Electron Devices, vol. 19, no. 1, pp. 111-121, 1972.
- [6] H. G. Kosmahl, P. Ramins, "Small-size 81- to 83.5-percent efficient 2- and 4-stage depressed collectors for octave-bandwidth high-performance TWT's", IEEE Trans. Electron Devices, vol. 24, no. 1, pp. 36-44, 1977.
- [7] J.A. Dayton, H. G. Kosmahl, P. Ramins, et al, "Analytical prediction and experimental verification of TWT and depressed collector performance using multidimensional computer programs", IEEE Trans. Electron Devices, vol. 26, no. 10, pp. 1589-1598, 1979.
- [8] A. Singh, W. W. Destler, D. Goutos, et al, "Study of an Energy Recovery System for a Large-orbit Gyrotron", International Electron Devices Meeting (IEDM '88), pp. 155-158, 1988.
- [9] M.E. Read, W.G. Lawson, A. J. Dudas, et al, "Depressed collectors for high-power Gyrotrons", IEEE Trans. Electron Devices, vol. 37, no. 6, Part 1, pp. 1579-1589, 1990.

- [10] F. Dolezal, R. Harvey, C. Parazzoli, "E-Guns and depressed collectors for two-stage free electron lasers", *IEEE J. Quantum Electronics*, vol.19, no. 3, pp. 309-315, 1983.
- [11] T.K. Ghosh and R.G. Carter, "Optimization of Multistage Depressed Collectors", *IEEE Trans. Electron Devices*, vol. 54, no. 8, pp. 2031-2039, 2007.
- [12] S. Coco, F. Emma, A. Laudani, et al, "COCA: a novel 3-D FE simulator for the design of TWT's multistage collectors", *IEEE Trans. Electron Devices*, vol. 48, no. 1, pp. 24-31, 2001.
- [13] J. Petillo, K. Eppley, D. Panagos, et al, "The MICHELLE three-dimensional electron gun and collector modeling tool: theory and design", *IEEE Trans. Plasma Sci.*, vol. 30, no. 3, Part 1, pp. 1238-1264, 2002.
- [14] H.G. Kosmahl, "Modern multistage depressed collectors—A review", *Proceedings of the IEEE*, vol. 70, no. 11, pp. 1325-1334, 1982.
- [15] T. G. Mihran, W. Neugebauer, "Multistage depressed electrostatic collector for magnetically focused space borne klystrons", NASA report, Report Number: NASA-CR-72767, 1970.
- [16] J. A. Dayton, H. G. Kosmahl, P. Ramins, et al, "Experimental verification of a computational procedure for the design of TWT-refocuser-MDC systems", *IEEE Trans. Electron Devices*, vol. 28, no. 12, pp. 1480-1489, 1981.
- [17] A. Singh, S. Rajapatirana, Y. Men, et al, "Design of a multistage depressed collector system for 1-MW CW Gyrotrons. I. Trajectory control of primary and secondary electrons in a two-stage depressed collector", *IEEE Trans. Plasma Sci.*, vol. 27, no. 2, pp. 490-502, 1999.
- [18] R.L. Ives, A. Singh, M. Mizuhara, et al, "Design of a multistage depressed collector system for 1-MW CW Gyrotrons. II. System consideration", *IEEE Trans. Plasma Sci.*, vol. 27, no. 2, pp. 503-511, 1999.
- [19] G. Ling, B. Piosczyk and M. K. Thumm, "A new approach for a multistage depressed collector for Gyrotrons", *IEEE Trans. Plasma Sci.*, vol. 28, no. 3, pp.

606-613, 2000.

- [20] Liu Ben-Tian, Jiao Chong-Qing and Zhang Yan-Sheng, "Experimental Study of a Ku-Band Gyrotron Backward-Wave Oscillator with a Single Stage Depressed Collector", IEEE Trans. Plasma Sci., vol. 35, no. 4, pp. 1065-1069, 2007.
- [21] J. R. Hechtel, "A novel electrostatic-focusing depressed collector for linear beam tubes", IEEE Trans Electron Devices, vol. ED-24, no. 1, pp. 45-52, 1977.
- [22] C. L. Jones and J. R. Hechtel, "Recent advances with high-power PPM-focused dual mode TWT's", Int. Electron Devices Meeting, vol. 22, pp. 530-533, 1976.
- [23] J. R. Hechtel and D. C. Wilson, "A high-efficiency, CW, PPM-focused TWT for ECM applications", Int. Electron Devices Meeting, pp. 354-356, 1977.
- [24] T. G. Mihran, and W. Neugebauer, "Analytic study of a depressed collector for linear beam microwave amplifiers", NASA report, Report Number: NASA-CR-72768, 1970.
- [25] T. Okoshi, E. Chiu, and S. Matanki, "The tilted electric field soft-landing collector and its application to a traveling-wave tube", IEEE Trans. Electron Devices, vol. ED-19, no. 1, pp. 104-111, 1972.
- [26] A. Singh, S. Rajapatirana, Y. Men, et al, "Design of a Multistage Depressed Collector System for 1-MW CW Gyrotrons. I. Trajectory Control of Primary and Secondary Electrons in a Two-stage Depressed Collector", IEEE Trans. Plasma Sci., vol. 27, no. 2, pp. 490-502, 1999.
- [27] G. Ling, B. Piosczyk and M. K. Thumm, "A New Approach for a Multistage Depressed Collector for Gyrotrons", IEEE Trans. Plasma Sci., vol. 8, no. 3, pp. 606-613, 2000.
- [28] M. A. Furman and M. T. Pivi, "Probabilistic Model for the Simulation of Secondary Electron Emission", Phys. Rev. S. T. - Accelerators and Beams,

vol. 5, no. 12, ID: 124404, 2002.

- [29] H. Salow, "Sekundare elektronen emission", *Physik. Z.*, vol. 41, pp. 434-442, 1940.
- [30] P. Lenard, *Ann Phys.*, vol. 12, pp. 714-744, 1903.
- [31] R. Whiddington, *Proceedings of the Royal Society of London*, A89, pp. 554, 1914.
- [32] E. M. Baroody, "A Theory of Secondary Electron Emission from Metals", *Phys. Rev.* vol. 78, pp. 780-787, 1950.
- [33] Robert g. Lye and a. J. Dekker, "Theory of Secondary Emission", *Phys. Rev.*, vol. 107, no. 4, pp: 977-981, 1957.
- [34] M. Salehi and E. A. Flinn, "An Experimental Assessment of Proposed Universal Yield Curves for Secondary Electron Emission", *J. Phys. D: Appl. Phys.*, vol. 13, no. 2, pp. 281-289, 1980.
- [35] H. Seiler, "Secondary Electron Emission in the Scanning Electron Microscope", *J. Appl. Phys.*, vol. 54, no. 11, pp. R1-R18, 1983.
- [36] S. Ono and K. Kana, "The Energy Dependence of Secondary Emission Based on the Range-energy Retardation Power Formula", *J. Phys. D: Appl. Phys.*, vol. 12, pp. 619-632, 1979.
- [37] E.W. Thomas, "Data Compendium for Plasma-Surface Interactions", *Nuclear Fusion special issue, IAEA, Vienna*, pp. 94, 1984.
- [38] J. Rodney and M. Vaughan, "New Formula for Secondary Emission Yield", *IEEE Trans. Electron Devices*, vol. 36, no. 9, pp: 1963-1967, 1989.
- [39] M. Vaughan, "Secondary Emission Formulas", *IEEE Trans. Electron Devices*, vol. 40, no. 4, pp. 830, 1993.
- [40] M.A. Furman, and M.T.F. Pivi, "Simulation of Secondary Electron Emission Based on a Phenomenological Probabilistic Model", LBNL-52807, SLAC-PUB-9912, 2003, <http://repositories.cdlib.org/lbnl/LBNL-52807/>.
- [41] H. J. Hunger and L. Kuchler, "Measurements of the Electron Backscattering

- Coefficient for Quantitative EPMA in the Energy Range of 4 to 40keV", *Phys. Stat. Sol.*, vol. 56, pp. K45, 1979.
- [42] L. Reimer, "Scanning Electron Microscopy, Physics of Image Formation and Microanalysis", in *Springer Ser. Opt. Science*. Berlin, Germany, Springer-Verlag, vol. 45, pp. 135–169, 1985.
- [43] A. Valfells, A. Singh, M. J. Kolander, et al, "Advancements in Codes for Computer Aided Design of Depressed Collectors and Tracing of Backscattered Electrons—Part II: Improvements in Modeling of the Physics of Secondary Electron Emission and Backscattering", *IEEE Trans. Plasma Science*, vol. 30, no. 3, pp. 1271-1276, 2002.
- [44] J. Petillo, K. Eppley, D. Panagos, et al, "The MICHELLE Three-Dimensional Electron Gun and Collector Modeling Tool: Theory and Design", *IEEE Trans. Plasma Science*, vol. 30, no. 3, pp. 1238-1264, 2002.
- [45] T.K. Ghosh and R.G. Carter, "Optimization of Multistage Depressed Collectors", *IEEE Trans. Electron Devices*, vol. 54, no. 8, pp. 2031-2039, 2007.
- [46] S. Illy, B. Piosczyk, "Simulation of High Power CW Gyrotron Collectors Including the Effect of Secondary Emission", *Joint 32nd International Conference on Infrared and Millimeter Waves and the 15th International Conference on Terahertz Electronics (IRMMW-THz)*, 2-9 Sept., pp. 50-51, 2007.
- [47] Jay Burns, "Angular distribution of secondary electrons from (100) faces of copper and nickel", *Phys. Rev.*, vol. 119, no. 1, pp. 102-114, 1960.
- [48] S. Goudsmit and J. L. Saunderson, "Multiple Scattering of Electrons", *Phys. Rev.*, vol. 57, no. 11940, pp. 24-29.
- [49] S. M. Seltzer, "Electron-photon Monte Carlo calculations: the ETRAN code", *Appl. Radia. Isot.*, vol. 42, no. 10, pp. 917-941, 1991.
- [50] H. A. Bethe, "Moliere's Theory of Multiple Scattering", *Phys. Rev.*, vol. 89, no. 6, pp. 1256-1266, 1953.

- [51] J. A. Halbleib, R. P. Kensek, G. D. Valdez, T. A. Mehlhorn, S. M. Seltzer, and M. J. Berger, "ITS: The integrated TIGER series of electron/photon transport codes—Version 3.0", IEEE Trans. Nucl. Sci., vol. 39, no. 4, pp. 1025–1030, 1992.
- [52] V. A. Flyagin, A. V. Gaponov, M. I. Petelin, and V. K. Yulpatov, "The Gyrotron", IEEE Trans. Microwave Theory Tech., vol. 25, no. 6, pp. 514-521, 1977
- [53] R. L. Geng, H. Padamsee, S. Belomestnykh, P. Goudket, D. M. Dykes, R. G. Carter, "Suppression of multipacting in rectangular coupler waveguides", Nuclear Instruments and Methods in Physics Research Section A: Accelerators, Spectrometers, Detectors and Associated Equipment, vol. 508, no. 3, pp. 227–238, 2003

Chapter 6

Simulation of the Depressed Collector

The design of depressed collector is a challenging work. It contains several problems such as how to choose the optimum potentials on the electrodes as well as the geometries of the electrodes. In this chapter, MAGIC and a genetic algorithm are employed to simulate the multi-stage depressed collector. Section 6.1 represents the simulation results of the gyro-BWO using a helically corrugated waveguide. Section 6.2 gives the particle-in-cell (PIC) simulation results after applying the Bragg reflector which is used to separate the radiation and the spent electron beam. In section 6.3, the optimum potentials on the electrodes are calculated and section 6.4 gives a detail description on the optimization of the depressed collector. Section 6.5 simulates the heat power distribution on the electrodes. And a brief conclusion was represented at the end of this chapter.

6.1 Simulation of gyro-BWO using MAGIC

A gyro-BWO with a helically corrugated waveguide has been demonstrated to allow a wide frequency tunability as well as pure frequency component due to large group velocity in the region of small axial wave number and the asymmetric geometry of the interaction region which ensures the electron beam can only interact with the wave in one direction [1]. An W-band (84 - 104 GHz) gyro-BWO based on threefold helically corrugated waveguide currently been built at the University of Strathclyde was predicted to achieve frequency tuning range of 20% and an electronic efficiency of 16.7% by using an axis-encircling large-orbit electron beam. The threefold helical

waveguide structure provided effective resonant coupling between the TE_{11} and TE_{21} mode [2].

The 3D PIC code MAGIC was used to simulate the electron beam trajectories, beam-wave interaction in the three-fold helically corrugated waveguide. MAGIC is a user-configurable code that solves Maxwell's equations together with Lorentz particle motion. The numerical calculations use the finite difference method to simulate the physical processes evolving in time and space from an initial specified state. From this initial specified state, time is advanced adding a single time step. At each new value of time, Maxwell's equations are solved throughout space to advance the electromagnetic fields in time. Using these new fields, the Lorentz equation is solved to advance the momentum and co-ordinates of all the electrons in the simulation. The continuity equation is then solved to map charge and current densities on to the grids which are then used as sources for Maxwell's equations on the next time step. This provides a self-consistent model of the interaction between the fields and particles [12].

The MAGIC tool suite includes MAGIC2D which is a 2.5 dimensional code (2D fields and 3D particle kinematics), MAGIC3D which is a fully three-dimensional code, and ReView which is a general-purpose post-processor [13].

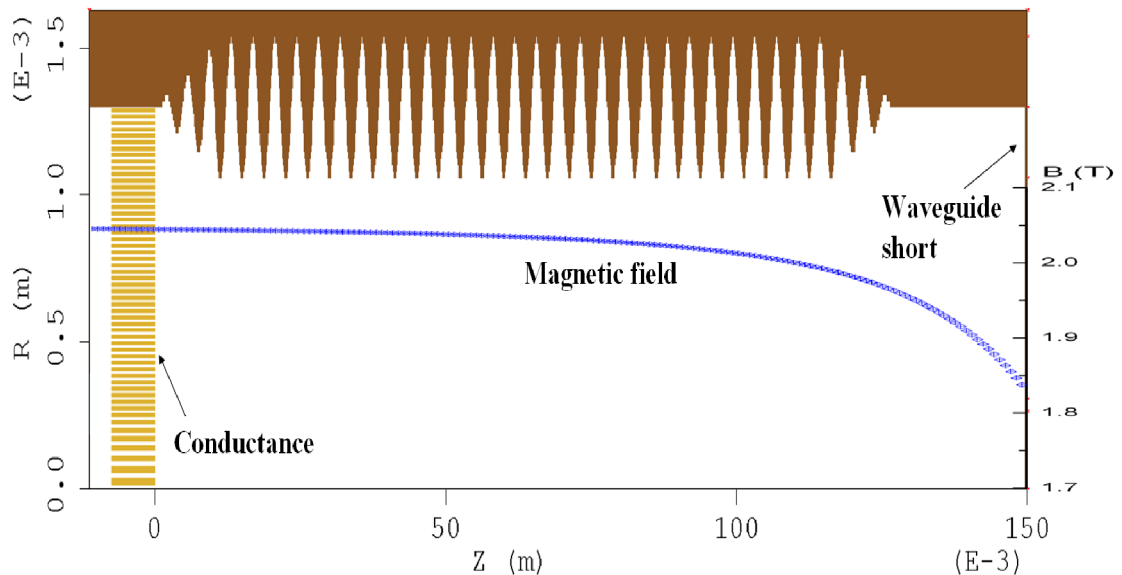
MAGIC provides configuration control based upon the MAGIC Command Language (MCL). MCL is a sophisticated scripting language with many powerful features. It allows the user to choose algorithms and define variable to create reusable configurations.

The configuration of the gyro-BWO in the 3D PIC code MAGIC is shown in Fig. 6.1. The waveguide was composed by 34 periods of helical length. According to the discussion in paper [3, 4], the electronic efficiency can be improved by using tapered magnetic field or tapered wall radius of the waveguide instead of the constant field or waveguide radius. Thus the waveguide in the simulation contains 3 periods of

tapered radius at both sides, as well as the amplitude of magnetic field tapered at the end of the interaction region.



(a)



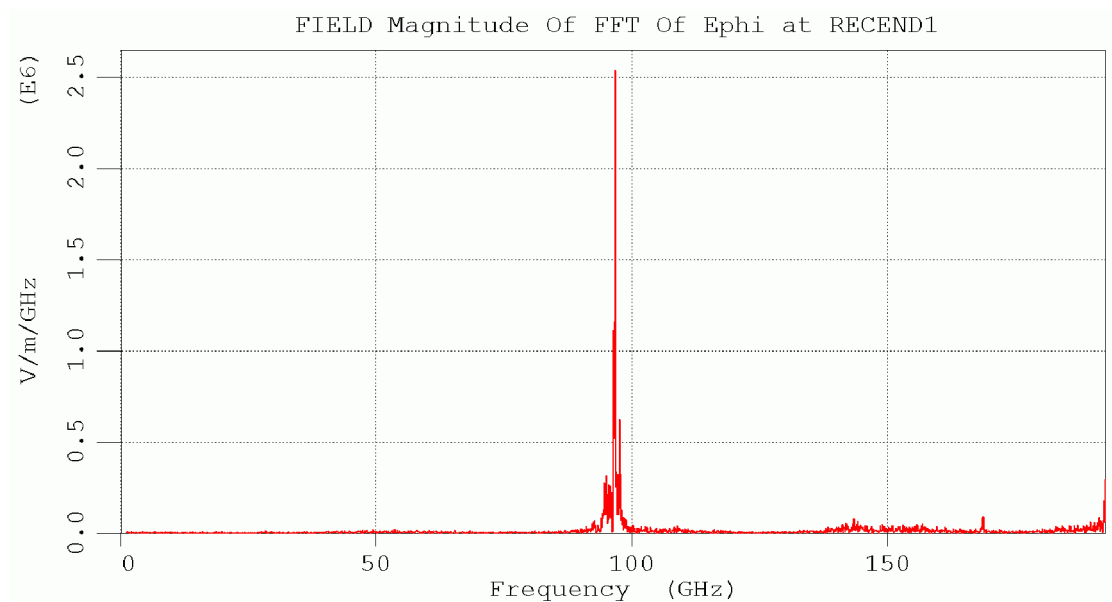
(b)

Fig. 6. 1 (a) Geometry of the helically corrugated waveguide and (b) the model in 3D PIC code MAGIC.

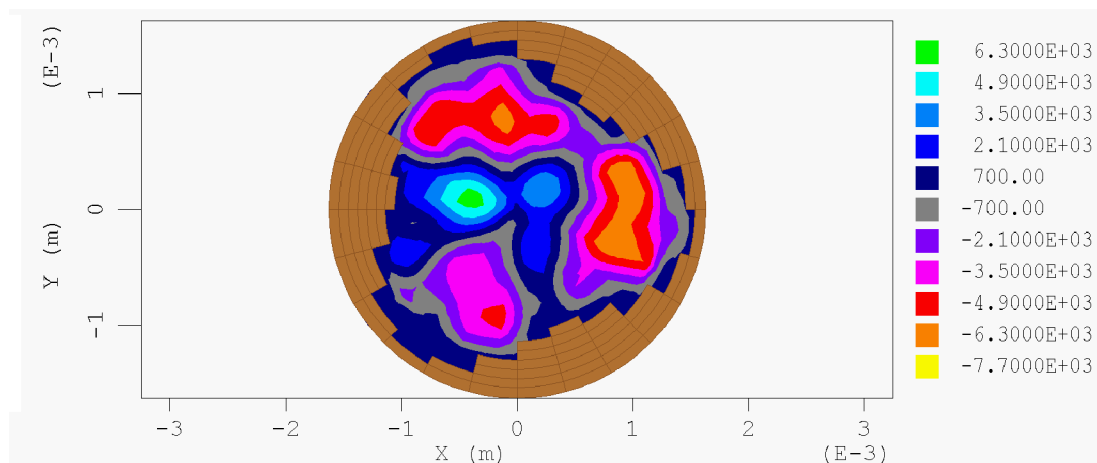
The radiation of the gyro-BWO can be coupled out either from an output coupler at the upstream side of the waveguide or through an output window at the downstream side. However, when considering the applications of a depressed collector at the end of the waveguide, coupling the radiation through the window at the downstream side will increase the difficulty in separating the radiation from the spent electron beam. Thus to use the output coupler is a more practical method. A short at the end of the microwave system was used to reflect the microwaves back upstream. To measure

the power of the radiation, a conductance was used to absorb the radiation without disturbing the propagation of the electron beam, as shown in Fig. 6.1.

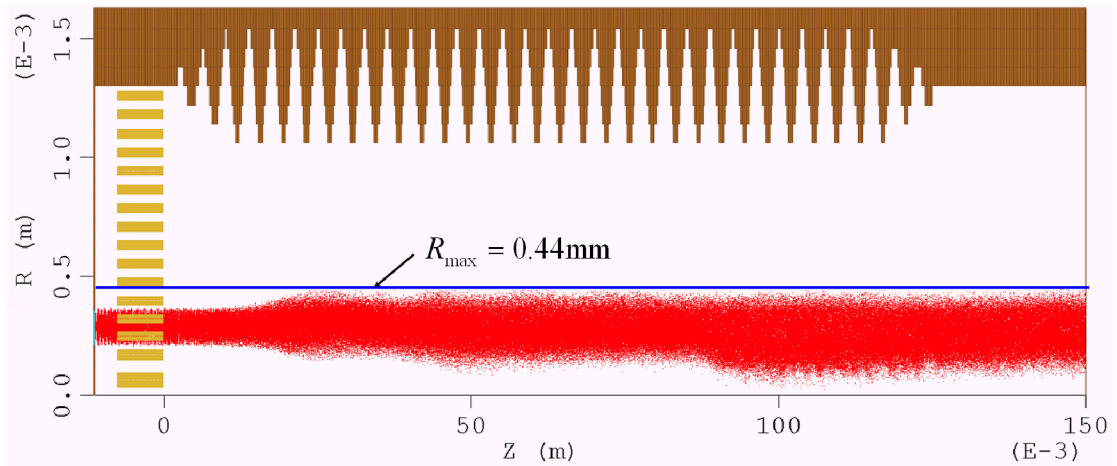
In the MAGIC simulation, an electron beam with energy 40 keV, current 1.5 A, and beam alpha 1.6 achieved an output power about 10 kW in a magnetic field of 1.90 T. A typical simulated output spectrum, mode pattern and beam trajectory are shown in Fig. 6.2.



(a)



(b)



(c)

Fig. 6. 2 (a) MAGIC simulation results of the output spectrum of 96.83 GHz, (b) mode pattern of TE_{11} mode and (c) beam trajectory.

The simulated output frequencies and powers of the gyro-BWO by the electron beam with the same energy, current and pitch angle as a function of the tuning cavity magnetic fields are given in Fig. 6.3. Also the frequency tuning characteristic of the gyro-BWO using beam voltage as a tuning parameter at fixed cavity magnetic field of 1.90 T was simulated and the results are presented in Fig. 6.4.

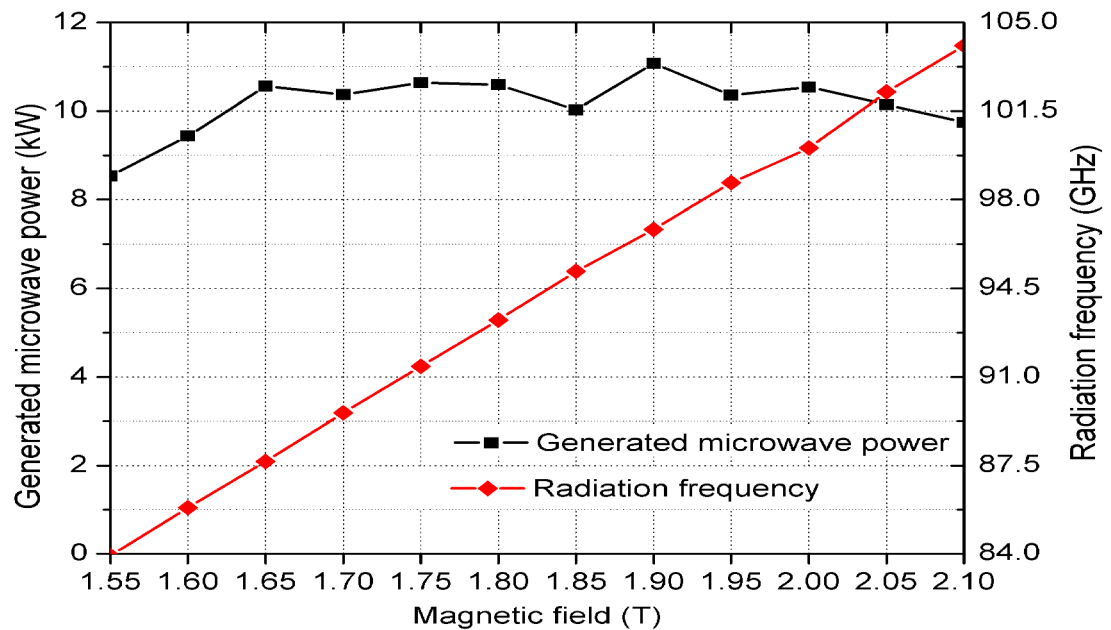


Fig. 6. 3 Simulated output frequency and power of the gyro-BWO as a function of tuning cavity magnetic field.

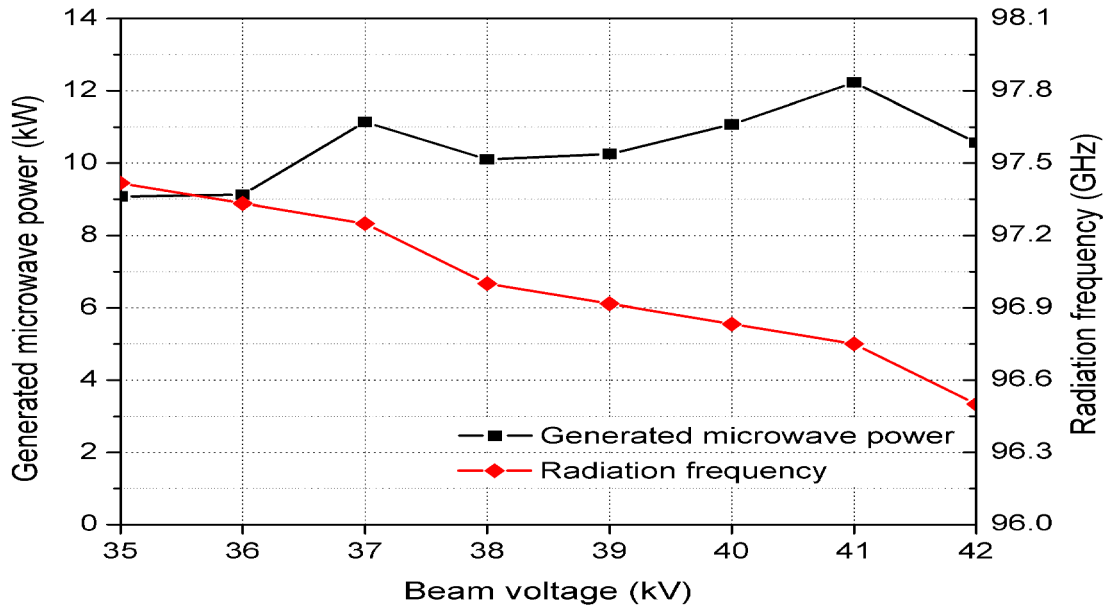


Fig. 6. 4 Simulated output frequency and power of the gyro-BWO as a function of tuning electron beam voltage when the magnetic field is 1.90 T.

6.2 Simulation results with Bragg reflectors

To allow the spent electrons passing through the interaction region and entering into the collection region, a Bragg reflector which is designed in chapter 3 can be used to take the place of the waveguide short in Fig. 6.1.

Another factor which affects the dimension of the Bragg reflector is the magnetic field in the interaction region. In the simulation of the W-band gyro-BWO, the electron beam was guided by a cylindrically symmetric magnetic field and the amplitude gradually reduced downstream. When the electrons travelled from a stronger magnetic field region into a weaker one, their Larmor radii become larger while the magnetic moment is kept constant [5, 6].

The Larmor radius for a gyrating electron in the magnetic field is defined as

$$R_L = \frac{mv_{\perp}}{eB} \quad (6.1)$$

where m and e are the mass and the charge of the electron, respectively. B is the magnetic field along the z direction and v_{\perp} is the velocity perpendicular to B .

The magnetic moment is defined by

$$\mu = \frac{mv_{\perp}^2}{2B} \quad (6.2)$$

Combing Eq. 6.1 and Eq. 6.2 then have

$$\mu = \frac{mv_{\perp}^2}{2B} = \frac{q^2}{2m} \cdot BR_L^2 = \text{constant} \quad (6.3)$$

As a conclusion of Eq. 6.3, the relationship between the Larmor radius of the spent electrons and the magnetic field follows

$$R_2 = \sqrt{B_1 R_1^2 / B_2} = R_1 \sqrt{B_1 / B_2} \quad (6.4)$$

In the simulation, the maximum radius of the hollow axis-encircling electron beam was about 0.44 mm, as marked in Fig. 6.2 (c). If we set B_1 as the maximum magnetic field in the interaction region, and R_1 as the maximum radius of the electron beam, B_2 as the magnetic profile along the axis direction, then we can get the maximum beam radius at different axial positions.

To avoid the spent electrons striking on the inner surface of the Bragg reflector, the maximum Larmor radius of the spent electrons inside the Bragg reflector should be less than the radius of the corrugated sections. As calculated from Eq. 6.4, the profile of the maximum beam radius at $B_1=1.90$ T is shown in Fig. 6.5. A similar profile can be obtained when sweeping B_1 from 1.55 T to 2.10 T.

When optimizing the Bragg reflector, the ranges of the radii of the corrugated sections whose distance is less than 45 mm to the beginning position are set as [1.3 mm, 2.0 mm]. The range of the radii of the corrugated sections whose distance is larger than 45 mm to the beginning position is set as [2.0 mm, 3.0 mm]. The range of the length of the corrugated sections is set as [2.0 mm, 5.5 mm]. The detail of the optimum result was discussed in chapter 3. The cross section view of the helically corrugated waveguide with the corrugated section is shown in Fig. 6.5. The radius of the waveguide is larger than the maximum trajectory radius of the spent electron beam, so that the spent electrons can pass the Bragg reflector without landing on it .

From the numerical simulations, the average microwave output power was about 10 kW while the power observed at the end of the reflector was 80 W under the conditions of electron beam voltage of 40 kV, beam current 1.5 A and beam alpha 1.6 where beam alpha is the ratio of the azimuthal velocity to the axial velocity of the electrons beam. The cavity magnetic field is 1.75 T. About 99% ($1 - 80W/10kW = 99.2\%$) of the microwave power was reflected back into the beam-wave interaction region. The simulated powers are shown in Fig. 6.6.

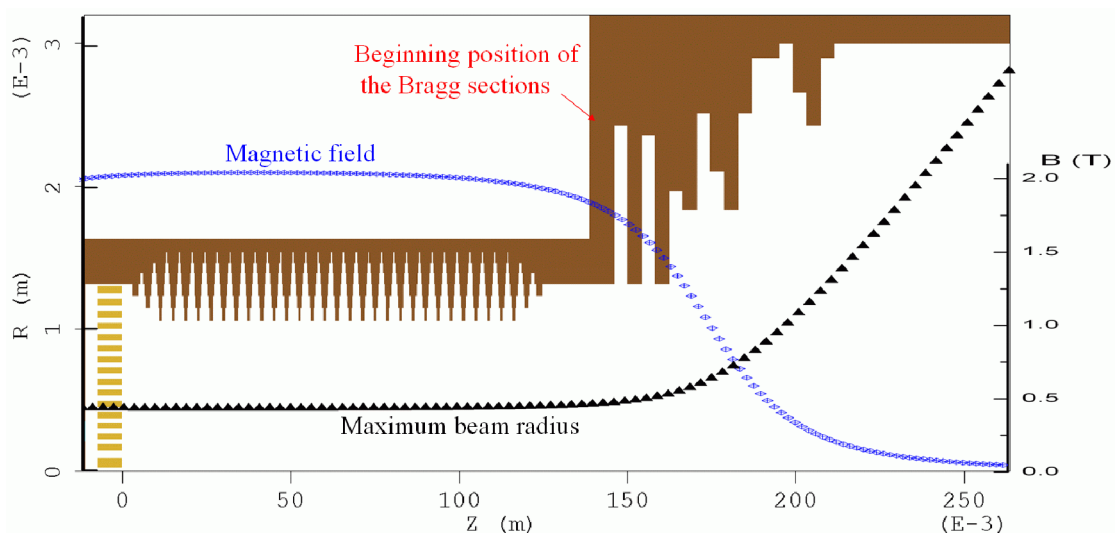
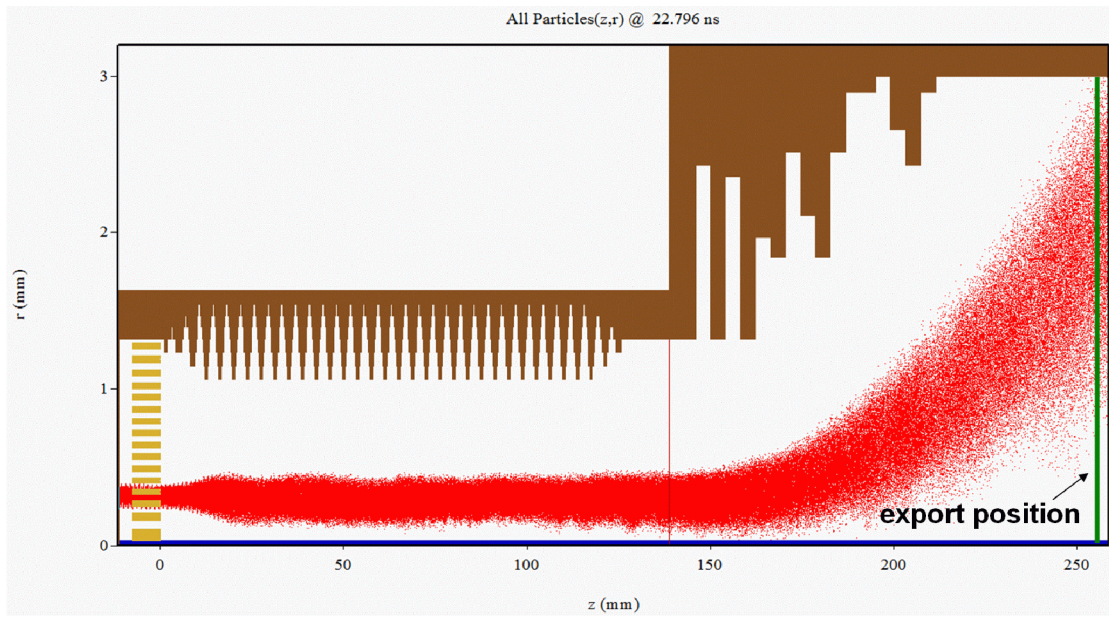
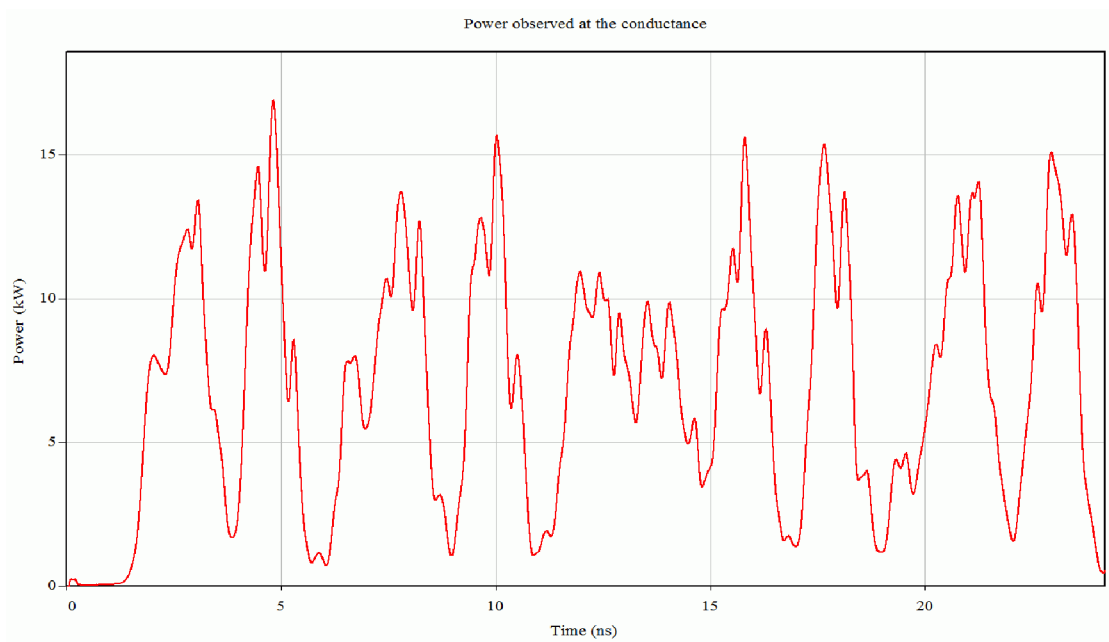


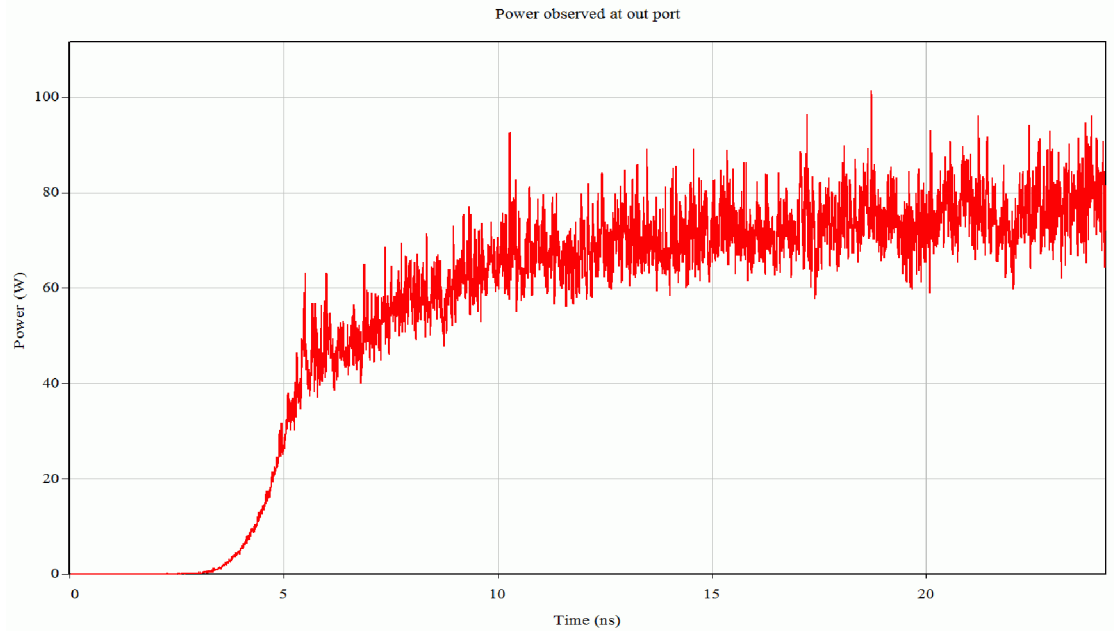
Fig. 6. 5 The overall magnetic field in the microwave tube.



(a)



(b)



(c)

Fig. 6. 6 Simulated structure using the 3D PIC code MAGIC (a) the trajectory of the electron beam, (b) Output microwave power, (c) Lost microwave power.

6.3 Collection efficiency

After the reflector, the spent electrons then entered into the depressed collector. The electrons lost their kinetic energy when passing through the retarding electrostatic field and finally landed on the collector surface with a significant reduction of their kinetic energy. They produced a loop current which results in a power recovery from the spent electrons.

The power recovered by depressed collectors is defined as

$$P_{\text{col}} = \sum_n V_n I_n \quad (6.5)$$

Here n is the number of stages and V_n, I_n are the potentials and collected current on the n th-stage electrode, respectively. For a given energy distribution of the spent electrons, increasing the number of stages resulted in more power be collected.

However, the design of the depressed collectors becomes more complex and the cost increases as the number of stages increases.

The electronic efficiency for a microwave tube is defined as

$$\eta_e = P_{mw} / P_b \quad (6.6)$$

where P_{mw} is the generated microwave power and the beam power P_b can be expressed as $P_b = U_b I_b$, where U_b is the beam voltage and I_b is the beam current.

The remaining power of the spent beam is given by $P_{spent_beam} = P_b - P_{mw}$ if other power losses such as the Ohmic wall loss from the beam loading are neglected.

The collection efficiency η_{col} for a depressed collector is defined as

$$\eta_{col} = P_{col} / P_{spent_beam} \quad (6.7)$$

Due to the intrinsic RF losses such as Ohmic wall losses and stray radiation, the output microwave power is determined by the generated microwave power and the output efficiency ε_{out} .

$$P_{out} = P_{mw} \cdot \varepsilon_{out} \quad (6.8)$$

It is suggested that the RF losses are between 10% and 15%, which means $\varepsilon_{out} = 0.85 \sim 0.9$.

By introducing a depressed collector with a collection efficiency of η_{col} , the overall efficiency of the microwave tube η_{tot} with an electronic efficiency η_e can be calculated using

$$\eta_{tot} = \frac{P_{out}}{P_b - P_{col}} = \frac{\varepsilon_{out} \eta_e}{1 - \eta_{col} (1 - \eta_e)} \quad (6.9)$$

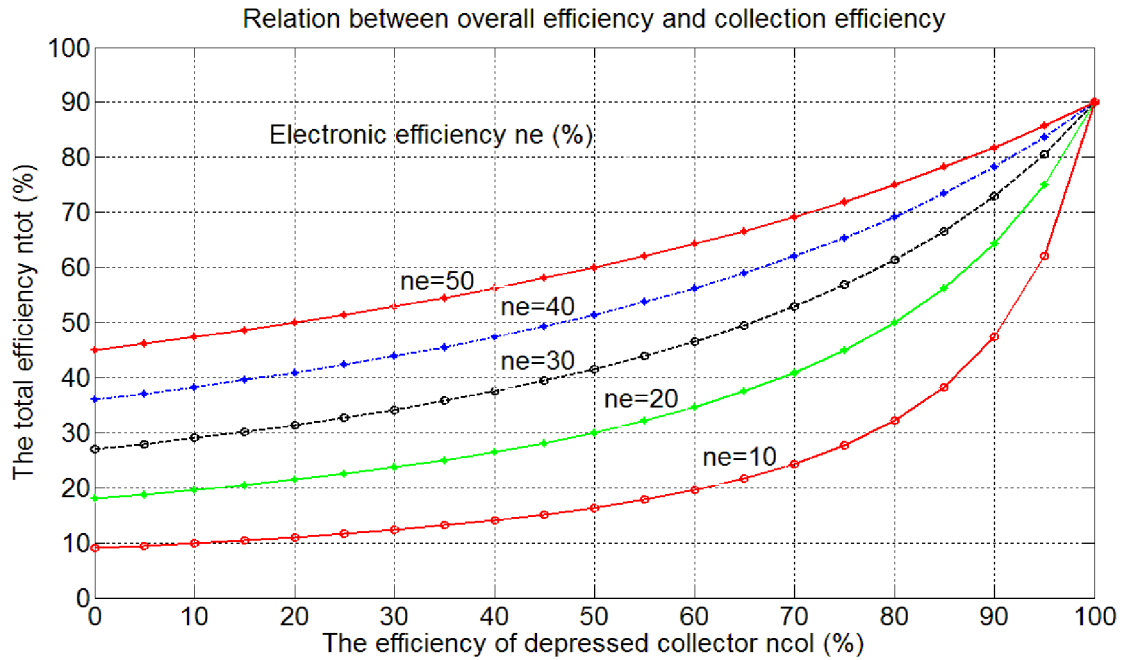
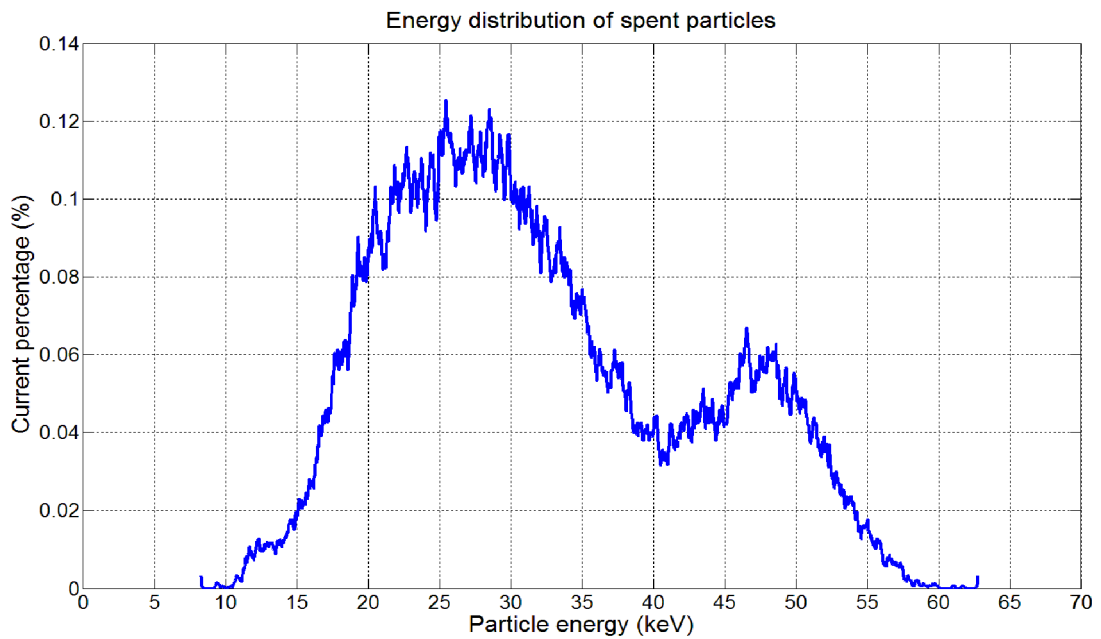


Fig. 6. 7 Overall device efficiency as a function of collector efficiency at different electronic efficiency.

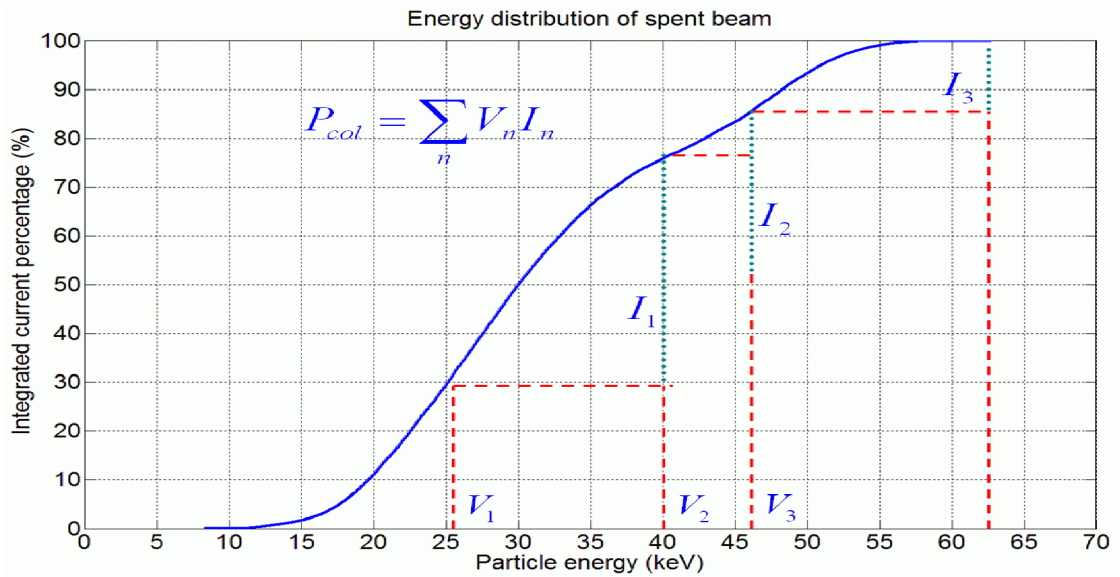
The relation between overall efficiency and collection efficiency is plotted in Fig. 6.7 at $\epsilon_{out} = 0.9$. For those inherently low efficiency high power microwave devices, depressed collectors with efficiency higher than 80% can significantly improve the overall efficiency. For a moderately efficient source with an electronic and collection efficiency of 30% and 80%, respectively, with the use of depressed collection the overall efficiency could be increased to 61.4%, increasing the overall efficiency by a factor of ~ 2 [7].

In the design of the energy recovery system, at the end of the Bragg reflector, the energy distribution of the electron beam was exported from the simulation of the gyro-BWO which was carried out using the MAGIC. The electrons in the export port with a time scale of 2 ns were selected to be the sample of the spent beam and used for the 3D PIC simulations of the depressed collector. Fig. 6.8 shows the spent beam distribution under the conditions of beam voltage 40 kV, beam current 1.5A and beam alpha 1.6. The cavity magnetic field is 1.75 T. Table 6.1 shows the optimum

potentials and the collection efficiency when a different number of stages are used [8]. In this calculation, it was assumed that all the electrons were collected on the electrodes without consideration of secondary emissions. The minimum electrode potential was set to be the minimum energy of electrons to avoid backstreaming and the maximum potential was set to be the electron beam voltage which was 40 kV in the gyro-BWO device. It was found that when the number of stages increased beyond four, the collection efficiency did not significantly increase. Four stages were therefore chosen as a compromise between the collection efficiency and complexity of the system.



(a)



(b)

Fig. 6. 8 (a) Energy distribution of the spent beam, (b) recovered energy from the spent electrons, under the condition of 40 kV electron beam voltage, 1.5 A beam current, beam alpha of 1.6 and a cavity magnetic field of 1.75 T.

Table 6. 1 Collection efficiency for different number of stages.

No.	Potentials on electrodes (kV)							Collection efficiency
	(relative to ground voltage)							
1	-9.24	-----	-----	-----	-----	-----	-----	28.8%
2	-9.24	-25.70	-----	-----	-----	-----	-----	63.6%
3	-9.24	-22.14	-36.57	-----	-----	-----	-----	75.7%
4	-9.24	-19.55	-27.31	-40.00	-----	-----	-----	82.5%
5	-9.24	-18.86	-24.96	-30.78	-40.00	-----	-----	85.7%
6	-9.24	-16.98	-22.14	-27.22	-32.66	-40.00	-----	87.5%
7	-9.24	-16.82	-21.33	-25.47	-29.53	-34.23	-40.00	88.7%

To keep the electrodes at the designed potentials, high voltage DC power supplies should be used. The spent electrons landing on the electrodes can be considered as the loads of the DC power sources. Fluctuations of the collected beam currents would give rise to the change of the potentials due to limited output impedances of the supplies and cause the collection efficiency to change. The collection efficiency influenced by potential fluctuation on the electrodes was also calculated and the results are shown in Fig. 6.9. When the potential fluctuation was limited to a $\pm 20\%$ range, the change in collection efficiency was less than 5%. In the experiment, less sensitivity of the collection efficiency caused by the fluctuation of the potentials on the electrodes is preferred.

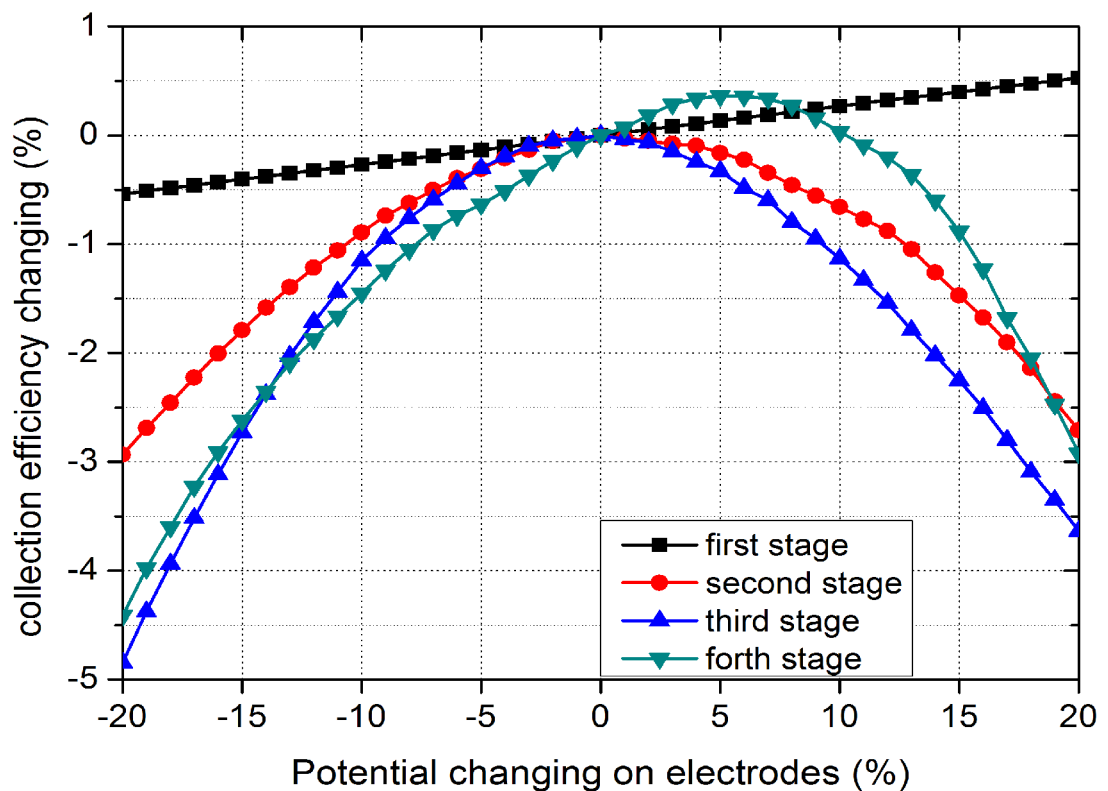


Fig. 6. 9 Collection efficiency as a function of potential fluctuation on each electrode.

6.4 Simulation of depressed collector

As shown in section 6.1, MAGIC was used to simulate the gyro-BWO with a helically corrugated waveguide because of the asymmetric structure, therefore the parameters of the spent electrons exported from the simulation of the gyro-BWO using 3D. MAGIC was also used to simulate the depressed collector. Simulation in 3D would also allow for the design of asymmetrical electrodes for the reduction of the possible backstreaming electrons.

The collection efficiency calculated in section 6.3 assumed that all the spent electrons were sorted by the electric and magnetic field in the collection region. In practice, the distribution of the electric field is determined by the geometry of the electrodes. Proper design of the electrode geometry not only acts to sort the electrons with different kinetic energies, but also to decrease the possibility of secondary emission and to avoid the backstreaming of the electrons in the collector.

One way to choose a good geometry is to use a searching algorithm such as a random walk and genetic algorithm to optimize the parameters [9]. An optimization program based on the MIT GALib was developed as mentioned in chapter 2. The optimization program firstly created an input file by inserting the new set of parameters to the template input file for MAGIC. Then MAGIC was invoked to simulate the new geometry and the result was read by the optimization program to evaluate the parameters.

6.4.1 Structure of the electrodes

The difficulty in the flow chart of the simulation was to design the template input file for MAGIC. The input file was required to have the capability to accept any sets of parameters produced by genetic algorithm and create the appropriate geometry. In this simulation, a basic geometry for each electrode was defined and parameterized.

The basic geometry of an electrode is shown in Fig. 6.10. It is determined completely by 4 parameters, the length of the electrode (L_i), the height of the electrode (H_i), the offset from the Z axis (O_i) and the tilt angle (A_i). There should be 16 parameters in a 4-stage collector. However, the outer radius of the depressed collector was restricted to 60 mm, and the overall length was restricted to be 150 mm. Thus 14 parameters were to be optimized. Before the optimization, many simulations were carried out to find a proper range for each parameter to ensure the searching range was as small as possible. For example, the O_i for the first electrode was set from 5.0 mm to 15.0 mm and the genome length was 6 bit using a binary code. The accuracy of each parameter was chosen to be consistent with the grid size in the MAGIC code.

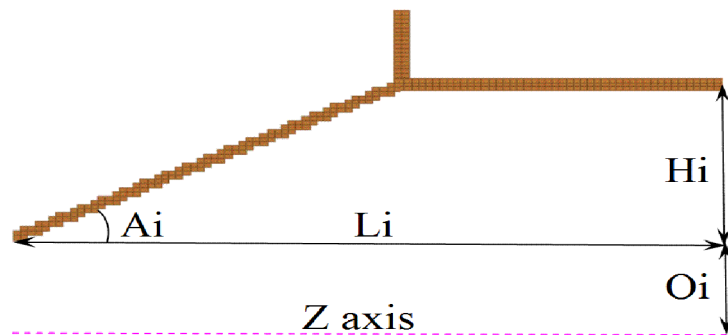


Fig. 6. 10 The basic geometry of an electrode.

6.4.2 Simulation results of the 4-stage depressed collector

The full geometry of the 4-stage depressed collector is shown in Fig. 6.11. A gap of 10 mm between the end of the collection region and the first stage of the collector was left to isolate the high voltage between them. The electrode shapes were modified as shown in S1, S2, S3 and S4 to avoid potential distortion in the simulation when the electric field was applied to the electrodes.

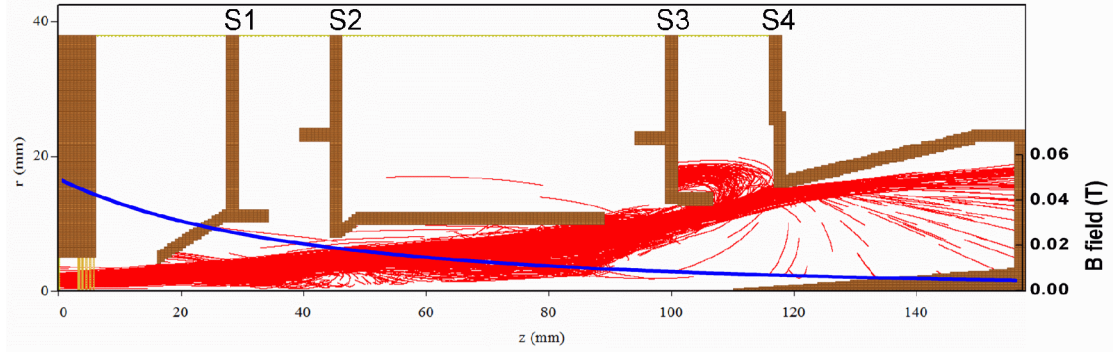


Fig. 6. 11 Full geometry of 4-stage depressed collector.

The potentials on each electrode were consistent with Table 6.1. After each simulation, the average current collected by each collector was read from a MAGIC output data file. Then the collected power was calculated from Eq. 6.5. The average power of the spent beam was calculated by counting all the energy from the spent electrons. The collection efficiency calculated by the collected power and power of the spent beam was used to evaluate the optimum geometric parameters. The crossover probability, mutation probability, and population size of the genetic algorithm were set to be 0.85, 0.05 and 12, respectively. The evaluation function is

$$\eta_{eva} = \eta_{col} - W\eta_{back} \quad (6.10)$$

where η_{back} was the percentage of the backstreaming electrons, and W was the weight. In our calculation, W was chosen as 1.5. The optimization was run with the magnetic field of 1.75 T. After 756 iterations, an optimum collection efficiency of 78.7% was achieved. It was 3.8% lower than the ideal collection efficiency calculated in the preceding section which assumed all the spent electrons were sorted perfectly. That was because not all the electrons were recovered by the optimum electrode and a small proportion were observed to backstream in the simulation. The trajectories of the spent electrons are also shown in Fig. 6.11.

Fig. 6.12 shows the optimum collection efficiency versus the number of the iterations. There is only a slight improvement in the collection efficiency after 408 iterations,

which means 34 generations in the genetic algorithm. A good convergence in searching for the parameters was achieved by using the genetic algorithm.

The emitted current in the simulation was 1.40 A, and the emitted power was about 48 kW. They all slightly changed for different simulations caused by a slight change in the size of the mesh grid. The top five collection efficiencies with collected current are shown in Table 6.2. It should be noticed that there was 4.5% of the current not collected which could stream back into the interaction region.

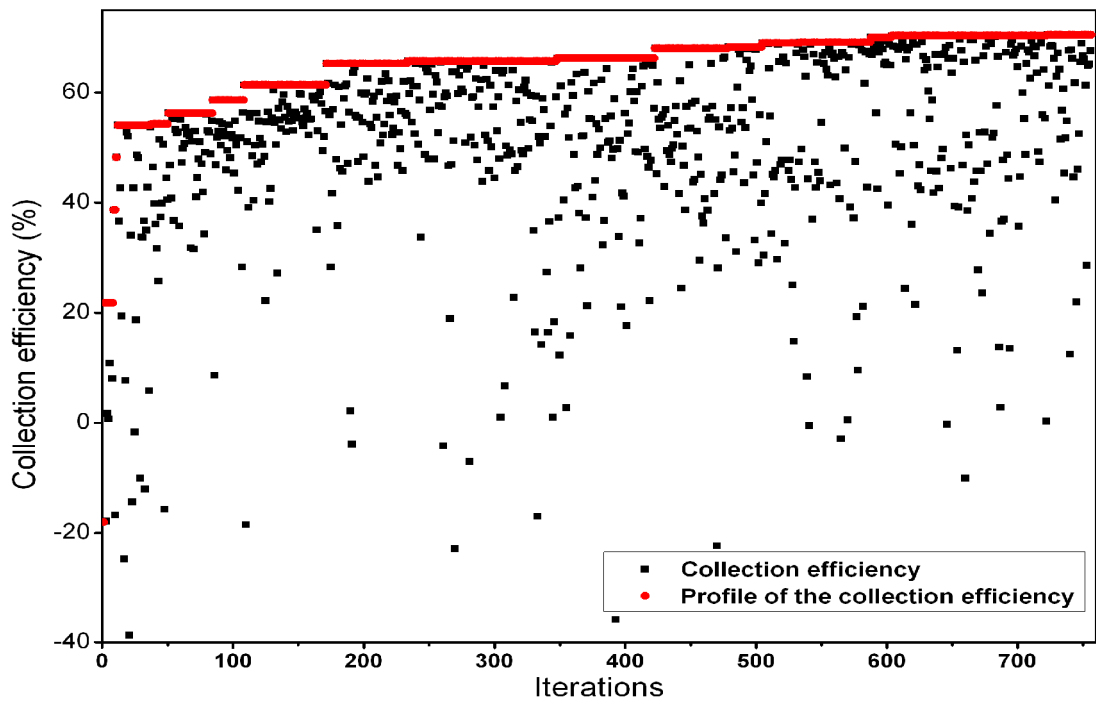


Fig. 6. 12 Collection efficiency versus iteration number.

The electronic efficiency of the W-band gyro-BWO was about

$$\eta_e = \frac{10.0 \text{ kW}}{40 \text{ kV} \times 1.5 \text{ A}} = 16.7\% \quad (6.11)$$

Without energy recovery, the overall efficiency of the microwave tube was

$$\eta_{tot} = \varepsilon_{out} \cdot \eta_e = 0.9 \times 0.167 = 15.0\% \quad (6.12)$$

By applying the optimum depressed collector using the data in iteration 604, the overall efficiency was

$$\eta_{tot} = \frac{0.15}{1 - 0.787 \times (1 - 0.167)} = 43.6\% \quad (6.13)$$

The overall efficiency was greatly improved by using the energy recovery system.

Table 6. 2 Collected currents and collection efficiencies

No.	P_{all} (kW)	I_1 (A)	I_2 (A)	I_3 (A)	I_4 (A)	P_{col}	Collection efficiency	Backward percentage	Evaluated value
604	48.11	-0.017	-0.44	-0.48	-0.40	37.87	78.7%	4.5%	72.0%
588	48.10	-0.016	-0.43	-0.47	-0.41	37.79	78.6%	5.3%	70.7%
653	47.98	-0.005	-0.41	-0.48	-0.42	37.97	79.1%	6.1%	70.0%
723	47.91	-0.002	-0.37	-0.53	-0.40	37.73	78.8%	7.0%	68.3%
683	48.11	-0.002	-0.37	-0.53	-0.40	37.73	78.4%	7.0%	67.9%

6.4.3 Simulation results for different magnetic fields

In different magnetic fields, the data could be dealt with in the same process, and the optimum potentials on the electrodes were also studied, as shown in Table 6.3 and Table 6.4.

Table 6. 3 The optimum potential on the electrodes

Magnetic field (T)	Potentials on the electrodes (kV) (Comparing with ground voltage)				Collection efficiency
	1 st stage	2 nd stage	3 rd stage	4 th stage	
1.55	-8.61	-19.43	-28.22	-40.00	82.9%
1.65	-8.61	-20.06	-28.44	-39.92	82.7%
1.75	-9.24	-19.55	-27.31	-39.99	82.5%
1.85	-9.70	-19.97	-28.63	-40.00	82.3%
1.95	-11.10	-21.88	-29.69	-39.99	83.4%
2.05	-12.33	-21.28	-29.01	-38.62	83.7%

Table 6. 4 The collected currents and the collection efficiencies

Magnetic field (T)	I_{all} (A)	P_{all} (kW)	I_1 (A)	I_2 (A)	I_3 (A)	I_4 (A)	P_{col}	Collection efficiency	Backward percentage
1.55	-1.40	48.32	-0.029	-0.34	-0.41	-0.53	39.63	82.0%	6.5%
1.65	-1.42	47.96	-0.037	-0.41	-0.43	-0.44	38.33	79.9%	7.3%
1.75	-1.40	48.11	-0.017	-0.44	-0.48	-0.40	37.87	78.7%	4.5%
1.85	-1.37	47.24	-0.016	-0.43	-0.45	-0.39	37.22	78.8%	6.1%
1.95	-1.53	53.67	-0.029	-0.46	-0.44	-0.46	41.85	78.0%	9.2%
2.05	-1.44	50.72	-0.01	-0.43	-0.37	-0.53	40.48	79.8%	6.9%

6.5 Simulation with secondary electron emission

6.5.1 Material property for the depressed collector

Copper is the most common material used for the electrodes of multi-stage depressed collectors due to its high thermal and electrical conductivity as well as its ease of fabrication. However, the biggest disadvantage of the untreated copper is its relatively high secondary electron emission characteristics making it a poor choice as the electrodes of a high performance depressed collector [10]. Table 6.5 lists the secondary electron yields of different materials.

Table 6. 5 The secondary electron yield of different materials

Material	$E_{0m}(0)$	$\delta_{0m}(0)$
Copper	500	1.3
Copper (sooted)	500	0.33
Texture carbon on copper	300	0.26
POCO Graphite (ion textured)	300	0.20

One of the approaches to lower the secondary emission level is to coat titanium carbide to the copper substrate.

6.5.2 Simulation results

The optimization simulation was run once again with the secondary electrons considered. Copper was chosen as the material of the electrodes. The collected power taking account of the secondary electrons was revised as [11]

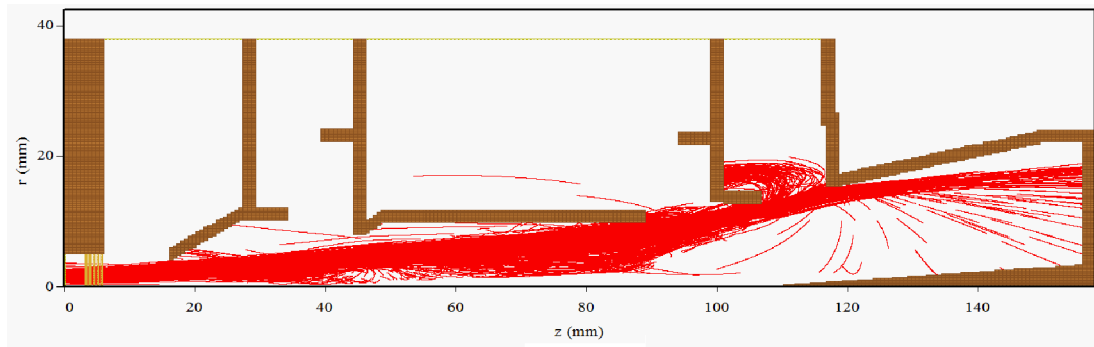
$$P_{col} = \sum_i^n V_i I_i + \sum_i^n \sum_j^n SIGN(i-j) I_{ij} (V_i - V_j) - \sum_i^n V_i I_{B_i} \quad (6.14)$$

$$SIGN(i-j) = \begin{cases} -1, i \leq j \\ 1, i > j \end{cases}$$

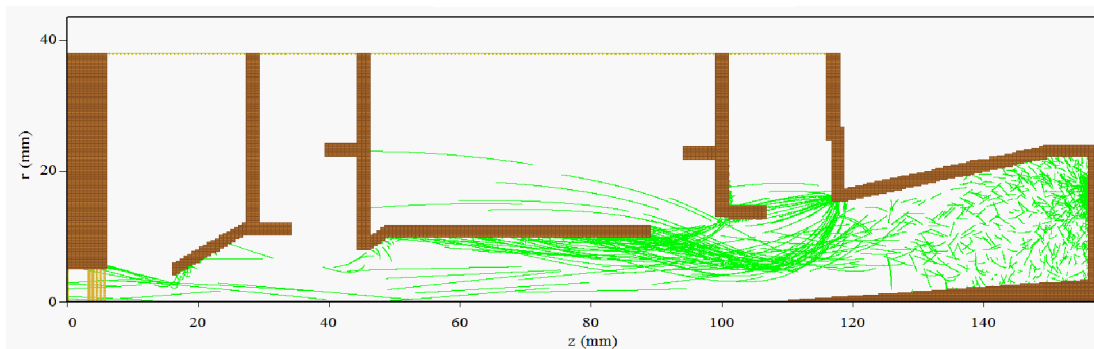
where n is the number of stages V_i, I_i are the potentials and the collected primary current on the i th-stage electrode, respectively. I_{ij} is the current of the secondary electrons emitted from the i th-stage electrode and collected on the j th-stage electrode. I_{B_i} is the backstreaming current by the secondary electrons emitted from the i th-stage electrode.

In the previous optimum geometry without considering the secondary electrons, a collection efficiency of 78.7% was obtained in the conditions of beam current of 1.5 A, beam voltage of 40 kV, magnetic field of 1.75 T, and the operation frequency of 91.4 GHz. The spent electron beam imported into the collector region had 1.4 A average current and approximately 48 kW average power. When taking the secondary electron emission into account, the collection efficiency reduced from 78.7% to 69.2% and the backstreaming increased from 4.5% to 9.4%. Vaughan's formula was used to simulate the true secondary electron emission. The trajectories of the primary electrons and the secondary electrons are shown in Fig. 6.13. The backstreaming was large thus modifications in the geometry were required.

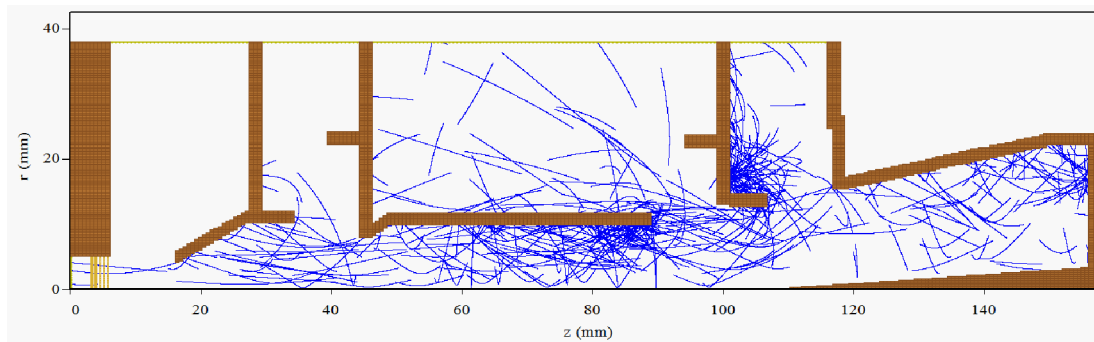
In Fig. 6.13, many secondary electrons were accelerated by the electric field in the z axis and returned to the interaction region. This backstreaming could be reduced if an acceleration field exists in the radial direction which is strong enough to push the secondary electrons back to the electrode surface. It could be improved by changing the tilt angle and the height of the spike in the fourth electrode. Together with the 14 parameters used in the previous geometry, the depressed collector was now completely determined by 16 parameters if we wanted to optimize the dimensions of the spike.



(a) Trajectories of the primary electrons;



(b) Trajectories of the true secondary electrons;



(c) Trajectories of the backscattered electrons;

Fig. 6. 13 Trajectories of the primary electrons and the secondary electrons in the optimized geometry.

With the same parameter setting in the genetic algorithm, after 552 iterations, an optimum collection efficiency of 69.0% was achieved when using Vaughan's true secondary emission model. The collection efficiency and the backstreaming

percentage were shown in Table 6.6. It only had slightly changed in the collection efficiency as compared with the previous geometry. However, the backstreaming was reduced from 9.4% to 4.9%. Table 6.7 presents the collection efficiencies and the percentages of the backstreaming currents in different cases. From the simulation results, by carefully designing the geometry of the depressed collector, the backstreaming could be reduced to a relatively low level.

Table 6. 6 The collected currents and the collection efficiencies.

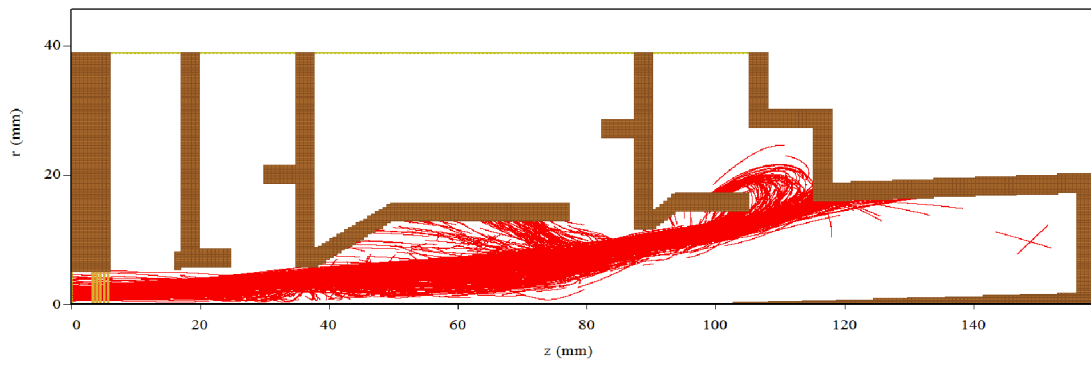
No.	P_{all} (kW)	I_1 (A)	I_2 (A)	I_3 (A)	I_4 (A)	P_{col}	Collection efficiency	Backward percentage
444	48.84	9.47E-05	0.49	0.39	0.41	69.0%	4.9%	61.7%
418	48.84	6.27E-05	0.49	0.39	0.41	68.1%	4.9%	60.8%
293	48.84	8.71E-05	0.49	0.40	0.41	68.1%	4.7%	61.1%
275	48.84	2.22E-04	0.53	0.35	0.41	67.5%	4.8%	60.3%
326	48.84	6.91E-05	0.48	0.41	0.42	66.7%	4.6%	59.8%

Table 6. 7 The collection efficiency and the backstreaming rate in different cases.

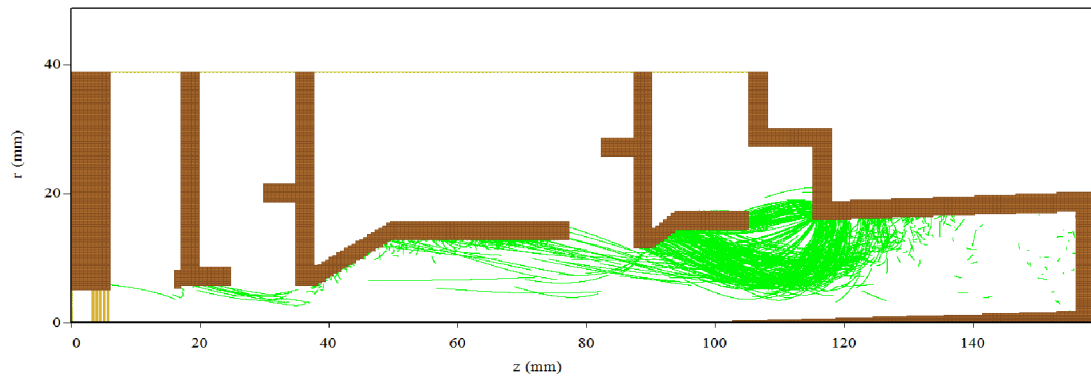
Cases	True SEE model	Collection efficiency	Percentage of backstreaming
without TSEs, without BSEs	---	75.7%	4.79%
with TSEs, without BSEs	Vaughan	71.1%	4.79%
	Furman	68.9%	4.80%
	Thomas	73.0%	4.80%
without TSEs, with BSEs	---	73.9%	4.89%
with TSEs, with BSEs	Vaughan	69.0%	4.89%
	Furman	66.8%	4.91%
	Thomas	71.0%	4.90%

From the simulation results, the backstreaming caused by the primary electrons was 4.79%, while TSEs and BSEs only contributed about 0.1%. Between BSEs and TSEs, the backstreaming was mostly composed by BSEs, as the BSEs had a higher energy than the TSEs thus they were better able to overcome the radial electric field and return to the interaction region. Fig. 6.14 shows the trajectories of the primary electrons, the true secondary electrons and the backscattered electrons in the designed depressed collector when using Vaughan's formula.

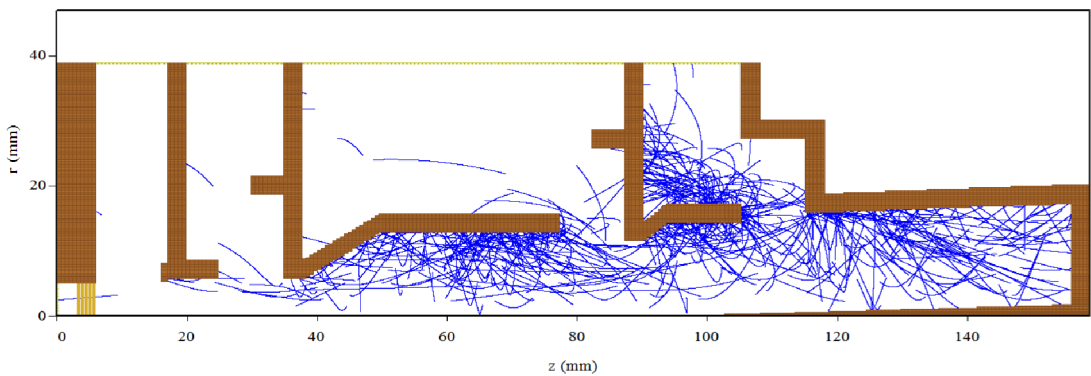
The reduction of the collection efficiency caused by the three different models of true secondary emission yield did not show a great difference and was about 4%. Each secondary emission model generated a different number of the true secondary electrons and impacted the second and third terms of Eq. 6.14. The second term was much smaller than the first term since $V_i - V_j$ was much smaller than V_i . In the simulation, the potentials on each electrode were -9.24 kV, -19.55 kV, -27.31 kV, -40.00 kV, respectively. From the trajectories of the true secondary electrons in Fig. 6.14(b), most of the true secondary electrons emitted from the fourth, third and second electrodes were collected by the third, second, and first electrode, respectively. That made the second term of Eq. 6.14 a small value. Since the difference between the collection efficiency and backstreaming rate associated with the different true secondary emission models were found to be small, in subsequent calculations, we only used Vaughan's formula because it has been widely accepted in the literature.



(a) Trajectories of the primary electrons;



(b) Trajectories of the true secondary electrons;



(c) Trajectories of the backscattered electrons;

Fig. 6. 14 Trajectories of the electrons in the depressed collector (using Vaughan's formulas)

The output frequency of the W-band gyro-BWO can be tuned by adjusting the amplitude of the cavity magnetic field. However the spent beam parameters were

also affected by this tuning. The collection efficiencies and the backstreaming rate of the W-band gyro-BWO were therefore simulated in the whole frequency tuning range for the optimized configuration of the four-stage depressed collector and the results are shown in Fig. 6.15. The collection efficiencies achieved were simulated to be about 70% and the backstreaming rate was lower than 7% in the working frequency band.

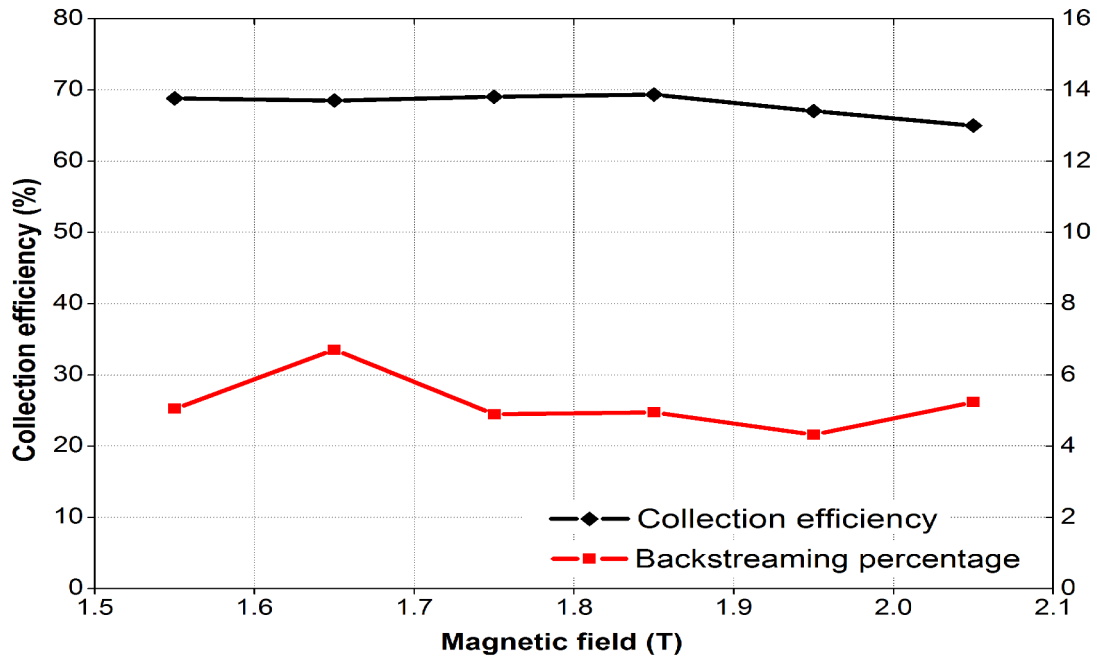


Fig. 6. 15 The collection efficiencies and the backstreaming rates over the frequency tuning range of the gyro-BWO.

6.6 Heat power density distribution on the collector

The heat power dissipation on the electrodes is another important issue in designing the depressed collector. Although the kinetic energy of the spent electrons reduced significantly when they passed through the retarded electric field, the heat due to the power of the remaining kinetic energy of the spent electrons when they struck the surface of the electrodes was still large, for our case, it could be up to 20 keV. The spent electrons with such high kinetic energy could damage the surface of electrodes

in the form of a "hot spot" and could reach the thermal stress threshold of the collector material.

To design an effective cooling system for the collector electrodes, the distribution of the heat power dissipated on the surface of the electrodes needs to be evaluated. In MAGIC, there is no way to obtain the heat power on the electrodes directly. However, it provides a command "OBSERVE COLLECTED POWER" to monitor the overall heat dissipation on a conductor. To obtain the heat power distribution on the surface of the electrodes, the four electrodes were divided into a large number of small conductors both in the azimuthal direction and the z direction and the heat power dissipated in each of these conductors was individually recorded, thus an approximate heat power distribution was obtained. The greater the number of conductors, the higher the resolution of the heat power distribution that could be achieved. The heat power densities on the conductors could be calculated by dividing the heat power by the area of the conductors' surface. There are two types of conductor surface, as shown in Fig. 6.16.

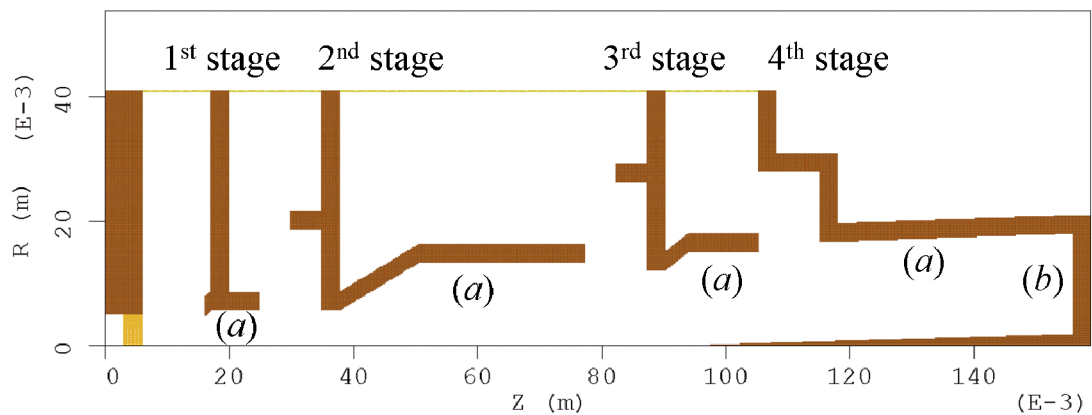


Fig. 6. 16 Two types of conductor surfaces.

A schematic of a single conductor in the electrode in case (a) is shown in Fig. 6.17.

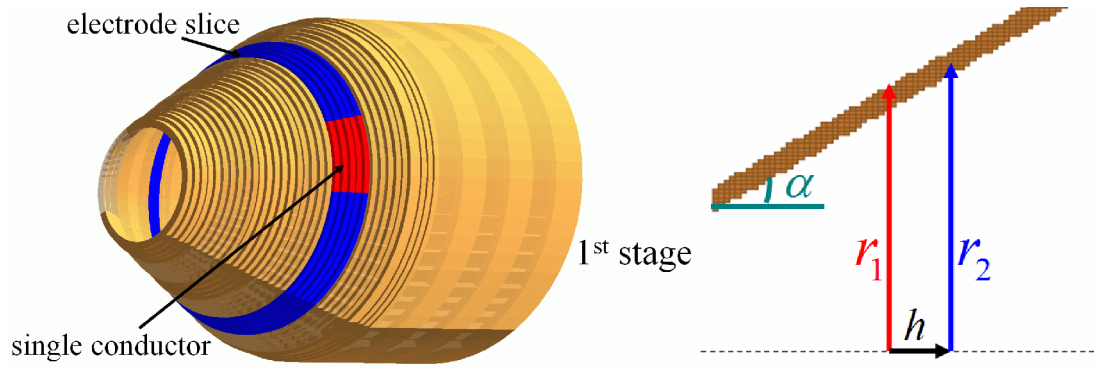


Fig. 6. 17 Schematic of the conductors in case (a).

In this case, the area of a single conductor has the following equation

$$S = \pi(r_2^2 - r_1^2) \sqrt{\frac{h^2}{(r_2 - r_1)^2} + 1} \quad (6.15)$$

The relation of the inner radius r_1 and outer radius r_2 is

$$r_2 = r_1 + h \tan \alpha \quad (6.16)$$

Thus we have

$$S = \pi(2r_1 + h \tan \alpha)h \sqrt{1 + \tan^2 \alpha} \quad (6.17)$$

In the simulation, h is the length of the electrode slice, α is the angle of the tilt part of each electrode, and 0 degree for the flat part.

A schematic of the electrode and a single conductor in case (b) are shown in Fig. 6.18. The area in this case follows

$$S = \frac{1}{2}(r_2^2 - r_1^2) \cdot \Delta\theta \quad (6.18)$$

where in the simulation, $\Delta\theta = \pi/12$ is a constant.

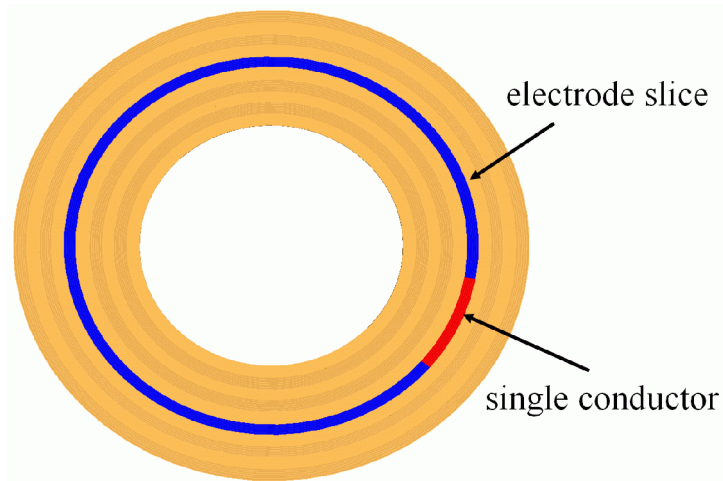


Fig. 6. 18 Schematic of the conductors in case (b).

The maximum value of the heat power densities in the azimuthal direction as a function of the axial position z was recorded and is shown in Fig. 6.19 when the magnetic field is 1.75 T and the beam voltage and current are 40 kV and 1.5 A, respectively. The average heat power density in the azimuthal direction as a function of the axial position z was recorded and shown. The largest heat power density was $\sim 220/\text{cm}^2$. Fig. 6.20 shows the maximum heat density in the designed depressed collector when different magnetic fields are applied. The maximum heat density was $\sim 240\text{W}/\text{cm}^2$. It is lower than the thermal stress threshold of the copper material thus the generation of "hot spots" can be avoided and no extra cooling system is required.

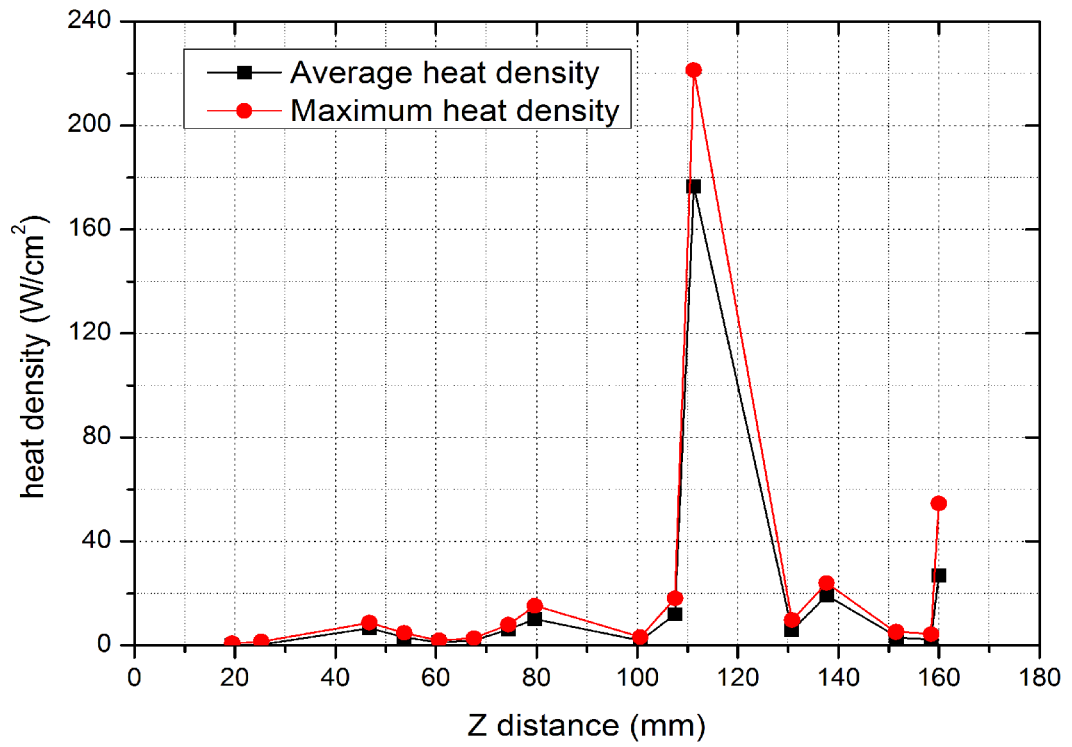


Fig. 6. 19 The average and maximum heat power density as a function of the axial position in the depressed collector.

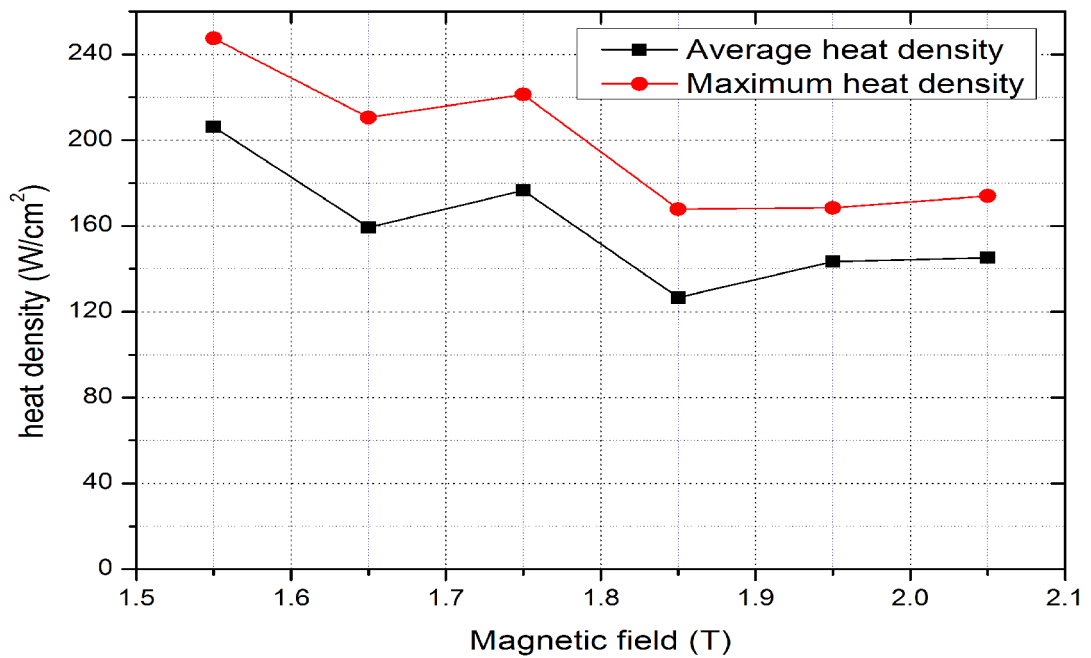
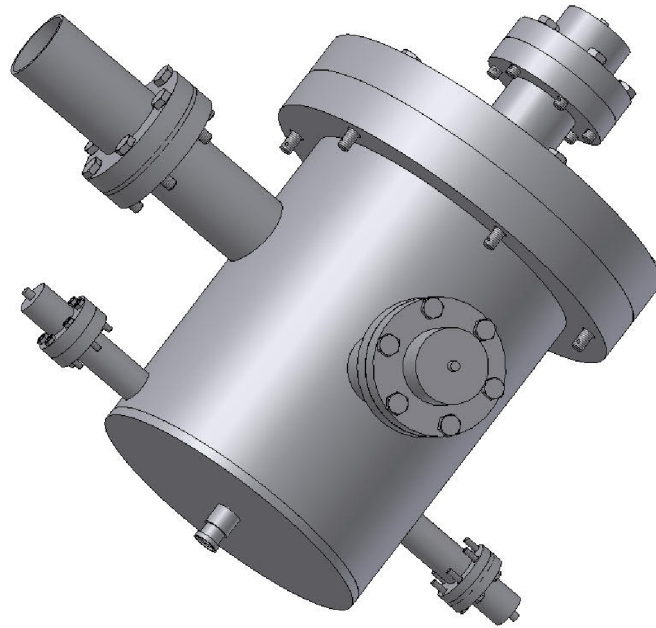
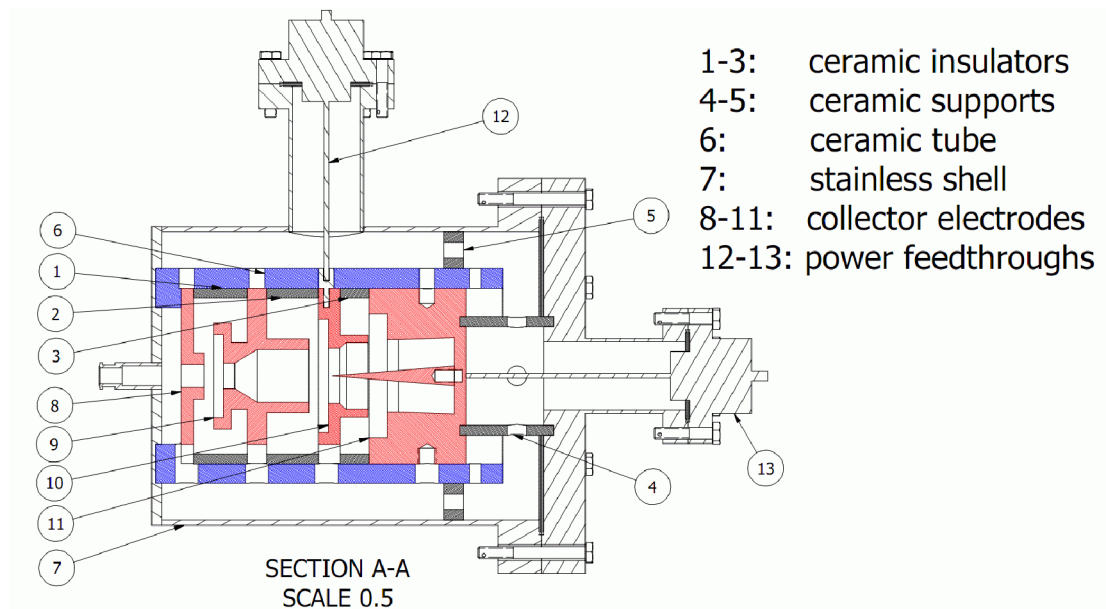


Fig. 6. 20 The maximum heat power density and maximum average power density in different magnetic fields.

6.7 CAD model of the depressed collector



(a) The 3D view;

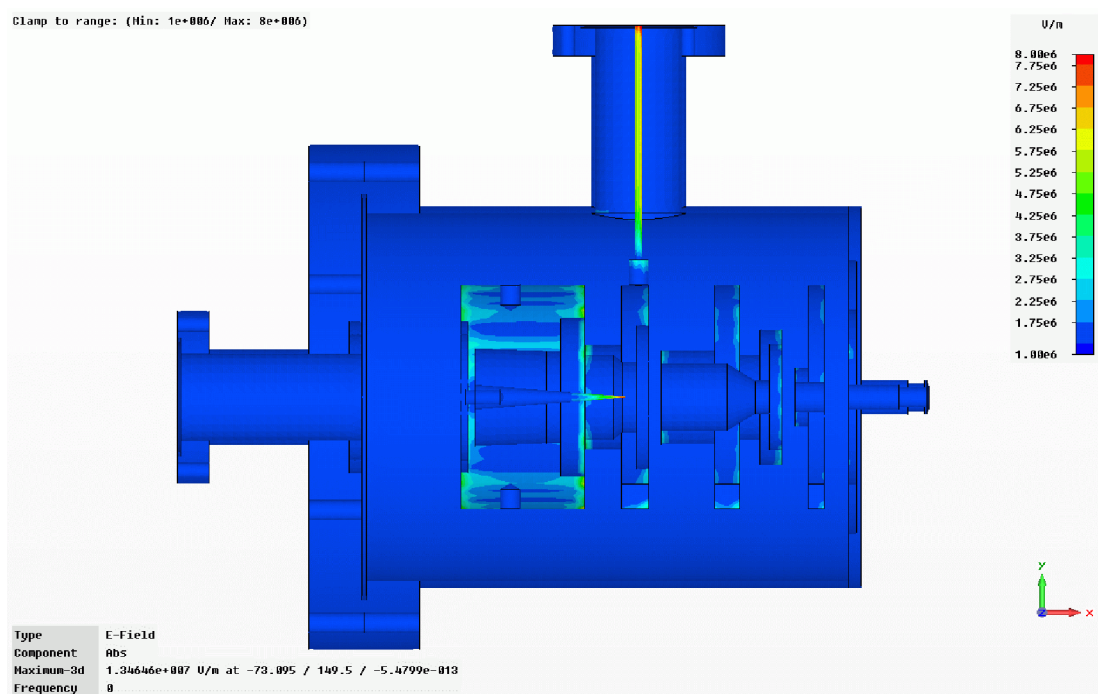


(b) The cross section view;

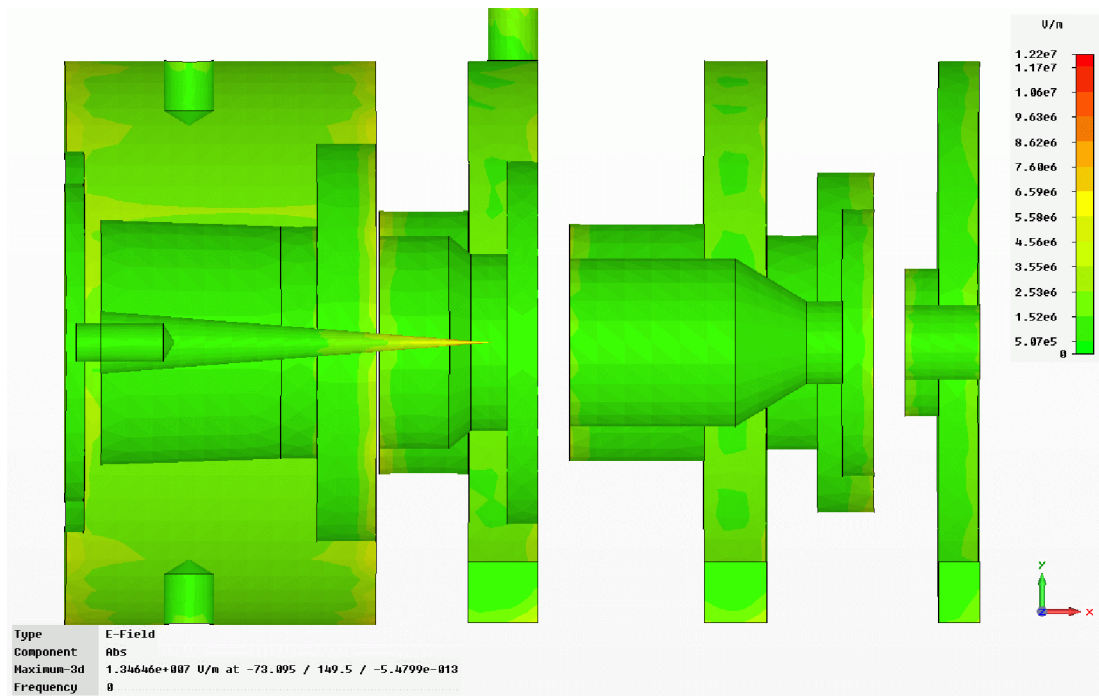
Fig. 6. 21 The 3D view (a) and the cross-section view (b) of the depressed collector.

The optimized geometry in MAGIC then was transferred to an AutoCAD drawing, as shown in Fig. 6.21. It contains the ceramic pieces which are used to isolate the high voltage between the electrodes, the electrodes, the power feedthroughs which are used to feed power from the power supply to the electrodes. To hold the high vacuum, the whole structure was connected by several flanges and the joined parts are welded together. A ceramic tube was used to hold the electrodes as well as to isolate the voltage between the electrodes and the outside shell. Small holes on the side of the ceramic tube were used to help pump the vacuum faster.

To avoid the voltage breakdown in the vacuum, the electric field strength inside the depressed collector was simulated using the CST studio. The calculation result of the original model is shown in Fig. 6.22. The maximum electric field inside the depressed collector was ~ 13.5 kV/mm. However, the vacuum breakdown electric field was ~ 10 kV/mm. The strong electric field mainly caused by the sharp spike and the sharp edge of the electrodes, and the power feedthroughs.



(a) The electric field distribution inside the depressed collector;



(b) The electric field distribution inside the electrodes;

Fig. 6. 22 The electric field distribution inside the depressed collector (a) and inside the electrodes (b)

The electric field around and between the input power feedthrough and the outside shell can be calculated using the following formula.

$$E = \frac{U}{\ln(r_2 / r_1)} \cdot \frac{1}{r}, \quad (r_1 \leq r \leq r_2) \quad (6.19)$$

where U is the potential between the feedthrough and the outside shell. r_2 and r_1 are the radius of the feedthrough and the outside shell. The maximum electric field appears when $r = r_1$. The maximum electric fields of the four power feedthroughs when the magnetic field is 1.75T are listed as Table 6.8.

Applying round corners on the spike and the electrodes can significantly reduce the electric field strength. The maximum electric fields on different radii of the round corners were also simulated to make sure the electric field was at a reasonably low level. Fig. 6.23 shows the simulated result when a round corner with radius of

2.2 mm on the spike, 2.0 mm on the first, second and third electrodes and 4.0 mm on the fourth electrode. The maximum electric field in the collector region was 5.4 kV/mm, which is acceptable for practical usage.

Table 6. 8 The maximum electric fields of the four power feedthroughs

No.	U (kV)	r_2 (mm)	r_1 (mm)	E (kV/mm)
1	9.24	7.9	1.2	4.1
2	19.55	7.9	3.0	6.7
3	27.31	17.5	3.0	5.2
4	40.00	17.5	5.0	6.4

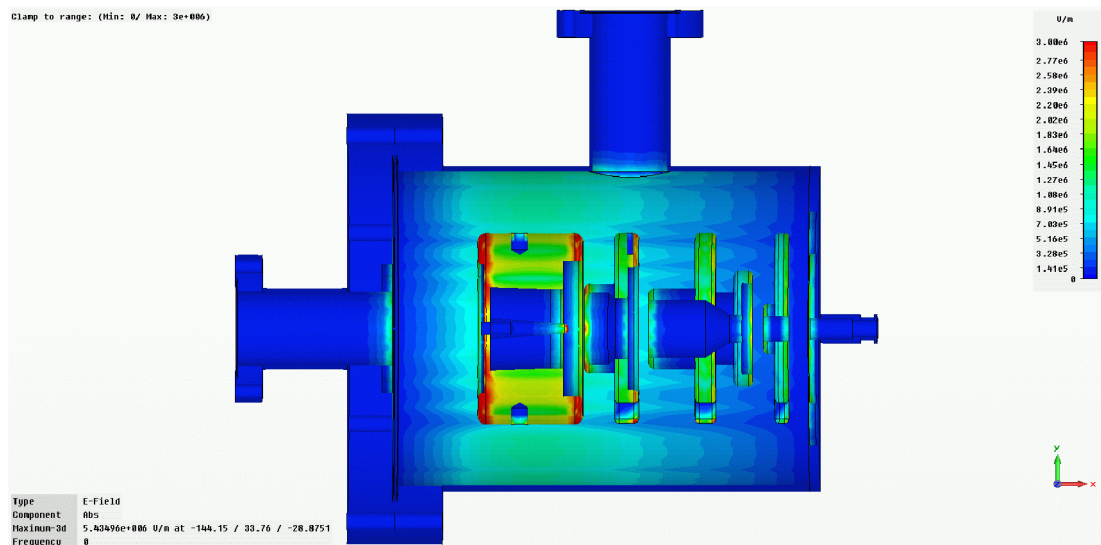


Fig. 6. 23 The electric field distribution inside the depressed collector.

6.8 Conclusion

In this chapter, the simulation results of the W-band Gyro-BWO were introduced and an energy recovery system containing a Bragg reflector and a four-stage depressed collector was designed. MAGIC and a genetic algorithm were used to simulate and optimize the geometry of the electrodes. In the simulation, 99% microwave power

was reflected back upstream by the Bragg reflector and 82.5% collection efficiency was achieved when the magnetic field was 1.75T.

Secondary electron emissions were simulated and a few emission models were compared to investigate their effects on the overall recovery efficiency and the backstreaming rate for the multistage collector. The optimization of the shape and dimensions of each stage of the collector using a genetic algorithm achieved an overall recovery efficiency of about 70%, with a minimized backstreaming rate of 4.9%. The backscattered electrons played a more important role than the true secondary electrons when understanding the backstreaming of electrons back into the beam wave interaction region. The heat distribution on the collector was calculated and the maximum heat density on the electrodes was 240 W/cm^2 and the generation of "hot spots" could be avoided. The electric field distribution inside the depressed collector was calculated and the electrode corners rounded to avoid the voltage breakdown in vacuum.

References

- [1] V. L. Bratman, G. G. Denisov, S.V. Samsonov, et. al, “High-Efficiency Wideband Gyro-TWTs and Gyro-BWOs With Helically Corrugated Waveguides”, *Radio Eng. Electron. Phys.*, vol. 50, no. 2, pp. 95-107, 2007.
- [2] W. He, K. Ronald, A.R. Young, et al, “Gyro-BWO experiments using a helical interaction waveguide”, *IEEE Trans. Electron Devices*, vol. 52, pp. 839-844, 2005.
- [3] G. S. Nusinovich, and O. Dumbrajs, “Theory of gyro-backward wave oscillators with tapered magnetic field and waveguide cross section”, *IEEE Trans. Plasma Sci.*, vol. 24, no. 3, pp. 620-629, 1996.
- [4] M.T. Walter, R.M. Gilgenbach, J.W. Luginsland, et al, “Effects of tapering on gyrotron backward-wave oscillators”, *IEEE Trans. Plasma Sci.*, vol. 24, no. 3, pp. 636-647, 1996.
- [5] M. A. Leontovitch, Ed., *Rev. Plasma Phys.*, NY: Consultants Bureau, New York, vol. 1, 1965.
- [6] F. F. Chen, *Introduction to Plasma Physics*, Plenum Press, New York, pp. 39, 1974.
- [7] L. Zhang, W. He, A. Cross, et. al, “Design of an Energy Recovery System for a Gyrotron Backward-Wave Oscillator”, *IEEE Trans. Plasma Sci.*, vol. 37, no. 3, pp. 390-394, 2009.
- [8] H. G. Kosmahl, “How to quickly predict the overall TWT and the multistage depressed collector efficiency”, *IEEE Trans. Electron Devices*, vol. 27, no. 3, pp. 526- 529, 1980.
- [9] T.K. Ghosh and R.G. Carter, “Optimization of Multistage Depressed Collectors”, *IEEE Trans. Electron Devices*, vol. 54, no. 8, pp. 2031-2039, 2007.
- [10] L. Zhang, W. He, A. Cross, et. al., "Numerical Optimization of a Multistage Depressed Collector With Secondary Electron Emission for an X-band

- Gyro-BWO", IEEE Trans. Plasma Sci., vol. 37, no.12, pp. 2328 - 2334, 2009.
- [11] A.N. Curren, Carbon and Carbon-coated Electrodes for Multistage Depressed Collectors for Electron-beam Devices—A Technology Review, IEEE Trans. Electron Devices, vol. 33, no. 11, pp:1902 - 1914, 1986.
- [12] B. Goplen, L. Ludeking, D. Smithe, and G. Warren, "User-Configurable MAGIC Code for Electromagnetic PIC Calculations," Computer Physics Communications, vol. 87, nos. 1 & 2, pp. 54-86, 1995.
- [13] MAGIC User Manual, mission research corporation, 2005.

,

Chapter 7

Experimental setup and results

7.1 Experiment setup for W-band gyro-BWO

The whole experimental setup for the W-band gyro-BWO is a complicated system. Fig. 7.1 is a schematic drawing of the preliminary experimental setup. In this setup, the microwave radiation was extracted out after the interaction region by a narrow band sapphire window. No depressed collector and output coupler were used. The experiments on the depressed collector is based on the current setup.

The whole system contains the cusp electron gun, the cavity solenoid and reverse coil, the high current DC power supply for solenoids, the beam-wave interaction waveguide, the vacuum system, the safety interlock system, the cooling water system, the electron beam diagnostic system, the microwave radiation detector and the power supply for accelerating the electron beam. Fig. 7.2 shows the gyro-BWO experimental bay and the electron beam device. A brief introduction to each component will be given in this section.

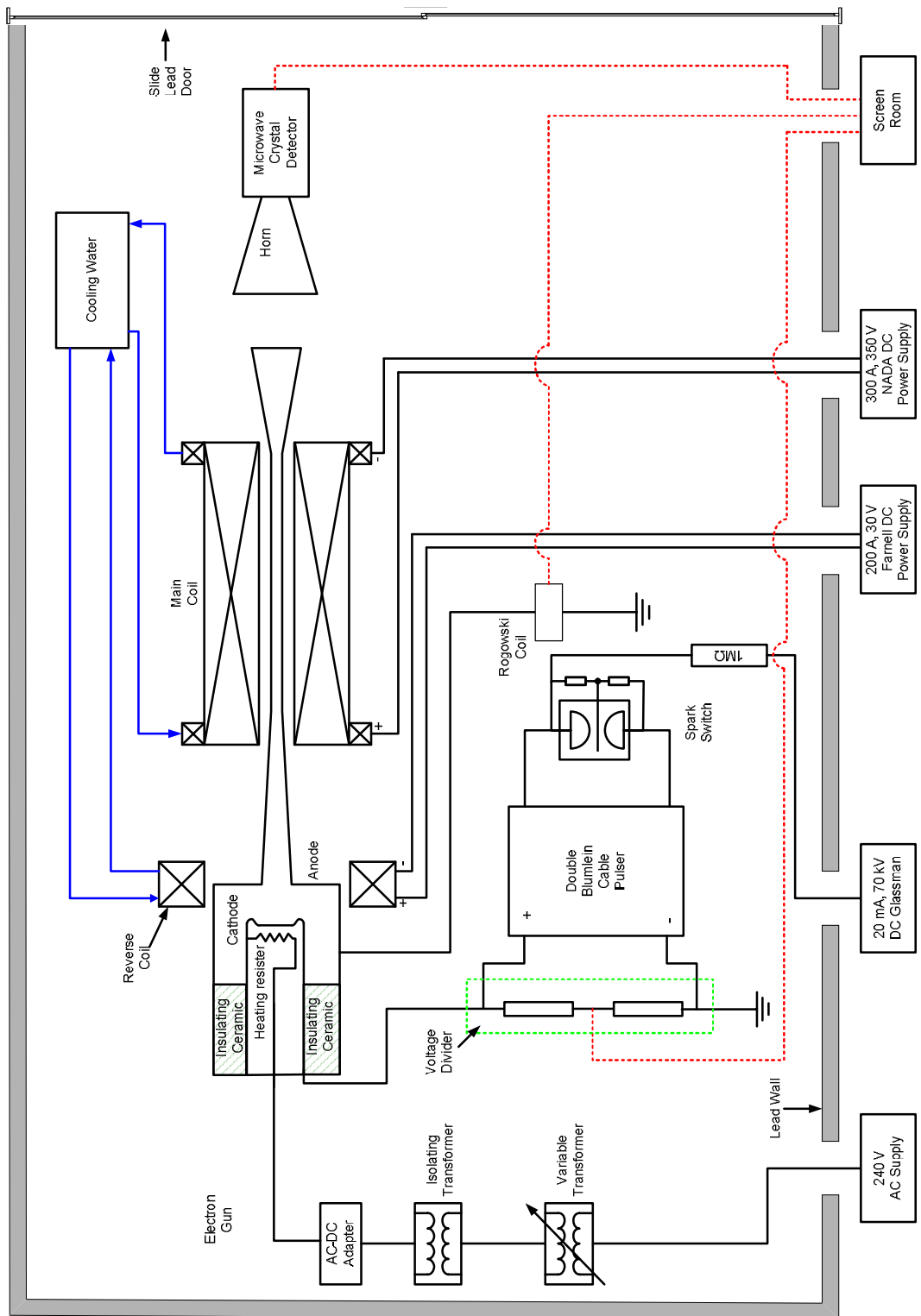
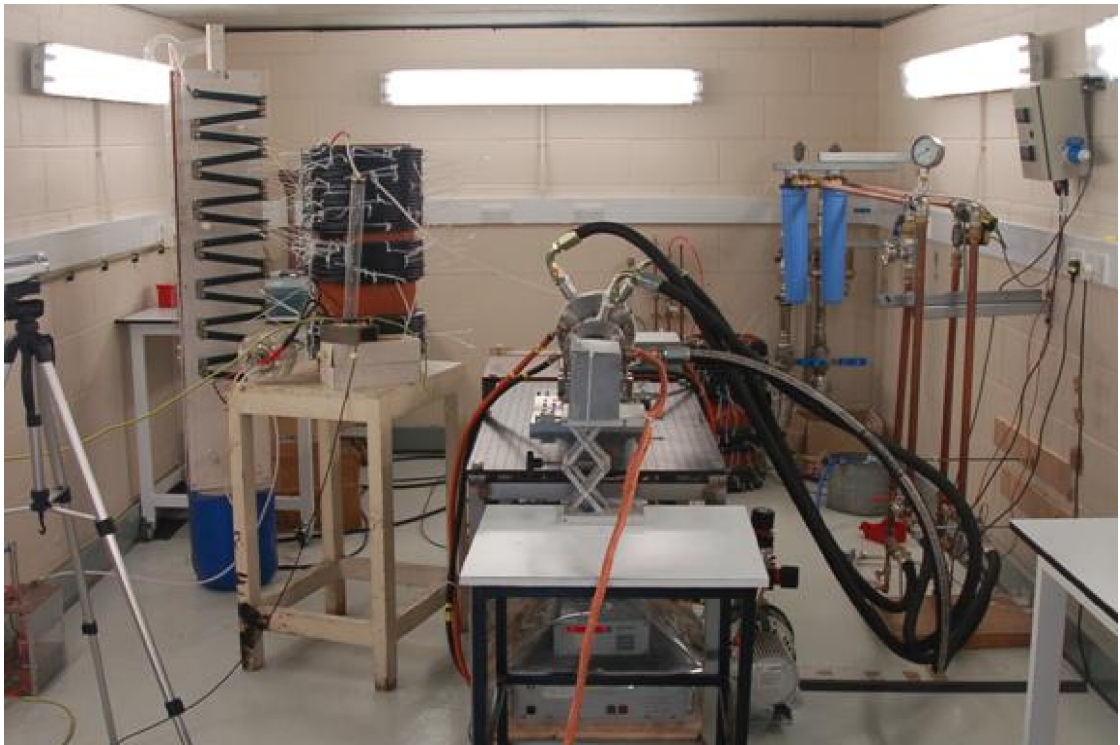
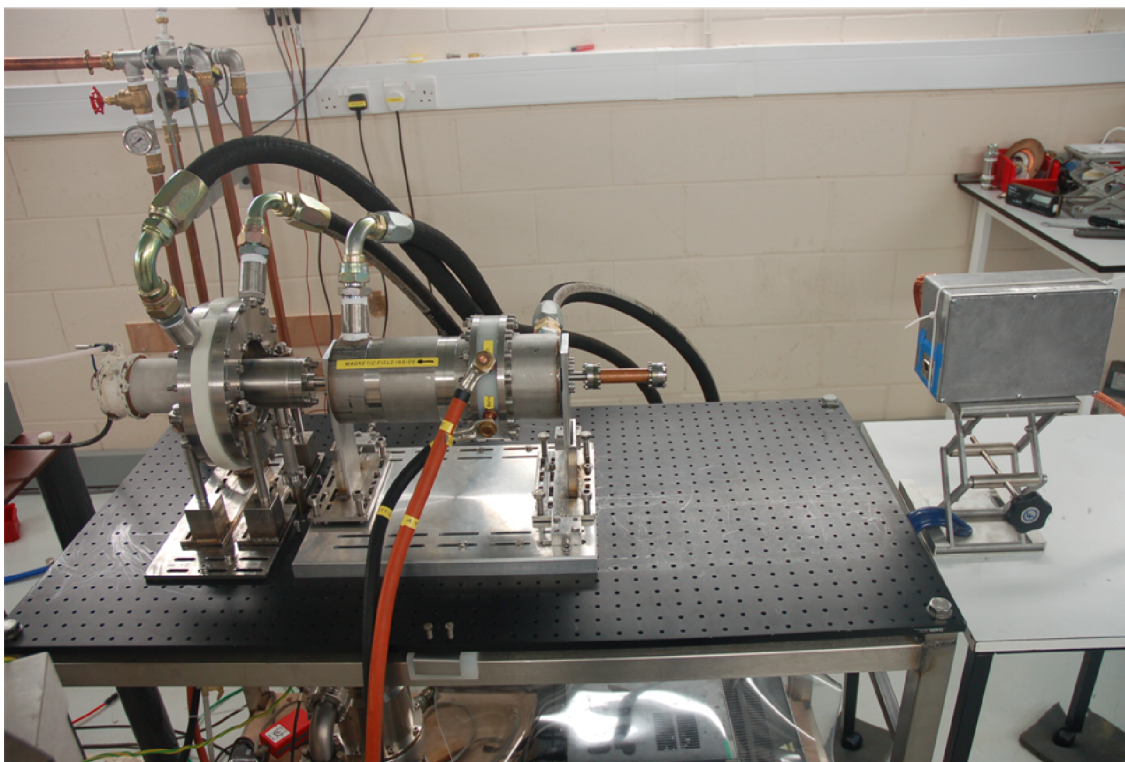


Fig. 7. 1 The schematic drawing of the experimental setup (Figure drawn by Craig Donoladson).



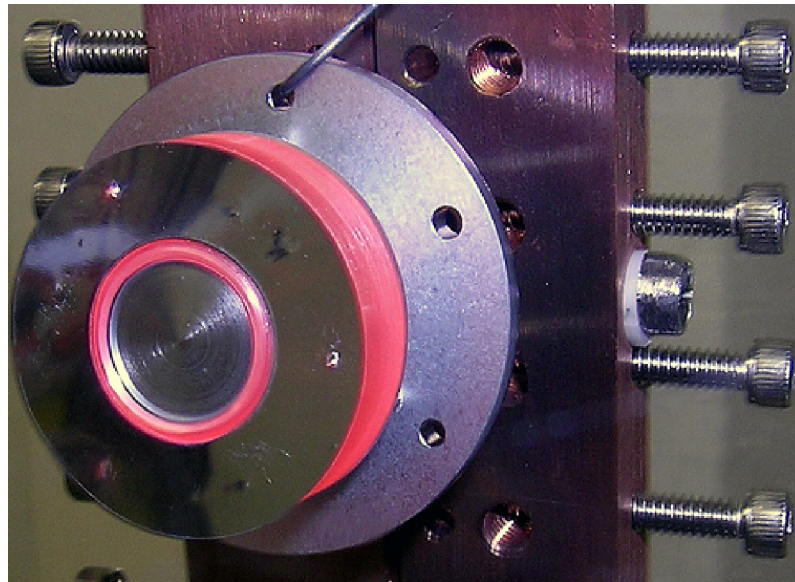
(a) The picture of the gyro-BWO experiment;



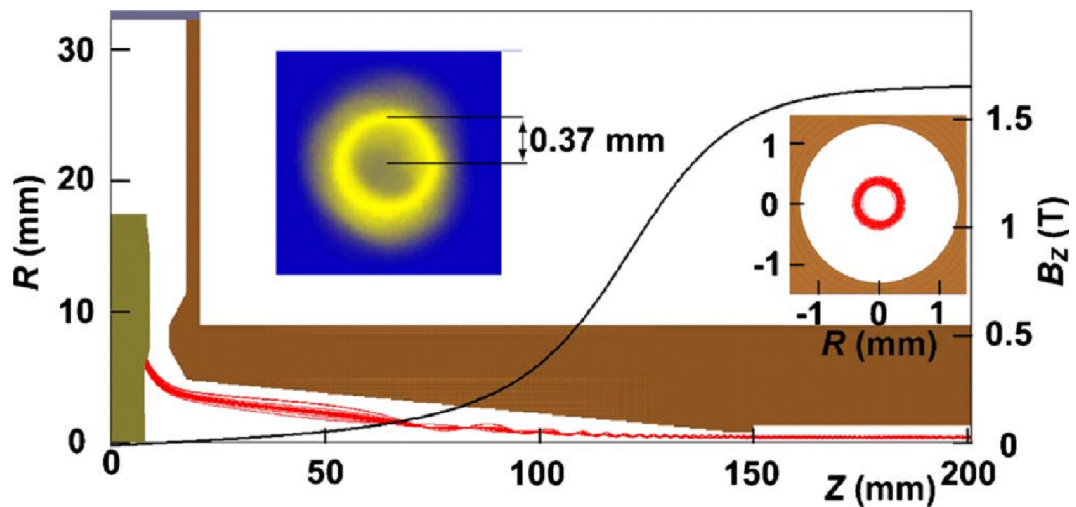
(b) the electron beam device;

Fig. 7. 2 The setup of the gyro-BWO experiments.

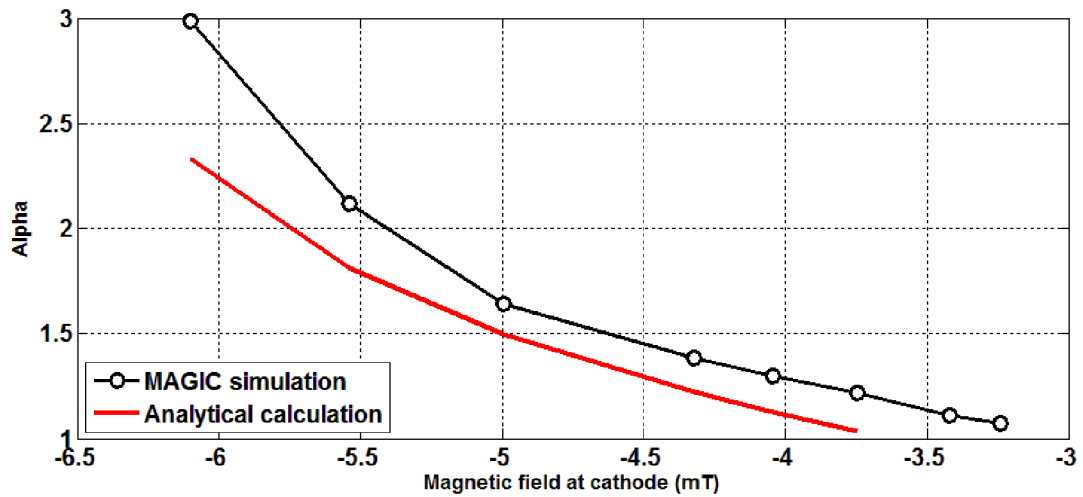
The cusp electron gun is designed to generate an annular-shaped, axis-encircling electron beam with 1.5 A current, and a adjustable beam alpha which is the ratio of the azimuthal velocity to the axial velocity of the electrons beam up to 3 at a beam voltage of 40 kV, as shown in Fig. 7.3 [1, 2]. The measurement of the generated electron beam shows a 0.37 mm in the mean radius, It matches well with the simulation, where the beam had an inner and an outer radius of 0.23 and 0.42 mm, at the central magnetic field of 1.82 T.



(a) A photograph of the cathode (RED part is the emitting surface);



(b) The simulated and measured electron beam of the cusp electron gun;



(c) The beam alpha in different magnetic fields at the cathode;

Fig. 7. 3 the properties of the cusp electron gun.

The cusp magnetic field is produced by two solenoids with opposite current direction. The reverse solenoid produces magnetic field with maximum value of ~ 68 mT at a current of 200 A. It has 4 layer and 10 turns per layer, as shown in Fig. 7.4. The cavity solenoid generates a magnetic field with opposite direction to form a cusp magnetic field for the electron gun, and also, it keeps an uniform magnetic field inside the interaction region. It contains 14 layers (each of 103 turns) and 2 extra layers (each of 15 turns) to compensate the magnetic field drop at both ends, as shown in Fig. 7.5. The resistance of the cavity solenoid is about 1Ω . The cavity solenoid can achieve a maximum magnetic field strength of 2.1 T at a current of 270 A. The power consumption of the solenoid is about 65 kW and a water cooling system is required. The cooling water is operating at a pressure of 4 bar to ensure a high flow rate to take away the heat power from the 0.5 mm gap between the solenoid layers.

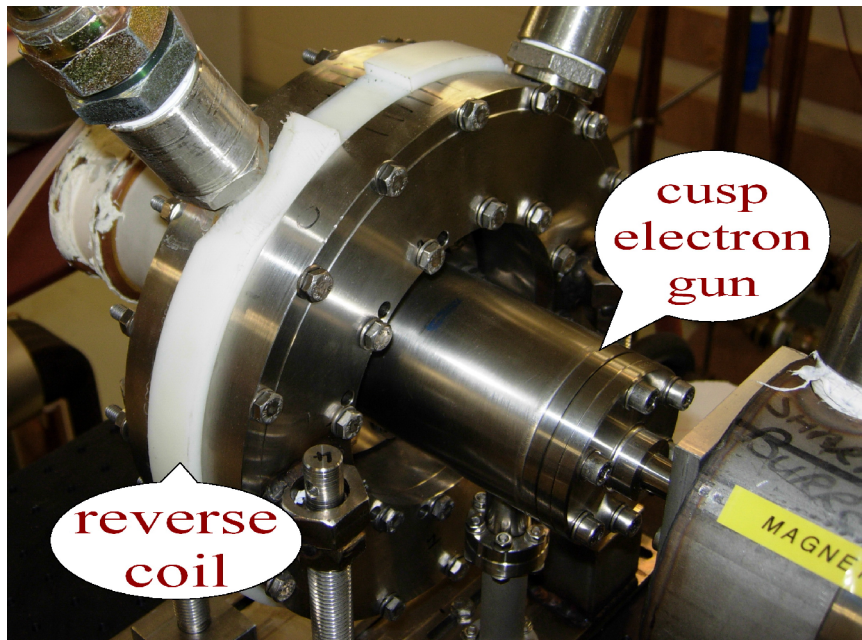
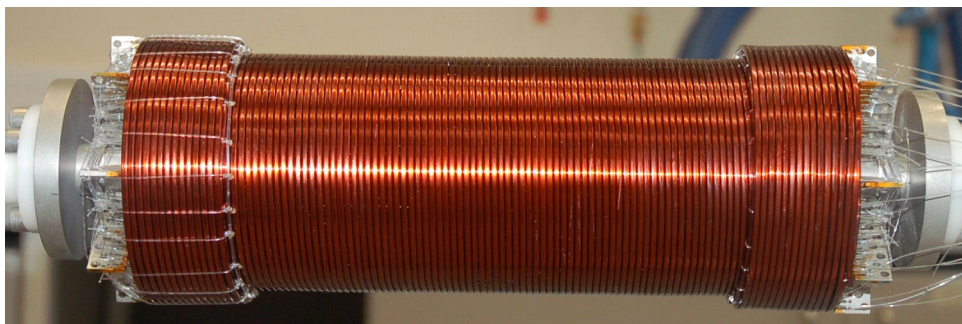
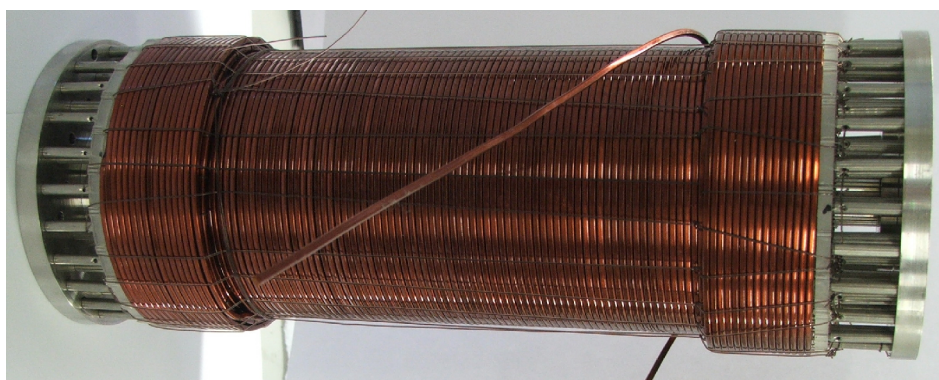


Fig. 7. 4 A photograph of the reverse coil.



(a) A photograph of the first cavity solenoid;



(b) A photograph of the second cavity solenoid.

Fig. 7. 5 Photographs of the cavity solenoids.

The magnetic field as the function of positions z on the axis generated by a single-layer solenoid of finite length L with a centre position of $z = 0$ can be written as

$$B(z) = \frac{\mu_0 n I}{2d} \left(\frac{z}{\sqrt{R^2 + z^2}} + \frac{L - z}{\sqrt{R^2 + (L - z)^2}} \right) \quad (7.1)$$

where μ_0 is the magnetic constant, n is the turns number of the solenoid, I is the current in the solenoid, d is the wire dimension, L is the length of the solenoid and R is the mean radius of the solenoid. For a multiple-layer solenoid, the magnetic field can be calculated by summing all the magnetic fields generated by all the layers.

The magnetic field profile of the reverse coil was measured by an axial Hall detector and the result is shown in Fig. 7.6. The measurement is taken at a driving current of 100 A. As seen from Fig. 7.6, the measurement result agrees well with the simulation result at 101.3 A.

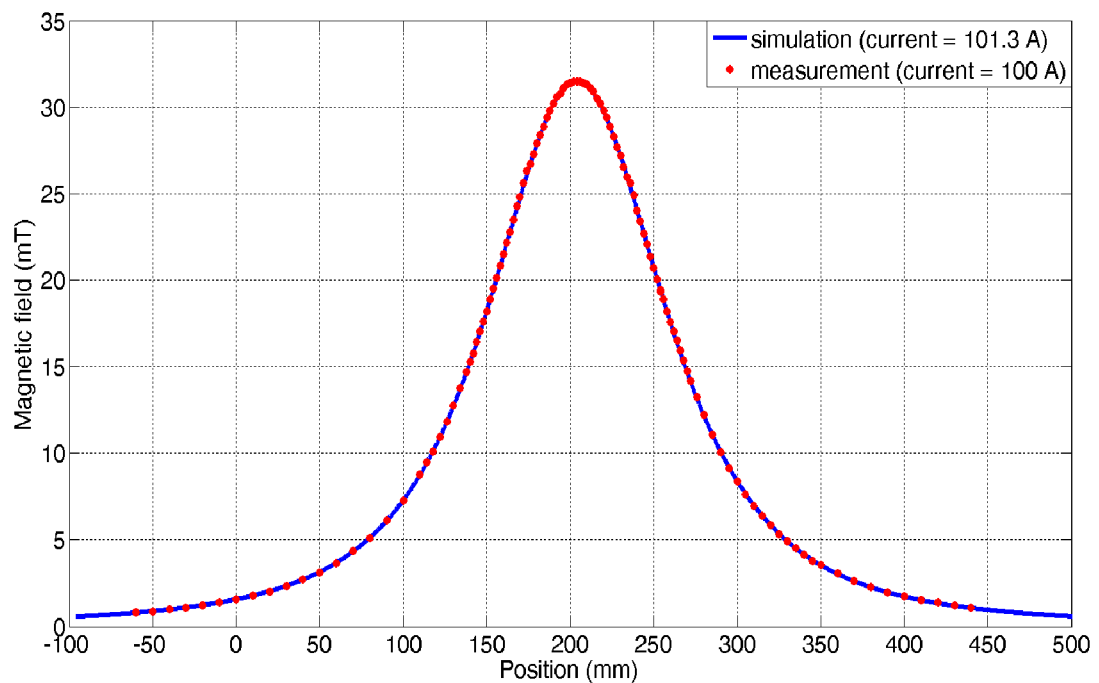
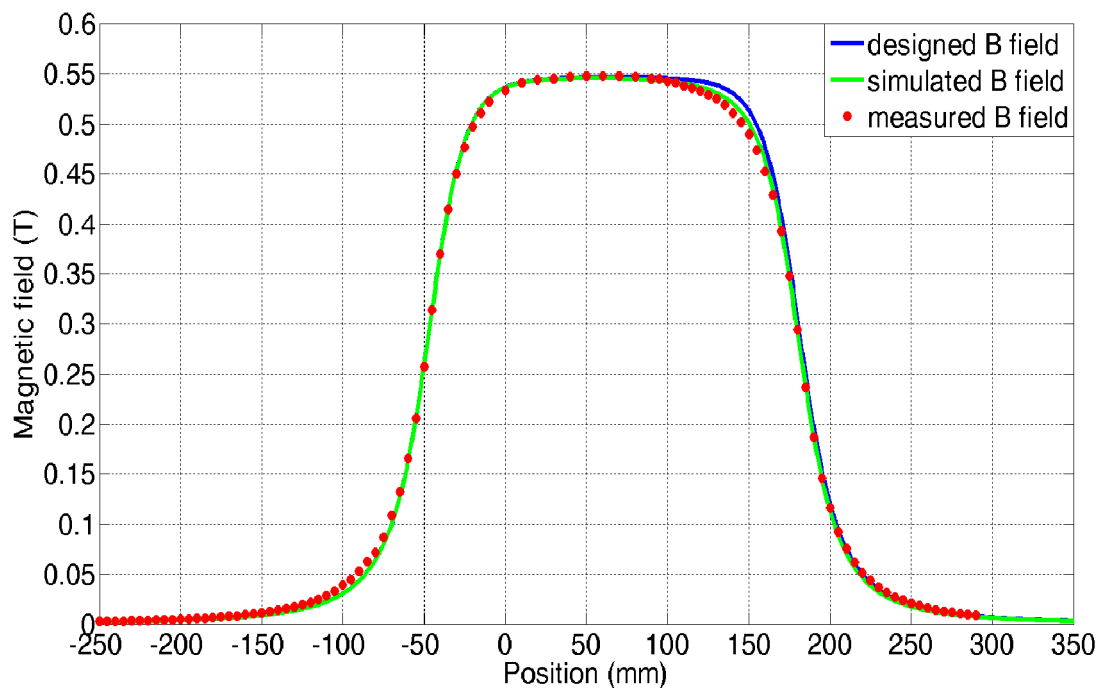


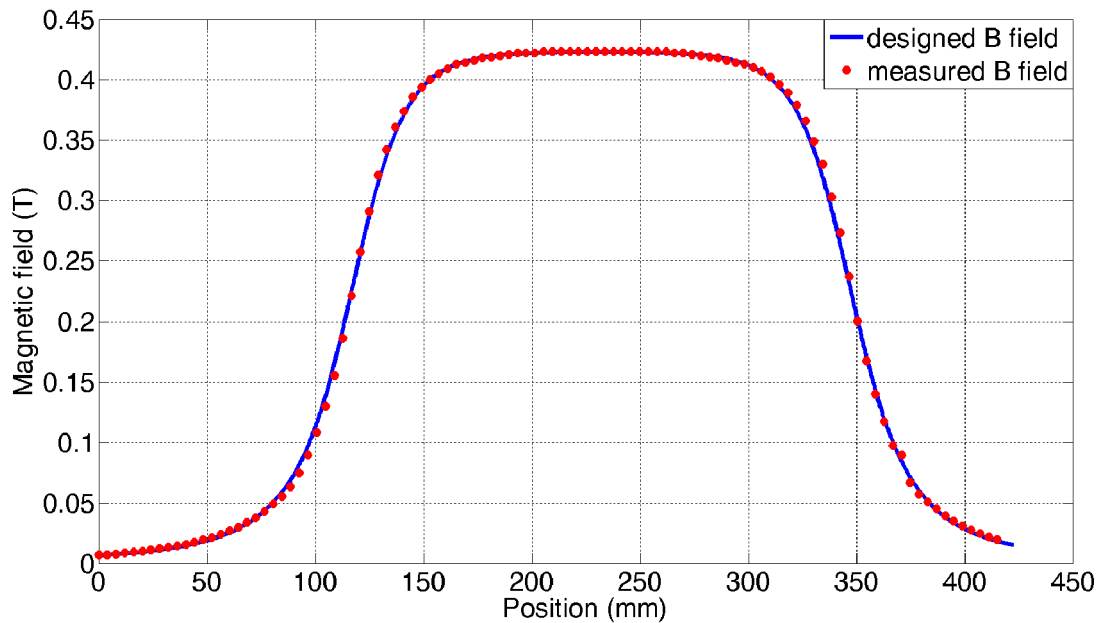
Fig. 7. 6 The simulation and measurement results of the reverse coil.

The magnetic field profile of the cavity coil was measured in the same way as the reverse coil and the result is shown in Fig. 7.7. The measurement of the first coil was taken at a driving current of 70.0 A. As seen from Fig. 7.7(a), the measurement agrees well with the simulation result at a current of 69.5 A on the left hand side. However, the measurement is slightly smaller than the designed magnetic field on the right hand side. Later it was found that the last extra layer in the right side was wound in the wrong direction. Thus the magnetic field created by the two extra layers on the right hand side cancelled each other to produce a lower magnetic field. The result of the verified simulation with 2 extra layers on the left hand side and 0 layers in the right hand side agrees well with the measurement and confirms the mistake when wiring the last extra layer in the right hand side.

The second cavity coil was then wound to correct the mistake in the first coil, and the measurement which was taken at a driven current of 55.0 A is shown in Fig. 7.7(b). It agrees well with the simulation result with a current of 53.8 A.



(a) The results of the first cavity solenoid;



(b) The results of the second cavity solenoid;

Fig. 7. 7 The simulation and measurement results of the cavity solenoid.

The power of the cavity solenoid was supplied by NADA high current power sources. Each NADA unit could provide 70 V maximum output voltage and 300 A maximum output current. As the resistance of the cavity solenoid was about 1Ω at room temperature, 5 units connected in series can provide enough voltage to generate the desired magnetic field for the interaction region. Fig. 7.8 shows a single unit of the NADA power supply. The reverse solenoid was powered by a Farnell power supply which can provide 30 V maximum output voltage and 200 A outputs current, as shown in Fig. 7. 9.



Fig. 7. 8 The NADA power supply (one unit).

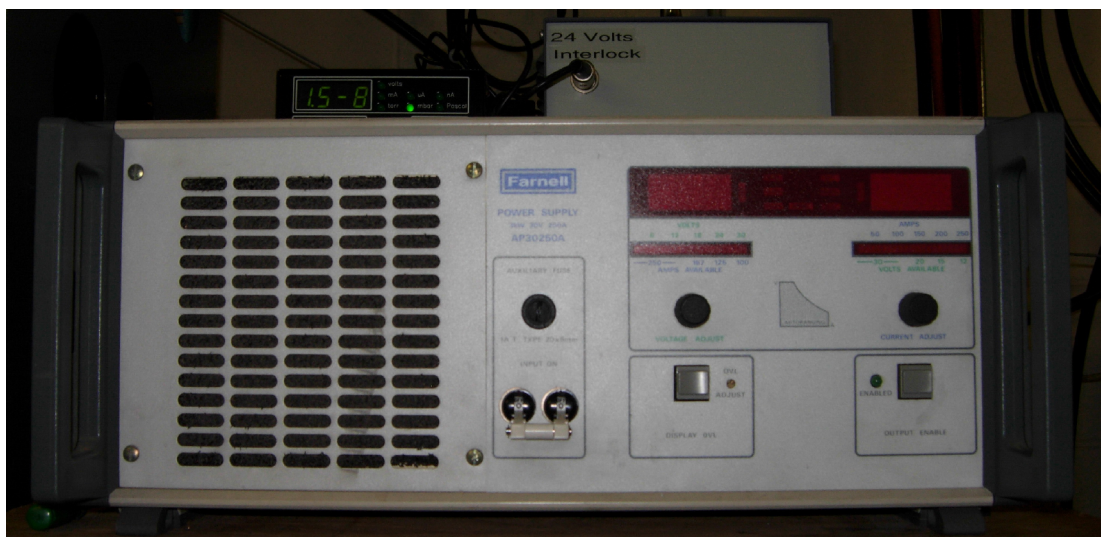


Fig. 7. 9 The Farnell power supply for reverse coil.

The vacuum system consisted of a mechanical scroll pump, a turbo-molecular pump, an ion pump, and two gauges to monitor the vacuum at both the high vacuum part and the lower vacuum part of the system. The mechanical scroll pump can obtain a vacuum with a pressure of 10^{-3} mBar; the turbo-molecular pump can reach a vacuum of 10^{-6} mBar; and the ion pump can finally get a vacuum down to 10^{-9} mBar.

The interlock system is connected with all the power supplies, the temperature monitor of the cavity solenoid and the door of the experiment bay. All the devices share the same ground plate for security purpose.

7.2 Construction of the depressed collector

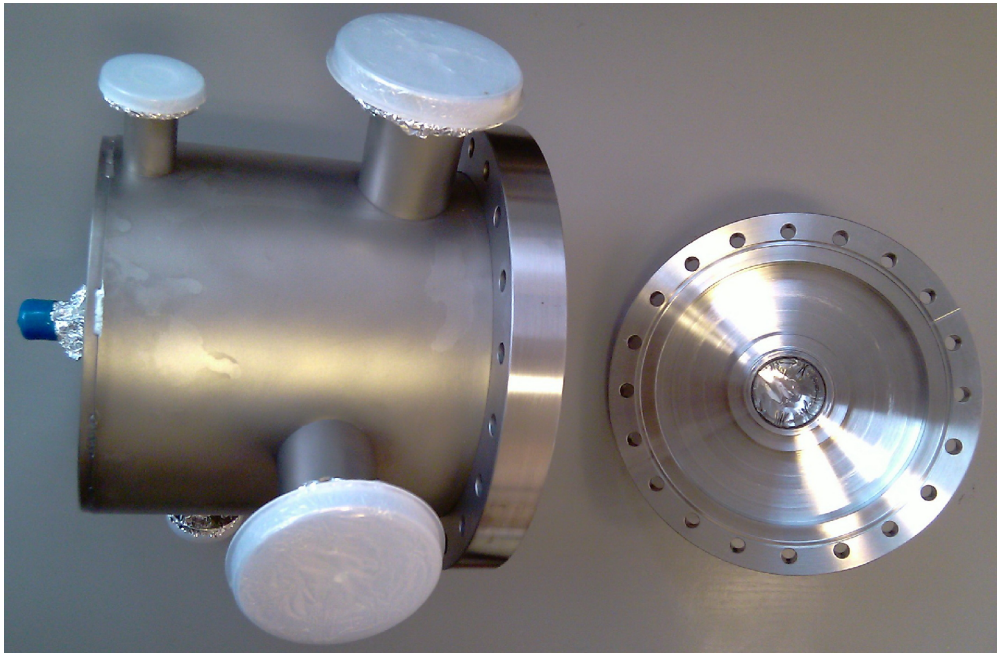
The components of the depressed collector contain the outside shell of the depressed collector, the connectors, the electrodes, the ceramic tubes and ceramic insulators, and the power feedthroughs. The photo of each component is shown in Fig. 7.10.

The outside shell of the depressed collector was welded by several standard flange half nipples, so as to reduce the machining complexity as well as the cost. The disadvantage is the thickness of the flanges is large and adds weight to the system. Several flange connection ports were left for the power feeding through and the vacuum pumping. The whole structure was sealed by a flange and copper gasket in order to obtain high vacuum with a pressure of 10^{-7} mBar.

The electrodes had the same inner shapes as the simulated results. They were machined in the copper and the holes on them were left as a vacuum pumping path.

The ceramic tube and insulators are made of machinable ceramic. The long ceramic tube with holes on the side was used to contain the electrodes and the insulators inside, while the insulators were used to insulate the high voltages between the electrodes, as well as the voltages between the electrodes and the outside shell which was at ground potential.

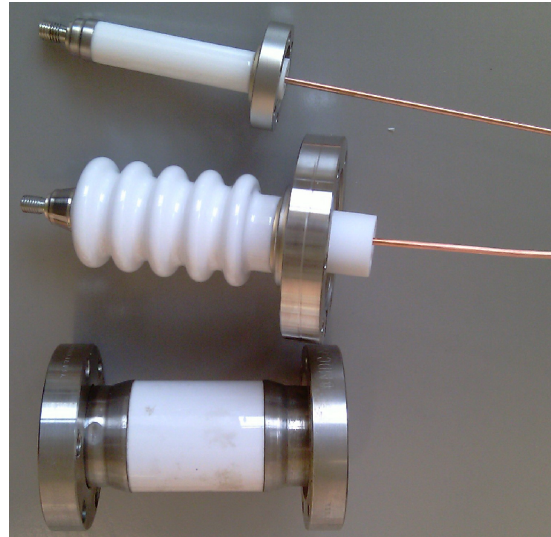
The high potential on the electrodes were fed into the depressed collector by the power feedthroughs from outside. The smallest one as shown in Fig. 7.10(c) can insulate 20 kV between the copper lead and the flange. The middle one can insulate 30 kV and the biggest one can insulate up to 40 kV.



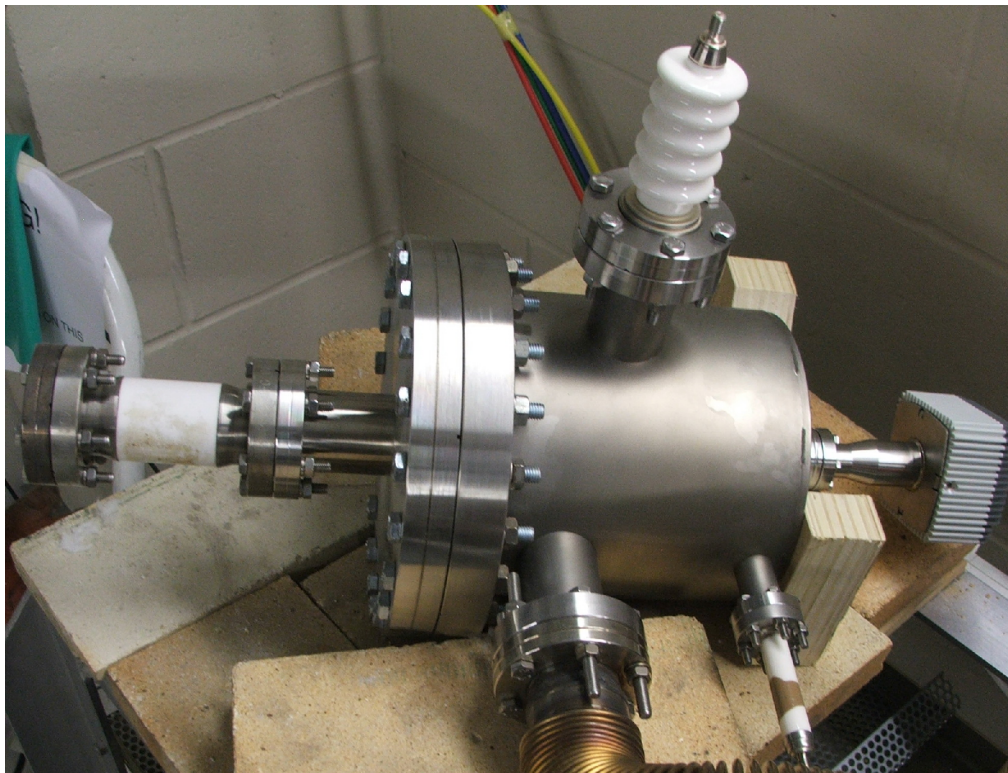
(a) The outside shell of the depressed collector;



(b) The electrodes of the depressed collector;



(c) The ceramic tube, insulators and the power feedthroughs;



(d) The assembly of the depressed collector;

Fig. 7. 10 The construction of the depressed collector.

7.3 Power supply

7.3.1 Double Blumlein line

The power for accelerating the electron beam in the W-band gyro-BWO is provided by a double Blumlein line pulser. The principle of the double Blumlein line is based on the pulse forming line (PFL).

The schematic of the pulse forming line is shown in Fig. 7.11. The transmission line with characteristic impedance Z_0 is charged by a voltage V with the charging current limit V/R_{Lim} when the switch is open at the beginning. Then if the switch is closed rapidly, the transmission line will output a pulse with length $2L/v$ and amplitude of

$$V_{out} = \frac{Z_L}{Z_L + Z_0} V \quad (7.2)$$

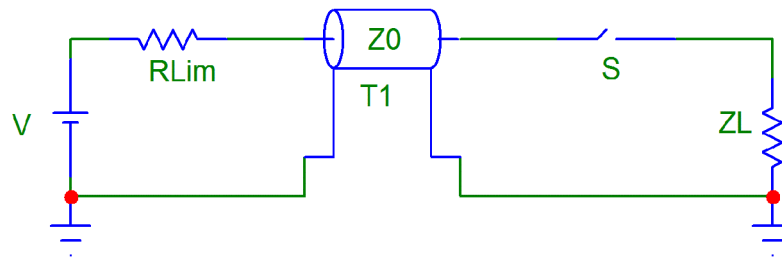


Fig. 7. 11 The schematic circuit of a pulse forming line.

where L is the length of the coaxial cable and v is the speed of the electromagnetic wave inside of the coaxial cable. The drawback of the pulse forming line is the output voltage can never exceed the charging voltage, as it is very clear from the equation. One way to double the output voltage without increasing the charging voltage is to use the Blumlein line [4], as shown in Fig. 7.12. The principle of the Blumlein is similar to the PFL, but two coaxial cables with the same lengths are

connected in series and charged at the same time. When the switch closes, the coaxial cables will discharge at the same time, and make the voltage between the two cables become twice as large as the single PFL if the load impedance is much larger than the characteristics impedance of the coaxial cable. The output voltage of the Blumlein line considering the impedance can be written as

$$V_{out} = \frac{2Z_L}{Z_L + Z_1 + Z_2} V \quad (7.3)$$

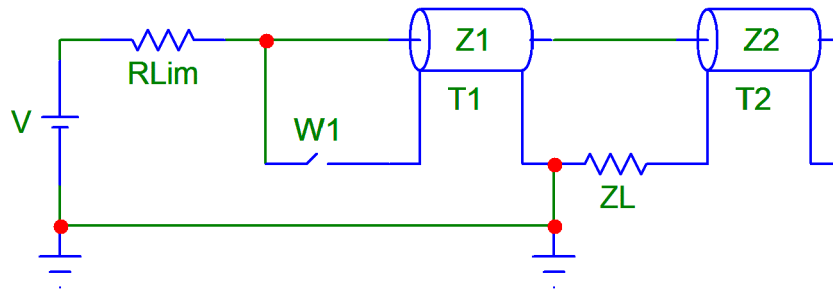


Fig. 7. 12 The schematic of a single Blumlein line.

With the same method, more coaxial cables can be charged in series and discharged in parallel to produce higher voltage. A schematic of the double Blumlein line is shown in Fig. 7.13. It is made by four cables. When the switch is open, the four cables were charged in series to voltage V . Once the switch is closed, a normal output voltage of $2V$ will be produced between b, c , and e, d from the principle of the Blumlein line. If we connect c, e together, then a voltage of $4V$ will be obtained between b and d . The output voltage of the double Blumlein line can be written as

$$V_{out} = \frac{4VZ_L}{Z_1 + Z_2 + Z_3 + Z_4 + Z_L} \quad (7.4)$$

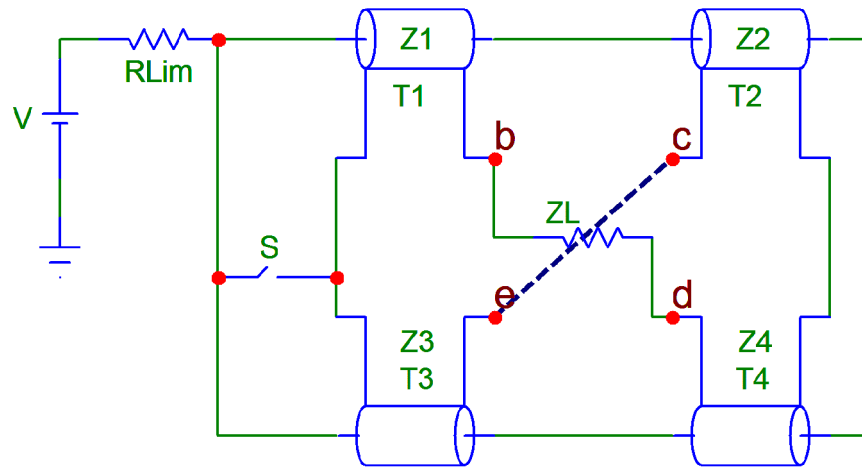


Fig. 7. 13 The schematic diagram of a double cable Blumlein line.

Although it is possible to produce triple Blumlein line, four Blumlein line, as many as it is needed to produce higher voltage, however, when looking into the equation of the output voltage, it can also be written in the following form

$$V_{out} = \frac{2NVZ_L}{\sum_1^N Z_i + Z_L} \quad (7.5)$$

suppose all the coaxial cables are with equal characteristic impedances, then we have

$$V_{out} = \frac{2NVZ_L}{NZ_i + Z_L} \quad (7.6)$$

if the impedance of the load is not large enough, increasing the cable number will not significantly increase the output voltage, but make the whole power system complex and difficult to make. In our experiment, a double Blumlein line was used to produce either a $+4V$ or $-4V$ pulse, as shown in Fig. 7.14. To produce a -40 kV output, the charging voltage needs to be around -10 kV.

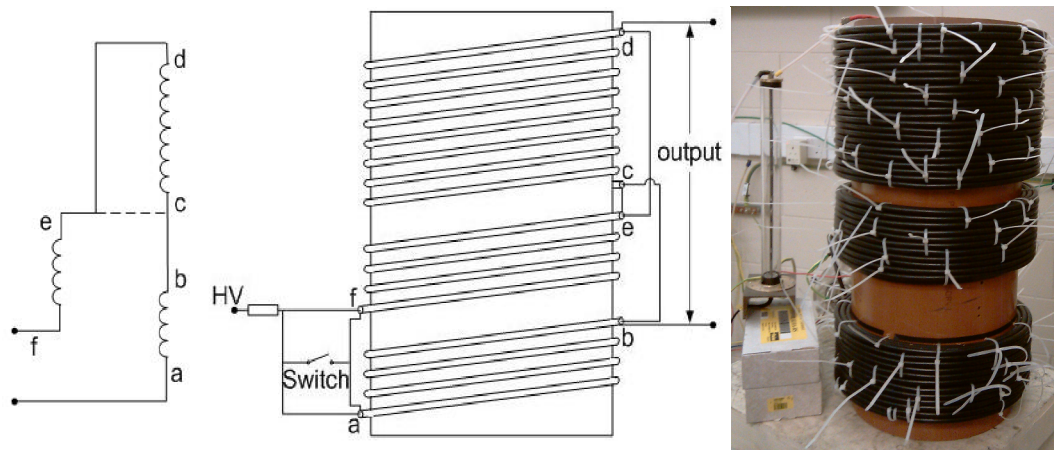


Fig. 7. 14 The schematic diagram of the double cable Blumlein in the experiments.

A spark-gap switch [5] was used to switch the double cable Blumlein pulser. The spark-gap switch normally consisted of an arrangement of two conducting electrodes separated by a gap usually filled with gas such as air, N_2 , Argon or SF_6 . A two-electrode spark-gap switch can only work on self-break-down mode. When the voltage between the two electrodes exceeded the break-down voltage in the gap, the switch would be closed and conducting. The drawback is the output voltage is completely determined by the maximum voltage that the switch can hold. If a higher or lower output pulse is required, adjustment on the gap distance or the pressure of the filled gas needs to be done, which is rather inconvenient. And also, the break-down voltage of the switch may change shot by shot, and the output voltage is not stable.

A three-electrode spark-gap switch is commonly used in practice, as shown in Fig. 7.15. It contains an extra trigger electrode between the main and ground electrodes. It can both operate on trigger and self-break-down mode. The mechanism of the trigger mode is: Firstly, the desired output voltage is applied on the main and ground electrodes. The switch does not conduct because the distance of the gaps is large enough. Then a fast and short trigger pulse is applied to the trigger electrode. If the electric field caused by the trigger voltage added to the one caused by the previous high voltage is high enough to break down a partial gap, for example, the gap between the trigger and ground electrode, this part of the switch will close first

forcing the trigger electrode to be the same potential as the ground electrode. As the gap between the trigger and the main electrodes is much narrower, the electric field in the gap will be large enough to break down the rest of the gap. Then the whole switch will be conducting. The mechanism of the self-break-down mode is similar to that of the triggered mode. The only difference is a voltage divider is applied to the three electrodes, when the high voltage is applied to the main and ground electrodes, the trigger electrode will also be charged to a certain potential which acts like the external trigger pulse.

The state of the three-electrode switch is mainly determined by the potential on the trigger electrode, which can be adjusted by the external trigger pulse or changing the resistance ratio of the voltage divider. The output voltage is determined by the applied high voltage which can be freely adjusted as long as it is high enough to break down the rest part of the gap and make it much easier to produce a suitable pulse used to drive the cusp electron gun.

The spark-gap switch used in the experiment is shown in Fig. 7.15, the resistors of the voltage divider are $R_1=250\text{ M}\Omega$, and $R_2=200\text{ M}\Omega$. This gap switch was operated without a trigger pulse in a self-break down mode.

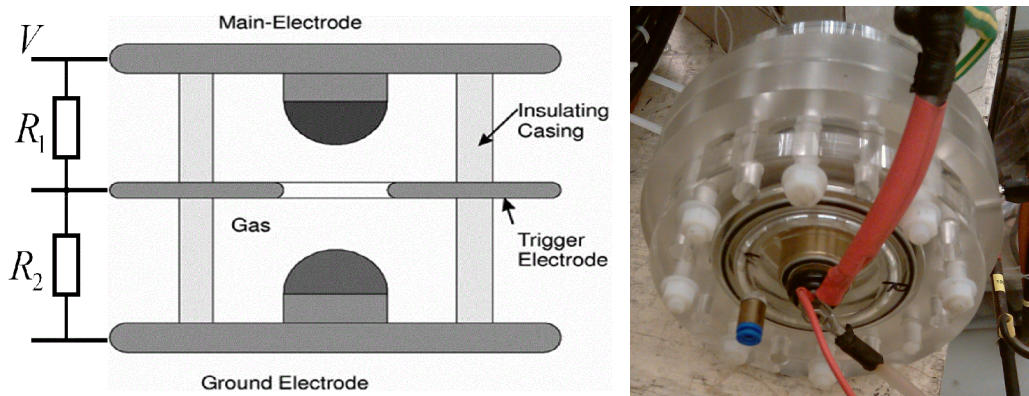


Fig. 7. 15 The schematic of the three-electrode spark-gap switch and the picture of the one used in the experiment.

The overall diagram of the power supply system for accelerating the electron beam is shown in Fig. 7.16. An adjustable DC power supply which could provide up to 70 kV output voltage with 20 mA current was used to charge the double Blumlein line.

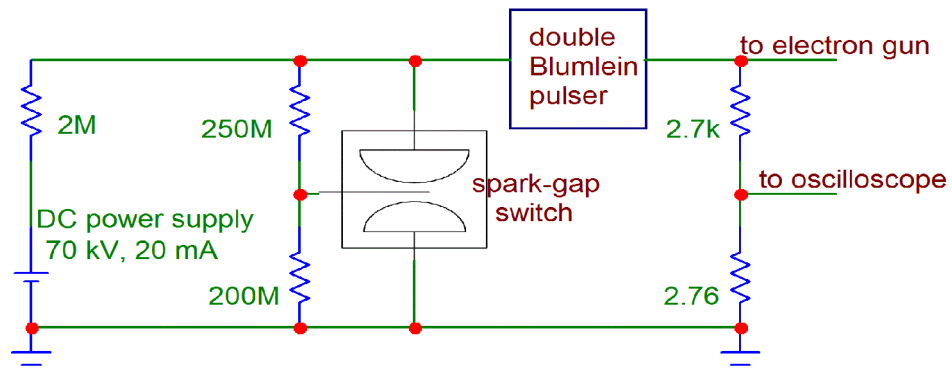


Fig. 7. 16 The schematic drawing of the power supply for the cathode.

7.3.2 Voltage dividers

The potentials on the electrodes for different stages of the depressed collector are different. Also, from the simulation results in chapter 6, the optimized potentials on the electrodes change when applying different cavity magnetic fields. The required range of the voltages on the electrodes is shown in table 7.1.

Table 7. 1 The minimum and maximum potentials on the electrodes

Electrode No.	Minimum potentials (kV)	Maximum potentials (kV)
1	-8.61	-12.33
2	-19.43	-21.88
3	-27.31	-29.69
4	-38.62	-40.00

To produce the required voltages from the double Blumlein line pulser, voltage dividers are necessary. The simplest schematic circuit of the voltage divider for the depressed collector is shown in Fig. 7.17.

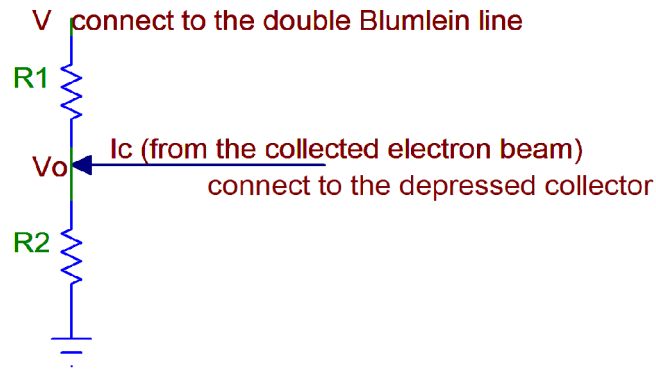


Fig. 7. 17 The schematic of the voltage divider for the depressed collector.

The potential on the electrode can be written as

$$V_o = \frac{V}{R_1 + R_2} R_2 + I_c R_2 = \left(\frac{V}{R_1 + R_2} + I_c \right) R_2 \quad (7.7)$$

In the experiment, the power should be applied to the depressed collector before applying the accelerating voltage to the electron gun. Thus initially, there is no spent electron beam collected by the electrode, and the potential on the electrode is completely determined by the output voltage from the double Blumlein line pulser and the resistance ratio R_1 / R_2 of the voltage divider. Properly choosing the ratio will produce the optimized electric field inside of the depressed collector. Then the collected current on the electrode increases and makes the voltage unable to stay at its optimized value. Chapter 6 also analyzes the effect caused by the changed potentials on the electrodes. As from the calculation, 20% variation of the potential on the electrode will cause about 5% difference in the collection efficiency. If we want to minimize the effect, the relation $V / (R_1 + R_2) \gg I_c$ needs to be satisfied. As from the simulation, the collected current of each electrode is 0.037 A, 0.46 A, 0.48A

and 0.53 A, respectively. If $V/(R_1 + R_2) = 5I_c$ was chosen, the voltage dividers need to provide current of the values 0.20 A, 2.30 A, 2.4 A, and 2.65 A, respectively. The resistors R_1, R_2 of the voltage dividers can therefore be calculated from these currents. It is surely better to make the currents in the voltage dividers as high as possible, however, the overall current on the dividers can not exceed the capability that the cable pulser can provide.

The voltage dividers need to have the capability to output adjustable voltages between minimum and maximum values. In the design, there are 20 stages which are implemented by a lot of resistors with small values connecting in serial.

A full schematic circuit of the voltage divider that can fulfill the requirements is shown in Fig. 7.18, and the picture is shown in Fig. 7.19. All the resistors are chosen as the available standard values.



Fig. 7. 18 A photograph of the voltage dividers.

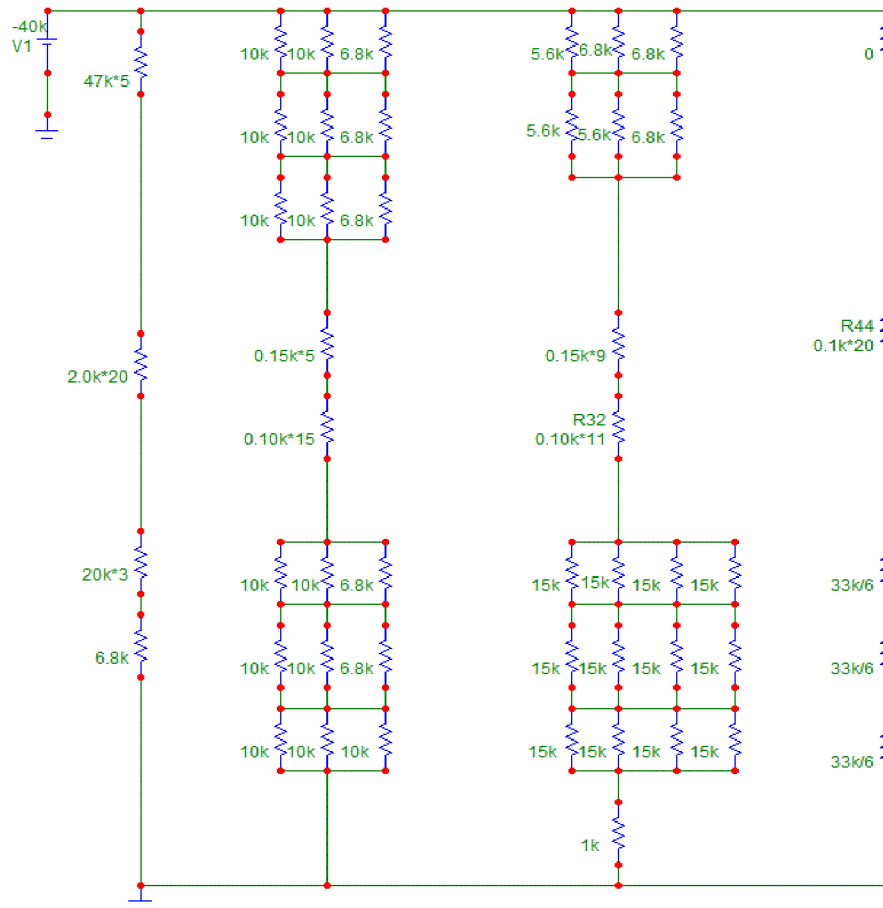


Fig. 7. 19 The schematic circuit of the voltage divider.

7.3.3 Measurement of the voltages and currents

In the experiment of the depressed collector, it is necessary to measure the high voltages applied to the collector electrodes as well as the collected currents from the spent electron beam on the electrodes.

The voltage signals applied to the electrodes are too high for the measuring instrument and they can be measured by the voltage dividers, as discussed in the last section. A precision resistor with a small resistance, such as 50 ohm, is connected in series into the circuit. The potential on the electrode can be easily calculated from the measured result and the resistor ratio between the precision resistor and the resistor parallel to the collector electrode.

It should be noted that, the calculation in last section assumes that the resistors are pure resistive. However, there are always stray capacitances and inductances existing either in the circuit. These distribution parameters, such as the stray capacitances will affect the rise time of measured waveform, and they should be reduced to as small as possible. When making the voltage divider, non-inductive, high frequency power resistors are chosen, and the resistors are soldered well to reduce the stray capacitances.

There are several methods that can be used to measure the electric current, such as magnetic probe method [6], Faraday cup [7] method and a current shunt [8]. A current shunt is a non-inductive resistor connected into the circuit, where the current to be measured is passed through the resistor. A standard resistor used for the voltage divider can also act as a current shunt. The current can be calculated from the measured voltage on the resistor. A Faraday cup normally captures the electrons, and it is a destructive method to measure the electron beam current. It is not suitable to measure the collected currents on the electrodes of the depressed collector although it can measure at both high and low frequencies. The Faraday cup is used to measure the beam current into the interaction region of the gyro-BWO when testing the performance of the cusp electron gun.

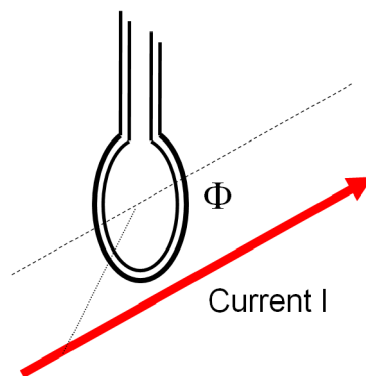


Fig. 7. 20 Basic schematic circuit of magnetic probe.

The magnetic probe method is accomplished by processing the signal from a pickup loop which is used to couple the magnetic field of the electron current. The pickup loop is also called a B-dot probe, which is shown in Fig. 7.20. A typical B-dot probe consists of N multiple turns of wire around a former which has an area of A in cross section. The B-dot probe produces an output voltage proportional to the time rate of change of the magnetic field component parallel to the axis of the coil. The voltage signal induced by the probe is given by Faraday's law in the form of

$$V = nA \frac{dB_n}{dt} = nM \frac{di}{dt} \quad (7.8)$$

where n is the turns of the probe, B_n is the component of the magnetic field parallel to the probe normal direction, and M is the mutual inductance. In general, it is hard to calculate M because the shape of the probe is usually non-uniform. A practical way to get the value is from experiments.

The current can be obtained by integrating the pickup voltage from the equation. A RC integrator is usually used to accomplish that in a practical circuit. The schematic of the electrical circuit is shown in Fig. 7.21. From the circuit, we can get

$$V = M \frac{di}{dt} \cong i_s R_T = i_4 R_l + \frac{1}{C} \int i_4 dt \quad (7.9)$$

Initially $i_4 \cong V / R_l$, and the voltage picked-up on the capacitor is

$$V_c = V - i_4 R_l = \frac{1}{C} \int \frac{V}{R_l} dt \quad (7.10)$$

Substitute Eq. 7.10 into Eq. 7.9, and suppose the pulse width is much less than the value of $R_l C$, we can get the relation between the current and the picked-up voltage

$$i_l = \frac{V_c R_l C}{M} \quad (7.11)$$

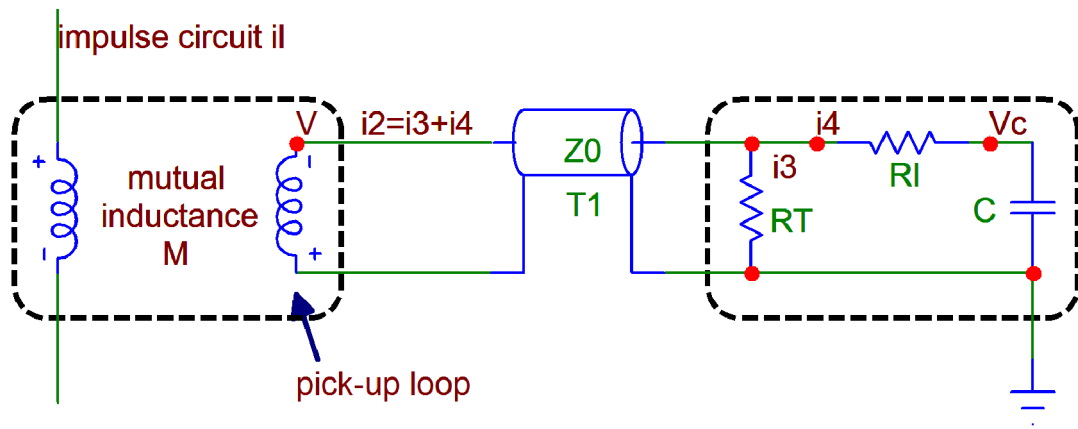


Fig. 7. 21 Magnetic probe method to measure the current.

The magnetic probe method has the advantage that it is electrically isolated from the monitored current and also it can have very small dimensions.

A typical example of the magnetic probe is the Rogowski coil [9]. A Rogowski coil is an air-cored coil placed around the conductor in a toroidal fashion. It is sensitive to flux changes created only by the current passing through the aperture of the coil, while the general B-dot probe is sensitive to the position with the electric current. A picture of the Rogowski coil is shown in Fig. 7.22. The Rogowski coil has the advantage of having a wide bandwidth, good linearity due to the absence of magnetic material and is capable of measuring large current. Rogowski coils are very suitable to measure high frequency current signals.

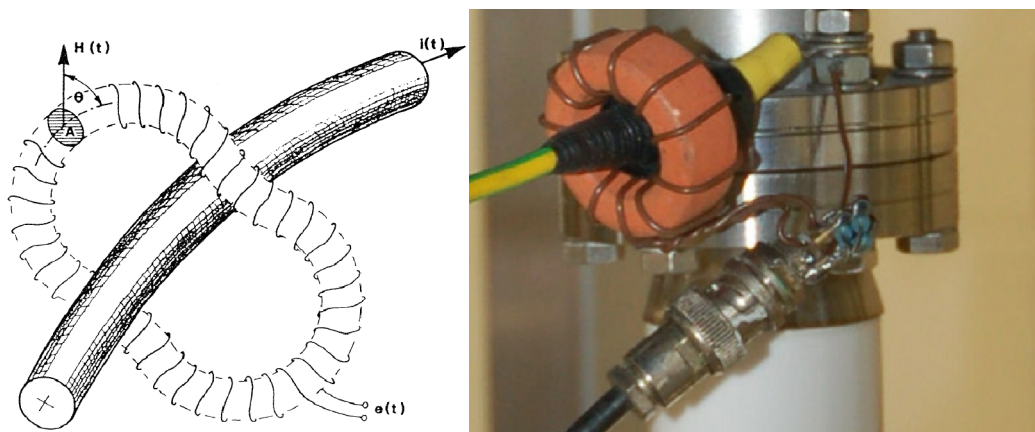


Fig. 7. 22 The Rogowski coil.

A typical output waveform from the double Blumlein cable pulser is shown in Fig. 7.23.

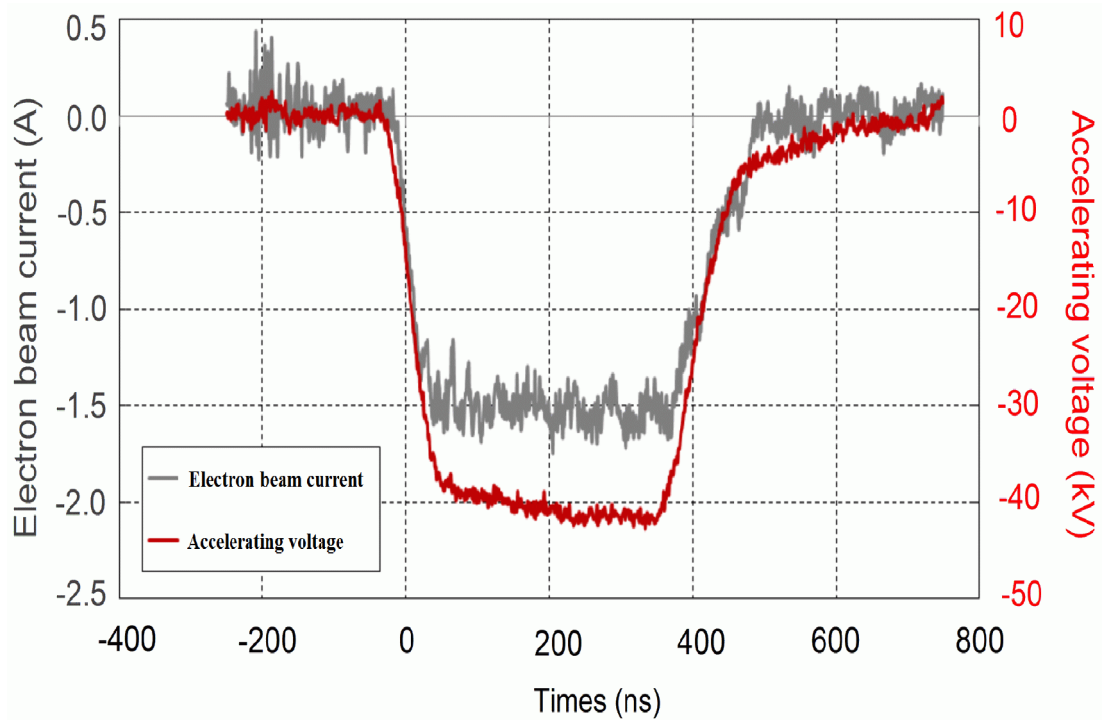


Fig. 7. 23 The typical traces of the measured beam voltage and beam current.

7.4 Experimental results of the microwave signal

The W-band gyro-BWO was tested in pulse mode of operation in the experiment, although it was designed with the capability of working continuously. There is no physics differences between the two modes, while operating in pulsed mode will greatly reduce the requirement of the power supply. The power supply for accelerating the electron beam was a 40 kV pulse with a width of ~ 370 ns seconds produced by a stacked double Blumlein line pulser. In the experiment, the microwave radiation was extracted out by a narrow band sapphire window and the radiation was measured by a crystal detector whose setup is shown in Fig. 7.24.

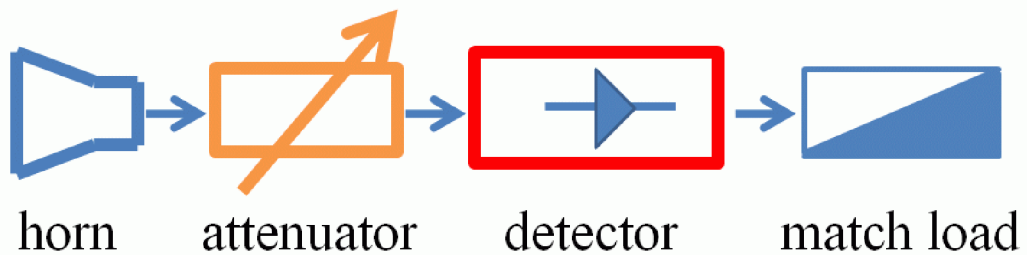
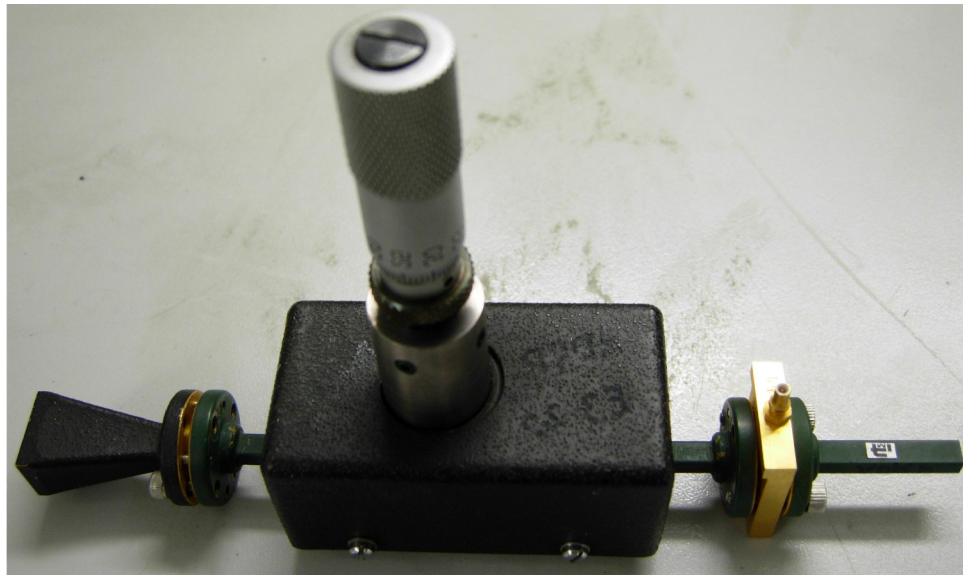


Fig. 7. 24 The setup of the microwave detector.

The microwave detector consists of a rectangular horn to collect the generated microwave signal, an attenuator to reduce the strength of the signal, a crystal detector to convert the microwave signal into a voltage signal. In the experiment, the microwave signal was observed when the cavity solenoid was driven by a current in the range of 230 - 245 A, which corresponds to the cavity magnetic field from 1.79 - 1.91 T. The frequency of the radiation can be approximately evaluated from the dispersion curve of the helically corrugated waveguide, which shows the frequency range of the radiation from 91 - 100 GHz. To verify the radiation frequency range, cut-off filters were connected after the microwave horn. For example, cut-off filters with diameters of 1.83 mm (with a cut-off frequency of 96.0 GHz) and 1.79 mm (with a cut-off frequency of 98.2 GHz) was used to verify the microwave signal with a predicted frequency of 96 GHz from the theory. The experimental frequency range

was found to be consistent with the theoretical prediction. A precise frequency measurement will be done using a microwave mixer.

Figure 7.25 shows the first measured microwave signal and the cathode voltage pulse. It was found that the microwave radiation was sensitive to the beam voltage. The microwave radiation appears at a beam voltage about -30 kV, and the power increased as the increment of the beam voltage was increased. The maximum power was observed at a beam voltage of about 35 kV. The microwave power was predicted to be about 370 W.

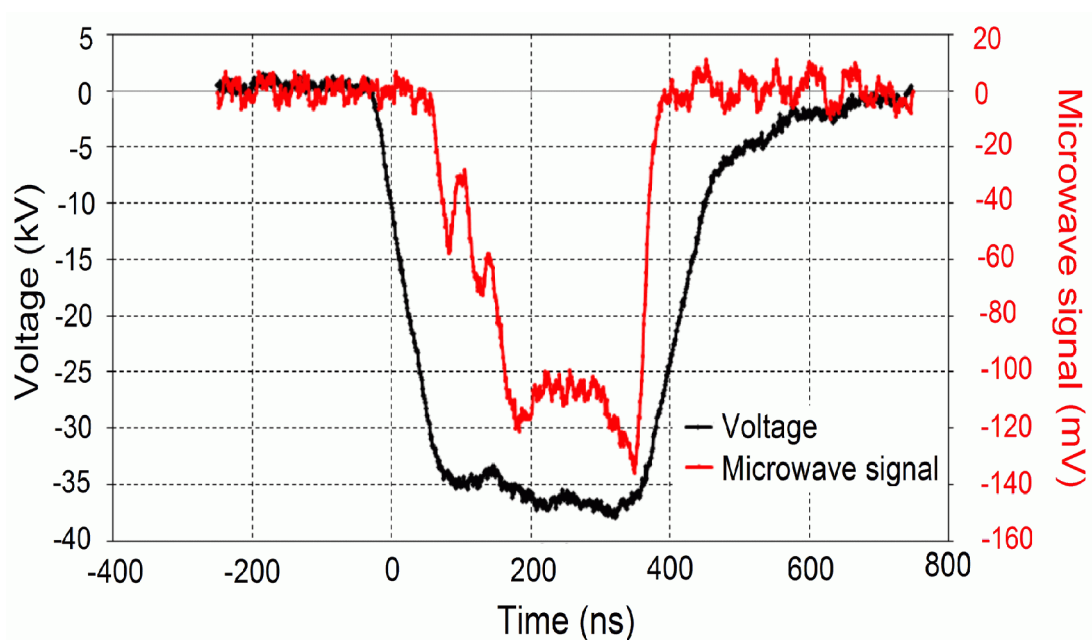


Fig. 7. 25 The measured voltage and microwave signal.

Further experiments that measure the precise microwave frequency and power will be carried out with a new updated designed three-layer output window and a W-band mixer.

The experiment of the depressed collector is based on the gyro-BWO experimental setup. Thus it can only be tested on pulse mode. However, as it was discussed before, the main purpose of the depressed collector is to reduce the heat dissipation and the power consumption, and these problems are only significant in CW operating. The

experiment of the depressed collector in pulse mode is not sufficient to exam all the performance but it will give results to prove the principle and the design. If there is no problem in the design, it will be no problem for the depressed collector to work in CW mode if the DC power supply for accelerating electron beam is available.

References

- [1] C. R. Donaldson, W. He, A. W. Cross, A. D. R. Phelps, F. Li, K. Ronald, C. W. Robertson, C. G. Whyte, A. R. Young, and L. Zhang, "Design and Numerical Optimization of a Cusp-Gun-Based Electron Beam for Millimeter-Wave Gyro-Devices", *IEEE Trans. Plasma Sci.*, vol. 37, no. 11, pp. 2153-2157, 2009.
- [2] C. R. Donaldson, W. He, A. W. Cross, F. Li, A. D. R. Phelps, L. Zhang, K. Ronald, C. W. Robertson, C. G. Whyte, and A. R. Young, "A cusp electron gun for millimeter wave gyrodevices", *Appl. Phys. Lett.* 96, 141501, 2010.
- [3] http://www.testequipmentconnection.com/specs/Anritsu_ME7808B.PDF.
- [4] I. C. Somerville, S. J. MacGregor and O. Farish, "An efficient stacked-Blumlein HV pulse generator", *Meas. Sci. Technol.*, vol. 1. no. 9, pp. 865-868, 1990.
- [5] H. Tang, V. Scuka, "The breakdown mechanism of a mid-plane triggered spark gap trigatron", *IEEE Trans. Dielectr. Electr. Insul.*, vol. 3, no. 6, pp. 843-848, 1996.
- [6] Thomas, Robert J., "High-Impulse Current and Voltage Measurement", *IEEE Instrum. Meas. Mag.*, vol. 19, pp. 102-117, 1970.
- [7] J. A. Jansen, G. J. Veenhof, C. D. Vries, "High Precision Electron Current Monitoring System", *Nuclear Instruments and Methods*, vol. 74, no. 1, pp. 20-26, 1969.
- [8] [http://en.wikipedia.org/wiki/Shunt_\(electrical\)](http://en.wikipedia.org/wiki/Shunt_(electrical)).
- [9] [17] J.D. Ramboz, "Machinable Rogowski coil, design, and calibration", *IEEE Instrum. Meas. Mag.*, vol. 45, pp. 511-515, 1996.

Chapter 8

Conclusions and future work

8.1 Introduction

The work represented in this thesis describes the analytic study, numerical simulation, optimization, and experimental measurement of the various components in the energy recovery system for the W-band gyro-BWO which is currently been built at the University of Strathclyde. These components include the Bragg reflector, and input/output side-wall coupler in chapter 3, the pillbox type and the multi-layer type microwave windows discussed in chapter 4, the four-stage depressed collector which takes into account secondary electrons described in chapter 6. The experimental setup and results are presented in chapter 7.

Chapter 8 will combine the results and conclusions from the previous chapters. This chapter also introduces the future work of the research on the energy recovery system for the W-band gyro-BWO.

8.2 Conclusions and future work

8.2.1 Conclusions

1 An optimization program based on the genetic algorithm package named MIT GALib was developed to optimize the microwave components as well as the geometry of the multi-stage depressed collector by using the CST microwave studio, the Mician μ Wave wizard as well as MAGIC. The other genetic algorithm packet Direct Search Toolbox in MATLAB was used to optimize the

Bragg reflector and the microwave window which were simulated by the mode-matching method implemented by MATLAB programming language.

2 A side-wall circular-to-rectangular coupler was designed and optimized to achieve a high transmission coefficient over the frequency range of 84 - 104 GHz. In the design, a Bragg reflector was used to replace the cut-off waveguide section for transportation of the electron beam to the interaction region without reducing the radius of the beam tunnel while avoiding the electromagnetic wave from propagating to the cathode region. The designed side-wall coupler achieved -1.0 dB transmission coefficient with a bandwidth of 19.5 GHz in the simulation. The measurement result of the Bragg reflectors agree well with the simulation results, and the input coupler achieves an average -13 dB reflection over the designed frequency band.

3 A pillbox window and a three-layer window were designed, fabricated and measured. The pillbox window was able to achieve an average -10 dB reflection in the operating frequency range and the three-layer window was able to achieve an average -15 dB reflection in the operating frequency range.

4 A four-stage depressed collector was designed to recover the energy from the spent electron beam. In 3D PIC code MAGIC, 99% microwave power was reflected back upstream by a 17-section Bragg reflector and 82.5% collection efficiency was achieved by the depressed collector when the magnetic field was 1.75T without considering the secondary electrons. Secondary electron emissions were also simulated and a few emission models were compared to investigate their effects on the overall recovery efficiency and the backstreaming rate for the multistage collector. The optimization of the shape and dimensions of each stage of the collector using a genetic algorithm achieved an overall recovery efficiency of about 70%, with a minimized backstreaming rate of 4.9%. The heat distribution on the collector was calculated and the maximum heat density on the electrodes was $240\text{W}/\text{cm}^2$ hence the parameter space was discovered which could avoid the generation of “hot spots”.

The electric field distribution inside the depressed collector was calculated using CST EM studio to avoid the voltage breakdown in the vacuum.

8.2.2 Future work

The research of the energy recovery system in this thesis does not contain every aspect and there is much future work that would provide interesting research opportunities.

1 The experimental measurements of the collected currents on the electrodes have not been finished due to the poisoning of the cathode. A new cathode needs to be installed and the electron beam measurement carried out, and then measurement of the microwave power and frequency to get the electronic efficiency. Finally the collected currents can be measured to get the collection efficiency and the overall efficiency.

2 The depressed collector itself still has the potential to be improved. The previous design has the disadvantage of weighing, about 20 kg which is still within the limit of being able to be lifted by one person nevertheless it would be possible to reduce the weight of future depressed collectors. A 20 kg depressed collector required additional precautions in the machining and assembly process. A better configuration could be employed, such as using thin electrodes, a smaller and thinner cavity to reduce the weight of the outside shell.

3 The gyro-BWO currently can only operate on pulse mode due to the limitation of the power supply. The depressed collector also has such limitation. To explore the full function of the depressed collector, an alternative power supply system that works either on CW mode or on a pulsed mode with a high duty factor is necessary. Further more, the power supply should be controllable within a fast switching time. The traditional switches, such as Thyatron, spark-gap switches are not sufficient due to either slow switching time or low repetition rate. A better option is to use solid

state switches, such as the insulated gate bipolar transistors (IGBT) [1], the metal oxide semiconductor field effect transistors (MOSFETs) [2, 3], and the photoconductive semiconductor switches (PCSSes) [4]. However, IGBTs can only achieve a rise time of tens of nanosecond. A single MOSFET is limited by the maximum voltage that it can hold, which is about 1500 V. That means more than 30 MOSFETs are required to operate in series. This would affect the jitter of the switching time. For PCSS, although the electric circuit is relative simple, a laser is required to turn it on therefore the whole system would be very expensive.

4 Another ongoing project on the same experimental platform is the W-band gyro-TWA. From the design, it is predicted to have a gain of 40 dB, with output power of 5 kW. A depressed collector for the gyro-TWA is also required when the gyro-TWA is operating in CW or high duty pulsed mode to improve the overall efficiency as well as reduce the heat dissipation. When inserting a depressed collector into the gyro-TWA system, it will be unavoidable to have some discontinuous in the geometry, such as the gap between the electrodes. These will cause some reflection. As the gyro-TWA is designed to have a gain of 40 dB, which also means the reflection caused by the depressed collector needs to be less than -30 dB if a -10 dB reflection from upstream input coupler is assumed. That is unrealistic in current experimental setup. An alterative method that may be used is based on Gaussian beam technology. A mode convertor [5] that converts the radiation mode from the gyro-TWA to a quasi-optical beam can be used before the depressed collector. The Gaussian beam has the advantage that it is not affected by the geometry if the waveguide is larger enough. Relevant research on the Gaussians beam mode converter has also been carried out in our group [6, 7].

References

- [1] R.L. Cassel, "A Hybrid Solid State Marx Magnetron modulator", IEEE Pulsed Power Conference (PPC '09), pp. 817 - 819, 2009.
- [2] P. A. Arnold, F. Barbosa, E. G. Cook, B. C. Hickman, G. L. Akana, C. A. Brooksby, "A high current, high voltage solid-state pulse generator for the NIF Plasma Electrode Pockels Cell", 16th IEEE International Pulsed Power Conference, pp. 1468 - 1472, 2007.
- [3] Liang Zhang, Ling Qin, Ziping Huang, Linwen Zhang, Chengjun Liu, Jin Li, "Experimental research on MHz repetition rate solid-state modulator", High Power Laser and Particle Beams, vol. 21, no. 8, 2009.
- [4] J. S. Sullivan and J. R. Stanley, "6H-SiC Photoconductive Switches Triggered at Below Bandgap Wavelengths", IEEE Trans. Dielectrics and Electrical Insulation, vol. 14, no. 4, pp. 980 - 985, 2007.
- [5] J. Teniente, "Modern Corrugated Horn Antennas", Ph.D. dissertation under direction of C. del Río. Public University of Navarra, Pamplona, Spain, 2003.
- [6] P. McElhinney, W. He, C. R. Donaldson, A. D. R. Phelps, L. Zhang, A. W. Cross, C. Robertson, C. Whyte and K. Ronald, "Simulation of a non-linear corrugated horn as a quasi-optical converter", Proc. National Vacuum Electronics Conference (NVEC), 2010.
- [7] Paul McElhinney, Craig R. Donaldson, Wenlong He, Liang Zhang, Kevin Ronald, Alan D.R. Phelps, and Adrian W. Cross, "A High Directivity Broadband Corrugated Horn for W-band Gyro-devices", to be submitted.

Appendix I Multi-mode Coupling Wave Theory

The equation of the helical profile of the inner surface in a cylindrical coordinate system (r, θ, z) can be written as

$$r(\theta, z) = R_0 + R_1 \cos(m_B \theta + 2\pi z / d) \quad (1)$$

where R_0 is the mean radius of the circular waveguide, R_1 is the corrugation depth, m_B is the fold number, and d is the axial period of the corrugation. When the corrugation depth is not zero, two modes will couple when their axial and azimuthal wave numbers satisfy the synchronism conditions

$$h_1 - h_2 = 2\pi / d, \quad m_1 - m_2 = m_B \quad (2)$$

where h_1 and h_2 are the axial wavenumbers of modes 1 and 2, and m_1 and m_2 are the azimuthal indices of modes 1 and 2, respectively.

In three-fold helically corrugated waveguide, the TE_{21} mode would couple with the TE_{11} circularly polarized mode of opposite rotation and generate an operating eigenwave, as shown in Fig. 1. From the synchronism condition, coupling between higher modes requires larger fold number m_B . However, with larger m_B more modes would satisfy the synchronism condition and they would couple with each other and hence contribute to the dispersion characteristic.

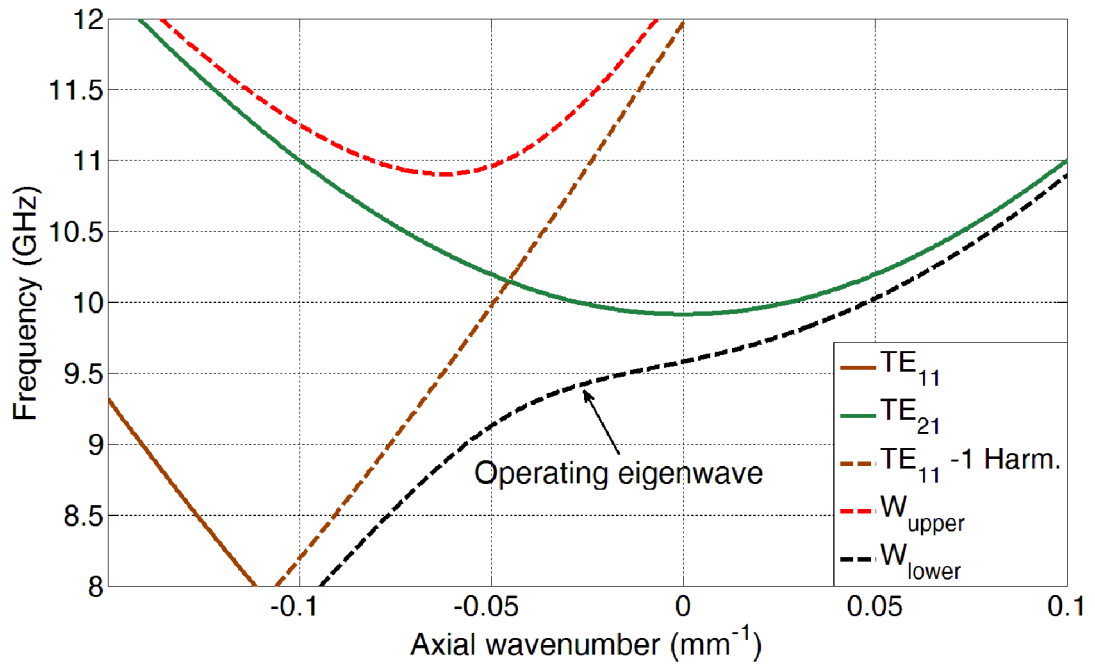


Fig. 1 The coupling between the TE₂₁ mode and the spatial harmonic TE₁₁ mode in a three-fold helical waveguide.

A. The Coupling Coefficients

The coupling coefficient is the basis of the coupled wave theory as it indicates how strong the coupling between two modes is. In this paper, we start from the general equations of the coupling coefficients between two TE modes, two TM modes and one TE (mode m) to one TM (mode j) modes as shown in (3). The derivation of these equations can be found in [1], which contains a detailed introduction to the coupled mode theory.

$$\begin{aligned}
 S_{jm} &= \frac{1}{2h_j(h_j - h_m)} \oint \nu(s) [\alpha_j^2 \alpha_m^2 \Psi^j \Psi^m + (h_j h_m - k^2) \frac{\partial \Psi^j}{\partial s} \frac{\partial \Psi^m}{\partial s}] ds \\
 S_{jm} &= \frac{k^2 - h_j h_m}{2h_j(h_j - h_m)} \oint \nu(s) \frac{\partial \phi^j}{\partial n} \frac{\partial \phi^m}{\partial n} ds \\
 S_{jm} &= -\frac{k}{2h_j} \oint \nu(s) \frac{\partial \phi^j}{\partial n} \frac{\partial \Psi^m}{\partial s} ds
 \end{aligned} \tag{3}$$

where $v(s)$ is the function to describe the difference between the perturbed non-uniform waveguide and the uniform waveguide. When $v(s)=0$, there is no coupling between the two modes. h_j, h_m are the axial wave numbers of the coupled modes and k is the free-space wave number. α_j, α_m are the transverse wave numbers of modes j and m . Ψ, φ are the transverse eigenfunctions of the TE and TM modes of the unperturbed regular waveguide. n is the normal vector directed towards the waveguide wall. s is chosen so that the axes n, s, z form a right-handed co-ordinate system.

In circular waveguide, the transverse wave number and eigenfunction in a cylindrical coordinate system are in the form of

$$\alpha_{nq} = \begin{cases} \xi_{nq} / R_0, & \text{(for TE mode)} \\ \varsigma_{nq} / R_0, & \text{(for TM mode)} \end{cases} \quad (4)$$

$$\begin{aligned} \Psi_{nq}(r, \theta) &= \sqrt{\frac{2}{\pi \epsilon_n}} \frac{1}{\sqrt{\xi_{nq}^2 - n^2} |J_n(\xi_{nq})|} J_n(\alpha_{nq} r) \begin{cases} \cos(n\theta) \\ \sin(n\theta) \end{cases} \\ \varphi_{nq}(r, \theta) &= \sqrt{\frac{2}{\pi \epsilon_n}} \frac{1}{\varsigma_{nq} |J'_n(\varsigma_{nq})|} J_n(\alpha_{nq} r) \begin{cases} \cos(n\theta) \\ \sin(n\theta) \end{cases} \\ \epsilon_n &= \begin{cases} 2, & (n = 1) \\ 1, & (n \neq 1) \end{cases} \end{aligned} \quad (5)$$

where ξ_{nq} is the q th zero of the derivation of J_n and J is the first kind of Bessel function. ς_{nq} is the q th root of J_n . In practical applications, the operating mode in the helically corrugated waveguide always satisfies $n \neq 0$. As the radial number q in the modes does not contribute to the following derivation, symbols j and m are used to denote the azimuthal number of the two coupling modes for simplicity.

The difference between the helically corrugated cross section and the circular waveguide at position $z = 0$ can be written as $v(s) = m_B R_1 \sin(m_B \theta)$. For a small

corrugation, we have $v(s) \ll R_0$. As $v(s)$ is in terms of the first-order derivation of the mean radius, if only the first-order approximation of the coupling coefficient is taken into account then only the zero-order approximation of the other terms in (3) needs to be considered. In polar coordinates, we can simply make $ds = rd\theta$ and $dn = dr$. Substituting these into (3), we can get a simpler form of the coupling coefficients, as

$$\begin{aligned}
S_{jm} &= \frac{R_1[\xi_m^2 \xi_j^2 + (h_j h_m + k^2) jm R_0^2]}{h_j (h_j - h_m) R_0^3 \sqrt{\xi_m^2 - m^2} \sqrt{\xi_j^2 - j^2}} \oint \frac{m_B}{\pi} \sin(m_B \theta) \begin{Bmatrix} \cos(m\theta) \\ \sin(m\theta) \end{Bmatrix} \begin{Bmatrix} \cos(j\theta) \\ \sin(j\theta) \end{Bmatrix} d\theta \\
S_{jm} &= \frac{R_1(k^2 - h_j h_m)}{R_0 h_j (h_j - h_m)} \oint \frac{m_B}{\pi} \sin(m_B \theta) \begin{Bmatrix} \cos(m\theta) \\ \sin(m\theta) \end{Bmatrix} \begin{Bmatrix} \cos(j\theta) \\ \sin(j\theta) \end{Bmatrix} d\theta \\
S_{jm} &= -\frac{R_1 km}{R_0 h_j \sqrt{\xi_m^2 - m^2}} \oint \frac{m_B}{\pi} \sin(m_B \theta) \begin{Bmatrix} \cos(m\theta) \\ \sin(m\theta) \end{Bmatrix} \begin{Bmatrix} \cos(j\theta) \\ \sin(j\theta) \end{Bmatrix} d\theta
\end{aligned} \tag{6}$$

In the helically corrugated waveguide, only the modes that satisfy the synchronism conditions can couple with each other. Thus we have $j-m=m_B$. It should be noted that, in the practical application, m is always chosen as a negative value indicating an opposite rotating mode and hence h_m also is a negative value. The integral in this equation will become unity if we apply the synchronism condition. Then the final coupling coefficients for the helically corrugated waveguide become

$$\begin{aligned}
S_{jm} &= \frac{R_1[\xi_m^2 \xi_j^2 + (h_j h_m + k^2) jm R_0^2]}{h_j (h_j - h_m) R_0^3 \sqrt{\xi_m^2 - m^2} \sqrt{\xi_j^2 - j^2}} \\
S_{jm} &= \frac{R_1(k^2 - h_j h_m)}{R_0 h_j (h_j - h_m)} \\
S_{jm} &= -\frac{R_1 km}{R_0 h_j \sqrt{\xi_m^2 - m^2}}
\end{aligned} \tag{7}$$

Eq. (7) has the same form as the ones in [2], while the coupling coefficient in [2] has been normalized to $h_j h_m$.

B. The Coupled Mode Equations

Although the coupling coefficient indicates the strength of the coupling between two modes, it is useful to know the strength of the coupling modes in the resultant eigenwave. They can be solved from the coupled mode equations [1] and the coupling coefficient, as

$$\begin{cases} \frac{dV_m}{dz} = -\frac{h_j}{h_m} S_{jm} \exp(-i(\sigma_j - \sigma_m)) V_j \\ \frac{dV_j}{dz} = S_{jm} \exp(i(\sigma_j - \sigma_m)) V_m \end{cases} \quad (8)$$

where V_m, V_j are the normalized voltages of mode m and j in the helically corrugated waveguide, respectively, and $\sigma_{j/m} = \int_0^z h_{j/m} dz$ is the phase of mode j or m in the waveguide, and $\sigma = \sigma_j - \sigma_m = (h_j - h_m)d$ is the phase difference between the two coupled modes in the waveguide with the length of one period d . σ becomes 2π if the synchronism conditions are applied.

The normalized voltages of mode m and j in the helically corrugated waveguide can be solved as

$$\begin{cases} V_m = -\left(\cos \kappa + \frac{i\pi}{\kappa} \sin \kappa\right) \\ V_j = \frac{\sqrt{\kappa^2 - \pi^2}}{\kappa} \sin \kappa \end{cases} \quad (9)$$

where $\kappa = 2\pi \sqrt{|h_j/h_m| S_{jm}^2 + 1/4}$.

They are completely determined by κ which is dependent on the axial wavenumbers of the coupling modes and the coupling coefficient.

C. The Dispersion Curve Function

The new dispersion curve caused by two-mode coupling will satisfy the following equation

$$f_j^2(h) \cdot f_m^2(h) = h_j^2 h_m^2 S_{jm}^2 \quad (10)$$

where f_j, f_m are the dispersion relations of the coupling modes which are functions of the axial wavenumber h . For a TE/TM mode in the circular waveguide, the dispersion relation can be written as

$$f_j^2(h) = k^2 - \alpha_j^2 - h^2 \quad (11)$$

Because mode m is the negative spatial harmonic wave, the dispersion curve is shifted to the left by $2\pi/d$ to produce the following dispersion relation

$$f_m^2(h) = k^2 - \alpha_m^2 - (h - 2\pi / d)^2 \quad (12)$$

Eq. (10) is a 4th order linear equation. Given a wave number k , we can get four eigenvalues by solving the equation. However, only two of them have practical physical meaning, and they are named as the upper coupled mode W_{upper} and the lower coupled mode W_{lower} . If there is no coupling between the two modes, that is $S_{jm}=0$, the eigenfunction will degenerate into two separate dispersion curve functions, i.e. $f_j^2(h) = 0$, and $f_m^2(h) = 0$. The W_{upper} and W_{lower} will degenerate into the previous uncoupled partial eigenwaves.

There is no straightforward dispersion curve equation available that can take into account all of the considered modes. However, from the dispersion diagram, it is clear that the coupling frequencies between any two modes, as shown in Fig. 2 which shows the five-fold helical waveguide case, are different. Thus an alternative method is to calculate the coupled eigenwaves in sequence by using the two-mode coupling equation, either from the lower frequency to the higher frequency, or vice versa.

Here the sequence from higher to lower frequencies is used. Firstly, two eigenwaves W_{upper1} and W_{lower1} can be resolved from (10), (11) and (12). Then eigenwave W_{upper1} does not have an intersection with the next mode, thus it is saved as an eigenwave (W_1 in Fig. 2). Eigenwave W_{lower1} couples with the next mode to generate W_{upper2} (W_2 in Fig. 2) and W_{lower2} by using (10), while here $fm(h)$ refers to the eigencurve W_{lower1} and h_j, h_m are the axial wavenumbers in the intersection of mode W_{lower1} and the next coupled mode. By repeating this process, all the eigenwaves caused by the mode coupling in the helically corrugated waveguide can be obtained.

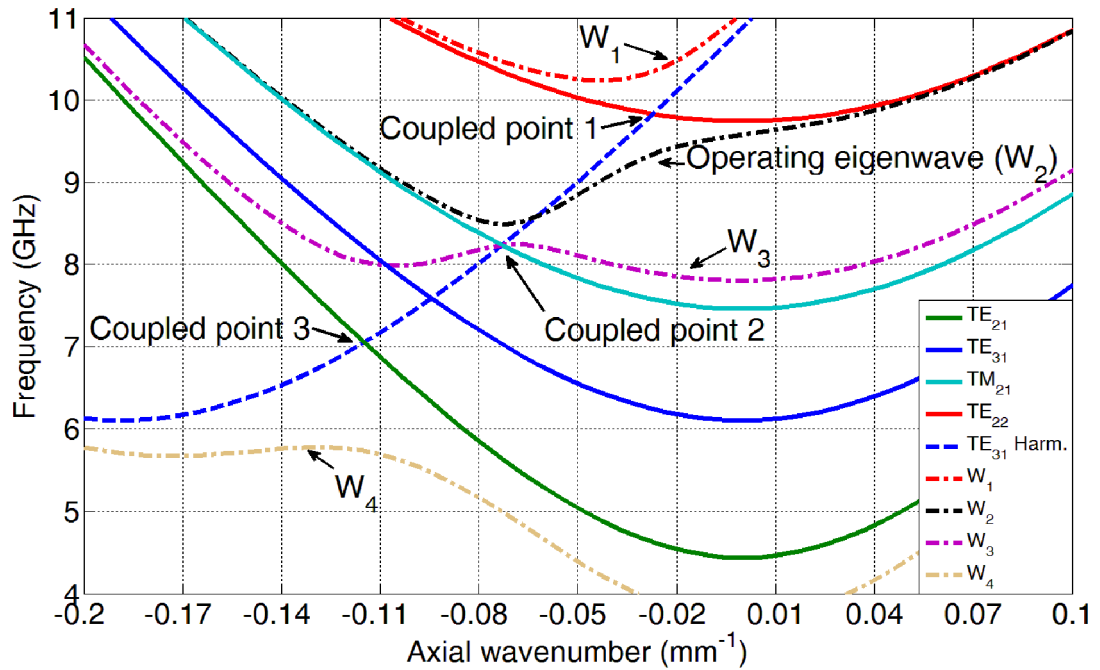


Fig. 2 The coupling modes in a five-fold helical waveguide.

D. Comparison between the calculation and the experiment

The five-fold helically corrugated waveguide was measured with dimensions of $R_0=32.84$ mm, $R_I=2.43$ mm and $d=33.26$ mm. The dispersion curve was also measured using a 65 GHz vector network analyzer (VNA) (Anritsu 37397A). The experimental setup is shown in Fig. 3. From left to right, a rectangular to circular mode converter (\odot in Fig. 3) was first used to convert the fundamental TE₁₀ mode

in rectangular waveguide to a linearly polarized TE_{11} mode in the circular waveguide. This is followed by an elliptical polarizer (② in Fig. 3) that converts the linearly polarized TE_{11} mode into a left hand rotating TE_{11} wave. A four-fold helical mode converter (③ in Fig. 3) was then used to convert the circularly polarized TE_{11} mode into a circularly polarized TE_{31} mode. The mode converter was designed to have a $>90\%$ conversion efficiency in the frequency range of 8.75 ~ 10.0 GHz. Finally a five-fold helical taper (④ in Fig. 3) was used before introducing the TE_{31} mode into the five-fold helically corrugated waveguide (⑤ in Fig. 3) to make sure the TE_{31} mode smoothly converted to the operating eigenwave without reflection. On the other side of the helical waveguide, the same configuration was used.

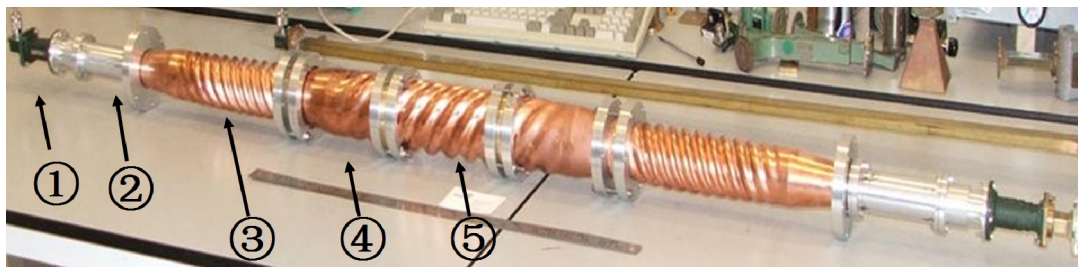


Fig. 3 Experimental setup for measuring the dispersion curve of the five-fold helical waveguide.

Fig. 4 shows the dispersion curves calculated from the coupled mode theory, simulated from the eigensolver in CST Microwave Studio as well as measured by the VNA. From the coupled mode calculation, there are four eigenwaves resulting from the mode coupling between the TE_{31} and the TE_{21} , the TM_{21} , and the TE_{22} modes. Eigenwave 2 is the operating eigenwave for compression of the microwave pulse. The dispersion curves from coupled mode theory, simulation using CST Microwave Studio and measurement using a VNA agree well with each other in the frequency range 8.75 ~ 10.0 GHz, as shown in Fig. 4.

However the measured dispersion at the lower frequency band (7.6 ~ 8.75 GHz) underwent a change of trend. This is due to the fact that the frequency is out of the

operating band of the TE_{11} -to- TE_{31} mode convertor. The dominant power in the helically corrugated waveguide is still in the TE_{11} mode in this lower frequency band. If the measured result in this frequency range is shifted by a factor of $2\pi N/L$, where N is an integer, and L is the length of the helically corrugated waveguide in the measurement, it agrees well with the dispersion curve of the TE_{11} mode, as shown in Fig. 4. At a frequency of 8.6 ~ 8.8 GHz a small content of the TE_{31} mode exists in the helical waveguide in conjunction with the TE_{11} mode, this causes the measured dispersion result in this frequency range to be spiky as it is the mixed phase information of the two modes.

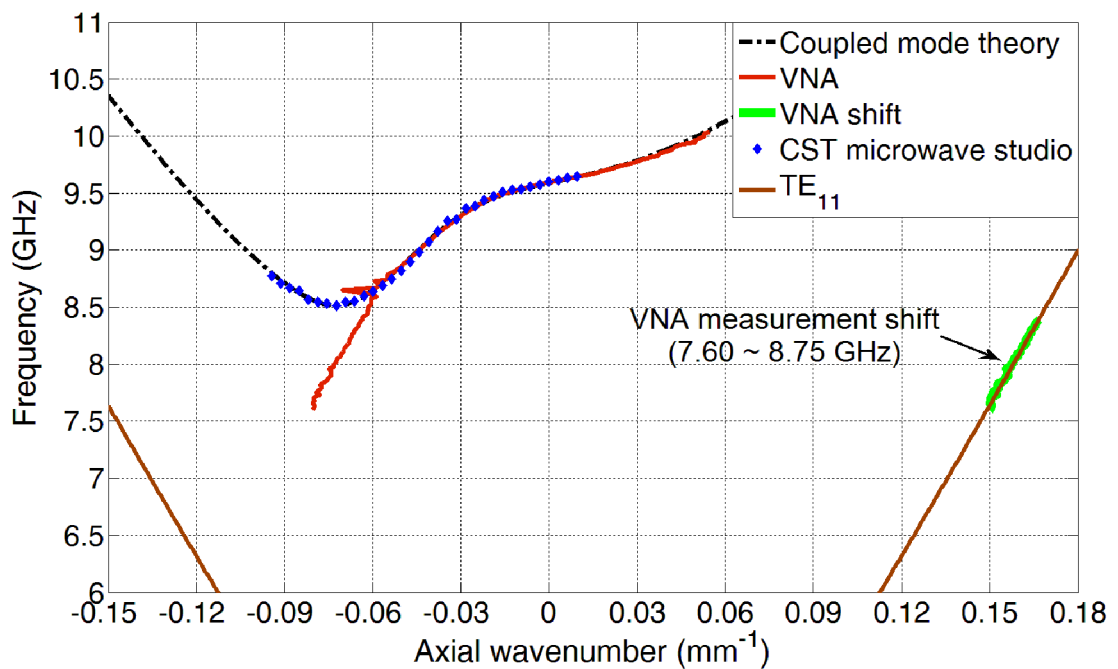


Fig. 4 The dispersion curve from coupled mode theory, CST Microwave Studio simulation and the VNA measurement.

Reference

- [1] B. Z. Katsenelenbaum, L. Mercader Del Río, M. Pereyaslavets, M. Sorolla Ayza, and M. K. A. Thumm, “Theory of Non-uniform Waveguides: the Cross-Section Method”, (The IET, London, U.K., 1999).

[2] G. G. Denisov and M. G. Reznikov, "Corrugated Cylindrical Resonators for Short-wavelength Relativistic Microwave Oscillators," *Radiophysics and Quantum Electronics*, vol. 25, no. 5, pp. 407-413, 1982

Appendix II The Optimization Program

The optimization program contains a GUI (graphic user interface) that makes it easily to be used, as shown in Fig. A1.1. The users can choose and set the optimizers and the simulators in the dialog, pause/continue or stop the optimization process, and change the thread number during the optimization.

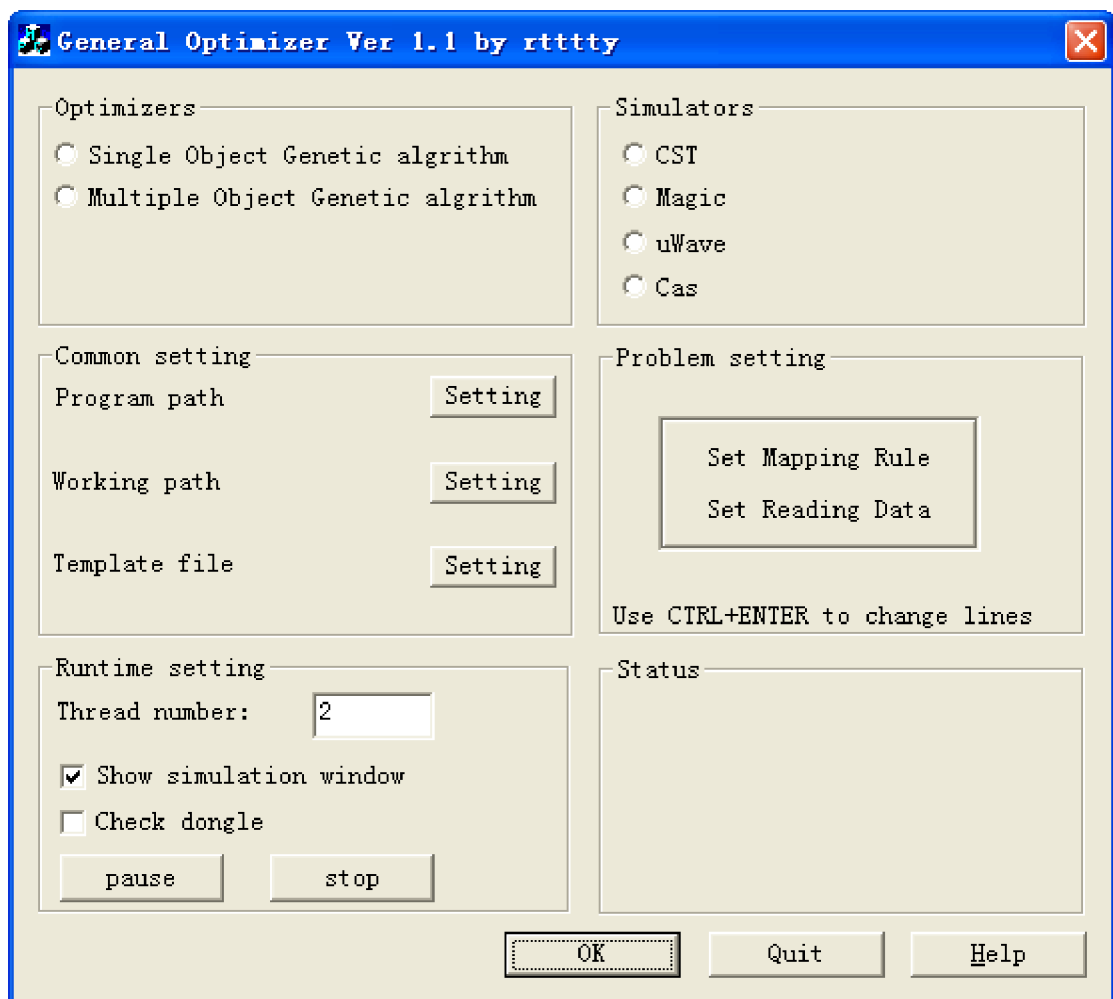


Fig. A1.1 The GUI of the optimization program

The architecture of the optimization program is well defined, as shown in Fig. A1.2, to produce a general solution of the optimization routing, and also make the program with good extensibility for more optimizers and simulators.

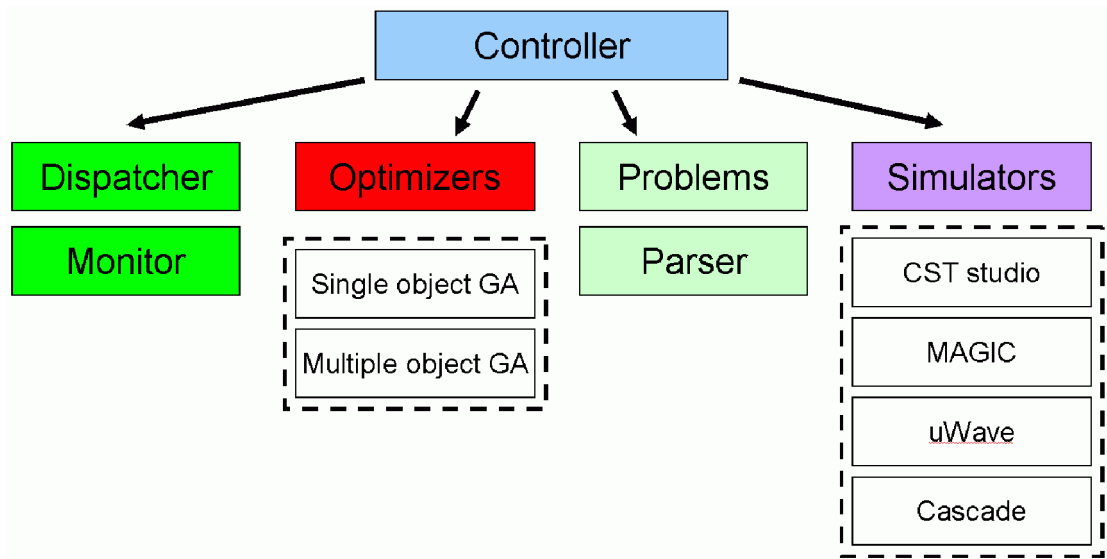


Fig. A1.2 The architecture of the program

The main object is the controller, it uses objects including:

- (1) The dispatcher which is used to assign tasks for the threads.
- (2) The monitor which is used to monitor the status of the simulations.
- (3) The optimizers which contains all the optimization algorithms. Currently only single object and multiple object genetic algorithms are implemented, and particle swan optimization is under tested.

The setting for the single object genetic algorithm is shown in Fig. A1.3. In this dialog, one can set the parameters for the optimization, such as the parameter number, the population size, the generation size, the crossover and mutation possibilities and so on. And also, one can give different genome length for each parameter to reduce the searching space.

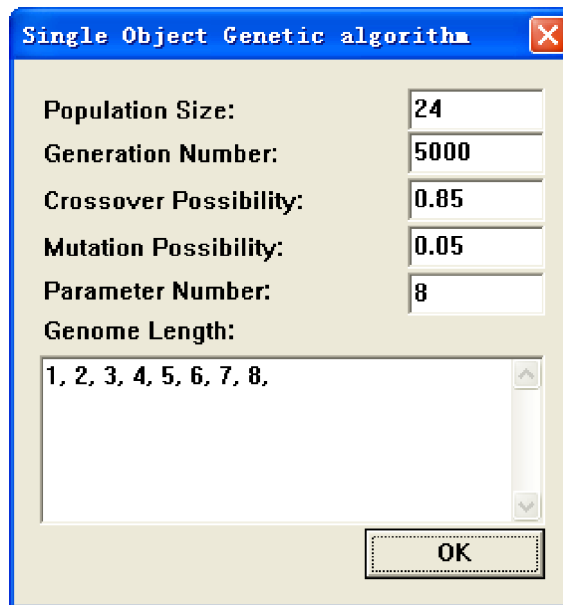


Fig. A1.3 The setting for single object genetic algorithm

The setting of the multiple object genetic algorithm is similar to the single object one. The difference is the user need to set the object number for the problem to be solved, as shown in Fig. A1.4.

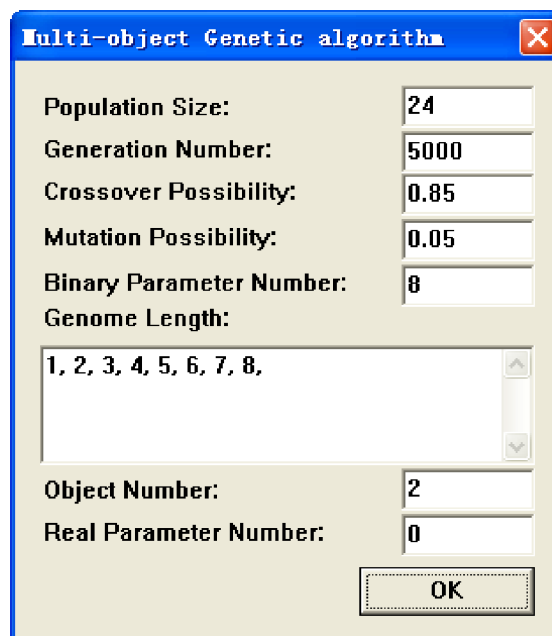
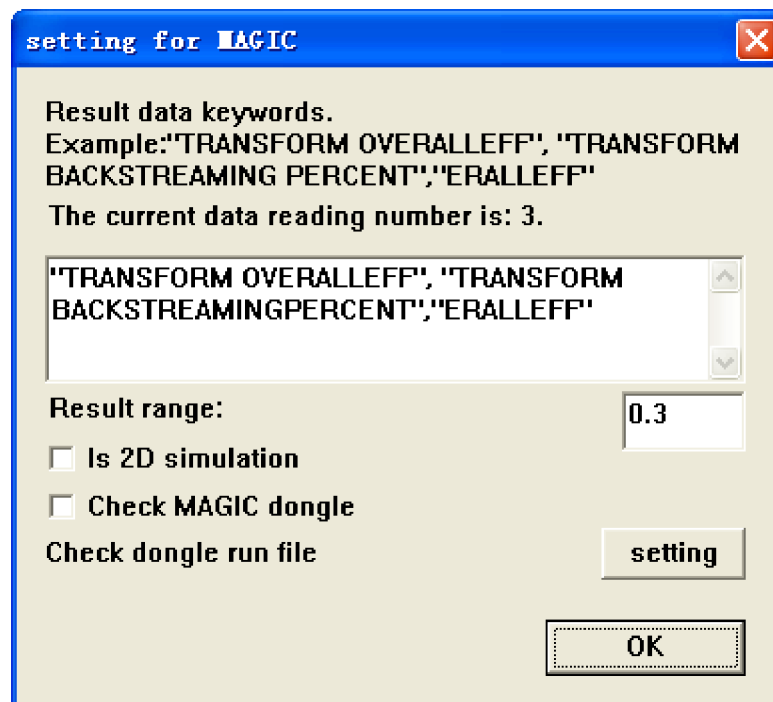


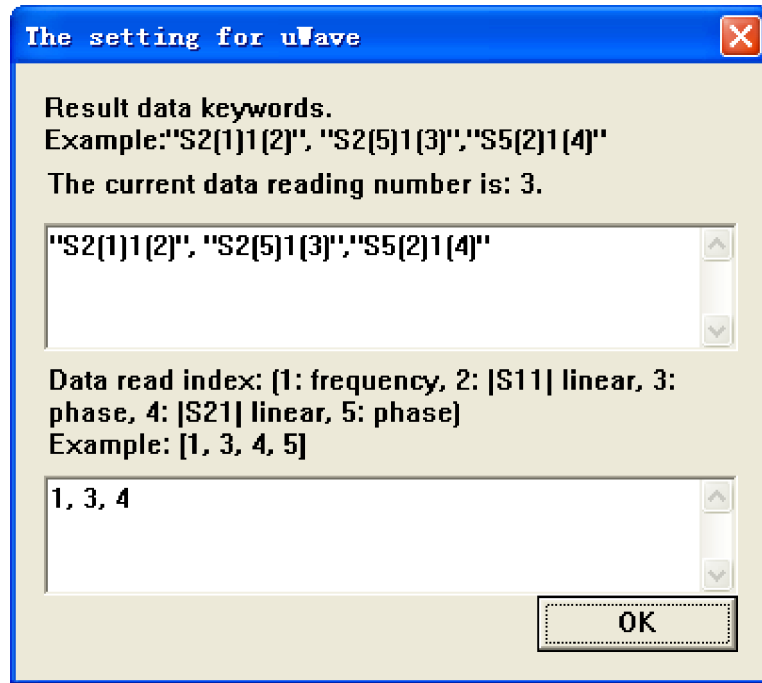
Fig. A1.4 The setting for multiple object genetic algorithm

(4) The simulators which is used to run the simulation of the problem to be solved and read the results from the result files. Currently, simulation programs such as CST microwave studio, the 3D PIC code MAGIC, and the Mician uWave are supported. It should be noticed that, besides MAGIC, the other programs all contain their own optimizers. However, the optimizer for CST microwave studio does not work perfectly because once it occurs some problem in an iteration then the whole optimization routing will stop and waste all the previous simulations. The developed optimizer can continue the optimization process even if there are errors when evaluating some bad individuals. The GUI of the uWave is not full functional for optimization. It is not allowed to optimize an arbitrary geometry. While in the early stage of the research, a full investigation on the parameter space is desired to get a full understand of the problem. The developed program can freely define the problem and create the simulation file more powerful than the GUI provided by uWave.

Fig. A1.5 shows the specifically setting for different simulation programs. There is no specific setting for CST microwave studio.



(a) the setting for MAGIC



(b) the setting for uWave

Fig. A1.5 The specific setting for MAGIC and uWave

The problem definition is the most important part of the program. A flexible mapping rule that maps the initial parameter range [0 1] to an arbitrary users' parameter space is developed. The mapping rule supports complicated equations between the new parameter space and the old parameter space. Besides the inbuilt functions like +, -, *, /, ^, *sin*, *cos*, *tan*, *ctan*, *asin*, *acos*, *log*, et, al, functions *max*, *min*, *sum*, *mean* are also provided to a vector result to a scale result.

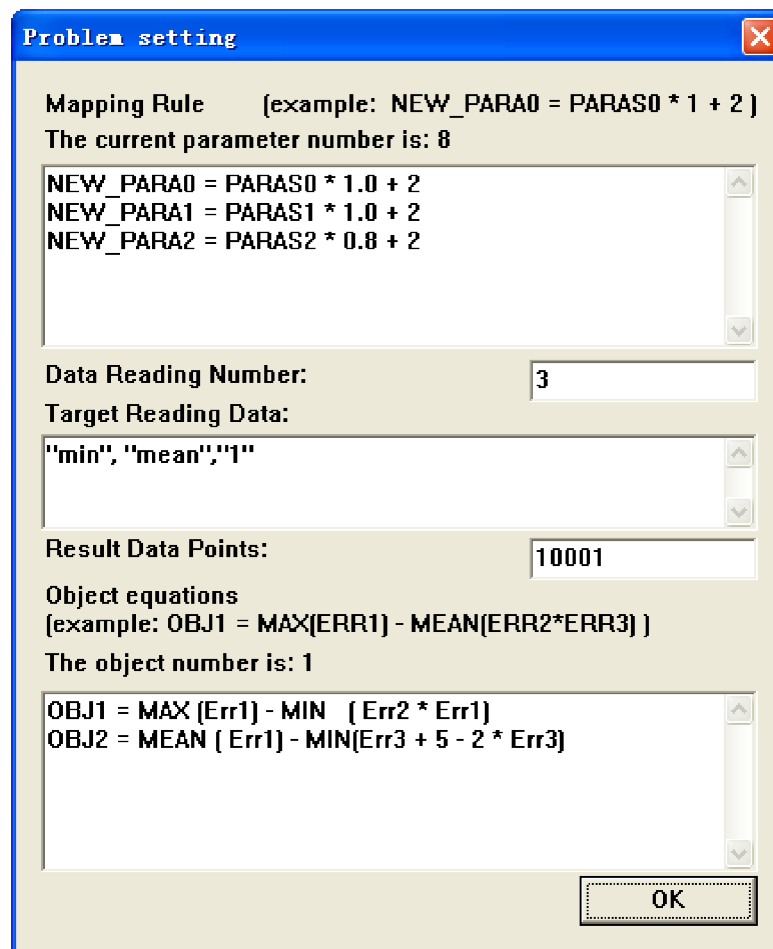


Fig. A1.6 The problem setting

Before the optimization routing, the program will generate a setting file for the problem to be solved. It records all the setting for the problem. The user can also write their own configure file without the need of the interface. In the following is a sample setting file for a problem.

To execute the simulations, one need to set the program that use to execute the simulation input file and the template file. Several keywords and wildcard matching are predefined when creating the simulation files from the template file, such as

```

"#ITERATION#"           // the iteration number that runs

"#RESULTFILENAME#"     // the path and name of the result file

"#PROJECTNAME#"       // the project's name

```

```

"#FILENAME#" // design name, sometimes used for CST, HFSS

"#DESIGNNAME#" // the design name, the same as project name

"#SUBPARAMUM#" // the number of parameters

"#BLOCKPARAMS#" // set block parameters in the format: PARAS0 = ...;

"#BLOCKPARAMSNOCOMMA#" // set block parameters in the format: PARAS0 = ..

"#BLOCKPARAMS_CST#" // set block parameters using vbs format:

    Const PARAS0 = ..

"#PARAS0", "#PARAS1" // the parameters

//here A, B are in double type, C, D are in string type, maybe will add more in the future.

"#IFGREATER(A,B,C,D)#" // means if A>B, then C else D, and C,D should not
                        contains any ","

"#IFLESS(A,B,C,D)#" //means if A<B, then C else D, and C,D should not
                     contains any ","

"#IFEQUAL(A,B,C,D)#" //means if A=B, then C else D, and C,D should not
                      contains any ","

```

Appendix III Non-uniform waveguide

The first study on the non-uniform waveguide with smooth variations on cross section along the axis was by Solymar in 1959. In this paper, the non-uniform waveguide was regarded as a system of coupled transmission lines, where the coupling coefficients were functions of the z axis. The field intensities in the non-uniform waveguide were represented by equivalent voltages and currents. And the differential equation for these voltages and currents was known as the generalized telegraphist's equation.

$$\begin{aligned} -\frac{dV_i}{dz} &= j\beta_i K_i I_i - \sum_p T_{pi} V_p \\ -\frac{dI_i}{dz} &= j\frac{\beta_i}{K_i} V_i - \sum_p T_{ip} V_p \end{aligned} \quad (\text{A.1})$$

where i and p denote arbitrary modes; V_i , and I_i are the equivalent voltage and current for mode i . β_i is the propagation coefficient, and K_i is the wave impedance. T_{ip} and T_{pi} represent the voltage and current transfer coefficients.

Introduce new variables A_i^+ and A_i^- which respectively represent the amplitudes of the forward travelling waves and backward travelling waves, and make the relations between them and the equivalent voltages and current to be

$$\begin{aligned} V_i &= K_i^{1/2} (A_i^+ + A_i^-) \\ I_i &= K_i^{-1/2} (A_i^+ - A_i^-) \end{aligned} \quad (\text{A.2})$$

The generalised telegraphist's equation rewritten as the functions of A_i^+ and A_i^- is

$$\begin{aligned}
\frac{dA_i^+}{dz} &= -j\beta_i A_i^+ - \frac{1}{2} \frac{d(\ln K_i)}{dz} A_i^- + \sum_p (S_{ip}^+ A_p^+ + S_{ip}^- A_p^-) \\
\frac{dA_i^-}{dz} &= j\beta_i A_i^- - \frac{1}{2} \frac{d(\ln K_i)}{dz} A_i^+ + \sum_p (S_{ip}^- A_p^+ + S_{ip}^+ A_p^-)
\end{aligned} \tag{A.3}$$

From Eq. A.3, the mode coupling has two sources. One is the reflection by the changing of impedance in the waveguide and the amplitude is indicated in the second term of the right-hand side of Eq. A.3. The other is the wall current in the waveguide and the coupling happens between any two modes.

S_{ip}^+ and S_{ip}^- are the forward and backward coupling coefficient arisen by the wall current, respectively. They are functions of transfer coefficients and the wave impedance.

$$S_{ip}^\pm = \frac{1}{2} \left[\frac{K_p^{1/2}}{K_i^{1/2}} T_{pi} \mp \frac{K_i^{1/2}}{K_p^{1/2}} T_{ip} \right] \tag{A.4}$$

S_{ip}^\pm can be expressed in terms of line integrals of the waveguide modes around the boundary of the waveguide. If the interaction is specialized to a single wave with forward and backward components, the subscripts i can be dropped, the sum over p vanishes and the coupling coefficient becomes

$$\begin{cases} S^- = -\frac{1}{2} \int_c \tan \theta \frac{\partial \psi}{\partial s} ds, & \text{for TE modes, and} \\ S^+ = 0 \end{cases} \tag{A.5}$$

$$\begin{cases} S^- = -\frac{1}{2} \int_c \tan \theta \frac{\partial \psi}{\partial n} ds, & \text{for TM modes.} \\ S^+ = 0 \end{cases} \tag{A.6}$$

where ψ is the wave function. The relationship between s , n and θ is shown in Fig. A.1.

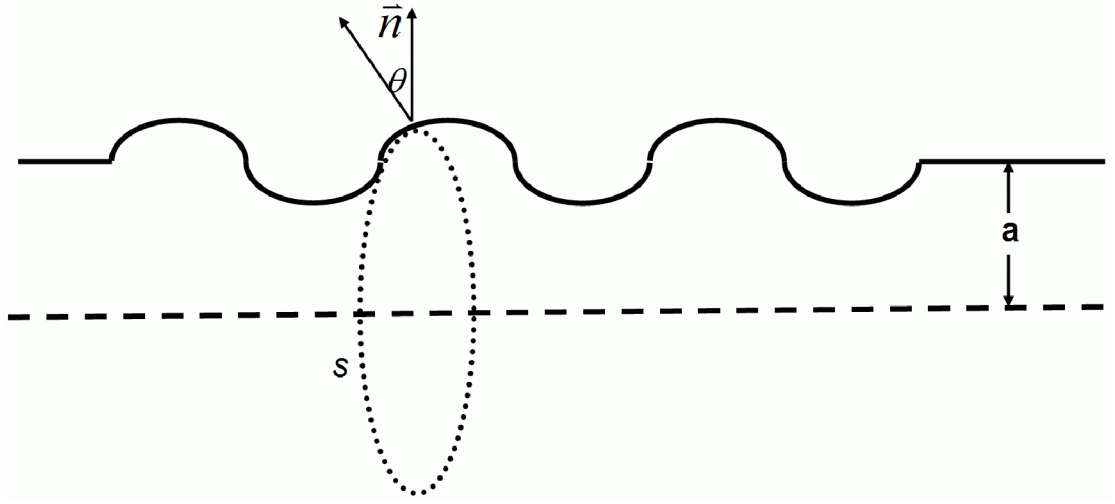


Fig. A.1 The relationship between s , n and θ

The wave function ψ for circular waveguide sections of radius a follows

$$\psi = \begin{cases} \frac{J_m\left(\frac{x'_{mn}r}{a}\right)e^{jm\phi}}{(\pi(x_{mn}^2 - m^2))^{1/2} J_m(x'_{mn})}, & \text{for TE modes.} \\ \frac{J_m\left(\frac{x_{mn}r}{a}\right)e^{jm\phi}}{\pi^{1/2} x_{mn} J'_m(x_{mn})}, & \text{for TM modes.} \end{cases} \quad (\text{A.7})$$

where J_m is the first kind of Bessel function and x_{mn} is the n^{th} zero of J_m . J'_m is the derivative of J_m and x'_{mn} is the n^{th} zero of J'_m . m, n are the azimuthal and radial mode indices, respectively. From Fig. A.1, we get the following equations

$$\begin{aligned} \frac{\partial \phi}{\partial n} &= \frac{\partial \phi}{\partial r} \\ \frac{\partial \phi}{\partial s} &= \frac{\partial \phi}{\partial(a\phi)} \end{aligned} \quad (\text{A.8})$$

Substituting Eq. A.7 and Eq. A.8 into Eq. A.5 and Eq. A.6, the coupling coefficients becomes

$$\begin{cases} S^- = \tan \theta \int_c \frac{(\frac{x'_{mn}}{a})^2 J_m^2(\frac{x'_{mn} r}{a})}{2\pi x_{mn}^2 J_m^2(x'_{mn})} ds & \text{for TE modes, and} \\ S^+ = 0 \end{cases} \quad (\text{A.9})$$

$$\begin{cases} S^- = -\frac{\tan \theta}{2\pi a^2} \int_c ds & \text{for TM modes.} \\ S^+ = 0 \end{cases} \quad (\text{A.10})$$

For the waveguide with axisymmetric variations in the wall radius, the line integral is independent of the angular variable and the value is $2\pi a$. Thus Eq. A.9 and Eq. A.10 can be evaluated as

$$\begin{cases} S^- = \tan \theta \frac{m^2}{a(x_{mn}^2 - m^2)}, & \text{for TE modes, and} \\ S^+ = 0 \end{cases} \quad (\text{A.11})$$

$$\begin{cases} S^- = -\frac{\tan \theta}{a}, & \text{for TM modes.} \\ S^+ = 0 \end{cases} \quad (\text{A.12})$$

The coupling coefficient caused by the impedance variation is

$$\frac{d}{dz}(\ln K) = \frac{d}{dz}(\ln \frac{\omega}{\beta}) = -\frac{1}{\beta} \frac{d\beta}{dz} \quad (\text{A.13})$$

Substituting the waveguide dispersion relation into Eq. A.13, we get

$$\begin{cases} \frac{d}{dz}(\ln K) = \frac{x_{mn}^2}{\beta^2 a^3} \frac{da}{dz}, & \text{for TE modes.} \\ \frac{d}{dz}(\ln K) = \frac{x_{mn}^2}{\beta^2 a^3} \frac{da}{dz}, & \text{for TM modes.} \end{cases} \quad (\text{A.14})$$

The impedance change arises from the changing of the wall radius which converts a forward wave to a backward wave of the same transverse structure. By the definition

of θ , we have $da/dz = \tan \theta$. From Eq. A.11, Eq. A.12 and Eq. A.14, the generalised telegraphist's equation is rewritten as

$$\begin{cases} \frac{dA^+}{dz} = j\beta A^+ - \frac{x_{mn}^2}{2\beta^2 a^3} \tan \theta A^- + \tan \theta \frac{m^2}{a(x_{mn}^2 - m^2)} A^- \\ \frac{dA^-}{dz} = -j\beta A^- + \frac{x_{mn}^2}{2\beta^2 a^3} \tan \theta A^+ + \tan \theta \frac{m^2}{a(x_{mn}^2 - m^2)} A^+ \end{cases}, \text{ for TE modes,} \quad (\text{A.15})$$

$$\begin{cases} \frac{dA^+}{dz} = j\beta A^+ - \frac{x_{mn}^2}{2\beta^2 a^3} \tan \theta A^- + \frac{\tan \theta}{a} A^- \\ \frac{dA^-}{dz} = -j\beta A^- + \frac{x_{mn}^2}{2\beta^2 a^3} \tan \theta A^+ + \frac{\tan \theta}{a} A^+ \end{cases}, \text{ for TM modes,} \quad (\text{A.16})$$

Eq. A.15 and Eq. A.16 can be written in a common form as

$$\begin{cases} \frac{dA^+}{dz} = j\beta A^+ - HA^- \\ \frac{dA^-}{dz} = -j\beta A^- + HA^+ \end{cases} \quad (\text{A.17})$$

Here

$$H = \begin{cases} \frac{\tan \theta}{2} \left\{ \frac{x_{mn}^4 - m^2 a^2 (\omega^2 / c^2 + \beta^2)}{\beta^2 a^3 (x_{mn}^2 - m^2)} \right\}, & \text{for TE modes,} \\ \frac{\tan \theta}{2} \frac{\omega^2 / c^2 + \beta^2}{\beta^2}, & \text{for TM modes.} \end{cases} \quad (\text{A.18})$$

Appendix IV Author's Publications

Book chapter

1 W. He, C. R. Donaldson, **L. Zhang**, K. Ronald, A. D. R. Phelps and A. W. Cross, "Numerical Simulation of a Gyro-BWO with a Helically Corrugated Interaction Region, Cusp Electron Gun and Depressed Collector", Numerical Simulations / Book 2, 2011

Journals

1 **Liang Zhang**, Wenlong He, Kevin Ronald, Alan D. R. Phelps, Colin G. Whyte, Craig W. Robertson, Alan R. Young, Craig R. Donaldson and Adrian W. Cross, "Multi-mode Coupling Wave Theory for Helically Corrugated Waveguide", IEEE Transaction on Microwave Theory and Technology, Vol. 60, No. 1, PP. 1-7, 2012

2 **Liang Zhang**, Wenlong He, Craig R. Donaldson, Adrian W. Cross, Alan D. R. Phelps, Paul McElhinney and Kevin Ronald, "W-band Gyro-BWO with a Four-stage Depressed Collector", International Journal of Terahertz Science and Technology, Vol. 4, No. 3, PP. 76-84, 2011

3 **Liang Zhang**, Wenlong He, Adrian W. Cross, Alan D. R. Phelps, Kevin Ronald, and Colin G. Whyte, Design of an Energy Recovery System for a Gyrotron Backward-Wave Oscillator, IEEE Transaction on Plasma Science, vol. 37, no. 3, 2009

4 **Liang Zhang**, Wenlong He, Adrian W. Cross, Alan D. R. Phelps, Kevin Ronald, and Colin G. Whyte, Numerical Optimization of a Multistage Depressed Collector With Secondary Electron Emission for an X-band Gyro-BWO, IEEE Transaction on Plasma Science, vol. 37, no.12, 2009

- 5 W. He, C. R. Donaldson, F. Li, **L. Zhang**, A. W. Cross, A. D. R. Phelps, K. Ronald, C. W. Robertson, C. G. Whyte, and A. R. Young, "W-band gyro-devices using helically corrugated waveguide and cusp gun: design, simulation and experiment", *International Journal of Terahertz Science and Technology*, vol. 4 no. 1, pp. 9 – 19, 2011
- 6 V. L. Bratman, G. G. Denisov, N. G. Kolganov, S. V. Mishakin, S. V. Samsonov, A. W. Cross, W. He, **L. Zhang**, M. McStravick, C. G. Whyte, A. R. Young, K. Ronald, C. W. Robertson, and A. D. R. Phelps, Generation of 3 GW microwave pulses in X-band from a combination of a relativistic backward-wave oscillator and a helical-waveguide compressor, *Physics of Plasma*, vol. 17, id: 110703, 2010
- 7 C. R. Donaldson, W. He, A. W. Cross, F. Li, A. D. R. Phelps, **L. Zhang**, K. Ronald, C. W. Robertson, C. G. Whyte, and A. R. Young, A cusp electron gun for millimeter wave gyrodevices, *Applied Physics Letters*, vol. 96, no. 14, id. 141501, 2010
- 8 Fengping Li, Wenlong He, Adrian W. Cross, Craig R. Donaldson, **Liang Zhang**, Alan D. R. Phelps and Kevin Ronald, Design and simulation of a ~390 GHz seventh harmonic gyrotron using a large orbit electron beam, *Journal of Physics D: Applied Physics*, vol. 43, no. 15, 2010
- 9 Craig R. Donaldson, Wenlong He, Adrian W. Cross, Alan D. R. Phelps, Fengping Li, Kevin Ronald, Craig W. Robertson, Colin G. Whyte, Alan R. Young, and **Liang Zhang**, Design and Numerical Optimization of a Cusp-Gun-Based Electron Beam for Millimeter-Wave Gyro-Devices, *IEEE Transactions on Plasma Science*, vol. 37, no. 11, 2009

Conferences

- 1 Liang Zhang**, Wenlong He, Craig Donaldson, Adrian Cross, Alan Phelps, Kevin Ronald, "A Four-stage Depressed Collector for a W-band Gyro-BWO", 36th International Conference on Infrared Millimeter and Terahertz Waves (IRMMW-THz), Houston, Texas, USA, October 2-7, 2011
- 2** Craig Donaldson, Wenlong He, **Liang Zhang**, Adrian Cross, Paul Mcelhinney, Alan Phelps, Kevin Ronald, "A W-band gyrotron traveling wave amplifier based on a cusp electron gun", 36th International Conference on Infrared Millimeter and Terahertz Waves (IRMMW-THz), Houston, Texas, USA, October 2-7, 2011
- 3** Paul Mcelhinney, Craig Donaldson, Wenlong He, **Liang Zhang**, Kevin Ronald, Alan Phelps, Adrian Cross, "Design of a Broadband Corrugated Horn for a W-band Gyro-TWA", 36th International Conference on Infrared Millimeter and Terahertz Waves (IRMMW-THz), Houston, Texas, USA, October 2-7, 2011
- 4 Liang Zhang**, Wenlong He, Adrian W. Cross, Alan D. R. Phelps, Craig Donaldson, Kevin Ronald, "Simulation of a four-stage depressed collector for a W-band Gyro-BWO", 35th International Conference on Infrared Millimeter and Terahertz Waves (IRMMW-THz), Rome, Italy, September 6-10, 2010
- 5** W. He, A.D.R. Phelps, C.R. Donaldson, A.W. Cross, **L. Zhang**, and K. Ronald, "A W-Band Gyro-TWA using a Helically Corrugated Waveguide", 35th International Conference on Infrared Millimeter and Terahertz Waves (IRMMW-THz), Rome, Italy, September 6-10, 2010
- 6** C. R. Donaldson, W. He, A. D. R. Phelps, F. Li, **L. Zhang**, A. W. Cross, K. Ronald, C. W. Robertson, C. G. Whyte, and A. R. Young, "Experimental demonstration of a W-band gyro-BWO using a helically corrugated waveguide", Rome, Italy, September 6-10, 2010
- 7** F. Li, W. He, A.D.R. Phelps, C.R. Donaldson, **L. Zhang**, A.W. Cross, and K. Ronald, "The Design of a 390 GHz Gyrotron Based on a Cusp Electron Gun", 35th

International Conference on Infrared Millimeter and Terahertz Waves (IRMMW-THz), Rome, Italy, September 6-10, 2010

8 C. R. Donaldson, W. He, A. W. Cross, F. Li, A. D.R. Phelps, **L. Zhang**, K. Ronald, C. W. Robertson, C. G. Whyte, and P. McElhinney, "Experimental Demonstration of a W-band gyro-BWO using a Helically Corrugated Waveguide", 11th International Vacuum Electronics Conference (IVEC), Monterey, California, USA, May 18-20, 2010

9 P. McElhinney, W. He, C. R. Donaldson, A. D. R. Phelps, **L. Zhang**, A. W. Cross, C. Robertson, C. Whyte and K. Ronald, " Simulation of a non-linear corrugated horn as a quasi-optical converter", Proc. National Vacuum Electronics Conference (NVEC), 2010.

10 W. He, C. R. Donaldson, A. D. R. Phelps, A. W. Cross, F. Li, K. Ronald, C. W. Robertson, C. G. Whyte, A.R. Young and **L. Zhang**, "W band Gyro-devices using helical interaction waveguides and cusp guns", 2nd UK/Europe-China Workshop on Millimetre Waves and Terahertz Technologies, p. 68, Rutherford Appleton Laboratory, UK, October 19-21, 2009.

11 **Liang Zhang**, Wenlong He, Adrian W. Cross, Alan D. R. Phelps, Kevin Ronald, and Colin G. Whyte, "Simulation of a Four-stage Depressed Collector for a W-band Gyro-BWO", 2nd UK/Europe-China Workshop on Millimetre Waves and Terahertz Technologies, p. 96, Rutherford Appleton Laboratory, UK, October 19-21, 2009.

12 W. He, C. R. Donaldson, F. Li, A. W. Cross, A. D. R. Phelps, K. Ronald, C. W. Robertson, C. G. Whyte, and **L. Zhang**, "Design, simulation and experiment of a cusp electron beam for millimeter wave gyro-devices", IEEE International Vacuum Electronics Conference (IVEC), Page(s): 517 - 518, Italy, Rome, April 28-30, 2009.

Multi-Mode Coupling Wave Theory for Helically Corrugated Waveguide

Liang Zhang, Wenlong He, Kevin Ronald, Alan D. R. Phelps, Colin G. Whyte, Craig W. Robertson, Alan R. Young, Craig R. Donaldson, and Adrian W. Cross

Abstract—Helically corrugated waveguide has been used in various applications such as gyro-backward wave oscillators, gyro-traveling wave amplifier and microwave pulse compressor. A fast prediction of the dispersion characteristic of the operating eigenwave is very important when designing a helically corrugated waveguide. In this paper, multi-mode coupling wave equations were developed based on the perturbation method. This method was then used to analyze a five-fold helically corrugated waveguide used for X-band microwave compression. The calculated result from this analysis was found to be in excellent agreement with the results from numerical simulation using CST Microwave Studio and vector network analyzer measurements.

Index Terms—Coupling coefficients, coupling wave theory (CWT), dispersion curve, helically corrugated waveguide.

I. INTRODUCTION

STRAIT hollow metal waveguides with uniform cross section can only support modes whose phase velocity is larger than the speed of light, while waveguides with periodic corrugations can propagate modes with phase velocity less than the speed of light and are suitable for particle beam-wave interactions. Periodically corrugated waveguides have been used in many applications, including slow-wave structures with axial periodicity for conventional backward wave oscillators (BWOs) and traveling wave tubes (TWTs)[1], and magnetrons [2] with azimuthal periodicity. Corrugated waveguide structures have also been used as Bragg reflectors [3], [4]. The helically corrugated waveguide, which contains both axial and azimuthal periodicity, has attracted significant interest in the last 10 years and has successfully found applications in the gyrotron traveling wave amplifier (gyro-TWA) [5], [6], as a dispersive medium for frequency-swept microwave pulse compression[7], [8] and in the gyrotron backward wave oscillator (gyro-BWO)[9], [10]. The electrodynamic properties of the helically corrugated waveguide are important, as the dispersion characteristic of the operating eigenwave can be changed by

choosing different corrugation depths and corrugation periods to meet the needs of different applications. In a gyro-TWA or gyro-BWO, a constant group velocity in the operating frequency range is desired, while in a microwave compressor, a linearly varying group velocity in the frequency band is preferred.

Several methods have been developed to investigate the dispersion characteristics of the helically corrugated waveguide by analytical and numerical techniques. The simplest and fastest method to calculate the dispersion curves is the coupled wave theory based on the method of perturbation [11]–[13]. It assumes that the change in the cross section is small and can be treated as a first order derivative of a regular cross section. Reference [12] gives the dispersion relation between two TE modes and [11] gives the results of the coupling coefficients between two TE modes, two TM modes, and one TE mode with one TM mode but no derivations were presented. It is found that when the corrugation depth is less than 15% of the mean radius of the waveguide, the coupled wave theory gives reasonably accurate results. The coupled wave theory played an important role in the preliminary design of the three-fold helical waveguide in which the dispersion of the operating eigenwave is simply a result from the coupling between two TE modes in the operating frequency range, i.e., the spatial harmonic TE_{11} mode and TE_{21} mode. However, the three-fold helical waveguide has limited power capability. A helical waveguide working with a higher eigenwave mode can achieve higher power capability as a larger radius can be used. However operating with higher mode means more modes would take part in the coupling and therefore the resultant dispersion curve would be more complicated to calculate. For example, in a five-fold helical waveguide the spatial harmonic of the TE_{31} mode would couple with the TE_{21} , TE_{22} , TM_{21} and TM_{22} modes. The coupled mode equation, which only considers two TE modes, would therefore not be accurate in obtaining the dispersion characteristics of the five-fold helical waveguide. Necessary modifications to include the coupling between TE and TM modes are required and will be presented in this paper.

The dispersion curve of the helically corrugated waveguide can also be numerically simulated by using some computer codes, such as the finite-element method (FEM), the eigensolver in CST Microwave Studio, the electromagnetic field solver in the particle-in-cell (PIC) code MAGIC and the transient solver in CST Microwave Studio, which use a finite-difference time-domain method (FDTD) [14]. By using these codes, accurate results can be obtained if the mesh grid is dense enough. However, these 3-D simulations have the disadvantage of requiring long computational times to complete the simulations,

Manuscript received March 28, 2011; revised September 13, 2011; accepted September 20, 2011. Date of publication November 02, 2011; date of current version December 30, 2011. This work was supported by the U.K. EPSRC Research Grant EP/E058868/1. The work of L. Zhang was supported by SUPA and SORSAS under the award of a SUPA prize research studentship.

The authors are with SUPA, Department of Physics, University of Strathclyde, Glasgow, G4 0NG, Scotland, U.K. (e-mail: liang.zhang@strath.ac.uk; w.he@strath.ac.uk; k.ronald@strath.ac.uk; a.d.r.phelps@strath.ac.uk; colin.whyte@strath.ac.uk; craig.robertson@strath.ac.uk; a.r.young@strath.ac.uk; craig.donaldson@strath.ac.uk; a.w.cross@strath.ac.uk).

Color versions of one or more of the figures in this paper are available online at <http://ieeexplore.ieee.org>.

Digital Object Identifier 10.1109/TMTT.2011.2170848

for example, two or three days on a powerful desktop PC using a reasonably dense mesh grid and they are therefore not suitable for optimizing the dimensions of the helical waveguide for a particular application.

It should be noticed that the helically corrugated waveguide can also be regarded as a type of twisted waveguide. A helicoidal coordinate transform can be employed to convert the twisted waveguide into a straight uniform waveguide, thus downgrading the 3-D problem into a 2-D one [15]. The price of using this technique is the uniform material properties in the twisted waveguide will become non-uniform and position dependent. This transformation method can greatly reduce the computing time in resolving the eigenwave dispersion when applying the FEM and FDTD methods in the 2-D geometries [16], [17]. It should be noted that the dispersions of the coupled waves and those initial partial waves are all existing and calculated at the same time when this method is used. The dispersion curves of these modes would be interweaved and very close to each other, especially when a higher modes are considered. Therefore the dispersion curves of the operating eigenwaves of the helically corrugated waveguide would be difficult to identify. The field patterns of the eigenmodes can be helpful when identifying the operating dispersion curve, however, it is very difficult to recognize by computer automatically, thus it is not suitable for the optimization routing. On the other hand, this operating eigenwave from the transformation method can be easily identified by using the calculated result from the coupled wave theory as a reference.

It is evident that the analytical calculation using the coupled wave theory is very useful in the preliminary design of the helically corrugated waveguide. It is also useful to accurately and rapidly predict the dispersion of the eigenwave when used in combination with the transformation method. In this paper, a detailed description of the coupling coefficient between TE modes and TM modes and the extended eigenwave equations caused by multi-mode coupling are discussed in Section II. Dispersion calculation of a five-fold helically corrugated waveguide is described in Section III. The comparison between the theoretical calculation and the experiment is presented in Section IV.

II. PRINCIPLE OF THE COUPLED WAVE THEORY

The equation of the helical profile of the inner surface in a cylindrical coordinate system (r, θ, z) can be written as

$$r(\theta, z) = R_0 + R_1 \cos\left(m_B \theta + \frac{2\pi z}{d}\right) \quad (1)$$

where R_0 is the mean radius of the circular waveguide, R_1 is the corrugation depth, m_B is the fold number, and d is the axial period of the corrugation. When the corrugation depth is not zero, two modes will couple when their axial and azimuthal wave numbers satisfy the synchronism conditions

$$h_1 - h_2 = \frac{2\pi}{d}, m_1 - m_2 = m_B \quad (2)$$

where h_1 and h_2 are the axial wavenumbers of modes 1 and 2, and m_1 and m_2 are the azimuthal indices of modes 1 and 2, respectively.

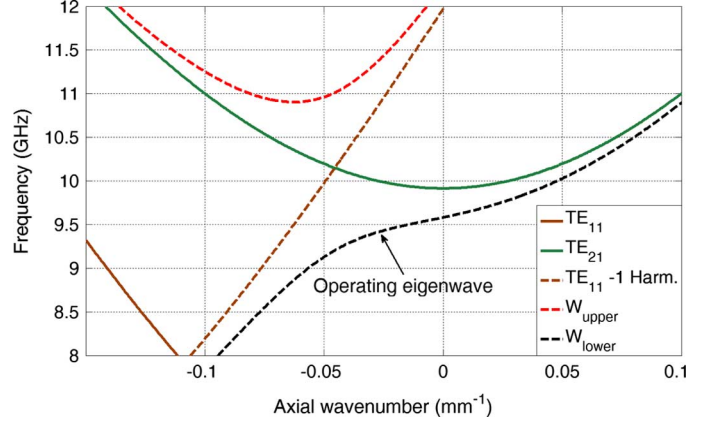


Fig. 1. Coupling between the TE_{21} mode and the spatial harmonic TE_{11} mode in a three-fold helical waveguide.

In three-fold helically corrugated waveguide, the TE_{21} mode would couple with the TE_{11} circularly polarized mode of opposite rotation and generate an operating eigenwave, as shown in Fig. 1. From the synchronism condition, coupling between higher modes requires larger fold number m_B . However, with larger m_B more modes would satisfy the synchronism condition and they would couple with each other and hence contribute to the dispersion characteristic.

A. Coupling Coefficients

The coupling coefficient is the basis of the coupled wave theory as it indicates how strong the coupling between two modes is. In this paper, we start from the general equations of the coupling coefficients between two TE modes, two TM modes and one TE (mode m) to one TM (mode j) modes as shown in (3). The derivation of these equations can be found in [18], which contains a detailed introduction to the coupled mode theory

$$\begin{aligned} S_{jm} &= \frac{1}{2h_j(h_j - h_m)} \oint v(s) \\ &\quad \times \left[\alpha_j^2 \alpha_m^2 \Psi_j \Psi_m + (h_j h_m - k^2) \frac{\partial \Psi_j}{\partial s} \frac{\partial \Psi_m}{\partial s} \right] ds \\ S_{jm} &= \frac{k^2 - h_j h_m}{2h_j(h_j - h_m)} \oint v(s) \frac{\partial \phi_j}{\partial u} \frac{\partial \phi_m}{\partial u} ds \\ S_{jm} &= -\frac{k}{2h_j} \oint v(s) \frac{\partial \phi_j}{\partial u} \frac{\partial \Psi_m}{\partial s} ds \end{aligned} \quad (3)$$

where $v(s)$ is the function to describe the difference between the perturbed non-uniform waveguide and the uniform waveguide. When $v(s) = 0$, there is no coupling between the two modes. h_j, h_m are the axial wave numbers of the coupled modes and k is the free-space wave number. α_j, α_m are the transverse wave numbers of modes j and m . Ψ, ϕ are the transverse eigenfunctions of the TE and TM modes of the unperturbed regular waveguide. u is the normal vector directed towards the waveguide wall. s is chosen so that axes u, s, z to form a right-handed coordinate system.

In circular waveguide, the transverse wave number and eigenfunction in a cylindrical coordinate system are in the form of

$$\alpha_{nq} = \begin{cases} \frac{\xi_{nq}}{R_0}, & \text{(for TE mode)} \\ \frac{\zeta_{nq}}{R_0}, & \text{(for TM mode)} \end{cases} \quad (4)$$

$$\begin{aligned} \Psi_{nq} &= \sqrt{\frac{2}{\pi \varepsilon_n}} \frac{1}{\sqrt{\xi_{nq}^2 - n^2} |J_n(\xi_{nq})|} \\ &\quad \times J_n(\alpha_{nq} r) \begin{cases} \cos(n\theta) \\ \sin(n\theta) \end{cases} \\ \varphi_{nq} &= \sqrt{\frac{2}{\pi \varepsilon_n}} \frac{1}{\zeta_{nq} |J'_n(\zeta_{nq})|} J_n(\alpha_{nq} r) \begin{cases} \cos(n\theta) \\ \sin(n\theta) \end{cases} \\ \varepsilon_n &= \begin{cases} 2, & (n = 1) \\ 1, & (n \neq 1) \end{cases} \end{aligned} \quad (5)$$

where ξ_{nq} is the q^{th} zero of the derivation of J_n and J is the first kind of Bessel function. ζ_{nq} is the q^{th} root of J_n . In practical applications, the operating mode in the helically corrugated waveguide always satisfies $n \neq 0$. As the radial number q in the modes does not contribute to the following derivation, symbols j and m are used to denote the azimuthal number of the two coupling modes for simplicity.

The difference between the helically corrugated cross section and the circular waveguide at position $z = 0$ can be written as $v(s) = m_B R_1 \sin(m_B \theta)$. For a small corrugation, we have $v(s) \ll R_0$. As $v(s)$ is in terms of the first-order derivation of the mean radius, if only the first-order approximation of the coupling coefficient is taken into account then only the zero-order approximation of the other terms in (3) needs to be considered. In polar coordinates, we can simply make $ds = r d\theta$ and $du = dr$. Substituting these into (3), we can get a simpler form of the coupling coefficients, as

$$\begin{aligned} S_{jm} &= \frac{R_1 [\xi_m^2 \xi_j^2 + (h_j h_m + k^2) j m R_0^2]}{h_j (h_j - h_m) R_0^3 \sqrt{\xi_m^2 - m^2} \sqrt{\xi_j^2 - j^2}} \\ &\quad \times \oint \frac{m_B}{\pi} \sin(m_B \theta) \begin{cases} \cos(m\theta) \\ \sin(m\theta) \end{cases} \begin{cases} \cos(j\theta) \\ \sin(j\theta) \end{cases} d\theta \\ S_{jm} &= \frac{R_1 (k^2 - h_j h_m)}{R_0 h_j (h_j - h_m)} \\ &\quad \times \oint \frac{m_B}{\pi} \sin(m_B \theta) \begin{cases} \cos(m\theta) \\ \sin(m\theta) \end{cases} \begin{cases} \cos(j\theta) \\ \sin(j\theta) \end{cases} d\theta \\ S_{jm} &= - \frac{R_1 k m}{R_0 h_j \sqrt{\xi_m^2 - m^2}} \\ &\quad \times \oint \frac{m_B}{\pi} \sin(m_B \theta) \begin{cases} \cos(m\theta) \\ \sin(m\theta) \end{cases} \begin{cases} \cos(j\theta) \\ \sin(j\theta) \end{cases} d\theta. \end{aligned} \quad (6)$$

In the helically corrugated waveguide, only the modes that satisfy the synchronism conditions can couple with each other. Thus we have $j - m = m_B$. It should be noted that, in the prac-

tical application, m is always chosen as a negative value indicating an opposite rotating mode and hence h_m also is a negative value. The integral in this equation will become unity if we apply the synchronism condition. Then the final coupling coefficients for the helically corrugated waveguide become

$$\begin{aligned} S_{jm} &= \frac{R_1 [\xi_m^2 \xi_j^2 + (h_j h_m + k^2) j m R_0^2]}{h_j (h_j - h_m) R_0^3 \sqrt{\xi_m^2 - m^2} \sqrt{\xi_j^2 - j^2}} \\ S_{jm} &= \frac{R_1 (k^2 - h_j h_m)}{R_0 h_j (h_j - h_m)} \\ S_{jm} &= - \frac{R_1 k m}{R_0 h_j \sqrt{\xi_m^2 - m^2}}. \end{aligned} \quad (7)$$

Equation (7) has the same form as the ones in [11], while the coupling coefficient in [11] has been normalized to $h_j h_m$.

B. Coupled Mode Equations

Although the coupling coefficient indicates the strength of the coupling between two modes, it is useful to know the strength of the coupling modes in the resultant eigenwave. They can be solved from the coupled mode equations [18] and the coupling coefficient, as

$$\begin{cases} \frac{dV_m}{dz} = \frac{-h_j}{h_m} S_{jm} \exp(-i(\sigma_j - \sigma_m)) V_j \\ \frac{dV_j}{dz} = S_{jm} \exp(i(\sigma_j - \sigma_m)) V_m \end{cases} \quad (8)$$

where V_m, V_j are the normalized voltages of mode m and j in the helically corrugated waveguide, respectively, and $\sigma_{j/m} = \int_0^z h_{j/m} dz$ is the phase of mode j or m in the waveguide, and $\sigma = \sigma_j - \sigma_m = (h_j - h_m)d$ is the phase difference between the two coupled modes in the waveguide with the length of one period d . σ becomes 2π if the synchronism conditions are applied.

The normalized voltages of mode m and j in the helically corrugated waveguide can be solved as

$$\begin{cases} V_m = - \left(\cos \kappa + \frac{i\pi}{\kappa} \sin \kappa \right) \\ V_j = \frac{\sqrt{\kappa^2 - \pi^2}}{\kappa} \sin \kappa \end{cases} \quad (9)$$

where

$$\kappa = 2\pi \sqrt{|h_j/h_m| S_{jm}^2 + 1/4}.$$

They are completely determined by κ which is dependent on the axial wavenumbers of the coupling modes and the coupling coefficient.

C. Dispersion Curve Function

The new dispersion curve caused by two-mode coupling will satisfy the following equation:

$$f_j^2(h) \cdot f_m^2(h) = h_j^2 h_m^2 S_{jm}^2 \quad (10)$$

where f_j, f_m are the dispersion relations of the coupling modes which are functions of the axial wavenumber h . For a TE/TM

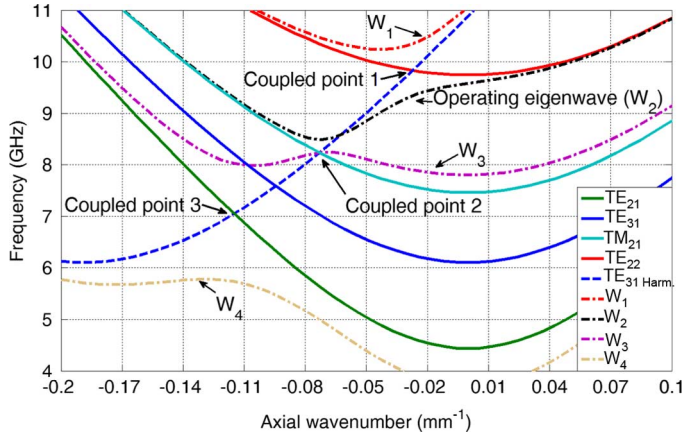


Fig. 2. Coupling modes in a five-fold helical waveguide.

mode in the circular waveguide, the dispersion relation can be written as

$$f_j^2(h) = k^2 - \alpha_j^2 - h^2. \quad (11)$$

Because, as noted in Section II-A, mode m is the negative spatial harmonic wave, the dispersion curve is shifted to the left by $2\pi/d$ to produce the following dispersion relation:

$$f_m^2(h) = k^2 - \alpha_m^2 - \left(h - \frac{2\pi}{d}\right)^2. \quad (12)$$

Equation (10) is a fourth-order linear equation. Given a wave number k , we can get four eigenvalues by solving the equation. However, only two of them have practical physical meaning, and they are named as upper coupled mode W_{upper} and lower coupled mode W_{lower} . If there is no coupling between the two modes, that is $S_{jm} = 0$, the eigenfunction will degenerate into two separate dispersion curve functions, i.e., $f_j^2(h) = 0$ and $f_m^2(h) = 0$. The W_{upper} and W_{lower} will degenerate into the previous uncoupled partial eigenwaves.

There is no straightforward dispersion curve equation available that can take into account all of the considered modes for a helically corrugated waveguide operating in a higher mode. However, from the dispersion diagram, it is clear that the coupling frequencies between any two modes, as shown in Fig. 2 which shows the five-fold helical waveguide case, are different. Thus an alternative method is to calculate the coupled eigenwaves in sequence by using the two-mode coupling equation, either from the lower frequency to the higher frequency, or vice versa. Here the sequence from higher to lower frequencies is used. First, two eigenwaves $W_{\text{upper}1}$ and $W_{\text{lower}1}$ can be resolved from (10)–(12). Then eigenwave $W_{\text{upper}1}$ does not have an intersection with the next mode, thus it is saved as an eigenwave (W_1 in Fig. 2). Eigenwave $W_{\text{lower}1}$ couples with the next mode to generate $W_{\text{upper}2}$ (W_2 in Fig. 2) and $W_{\text{lower}2}$ by using (10), while here $f_m(h)$ refers to the eigencurve $W_{\text{lower}1}$ and h_j, h_m are the axial wavenumbers in the intersection of mode $W_{\text{lower}1}$ and the next coupled mode. By repeating this process, all the eigenwaves caused by the mode coupling in the helically corrugated waveguide can be obtained.

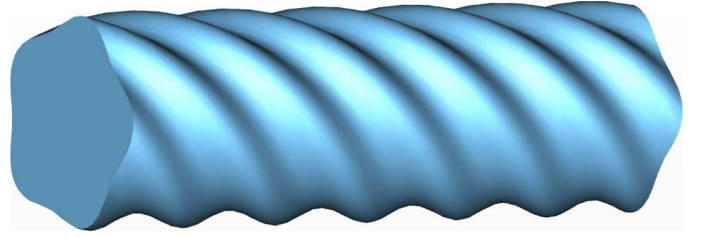


Fig. 3. Schematic view of the five-fold helical waveguide.

III. DISPERSION CALCULATION OF A FIVE-FOLD HELICALLY CORRUGATED WAVEGUIDE

One of the applications of the helically corrugated waveguide is as a dispersive medium for pulse compression. A three-fold corrugated waveguide operating in X-band was previously designed and was used in an experiment that achieved a compression factor of 25 [19]. The maximum power capability of the waveguide is about 1 MW. To pursue higher power capability [20], a five-fold helically corrugated waveguide with larger radius operating in the same frequency range has been investigated. A general schematic view of a five-fold helical waveguide is shown in Fig. 3. The desired coupled modes are the spatial harmonic TE_{31} mode and the TE_{22} mode. As known from the synchronism condition, besides the TE_{22} mode, the possible modes that can couple with the TE_{31} are the TE_{21} and TM_{21} modes in the lower frequency range and the effects need to be investigated.

A fast prediction of the operating dispersion curve can be obtained by using the multi-mode coupling method, as shown in Fig. 2. The cut-off frequency of the TE_{21} mode is much smaller than the TM_{21} and TE_{22} modes, thus it will not contribute to the operating eigenwave in the frequency range of interest for the microwave compressor. The choice of the mean radius of the helically corrugated waveguide needs to balance the dispersion characteristic as well as the power capability. A smaller R_0 has a larger cut-off frequency gap between the TM_{21} , TE_{31} and TE_{22} modes, thus it is possible to reduce the effect caused by the coupling between the TE_{31} and TM_{21} modes. However, a small radius can also reduce the power capability, which is opposite to the original aim. The axial period of the helical waveguide d determines the intersection points of the coupled modes, and the corrugation depth R_1 greatly contributes to the coupling coefficients, a larger corrugation depth results in stronger coupling. An optimum set of parameters can be searched for simply by parameter sweeping, or from an optimization algorithm to find an optimum balance among the requirements, such as the power capability, the operating frequency range, and the dispersion characteristic of the operating eigenwave.

IV. COMPARISON BETWEEN THE CALCULATION AND THE EXPERIMENT

The five-fold helically corrugated waveguide was studied with dimensions of $R_0 = 32.84$ mm, $R_1 = 2.43$ mm, and $d = 33.26$ mm. The dispersion curve was also measured using a 65 GHz vector network analyzer (VNA) (Anritsu 37397A). The experimental setup is shown in Fig. 4. From left to right, a rectangular to circular mode converter (① in Fig. 4) was first

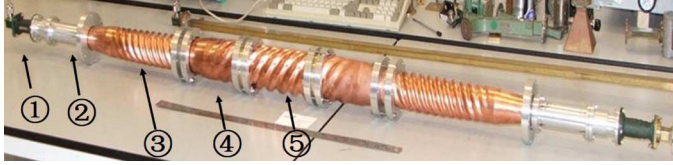


Fig. 4. Experimental setup for measuring the dispersion curve of the five-fold helical waveguide.

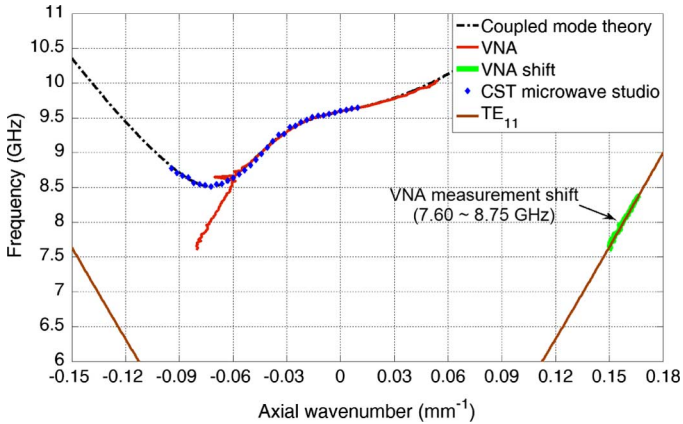


Fig. 5. Dispersion curve from coupled mode theory, CST Microwave Studio simulation, and the VNA measurement.

used to convert the fundamental TE_{10} mode in rectangular waveguide to a linearly polarized TE_{11} mode in the circular waveguide. This is followed by an elliptical polarizer (② in Fig. 4) that converts the linearly polarized TE_{11} mode into a left hand rotating TE_{11} wave. A four-fold helical mode converter (③ in Fig. 4) was then used to convert the circularly polarized TE_{11} mode into a circularly polarized TE_{31} mode. The mode convertor was designed to have $> 90\%$ conversion efficiency in the frequency range of $8.75 \sim 10.0$ GHz. Finally a five-fold helical taper (④ in Fig. 4) was used before introducing the TE_{31} mode into the five-fold helically corrugated waveguide (⑤ in Fig. 4) to make sure the TE_{31} mode smoothly converted to the operating eigenwave without reflection. On the other side of the helical waveguide, the same configuration was used.

Fig. 5 shows the dispersion curves calculated from the coupled mode theory, simulated from the eigensolver in CST Microwave Studio as well as measured by the VNA. From the coupled mode calculation, there are four eigenwaves resulting from the mode coupling between the TE_{31} and the TE_{21} , the TM_{21} , and the TE_{22} modes. Eigenwave 2 is the operating eigenwave for microwave compression. The dispersion curves from coupled mode theory, simulation using CST Microwave Studio and measurement using a VNA agree well with each other in the frequency range $8.75 \sim 10.0$ GHz, as shown in Fig. 5.

However the measured dispersion at the lower frequency band ($7.6 \sim 8.75$ GHz) underwent a change of trend. This is due to the fact that the frequency is out of the operating band of the TE_{11} -to- TE_{31} mode convertor. The dominant power in the helically corrugated waveguide is still in the TE_{11} mode in this lower frequency band. If the measured result in this frequency range is shifted by a factor of $2\pi N/L$, where N is

an integer, and L is the length of the helically corrugated waveguide in the measurement, it agrees well with the dispersion curve of the TE_{11} mode, as shown in Fig. 5. At a frequency of $8.6 \sim 8.8$ GHz a small content of the TE_{31} mode exists in the helical waveguide in conjunction with the TE_{11} mode, this causes the measured dispersion result in this frequency range to be spiky as it is the mixed phase information of the two modes.

V. CONCLUSION

In this paper, a detailed description of the multi-mode coupled wave theory for calculation of the dispersion characteristic of helically corrugated waveguide is given and it is applied to analyze a five-fold helical waveguide. This calculated result from the theory was found to be in good agreement with the CST Microwave Studio simulation result, as well as the VNA measurements.

ACKNOWLEDGMENT

The authors would like to thank V. L. Bratman, G. G. Denisov, S. V. Samsonov, and S.V. Mishakin for their helpful discussions.

REFERENCES

- [1] A. S. Gilmour, *Principles of Traveling Wave Tubes*. Boston, MA: Artech House, 1994.
- [2] R. J. Barker, J. H. Booske, N. C. Luhmann, and S. N. Gregory, Eds., *Modern Microwave and Millimeter-Wave Power Electronics*. New York: IEEE, 2005.
- [3] C. K. Chong, D. B. McDermott, M. M. Razegh, N. C. Luhmann, J. Pretterebner, D. Wagner, M. Thumm, M. Caplan, and B. Kulke, "Bragg reflectors," *IEEE Trans. Plasma Sci.*, vol. 20, no. 3, pp. 393–402, Mar. 1992.
- [4] N. Ginzburg, N. Peskov, A. Sergeev, A. D. R. Phelps, A. W. Cross, and I. V. Konoplev, "The use of a hybrid resonator consisting of one dimensional and two dimensional bragg reflectors for generation of spatially coherent radiation in a coaxial free-electron laser," *Phys. Plasmas*, vol. 9, no. 6, pp. 2798–2802, 2002.
- [5] V. L. Bratman, A. W. Cross, G. G. Denisov, W. He, A. D. R. Phelps, K. Ronald, S. V. Samsonov, and C. G. W. A. R. Young, "High-gain wide-band gyrotron traveling wave amplifier with a helically corrugated waveguide," *Phys. Rev. Lett.*, vol. 84, no. 12, pp. 2746–2749, 2000.
- [6] A. W. Cross, W. He, A. D. R. Phelps, K. Ronald, C. G. Whyte, A. R. Young, C. W. Robertson, E. G. Rafferty, and J. Thomson, "Helically corrugated waveguide gyrotron traveling wave amplifier using a thermionic cathode electron gun," *Appl. Phys. Lett.*, vol. 90, p. 253501, 2007.
- [7] S. V. Samsonov, A. D. R. Phelps, V. L. Bratman, G. Burt, G. G. Denisov, A. W. Cross, K. Ronald, W. He, and H. Yin, "Compression of frequency-modulated pulses using helically corrugated waveguides and its potential for generating multigigawatt rf radiation," *Phys. Rev. Lett.*, vol. 92, p. 118301, 2004.
- [8] G. Burt, S. V. Samsonov, A. D. R. Phelps, V. L. Bratman, K. Ronald, G. G. Denisov, W. He, A. R. Young, A. W. Cross, and I. V. Konoplev, "Microwave pulse compression using a helically corrugated waveguide," *IEEE Trans. Plasma Sci.*, vol. 33, no. 2, pp. 661–667, Feb. 2005.
- [9] W. He, A. W. Cross, A. D. R. Phelps, K. Ronald, C. G. Whyte, S. V. Samsonov, V. L. Bratman, and G. G. Denisov, "Theory and simulations of a gyrotron backward wave oscillator using a helical interaction waveguide," *Appl. Phys. Lett.*, vol. 89, p. 091504, 2006.
- [10] W. He, K. Ronald, A. R. Young, A. W. Cross, A. D. R. Phelps, C. G. Whyte, E. G. Rafferty, J. Thomson, C. W. Robertson, D. C. Speirs, S. V. Samsonov, V. L. Bratman, and G. G. Denisov, "Gyro-BWO experiments using a helical interaction waveguide," *IEEE Trans. Electron Devices*, vol. 52, no. 5, pp. 839–844, May 2005.

- [11] G. G. Denisov and M. G. Reznikov, "Corrugated cylindrical resonators for short-wavelength relativistic microwave oscillators," *Radiophys. Quantum Electron.*, vol. 25, no. 5, pp. 407–413, 1982.
- [12] S. J. Cooke and G. G. Denisov, "Linear theory of a wide-band gyro-TWT amplifier using spiral waveguide," *IEEE Trans. Plasma Sci.*, vol. 26, no. 3, pp. 519–530, Mar. 1998.
- [13] G. G. Denisov, V. L. Bratman, A. D. R. Phelps, and S. V. Samsonov, "Gyro-TWT with a helical operating waveguide: New possibilities to enhance efficiency and frequency bandwidth," *IEEE Trans. Plasma Sci.*, vol. 26, no. 3, pp. 508–518, Mar. 1998.
- [14] G. Burt, S. V. Samsonov, K. Ronald, G. G. Denisov, A. R. Young, V. L. Bratman, A. D. R. Phelps, A. W. Cross, I. V. Konoplev, W. He, J. Thomson, and C. G. Whyte, "Dispersion of helically corrugated waveguides: Analytical, numerical, and experimental study," *Phys. Rev. E*, vol. 70, no. 4, p. 046402, 2004.
- [15] L. Lewin, *Theory of Waveguides: Techniques for the Solution of Waveguide Problems*. London, U.K.: Newnes Butterworths, 1975.
- [16] A. Nicolet and F. Zolla, "Finite element analysis of helicoidal waveguides," *IET Sci., Meas., Technol.*, vol. 1, no. 1, pp. 67–70, 2007.
- [17] J. L. Wilson, C. Wang, A. E. Fathy, and Y. W. Kang, "Analysis of rapidly twisted hollow waveguides," *IEEE Trans. Plasma Sci.*, vol. 57, no. 1, pp. 130–139, Jan. 2009.
- [18] B. Z. Katsenelenbaum, L. M. D. Ro, M. Pereyaslavets, M. S. Ayz, and M. K. A. Thumm, *Theory of Non-Uniform Waveguides: The Cross-Section Method*. London, U.K.: The IET, 1999.
- [19] M. McStravick, S. V. Samsonov, K. Ronald, S. V. Mishakin, W. He, G. G. Denisov, C. G. Whyte, V. L. Bratman, A. W. Cross, A. R. Young, P. MacInnes, C. W. Robertson, and A. D. R. Phelps, "Experimental results on microwave pulse compression using helically corrugated waveguide," *J. Appl. Phys.*, vol. 108, no. 5, p. 054908, 2010.
- [20] V. L. Bratman, G. G. Denisov, N. G. Kolganov, S. V. Mishakin, S. V. Samsonov, A. W. Cross, W. He, L. Zhang, M. McStravick, C. G. Whyte, A. R. Young, K. Ronald, C. W. Robertson, and A. D. R. Phelps, "Generation of 3 GW microwave pulses in x-band from a combination of a relativistic backward-wave oscillator and a helical-waveguide compressor," *Phys. Plasmas*, vol. 17, p. 110703, 2010.



oscillators.

Liang Zhang received the B.Sc. degree in applied physics from the University of Science and Technology of China, Hefei, China, in 2004 and the M.Sc. degree in application of nuclear techniques from the China Academy of Engineering Physics, Chengdu, China, in 2007, respectively. He is currently pursuing the Ph.D. degree in physics from the Scottish Universities Physics Alliance, Department of Physics, University of Strathclyde, Glasgow, U.K.

His main research interests include pulse-power technology, and Gyrotron-TWT/backward-wave



beams, CARMs, FELs, Gyrotron-TWT/backward-wave oscillators, and other highpower microwave devices.

Wenlong He received the B.Sc. degree in physics from Suchow University, Jiangsu, China, in 1983, the M.Sc. degree in accelerator physics from the China Academy of Engineering Physics, Chengdu, China, in 1988, and the Ph.D. degree in relativistic electron beams and masers from the Department of Physics, University of Strathclyde, Glasgow, U.K., in 1995.

He is currently a Senior Research Fellow with the Scottish Universities Physics Alliance, Department of Physics, University of Strathclyde. His main research interests include relativistic electron



Kevin Ronald was born in Glasgow, U.K. He received the B.Sc. (with honors) and Ph.D. degrees in physics from the University of Strathclyde, Glasgow, U.K., in 1992 and 1997, respectively.

He is currently a Lecturer with the Scottish Universities Physics Alliance, Department of Physics, University of Strathclyde.



Alan D. R. Phelps was born in the U.K. in 1944. He received the B.A. degree (with honors) in physics and the M.A. degree from Cambridge University, Cambridge, U.K., in 1966 and 1970, respectively, and the D.Phil. degree for plasma research from Oxford University, Oxford, U.K., in 1970.

He has been with the University of Strathclyde, Glasgow, U.K., since 1978, where he initially founded a research group, became a Full Professor in 1993, and is currently with the Scottish Universities Physics Alliance, Department of Physics, where he

was the Head of the department from 1998 to 2001. His research interests include high-power free-electron radiation sources and plasmas.

Dr. Phelps is a Fellow of the Institute of Physics and of the Royal Society of Edinburgh.



Colin G. Whyte was born in Selkirk, U.K., in 1969. He received the B.Sc. degree in physics from the University of Glasgow, Glasgow, U.K., in 1991 and the M.Sc. degree in laser physics and pulsed-power technology and the Ph.D. degree in physics from the University of St Andrews, St Andrews, U.K., in 1992 and 1996, respectively.

He has been with the University of Strathclyde, Glasgow, U.K., since 1996 in the ABP Group, Department of Physics, where he is also currently with SUPA. His research interests include the design and

experimental investigation of high-power broadband microwave amplifiers and oscillators, including novel helical gyro-TWT devices and reverse-guide-field free-electron lasers. He also designs and builds high-voltage pulsed-power supplies.



Craig W. Robertson was born in Ayrshire, U.K., in 1977. He received the B.Sc. (with honors) degree in physics and the Ph.D. degree from the University of Strathclyde, Glasgow, U.K., in 1999 and 2004, respectively.

He is currently with SUPA, Department of Physics, University of Strathclyde. His interests include low-temperature plasma production and diagnostics, as well as high-power microwave sources.



Alan R. Young received the B.Sc. degree in physics, the M.Sc. degree in information technologies systems, and the Ph.D. degree, with a dissertation on high-quality electron beams for CARMs, from the University of Strathclyde, Glasgow, U.K., in 1993, 1994, and 1998, respectively.

He has since continued to work as a Research Fellow with the Department of Physics, University of Strathclyde, on a variety of gyro-devices, including CARM and gyro-TWT, where he is also currently with SUPA.



Craig R. Donaldson received the B.Sc. (with honors) degree in physics, the M.Sc. degree in high power RF and the Ph.D. degree in physics from the University of Strathclyde, Glasgow, U.K., in 2005, 2006, and 2009, respectively.

He is currently with SUPA, Department of Physics, University of Strathclyde. His main research interests include electron-beam generation, gyro-TWT/BWOs, and helically corrugated waveguides.



Adrian W. Cross received the B.Sc. degree (with honors) in physics and the Ph.D. degree from the University of Strathclyde, Glasgow, U.K., in 1989 and 1993, respectively.

He joined the Atoms, Beams, and Plasmas Group, University of Strathclyde, in 1993 initially as a Research Fellow and then as a Lecturer in 2000, Senior Lecturer in 2005, and is now a Reader with the Department of Physics. From 2002 to 2007, he was an Engineering and Physical Science (EPSRC) Advanced Fellow. He has been involved in various aspects of research on gyrotrons, cyclotron autoresonance masers, free-electron lasers, superradiant sources, gyrotron travelling wave amplifiers and plasma applications. More recently, he has primarily been concerned with research on microwave pulse compression, THz radiation sources and pseudospark physics.

W-band Gyro-BWO with a Four-stage Depressed Collector

Liang Zhang*, Wenlong He, Craig R. Donaldson, Adrian W. Cross, Alan D. R. Phelps, Paul McElhinney and Kevin Ronald

SUPA, Department of Physics, University of Strathclyde, Glasgow, G4 0NG, Scotland, UK

*Email: liang.zhang@strath.ac.uk

Abstract: An energy recovery system using a four-stage depressed collector was simulated and designed to improve the overall efficiency of the W-band gyrotron backward wave oscillator (gyro-BWO) at the University of Strathclyde. The spent beam information was exported from the simulation of the gyro-BWO using the 3D PIC code MAGIC. The geometry of the depressed collector was optimized using a genetic algorithm to achieve the optimum overall recovery efficiency for specific parameters of the spent beam. Secondary electron emissions and their effects on the recovery efficiency and the backstreaming of the electrons from the collector region were simulated. The heat power distribution on the electrodes was also simulated to avoid the “hot spot”.

Keywords: Gyro-BWO, Depressed collector, Energy recovery, Secondary electron emission.

1. INTRODUCTION

Gyro-BWOs are gyrodevices based on the electron cyclotron maser instability. They are with wide frequency tuneability and high power capability from the microwave to terahertz frequency range. The gyro-BWOs have attracted many interests for their potential applications such as radar, communication, and plasma diagnostics. Gyro-BWOs based on helically corrugated waveguides can achieve even wider frequency tuning range and higher efficiency. The helically corrugated waveguide couples two modes in the circular waveguide to generate a new operating eigen-mode which has large group velocity in low axial wavenumber range to make it less sensitive to the electron beam energy[4]. Gyro-BWOs based on helically corrugated waveguides have demonstrated excellent results in X-band and Ka-band [1-3]. A W-band gyro-BWO currently being built at the university of Strathclyde was predicted to have a 3 dB frequency bandwidth of 84–104 GHz, output power of 10 kW with an electronic efficiency of 17% [5, 6].

The gyro-BWOs suffer slightly lower interaction efficiency when comparing with the gyromonotron and gyroklystron. In gyro-BWOs, the amplitude of the RF field increases as the RF wave traveling to the entrance. In the entrance, the amplitude of RF field reaches its maximum and it causes an abrupt electron bunching, while the RF field is weak in the exit of the interaction region resulting in a weak beam-wave interaction. The electrons lose less energy to the wave and the efficiency is low. Several methods have been developed to improve the efficiency of beam-wave interaction. One is to change the profile of the waveguide, such as employing slot structure [7], helical structure [1-6] and slice structure [8]. The other way is using tapered magnetic field or tapered wall radius instead of the constant ones [9, 10]. However, once the electronic tube has been established, the electronic efficiency would be fixed too. Another way to increase the overall efficiency is to recover energy using single or multi-stage depressed collectors from the spent beam. It has been proved that it is an efficiency way to improve the overall efficiency of microwave tubes, such as conventional klystrons, BWOs and TWTs [11, 12].

However, it is still a challenge to employ multi-stage depressed collectors in gyrotron devices as the electrons always have large transverse velocity which makes them hard to be sorted.

In this paper, an energy recovery system using multi-stage depressed collectors to recover the energy from the spent beam was designed for a W-band gyro-BWO. This gyro-BWO was based on the helically corrugated waveguide and a cusp electron gun. The experimental setup and the schematic of the W-band gyro-BWO are shown in Fig. 1 and Fig. 2. The cusp electron gun was designed to produce an axis-encircling annular beam of 40 kV, 1.5 A with a beam alpha of 1.65 [13-15]. The microwave radiation was generated in the helically corrugated interaction region and then the spent electron beam entered into the collection region. To extract the radiation out of the interaction region, a side-wall coupler that achieves a good transmission over the operating frequency range was designed and placed at the upstream of the interaction region. A Bragg reflector acting as a microwave short in the operating frequency range at the end of the helical waveguide, was used to reflect the radiation back into the interaction region.

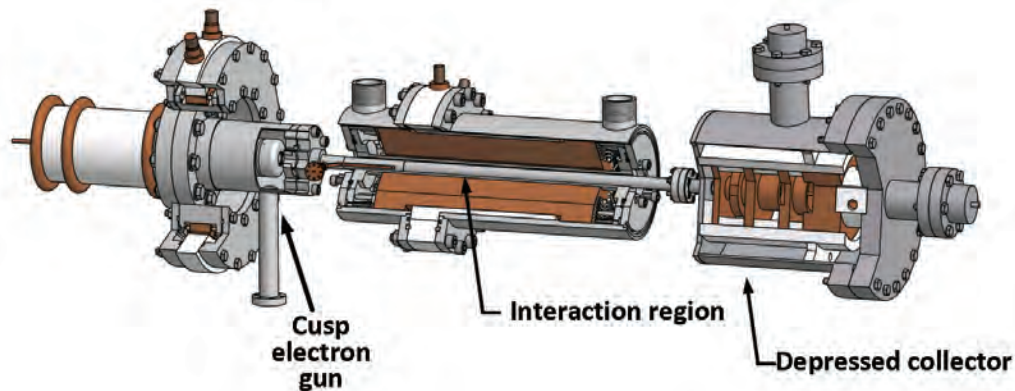


Fig. 1 The experimental setup of the W-band gyro-BWO.

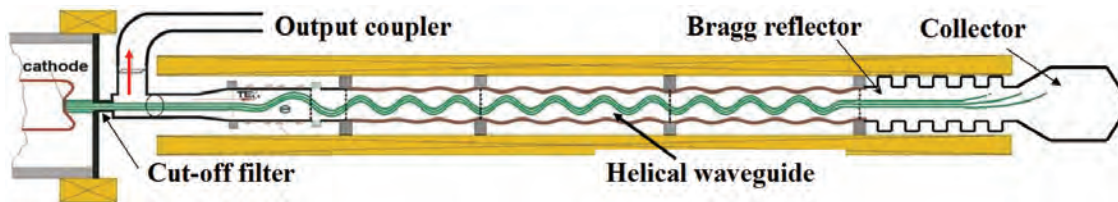


Fig. 2 The schematic of the W-band gyro-BWO.

2. PRINCIPLE OF THE DEPRESSED COLLECTOR

Depressed collectors are passive converters that can transfer the kinetic energy of the spent electrons into potential electric energy. “Depressed” means that the collector has a depressed potential as compared with the main body of the tube. The electrons lose their kinetic energy when passing through the retarding electrostatic field and finally land on the collector surface with a significant reduction in kinetic energy. They produce a loop current which results in a

power recovery from the spent electrons. The collected power by a depressed collector can be written as

$$P_{col} = \sum_n V_n I_n \quad (1)$$

where n is the number of stages and V_n, I_n are potentials and collected current on the n th-stage electrode, respectively. By introducing a depressed collector with a collection efficiency of η_{col} , the overall efficiency of the microwave tube η_{tot} with an electronic efficiency η_e can be calculated using

$$\eta_{tot} = \frac{P_{out}}{P_b - P_{col}} = \frac{\varepsilon_{out} \eta_e}{1 - \eta_{col}(1 - \eta_e)} \quad (2)$$

where ε_{out} , the output efficiency, is the ratio of the output microwave power and generated microwave power in the cavity. For those inherently low efficiency high power microwave devices, depressed collectors with efficiencies higher than 80% can significantly improve the overall efficiencies. For a moderately efficient source with an electronic and collection efficiency of 30% and 80%, respectively, with the use of depressed collection the overall efficiency could be increased to 61.4% when $\varepsilon_{out} = 0.9$, increasing the overall efficiency by a factor of 2.

3. SIMULATION OF THE DEPRESSED COLLECTOR

The design of a depressed collector involves several issues like determining the potentials and the geometry of the electrodes to reach the optimum collection efficiency, the effect of the secondary electrons and the heat distribution on the electrodes.

The collection efficiency of a depressed collector is mainly dependent on the potentials on the electrodes and the geometry of the electrodes. When specifying a stage number, the optimum potentials on the electrodes can be evaluated by the energy distribution of the spent electron beam which was exported from the simulation of the gyro-BWO using the 3D PIC code MAGIC. It should be noted that, in the calculation, it was assumed that all the electrons were collected on the electrodes without consideration of secondary emissions. To avoid backstreaming, the minimum electrode potential was set to be the minimum energy of electrons, and the maximum potential was set to be the electron beam voltage which was 40 kV in the considered W-band gyro-BWO. The energy distribution of the spent electron beam is shown as Fig. 3 and the collection efficiency at different stage number is shown in Table 1.

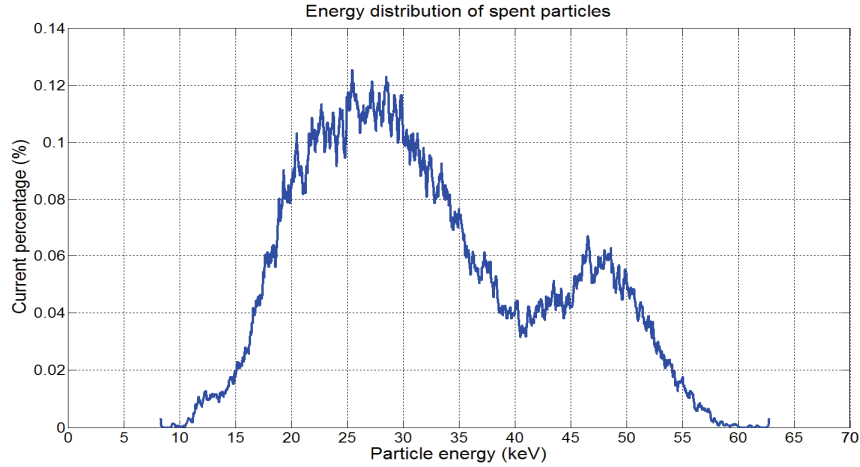


Fig. 3 The energy distribution of the spent electron beam

Tab. 1 Collection efficiency at different stage number

No.	Potentials on electrodes (kV) (relative to ground voltage)							Collection efficiency
1	-9.24	-----	-----	-----	-----	-----	-----	28.8%
2	-9.24	-25.70	-----	-----	-----	-----	-----	63.6%
3	-9.24	-22.14	-36.57	-----	-----	-----	-----	75.7%
4	-9.24	-19.55	-27.31	-40.00	-----	-----	-----	82.5%
5	-9.24	-18.86	-24.96	-30.78	-40.00	-----	-----	85.7%
6	-9.24	-16.98	-22.14	-27.22	-32.66	-40.00	-----	87.5%
7	-9.24	-16.82	-21.33	-25.47	-29.53	-34.23	-40.00	88.7%

The depressed collectors with different geometries of the electrodes were simulated by 3D PIC code MAGIC and the parameters for the geometries were optimized by the genetic algorithm. A detail description of the simulation flow chart can be found in paper [16]. In the optimization, the evaluation function was chosen as

$$\eta_{eva} = \eta_{col} - W\eta_{back} \tag{3}$$

where η_{back} was the percentage of the backstreaming electrons, and W was the weight. In the simulation, W was chosen as 1.5. The optimization was run with the magnetic field of 1.75 T and an optimum collection efficiency of 78.7% was achieved. It was 3.8% lower than the ideal collection efficiency which assumes all the spent electrons were sorted perfectly. That was because not all the electrons were collected by the electrodes and a small proportion were observed to become backstreaming in the simulation. The trajectories of the spent electrons are shown in Fig. 4.

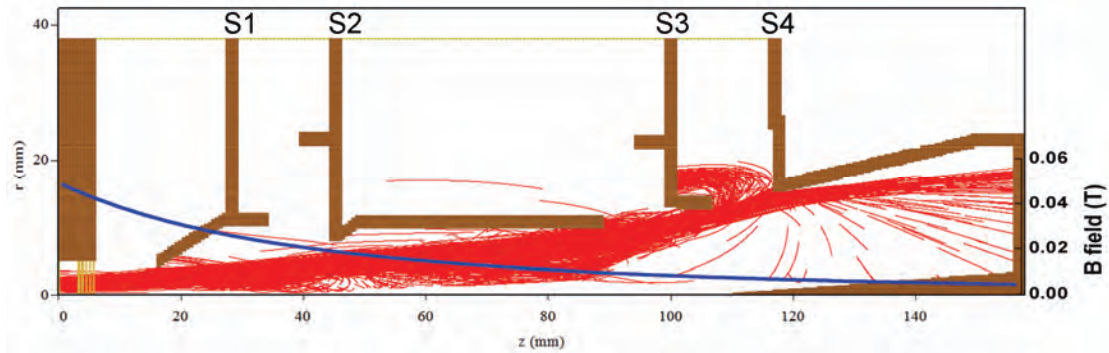


Fig. 4 The trajectories of the spent electron beam.

The secondary electrons have several negative effects on high power microwave devices. First of all, secondary electrons carrying velocities with opposite direction to the primaries will be accelerated by the electrostatic field in the collection region and some of them will become backstreaming. The secondary electrons absorb energy from the electrostatic field and decrease the collection efficiency. Secondly, the backstreaming entered into the RF interaction region, which will generate noise on the microwave output and decrease the performance of the microwave tube. Thirdly, in high average power devices, the backstreaming may contribute an additional thermal power on the thermally stressed waveguide structure. Thus in depressed collectors, it is essential to reduce the current of secondary electrons to be as low as possible. Secondary electrons are generally divided into two classes. The first class is the true secondary electrons (TSEs) which are knocked out from the surface of the material due to the bombardment of the primary electrons. The other class is the backscattered electrons (BSEs) including the re-diffused electrons and the elastic scattering electrons.

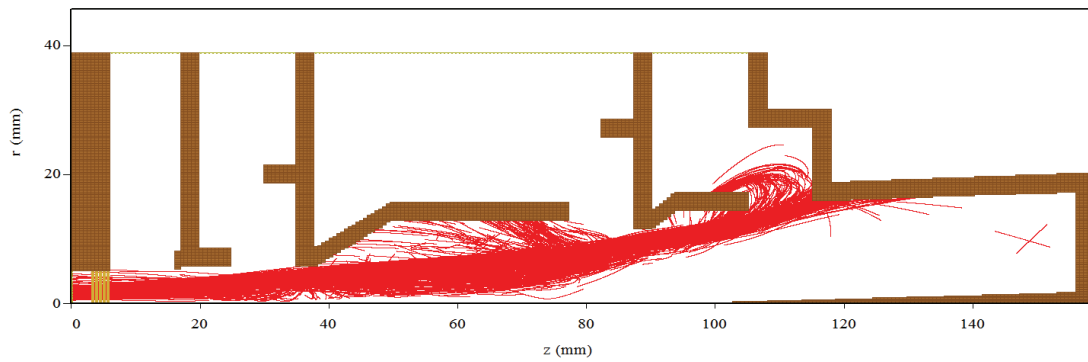
Secondary electron emission models were applied in the simulation of the depressed collector to investigate the effect of the secondary electrons. The TSE yield function in MAGIC is based on that by Thomas [17]. However, MAGIC also allows users to define their own SEY functions and the energy distribution function for TSEs by using the command “EMISSION SECONDARY.” In our simulation, different formulas were tested including the Vaughan’s [18], Furman’s [19] and Thomas’s equations and the effect on the collection efficiency was studied.

The scattering process of the BSEs in MAGIC is carried out by the ITS code. The “BACKSCATTER” option in MAGIC allows ITS to be invoked automatically to simulate the emission of both the rediffused and backscattered elastic electrons. The TSE and BSE models used in the MAGIC simulations were discussed in detail in the paper [20]. Table 2 is a summary of the simulation results with consider different TSE models and the BSEs. The optimum geometry of the four-stage depressed collector as well as the trajectories of the primary electron, true secondary electrons and the backscattered electrons is shown in Fig. 5.

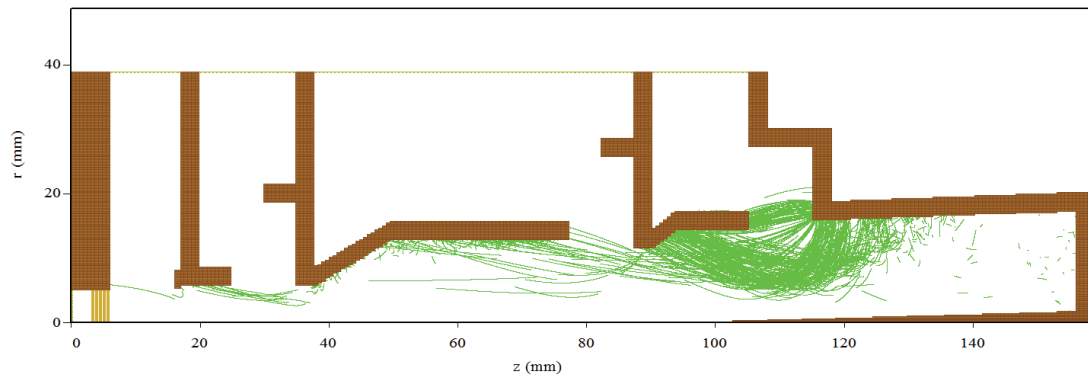
The collection efficiencies and the backstreaming rate of the W-band gyro-BWO were simulated in the whole frequency tuning range by the optimized configuration of the designed four-stage depressed collector. The collection efficiencies achieved were about 70% and the backstreaming rate was lower than 7% in the working frequency band. Thus an overall efficiency of 40% can be achieved.

Tab. 2 Collection efficiency at different stage number.

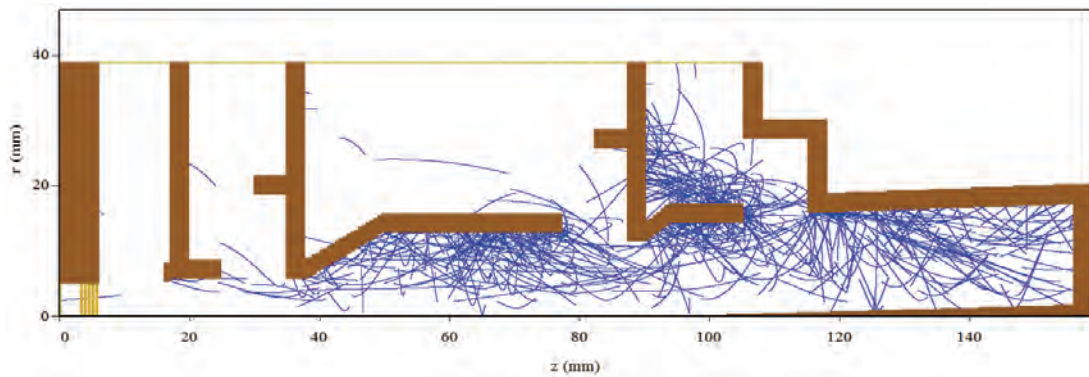
Cases	TSE model	Collection efficiency	Percentage of backstreaming
without TSEs, without BSEs	-----	75.7%	4.79%
with TSEs, without BSEs	Vaughan	71.1%	4.79%
	Furman	68.9%	4.80%
	Thomas	73.0%	4.80%
without TSEs, with BSEs	-----	73.9%	4.89%
with TSEs, with BSEs	Vaughan	69.0%	4.89%
	Furman	66.8%	4.91%
	Thomas	71.0%	4.90%



(a) Trajectories of the primary electrons.



(b) Trajectories of the true secondary electrons.



(c) Trajectories of the backscattered electrons.

Fig. 5 Trajectories of the electrons in the depressed collector (using Vaughan's formulas).

The heat power dissipation on the electrodes is another important issue in designing the depressed collector. Although the kinetic energy of the spent electrons reduced significantly when they passed through the retarded electric field, the heat due to the power of the remaining kinetic energy of the spent electrons when they struck the surface of the electrodes was still large, for our case, it could be up to 20 keV. The spent electrons with such high kinetic energy could damage the surface of electrodes in the form of a “hot spot” and could reach the thermal stress threshold of the collector material.

To design effective cooling system for the collector electrodes, the distribution of the heat power dissipated on the surface of the electrodes needs to be evaluated. In MAGIC, there is no straightforward way to get the heat power on the electrodes directly. However, it provides a command “OBSERVE COLLECTED POWER” to observe the overall heat dissipation on a conductor. To obtain the heat power distribution on the surface of the electrodes, the electrodes were divided into a large number of small conductors both in the azimuthal direction and the z direction and the heat power dissipated in each of these conductors was individually measured, thus an approximate heat power distribution was obtained. The heat power densities on the conductors calculated from the collected electric power and the area of the conductors. In the simulation, the maximum heat density was $\sim 240\text{W}/\text{cm}^2$. It is lower than the thermal stress threshold of the copper material thus the generation of “hot spots” can be avoided.

Reference

- [1] W. He, K. Ronald, A. R. Young, A. W. Cross, A. D. R. Phelps, C. G. Whyte, E. G. Rafferty, J. Thomson, C. W. Robertson, D. C. Speirs, S. V. Samsonov, V. L. Bratman, and G. G. Denisov, “Gyro-BWO experiments using a helical interaction waveguide”, *IEEE Trans. Electron Devices*, 52, 5, 839–844 (2005).
- [2] W. He, A. W. Cross, A. D. R. Phelps, K. Ronald, C. G. Whyte, S. V. Samsonov, V. L. Bratman, and G. G. Denisov, “Theory and simulations of a gyrotron backward wave oscillator using a helical interaction waveguide”, *Appl. Phys. Lett.*, 8, 091504 (2006).

- [3] V. L. Bratman, G. G. Denisov, V. N. Manuilov, S. V. Samsonov, and A. B. Volkov, "Development of helical-waveguide gyro-devices based on low-energy electron beams", *Int. Conf. Infrared and Millimeter Waves, France*, 5–105 (2001).
- [4] Gregory G. Denisov, Vladimir L. Bratman, Alan D. R. Phelps, and Sergei V. Samsonov, "Gyro-TWT with a Helical Operating Waveguide: New Possibilities to Enhance Efficiency and Frequency Bandwidth", *IEEE Trans. Plasma Sci.*, 26, 3, 508-518 (1998).
- [5] W. He, C. R. Donaldson, F. Li, L. Zhang, A. W. Cross, A. D. R. Phelps, K. Ronald, C. W. Robertson, C. G. Whyte, and A. R. Young, "W-band gyro-devices using helically corrugated waveguide and cusp gun: design, simulation and experiment", *T. S. T.*, 4, 9-19 (2011).
- [6] W. He, C. R. Donaldson, L. Zhang, K. Ronald, A. D. R. Phelps, and A. W. Cross, "Numerical Simulation of a Gyro-BWO with a Helically Corrugated Interaction Region, Cusp Electron Gun and Depressed Collector", *Numerical Simulations / Book 2*, Intech publisher (2011).
- [7] N. C. Chen, C. F. Yu, and T. H. Chang, "A TE₂₁ Second-harmonic Gyrotron Backward-wave Oscillator with Slotted Structure", *Phys. Plasmas*, 14, 123105 (2007).
- [8] Q. S. Wang, D. B. McDermott, and N. C. Luhmann, "Demonstration of Marginal Stability Theory by a 200-kW Second-Harmonic Gyro-TWT Amplifier", *Phys. Rev. Lett.*, 75, 4322 (1995).
- [9] G. S. Nusinovich, and O. Dumbrajs, "Theory of gyro-backward wave oscillators with tapered magnetic field and waveguide cross section", *IEEE Trans. Plasma Sci.*, 24, 3, 620-629 (1996).
- [10] Mark T. Walter, Ronald M. Gilgenbach, John W. Luginsland, Jonathan M. Hochman, J. I. Rintamaki, Reginald L. Jaynes, Y. Y. Lau, and Thomas A. Spencer, "Effects of tapering on gyrotron backward-wave oscillators", *IEEE Trans. Plasma Sci.*, 24, 3, 636-647 (1996).
- [11] W. Neugebauer, and T. G. Mihran, "A ten-stage electrostatic depressed collector for improving klystron efficiency", *IEEE Trans. Electron Devices*, 19, 1, 111- 121 (1972).
- [12] J. D. Wilson, E. G. Wintucky, K. R. Vaden, D. A. Force, I. L. Krainsky, R. N. Simons, N. R. Robbins, W. L. Menninger, D. R. Dibb, and D. E. Lewis, "Advances in Space Traveling-Wave Tubes for NASA Missions", *Proceedings of the IEEE*, 95, 10, 1958-1967 (2007).
- [13] W. He, C. G. Whyte, E. G. Rafferty, A. W. Cross, A. D. R. Phelps, K. Ronald, A. R. Young, C. W. Robertson, D. C. Speirs, and D. H. Rowlands, "Axis-encircling electron beam generation using a smooth magnetic cusp for gyrodevices", *Appl. Phys. Lett.*, 93, 121501 (2008).
- [14] C. R. Donaldson, W. He, A. W. Cross, A. D. R. Phelps, F. Li, K. Ronald, C. W. Robertson, C. G. Whyte, A. R. Young, and L. Zhang, "Design and numerical optimization of a cusp-gun-based electron beam for millimeter-wave gyro-devices", *IEEE Trans. Plasma Sci.*, 37, 2153–2157 (2009).
- [15] C. R. Donaldson, W. He, A. W. Cross, F. Li, A. D. R. Phelps, L. Zhang, K. Ronald, C. W. Robertson, C. G. Whyte, and A. R. Young, "A Cusp Electron Gun for Millimeter Wave Gyro-Devices", *Appl. Phys. Lett.*, 96, 141501 (2010).
- [16] L. Zhang, W. He, A. W. Cross, A. D. R. Phelps, K. Ronald, and C. G. Whyte, "Design of an energy recovery system for a gyrotron backward-wave oscillator", *IEEE Trans. Plasma Sci.*, 37, 3, 390-394 (2009).
- [17] MAGIC User's Manual, *Mission Res. Corp.*, Newington, VA (2002).

- [18] M. Vaughan, "Secondary emission formulas", *IEEE Trans. Electron Devices*, 40, 4, 830 (1993).
- [19] M. A. Furman and M. T. Pivi, "Probabilistic Model for the Simulation of Secondary Electron Emission", *Phys. Rev. ST Accel. Beams*, 5, 12, 124404 (2002).
- [20] L. Zhang, W. He, A. W. Cross, A. D. R. Phelps, K. Ronald, and C. G. Whyte, "Numerical Optimization of a Multistage Depressed Collector With Secondary Electron Emission for an X-band Gyro-BWO", *IEEE Trans. Plasma Sci.*, 37, 12, 2328-2334 (2009).

Design of an Energy Recovery System for a Gyrotron Backward-Wave Oscillator

Liang Zhang, Wenlong He, Adrian W. Cross, Alan D. R. Phelps, Kevin Ronald, and Colin G. Whyte

Abstract—To realize the full potential of a gyrotron backward-wave oscillator (gyro-BWO), an energy recovery system was designed using Particle-In-Cell (PIC) simulations and optimized using both a genetic algorithm and PIC simulations. Simulations were carried out to optimize a periodic structure for separation of the spent electron beam and the output radiation produced by a gyro-BWO in the 8.0–9.5 GHz frequency range. The spent electron beam can be collected using a multistage depressed collector. The number and electric potentials of the electrodes were optimized to achieve the best overall recovery efficiency for specific parameters of the spent beam. The 3-D PIC code MAGIC was used to simulate the electrons' trajectories and a genetic algorithm was used to refine the electrode shapes for optimum efficiency.

Index Terms—Depressed collector, energy recovery, genetic algorithm, gyrotron backward-wave oscillator (gyro-BWO).

I. INTRODUCTION

GYROTRON backward-wave oscillators (gyro-BWOs) are gyrodevices based on the electron cyclotron maser instability [1]. They can be used in applications such as high-resolution radar, plasma heating, high-energy accelerators, and deep-space communication. The main advantage of gyro-BWOs is their wide frequency tunability. They also promise high-power capability in the millimeter and submillimeter ranges.

Theoretical studies of the gyro-BWO first appeared in the mid-1960s, and experiment results have been published. Gyro-BWO operation in the Ka-band (26.5–40 GHz) at a maximum power of 113 kW at ~19% efficiency was demonstrated [2]. The experimental study of a Ku-band (12–18 GHz) gyro-BWO with a single-stage depressed collector achieved a maximum power of 48 kW with an efficiency of 21% [3].

Research of gyro-BWOs based on a helically corrugated waveguide demonstrated excellent results in achieving high-power and wide frequency tunability. As predicted in the study of a W-band (75–110 GHz) gyro-BWO, it is possible to increase the frequency-tuning band to more than 20% [4]. A Ka-band gyro-BWO operating at the second cyclotron harmonic was reported, with maximum output power of about 1 MW, 10% efficiency, and 15% frequency-tuning range [5]. In 2005, an

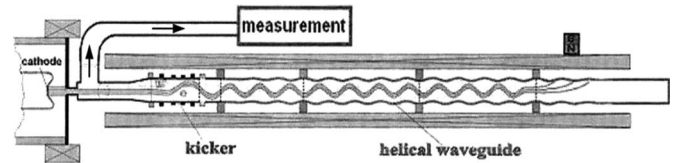


Fig. 1. Gyro-BWO experimental setup [5].

X-band (7–12.5 GHz) gyro-BWO, with a helically corrugated interaction waveguide, achieved a frequency-tuning band of 17% and 16.5% electronic efficiency [6]. Two ways can be used to improve the microwave tube efficiency. One is to improve the electronic efficiency of the beam–wave interaction, such as by introducing a tapered magnetic field [7]. Another way is to recover the energy of the spent beam, which is lost in processes such as heating of the walls of the collection region [8], [9], using single- or multistage depressed collectors. To increase the overall efficiency of a gyro-BWO device, an energy recovery system using a depressed collector has been designed to recover the energy of the spent electron beam, and this design is presented in this paper. In this device, a solid axis-encircling beam (so-called large-orbit beam) was used for the beam–wave interaction. The design methodology of the depressed collector could be applied to other gyrodevices, either using a large-orbit beam or a beam produced by a magnetron injection gun.

The basic diagram of the X-band gyro-BWO experimental setup is shown in Fig. 1. A reduced radius reflector, acting as a microwave short at the output end of the device, can be used to reflect the radiation back into the system; the backward propagating microwaves can then be extracted using a waveguide coupler. The spent electrons propagating in the opposite forward direction, on exiting the focusing solenoid field, strike the waveguide surface and dissipate their kinetic energy as heat.

To recover the energy from the spent beam of the X-band gyro-BWO shown in Fig. 1, instead of using a short at the output of the device, a Bragg reflector can be used to reflect the microwave radiation back into the system, while the spent electrons continue to propagate in the forward direction to the collection region. After the Bragg reflector, a three-stage depressed collector was designed to recover the energy from the spent electrons. A genetic algorithm was used to optimize the geometry to achieve optimum recovery efficiency.

II. BRAGG REFLECTOR

Extensive theoretical and experimental research indicated that a near unity reflection could be achieved by a Bragg

Manuscript received August 26, 2008; revised October 14, 2008 and November 29, 2008. Current version published March 11, 2009. This work was supported in part by the Scottish Universities Physics Alliance (SUPA) and in part by the Overseas Research Students Awards Scheme (ORSAS).

The authors are with the Scottish Universities Physics Alliance, Department of Physics, University of Strathclyde, G4 0NG Glasgow, U.K. (e-mail: liang.zhang@strath.ac.uk).

Color versions of one or more of the figures in this paper are available online at <http://ieeexplore.ieee.org>.

Digital Object Identifier 10.1109/TPS.2008.2012108

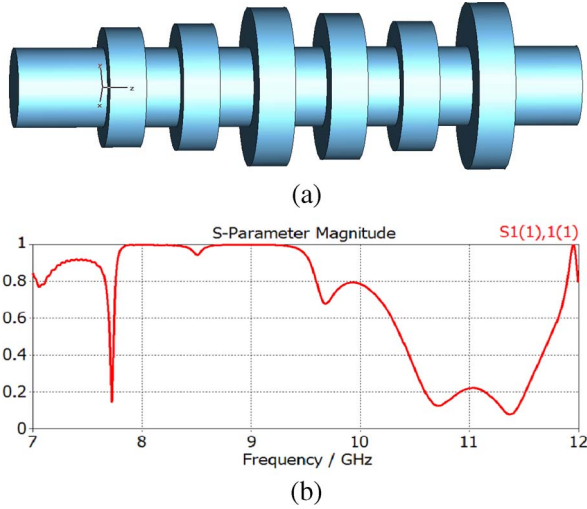


Fig. 2. (a) Geometry of a six-period Bragg reflector. (b) Simulated S_{11} parameter.

reflector composed of a cylindrically symmetric corrugated structure [10]. In this application, a high reflection was desired in the gyro-BWO's frequency-tuning range of 8.0–9.5 GHz. The total length of the reflector should be as short as possible to reduce the length and, hence, the driving power of the solenoid required for beam–wave interaction.

A genetic algorithm was used to optimize the corrugated depths of the reflector in a CST microwave studio. A Visual Basic for Applications script was developed to control the simulation process, such as the determination of the dimensions, simulation, and the evaluation of the S_{11} parameter for a given geometry. The period of the reflectors was fixed at 12.4 mm, and reflectors with a different number of periods were simulated. The final geometry of the reflector and the corresponding S_{11} magnitude are shown in Fig. 2.

The Bragg reflector was then transferred to a MAGIC model of an X-band helically corrugated gyro-BWO. From the numerical simulation results, the average microwave output power was 33.0 kW, while the power observed at the end of the reflector was 0.4 kW under the condition of an electron beam voltage of 185 kV, beam current of 3 A, and cavity magnetic field of 0.20 T. About 98.8% of the microwave power was reflected back into the beam–wave interaction region.

III. OPTIMUM POTENTIAL ON DEPRESSED COLLECTOR

After the reflector, the spent electrons then entered the depressed collector. “Depressed” means that the collector has a depressed potential compared with the main body of the tube. The electrons lost their kinetic energy when passing through the retarding electrostatic field and finally landed on the collector surface, with a significant reduction in kinetic energy. They produced a loop current which results in power recovery from the spent electrons [11].

The power recovered by the depressed collectors is defined as

$$P_{\text{col}} = \sum_n V_n I_n. \quad (1)$$

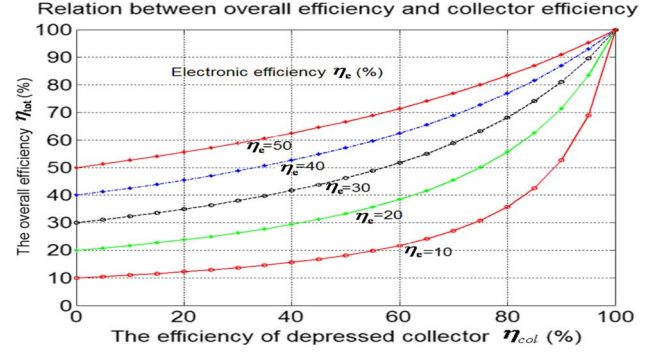


Fig. 3. Overall device efficiency as a function of collector efficiency at different electronic efficiencies.

Here, n is the number of stages, and V_n and I_n are the potentials and collected current on the n th-stage electrode, respectively. For a given energy distribution of the spent electrons, increasing the number of stages resulted in the collection of more power. However, the design of depressed collectors becomes more complex, and the cost increases as the number of stages increases.

The electronic efficiency for a microwave tube is defined as

$$\eta_e = P_{\text{mw}}/P_b \quad (2)$$

where P_{mw} is the generated microwave power and the beam power P_b can be expressed as $P_b = U_b I_b$, where U_b is the beam voltage and I_b is the beam current. The remaining power of the spent beam is given by $P_{\text{spent_beam}} = P_b - P_{\text{mw}}$ if other power losses, such as the ohmic wall loss from the beam loading, are neglected.

The collection efficiency η_{col} for a depressed collector is defined as

$$\eta_{\text{col}} = P_{\text{col}}/P_{\text{spent_beam}}. \quad (3)$$

Due to the intrinsic RF losses, such as the ohmic wall losses and stray radiation, the output microwave power is determined by the generated microwave power and the output efficiency ε_{out}

$$P_{\text{out}} = P_{\text{mw}} \cdot \varepsilon_{\text{out}}. \quad (4)$$

It is suggested that the RF losses are between 10% and 15%, which, in practice, means that $\varepsilon_{\text{out}} = 0.85 \sim 0.9$.

By introducing a depressed collector with a collection efficiency of η_{col} , the overall efficiency of the microwave tube η_{tot} , with an electronic efficiency η_e , can be calculated using

$$\eta_{\text{tot}} = \frac{P_{\text{out}}}{P_b - P_{\text{col}}} = \frac{\varepsilon_{\text{out}} \eta_e}{1 - \eta_{\text{col}}(1 - \eta_e)}. \quad (5)$$

The relation between the overall efficiency and the collection efficiency is shown in Fig. 3 ($\varepsilon_{\text{out}} = 0.9$). For those inherently low efficiency high-power microwave devices, depressed collectors with efficiency higher than 80% can significantly improve the overall efficiency.

In the design of the energy recovery system, at the end of the Bragg reflector, the energy distribution of the spent beam was exported from the simulation of the gyro-BWO using the

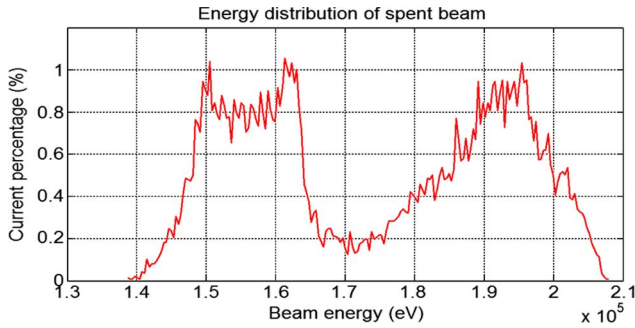


Fig. 4. Energy distribution of the spent electrons before entering into the energy recovery system.

TABLE I
COLLECTION EFFICIENCY AT DIFFERENT STAGE NUMBERS

No.	Potentials on electrodes (kV) (Comparing with ground voltage)					Col. Eff.
1	-138.9	----	----	----	----	79.8%
2	-138.9	-158.7	----	----	----	90.5%
3	-138.9	-158.1	-179.1	----	----	93.8%
4	-138.9	-153.3	-164.0	-183.4	----	95.1%
5	-138.9	-150.8	-159.3	-169.6	-185.0	96.0%

(Col. Eff. = Collection efficiency)

3-D PIC code MAGIC, as shown in Fig. 4. Table I shows the optimum potentials and the collection efficiency when different numbers of stages are used. In this calculation, it was assumed that all the electrons were collected on the electrodes without consideration of secondary emissions. The minimum electrode potential was set to be the minimum energy of electrons to avoid backstreaming, and the maximum potential was set to be the electron beam voltage which was 185 kV in the gyro-BWO device. It was found that when the stage number increased beyond three stages, the collection efficiency did not significantly increase. The number of stages was therefore chosen to be three, as a compromise between the collection efficiency and the complexity of the system.

To keep the electrodes at the designed potentials, high-voltage dc power supplies should be used. The spent electrons landing on the electrodes can be considered as the loads of the dc power sources. Fluctuations of the collected beam currents would give rise to the change of the potentials due to limited output impedances of the supplies and cause the collection efficiency to change. Fig. 5 shows the collector efficiency influenced by potential fluctuation on the electrodes in the three-stage case. When the potential fluctuation was limited to the $\pm 5\%$ range, the change in collection efficiency was less than 3%. However, the collection efficiency decreased rapidly when the potential fluctuation exceeded 5%, particularly on the first electrode.

IV. OPTIMIZED ELECTRODE GEOMETRY

The collection efficiency calculated in Section III assumed that all the spent electrons were sorted by the electric and magnetic fields in the collection region. The electrode geometry is important to the collection efficiency. Proper design of the

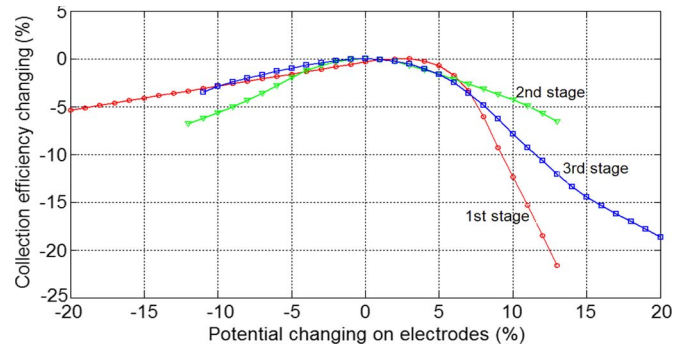


Fig. 5. Collection efficiency as a function of potential fluctuation on each electrode.

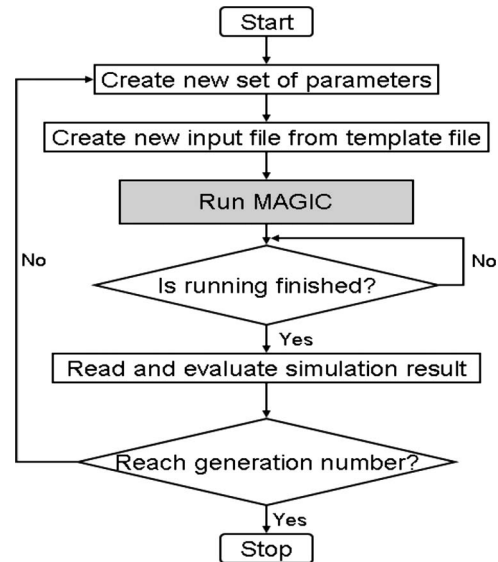


Fig. 6. Flow diagram of the optimization program.

electrode geometry not only acts to sort electrons with different kinetic energies, to decrease the possibility of secondary emission, and to avoid the backstreaming of the electrons in the collector. A 3-D PIC code was used to simulate the gyro-BWO with a helically corrugated waveguide because of the asymmetric structure. The parameters of the spent electrons exported from the simulation of the gyro-BWO were used as the input to the 3-D PIC code used to simulate the depressed collector, and therefore, the simulation of the depressed collector was also in 3-D. Simulation in 3-D would also allow for the design of asymmetrical electrodes for the reduction of the possible backstreaming electrons. One way to choose a better geometry is to use a searching algorithm, such as a random walk, and a genetic algorithm to optimize the parameters [12]. An optimization program integrating a genetic algorithm was developed to optimize the depressed geometry parameters by controlling the 3-D PIC code MAGIC without the need to know the source code. The optimization program first created an input file by filling the new set of parameters to the template input file for MAGIC. Then, MAGIC was invoked to simulate the new geometry, and the result was read by the optimization program to evaluate the parameters. The flow diagram of this process is shown in Fig. 6.

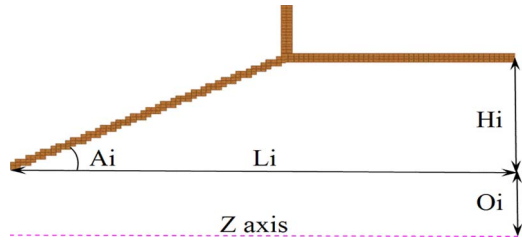


Fig. 7. Basic geometry of an electrode.

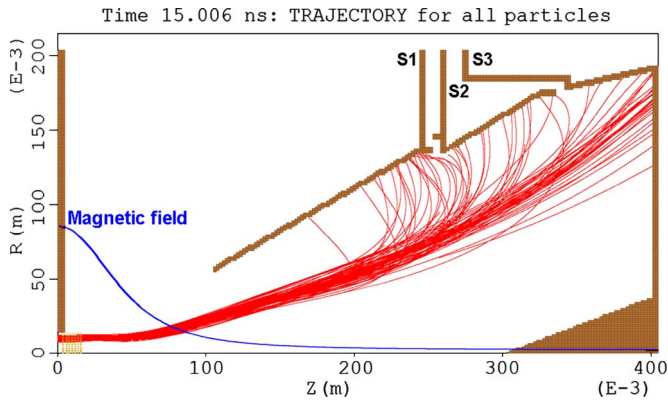


Fig. 8. Full geometry of a three-stage depressed collector.

The basic geometry of an electrode is shown in Fig. 7. It is determined completely by four parameters, namely, the length of the electrode (L_i), the height of the electrode (H_i), the offset from the Z -axis (O_i), and the tilt angle (A_i). There should be 12 parameters in a three-stage collector. However, the outer radius of the depressed collector was restricted to be 200 mm, and the overall length was restricted to be 400 mm. Thus, ten parameters were to be optimized. Before the optimization, many simulations were carried out to find a proper range for each parameter to ensure that the searching range was as small as possible. For example, the O_i for the first electrode was set from 24 to 70, mm and the genome length was 5 b, using a binary code. The accuracy of each parameter was chosen to be consistent with the grid size in the MAGIC code.

The full geometry of the three-stage depressed collector is shown in Fig. 8. A gap with a distance of 100 mm between the Bragg reflector and the first stage of the collector was left to allow the magnetic field to decrease to a small value. As the magnetic field decreased in this gap, the angular momentum decreased, as shown in Fig. 9. More than 70% of the angular kinetic momentum was transferred to the axial momentum in the gap for energy collection. Spent electrons with smaller oscillating energy would be easier to sort. The electrode shape was modified, as shown in S1, S2, and S3 in Fig. 8, to avoid potential distortion when the electric field was applied to the electrodes.

The potentials on each electrode were set to be the values shown in Table I. After each simulation, the average current collected by each collector was read from a MAGIC output data file. Then, the collected power was calculated from (1). The average power of the spent beam was calculated by counting all the energy from the spent electrons. It was implemented by extracting the energy of all the electrons in the

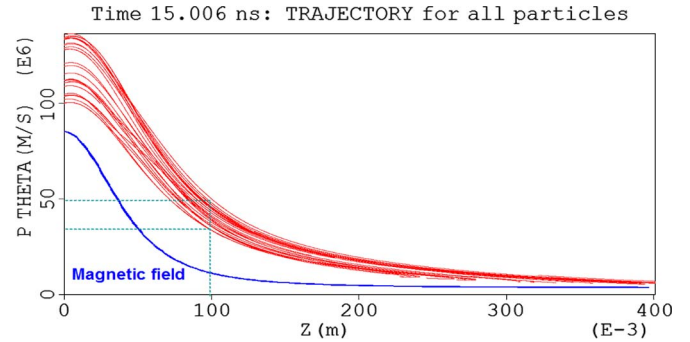

 Fig. 9. Angular momentum of the spent electrons along the Z -direction.

 TABLE II
COLLECTED CURRENT AND COLLECTION EFFICIENCY

No.	I1 (A)	I2 (A)	I3 (A)	I_{total} (A)	Collection efficiency
460	-0.88	-0.65	-1.38	-2.91	90.4%
444	-0.93	-0.60	-1.39	-2.91	90.3%
472	-0.88	-0.67	-1.36	-2.90	90.2%

3-D PIC code MAGIC. The collection efficiency calculated by the collected power and power of the spent beam was used to evaluate the optimum geometric parameters. The crossover probability, mutation probability, and population size of the genetic algorithm were set to be 0.9, 0.01, and 8, respectively. After 560 iterations, an optimum collection efficiency of 90.4% was achieved. It is 3% lower than the collection efficiency calculated in Section III, which assumed that all the spent electrons are sorted perfectly. It is because not all the electrons were recovered by the electrode, and a small proportion was observed to back stream in the simulation. The trajectories of the spent electrons are shown in Fig. 8.

The top three collection efficiencies with the collected current are shown in Table II. It should be noticed that there was 2.9% of the current not collected, which could stream back into the interaction region.

The electronic efficiency of the microwave tube is

$$\eta_e = \frac{33.0 \text{ kW}}{185 \text{ kV} \times 3 \text{ A}} = 5.9\%.$$

Without energy recovery, the overall efficiency of the microwave tube is

$$\eta_{tot} = \varepsilon_{out} \cdot \eta_e = 0.9 \times 0.059 = 5.3\%.$$

By applying the optimum depressed collector designed in this paper, the overall efficiency is

$$\eta_{tot} = \frac{5.3\%}{1 - 0.904 \times (1 - 0.059)} = 35.5\%.$$

It is obvious that the overall efficiency is greatly improved by using the energy recovery system.

V. CONCLUSION

An energy recovery system containing a Bragg reflector and a three-stage depressed collector was designed. A genetic

algorithm was used to optimize the geometry. In the 3-D PIC code MAGIC, 98.8% of microwave power was reflected back upstream by the Bragg reflector, and a 90.4% collection efficiency was achieved. In the future work, we plan to construct an energy recovery system with a three-stage depressed collector with the structure optimized in the X-band (8.5–12.4 GHz).

REFERENCES

- [1] W. He, A. W. Cross, A. D. R. Phelps, K. Ronald, C. G. Whyte, S. V. Samsonov, V. L. Bratman, and G. G. Denisov, "Theory and simulation of a gyro-BWO using a helical interaction waveguide," *Appl. Phys. Lett.*, vol. 89, no. 9, p. 091504, Aug. 2006.
- [2] C. S. Kou, S. H. Chen, L. R. Barnett, H. Y. Chen, and K. R. Chu, "Experimental study of an injection-locked gyrotron backward wave oscillator," *Phys. Rev. Lett.*, vol. 70, no. 7, pp. 924–927, Feb. 1993.
- [3] B.-T. Liu, C.-Q. Jiao, Y.-S. Zhang, G.-J. Yuan, W. Guo, and L. Zheng, "Experimental study of a Ku-band gyrotron backward-wave oscillator with a single stage depressed collector," *IEEE Trans. Plasma Sci.*, vol. 35, no. 4, pp. 1065–1069, Aug. 2007.
- [4] W. He, A. D. R. Phelps, C. R. Donaldson, A. W. Cross, and K. Ronald, "The design and simulation of a W-band gyro-BWO," in *Proc. 8th IEEE Int. Vacuum Electron. Conf.*, Kitakyushu, Japan, May 15–17, 2007, pp. 1–2.
- [5] W. He, K. Ronald, A. R. Young, A. W. Cross, A. D. R. Phelps, C. G. Whyte, E. G. Rafferty, J. Thomson, C. W. Robertson, D. C. Speirs, S. V. Samsonov, V. L. Bratman, and G. G. Denisov, "Gyro-BWO experiments using a helical interaction waveguide," *IEEE Trans. Electron Devices*, vol. 52, no. 5, pp. 839–844, May 2005.
- [6] S. V. Samsonov, G. G. Denisov, V. L. Bratman, A. A. Bogdashov, M. Y. Glyavin, A. G. Luchinin, V. K. Lygin, and M. K. Thumm, "Frequency-tunable CW gyro-BWO with a helically rippled operating waveguide," *IEEE Trans. Plasma Sci.*, vol. 32, no. 3, pp. 884–889, Jun. 2004.
- [7] G. S. Nusinovich and O. Dumbrajs, "Theory of gyro-backward wave oscillators with tapered magnetic field and waveguide cross section," *IEEE Trans. Plasma Sci.*, vol. 24, no. 3, pp. 620–629, Jun. 1996.
- [8] R. L. Ives, A. Singh, M. Mizuhara, R. Schumacher, J. Neilson, M. Gaudreau, J. A. Casey, and V. L. Granatstein, "Design of a multistage depressed collector system for 1 MW CW gyrotrons—Part II: System consideration," *IEEE Trans. Plasma Sci.*, vol. 27, no. 2, pp. 503–511, Apr. 1999.
- [9] M. E. Read, W. G. Lawson, A. J. Dudas, and A. Singh, "Depressed collectors for high-power gyrotrons," *IEEE Trans. Electron Devices*, vol. 37, no. 6, pt. 1, pp. 1579–1589, Jun. 1990.
- [10] C. K. Chong, D. B. McDermott, M. M. Razeghi, N. C. Luhmann, Jr., J. Pretterebner, D. Wagner, M. Thumm, M. Caplan, and B. Kulke, "Bragg reflectors," *IEEE Trans. Plasma Sci.*, vol. 20, no. 3, pp. 393–402, Jun. 1992.
- [11] G. Ling, B. Piosczyk, and M. K. Thumm, "A new approach for a multistage depressed collector for gyrotrons," *IEEE Trans. Plasma Sci.*, vol. 28, no. 3, pp. 606–613, Jun. 2000.
- [12] T. K. Ghosh and R. G. Carter, "Optimization of multistage depressed collectors," *IEEE Trans. Electron Devices*, vol. 54, no. 8, pp. 2031–2039, Aug. 2007.



Liang Zhang received the B.Sc. degree in applied physics from University of Science and Technology of China, Hefei, China, and the M.Sc. degree in application of nuclear techniques from the China Academy of Engineering Physics, Chengdu, China, in 2004, and 2007, respectively. He is currently working toward the Ph.D. degree in relativistic electron beams in the Scottish Universities Physics Alliance, Department of Physics, University of Strathclyde, Glasgow, U.K.

His main research interests include pulse power technology, electron beam generation, and gyrotron-TWT/backward-wave oscillators.



Wenlong He received the B.Sc. degree in physics from Suchow University, Jiangsu, China, in 1983, the M.Sc. degree in accelerator physics from the China Academy of Engineering Physics, Chengdu, China, in 1988, and the Ph.D. degree in relativistic electron beams and masers from the Department of Physics, University of Strathclyde, Glasgow, U.K., in 1995.

He is currently a Senior Research Fellow with the Scottish Universities Physics Alliance, Physics Department, University of Strathclyde. His main research interests include relativistic electron beams, CARMs, FELs, gyrotron-TWT/backward-wave oscillators, and other high-power microwave devices.



Adrian W. Cross received the B.Sc. (Honors) degree in physics and the Ph.D. degree from the University of Strathclyde, Glasgow, U.K., in 1989 and 1993, respectively.

Since 1993, he has been with the University of Strathclyde, where he was initially a Research Fellow and then, in 2000, was a Lecturer with the Atoms, Beams, and Plasmas Group, and where he is currently a Senior Lecturer with the Scottish Universities Physics Alliance, Department of Physics. He has been involved in various aspects of research on gyrotrons, cyclotron autoresonance masers, free-electron lasers, superradiant sources, and plasma applications. More recently, he has primarily been concerned with research on radiation sources for use in accelerators and pseudospark physics.



Alan D. R. Phelps was born in 1944 in the U.K. He received the B.A. (Honors) degree in physics and the M.A. degree from Cambridge University, Cambridge, U.K., in 1966 and 1970, respectively, and the Dr.Phil. degree for plasma research from Oxford University, Oxford, U.K., in 1970.

He has been with the University of Strathclyde, Glasgow, U.K., since 1978, where he initially founded a research group, became a Full Professor in 1993, and is currently with the Scottish Universities Physics Alliance, Physics Department, where he was the Head of the department from 1998 to 2001. His research interests include high-power free-electron radiation sources and plasmas.

Dr. Phelps is a Fellow of the Institute of Physics and of the Royal Society of Edinburgh.



Kevin Ronald was born in Glasgow, U.K. He received the B.Sc. (Honors) and Ph.D. degrees in physics from the University of Strathclyde, Glasgow, in 1992 and 1997, respectively.

He is currently a Lecturer with the Scottish Universities Physics Alliance, Physics Department, University of Strathclyde.



Colin G. Whyte was born in Selkirk, U.K., in 1969. He received the B.Sc. degree in physics from the University of Glasgow, Glasgow, U.K., in 1991, and the M.Sc. degree in laser physics and pulsed-power technology and the Ph.D. degree in physics from the University of St. Andrews, St. Andrews, U.K., in 1992 and 1996, respectively.

He has been with the Scottish Universities Physics Alliance, Department of Physics, University of Strathclyde, Glasgow, since 1996 in the RELD Group. His research interests include the design and experimental investigation of high-power broadband microwave amplifiers and oscillators, including novel helical gyro-TWT devices and reverse guide field free-electron lasers. He also designs and builds high-voltage pulsed-power supplies.

Numerical Optimization of a Multistage Depressed Collector With Secondary Electron Emission for an X-band Gyro-BWO

Liang Zhang, Wenlong He, Adrian W. Cross, *Member, IEEE*, Alan D. R. Phelps, Kevin Ronald, and Colin G. Whyte

Abstract—A three-stage depressed collector was previously designed and simulated to recover the kinetic energy of the spent electron beam in an X-band Gyrotron backward wave oscillator (Gyro-BWO) by using the 3-D particle-in-cell code MAGIC. The geometry of the depressed collector was optimized using a genetic algorithm to achieve the optimum overall recovery efficiency for specific parameters of the spent beam. In this paper, secondary electron emissions were simulated, and a few emission models were compared to investigate the effects of the secondary electrons on the overall recovery efficiency and the backstreaming of the electrons from the collector region. The optimization of the shape and dimensions of each stage of the collector using a genetic algorithm achieved an overall recovery efficiency of more than 80% over the entire operating regime of the Gyro-BWO, with a minimized backstreaming of 1.4%. The heat distribution on the collector was calculated, and the maximum heat density on the electrodes was approximately 195 W/cm^2 , hence avoiding the generation of “hot spots.”

Index Terms—Depressed collector, Gyrotron backward wave oscillator (Gyro-BWO), heat distribution, secondary electron emission.

I. INTRODUCTION

THE GYROTRON backward wave oscillator (Gyro-BWO) is known as a source of frequency-tunable high-frequency high-power coherent radiation and is based on the resonant cyclotron interaction of electrons gyrating in the external magnetic field with an oppositely traveling electromagnetic wave [1]. It can be used in applications such as high-resolution radar, plasma heating, high-energy accelerators, electron spin resonance spectroscopy, and deep-space communication. Research of Gyro-BWOs based on a helically corrugated waveguide demonstrated excellent results in achieving high-power and wide-frequency tunability. An X-band Gyro-BWO, with a helically corrugated interaction waveguide, which achieved a maximum power of 62 kW, a frequency tuning band of 17% (8.0–9.5 GHz), and an electronic efficiency of 16.5%, was reported in 2005. The pulselength was approximately $1 \mu\text{s}$

[2]. The Gyro-BWO promises high-power capability in the millimeter and submillimeter ranges.

Two ways can be used to improve microwave tube efficiency. One is to improve the electronic efficiency of the beam-wave interaction, such as introducing a tapered magnetic field [3]. Another way is to recover energy from the spent beam using single- or multistage depressed collectors to recover the energy of the spent beam that is lost in processes such as heating of the walls of the collection region.

Depressed collectors are passive converters that can transfer the kinetic energy of the spent electrons into potential electric energy. “Depressed” means that the collector has a depressed potential as compared with the main body of the tube. The electrons lose their kinetic energy when passing through the retarding electrostatic field and finally land on the collector surface with a significant reduction in kinetic energy. They produce a loop current which results in a power recovery from the spent electrons [4]. The collection efficiency for a depressed collector is defined by the ratio of the collected power and the spent electron-beam power. Depressed collectors are essential for megawatt Gyrotrons used as electron cyclotron heating power sources for the international thermonuclear experimental reactor and in traveling-wave tubes (TWTs) utilized in space communication [5], [6]. For Gyrotrons and cavity-coupled TWTs, the operation frequency is rather narrow, and the depressed collector can always achieve optimum collection efficiency once the collector is designed. For a broadband helix TWT, the parameter of its spent beam has rather small variations in its operating frequency band. Therefore, its depressed collector can be designed to high efficiency. However, designing a depressed collector in a frequency tunable Gyro-BWO is a much harder task because the parameters of the spent electron beam are different over the frequency tuning range. The structure of the depressed collector should have an overall high performance in the frequency tuning range of operation.

In our previous work, a three-stage depressed collector was designed by using the 3-D particle-in-cell (PIC) code MAGIC. A genetic algorithm was used to optimize the geometry, and 90.4% collection efficiency was achieved without considering the secondary electron emission [7]. The secondary emission is an important issue in the design of multistage depressed collectors. The collection efficiency can be approximately 10% lower when the secondaries are taken into account. In [8], the collection efficiency of a two-stage depressed collector for 1-MW CW Gyrotrons varied from 68% to 60% when the secondaries were considered.

Manuscript received July 3, 2009; revised September 3, 2009. First published November 3, 2009; current version published December 11, 2009. This work was supported in part by the Scottish Universities Physics Alliance (SUPA) and in part by the Overseas Research Students Awards Scheme (ORSAS).

The authors are with SUPA, Department of Physics, University of Strathclyde, G4 0NG Glasgow, U.K. (e-mail: liang.zhang@strath.ac.uk; w.he@strath.ac.uk; a.w.cross@strath.ac.uk; a.d.r.phelps@strath.ac.uk; k.ronald@strath.ac.uk; colin.whyte@strath.ac.uk).

Color versions of one or more of the figures in this paper are available online at <http://ieeexplore.ieee.org>.

Digital Object Identifier 10.1109/TPS.2009.2034164

In this paper, secondary-electron-emission models were supplemented to the simulation to investigate the effect of the secondary electrons. The collection efficiency of the designed depressed collector among the frequency tuning band of the X-band Gyro-BWO was simulated as well as the heat distribution on the electrodes in order to avoid the generation of “hot spots.”

II. MODELS OF SECONDARY ELECTRON EMISSION

The secondary electrons have several negative effects on high-power microwave devices. First of all, secondary electrons carrying velocities with opposite direction to the primaries will be accelerated by the electrostatic field in the collection region, and some of them will be backstreamed. The secondary electrons absorb energy from the electrostatic field and decrease the collection efficiency. Second, the backstreaming entered into the RF interaction region will generate noise on the microwave output and decrease the performance of the microwave tube. Third, in high-average-power devices, the backstreaming may contribute an additional thermal power on the thermally stressed waveguide structure [9]. Thus, in depressed collectors, it is essential to reduce the current of secondary electrons to be as low as possible.

Secondary electrons are generally divided into three classes [10]. The first class is the true secondary electrons (TSEs) which are knocked out from the surface of the material due to the bombardment of the primary electrons. The true secondaries are always with energy less than a few tens of electronvolts, normally regarded as 50 eV. The second class is the rediffused electrons. The primary electron impacts with one or more atoms inside the material and then is reflected back out. The collision is inelastic, and the energy of the rediffused secondaries can be any value from a few tens of electronvolts to the incident energy. The other class is the backscattered elastic electrons in which the incident electron is reflected back without losing its kinetic energy. In our simulation, the rediffused electrons and the backscattered elastic electrons were treated by a uniform model for they had the same physical nature. The term “backscattered electrons” (BSEs) was used to indicate these two types of secondary electrons in this paper.

A. Simulation of TSEs

In the 3-D PIC code MAGIC, the numbers, the energies, and the angles of the emitted TSEs were sampled from the probability function of the yield, the energy distribution, and the angular distribution by using the Monte Carlo algorithm. Therefore, the true secondary yield, the emitted angular distribution, and the emitted-energy spectrum are considered as important quantities in the simulation. The original data of the secondary electron yield (SEY), the emitted angle distribution, and the emitted-energy spectrum can be obtained from experiments, and several semiempirical formulas have been developed to fit the experimental data.

1) *TSE Yield*: The SEY represents the number of secondary electrons emitted per incident particle, which is

$$\delta = I_s/I_0 = \delta_T + \eta \quad (1)$$

where I_0 is the incident electron-beam current and I_s is the secondary current. SEY is composed by the true secondary yield δ_T and the backscatter coefficient η .

The true secondary yield δ_T can be calculated using (1) because the SEY and the backscatter coefficient were measured by various parties and semiempirical formulas were obtained.

A formula widely used for SEY was by Vaughan in 1993 [11]. It followed

$$\delta/\delta_{0m} = (ve^{1-v})^k \quad (2)$$

where δ_{0m} was the maximum SEY

$$v = (E_0 - E_{\min})/(E_{0m} - E_{\min}).$$

E_0 was the energy of the incident primary electron. E_{\min} was the minimum primary energy that could generate the secondary electrons, which was commonly accepted as 12.5 eV. E_{0m} was the energy of the incident primary electron producing the maximum SEY. The value of parameter k was suggested as

$$\begin{aligned} k &= k_1 = 0.56, & \text{for } v < 1 \\ k &= k_2 = 0.25, & \text{for } 1 < v \leq 3.6 \\ \delta &= 1.125\delta_{0m}/v^{0.35}, & \text{for } v > 3.6. \end{aligned} \quad (3)$$

Aside from the incident primary energy E_0 , the incident angle is another important parameter of the secondary-electron-emission yield. The angular dependent SEY in Vaughan’s formula was

$$\begin{cases} E_{0m}(\theta) = E_{0m}(0)(1 + k_{sE}\theta^2/2\pi) \\ \delta_{0m}(\theta) = \delta_{0m}(0)(1 + k_{s\delta}\theta^2/2\pi) \end{cases} \quad (4)$$

where θ was the incident angle and $0 \leq \theta < \pi/2$. $\delta_{0m}(0)$ was the maximum SEY normal to the surface. k_{sE} and $k_{s\delta}$ were the smooth factors for $E_{0m}(0)$ and $\delta_{0m}(0)$, respectively. They were normally set at a default value of 1.0 to represent the surface of the tube.

In 2002, Furman suggested another semiempirical formula based on a probability model and the experimental data from the large hadron collider (LHC) for the low primary energy part ($E_0 < 1$ kV) of the electrons [12] and is given by

$$\frac{\delta}{\delta_{0m}} = \frac{s(E_0/E_{0m})}{s - 1 + (E_0/E_{0m})^s} \quad (5)$$

where s is a constant and $s > 1$.

The SEY considering incident angle in Furman’s formula based on the experimental results obtained at the LHC was

$$\begin{cases} E_{0m}(\theta) = E_{0m}(0) [1 + t_1(1 - \cos^{t_2} \theta)] \\ \delta_{0m}(\theta) = \delta_{0m}(0) [1 + t_3(1 - \cos^{t_4} \theta)] \end{cases} \quad (0 \leq \theta \leq 84^\circ) \quad (6)$$

where t_1 , t_2 , t_3 , and t_4 were coefficients varying for different materials. Fig. 1 shows the SEY as a function of the incident energy of the primary electrons obtained by different researches since 1950 [11]–[15].

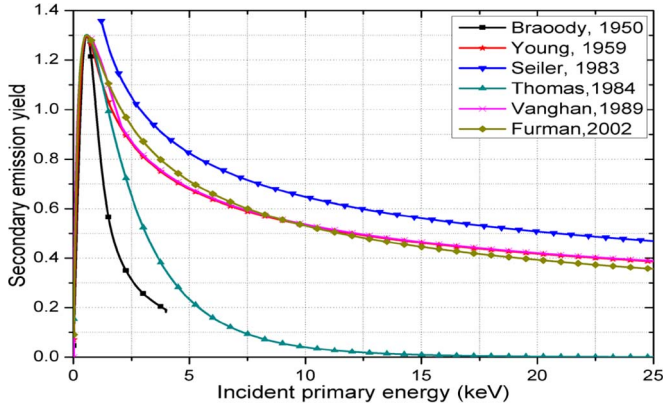


Fig. 1. Relation between SEY and the incident primary energy in different models for copper where $\delta_{0m} = 1.3$, $E_{0m} = 580$ eV, and $s = 1.44$.

The backscatter coefficient could be evaluated by the Hunger–Kuchler formula which was obtained by fitting the experimental data in the energy range of 4–40 keV [16]

$$\begin{aligned} \eta(E_0, Z) &= E_0^{m(Z)} C(Z) \\ m(Z) &= 0.13182 - 0.9211/Z^{0.5} \\ C(Z) &= 0.1904 - 0.2236 \ln Z \\ &\quad + 0.1292(\ln Z)^2 - 0.01491(\ln Z)^3 \end{aligned} \quad (7)$$

where Z was the atomic number of the material. The angular dependence of the backscatter coefficient could be evaluated by [17]

$$\eta(\theta) = 0.89(\eta_0/0.89)^{\cos \theta}. \quad (8)$$

In our simulation using the 3-D PIC code MAGIC, the TSE yield function is based on that by Thomas [15]. However, MAGIC also allows users to define their own SEY functions and the energy distribution function for TSEs by using the command “EMISSION SECONDARY.” In the simulation, Vaughan’s and Furman’s SEY formulas and the backscatter coefficient in (7) were used to evaluate the true secondary yield as they have been proved to be in good agreement with the experimental data [12], [18].

2) *Energy Spectrum and Angular Distribution of the TSEs:* It was found that the incident angle and energy of the primary electron did not affect the energy distribution of the TSEs [19]. Therefore, in the simulation, the secondary energy distribution of the TSEs was assumed to have a peak at 7.5 eV with a full-width at half-maximum of 10 eV. While, in the 3-D PIC code MICHELLE [20], a normalized Maxwellian probability distribution function was suggested with

$$f(E/E_{pk}) = (E/E_{pk})e^{-(E/E_{pk})} \quad (9)$$

where E_{pk} is the empirical energy peak which is regarded as 3.3 eV for copper material. In BSCAT code [21], a probability distribution function of

$$f(E) = 6u^2E/(E+u)^4 \quad (10)$$

was used, where u is the work function of the material (4.7 eV for copper). Because the kinetic energy of the true secondary (always less than 50 eV) is much smaller than the electric

potential difference between the electrodes of the designed depressed collector (larger than 10 kV), the differences caused by using these different energy distribution functions could be neglected.

The angular distribution of TSEs was chosen to be homogeneous in the 3-D PIC code MAGIC [15], while a more accurate distribution was suggested to follow the cosine distribution [20]. The inaccurate angular distribution might cause error in the simulation. However, from the trajectories of the TSEs in our simulation, almost all of the TSEs emitted from the second and third electrodes were collected by the first electrode. Thus, the difference in the emitted angular distribution would not affect much of the overall collection efficiency.

B. Multiple Scattering Model for the BSEs

In our simulation using the 3-D PIC code MAGIC, the way to deal with the BSEs was different from the TSEs. In the process of producing TSEs, the microcosmic interaction between the incident electrons and the target material was treated as a “black box.” However, in the process of producing BSEs, a real multiple scattering model between the incident electrons and the target material was used in the simulation. In this process, the traces of the electrons were divided into a sequence of random moves and interaction events that the electrons changed their direction and energy. The energy loss straggling (including collision energy-loss straggling and radiative energy-loss straggling) and angular deflection for each step were sampled from a multiple scattering distribution. The parameters for the multiple scattering models were the energy and angle of the incident electrons, as well as the properties of the target material. The backscatter coefficient, the emitted energy spectrum, and the angular distribution of the BSEs are obtained from the statistical results of a large number of interaction events in the multiple scattering process.

The research on the multiple scattering models began in the 1940’s with Goudsmit and Saunderson [22], and sufficient papers have been published. Several useful codes based on the Monte Carlo algorithm and multiple scattering models together with the experimental data, such as EGS4, GRANT, ETRAN, ITS, MCNP, PENELOPE, etc., have been developed and widely used in the study of the transportation of the electrons and photons in various media. References [23] and [24] are good review papers on the multiple scattering models and the electron–photon Monte Carlo calculations.

The scattering process in MAGIC was carried out by ITS (The Integrated TIGER Series of Coupled Electron/Photon Monte Carlo Transport Codes) code, and it has been proven that the simulation results of the ITS code were in good agreement with the experiments [25]. “BACKSCATTER” option in MAGIC allows ITS to be invoked automatically to simulate the emission of both the rediffused and backscattered elastic electrons.

III. SIMULATION RESULTS OF THE DEPRESSED COLLECTOR WITH SECONDARY ELECTRONS

In the simulation of the depressed collector, the information of the spent electrons was exported from the simulation of the

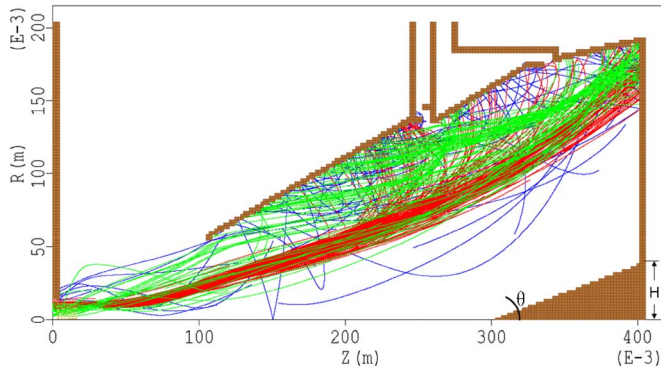


Fig. 2. Trajectories of the primary electrons and the secondary electrons in the previous geometry [(Red) Primary electrons; (green) TSEs; (blue) BSEs].

X-band Gyro-BWO using the 3-D PIC code MAGIC and then imported into the collector region. Copper was chosen as the material of the electrodes. The collected power taking account of the secondary electrons was revised as

$$P_{\text{col}} = \sum_i^n V_i I_i + \sum_i^n \sum_j^n \text{SIGN}(i-j) I_{ij} (V_i - V_j) - \sum_i^n V_i I_{B_i},$$

$$\text{SIGN}(i-j) = \begin{cases} -1, & i \leq j \\ 1, & i > j \end{cases} \quad (11)$$

where n is the number of stages and V_i and I_i are the potentials and the collected primary current on the i th-stage electrode, respectively. I_{ij} is the current of the secondary electrons emitted from the i th-stage electrode and collected on the j th-stage electrode. I_{B_i} is the backstreaming current by the secondary electrons emitted from the i th-stage electrode.

In the previous optimum geometry without considering the secondary electrons, a collection efficiency of 90.4% was obtained in the conditions of beam current of 3 A, beam voltage of 185 kV, magnetic field of 0.2008 T, and operation frequency of 8.63 GHz. The spent electron beam imported into the collector region had a 3-A average current and a 522-kW average power. When taking account of the secondary electron emission, the collection efficiency was reduced to 79.3%, and the backstreaming increased from 3.0% to 11.1%. Vaughan's formula was used to simulate the TSE emission. The trajectories of the primary electrons and the secondary electrons are shown in Fig. 2. The backstreaming was large; thus, modifications in the geometry were required.

In Fig. 2, many secondary electrons were accelerated by the electric field in the z -axis and returned to the interaction region. The backstreaming could be reduced if an acceleration field exists in the radial direction which is strong enough to push the secondary electrons toward the collector. It could be improved by changing the tilt angle and the height of the spike structure of the third electrode, as shown in Fig. 2. Together with the ten parameters used in the previous geometry, the depressed collector was now completely determined by 12 parameters.

TABLE I
COLLECTION EFFICIENCY AND THE BACKSTREAMING RATE IN DIFFERENT CASES

Cases	True secondary model	Collection efficiency	Percentage of backstreaming
Without TSEs, without BSEs	---	88.9%	0.40%
With TSEs, without BSEs	Vaughan	84.9%	0.59%
	Furman	82.7%	0.66%
	Thomas	86.4%	0.58%
Without TSEs, with BSEs	---	86.8%	1.54%
With TSEs, with BSEs	Vaughan	82.9%	1.80%
	Furman	80.8%	1.90%
	Thomas	84.3%	1.72%

The optimization program integrating a genetic algorithm which was described in detail in [7] was executed once again to optimize the parameters by controlling the 3-D PIC code MAGIC. The crossover probability, mutation probability, and population size of the genetic algorithm were set to be 0.9, 0.01, and 12, respectively. After 540 iterations, an optimum collection efficiency of 82.9% was achieved when using Vaughan's true secondary emission model. It was only a small improvement in the collection efficiency as compared to the previous geometry. However, the backstreaming was significantly reduced from 11.1% to 1.80%. Table I presents the collection efficiency and the percentage of the backstreaming current in different cases, including with or without the BSEs as well as with or without the TSEs. From the simulation results, by carefully designing the geometry of the depressed collector, the backstreaming could be reduced to a very low level.

From the simulation results, the BSEs contributed more backstreaming than TSEs. That was because the BSEs had a higher energy than the TSEs, and thus, they had a larger probability to overcome the radial electric field and return to the interaction region. Fig. 3 shows the trajectories of the primary electrons, the TSEs, and the BSEs, in the designed depressed collector when using Vaughan's formula.

The collection efficiency with three different formulas of true secondary emission yield, including Vaughan's, Furman's and Thomas', did not show a great difference, which was 4%. A different secondary emission model generated a different number of TSEs and impacted the second and third terms of (11). The value of the second term was much smaller than the first term for $V_i - V_j$ was much smaller than V_i . In the simulation, the potentials on each electrode were -138.7 , -154.7 , and -183.8 kV, respectively. From the trajectories of the TSEs in Fig. 3(b), almost all of the TSEs emitted from the second and third electrodes were collected by the first electrode. That made the third term of (11) to be a small value. As the difference of the effects on the collection efficiency and backstreaming rate from different true secondary emission models were simulated and were found to be negligible; in later calculations, we only used Vaughan's formula for it has been widely accepted in the literature.

The output frequency of the X-band Gyro-BWO can be tuned by adjusting the amplitude of the cavity magnetic field. However, the spent beam parameters at different output frequencies were different. The collection efficiencies and the

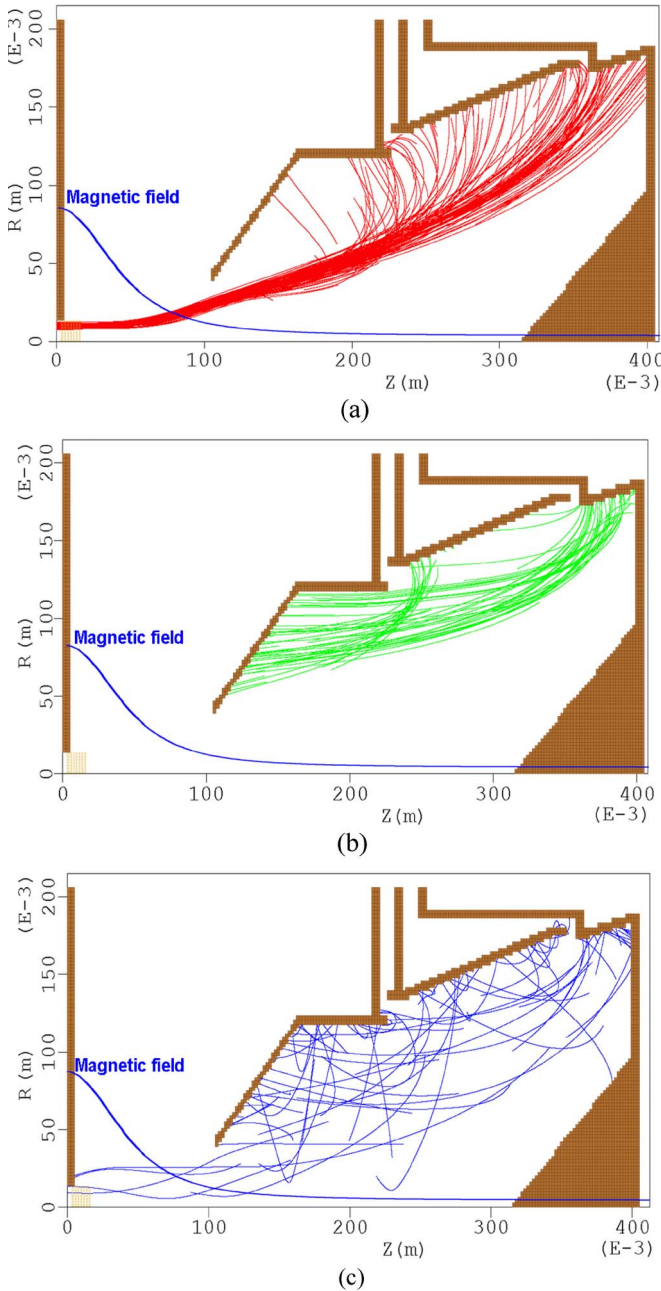


Fig. 3. Trajectories of the electrons in the depressed collector (using Vaughan’s formulas). (a) Trajectories of the primary electrons. (b) Trajectories of the TSEs. (c) Trajectories of the BSEs.

backstreaming rate of the X-band Gyro-BWO were therefore simulated in the whole frequency tuning range by the optimized configuration of the designed three-stage depressed collector and are shown in Fig. 4. The collection efficiencies achieved were simulated to be higher than 80%, and the backstreaming rate was lower than 5% when the operation frequencies were lower than 9.0 GHz. However, the backstreaming grew as the operation frequency increased.

IV. HEAT POWER DENSITY DISTRIBUTION ON THE COLLECTOR

The cooling of the electrodes is another important issue in designing the depressed collector. Although the kinetic energy

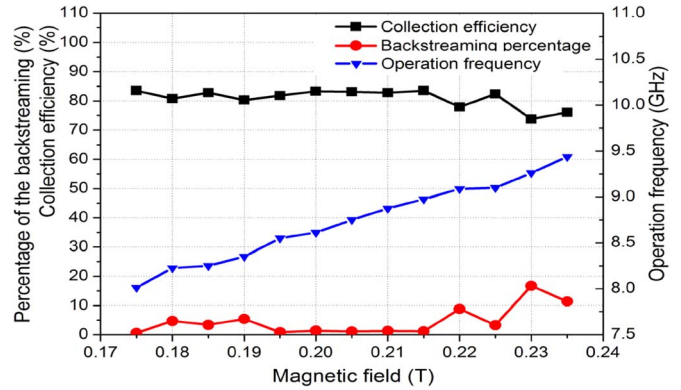


Fig. 4. Collection efficiencies and the backstreaming rate over the frequency-tuning range of the Gyro-BWO.

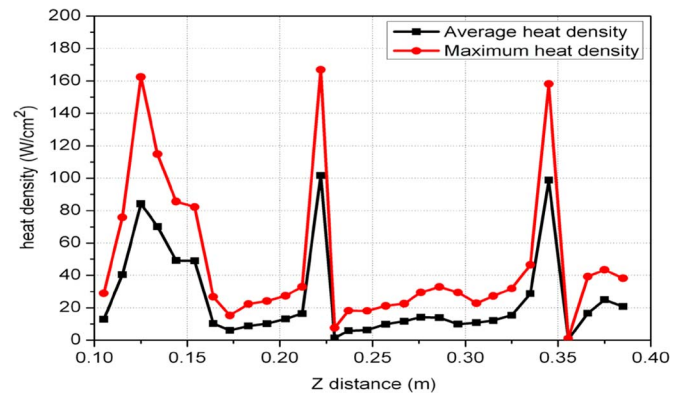


Fig. 5. Average and maximum heat power density as a function of the axial position in the depressed collector.

of the spent electrons reduced significantly when they passed through the retarded electric field, the heat due to the power of the remaining kinetic energy of the spent electrons when they struck the surface of the electrodes was still large; for our case, it could be up to 40 keV. The spent electrons with such high kinetic energy could damage the surface of electrodes in the form of a “hot spot” and could reach the thermal stress threshold of the collector material.

To design the effective cooling system for the collector electrodes, the distribution of the heat power dissipated on the surface of the electrodes needs to be evaluated. In the 3-D PIC code MAGIC, the overall heat dissipation on a conductor can be calculated by the command “OBSERVE COLLECTED POWER.” To obtain the heat power distribution on the surface of the electrodes, the three electrodes were divided into a large number of small conductors both in the azimuthal direction and the z -direction, and the heat power dissipated in each of these conductors was individually measured; thus, an approximate heat power distribution was obtained. The greater the number of conductors, the more accurate the heat power distribution that could be achieved. The heat power densities on the conductors could be calculated by dividing the heat power by the area of the conductors’ surface. The maximum value of the heat power densities in the azimuthal direction as a function of the axial position z was recorded and is shown in Fig. 5 when the magnetic field is 0.2008 T and the beam voltage and current are 185 kV and 3 A, respectively. The average heat power density in

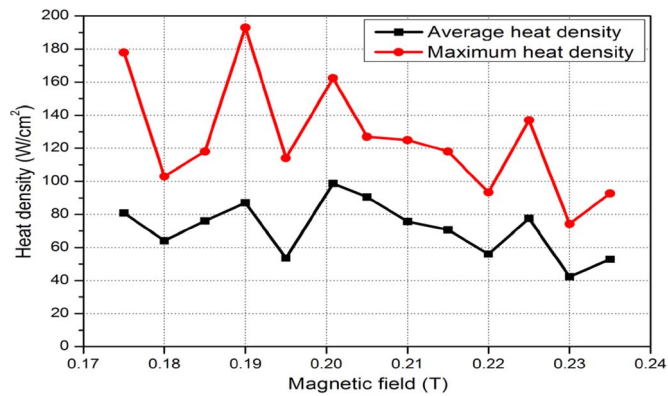


Fig. 6. Maximum heat power density and maximum average power density in different magnetic fields.

the azimuthal direction as a function of the axial position z was recorded and is shown in Fig. 5 also. The largest heat power density was ~ 170 W/cm². Fig. 6 shows the maximum heat density and the maximum average heat density in the designed depressed collector when different magnetic fields are applied. The maximum heat density was ~ 195 W/cm². It is lower than the thermal stress threshold of the copper material; thus, the generation of hot spots can be avoided.

V. CONCLUSION

Secondary electron emissions were simulated and a few emission models were compared to investigate their effects on the overall recovery efficiency and the backstreaming rate for the multistage collector. The optimization of the shape and dimensions of each stage of the collector using a genetic algorithm achieved an overall recovery efficiency of more than 80%, with a minimized backstreaming rate of 1.4%. The BSEs played a more important role than the TSEs when understanding the backstreaming of electrons back into the beam-wave-interaction region. The heat distribution on the collector was calculated, and the maximum heat density on the electrodes was 195 W/cm²; hence, parameter space was discovered which could avoid the generation of “hot spots.”

REFERENCES

- [1] W. He, A. W. Cross, A. D. R. Phelps, K. Ronald, C. G. Whyte, S. V. Samsonov, V. L. Bratman, and G. G. Denisov, “Theory and simulation of a Gyro-BWO using a helical interaction waveguide,” *Appl. Phys. Lett.*, vol. 89, no. 9, p. 091 504, Aug. 2006.
- [2] W. He, K. Ronald, A. R. Young, A. W. Cross, A. D. R. Phelps, C. G. Whyte, E. G. Rafferty, J. Thomson, C. W. Robertson, D. C. Speirs, S. V. Samsonov, V. L. Bratman, and G. G. Denisov, “Gyro-BWO experiments using a helical interaction waveguide,” *IEEE Trans. Electron Devices*, vol. 52, no. 5, pp. 839–844, May 2005.
- [3] G. S. Nusinovich and O. Dumbrajs, “Theory of gyro-backward wave oscillators with tapered magnetic field and waveguide cross section,” *IEEE Trans. Plasma Sci.*, vol. 24, no. 3, pp. 620–629, Jun. 1996.
- [4] F. Sterzer and N. J. Princeton, “Improvement of traveling-wave tube efficiency through collector potential depression,” *IRE Trans. Electron Devices*, vol. 5, no. 4, pp. 300–305, Oct. 1958.
- [5] R. L. Ives, A. Singh, M. Mizuhara, R. Schumacher, J. Neilson, M. Gaudreau, J. A. Casey, and V. L. Granatstein, “Design of a multistage depressed collector system for 1 MW CW Gyrotrons—Part II: System consideration,” *IEEE Trans. Plasma Sci.*, vol. 27, no. 2, pp. 503–511, Apr. 1999.
- [6] J. D. Wilson, E. G. Wintucky, K. R. Vaden, D. A. Force, I. L. Krainsky, R. N. Simons, N. R. Robbins, W. L. Menninger, D. R. Dibb, and

- D. E. Lewis, “Advances in space traveling-wave tubes for NASA missions,” *Proc. IEEE*, vol. 95, no. 10, pp. 1958–1967, Oct. 2007.
- [7] L. Zhang, W. He, A. W. Cross, A. D. R. Phelps, K. Ronald, and C. G. Whyte, “Design of an energy recovery system for a Gyrotron backward-wave oscillator,” *IEEE Trans. Plasma Sci.*, vol. 37, no. 3, pp. 390–394, Mar. 2009.
- [8] A. Singh, S. Rajapatirana, Y. Men, V. L. Granatstein, R. L. Ives, and A. J. Antolak, “Design of a multistage depressed collector system for 1-MW CW Gyrotrons—Part I: Trajectory control of primary and secondary electrons in a two-stage depressed collector,” *IEEE Trans. Plasma Sci.*, vol. 27, no. 2, pp. 490–502, Apr. 1999.
- [9] G. Ling, B. Piosczyk, and M. K. Thumm, “A new approach for a multistage depressed collector for Gyrotrons,” *IEEE Trans. Plasma Sci.*, vol. 28, no. 3, pp. 606–613, Jun. 2000.
- [10] M. A. Furman and M. T. F. Pivi, “Probabilistic model for the simulation of secondary electron emission,” *Phys. Rev. Spec. Top., Accel. Beams*, vol. 5, no. 12, p. 124404, Dec. 2002.
- [11] M. Vaughan, “Secondary emission formulas,” *IEEE Trans. Electron Devices*, vol. 40, no. 4, p. 830, Apr. 1993.
- [12] M. A. Furman and M. T. F. Pivi, Simulation of Secondary Electron Emission Based on a Phenomenological Probabilistic Model, 2003, LBNL-52807, SLAC-PUB-9912. [Online]. Available: <http://repositories.cdlib.org/lbnl/LBNL-52807/>
- [13] R. G. Lye and A. J. Dekker, “Theory of secondary emission,” *Phys. Rev.*, vol. 107, no. 4, pp. 977–981, Aug. 1957.
- [14] H. Seiler, “Secondary electron emission in the scanning electron microscope,” *J. Appl. Phys.*, vol. 54, no. 11, pp. R1–R18, Nov. 1983.
- [15] *MAGIC User’s Manual*, Mission Res. Corp., Newington, VA, 2002.
- [16] H. J. Hunger and L. Kuchler, “Measurements of the electron backscattering coefficient for quantitative EPMA in the energy range of 4 to 40 keV,” *Phys. Stat. Sol.*, vol. 56, pp. K45–K48, 1979.
- [17] L. Reimer, *Scanning Electron Microscopy, Physics of Image Formation and Microanalysis*. Berlin, Germany: Springer-Verlag, 1985, ch. 4, pp. 135–169.
- [18] J. Rodney and M. Vaughan, “A new formula for secondary emission yield,” *IEEE Trans. Electron Devices*, vol. 36, no. 9, pp. 1963–1967, Sep. 1989.
- [19] J. Burns, “Angular distribution of secondary electrons from (100) faces of copper and nickel,” *Phys. Rev.*, vol. 119, no. 1, pp. 102–114, Jul. 1960.
- [20] J. Petillo, K. Eppley, D. Panagos, P. Blanchard, E. Nelson, N. Dionne, J. Deford, B. Held, L. Hernyakova, W. Krueger, S. Humphries, T. McLure, A. Mondelli, J. Burdette, M. Cattelino, R. True, K. T. Nguyen, and B. Levush, “The MICHELLE three-dimensional electron gun and collector modeling tool: Theory and design,” *IEEE Trans. Plasma Sci.*, vol. 30, no. 3, pp. 1238–1264, Jun. 2002.
- [21] A. Valfells, A. Singh, M. J. Klander, and V. L. Granatstein, “Advancements in codes for computer aided design of depressed collectors and tracing of backscattered electrons—Part II: Improvements in modeling of the physics of secondary electron emission and backscattering,” *IEEE Trans. Plasma Sci.*, vol. 30, no. 3, pp. 1271–1276, Jun. 2002.
- [22] S. Goudsmit and J. L. Saunderson, “Multiple scattering of electrons,” *Phys. Rev.*, vol. 57, no. 1, pp. 24–29, Jan. 1940.
- [23] S. M. Seltzer, “Electron–photon Monte Carlo calculations: The ETRAN code,” *Int. J. Appl. Radiat. Isot.*, vol. 42, no. 10, pp. 917–941, 1991.
- [24] H. A. Bethe, “Moliere’s theory of multiple scattering,” *Phys. Rev.*, vol. 89, no. 6, pp. 1256–1266, Mar. 1953.
- [25] J. A. Halbleib, R. P. Kensek, G. D. Valdez, T. A. Mehlhorn, S. M. Seltzer, and M. J. Berger, “ITS: The integrated TIGER series of electron/photon transport codes—Version 3.0,” *IEEE Trans. Nucl. Sci.*, vol. 39, no. 4, pp. 1025–1030, Aug. 1992.



Liang Zhang received the B.Sc. degree in applied physics from the University of Science and Technology of China, Hefei, China, in 2004 and the M.Sc. degree in application of nuclear techniques from the China Academy of Engineering Physics, Chengdu, China, in 2007, respectively. He is currently working toward the Ph.D. degree in relativistic electron beams in the Scottish Universities Physics Alliance, Department of Physics, University of Strathclyde, Glasgow, U.K.

His main research interests include pulse-power technology, electron-beam generation, and Gyrotron-TWT/backward-wave oscillators.



Wenlong He received the B.Sc. degree in physics from Suchow University, Jiangsu, China, in 1983, the M.Sc. degree in accelerator physics from the China Academy of Engineering Physics, Chengdu, China, in 1988, and the Ph.D. degree in relativistic electron beams and masers from the Department of Physics, University of Strathclyde, Glasgow, U.K., in 1995.

He is currently a Senior Research Fellow with the Scottish Universities Physics Alliance, Department of Physics, University of Strathclyde. His main research interests include relativistic electron beams,

CARMs, FELs, Gyrotron-TWT/backward-wave oscillators, and other high-power microwave devices.



Kevin Ronald was born in Glasgow, U.K. He received the B.Sc. (with honors) and Ph.D. degrees in physics from the University of Strathclyde, Glasgow, U.K., in 1992 and 1997, respectively.

He is currently a Lecturer with the Scottish Universities Physics Alliance, Department of Physics, University of Strathclyde.



Adrian W. Cross (M'02) received the B.Sc. degree (with honors) in physics and the Ph.D. degree from the University of Strathclyde, Glasgow, U.K., in 1989 and 1993, respectively.

Since 1993, he has been with the University of Strathclyde, where he was initially a Research Fellow and then, in 2000, was a Lecturer with the Atoms, Beams, and Plasmas Group, and where he is currently a Senior Lecturer with the Scottish Universities Physics Alliance, Department of Physics.

He has been involved in various aspects of research

on Gyrotrons, cyclotron autoresonance masers, free-electron lasers, superradiant sources, and plasma applications. More recently, he has primarily been concerned with research on radiation sources for use in accelerators and pseudospark physics.



Colin G. Whyte was born in Selkirk, U.K., in 1969. He received the B.Sc. degree in physics from the University of Glasgow, Glasgow, U.K., in 1991 and the M.Sc. degree in laser physics and pulsed-power technology and the Ph.D. degree in physics from the University of St. Andrews, St. Andrews, U.K., in 1992 and 1996, respectively.

He has been with the Scottish Universities Physics Alliance, Department of Physics, University of Strathclyde, Glasgow, since 1996 with the RELD Group. His research interests include the design and

experimental investigation of high-power broadband microwave amplifiers and oscillators, including novel helical gyro-TWT devices and reverse guide field free-electron lasers. He also designs and builds high-voltage pulsed-power supplies.



Alan D. R. Phelps was born in U.K. in 1944. He received the B.A. degree (with honors) in physics and the M.A. degree from Cambridge University, Cambridge, U.K., in 1966 and 1970, respectively, and the Dr.Phil. degree for plasma research from Oxford University, Oxford, U.K., in 1970.

He has been with the University of Strathclyde, Glasgow, U.K., since 1978, where he initially founded a research group, became a Full Professor in 1993, and is currently with the Scottish Universities Physics Alliance, Department of Physics, where he

was the Head of the department from 1998 to 2001. His research interests include high-power free-electron radiation sources and plasmas.

Dr. Phelps is a Fellow of the Institute of Physics and of the Royal Society of Edinburgh.

Generation of 3 GW microwave pulses in X-band from a combination of a relativistic backward-wave oscillator and a helical-waveguide compressor

V. L. Bratman,¹ G. G. Denisov,¹ N. G. Kolganov,¹ S. V. Mishakin,¹ S. V. Samsonov,¹ A. W. Cross,² W. He,² L. Zhang,² M. McStravick,² C. G. Whyte,² A. R. Young,² K. Ronald,² C. W. Robertson,² and A. D. R. Phelps²

¹*Institute of Applied Physics, Russian Academy of Sciences, Nizhny Novgorod 603950, Russia*

²*Department of Physics, Scottish Universities Physics Alliance, University of Strathclyde, Glasgow, Scotland G4 0NG, United Kingdom*

(Received 20 September 2010; accepted 5 October 2010; published online 2 November 2010)

The phenomenon of passive compression of frequency-modulated (FM) pulses in a dispersive media (DM) was used to increase the peak microwave power up to the multigigawatt level. A helically corrugated waveguide was used as the DM, while a relativistic X-band backward-wave oscillator (RBWO) with a descending-during-the-pulse accelerating voltage served as a source of FM pulses. Compression of pulses down to a halfwidth of 2.2 ns accompanied by a 4.5-fold power increase up to a value of about 3.2 GW has been demonstrated. © 2010 American Institute of Physics. [doi:10.1063/1.3505825]

Radio frequency (rf) pulses with multigigawatt peak power levels have recently become available owing to progress in relativistic vacuum electronics. Multigigawatt powers open up many opportunities for fundamental plasma studies and promising applications.¹ For example, the power of 8.7 GW if focused on an area of the order of the wavelength squared imparts a relativistic oscillatory velocity to electrons. In contrast with challenging ways of generating gigawatt power level radiation by increasing directly the power of electron beams up to a few MeVs and tens of kiloamperes,² some advanced methods using substantially less intense beams are being actively developed. Among these methods, results achieved based on superradiance effects³ and pulse compression (active and passive) (see, e.g., Refs. 1 and 4–7 and references cited there) show great promise.

In a series of publications, the well-known phenomenon of passive pulse compression (reduction in duration accompanied with an increase in amplitude), widely used in optics (see, e.g., Refs. 8 and 9), has been proposed and investigated both theoretically and in low-power proof-of-principle experiments^{6,7} as a method of achieving microwave radiation with multigigawatt peak powers. The method is based on generation of a frequency modulated (FM) pulse by a relativistic backward-wave oscillator (RBWO) following its compression due to propagation through a DM in the form of a hollow metallic waveguide with helical corrugation of the inner surface. In this letter we present the first pulse compression experiment in which multigigawatt peak power of X-band radiation has been achieved. The experimental setup comprises two key elements (Fig. 1): the source of FM radiation (an RBWO) and the DM [a helical-waveguide (HW) compressor].

A *helical-waveguide compressor* with appropriate parameters, namely, having a relatively shallow helical corrugation (periodical in both axial and azimuthal directions) of

the inner wall of a waveguide with circular cross-section, can resonantly couple a pair of circularly polarized partial modes of the unperturbed waveguide, having significantly different group velocities where one mode is far from the cutoff and the other mode is close to cutoff.⁶ As a result, in the frequency region of their resonant coupling, an eigenmode appears having a strong frequency dependent group velocity, which is favorable for the pulse compression. In contrast with a smooth or axially symmetric corrugated waveguide, the helical corrugation allows the frequency regions with zero or negative group velocity of the eigenwave to be avoided. This ensures good rf matching of the compressor to the input source over a suitably wide frequency band.

In the experiment under discussion, a fivefold sinusoidal corrugation was used which coupled a circularly polarized TE_{3,1} mode having large group velocity with a near-cutoff counter-rotating TE_{2,2} mode. The use of these relatively high-order modes ensured sufficient rf breakdown strength at the gigawatt power level.⁷ The inner surface of the waveguide in cylindrical coordinates r , φ , and z had the following form: $r(\varphi, z) = 31.5 + 2.7 \sin(2\pi z/32.4 - 5\varphi)$ (all dimensions are in millimeters). The HW consisted of four aluminum sections and had a total length of the regular corrugation of 972 mm, bounded from each side by three-period sections with linearly increasing/decreasing amplitude of corrugation for adiabatic conversion of the radiation from the incident TE_{3,1} mode into the operating eigenwave of the HW, at the input, and back to the TE_{3,1} mode, at the output. The most favorable frequency region for the pulse compression is a part of the dispersion characteristic where the operating wave group velocity has a large negative gradient as a function of frequency, which, for the HW under consideration, is the region from 9.4 to 9.95 GHz (Fig. 2). Therefore, in order to be effectively compressed, an input pulse should have a negative frequency sweep within the mentioned frequency interval.

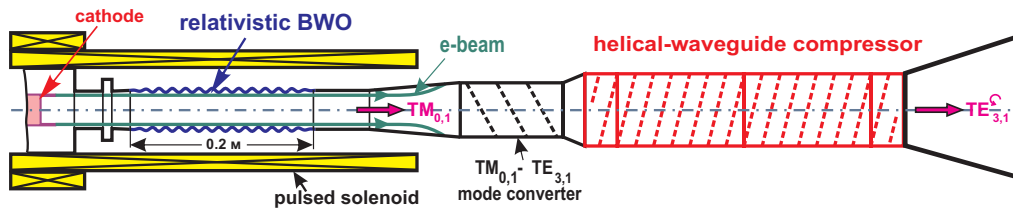


FIG. 1. (Color online) Scheme of the experimental setup.

Relativistic backward-wave oscillator. An analysis, based on a 1D theoretical model,¹⁰ and more detailed numerical simulations using the time-domain particle-in-cell code KARAT (Ref. 11) were performed, resulting in the design of an RBWO which combined high output power, high efficiency which was able to be frequency tuned over a sufficiently wide range for a moderately relativistic electron beam.⁷ According to the simulations, the RBWO oscillation frequency should smoothly sweep from 10 to 9.5 GHz when the accelerating voltage gradually changes in time from 600 to 300 kV.

The experiments were performed using a SINUS-6 accelerator (IAP RAS) where an accelerating voltage pulse was formed by a combination of a Tesla transformer and a coaxial transmission line. When operating to a matched load it produces pulses of voltage up to 600 kV and current of 6–7 kA with about 15 ns long flat top and 5–10 ns long rising/falling edges. Because of the principle of operation of the SINUS-6 accelerator it is very problematic to realize the necessary voltage sweep for the RBWO voltage over the main central region of the pulse by modifying the external circuit. Nevertheless, it was experimentally found how to realize an appropriate voltage drop “internally.”¹² To achieve this change in voltage a dielectric cylinder was introduced into the region of the magnetically insulated coaxial diode where the electron beam was formed. Presumably due to some plasma effects, this dielectric insert led to a significant decrease (with characteristic time of 10–20 ns) of the diode impedance during the process of explosive-emission beam

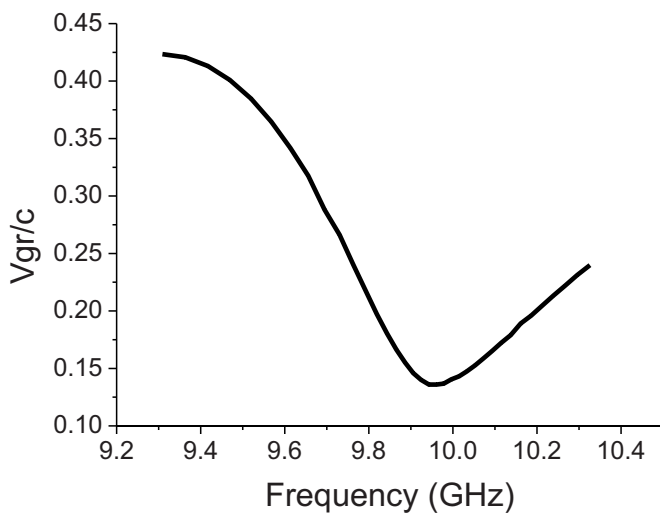


FIG. 2. Group velocity (normalized to the speed of light) of the helical waveguide operating wave.

generation, resulting in a decrease in the accelerating voltage and an increase in the beam current at the top of the pulse [Fig. 3(a)]. Moreover, varying the axial distance between edges of the cathode and dielectric insert within several millimeters we could control the magnitude of the voltage drop and hence control the frequency sweep interval, which was used in the final experimental optimization of the combination of the RBWO with the compressor. At optimum configuration, when the top-pulse voltage decreased from 550 to 300 kV and beam current increased from 7 to 9 kA the RBWO generated radiation with power of 0.6–0.8 GW when frequency sweeping from 10 to 9.6 GHz during about 15 ns (Fig. 3).

The frequency sweep was measured by means of a heterodyne technique, when a small fraction of output radiation from the RBWO was nonlinearly mixed with radiation of a

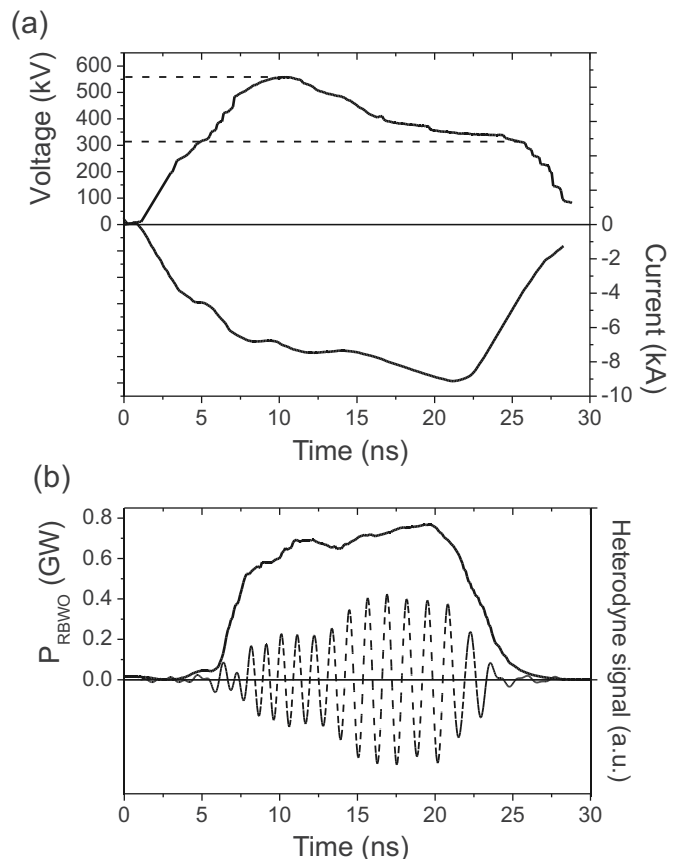


FIG. 3. Time characteristics of the relativistic backward-wave oscillator: (a) accelerating voltage (upper curve) and beam current (lower curve); (b) output power (solid curve) and heterodyne signal (dashed curve) at the master oscillator frequency of 9.1 GHz.

pulsed magnetron at a fixed frequency, resulting in a waveform at the intermediate frequency [Fig. 3(b), dashed curve]. The power of the output rf pulse [Fig. 3(b), solid curve] from the RBWO was obtained by processing of the rf detector signal, detector voltage-power calibration, and data from a calorimeter measuring the total rf energy in the pulse.

Combination of the RBWO and the HW compressor. The RBWO was combined with the HW compressor in a common vacuum system via a mode converter which transformed the power from the RBWO in the form of the $TM_{0,1}$ mode into the incident operating mode of the compressor, namely, the circularly polarized $TE_{3,1}$ mode (Fig. 1). The output power in the form of the $TE_{3,1}$ mode from the whole system was radiated through a horn terminated with a 300 mm diameter 0.3 mm thick lavsan window and then absorbed in a calorimeter with an aperture of 600 mm in diameter.

The experimental optimization aiming to obtain the maximum peak power of the compressed pulse was performed by variation of the axial distance between the cathode and dielectric insert, electron beam diameter (factors influencing the RBWO power and frequency sweep) and the length of the HW which could be adjusted in six-period-long sections. As a result the maximum peak power of the compressed pulse was measured to be as high as 3.2 GW while its halfwidth amounted to 2.2 ns with a total pulse energy of 9.7 ± 0.2 J (Fig. 4). As compared to the RBWO having approximately 0.7 GW pulse-averaged output power and 10.2 ± 0.2 J of pulse energy, a 4.5-fold power amplification due to the compression was achieved. Assuming the energy content in a “useful” pulse as a product of its peak power and halfwidth an compressing efficiency of nearly 70% was realized. (The rest of energy goes to Ohmic losses and the pulse sidelobes.)

It should be noted that the achievable power compression ratio by the method discussed is approximately proportional to the input FM pulse width. Therefore if the duration of the RBWO accelerating voltage pulse (which should have a negative slope) is increased from 15 ns, as used in the experiment presented, to 40–50 ns and the HW compressor is proportionally elongated a further threefold power increase of the compressed pulse is achievable. In conclusion, the method of generation of ultra-high-power microwave pulses based on a combination of a voltage-swept RBWO and an HW compressor has been experimentally demonstrated at

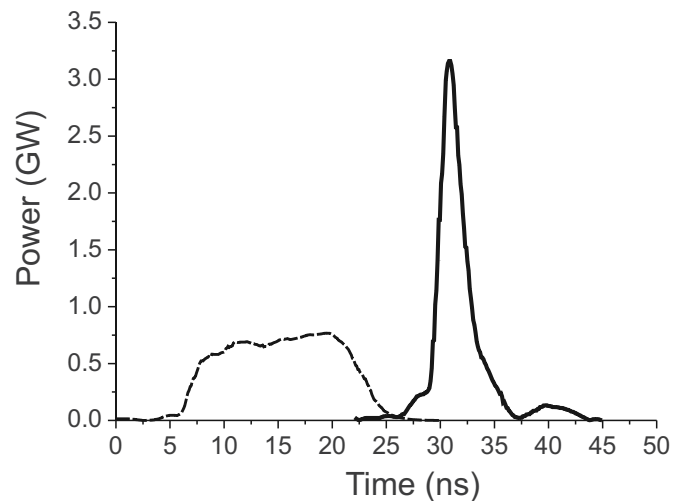


FIG. 4. The resultant compressed pulse (solid curve) shown in contrast with the relativistic backward-wave oscillator output pulse (dashed curve).

multigigawatt power levels and has a serious potential for further peak power enhancement.

This work was supported by the Russian Foundation for Basic Research (Grant No. 10-02-00975) and the EPSRC U.K. (Grant No. EP/E058868/1).

- ¹*Applications of High-Power Microwaves*, edited by A. V. Gaponov-Grekhov and V. L. Granatstein (Artech, Norwood, MA, 1994).
- ²S. P. Bugaev, V. A. Cherepenin, V. I. Kanavets, V. I. Koshelev, V. A. Popov, and A. N. Vlasov, *IEEE Trans. Plasma Sci.* **18**, 525 (1990).
- ³A. A. Eltchaninov, S. D. Korovin, G. A. Mesyats, I. V. Pegel, V. V. Rostov, V. G. Shpak, and M. I. Yalandin, *IEEE Trans. Plasma Sci.* **32**, 1093 (2004).
- ⁴W. M. Manheimer and B. H. Ripin, *Phys. Fluids* **29**, 2283 (1986).
- ⁵M. K. Thumm and W. Kasperek, *IEEE Trans. Plasma Sci.* **30**, 755 (2002).
- ⁶S. V. Samsonov, A. D. R. Phelps, V. L. Bratman, G. Burt, G. G. Denisov, A. W. Cross, K. Ronald, W. He, and H. Yin, *Phys. Rev. Lett.* **92**, 118301 (2004).
- ⁷V. Bratman, G. G. Denisov, S. V. Samsonov, A. W. Cross, K. Ronald, and A. D. R. Phelps, *Radiophys. Quantum Electron.* **50**, 36 (2007).
- ⁸O. Svelto and D. C. Hanna, *Principles of Lasers*, 4th ed. (Springer, New York, NY, 1998).
- ⁹R. H. Lehberg and J. M. McMahon, *Appl. Phys. Lett.* **28**, 204 (1976).
- ¹⁰B. Levush, T. Antonsen, A. Bromborsky, W. R. Lou, and Y. Carmel, *Phys. Fluids B* **4**, 2293 (1992).
- ¹¹V. P. Tarakanov, *User's Manual for Code KARAT* (Berkley Research, Springfield, VA, 1992).
- ¹²A. M. Bechasnov, V. L. Bratman, N. G. Kolganov, S. V. Mishakin, and S. V. Samsonov, *Tech. Phys. Lett.* **36**, 140 (2010).

*Invited Paper***W-band Gyro-devices Using Helically Corrugated Waveguide and Cusp Gun: Design, Simulation and Experiment**

W. He*, C. R. Donaldson, F. Li, L. Zhang, A. W. Cross, A. D. R. Phelps, K. Ronald,
C. W. Robertson, C. G. Whyte, A. R. Young
SUPA, Department of Physics, University of Strathclyde,
Glasgow, G4 0NG, Scotland, UK
*Email: w.he@strath.ac.uk

(Received 18 November 2010)

Abstract: This paper presents the design and simulation of W-band Gyro-devices using helically corrugated waveguides as the beam-wave interaction region and a cusp gun as the electron beam source. The electron beam system and the beam-wave interaction were optimized through numerical simulations by using a particle-in-cell (PIC) code MAGIC to predict (calculate) the output power and frequency bandwidth. The beam cross sectional measurement using a scintillator plate confirmed that an axis encircling electron beam was achieved with the designed beam parameters of current 1.5 A and energy 40 keV. The W-band helically corrugated interaction region for the gyrotron backward wave oscillator (Gyro-BWO) was manufactured with a dispersion from 80 GHz to 110 GHz measured using a vector network analyser which was found to be in good agreement with simulations and theory. The Gyro-BWO achieved frequency-tuneable operation by adjusting the magnetic field in the interaction cavity. A -3 dB bandwidth of ~84-104 GHz and output power ~10 kW were simulated using the electron beam from the cusp gun. The gyrotron travelling wave amplifier (Gyro-TWA) is designed to have a -3 dB frequency bandwidth of 90-100 GHz, output power of 10 kW and saturated amplification gain of 40 dB.

Keywords: Gyro-devices, Gyro-BWO, Gyro-TWA, Helically Corrugated Waveguide, Cusp Gun

1. Introduction

High-power, high-frequency, coherent radiation sources, especially in the range of mm and sub-mm wavelengths, have attracted significant research interest recently due to their desirable applications in many areas such as remote sensing [1], medical imaging [2], plasma heating [3] and spectroscopy [4]. Gyro-devices are promising candidates to fulfill such a demand due to their inherent characteristic fast wave interaction. A helically corrugated waveguide has been demonstrated with a wave dispersion that has a near constant group velocity in the region of small axial wave number [5]. This allows broadband microwave amplification to be achieved in a gyrotron travelling wave amplifier (Gyro-TWA) and wide frequency tuning in a Gyro-BWO as demonstrated by our previous experiments in X-band [6,7,8].

A number of Gyro-BWOs have been investigated both in theory and experiments. Two such experiments at the Naval Research Laboratory [9] and the National Tsing Hua University [10] operating at the fundamental cyclotron harmonic and the fundamental mode of a smooth cylindrical waveguide demonstrated impressive voltage and frequency tuning up to 5% and 13%, respectively with a very high efficiency of nearly 20% at power levels of up to 100 kW at Ka-band frequencies. A Gyro-BWO using a helically corrugated waveguide has demonstrated improved frequency tuning range without compromising interaction efficiency

and output power when compared with its counterparts using cylindrical smooth bore waveguides. Previous experiments using such a microwave system at Ka-band achieved an output power of ~ 1 MW, an efficiency of 10%, a frequency tuning band of 15% using a 20 ns, 300 keV electron beam [11]. Recently a relative frequency-tuning band of 17% at X-band with 16.5% electronic efficiency was achieved [12,13] at the second harmonic of the electron cyclotron mode using a three-fold helically corrugated waveguide and an axis-encircling electron beam.

Variations to increase the bandwidth of gyrotron amplifiers have been investigated [14,15]. For example, a series of gyro-amplifiers have obtained 16% efficiency at a frequency of 5 GHz with a uniform magnetic field, increasing to 26% efficiency with 7% bandwidth using a tapered field [16]. Recently, impressive experimental results on a gyro-TWT were achieved by Chu et al., who studied the amplifier at the fundamental cyclotron harmonic. By stabilizing oscillations with the use of an interaction structure with distributed wall losses, this 35 GHz Ka-band amplifier produced 93 kW of power at 26.5% efficiency and 70 dB gain with a -3 dB bandwidth of 8.6% [17]. Gyro-TWA experiments based on a helically corrugated waveguide have been undertaken at Strathclyde University for the last few years. Experiments in X-band achieved 1.1 MW output power with 30% electronic efficiency, 21% relative -3 dB bandwidth [18,19].

Research projects investigating Gyro-BWOs and Gyro-TWAs in the W-band using helically corrugated waveguides started at Strathclyde University in 2010. Presented in this paper is the design, simulation of the gyro-devices and initial experimental results of the W-band Gyro-BWO.

2. Cusp electron gun

A novel cusp electron beam source is used to drive the beam wave interaction in the W-band Gyro-BWO and Gyro-TWA. This electron gun is required to produce an axis-encircling, annular shaped electron beam of current 1.5 A, energy 40 keV and a pitch alpha (= the ratio between the transverse momentum and the axial momentum of the electron beam) of up to 2 with the beam optimized for interaction with an operating eigenwave in the cavity. For the gyro-BWO interaction a pitch alpha of 1.5-2 could be used to drive the high efficiency beam-wave interaction. However for the Gyro-TWA a slightly lower pitch alpha in the range of 1.0-1.2 is preferred to maintain zero-drive stability of the amplifier.

The cusp electron gun is a novel way of creating an axis-encircling annular electron beam ideal for use in gyrotron devices. Conventional electron guns mainly used in gyrotron devices are the Magnetron Injection Gun (MIG) and Pierce gun. Mode selectivity is poor in the MIG as the coupling for such a beam is strongest to the fundamental mode. In the Pierce gun case, a straight linear electron beam is kicked into an axis-encircling path. However, for this CW source the Pierce gun would not be a suitable source as the kicker magnet is feasible primarily in pulsed mode. Due to the high power of the spent electron beam, an annular shaped electron beam is desirable for beam energy recovery using a depressed collector method. Therefore, the cusp gun is the best choice of electron gun for this Gyro-BWO and Gyro-TWA.

Initially, transport of an electron beam through opposing magnetic fields (the so-called "magnetic cusp") was investigated in the 1960s [20,21] for plasma-containment applications.

Schmidt described a threshold for magnetic mirroring and the effects on the electrons after they have passed through the cusp region, namely, azimuthal rotation around the central axis of symmetry due to conservation of the electron canonical momentum given in equation (1) which is satisfied by an off-axis beam, where v_θ is zero.

$$P_\theta - qrA_\theta = mv_\theta r \quad (1)$$

When the magnetic field changes sign the vector potential A_θ also changes sign therefore v_θ cannot be zero to still satisfy this equation.

Following Schmidt et al. [20] continuous efforts and progress have been made through both theoretical analysis and experimental study in the generation of cusp-based electron-beam sources [22,23]. Special concentration was paid on the methods to produce an ideal sharp cusp shape by using complex arrays of magnetic coils, magnetic poles, and, possibly, magnetic material inside the cathode [24,25,26]. These studies have been based on the configuration where a magnetic cusp was located at or after the anode where large cusp amplitude was required due to a fully accelerated electron momentum. However the electron gun designed for W-band gyro-devices was based on a “smooth” cusp [27], formed by two simple coils without any magnetic shaping poles, located immediately after the cathode.

3. Numerical simulation of the cusp gun

The 3D PIC (Particle in Cell) code MAGIC was used to simulate the cusp gun. A slice through the geometry, in polar coordinates, can be seen in Fig. 1. Two solenoids are used, one with a negative polarity. The negative coil is positioned immediately behind the cathode and the cavity coil midway along the waveguide. An accelerating voltage of 40 kV is applied to the diode which results in an emitted current density of $9.6 A/cm^2$ from the cathode. The shape of the cathode and the electron emitting surface, the positions and dimensions of the solenoids have been optimized to ensure the best electron beam qualities when it gets compressed, passes through the magnetic cusp and enters the higher magnetic field region. Desirable electron beam properties include a uniform beam density, less off-centering coupling with a low velocity spread. At the end of the electron beam drift region a cylindrical step down reflector of radius 0.837 mm is used to stop microwaves returning to the diode. The input waveguide to the helical structure has a radius of 1.3 mm suitable for use at W-Band frequencies.

The simulated electron-beam trajectory from the cusp gun with its magnetic-field profile ($B_0 = 1.82 T$) is shown in Fig. 1. The cross-sectional shape of the beam at the downstream region is also shown in Fig. 1, and it clearly shows an annular-shaped axis-encircling beam. The magnetic field profile is a smooth transition from the cathode to the downstream uniform magnetic-field region, with the cusp being located at $\sim 4.6 mm$ in front of the emission surface.

From simulation, to obtain an alpha value of one to three, the required magnetic field at the cathode was $\sim 3.0-6.7 mT$. At a constant value of B_0 , a larger α value could be achieved by increasing the magnetic-field amplitude at the cathode (B_c). The simulated average alpha of the electron beam as a function of the magnetic-field amplitude at the cathode is shown in Fig. 2 for $B_0 = 1.82 T$. The spread in alpha is also shown in this figure as bars, deviating from the

average values. The alpha values calculated from the previous equation are also shown in Fig. 2 for comparison. Minimum axial velocity spreads of $\sim 8\%$ and relative alpha spreads of $\sim 10\%$ were achieved at an alpha value of 1.65 at this constant magnetic field. At B_0 values of 2.1 and 1.7 T, the optimum alpha spreads were $\sim 23\%$ and $\sim 15\%$ for alpha values of 3 and 1.2, respectively, and the corresponding axial velocity spreads for these cases were $\sim 20\%$ and $\sim 10\%$. At the central magnetic field B_0 of 1.82 T, the beam had an inner and an outer radius of 0.23 mm and 0.42 mm, respectively, with an envelope ripple $\sim 13\%$. Beam transport through the tube was measured to be 100% after the initial low potential electrons were reflected.

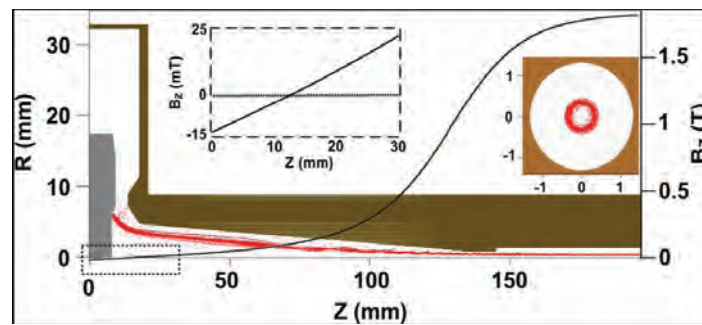


Fig. 1 Cross-section of cusp geometry with simulated electron beam trajectories.

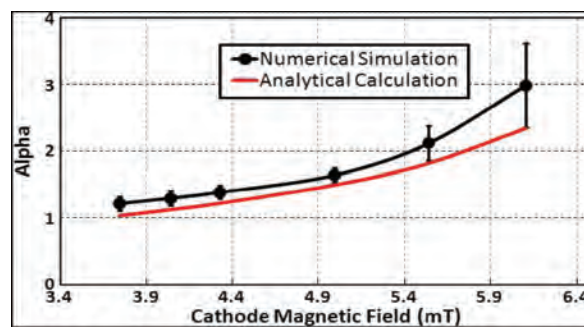


Fig. 2 Numerically simulated and analytically calculated alpha values for different values of cathode magnetic field at $B_0 = 1.82$ T.

4. Cusp gun experiment

Based on the simulation results for one particular set of parameters which yields an optimized beam for an alpha range of 1–2, the cusp electron gun of Fig. 3 was manufactured. The cathode assembly and the anode were arranged in a coaxial configuration Fig. 3. The cathode head included three following interchangeable parts: outer, inner focusing electrodes, and the thermionic cathode emitter which was located between the electrodes and constructed from porous tungsten impregnated with barium oxide. Facing the cathode head was an interchangeable anode tip.

The beam cross-sectional shape and dimensions were recorded by a phosphor scintillator plate and digital camera system [28] after the Faraday cup was removed. The scintillator, a round transparent disk coated with a thin layer of phosphor, produces visible light when electrons impact on the surface. A typical scintillator image, after the optical noise was removed, is shown in Fig. 4. The image shows clearly that an axis-encircling electron beam was generated.

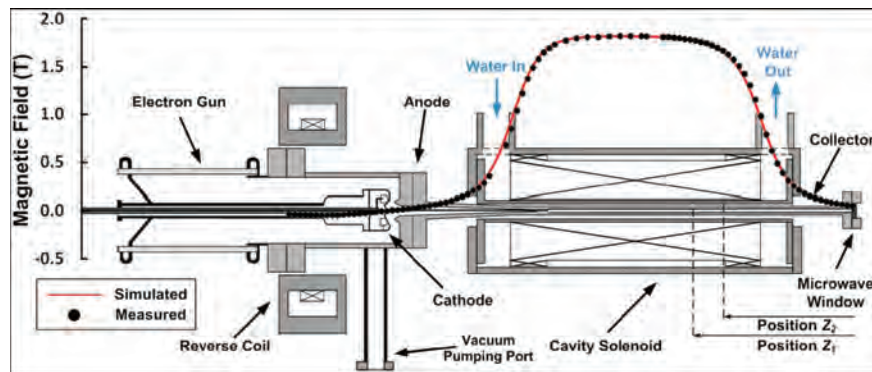


Fig. 3 Schematic diagram of the cusp electron gun with simulated and measured magnetic field profiles overlaid.

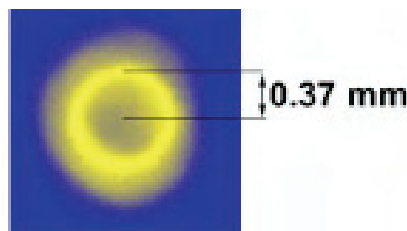


Fig. 4 Scintillator recorded beam cross-sectional shape at the downstream region.

5. Interaction cavity of Gyro-BWO

Fig. 5 shows the photo of the helically corrugated interaction region. The 3-fold helically corrugated waveguide resonantly couples two partial waves, one the A wave (Fig. 6), is the near cutoff TE_{21} mode, the other, the B wave, is a traveling TE_{11} mode. When Bragg resonant conditions are met, the coupling results in two eigenwaves W_1 and W_2 as shown in Fig. 6. One of the eigenwaves (W_1) has a near constant group velocity at small wavenumber over a wide frequency range. This ideal dispersion property allows wide frequency bandwidth to be achieved for a gyrotron travelling wave amplifier as well as for gyro-BWOs.

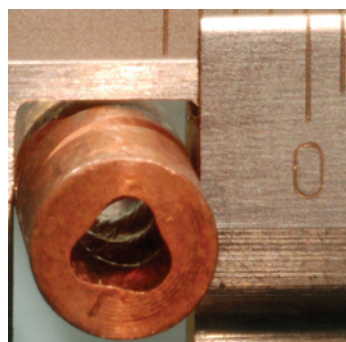


Fig. 5 A photo of the helically corrugated waveguide for the W-band Gyro-BWO.

The helically corrugated waveguide was designed for the optimized frequency bandwidth and interaction efficiency. The dispersion of the operating eigenwave was measured by measuring the phase evolution of a counter-rotating circular polarized wave when it propagates through the waveguide by using an Anritsu 7808B 40 MHz - 110 GHz VNA broadband vector network analyser and is shown in Fig. 6. Two partial waves A and B, together with two eigenwaves calculated using perturbation theory, electron beam dispersion

line and the growth rate at an interaction frequency of ~ 94 GHz as it interacts with the operating eigenwave at a magnetic field of ~ 1.83 T are shown in Fig. 6.

The measured operating eigenwave was found to be in very good agreement when compared with the results simulated from MAGIC and calculations based on perturbation theory. In the simulation using the MAGIC code, a left-polarized circular wave of one frequency was injected into the right-hand helical waveguide, and a component of the electric field inside the waveguide was measured along the axial direction. The measured field was then numerically analyzed and the axial wavenumber of the eigenwave was therefore obtained for that frequency.

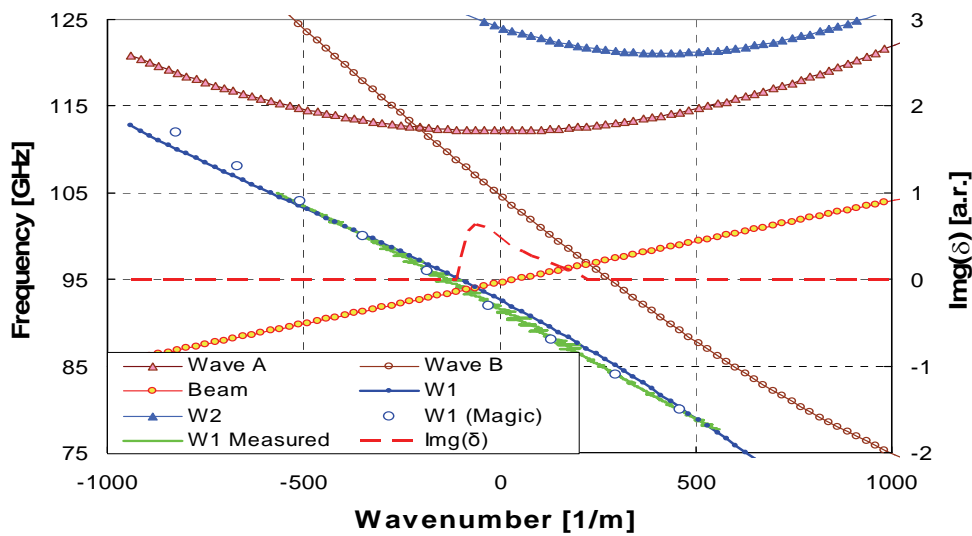


Fig. 6 Dispersion diagram of the operating eigenwave, the second harmonic electron cyclotron mode, an interaction at ~ 94 GHz and corresponding growth rate of the W-band Gyro-BWO.

6. Simulation of Beam-wave interaction in a Gyro-BWO

The beam-wave interaction of the Gyro-BWO was simulated using Magic when driven by a large-orbit annular shaped electron beam of voltage 40 kV, current 1.5 A and a pitch alpha of 1.6, and the simulated output power and frequency are shown in Fig. 7.

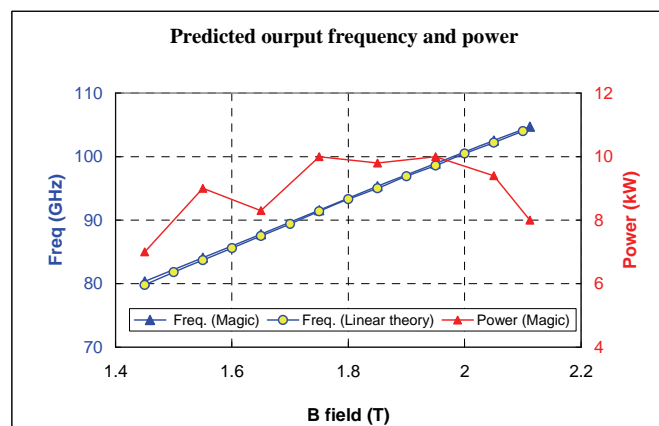


Fig. 7 Simulated output power and frequency as a function of cavity magnetic field.

7. Gyro-BWO Experiment

The setup of the experiment is shown in Fig. 8 with the cusp gun shown in the left, helical interaction region in the middle and output window at the right. Two coils, which form a magnetic cusp at the front of the cathode surface, are also shown in Fig. 8.

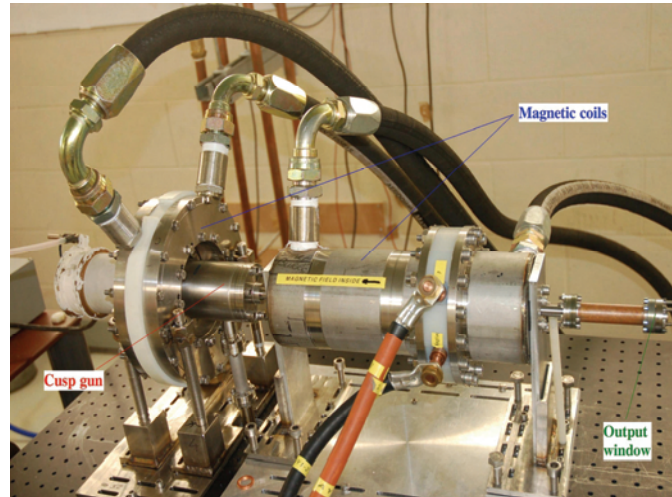


Fig. 8 The setup of the W-band Gyro-BWO experiment.

The cusp gun was firstly tested under a pulsed operation mode using a double Blumlein pulsed power system made from a cable. The thermionic cathode is designed to operate in a temperature-limited regime. Microwave radiation has been observed in the Gyro-BWO operation. Typical measured beam voltage, emitting current from cathode, transported current at the downstream side of the cavity and detected microwave traces were recorded and are shown in Fig. 9.

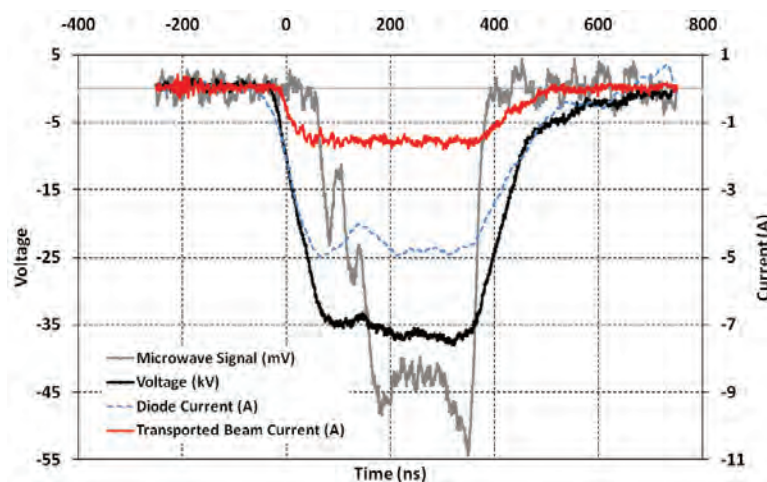


Fig. 9 Recorded traces of beam voltage, emitting current, beam current and microwave radiation.

8. Design of Gyro-TWA

The coupling of the beam and the eigenwave that exists inside the helically corrugated waveguide can be described by the following equation:

$$\begin{aligned}
 & [(h^2 - 2\delta)(h + \Delta_g - \delta/h_0) + 2\sigma^2/h_0][h - (\delta - \Delta_H)/\beta_{z0}]^2 \\
 & = C^3(h + \Delta_g - \delta/h_0) \left\{ 1 + \frac{2s}{\alpha_0^2 \beta_{z0}} [h - (\delta - \Delta_H)/\beta_{z0}] \right\}
 \end{aligned}
 \tag{2}$$

The resultant dispersions of the eigenwave and beam cyclotron mode as well as the small signal growth rate are shown in Fig. 10.

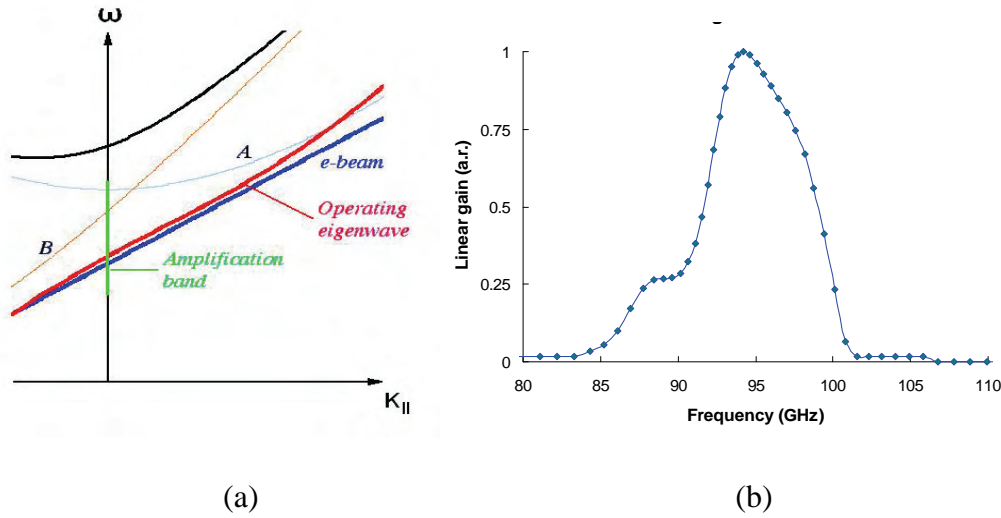


Fig. 10 (a) The dispersion of the eigenwave and electron beam and (b) the small signal growth rate.

The beam-wave interaction inside the helically corrugated waveguide was simulated by using the 3D PIC code MAGIC. The simulated output power as a function of input power at 96 GHz is shown in Fig. 11.

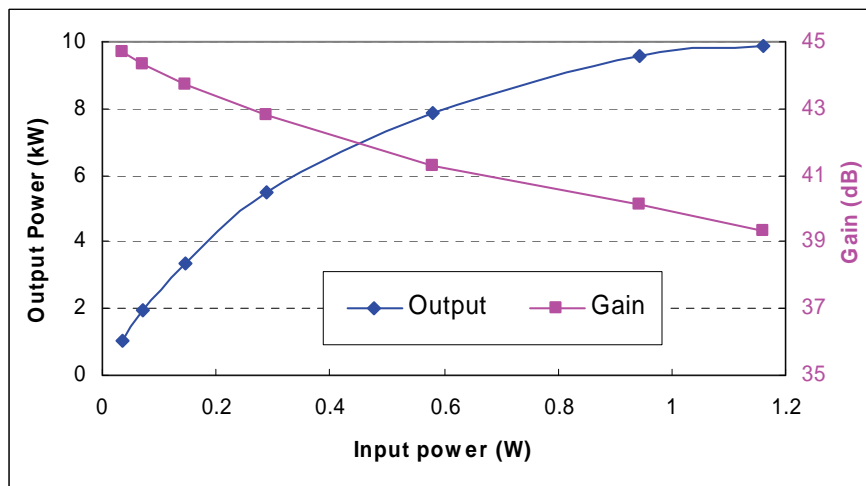


Fig. 11 Simulated output power as a function of input power.

At a constant cavity magnetic field of 1.83 T, the W-band Gyro-TWA was simulated to output a maximum power of 10 kW, with a -3 dB bandwidth of 90-100 GHz and a saturated gain of 40 dB at the centre frequency of the amplification band. The output power and gain curve are shown in Fig. 12.

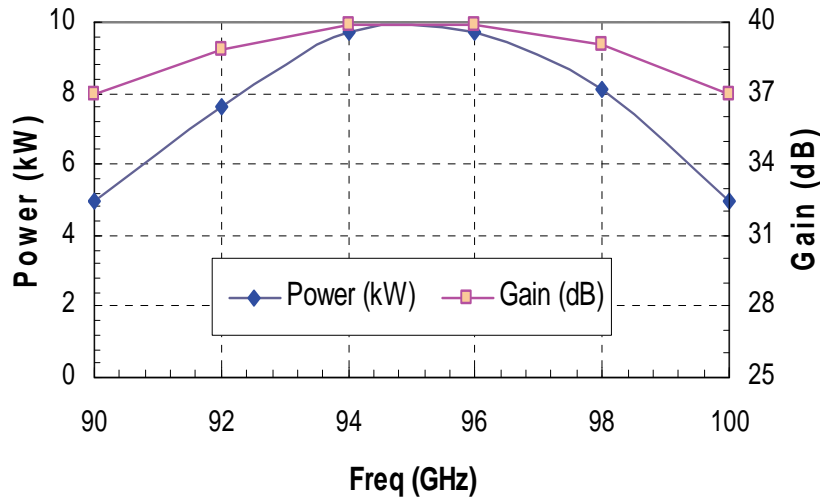


Fig. 12 Simulated performance of the W-band Gyro-TWA.

A side-wall rectangular-to-circular coupler was used to seed the input signal for the Gyro-TWA. A ceramic window constructed in a pillbox cavity was used to serve as a vacuum boundary. This same input coupler of the Gyro-TWA can be used as an output coupler for Gyro-BWO operation. Therefore the coupler was aimed to achieve a high transmission coefficient for a W-band Gyro-BWO working in the frequency range of 84 GHz - 104 GHz as well as a W-band Gyro-TWA working in the frequency range of 90 GHz - 100 GHz. In the design, a Bragg reflector was employed to prevent the microwave radiation from travelling into the cusp gun region. Usage of a Bragg reflector instead of the cut-off waveguide resulted in an increase of the size of the beam tunnel and made it easier for the beam to pass into the interaction region. The optimized coupler achieved a transmission coefficient of better than -1 dB over the whole operating frequency range.

The output window, positioned at the output end of the interaction region, consisted of 3 pieces of dielectric disks, with the middle sapphire disk serving as the vacuum boundary and two quartz disks at the both sides to increase the operating bandwidth. The thickness of the disks and the separation distances of the disks were optimized by analytical calculation and finally simulated by CST Microwave Studio. The configuration of the output window and optimized S_{11} parameter are shown in Fig. 13.

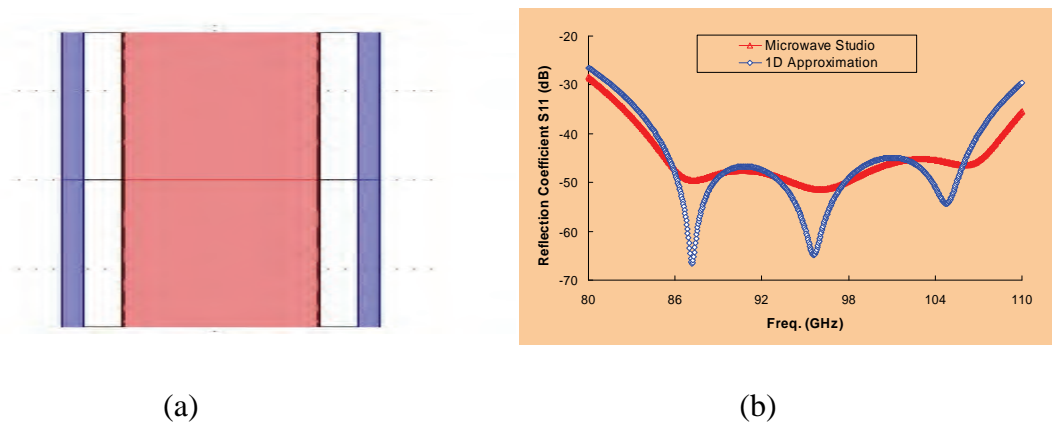


Fig. 13 (a) The geometry of the output window, (b) calculated and simulated reflection coefficient S_{11} .

9. Conclusion

A Gyro-BWO with a -3 dB frequency tuning range of 84-104 GHz and a Gyro-TWA with an instantaneous amplification bandwidth of 90 – 100 GHz were designed and manufactured for high power CW output of up to 10 kW. The thermionic cusp gun based electron beam to drive the beam-wave interactions of the gyro-devices was successfully operated and the measured beam energy, current and pitch alpha were in excellent agreement with the simulated results from the PIC code MAGIC. Microwave radiation from the Gyro-BWO was observed and continuous tuning of the output frequency from 92-102 GHz achieved in the initial experiment by changing the cavity magnetic field. Furthermore, the W-band Gyro-TWA was predicted to have a saturated gain of ~ 40 dB and interaction efficiency of 17%. The interaction cavity, input coupler and output window were designed and optimized.

References

- [1] W. M. Manheimer, G. Mesyats, and M. I. Petelin, in *Applications of High-Power Microwaves*, edited by A.V.Gaponov-Grekhov and V.L. Granatstein, Artech House, Boston, pp. 169-207, (1994).
- [2] D. D. Amone, C. M. Cielsla, A. Corchia, S. Egusa, et al, *Proc. SPIE Terahertz Spectroscopy Applicat. II.*, pp. 3823, Munich, Germany, (1999).
- [3] T. Imani, N. Kobayashi, R. Temkin, M. Thumm, M.Q. Tran and V. Alikeev, "Electron Cyclotron Heating and Current Drive System", *Fusion Eng. Design*, 55, no. 2-3, pp. 281, (2001).
- [4] T. I. Smirnova, A. I. Smirnov and R. B. Clarkson, "W-band(95GHz)EPR Spectroscopy of Nitroxide Radicals With Complex Proton Hyperfine Structures: Fast Motion", *J. Phys. Chem.*, 99, No. 22, pp. 9008, (1995).
- [5] G. Burt, S. V. Samsonov, K. Ronald, G. G. Denisov, et al., 'Dispersion of helically corrugated waveguides: Analytical, numerical, and experimental study', *Phys. Rev. E*, 70, (4), 046402, (2004).
- [6] A. W. Cross, W. He, A. D. R. Phelps, K. Ronald, et al., 'Helically corrugated waveguide gyrotron traveling wave amplifier using a thermionic cathode electron gun', *Appl. Phys. Lett.*, 90, (25), 253501, (2007).
- [7] W. He, K. Ronald, A. R. Young, A. W. Cross, et al., 'Gyro-BWO experiments using a helical interaction waveguide', *IEEE Trans. Electron Devices*, 52, (5), pp. 839, (2005).
- [8] W. He, A. W. Cross, A. D. R. Phelps, K. Ronald, et al., 'Theory and simulations of a gyrotron backward wave oscillator using a helical interaction waveguide', *Appl. Phys. Lett.*, 89, (9), 091504, (2006).
- [9] S. Y. Park, R. H. Kyser, C. M. Armstrong, R. K. Parker and V. L. Granatstein, "Experimental study of a Ka-band gyrotron backward-wave oscillator", *IEEE Trans. Plasma Sci.*, vol.18, pp321-325, June, (1990).
- [10] C. S. Kou, S. G. Chen, L. R. Barnett, H. Y. Chen and K. R. Chu, "Experimental study of an injection-locked gyrotron backward-wave oscillator", *Phys. Rev. Lett.*, vol. 70, no. 7, pp924-927, (1993).
- [11] V. L. Bratman, G. G. Denisov, V. N. Manuilov, S. V. Samsonov and A. B. Volkov, *Digest of Int. Conf. Infrared and Millimeter Waves*, Toulouse, France, O. Portugall and J. Leotins Eds. (ISBN 2-87649-035-8), (2001).
- [12] W. He, K. Ronald, A.R. Young, A.W. Cross, A.D.R. Phelps, C.G. Whyte, E.G. Rafferty, J. Thomson, C.W. Robertson and D.C. Speirs, S.V. Samsonov, V.L. Bratman and G.G. Denisov, *IEEE Trans. Electron Devices*, 52, 839, (2005).

- [13] W. He, A. W. Cross, A. D. R. Phelps, K. Ronald, C. G. Whyte, S. V. Samsonov, V. L. Bratman, and G. G. Denisov, *Appl. Phys. Lett.* 89, 091504, (2006).
- [14] K. R. Chu, A. T. Drobot, V. L. Granatstein, and J. L. Seftor, *IEEE Trans. Electron Devices* MTT-27, 178–187, (1979).
- [15] M. Blank, in *Generation and Application of High Power Microwaves*, edited by R. A. Cairns and A. D. R. Phelps, Proceedings of the 48th Scottish Universities Summer School in Physics, IOP, Bristol, (1996).
- [16] P. E. Ferguson, G. Valier, and R. S. Symons, *IEEE Trans. Microwave Theory Tech.* 29, 794–799, (1981).
- [17] K. R. Chu, H.Y. Chen, C. L. Hung, T. H. Chang, L. R. Barnett, S. H. Chen, and T. T. Yang, *Phys. Rev. Lett.* 81, 4760–4763 (1998).
- [18] G. G. Denisov, V. L. Bratman, A. W. Cross, W. He, A. D. R. Phelps, K. Ronald, S. V. Samsonov and C. G. whyte, “Gyrotron travelling wave amplifier with a helical interaction region”, *Phys. Rev. Lett.*, 81, pp5680-5683, (1998).
- [19] V. L. Bratman, A. W. Cross, G. G. Denisov, W. He, A.D.R. Phelps, K. Ronald, S.V. Samsonov, C. G. Whyte and A. R. Young, ‘High Gain Wide-Band Gyro-Travelling Wave Amplifier With A Helically Corrugated Waveguide’, *Phys. Rev. Lett.*, 84, Pp2746-2749, (2000).
- [20] Schmidt G., Nonadiabatic Particle Motion in Axialsymmetric Fields, *The Physics of Fluids*, 5, 994-1002, (1962).
- [21] J. Sinnis and G. Schmidt, “Experimental trajectory analysis of charged particles in a cusped geometry,” *Phys. Fluids*, vol. 6, no. 6, pp. 841–845, Jun. (1963).
- [22] M. J. Rhee and W. W. Destler, “Relativistic electron dynamics in a cusped magnetic field,” *Phys. Fluids*, vol. 17, no. 8, pp. 1574–1581, Aug. 1974.
- [23] W.W.Destler and M.J. Rhee, “Radial and axial compression of a hollow electron beam using an asymmetric magnetic cusp,” *Phys. Fluids*, vol. 20, no. 9, pp. 1582–1584, Sep. (1977).
- [24] G. P. Scheitrum, R. S. Symons, and R. B. True, “Low velocity spread axis encircling electron beam forming system,” in *IEDM Tech. Dig.*, pp. 743–746, (1989).
- [25] K. T. Nguyen, D. N. Smithe, and L. D. Ludeking, “The double-cusp gyrogun,” in *IEDM Tech. Dig.*, pp. 219–222, (1992).
- [26] D.A.Gallagher, M. Barsanti, F. Scafuri, and C. Armstrong, “High-power cusp gun for harmonic gyro-device applications,” *IEEE Trans. Plasma Sci.*, vol. 28, no. 3, pp. 695–699, Jun. (2000).
- [27] W. He, C. G. Whyte, E. G. Rafferty, A. W. Cross, A. D. R. Phelps, K. Ronald, A. R. Young, C. W. Robertson, D. C. Speirs, and D. H. Rowlands, “Axis-encircling electron beam generation using a smooth magnetic cusp for gyrodevices,” *Appl. Phys. Lett.*, vol. 93, no. 12, 121501, Sep. (2008).
- [28] W. He, H. Yin, A. D. R. Phelps, A. W. Cross, and S. N. Spark, *Rev. Sci. Instrum.* 72, pp. 4266, (2001).

A cusp electron gun for millimeter wave gyrodevices

C. R. Donaldson,^{a)} W. He, A. W. Cross, F. Li, A. D. R. Phelps, L. Zhang, K. Ronald, C. W. Robertson, C. G. Whyte, and A. R. Young

Department of Physics, SUPA, University of Strathclyde, Glasgow G4 0NG, United Kingdom

(Received 18 January 2010; accepted 8 March 2010; published online 5 April 2010)

The experimental results of a thermionic cusp electron gun, to drive millimeter and submillimeter wave harmonic gyrodevices, are reported in this paper. Using a “smooth” magnetic field reversal formed by two coils this gun generated an annular-shaped, axis-encircling electron beam with 1.5 A current, and an adjustable velocity ratio α of up to 1.56 at a beam voltage of 40 kV. The beam cross-sectional shape and transported beam current were measured by a witness plate technique and Faraday cup, respectively. These measured results were found to be in excellent agreement with the simulated results using the three-dimensional code MAGIC. © 2010 American Institute of Physics. [doi:10.1063/1.3374888]

Further to the design and numerical optimization of a cusp electron beam source,¹ in this paper we present the experiment of the cusp gun and the measured results of the generated axis-encircling electron beam. Due to its small cross-sectional size (less than 1 mm in diameter) in a large magnetic field (a few tesla) such a beam is capable of driving millimeter and submillimeter wave gyrodevices which have many modern applications notably in remote sensing,² medical imaging,³ plasma heating,⁴ and electron spin resonance spectroscopy.⁵ In order to reach higher frequencies, gyrodevices are more commonly operating at a higher indexed waveguide mode and a harmonic of the electron cyclotron frequency;^{6–10} the advantage being that it lowers the required magnetic field strength by a factor of s , the harmonic number. However, operating at harmonics could introduce undesired mode competition, as well as parasitic oscillations. An axis-encircling electron beam is ideal for harmonic gyrodevices due to its good mode selectivity as the beam-wave coupling requires that the azimuthal index of the waveguide mode, m be equal to s .¹¹ Compared to previous cusp guns,^{12–15} this cusp gun has the advantage of (1) simple design and structure with reduced manufacturing complexity due to the “smooth cusp” configuration¹⁶ using two coils without any need for extra magnetic poles and/or material and (2) smaller cusp amplitude because the cusp is located immediately after the cathode where the electron is not fully accelerated.

The electron gun was designed and optimized using the three-dimensional particle-in-cell code MAGIC. The applications were for three microwave sources being developed including a W-band gyrotron backward-wave oscillator (gyro-BWO)¹⁷ and a W-band gyrotron traveling-wave tube¹⁸ both using a helically corrugated waveguide and a terahertz seventh harmonic gyrotron.¹⁹ These devices are based on the previous radiation sources operating at X-band (8.4 to 12 GHz) frequencies.^{20–22} The cusp gun was designed to generate an electron beam of 1.5 A, 40 kV with velocity ratio $\alpha = 1–3$ in order to generate millimeter and submillimeter waves of 75 GHz to 390 GHz over a magnetic field range of 1.50–2.1 T. Based on the simulation results for one particular set of parameters which yields an optimized beam for an

alpha range of 1–2, the cusp electron gun of Fig. 1 was manufactured.

The cathode assembly and the anode were arranged in a coaxial configuration (Fig. 1). The cathode head included three following interchangeable parts: outer, inner focusing electrodes, and the thermionic cathode emitter which was located between the electrodes and constructed from porous tungsten impregnated with barium oxide. Facing the cathode head was an interchangeable anode tip. The beam trajectories are determined by the dimensions of these interchangeable parts. The cathode heating coil was bifilar wound in order to minimize any contribution to the field at the cathode.¹ Two fine gaps of 0.1 mm in width between the emitter and the focusing electrodes were used to reduce the thermal loading of the cathode and to stop the migration of barium from the emitter. Layers of thin tubes and disks made from molybdenum, located between the outer electrodes and the emitter and behind the emitter, respectively, were used as radiation shields to further reduce the thermal loading of the cathode. The beam tunnel tapered down from the anode aperture (radius 4 mm) to the cut-off filter (radius 0.84 mm), followed by an experimental region, a cylindrical tunnel of radius 3.0 mm and length 292 mm, and then to the up-taper and finally the window region. This experimental region allowed the beam diagnostic apparatus such as the Faraday cup and the scintillator witness plate to be inserted. A single layer sapphire window was used in this beam experiment for observation of the visible light generated by the scintillator. The whole system was evacuated to 10^{-9} mBar.

The magnetic field coils were wound from annealed, varnish-coated, square copper wire of cross section 2.2×2.2 mm², enclosed in watertight, stainless steel chambers, and cooled by high pressure recirculating water when in operation. The cavity solenoid which generates a uniform B-field in the beam-wave interaction region has 14 layers each of 103 turns. Two extra layers of coils were added to both ends of the main solenoid to reduce the rise and fall distance of its B-field profile for a certain length of the flat-top so that the overall turns, length of the solenoid, and hence the driving electric power were reduced. At maximum achievable magnetic field strength of 2.1 T the required driving power was ~ 65 kW at a current of ~ 270 A. The layers were separated by 0.4 mm gaps to allow cooling water to

^{a)}Electronic mail: craig.donaldson@strath.ac.uk.

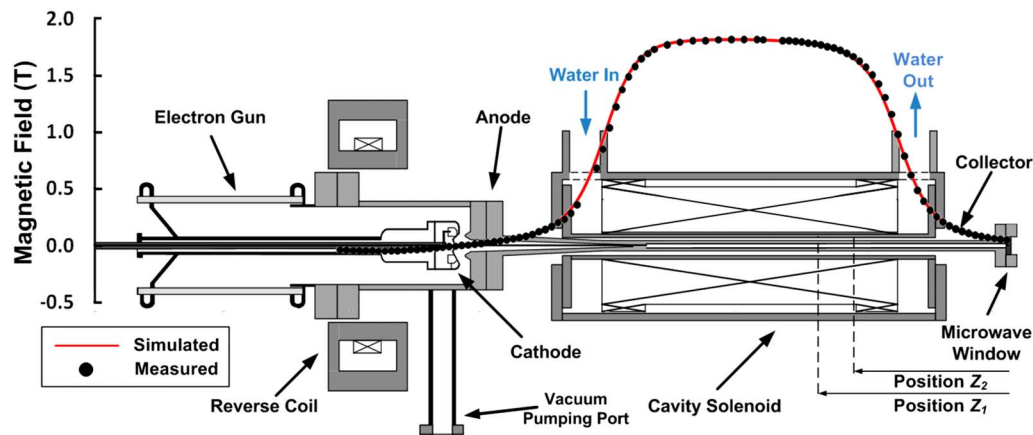


FIG. 1. (Color online) Schematic diagram of the cusp electron gun with simulated and measured magnetic field profile overlaid.

pass from one end to the other end of the solenoid. Simulations of the fluid dynamics and heat exchange including heat conduction, convection, and diffusion were performed by using the MultiPhysics code COMSOL.²³ The reverse coil, having four layers each of ten turns, produced the reverse B-field for the cusp gun. The magnetic field profiles measured using an axial Hall probe and calculated from MAGIC are shown in Fig. 1.

A double cable Blumlein²⁴ which could output a ~ 380 ns, 40 kV pulse was used to drive the cusp gun. The beam voltage was measured using a two-stage voltage divider made from metal film resistors. The emitted current was measured with a Rogowski coil located in the earth line between the anode and the cable Blumlein and the beam current by a Faraday cup at Z_1 location (see Fig. 1).

The beam cross-sectional shape and dimensions were recorded by a phosphor scintillator plate and digital camera system²⁵ after the Faraday cup was removed. The scintillator, a round transparent disk coated with a thin layer of phosphor, produces visible light when electrons impact on the surface. A thin titanium disk of thickness ~ 8 μm was placed before the scintillator to reduce the impact energy of the beam. The scintillator disk was located at position Z_2 (see Fig. 1), 10.5 cm from the window so as to match with the focal length of the camera, at this position the magnetic field tailed off to 90% of the cavity B-field. By using the equation in Ref. 16, the α value in the cavity (in particular, at Z_1) could be calculated from the B-field and α values at Z_2 .

Typical traces of beam voltage and beam current are shown in Fig. 2. The emitted current from the cathode could be varied from 0 to ~ 1.6 A by increasing the operating

temperature of the cathode, at the applied beam voltage of 40 kV. Further increase in the temperature did not result in an increase in the beam current. This indicated that the operation of the cathode had become space-charge limited. In Fig. 2, we can see the beam current reached a steady value of 1.5 A. When the cavity B-field was 1.82 T $\sim 96\%$ of this current reached the Faraday cup.

A typical scintillator image, after the optical noise was removed, is shown in Fig. 3. The image shows clearly that an axis-encircling electron beam was generated. The simulated beam cross-sectional shape is shown for comparison together with beam trajectories in the R - Z plane. For this particular measurement, at a cavity B-field of 1.64 T, the annular beam was measured to have an average radius of ~ 0.37 mm. It was calculated from the equation in Ref. 16 that the corresponding α was 1.34 ± 0.11 . This corresponded to an α value of 1.56 ± 0.16 at the Z_1 position.

By adjusting the reverse coil current the magnetic field at the cathode and hence the value of the velocity ratio of the beam in the cavity could be controlled. At $B_0 = 1.64$ T the velocity ratio at position Z_2 as a function of cathode B-field was measured and is shown in Fig. 4. For comparison of the simulated α at Z_1 and Z_2 as well as analytically calculated value at Z_2 are also shown in Fig. 4. From the diagram, the measured α value had the same trend and good agreement with both the numerical simulated and analytically calculated values. However investigation at higher alphas was limited by the capability of the existing power supply.

In summary, when the thermionic cusp gun for millimeter/submillimeter wave gyrodevices was tested, the

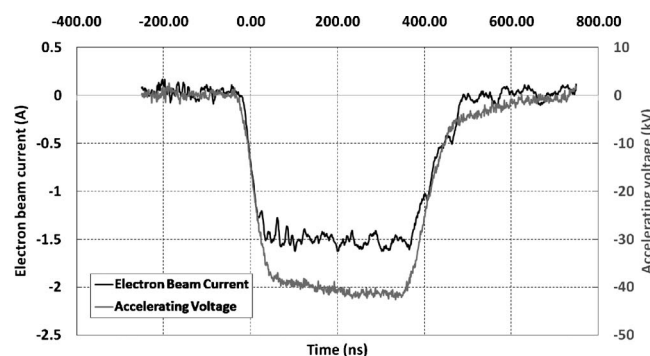


FIG. 2. The typical traces of the measured beam voltage and beam current.

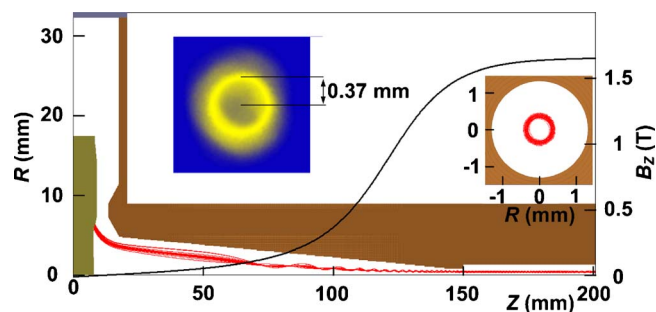


FIG. 3. (Color online) Snapshot of the simulated electron beam trajectory with magnetic field profile overlaid, also simulated and scintillator recorded beam cross-sectional shape at the downstream region.

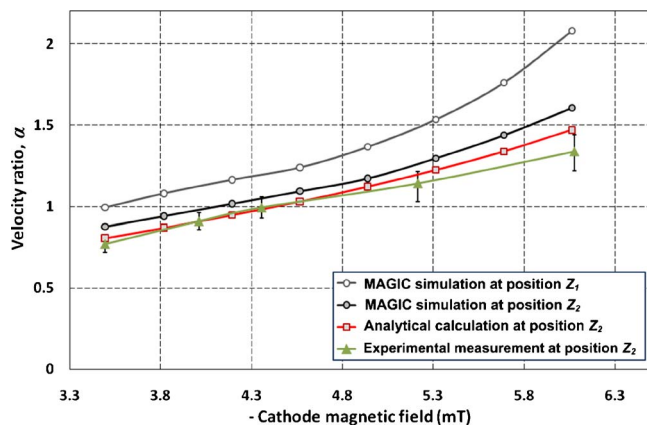


FIG. 4. (Color online) The measured, simulated, and analytically calculated beam velocity ratio as a function of cathode magnetic field at $B_0=1.64$ T.

measured beam parameters were in excellent agreement with the MAGIC simulation. In addition, in a recent experiment, the beam from this cusp gun has been used in a helical waveguide gyro-BWO which generated microwave radiation in the frequency range 92–100 GHz.²⁶

The authors would thank the UK Engineering and Physical Sciences Research Council, the UK Faraday Partnership in High Power RF, the Scottish Universities Physics Alliance and Overseas Research Students Awards Scheme for supporting this work.

¹C. R. Donaldson, W. He, A. W. Cross, A. D. R. Phelps, F. Li, K. Ronald, C. W. Robertson, C. G. Whyte, A. R. Young, and L. Zhang, *IEEE Trans. Plasma Sci.* **37**, 2153 (2009).

²W. M. Manheimer, G. Mesyats, and M. I. Petelin, in *Applications of High-Power Microwaves*, edited by A. V. Gaponov-Grekhov and V. L. Granatstein (Artech House, Norwood, 1994), pp. 169–207.

³R. M. Woodward, B. E. Cole, R. J. Pye, D. D. Amone, E. H. Linfield, and M. Pepper, *Phys. Med. Biol.* **47**, 3853 (2002).

⁴T. Imai, N. Kobayashi, R. Temkin, M. Thumm, M. Q. Tran, and V. Alikaev, *Fusion Eng. Des.* **55**, 281 (2001).

⁵H. M. Assenheim, *Introduction to Electron Spin Resonance* (Plenum, New York, 1966).

⁶M. Garven, J. P. Calame, B. G. Danly, K. T. Nguyen, B. Levush, F. N. Wood, and D. E. Pershing, *IEEE Trans. Plasma Sci.* **30**, 885 (2002).

⁷G. F. Brand, P. W. Fekete, K. Hong, K. J. Moore, and T. Idehara, *Int. J. Electron.* **68**, 1099 (1990).

⁸T. Idehara, I. Ogawa, S. Mitsudo, Y. Iwata, S. Watanabe, Y. Itakura, K. Ohashi, H. Kobayashi, T. Yokoyama, V. E. Zapevalov, M. Y. Glyavin, A. N. Kufin, O. V. Malygin, and S. P. Sabchevski, *IEEE Trans. Plasma Sci.* **32**, 903 (2004).

⁹T. H. Chang, C. F. Yu, C. L. Hung, Y. S. Yeh, M. C. Hsiao, and Y. Y. Shin, *Phys. Plasmas* **15**, 073105 (2008).

¹⁰Q. S. Wang, H. E. Huey, D. B. McDermott, Y. Hirata, and N. C. Luhmann, Jr., *IEEE Trans. Plasma Sci.* **28**, 2232 (2000).

¹¹K. R. Chu, *Rev. Mod. Phys.* **76**, 489 (2004).

¹²J. Sinnis and G. Schmidt, *Phys. Fluids* **6**, 841 (1963).

¹³M. Friedman, *Phys. Rev. Lett.* **24**, 1098 (1970).

¹⁴W. Lawson, *Appl. Phys. Lett.* **50**, 1477 (1987).

¹⁵S. G. Jeon, C. W. Baik, D. H. Kim, G. S. Park, N. Sato, and K. Yokoo, *Appl. Phys. Lett.* **80**, 3703 (2002).

¹⁶W. He, C. G. Whyte, E. G. Rafferty, A. W. Cross, A. D. R. Phelps, K. Ronald, A. R. Young, C. W. Robertson, D. C. Speirs, and D. H. Rowlands, *Appl. Phys. Lett.* **93**, 121501 (2008).

¹⁷C. R. Donaldson, W. He, A. D. R. Phelps, F. Li, A. W. Cross, K. Ronald, A. R. Young, and C. G. Whyte, *Joint 33rd International Conference on Infrared and Millimeter and 16th International Conference on Terahertz Electronics*, Pasadena, CA, 2008 (IEEE, New York, 2008).

¹⁸W. He, A. D. R. Phelps, A. W. Cross, C. R. Donaldson, and K. Ronald, The 17th High-Power Particle Beams Conference (Beams' 08), Xi'an, China (Chinese Pulsed Power Society, Chinese Particle Accelerator Society, 2008), p. 646.

¹⁹F. Li, W. He, A. D. R. Phelps, A. W. Cross, C. R. Donaldson, and K. Ronald, *Joint 33rd International Conference on Infrared and Millimeter and 16th International Conference on Terahertz Electronics*, Pasadena, CA, 2008 (IEEE, New York, 2008).

²⁰A. W. Cross, W. He, A. D. R. Phelps, K. Ronald, C. G. Whyte, A. R. Young, C. W. Robertson, E. G. Rafferty, and J. Thomson, *Appl. Phys. Lett.* **90**, 253501 (2007).

²¹W. He, K. Ronald, A. R. Young, A. W. Cross, A. D. R. Phelps, C. G. Whyte, E. G. Rafferty, J. Thomson, C. W. Robertson, E. C. Speirs, S. V. Samsonov, V. L. Bratman, and G. G. Denisov, *IEEE Trans. Electron Devices* **52**, 839 (2005).

²²W. He, A. W. Cross, A. D. R. Phelps, K. Ronald, C. G. Whyte, S. V. Samsonov, V. L. Bratman, and G. G. Denisov, *Appl. Phys. Lett.* **89**, 091504 (2006).

²³COMSOL, Multiphysics, Comsol, Inc., www.comsol.com

²⁴I. C. Somerville, S. J. MacGregor, and O. Farish, *Meas. Sci. Technol.* **1**, 865 (1990).

²⁵W. He, H. Yin, A. D. R. Phelps, A. W. Cross, and S. N. Spark, *Rev. Sci. Instrum.* **72**, 4266 (2001).

²⁶W. He, C. R. Donaldson, A. W. Cross, F. Li, A. D. R. Phelps, L. Zhang, K. Ronald, C. W. Robertson, C. G. Whyte, and A. R. Young, The 34th International Conference on Infrared, Millimeter, and Terahertz Waves, Busan, Korea (IEEE, New York, 2009).

Design and simulation of a ~ 390 GHz seventh harmonic gyrotron using a large orbit electron beam

Fengping Li, Wenlong He, Adrian W Cross, Craig R Donaldson,
Liang Zhang, Alan D R Phelps and Kevin Ronald

SUPA, Department of Physics, University of Strathclyde, Glasgow, G4 0NG, UK

E-mail: Fengping.li@strath.ac.uk

Received 15 January 2010, in final form 1 March 2010

Published 30 March 2010

Online at stacks.iop.org/JPhysD/43/155204

Abstract

A ~ 390 GHz harmonic gyrotron based on a cusp electron gun has been designed and numerically modelled. The gyrotron operates at the seventh harmonic of the electron cyclotron frequency with the beam interacting with a TE_{71} waveguide mode. Theoretical as well as numerical simulation results using the 3D particle-in-cell code MAGIC are presented. The cusp gun generated an axis-encircling, annular shaped electron beam of energy 40 keV, current 1.5 A with a velocity ratio α of 3. Smooth cylindrical waveguides have been studied as the interaction cavities and their cavity Q optimized for 390 GHz operation. In the simulations ~ 600 W of output power at the design frequency has been demonstrated.

(Some figures in this article are in colour only in the electronic version)

1. Introduction

Microwave radiation sources are one of the crucial technologies for modern society. High power sub-millimetre wave sources have attracted significant interest recently due to their potential applications in electron cyclotron resonance heating [1], plasma diagnostics [2], space radar systems [3], communication systems [4], materials science and medical imaging and spectroscopy [5, 6].

The gyrotron is well known as a coherent millimetre wave source capable of high power and high frequency output which is extendable to the terahertz (THz) frequency region. Recently a gyrotron achieved kilowatts of output power operated at the fundamental electron cyclotron frequency of 1 THz [7] by using a pulsed solenoid. However, continuous wave (CW) operation at such a frequency is a formidable task because of the large magnetic field (~ 40 T) that is required. As the output frequency increases, both larger magnetic fields and reduced interaction region size are needed when operating at the fundamental cyclotron frequency. An alternative approach to generate CW high frequency radiation is to work at higher cyclotron harmonics [8–11] which allow the use of larger cavity sizes and smaller magnetic fields by a factor of s , where s is the harmonic number.

A CW high harmonic gyrotron operating at a frequency of ~ 390 GHz at relatively lower B -field was designed and is presented in this paper. In this gyrotron cyclotron resonance takes place between the seventh harmonic of the electron cyclotron frequency ($s = 7$) and the TE_{71} waveguide mode. A large orbit electron beam from a cusp gun is used to reduce the possibility of parasitic interactions. The small-signal theory of the beam–wave interaction was used to calculate the growth rate and the starting current. A smooth-bore cavity was designed with a suitable Q value by optimizing the angle of the output taper and the length of the cavity so that the starting current requirement is met. Finally, the beam–wave interaction of the gyrotron was simulated using the 3D particle-in-cell (PIC) code MAGIC and the results are presented.

2. Cusp electron gun

While operating at harmonics, undesired mode competition as well as parasitic oscillations will be more problematic as the harmonic number increases; therefore, it is advantageous for an electron gun to be able to generate a mode-selective beam. A large orbit electron beam from a cusp gun was selected because, for such a beam, its harmonic of the cyclotron mode (s) only interacts with a TE_{mn} waveguide mode (m and n are

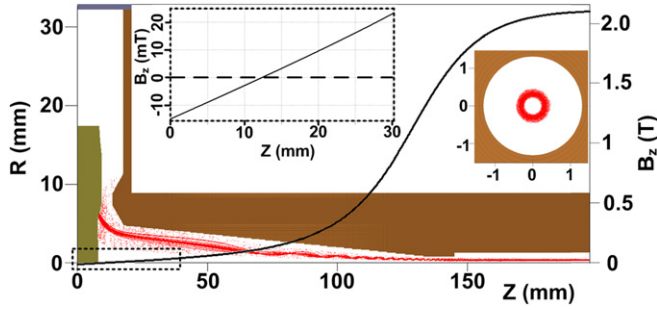


Figure 1. Simulated cusp gun and resultant beam trajectories with the detailed magnetic field configuration at the cusp point.

the azimuthal and the radial mode index, respectively) when $s = m$ [12]. A cusp electron gun operates by an electron beam passing through a non-adiabatic magnetic field reversal from negative to positive sign. Invariance of the magnetic moment results in a large orbit, annular electron beam [13–15].

Several successful terahertz range large orbit harmonic gyrotron experiments have been carried out at resonant magnetic fields 10.5–14 T [16, 17].

The 3D PIC code MAGIC was used to simulate and optimize the design of the cusp electron beam source. The optimized geometry of the cusp gun including the magnetic field profile and the resultant beam trajectories are shown in figure 1. An insertion shows in detail the B -field reversal in the cusp region.

The B -field profile of the cusp was produced by two coils, a main coil and a reverse coil. The main coil produces a uniform magnetic field at the downstream region which should have a certain length of the flat-top region required by the beam–wave interaction in the cavity. Two extra layers of coils were added to both ends of the main solenoid to sharpen its B -field profile so that the overall turns and length of the solenoid were reduced. These extra coils were carefully designed to avoid any bumps in the magnetic field profile while minimizing the rise and fall distance of the magnetic field. The design parameters were optimized resulting in the production of a 40 kV, 1.5 A large orbit electron beam in the simulations. This electron beam has been optimized through adjustment of the magnetic coil arrangement to operate at a velocity ratio α from 1.2 to 3 [18, 19] with an inner radius of 0.27 mm and an outer radius of 0.36 mm. This is consistent with the analytical calculated Larmor radius of 0.31 mm. The reflected electrons in figure 1 are low energy electrons emitted during the rise-time of the applied voltage pulse. A velocity pitch α spread of $\sim 25\%$ was simulated when α reaches 3. Further increase in the beam α would result in a significant increase in beam spread in α , hence the reflection of some beam electrons.

3. Gyrotron design

Gyrotrons are based on the cyclotron resonance maser (CRM) [20] instability and operate through a fast cyclotron wave interaction, which takes place near the frequency cut-off region of the waveguide mode. In a high harmonic gyrotron, the beam (harmonic number $s > 1$) interacts with a high order TE_{mn} waveguide mode where $m = s$.

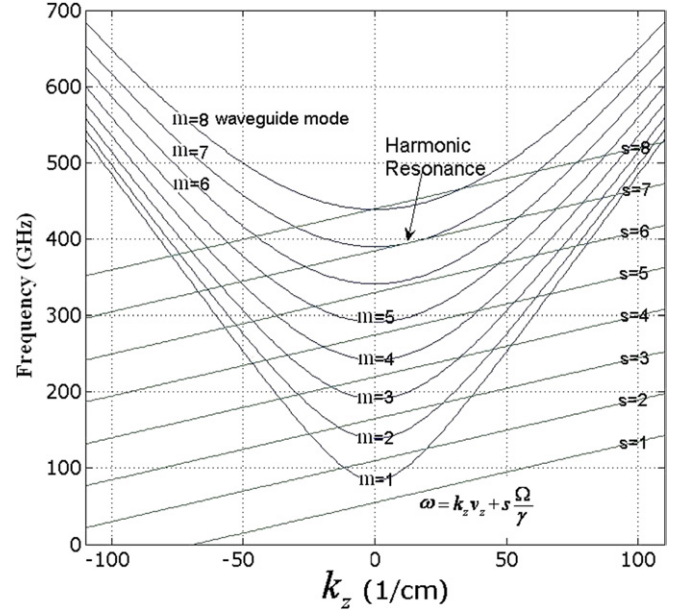


Figure 2. Dispersion of the TE_{m1} waveguide modes ($m = 1–8$) and beam–wave resonances at different harmonics.

All the possible interactions are shown in figure 2. When the seventh harmonic of the electron cyclotron frequency is in resonance with the TE_{71} mode, interactions below this mode are eliminated because the corresponding harmonic beam lines are far below their corresponding TE_{m1} waveguide mode curves except for the case of the TE_{61} mode and $s = 6$. The other possible parasitic interactions might be from higher modes, i.e. TE_{81} with $s = 8$ and TE_{91} with $s = 9$, etc. However, the most dangerous one is with the neighbouring TE_{81} interaction as the starting current increases as the mode index increases. But the TE_{81} interaction has a starting current higher than the beam current. In this way any other parasitic interactions of higher modes are automatically eliminated.

As the gyrotron works near the cut-off frequency region, and a large orbit gyrotron requires $s = m$, the operating frequency (390 GHz) and harmonic number ($s = 7$) as well as the azimuthal index of the waveguide mode ($m = 7$) were chosen prior to the cavity size.

The interaction of the waveguide mode and axis-encircling electron beam cyclotron mode can be described by the equation below [21, 22]:

$$\omega^2 - k_z^2 c^2 = - \frac{4\beta_{\perp}^2}{(x_{mn}^2 - m^2) (\omega - k_z v_z - s\Omega)^2} \times \left(\frac{I}{I_A} \right) \left(\frac{x_{mn} c}{r_w} \right)^4 \left(\frac{J'_m(x_{mn} r_L / r_w)}{J_m(x_{mn})} \right)^2, \quad (1)$$

where k_z is the propagation constant; x_{mn} is the n th root of $J'_m(x) = 0$. r_w is the radius of the cylindrical cavity; N_e is the axial linear density of electrons. $\gamma_0 = 1 + eV/m_0 c^2$ is the relativistic Lorentz factor; m_0 is the rest mass of an electron, V is the electron beam voltage. $\beta_{\perp} = v_{\perp}/c$; $r_L = v_{\perp}/\Omega$ is the electron Larmor radius. $\Omega = eB/\gamma_0 m_0$ is the electron gyration frequency, where B is the magnetic field. I is the beam current and $I_A = 4\pi\epsilon_0 m_0 c^3/e \approx 17$ kA is the Alfvén current.

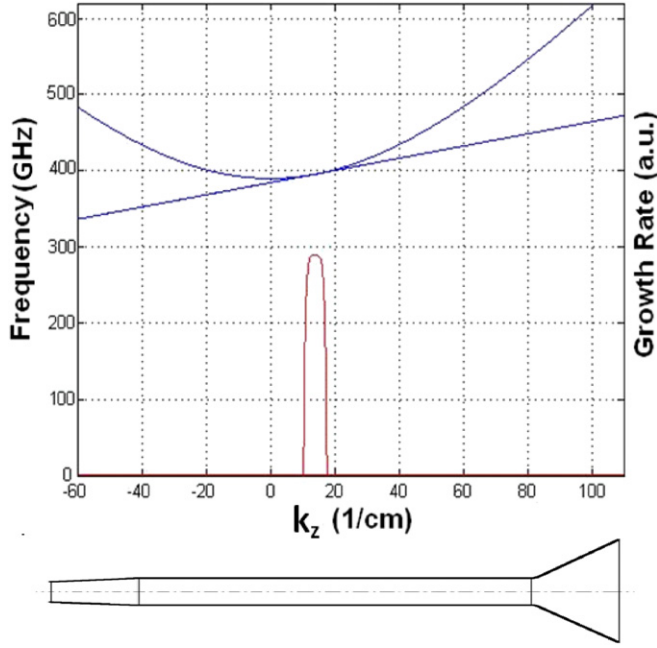


Figure 3. The growth rate at the seventh harmonic interaction (upper diagram) and the schematic gyrotron geometry (lower diagram).

The growth rate of this interaction can be obtained by solving the imaginary part of ω in equation (1) as a function of axial wavenumber k_z and is shown in figure 3. In the diagram the TE₇₁ cylindrical waveguide mode is interacting with the seventh harmonic of the electron cyclotron frequency of a beam with a velocity ratio α of 3 at a magnetic field of 2.09 T. The radius of the cylindrical cavity is 1.055 mm and the cavity length is 50 mm at a reasonable cavity Q of 2000.

The cavity length L and the output taper angle are optimized for a reasonably high Q which is a very important parameter in any gyrotron design. The total Q of the resonant cavity is given by

$$\frac{1}{Q} = \frac{1}{Q_d} + \frac{1}{Q_\Omega}. \quad (2)$$

The diffraction quality factor Q_d and the ohmic quality factor Q_Ω which are caused by diffraction and ohmic losses, respectively, can be calculated using the equations below:

$$Q_d = 4\pi \frac{(L/\lambda)^2}{1 - |R_1 R_2|}, \quad (3)$$

$$\frac{1}{Q_\Omega} = \left(\frac{\delta}{r_w} \right) \left[\frac{c^2}{\omega^2} \frac{x_{mn}^2}{r_w^2} + \left(\frac{x_{mn}^2}{x_{mn}^2 - m^2} \right) \right], \quad (4)$$

where $\delta = \sqrt{2/\omega\mu\sigma}$ is the skin depth of the cavity wall, σ is the conductivity of the cavity material, μ is the absolute permeability. R_1 and R_2 are the reflection coefficients at both ends of the cavity interaction region.

The cavity Q was calculated using the code Cascade [23]. In figure 4(a) the curve shows the simulated cavity Q as a function of the output taper angle at 390 GHz. In this diagram, the cavity was a 40 mm long smooth cylindrical cavity with a radius of $r_w = 1.055$ mm. The output taper was 10 mm in

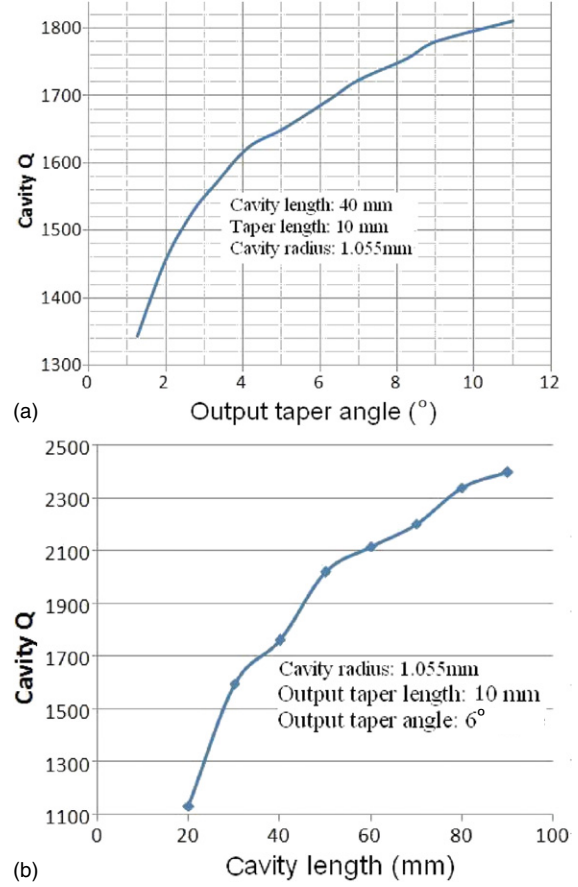


Figure 4. (a) Cavity Q as a function of output taper angle and (b) cavity Q as a function of cavity length.

length and the input section of the cut-off taper had a fixed radius of 0.8 mm and a length of 20 mm. Though in a real situation the tolerance of the cavity dimensions, roughness of the cavity surface [24] and the purity of the materials will affect the value of the ohmic losses at high frequencies, the ideal surfaces and oxygen free high conductivity copper were applied to these calculations. From the diagram we can see the cavity Q increases as the angle increases, but in order to sustain enough output power and to decrease the heat load of the cavity [25], the taper angle needs to be properly selected. Considering all of these factors a 6° output taper was chosen in the cavity design. The cut-off taper angle was also studied by changing the length of the taper with a fixed cut-off input radius 0.8 mm. Cascade simulations show that these changes do not affect the cavity Q value very much (less than 20 when the cut-off taper length was varied from 5 to 20 mm).

Figure 4(b) shows the simulated cavity Q as a function of cavity length using the code Cascade. In the simulation the input end had a 20 mm taper with an input radius of 0.8 mm. The cavity radius remains the same as before, which was 1.055 mm, and at the end it had a 6° output taper. Simulations using CST Microwave Studio showed that there is no significant mode conversion (<10% of power) for this output taper at the operating mode. However, further increase in the output taper length or output taper angle will cause significant mode conversion. For example, when the

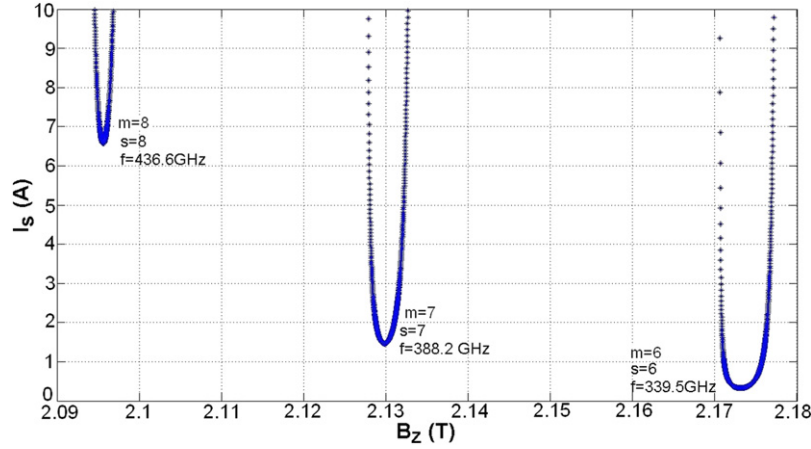


Figure 5. Starting currents for the seventh harmonic TE₇₁ mode and its neighbouring TE_{m1} modes.

taper length was increased to 20 mm, 70% of the power was converted to the TM₅₂ mode.

The starting oscillation currents for this cavity at the design mode and competing modes can be calculated using the equation shown below [12]:

$$I_s = \left(\frac{I_A}{Q} \right) \left(\frac{\omega}{s\Omega} \right) \left(\frac{\gamma L r_w^2 \omega k_z^2 \beta_z^2}{16c} \right) \left(1 - \frac{m^2}{x_{mn}^2} \right) \times \left(\frac{J_m(x_{mn})}{J'_m(x_{mn} \beta_{\perp} c / r_w \Omega)} \right)^2 R(X)^{-1}, \quad (5)$$

where

$$R(X) = \left\{ 2 - 2x \left(\frac{\beta_{\perp}^2}{\beta_z} \right) \left(\frac{k_z c}{s\Omega} \right) + \left[\left(\frac{r_w s \Omega}{\beta_{\perp} c x_{mn}} \right)^2 - 1 \right] \times \left(\frac{J_n(x_{mn} \beta_{\perp} c / r_w \Omega)}{J'_n(x_{mn} \beta_{\perp} c / r_w \Omega)} \right)^2 + \left(\frac{2x_{mn} \beta_{\perp} c}{r_w \Omega} \right) \times \left(\frac{J''_n(x_{mn} \beta_{\perp} c / r_w \Omega)}{J'_n(x_{mn} \beta_{\perp} c / r_w \Omega)} \right) \right\} G(X) + \left(\frac{\beta_{\perp}^2}{\beta_z} \right) \left(\frac{\omega}{s\Omega} \right) \left[\frac{\omega}{ck_z} - \left(\frac{ck_z}{\omega} \right) X^2 \right] G'(X) \quad (6)$$

and $X = (\omega - s\Omega) / k_z \beta_z c$,

$$G(X) = \begin{cases} [\cos(\pi q X / 2) / (1 - X^2)]^2 & (\text{odd } q), \\ [\sin(\pi q X / 2) / (1 - X^2)]^2 & (\text{even } q). \end{cases} \quad (7)$$

Here $q = k_z L / \pi$, and the calculation result is shown in figure 5. In this calculation the cavity $Q = 2000$ and the electron beam velocity ratio α was 3.

The minimum starting current for the seventh harmonic mode is 1.4 A, at a magnetic field of 2.13 T which are both within the capability of our cusp gun design current of 1.5–1.7 A and the solenoid magnetic field of 2.16 T. This diagram clearly shows that the neighbouring modes $s = 8$ and $s = 6$ will be eliminated as the starting current for the eighth harmonic requires a starting current of more than 6 A and the magnetic field requirement for the sixth harmonic is above 2.17 T.

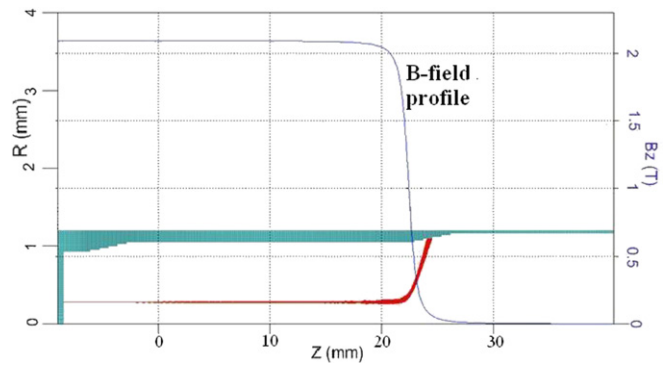


Figure 6. A schematic diagram of the gyrotron in the R – Z plane with simulated electron beam trajectories.

4. Simulation results

In order to demonstrate the beam–wave interaction can take place in the designed gyrotron cavity, the code MAGIC was used to simulate the harmonic gyrotron interaction. The R – Z plane geometries of the smooth cylindrical structures and electron trajectories are shown in figure 6. An ideal beam with the parameters from the cusp electron simulation but without velocity and radius spreads was emitted from the left end of the cavity and propagated in a uniform B -field produced by a solenoid in the MAGIC simulation. The right end of the solenoid sits in the middle of the output taper in the Z -axis. During the simulation, the cavity length was reduced from 50 to 30 mm as the cavity ohmic loss was neglected in the simulation. A schematic diagram of the simulation is shown in figure 6 with the magnetic field profile produced by the solenoid.

The simulation result is shown in figure 7. In the simulation the large orbit annular electron beam had a voltage of 40 kV, a current of 1.5 A and a beam velocity ratio α of 3. The magnetic B -field applied in the cavity was 2.09 T. The magnetic field difference between the MAGIC and the analytical calculation is due to the grid density in the gyrotron simulation; when a higher grid density is used, the B -field required in the simulation will be larger and closer to the analytically calculated value.

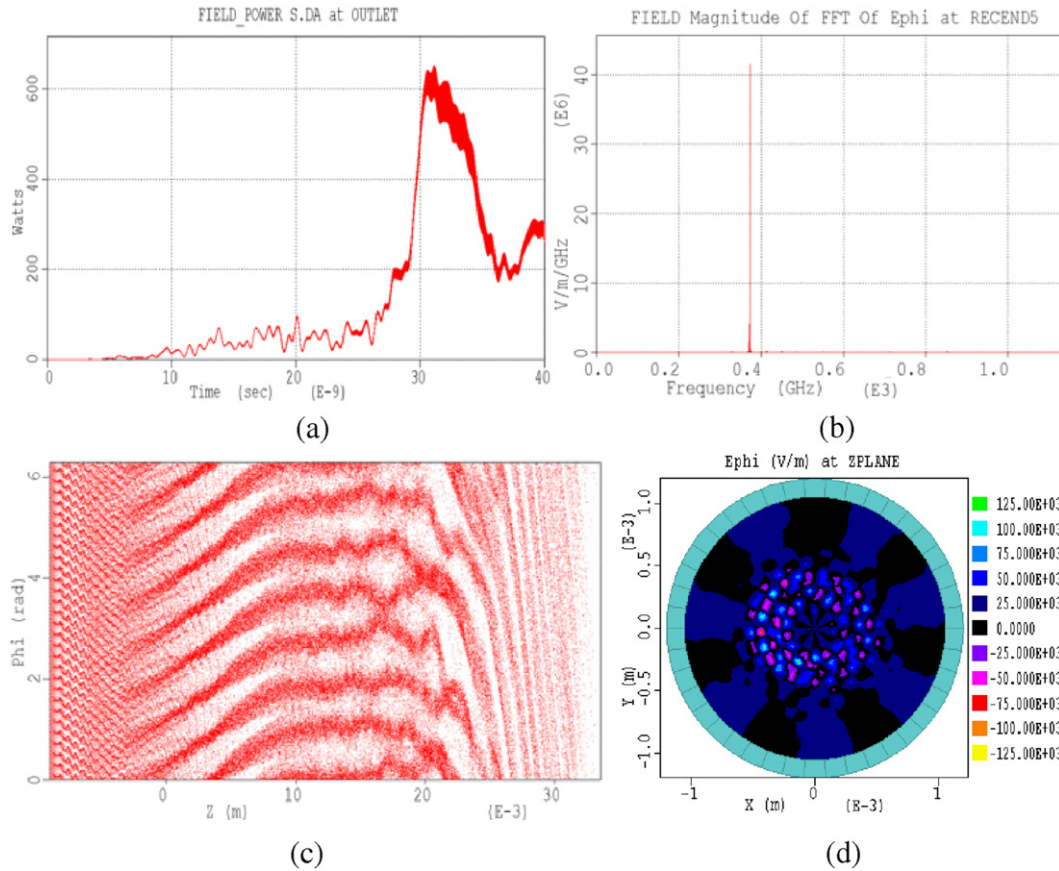


Figure 7. Simulation results of the seventh harmonic gyrotron with a smooth cavity: (a) output power, (b) output spectrum and (c) electron phase angle as a function of axial position (d) microwave E_{ϕ} field pattern at resonance.

The electron phase angle as a function of axial position Z (figure 7(c)) indicates the interaction occurred at the seventh harmonic of the electron cyclotron frequency. Very pure radiation output at a frequency of 384 GHz was observed in the simulation as shown in figure 7(b), and ~ 600 W of output power was achieved in this simulation. The reduction in power observed after ~ 30 ns arises due to the cavity of 30 mm in length being sufficiently long in the absence of wall loss, for the interaction to enter phase trapped saturation resulting in re-absorption of the wave energy—this can be seen in figure 7(c) where the electron distribution in phase angle illustrates the trapping occurring. When 0.1 mm beam thickness and 25% beam spread were introduced in the simulation, it was found that the total output power dropped to ~ 500 W while a competing TE_{61} became slightly dominant at the output. The output power at the designed frequency and mode dropped to ~ 200 W.

5. Conclusion

In conclusion a ~ 390 GHz harmonic gyrotron based on a large orbit electron beam was designed and simulated. The cavity has been analysed and optimized. Theoretical and numerical simulation results demonstrate that the beam interacts with the single TE_{71} mode and a simulated output power of ~ 600 W was achieved while using a 40 kV, 1.5 A, large orbit electron beam with velocity ratio α of 3. It was found from simulation that

a spread in α will cause the reduction in the output power and start-up of mode competition. The effect that beam parameters, such as velocity spread and envelop ripple, might have on the starting current and mode excitation [26] will be studied both numerically and experimentally in the future.

Acknowledgments

The authors would like to thank the Faraday Partnership in High Power RF and the Scottish Universities Physics Alliance (SUPA) and the Overseas Research Students Awards Scheme (ORSAS) for supporting this project. The authors would also like to thank ‘Calabazas Creek Research’ for providing the one month free licence for Cascade.

References

- [1] Wagner D *et al* 2007 The new multi-frequency electron cyclotron resonance heating system for ASDEX Upgrade *Fusion Sci. Technol.* **52** 313–20
- [2] Saito T *et al* 2008 Development of a sub terahertz high power pulse gyrotron for collective Thomson scattering *Presented at the Joint 33rd Int. Conf. Infrared Millimeter, 16th Int. Conf. Terahertz Electronics (Pasadena, CA, 2008)* Paper ICIMW.2008.4665739
- [3] Bhartia P and Bahl I J 1984 *Millimeter Wave Engineering and Applications* (New York: Wiley)
- [4] Siegel P H 2002 Terahertz Technology *IEEE Trans. Microw. Theory Tech.* **50** 910–28

- [5] Clery D 2002 Brainstorming their way to an imaging revolution *Science* **297** 761–3
- [6] Torrezan A C *et al* 2008 CW Operation of a tunable 330/460 GHz gyrotron for enhanced nuclear magnetic resonance Presented at the Joint 33rd Int. Conf. Infrared Millimeter, 16th Int. Conf. Terahertz Electronics (Pasadena, CA, 2008) Paper ICIMW.2008.4665733
- [7] Glyavin M Yu, Luchinin A G and Golubiantnikov G Yu 2008 Generation of 1.5 kW 1 THz coherent radiation from a gyrotron with a pulsed magnetic field *Phys. Rev. Lett.* **100** 015101
- [8] Idehara T *et al* 2004 A high harmonic gyrotron with an axis-encircling electron beam and a permanent magnet *IEEE Trans. Plasma Sci.* **32** 903–9
- [9] Wang Q S *et al* 1994 Stable 1 MW, third-harmonic gyro-TWT amplifier *IEEE Trans. Plasma Sci.* **22** 608–15
- [10] Wang Q S *et al* 2000 Design of a W-band second-harmonic TE₀₂ gyro-TWT amplifier *IEEE Trans. Plasma Sci.* **28** 2232–7
- [11] La Agusu *et al* 2006 Design of a 400 GHz gyrotron for DNP-NMR spectroscopy Presented at the Joint 31st Int. Conf. Infrared Millimeter, 14th Int. Conf. Terahertz Electronics (Shanghai, China, 2006) Paper ICIMW.2006.368290
- [12] McDermott D B, Luhmann N C Jr, Kupisedwski A and Jory H R 1983 Small-signal theory of a large-orbit electron-cyclotron harmonic maser *Phys. Fluids* **26** 1936–41
- [13] Schmidt G 1962 Nonadiabatic particle motion in axiallysymmetric fields *Phys. Fluids* **5** 994–1002
- [14] He W *et al* 2006 A W-band gyro-BWO based on a helically corrugated waveguide *Infrared Millimeter Waves and 14th Int. Conf. on Terahertz Electronics, Joint 31st Int. Conf. on IRMMW-THz (Shanghai, Sept. 2006)* pp 88–8
- [15] He W 2008 Axis-encircling electron beam generation using a smooth magnetic cusp for gyro-devices *Appl. Phys. Lett.* **93** 121501
- [16] Bratman V L *et al* 2005 Submillimeter-wave large-orbit gyrotron *Radiophys. Quantum Electron.* **48** 731–6
- [17] Bratman V L, Kalynov Yu K and Manuilov V N 2009 Large-orbit gyrotron operation in the terahertz frequency range *Phys. Rev. Lett.* **102** 245101
- [18] He W *et al* 2009 Design, simulation and experiment of a cusp electron beam for millimeter wave gyro-devices *IVEC (Rome, Italy, 2009)*
- [19] Donaldson C R *et al* 2009 Design and numerical optimization of a cusp-gun-based electron beam for millimeter-wave gyro-devices *IEEE Trans. Plasma Sci.* **37** 2153–7
- [20] Chu K R 2004 The electron cyclotron maser *Rev. Mod. Phys.* **76** 489–540
- [21] Chu K R and Anthony T Lin 1988 Gain and bandwidth of the gyro-TWT and CARM amplifiers *IEEE Trans. Plasma Sci.* **16** 90–104
- [22] Furuno D S *et al* 1990 Operation of a large-orbit high-harmonic gyro-traveling-wave tube amplifier *IEEE Trans. Plasma Sci.* **18** 313–20
- [23] Ives L, Nelson J and Vogler W 2003 Cascade—an advanced computational tool for waveguide components and window design *Proc. 2003 Particle Accelerator Conf. (Portland, OR, 2003)*
- [24] Thorpe T S 1954 RF conductivity in copper at 8 mm wavelengths *Proc. Instn. Electr. Eng. (Part III)* **101** 357–9
- [25] Zapevalov V E *et al* 1994 Low-Q cavities for high-power gyrotrons *Radiophys. Quantum Electron.* **37** 233–6
- [26] Bratman V L, Kalynov Yu K and Fedotov A E 1998 Theory of gyro devices with thin electron beams (large-orbit gyrotron) *Tech. Phys.* **43** 1219–25

Design and Numerical Optimization of a Cusp-Gun-Based Electron Beam for Millimeter-Wave Gyro-Devices

Craig R. Donaldson, Wenlong He, Adrian W. Cross, Alan D. R. Phelps, Fengping Li, Kevin Ronald, Craig W. Robertson, Colin G. Whyte, Alan R. Young, and Liang Zhang

Abstract—A novel thermionic cusp electron gun operating in the temperature-limited regime that produces a large-orbit electron beam through a nonadiabatic magnetic-field reversal was designed, analyzed, and optimized to give an electron-beam ideal for driving gyro-devices, particularly in the millimeter-to-submillimeter-wavelength range due to its small cross-sectional size. The annular-shaped axis-encircling electron beam had a beam current of 1.5 A at an acceleration potential of 40 kV, a tunable velocity ratio α ($= v_{\perp}/v_z$) between one and three, an optimized axial velocity spread $\Delta v_z/v_z$ of $\sim 8\%$, and a relative alpha spread $\Delta\alpha/\alpha$ of $\sim 10\%$ at an alpha value of 1.65.

Index Terms—Axis-encircling electron beam, cusp electron gun, gyro-BWO, gyro-TWT, high-harmonic gyrotron, THz electron-beam source, W-band.

I. INTRODUCTION

HIGH-POWER high-frequency coherent radiation sources, particularly in the range of millimeter and submillimeter wavelengths, have attracted significant research interest recently due to their desirable applications in many areas such as remote sensing [1], medical imaging [2], plasma heating [3], and spectroscopy [4]. Gyro-devices [5] are promising candidates to fulfil such a demand due to their inherent characteristic fast-wave interaction. Many high-frequency gyro-devices operate at harmonics [6]–[9] to allow for the use of a larger cavity size and to decrease magnetic fields by a factor of s , the harmonic number. However, operating at harmonics could introduce undesired-mode competition, as well as parasitic oscillations. Therefore, it is advantageous for an electron gun to be able to generate a mode-selective beam. This paper presents the innovative design and performance of such a beam from a novel electron gun that is capable of driving high-power millimeter-wave vacuum electron devices through generation of an annular-shaped axis-encircling electron beam. An axis-

Manuscript received July 2, 2009; revised August 24, 2009. First published October 9, 2009; current version published November 11, 2009. This work was supported in part by the U.K. Engineering and Physical Sciences Research Council, by the Scottish Universities Physics Alliance (SUPA), by the Overseas Research Studentship, and by the U.K. High Power RF Faraday Partnership.

The authors are with SUPA, Department of Physics, University of Strathclyde, G4 0NG Glasgow, U.K. (e-mail: craig.donaldson@strath.ac.uk; h.e.wenlong@strath.ac.uk; a.w.cross@strath.ac.uk; a.d.r.phelps@strath.ac.uk; fengping.li@strath.ac.uk; k.ronald@strath.ac.uk; craig.robertson@strath.ac.uk; colin.whyte@strath.ac.uk; a.r.young@strath.ac.uk; liang.zhang@strath.ac.uk).

Color versions of one or more of the figures in this paper are available online at <http://ieeexplore.ieee.org>.

Digital Object Identifier 10.1109/TPS.2009.2031470

encircling electron beam is ideal for harmonic operation of gyro-devices as the mode-selectivity nature of such a beam requires that the harmonic number is equal to the azimuthal index of a waveguide mode for effective beam-wave coupling [10], which leads to a reduced possibility of parasitic oscillations. Furthermore, due to the high power of the spent electron beam, an annular-shaped electron beam is desirable for beam-energy recovery using a depressed collector.

Initially, transport of an electron beam through opposing magnetic fields (the so-called “magnetic cusp”) was investigated in the 1960s [11], [12] for plasma-heating applications. Schmidt [11] described a threshold for magnetic mirroring and the effects on the electrons after they have passed the cusp region, namely, azimuthal rotation around the central axis of symmetry due to conservation of the electron canonical momentum. Building on the work of Schmidt *et al.*, continuous efforts and progress have been made through both theoretical analysis and experimental study in the generation of cusp-based electron-beam sources [13], [14]. Special concentration was paid on the methods to produce an ideal sharp cusp shape by using complex arrays of magnetic coils, magnetic poles, and, possibly, magnetic material inside the cathode [15]–[18]. This culminated in a “state-of-the-art” cusp gun in 2000 by Northrop Grumman [19], which generated an electron beam of 70-kV energy, 3.5-A current, and 1.5 velocity ratio with a small axial velocity spread of 5% at a magnetic field of ~ 0.25 T. These studies have been based on the configuration where a magnetic cusp was located at or after the anode where a large cusp amplitude was required due to a fully accelerated electron momentum. However, in this paper, an electron gun based on a “smooth” cusp [20], formed by two simple coils without any magnetic shaping poles, located immediately after the cathode, is presented.

Despite these theoretical and experimental studies over the last few decades, it was not until 1983 that a cusp electron gun was first used in microwave sources, specifically in a magnetron [21]. Recently, gyro-devices have begun to adopt cusp guns as their electron beam sources, notably in lower frequency harmonic gyro-devices [22].

A cold cusp gun was developed for an X-band gyrotron traveling-wave amplifier (gyro-TWA) at the University of Strathclyde in 2007 [18]. The methodology of the design was validated through results from numerical simulations, from the 3-D particle-in-cell code MAGIC [23], agreeing well with the

experimental results. In this paper, we present a thermionic cusp gun that was designed and numerically optimized based on the valid methodology for millimeter-wave gyro-devices. It was designed for three high-frequency devices, including a W-band gyro-BWO [24], a W-band gyro-TWA [25], and a THz harmonic gyrotron [26]. The second-harmonic W-band gyro-BWO uses a helically corrugated waveguide [27], [28] and is calculated to produce 10-kW CW at 18% efficiency, with a 3-dB frequency tuning bandwidth between 85 and 105 GHz. A W-band gyro-TWA has been designed to operate at an alpha of 1.2 and give an output of 5-kW CW. The THz harmonic gyrotron that operates at the seventh harmonic has been simulated to produce 600-W CW at 390 GHz with a TE₇₁ output at an $\alpha = 3$. These devices operate over a wide range of frequencies from 75 GHz to 390 GHz with an α value of one to three.

II. DIODE DESIGN

It is possible to show [18] that the velocity ratio in the downstream uniform magnetic-field (B_0) region can be described approximately by the equation $\alpha = \sqrt{(-r_c^2 \omega_c \omega_0 / v_0^2 + r_c^2 \omega_c \omega_0)}$. Here, r_c is the average radius of the cathode; v_0 is the total electron velocity; $\omega = eB/\gamma m_e$ is the electron cyclotron frequency, where γ is the Lorentz factor of the electrons at the downstream region and e and m_e are the charge and the rest mass of the electron, respectively; and subscripts “c” and “0” denote the cathode and the downstream uniform magnetic-field region, respectively.

The parameters of the electron beam were chosen to be as follows: beam energy $E = 40$ keV and current of ~ 1.5 A, with $\alpha = 1-3$ and $B_0 = 1.7-2.1$ T for high-frequency gyro-device experiments. Assuming the cathode operation with a current density of 6 A/cm² in the temperature-limited regime [29], a cathode with $r_c = 6.0$ mm and $\Delta r_c = 0.5$ mm was chosen. Therefore, a magnetic-field amplitude of ~ 50 G at the cathode is required to achieve an alpha value of 1.65, at $B_0 = 1.82$ T, which corresponds to a magnetic compression ratio of ~ 360 and a radial compression of ~ 19 for the electron beam. It is important that a small value of $\Delta r_c / r_c$ was chosen because the smaller it is, the smaller the alpha spread in the electron beam. The thermal loading of the gun was estimated to be ~ 100 W at an operating temperature of ~ 1000 °C. To reduce the stray magnetic field, the heating coil should be wired in a bifilar format. A stray magnetic field of $\sim 10^{-4}$ T was simulated by using CST Microwave Studio at a driving current of the heating coil of 10 A. It is of primary importance that the stray magnetic field from the heating coil is significantly lower than the magnetic field at the cathode to achieve a stable alpha and axial velocity of the electron beam.

The geometry of the cusp gun is shown in Fig. 1. The emitting surface is annular shaped and porous tungsten impregnated with barium oxide to reduce the work function to achieve the designed beam current at an operating temperature of ~ 1000 °C. Two fine gaps of 0.1-mm width were used to separate the cathode ring from the outer and inner focusing electrodes for the following purposes: 1) reducing the thermal loading and 2) stopping the migration of the barium of the cathode. The length of the cathode–anode gap is chosen so

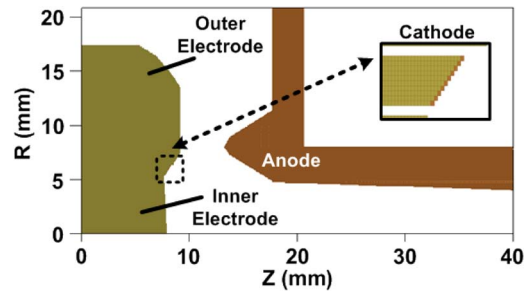


Fig. 1. Geometry of the cathode and anode of the cusp electron gun.

that the electric fields at the cathode are below 10 MV/m at an applied voltage of 40 kV to avoid problems such as field emission and vacuum breakdown. An anode tip is further used in the design to focus and transport the electron beam to the downstream region. The outer radius of the outer electrode was chosen to be large enough so that its effects on the electric field distribution between the cathode and anode are negligible while keeping its distance to the anode large enough to avoid problems such as field emission and vacuum breakdown. To avoid microwaves entering the gun region, a cylindrical low-frequency cutoff waveguide of 0.84-mm radius is used.

Two coils, namely, one “reverse” coil behind the cathode producing negative magnetic field, and the other a solenoid producing a uniform positive magnetic field B_0 at the downstream region, were used to form a magnetic cusp at the front of the cathode. Because of the relative low energy (approximately a few kiloelectron volts) of the electrons at the cusp, the amplitude of the cusp was greatly reduced (a few tens of gauss), and the Larmor step is on the order of meters due to the small amplitude of the cusp and the small transverse velocity component. This allows a field reversal over a longer distance. Therefore, in this design, it is not necessary to use any magnetic poles to sharpen the shape of the magnetic cusp. This makes this cusp gun a simple and effective alternative because of its simplified manufacture and optimization process, as well as flexibility in its operation. For example, the driving currents, averaged radius, and start and end positions of the coils can be changed to allow the adjustment of cusp position.

Various configurations of the cusp gun were optimized to give the highest quality electron beam, which include the following: the length of the cathode–anode gap, the shape of the anode tip, the cathode slope, the inner and outer focusing electrode geometries, and the size and position of the coils relative to the cathode surface. After the average radius and width are decided, the sizes of the dimensions of a, b, c, d, e, f, g, h, i, and j, as shown in Fig. 1, are varied for optimized beam quality in the simulation. Dimensions c, d, e, and f are used to adjust the slope angle relative to the z -axis of the inner and outer electrodes, as well as the relative position of the emitting surface to the electrodes. Adjustment of the relative position in the z -axis between the emitting surface and the electrodes is important to compensate the defocusing effect of the gaps on the electrons emitted from the corners of the cathode. Optimization of the slope of the electrodes and dimensions a and b is important because this decides the beam trajectory in the gun region. Dimension g should be chosen large enough to avoid

TABLE I
LIST OF OPTIMIZATION PARAMETERS, OPTIMIZED VALUES, AND OPTIMIZATION RANGES

Dimension Denotation	Optimised Value (mm)	Range of optimisation (mm)
a	0.30	0.00-0.60
b	5.44	5.30-6.00
c	0.27	0.10-0.45
d	0.25	0.10-0.45
e	0.60	0.40-0.80
f	1.01	0.70-1.30
g	4.48	2.50-5.00
h	3.23	2.00-4.00
i	4.13	3.50-5.10
j	4.80	4.00-5.20

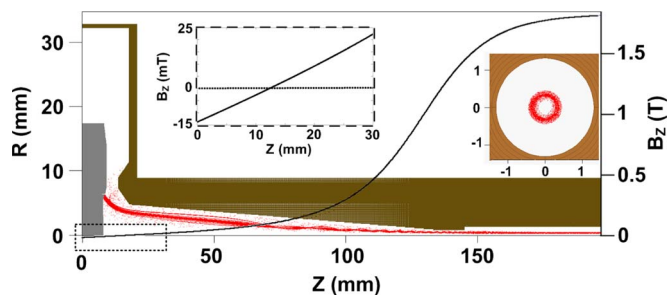


Fig. 2. Snapshot of the simulated electron-beam trajectory with magnetic-field profile and a cross-sectional shape of the beam at the downstream region.

vacuum breakdown and field emission. Dimensions h, i, and j are used to optimize the focusing effect at the anode region. Simulations of the electron beam aim to reduce beam envelope oscillation, axial velocity spread, and alpha spread over a wide range of magnetic fields. Table I summarizes the optimized dimensions and the optimization ranges of these variables used in the simulation.

III. SIMULATION RESULT

Electron-beam emission was modeled using the Richardson–Dushman equation for thermionic emission. The accelerating voltage was applied using a smooth rising function with a rise time of 1 ns to avoid high-frequency loading of the gun. The simulated electron-beam trajectory from the cusp gun with its magnetic-field profile ($B_0 = 1.82$ T) is shown in Fig. 2. The cross-sectional shape of the beam at the downstream region is also shown in Fig. 2, and it clearly shows an annular-shaped axis-encircling beam. The magnetic-field profile is a smooth transition from the cathode to the downstream uniform magnetic-field region, with the cusp being located at ~ 4.6 mm in front of the emission surface. It should be noted that some low-energy electrons of a few milliamperes over a period of a few nanoseconds (emitted when the accelerating voltage was rising) were reflected back at a high alpha value due to the magnetic-mirror effect, as

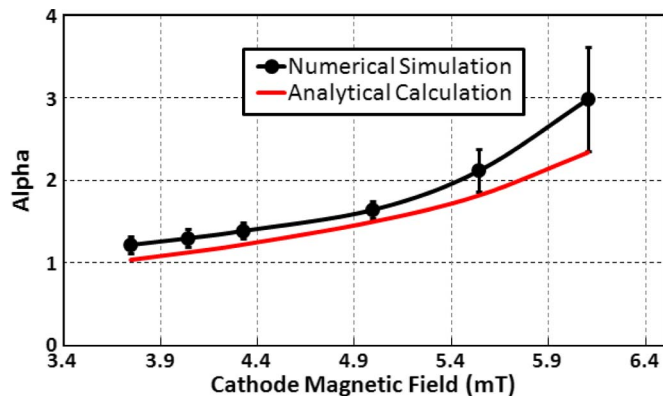


Fig. 3. Numerically simulated and analytically calculated alpha values for different values of cathode magnetic field at $B_0 = 1.82$ T.

shown in Fig. 1. However, after a few nanoseconds, 100% of the emitted current was transported to the downstream region. From simulation, to obtain an alpha value of one to three, the required magnetic field at the cathode was ~ 3.0 – 6.7 mT. At a constant value of B_0 , a larger α value could be achieved by increasing the magnetic-field amplitude at the cathode (B_c). The simulated average alpha of the electron beam as a function of the magnetic-field amplitude at the cathode is shown in Fig. 3 at $B_0 = 1.82$ T. The spread in alpha is also shown in this figure as bars, deviating from the average values. The alpha values calculated from the previous equation are also shown in Fig. 3 for comparison. Minimum axial velocity spreads of $\sim 8\%$ and relative alpha spreads of $\sim 10\%$ were achieved at an alpha value of 1.65 at this constant magnetic field. At B_0 values of 2.1 and 1.7 T, the optimum alpha spreads were $\sim 23\%$ and $\sim 15\%$ for alpha values of 3 and 1.2, respectively, and the corresponding axial velocity spreads for these cases were $\sim 20\%$ and $\sim 10\%$. At the central magnetic field B_0 of 1.82 T, the beam had an inner and an outer radius of 0.23 and 0.42 mm, with an envelope ripple $\sim 13\%$. Beam transport through the tube was measured to be 100% after the initial low potential electrons were reflected. The feasibility of

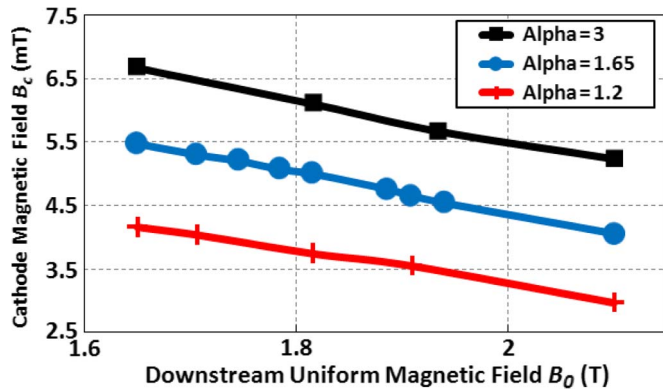


Fig. 4. Magnetic-field operation ranges for different values of velocity ratio (α).

operating this cathode at different alpha values for the three aforementioned microwave sources was also investigated with different magnetic-field operation ranges and is shown in Fig. 4. The gun is able to operate at an alpha from one to three over the magnetic-field tuning range of 1.65–2.1 T.

IV. CONCLUSION, DISCUSSION, AND FUTURE WORK

In conclusion, a cusp electron gun was simulated and optimized to generate an axis-encircling annular-shaped electron beam to drive millimeter-wave gyro-devices. At a velocity alpha of 1.65, the beam was optimized to achieve an axial velocity spread of 8% and a velocity spread of 10%. The viability of using the designed gun over a large alpha and magnetic-field range was demonstrated. It should be noted that the optimization for the generation of electron beams with alpha values of 1.2 and 3 has been performed by adjusting the position of the cusp, i.e., by adjusting the positions of the reversed and cavity coil only while the shape and size of the inner and outer electrodes are kept unchanged. Therefore, future work includes the optimization of the focusing electrodes to achieve optimized beam quality for harmonic-gyrotron and gyro-TWA applications. The structure of the cusp gun was designed in a way that allows the focusing electrodes to be changed.

REFERENCES

- [1] W. M. Manheimer, G. Mesyats, and M. I. Petelin, *Applications of High-Power Microwaves*, A. V. Gaponov-Grekhov and V. L. Granatstein, Eds. Norwood, MA: Artech House, 1994, pp. 169–207.
- [2] D. D. Amone, C. M. Cielsla, A. Corchia, S. Egusa, M. Pepper, J. Chamberlain, C. Bezant, E. H. Linfield, R. Clothier, and N. Khammo, "Application of terahertz (THz) technology to medical imaging," in *Proc. SPIE—Terahertz Spectroscopy Applications II*, Munich, Germany, 1999, vol. 3823, pp. 209–219.
- [3] T. Imai, N. Kobayashi, R. Temkin, M. Thumm, M. Q. Tran, and V. Alikae, "ITER R&D: Auxiliary systems: Electron cyclotron heating and current drive system," *Fusion Eng. Des.*, vol. 55, no. 2/3, pp. 281–289, Jul. 2001.
- [4] T. I. Smirnova, A. I. Smirnov, and R. B. Clarkson, "W-band (95 GHz) EPR spectroscopy of nitroxide radicals with complex proton hyperfine structure: Fast motion," *J. Phys. Chem.*, vol. 99, no. 22, pp. 9008–9016, Jun. 1995.
- [5] G. S. Nusinovich and O. Dumbrajs, "Theory of gyro-backward wave oscillators with tapered magnetic field and waveguide cross section," *IEEE Trans. Plasma Sci.*, vol. 24, no. 3, pp. 620–629, Jun. 1996.
- [6] M. Garven, J. P. Calame, B. G. Danly, K. T. Nguyen, B. Levush, F. N. Wood, and D. E. Pershing, "A gyrotron-traveling-wave tube amplifier experiment with a ceramic loaded interaction region," *IEEE Trans. Plasma Sci.*, vol. 30, no. 3, pp. 885–893, Jun. 2002.
- [7] T. Idehara, I. Ogawa, S. Mitsudo, Y. Iwata, S. Watanabe, Y. Itakura, K. Ohashi, H. Kobayashi, T. Yokoyama, V. E. Zapevalov, M. Y. Glyavin, A. N. Kuftin, O. V. Malygin, and S. P. Sabchevski, "A high harmonic gyrotron with an axis-encircling electron beam and a permanent magnet," *IEEE Trans. Plasma Sci.*, vol. 32, no. 3, pp. 903–909, Jun. 2004.
- [8] T. H. Chang, C. F. Yu, C. L. Hung, Y. S. Yeh, M. C. Hsiao, and Y. Y. Shin, "W-band TE₀₁ gyrotron backward-wave oscillator with distributed loss," *Phys. Plasmas*, vol. 15, no. 7, p. 073 105, Jul. 2008.
- [9] Q. S. Wang, H. E. Huey, D. B. McDermott, Y. Hirata, and N. C. Luhmann, Jr., "Design of a W-band second-harmonic TE₀₂ gyro-TWT amplifier," *IEEE Trans. Plasma Sci.*, vol. 28, no. 6, pp. 2232–2237, Dec. 2000.
- [10] K. R. Chu, "Theory of electron cyclotron maser interaction in a cavity at the harmonic frequencies," *Phys. Fluids*, vol. 21, no. 12, pp. 2354–2364, Dec. 1978.
- [11] G. Schmidt, "Nonadiabatic particle motion in axialsymmetric fields," *Phys. Fluids*, vol. 5, no. 8, pp. 994–1002, Aug. 1962.
- [12] J. Sillis and G. Schmidt, "Experimental trajectory analysis of charged particles in a cusped geometry," *Phys. Fluids*, vol. 6, no. 6, pp. 841–845, Jun. 1963.
- [13] M. J. Rhee and W. W. Destler, "Relativistic electron dynamics in a cusped magnetic field," *Phys. Fluids*, vol. 17, no. 8, pp. 1574–1581, Aug. 1974.
- [14] W. W. Destler and M. J. Rhee, "Radial and axial compression of a hollow electron beam using an asymmetric magnetic cusp," *Phys. Fluids*, vol. 20, no. 9, pp. 1582–1584, Sep. 1977.
- [15] G. P. Scheitrum and R. True, "A triple pole piece magnetic field reversal element for generation of high rotational energy beams," in *IEDM Tech. Dig.*, Washington, DC, 1981, vol. 27, pp. 332–335.
- [16] K. T. Nguyen, D. N. Smithe, and L. D. Ludeking, "The double-cusp gyro-gun," in *IEDM Tech. Dig.*, 1992, pp. 219–222.
- [17] G. P. Scheitrum, R. S. Symons, and R. B. True, "Low velocity spread axis encircling electron beam forming system," in *IEDM Tech. Dig.*, 1989, pp. 743–746.
- [18] S. G. Jeon, C. W. Baik, D. H. Kim, G. S. Park, N. Sato, and K. Yokoo, "Study on velocity spread for axis-encircling electron beams generated by single magnetic cusp," *Appl. Phys. Lett.*, vol. 80, no. 20, pp. 3703–3705, May 2002.
- [19] D. A. Gallagher, M. Barsanti, F. Scafuri, and C. Armstrong, "High-power cusp gun for harmonic gyro-device applications," *IEEE Trans. Plasma Sci.*, vol. 28, no. 3, pp. 695–699, Jun. 2000.
- [20] W. He, C. G. Whyte, E. G. Rafferty, A. W. Cross, A. D. R. Phelps, K. Ronald, A. R. Young, C. W. Robertson, D. C. Speirs, and D. H. Rowlands, "Axis-encircling electron beam generation using a smooth magnetic cusp for gyrodevices," *Appl. Phys. Lett.*, vol. 93, no. 12, p. 121 501, Sep. 2008.
- [21] W. W. Destler, R. Kulkarni, C. D. Striffler, and R. L. Weiler, "Microwave generation from rotating electron beams in magnetron-type waveguides," *J. Appl. Phys.*, vol. 54, no. 7, pp. 4152–4162, Jul. 1983.
- [22] D. B. McDermott, A. J. Balkcum, and N. C. Luhmann, Jr., "35-GHz 25-kW CW low-voltage third-harmonic gyrotron," *IEEE Trans. Plasma Sci.*, vol. 24, no. 3, pp. 613–619, Jun. 1996.
- [23] T. Gray, D. N. Smithe, and L. D. Ludeking, *Introduction to MAGIC*. Washington, DC: Mission Research Corp., 2003.
- [24] C. R. Donaldson, W. He, A. D. R. Phelps, F. Li, A. W. Cross, K. Ronald, A. R. Young, and C. G. Whyte, "A ~10 kW W-band gyro-BWO using a helically corrugated waveguide," presented at the Joint 33rd Int. Conf. Infrared Millimeter, 16th Int. Conf. Terahertz Electronics, Pasadena, CA, 2008, Paper ICIMW.2008.4665519.
- [25] W. He, A. D. R. Phelps, A. W. Cross, C. R. Donaldson, and K. Ronald, "A W-band gyrotron travelling wave amplifier using a helically corrugated waveguide," in *Proc. 17th High-Power Particle Beams Conf. (Beams)*, Xi'an, China, 2008, p. 646.
- [26] F. Li, W. He, A. D. R. Phelps, A. W. Cross, C. R. Donaldson, and K. Ronald, "The design of a 390 GHz gyrotron based on a cusp electron gun," presented at the Joint 33rd Int. Conf. Infrared Millimeter, 16th Int. Conf. Terahertz Electronics, Pasadena, CA, 2008, Paper ICIMW.2008.4665500.
- [27] G. G. Denisov, V. L. Bratman, A. D. R. Phelps, and S. V. Samsonov, "Gyro-TWT with a helical operating waveguide: New possibilities to enhance efficiency and frequency bandwidth," *IEEE Trans. Plasma Sci.*, vol. 26, no. 3, pp. 508–518, Jun. 1998.
- [28] W. He, A. W. Cross, A. D. R. Phelps, K. Ronald, C. G. Whyte, S. V. Samsonov, V. L. Bratman, and G. G. Denisov, "Theory and simulations of a gyrotron backward wave oscillator using a helical interaction waveguide," *Appl. Phys. Lett.*, vol. 89, no. 9, p. 091 504, Sep. 2006.
- [29] S. Humphries, *Charged Particle Beams*. New York: Wiley, 1990.



Craig R. Donaldson received the B.Sc.(Hons.) degree in physics and the M.Sc. degree in high power RF from the University of Strathclyde, Glasgow, U.K., in 2005 and 2006, respectively, where he is currently working toward the Ph.D. degree in physics in the Department of Physics.

He is also currently with SUPA, University of Strathclyde. His main research interests include electron-beam generation, gyro-TWT/BWOs, and helically corrugated waveguides.



Kevin Ronald was born in Glasgow, U.K. He received the B.Sc.(Hons.) and Ph.D. degrees in physics from the University of Strathclyde, Glasgow, in 1992 and 1997, respectively.

He is currently a Lecturer with the Department of Physics, University of Strathclyde, where he is also with SUPA.



Wenlong He received the B.Sc. degree in physics from Suzhou University, Jiangsu, China, in 1983, the M.Sc. degree in accelerator physics from the China Academy of Engineering Physics, Chengdu, China, in 1988, and the Ph.D. degree in relativistic electron beams and masers from the Department of Physics, University of Strathclyde, Glasgow, U.K., in 1995.

He is currently a Senior Research Fellow with the Department of Physics, University of Strathclyde, where he is also with SUPA. His main research interests include relativistic electron beams, CARMs, FELs, gyro-TWT/BWOs, and other high-power microwave devices.



Craig W. Robertson was born in Ayrshire, U.K., in 1977. He received the B.Sc.(Hons.) degree in physics and the Ph.D. degree from the University of Strathclyde, Glasgow, U.K., in 1999 and 2004, respectively.

He is currently with SUPA, Department of Physics, University of Strathclyde. His interests include low-temperature plasma production and diagnostics, as well as high-power microwave sources.



Adrian W. Cross received the B.Sc.(Hons.) degree in physics and the Ph.D. degree from the University of Strathclyde, Glasgow, U.K., in 1989 and 1993, respectively.

He joined the ABP Group, University of Strathclyde, initially as a Research Fellow in 1993 and then as a Lecturer in 2000, where he is currently a Reader with the Department of Physics and also with SUPA. He has been involved in various aspects of research on gyrotrons, cyclotron autoresonance masers, free-electron lasers, superradiant sources, and plasma applications. More recently, he has primarily been concerned with research on radiation sources for use in accelerators and pseudospark physics.



Colin G. Whyte was born in Selkirk, U.K., in 1969. He received the B.Sc. degree in physics from the University of Glasgow, Glasgow, U.K., in 1991 and the M.Sc. degree in laser physics and pulsed-power technology and the Ph.D. degree in physics from the University of St Andrews, St Andrews, U.K., in 1992 and 1996, respectively.

He has been with the University of Strathclyde, Glasgow, since 1996 in the ABP Group, Department of Physics, where he is also currently with SUPA. His research interests include the design and experimental investigation of high-power broadband microwave amplifiers and oscillators, including novel helical gyro-TWT devices and reverse-guide-field free-electron lasers. He also designs and builds high-voltage pulsed-power supplies.



Alan D. R. Phelps was born in 1944 in the U.K. He received the B.A.(Hons.) degree in physics and the M.A. degree from Cambridge University, Cambridge, U.K., in 1966 and 1970, respectively, and the Dr.Phil. degree in plasma research from Oxford University, Oxford, U.K., in 1970.

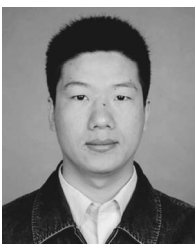
He founded a research group at the University of Strathclyde, Glasgow, U.K., in 1978, where he became a Full Professor in 1993. He is currently with the Department of Physics, University of Strathclyde, where he was the Head from 1998 to 2001, and also with SUPA. His research interests include high-power free-electron radiation sources and plasmas.

Prof. Phelps is a fellow of the Institute of Physics and The Royal Society of Edinburgh.



Alan R. Young received the B.Sc. degree in physics, the M.Sc. degree in information technologies systems, and the Ph.D. degree, with a dissertation on high-quality electron beams for CARMs, from the University of Strathclyde, Glasgow, U.K., in 1993, 1994, and 1998, respectively.

He has since continued to work as a Research Fellow with the Department of Physics, University of Strathclyde, on a variety of gyro-devices, including CARM and gyro-TWT, where he is also currently with SUPA.



Fengping Li received the B.Sc. degree in applied physics from the University of Science and Technology of China, Hefei, China, in 2001 and the M.Sc. degree in accelerator physics from the China Academy of Engineering Physics, Chengdu, China, in 2004. He is currently working toward the Ph.D. degree in relativistic electron beams in the Department of Physics, University of Strathclyde, Glasgow, U.K.

He was awarded a SUPA prize studentship in 2006 and is with SUPA, Department of Physics. His main research interests include pulsed-power technology, X-ray diagnostics, lasers, plasma science, electron-beam generation and gyro-TWT/BWOs.



Liang Zhang received the B.Sc. degree in applied physics from the University of Science and Technology of China, Hefei, China, in 2004 and the M.Sc. degree in application of nuclear techniques from the China Academy of Engineering Physics, Chengdu, China, in 2007. He is currently working toward the Ph.D. degree in relativistic electron beams in the Department of Physics, University of Strathclyde, Glasgow, U.K.

He was awarded a SUPA prize studentship in 2007 and is with SUPA, Department of Physics, University of Strathclyde. His main research interests include pulsed-power technology, electron-beam generation, and gyro-TWT/BWOs.